The Performance of Fully Grouted Rock Bolts Subjected to Combined Pull and Shear Loads Under Constant Normal Stiffness Condition

A Thesis submitted for the Degree of Doctor of Philosophy

School of Civil, Environmental and Mining Engineering, the University of Adelaide

by

Mahdi Saadat

August 2019

Abstract

The Performance of Fully Grouted Rock Bolts Subjected to Combined Pull and Shear Loads Under Constant Normal Stiffness Condition

A Thesis Submitted for the Degree of Doctor of Philosophy

Mahdi Saadat

School of Civil, Environmental and Mining Engineering

The University of Adelaide, August 2019

The natural discontinuities in rock masses, which form unstable rock blocks, have a profound impact on the stability and safety of mining structures. The most commonly used means of rock block reinforcement in the field is fully grouted rock bolt because of its high tension capacity and its efficient anchoring. Rock bolting system forms a self-supporting structure in rock mass through reinforcing loosened rock blocks, improving shear strength of rock joints. According to field observations the failure of rock bolts occurs due to a combination of both pull-out and shear forces. Thus, understanding the failure mechanism of bolted rock joint under such a mixing loading condition is essential for rock support system design. The surface roughness characteristics, Constant Normal Load (CNL) and Constant Normal Stiffness (CNS) conditions, and the presence of infill material within rock joint can significantly influence its shear strength. Moreover, the mechanical and failure behaviour of rock as a heterogeneous material is controlled by various microstructural parameters, such as grain shape and size, type of minerals, and the existence of pre-existing flaws. Any damage due to the mine roof fall (e.g. rock block collapse in roadways and tunnels) or the failure of rock in open pit slopes can hinder mining activities, and results in penalties being imposed on mining companies. Therefore, an appropriate evaluation of rock block instability and response of rock bolting system is critical when designing both surface and underground mining structures.

Recent developments in computational mechanics and distinct element numerical method (DEM) enable more efficient and faster design of mining structures. However, a

promising DEM framework requires a robust and rigorous contact constitutive model, which is capable of mimicking the failure and mechanical response of material at microscopic scale. The key aspect of DEM contact model is its contact force-displacement law, which is responsible for capturing the essential macroscopic features of material failure and deformation. For rock joints reinforced with fully grouted rock bolts, these macroscopic features include brittle or softening behaviour of rock and grout, the cohesive or non-cohesive behaviour of infill material during shearing, and the failure of bolt-grout interface due to tension load. In the case of polycrystalline rock (e.g. granite), the inter- and intra-granular micro-cracking behaviour should also be taken into considerations.

The focus of this study is on development of a DEM-based cohesive contact model for simulating the failure behaviour of rock, cohesive infill material (e.g. clay), grout, and bolt-grout interface. The proposed DEM-based cohesive model couples damage mechanics and plasticity theory in both modes I and II, and features an exponential decay damage function that considers the influence of both normal and shear stresses in reproducing a gradual, post-peak softening response in DEM contacts. Unlike conventional contact models such as Parallel Bond Model (PBM), flat-joint model (FJM), and smooth joint model (SJM), which feature no gradual degradation of contact strength after yield point, the cohesive softening behaviour incorporated in the new contact model inhibits the abrupt contact failure that enhances the macroscopic softening response of the DEM model. The proposed contact model is implemented in DEM code (PFC2D) to develop a cohesive DEM framework. A Stepwise Pull-Shear Test (SPST) scheme is developed to investigate the influence of pretension load, rib angle, and CNS boundary condition on the ultimate shear resistance of rock joints. The SPST approach allows simulation of bolted rock joints subjected to a combined pull-shear load, which is more realistic compared to previous shear testings that neglect the impact of simultaneous pull-out and shear loads. The proposed cohesive contact model is also incorporated into a Grain Based Model (GBM) to develop a cohesive GBM framework for simulating the micro-cracking behaviour of polycrystalline rocks.

The numerical validations against a range of laboratory tests demonstrate that the proposed cohesive DEM and GBM frameworks are effective in reproducing the mechanical and failure behaviour of rock and grout materials as well as bolt-grout interface, the cohesive macroscopic response of clay-infilled rock joints, and micro-cracking behaviour of granitic rocks. The proposed modelling method, in conjunction with the SPST scheme, provided an efficient and inexpensive numerical framework that can be used by designers and geotechnical engineers for

carrying out realistic experiments (i.e., combined pull–shear loads). Doing so will give them new insights into the mechanical performance of fully grouted rock bolts and failure behaviour of rock mass.

Declaration

I, Mahdi Saadat, certify that this work contains no material which has been accepted for the award of any other degree or diploma in my name, in any university or other tertiary institution and, to the best of my knowledge and belief, contains no material previously published or written by another person, except where due reference has been made in the text. In addition, I certify that no part of this work will, in the future, be used in a submission in my name, for any other degree or diploma in any university or other tertiary institution without the prior approval of the University of Adelaide and where applicable, any partner institution responsible for the joint-award of this degree.

I acknowledge that copyright of published works contained within this thesis resides with the copyright holder(s) of those works.

I also give permission for the digital version of my thesis to be made available on the web, via the University's digital research repository, the Library Search and also through web search engines, unless permission has been granted by the University to restrict access for a period of time.

I acknowledge the support I have received for my research through the provision of an Australian Government Research Training Program Scholarship.

August 7th 2019

Mahdi Saadat

Acknowledgements

I would like to express my deep gratitude to my principle supervisor, Dr Abbas Taheri, for being supportive and encouraging of my research pursuits. Abbas willingly offered his time, wit, and erudition during many efficacious discussions. He has an incredible ability to target directly the root of any matter. I am immensely grateful to Associate Professor Giang D. Nguyen, who introduced me to the topic of DEM modelling. Giang is a true professional and great mentor, and engaged me to tackle complex numerical problems that really set fire to my enthusiasm in pursuing this topic. The cohesive model developed in this study was formulated based on a generic framework by Giang and Ha H. Bui (Monash University), with Giang's help in the development and revision of the model.

I would also like to acknowledge Mr. Sacha Emam from Itasca Consulting group (France). As a geomechanics and software engineer, Sacha introduced me to C++ programming and PFC2D FISH script editor, and was instrumental in initiating this research. It was truly a pleasure to be able to interact with someone of such creative talent and technical expertise. Another individual form Itasca Consulting group I would like to recognize is Dr David Potyondy for his clear and perceptive discussions on the simulation of natural rock joints in PFC2D.

I would also like to thank Ms Leticia Mooney for her proofreading of several chapters of this thesis. Her insightful comments and suggestions on my writing-style, and elaboration of the chapters, is also gratefully acknowledged.

I would like to thank all my office mates and friends for many good times in and out of Adelaide University. I would also like to express my respect, gratefulness and love to Zaynab, who has been an immense source of inspiration and infinite hope. And thank you, Ali, for being an awesome Persian-poem-reader friend, whose company induces feelings of well-being.

Finally, I would like to acknowledge my family. For my mom, dad, brother, and sister who have been so loving and supportive. They provided the foundation in my study to make this work possible. An additional thanks to my mom for her unconditional love and faith in me all my life.

List of publications

Saadat M, Taheri A. (2019) Effect of Contributing Parameters on the Behaviour of a Bolted Rock Joint Subjected to Combined Pull-and-Shear Loading: A DEM Approach. *Rock Mechanics and Rock Engineering*. doi: 10.1007/s00603-019-01921-6

Saadat M, Taheri A. (2019) A cohesive discrete element based approach to characterizing the shear behavior of cohesive soil and clay-infilled rock joints. *Computers and Geotechnics 114*: 103109. doi: https://doi.org/10.1016/j.compgeo.2019.103109

Saadat M, Taheri A. (2019) Modelling Micro-cracking Behaviour of Pre-cracked Granite Using Grain-Based Distinct Element Model. *Rock Mechanics and Rock Engineering*. doi: 10.1007/s00603-019-01862-0

Saadat M, Taheri A. (2019) A numerical approach to investigate the effects of rock texture on the damage and crack propagation of a pre-cracked granite. *Computers and Geotechnics 111*: 89-111. doi: https://doi.org/10.1016/j.compgeo.2019.03.009

Saadat M, Taheri A. (2019) A cohesive grain based model to simulate shear behaviour of rock joints with asperity damage in polycrystalline rock. *Computers and Geotechnics (Under Review)*

Contents

List of Figures

List of tables

List of acronyms

CCM	Cohesive Contact Model
CNL	Constant Normal Load
CNS	Constant Normal Stiffness
CSJM	Cohesive Smooth Joint Model
DEM	Distinct Element Method
DLL	Dynamic Link Library
GBM	Grain Based Model
ISRM	International Society for Rock Mechanics
JRC	Joint Roughness Coefficient
PBM	Parallel Bond Model
PFC	Particle Flow Code
SJM	Smooth Joint Model
SPST	Stepwise Pull-and-Shear Test

List of symbols

All symbols related to numerical modelling are defined where they first appear in the text. For convenience, they are also listed in the followings:

$\boldsymbol{u}$	Relative displacement
$\boldsymbol{u}^e$	Relative elastic displacement
$\boldsymbol{u}^p$	Relative plastic displacement
σ_n	Contact normal stress
σ_s	Contact shear stress
k_n^0	Contact normal stiffness
k_s^0	Contact shear stiffness
u_n^p	Total normal plastic displacement
u_s^p	Total shear plastic displacement
F	Yield function
C	Cohesion of contact
C^0	Initial cohesion of contact
μ	Friction coefficient of contact
κ	Softening parameter
u^p	Accumulated plastic displacement of contact
D	Damage parameter
G	Plastic potential

β	Dilation coefficient of contact
$d\lambda$	Plastic multiplier
σ_n^{trial}	Trial normal stress of contact
σ_s^{trial}	Trial shear stress of contact
F^{trial}	Trial yield function
$\bar{A}$	Cross-sectional area of contact
$\bar{R}$	Radius of DEM particle
$\bar{E}_c$	Elastic modulus of contact
L	Contact length
k^*	Normal to shear stiffness ratio of contact
υ	Poisson's ratio
r_{max}	Maximum radius of DEM particle
r_{min}	Minimum radius of DEM particle
α	Rib angle
$\bar{E}_{c,CCM}$	CCM elastic modulus
C_{CCM}^0	CCM initial cohesion
μ_{CCM}	CCM friction coefficient
β_{CCM}	CCM dilation coefficient
k_{CCM}^*	CCM normal to shear stiffness ratio

κ_{CCM}	CCM softening parameter
D_{CCM}	CCM damage parameter
k_n^{sj}	Normal stiffness of SJM contact
k_s^{sj}	Shear stiffness of SJM contact
μ^{sj}	Friction coefficient of SJM contact
$k_{s,CSJM}^0$	CSJM shear stiffness
$k_{n,CSJM}^0$	CSJM normal stiffness
C_{CSJM}^0	CSJM initial cohesion
μ_{CSJM}	CSJM friction coefficient
β_{CSJM}	CSJM dilation coefficient
κ_{CSJM}	CSJM softening parameter
D_{CCM}	CSJM damage parameter
λ^{RJ}	Wavelength of idealized rock joint
σ_n^0	Applied normal stress in CNL direct shear test
σ_c	Rock compressive strength
σ_n^i	Induced normal stress on rock joint interface
$d\sigma_n$	Change in the normal stress during CNS direct shear test
k^{cns}	CNS stiffness
$d\delta_n$	Change in the normal displacement of rock joint

σ_n^u Updated normal stress in CNS direct shear test

σ_n^{total} Applied normal stress in pull-and-shear test

Chapter 1: Introduction

1.1 Problem statement

Rocks in mining structures, e.g. open pits, roadways, and tunnels, are inhomogeneous and commonly contain discontinuities such as joints, fractures, and defects. The natural discontinuities in rock mass have a profound impact on the stability and safety of underground mining excavations. Moreover, the microstructural properties of rock mass (e.g. grain size, mineral content, pre-existing fractures and etc.) have significant influence on its mechanical and fracture behaviour. Any damage due to roof fall or rock slopes failure can hinder mining activities and impose penalties to mining companies. Therefore, sufficient knowledge about the geometrical parameters of rock joints (e.g. surface roughness, filling etc.) is necessary for the process of cost-effective, reliable design of mining structures (Harrison and Hudson 1977). Hence, this thesis deals with the mechanical and failure behaviour of bolted rock joint, infilled rock joint, and polycrystalline rock.

The concept of rock joint shear behaviour and stability of rock blocks in underground mining is depicted in Figure 1.1. This figure illustrates the characterisation of discontinuities at both field and laboratory scales. Figure 1.1a depicts a tunnel (e.g. roadway in an underground mine) reinforced by fully grouted rock bolts. The role of rock bolts is to improve the shear resistance of unstable rock blocks surrounding the tunnel. In order to characterise the shear failure of bolted rock joints, the direct shear test can be conducted at a laboratory scale (Figure 1.1b). It can be seen that the field scale conditions (i.e. combined pull-shear load, and CNS condition) can be achieved in the laboratory environment. Figure 1.1c illustrates a distinct element model (DEM) of the infilled rock joint. This laboratory scale testing can enhance our understanding of the influence of infill material on the shear behaviour of rock joint. Figure 1.1d shows a grain based DEM model including a natural rock joint profile. In such modelling scheme, the microstructural characteristics of the rock should be incorporated in the model to explicitly characterise rock joint asperity damage (i.e. grain crushing) at the grain scale.

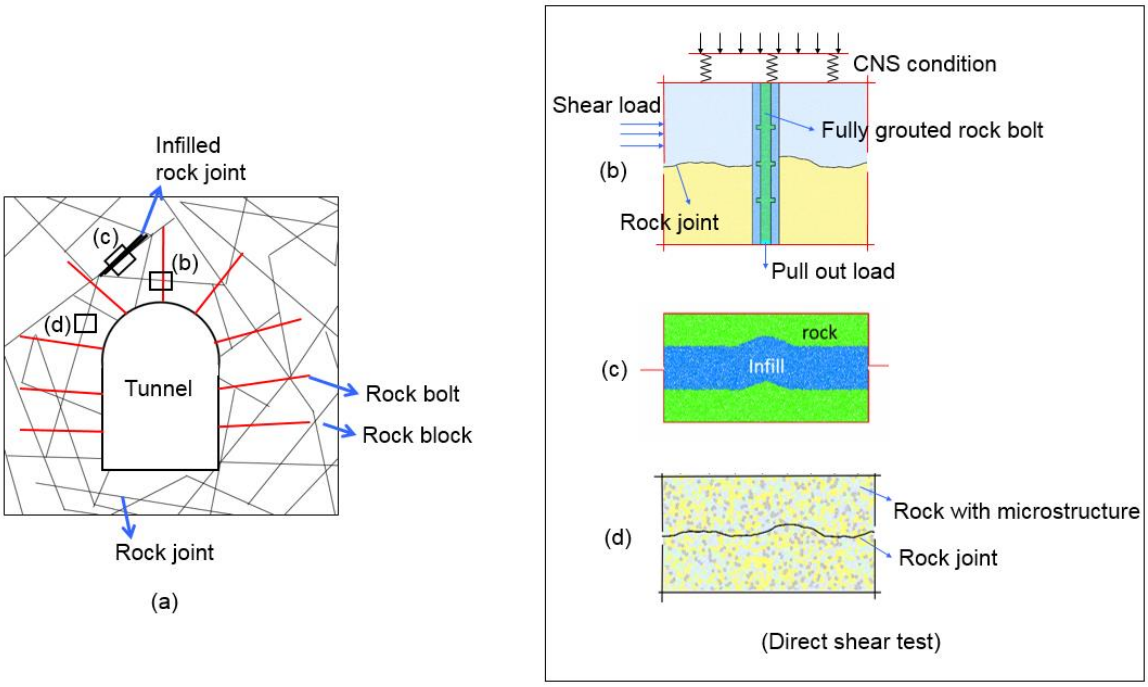

Figure 1.1 The characterisation of rock discontinuities at field and laboratory scale. (a) An underground mining excavation reinforced with rock bolts. (b) Direct shear test of bolted rock joint subjected to combined pull-shear load. (c) Direct shear test of infilled rock joint with idealized saw-tooth asperity. (d) Direct shear test of jointed crystalline rock (the minerals are depicted in different colours).

1.1.1 Bolted rock joint

In the mining industry, reinforcement measures are taken to control the rock mass deformability and ensure the stability and safety of the mining structures. Fully grouted rock bolt has been widely used as a reinforcement element in underground mining due to its economic benefits and advancement in the bolt system technology (He et al. 2018; Huang et al. 2002; Jin-feng and Peng-hao 2019). The fully grouted rock bolt also fully utilises the bolt strength (He et al. 2018). Rock bolting system forms a self-supporting structure in rock mass through supporting loosened rock blocks, improving shear resistance of rock joints (He et al. 2018; Ma et al. 2017), and restraining rock mass deformation (Chen and Li 2015b). The load transfer capacity of fully grouted rock bolts is largely controlled by the shear strength of the bolt-grout interface and the mechanical interlocking between the grout and the rock bolt ribs (Cao et al. 2014; Li et al. 2019a; Ma et al. 2017; Shang et al. 2018a). Pull-out testing is commonly used to study the load transfer mechanism of fully grouted rock bolt (Jin-feng and Peng-hao 2019). However, in field conditions, the failure of rock bolts occurs due to a combination of both pull-out and shear forces (Li et al. 2016c). Therefore, understanding the

failure mechanism of bolted rock joint under such a mixing loading condition is useful for rock support system design (Chen and Li 2015b; Li 2010).

The behaviour of a bolted rock joint is depicted in Figure 1.2. Several parameters can influence the mechanical behaviour of bolted rock joints (Figure 1.2). These include boundary conditions imposed by the surrounding rock block, the rib angle of the rebar bolt, the surface roughness of the rock joint, the confining pressure applied on the rock joint profile, the presence of infill material inside the rock joint, and so on.

In conventional laboratory investigations, the mechanical behaviour of rock joints is usually investigated under a constant normal load/stress (CNL) boundary condition where the applied normal stress on the rock joint profile is constant. However, in underground mining, the unstable rock block is restricted by neighbouring rock blocks; the applied normal stress is not constant, and the analysis of the rock joint requires a constant normal stiffness (CNS) condition (Bewick et al. 2014b; Indraranta et al. 2005; Indraratna and Welideniya 2003; Shang et al. 2018b; Thirukumaran and Indraratna 2016; Thirukumaran et al. 2016).

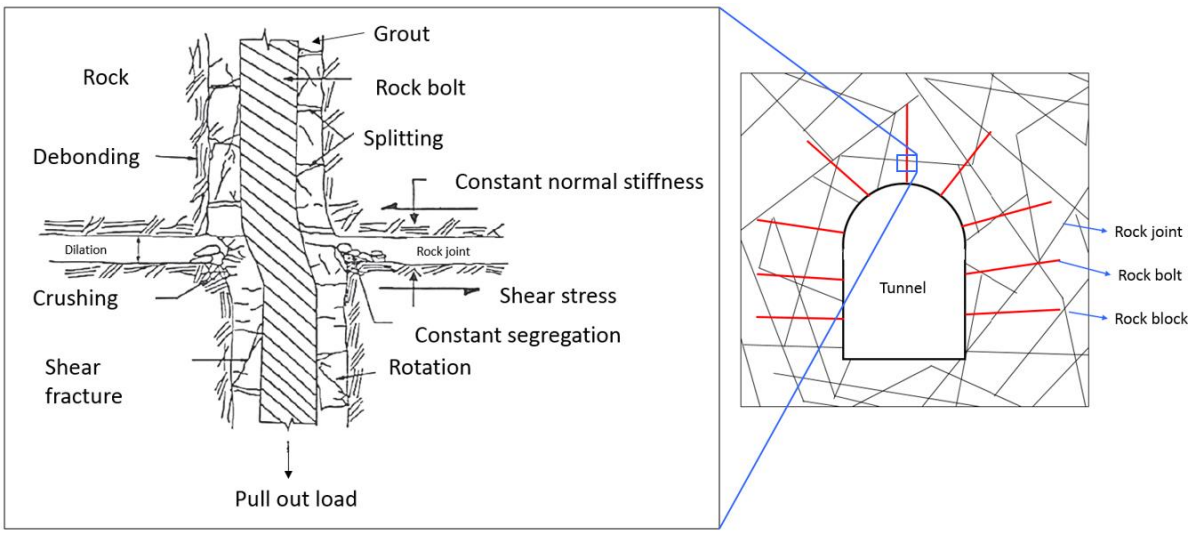

Figure 1.2 The mechanical behaviour of bolted rock joint subjected to a combined pull-shear load (inspired after Indraratna and Haque (2000))

1.1.2 Infilled rock joint

The presence of infill material within a joint can significantly influence its shear strength. Infill thickness and asperity angle are the most important parameters controlling the shear behaviour of infilled rock joints (Indraranta et al. 1999; Mylvaganam 2007; Oliveira et al. 2009). The characterisation and prediction of the shear mechanism of infilled rock joints is a significant problem in rock engineering projects. For instance, Indraratna et al. (2010a) reported that using

an oversimplified constitutive model in the design process, which neglected the role of infill material, could have contributed to the collapse of São Paulo metro station. Thus, improving the understanding of the shear behaviour of infilled rock joints for better prediction of failure is crucial to practical applications in mining and geotechnical engineering.

1.1.3 Polycrystalline rock

Apart from rock joints, other factors such as microstructural properties of grains (i.e. shape and size), mineral composition, pre-existing defects, cavities can also control the mechanical and damage response of rock. The laboratory observations of Meng et al. (2018) showed that in polycrystalline rock, the development of inter- and intra-grain micro-cracks contributed to the asperity damage of rock joint profiles. They also concluded that there would be a possible correlation between surface roughness and grain size. It is, therefore, necessary to assess the influence of mineral composition on the mechanism of asperity damage.

The multiscale heterogeneity and presence of discontinuities make the realistic characterisation of rock fracture and damage behaviour difficult (Zhang et al. 2019). Figure 1.3 illustrates multiscale characterisation of mining engineering projects. In mining structures (e.g. the open pit iron mine shown in Figure 1.3a), rock mass stability is profoundly affected by the propagation and coalescence of macroscopic cracks initiating from the pre-existing flaws, on various rock mass scales. The macroscopic cracking process is the dominant damage mechanism controlling the mechanical behaviour and the integrity of brittle rocks (Morgan et al. 2013). It is well documented in the literature that the macroscopic fracture behaviour is attributed to complicated micro-cracking mechanism (Hajiabdolmajid and Kaiser 2003), thus a reliable knowledge about the microstructural properties of rock is crucial in the design procedure of mining structures. The numerical study of Farahmand et al. (2018) showed that in large scale jointed specimens (with 10m height) the dominant failure mechanism is the coalescence between rock joints (Figure 1.3b). The experimental observations of Moradian et al. (2016) showed that, for laboratory scale specimens of pre-cracked Barre granite, the coalescence of pre-existing cracks is due to the extension of macroscopic fractures (Figure 1.3c), which are the results of coalescence of inter- and intra-grain micro-cracks at microscopic scale (Figure 1.3d). Figure 1.3 indicates that the microstructure of polycrystalline rock needs to be taken into account to link the damage initiation and evolution of grain microstructure (e.g. micro-cracking response of grain boundaries, grain crushing, and etc.) to macroscopic failure behaviour.

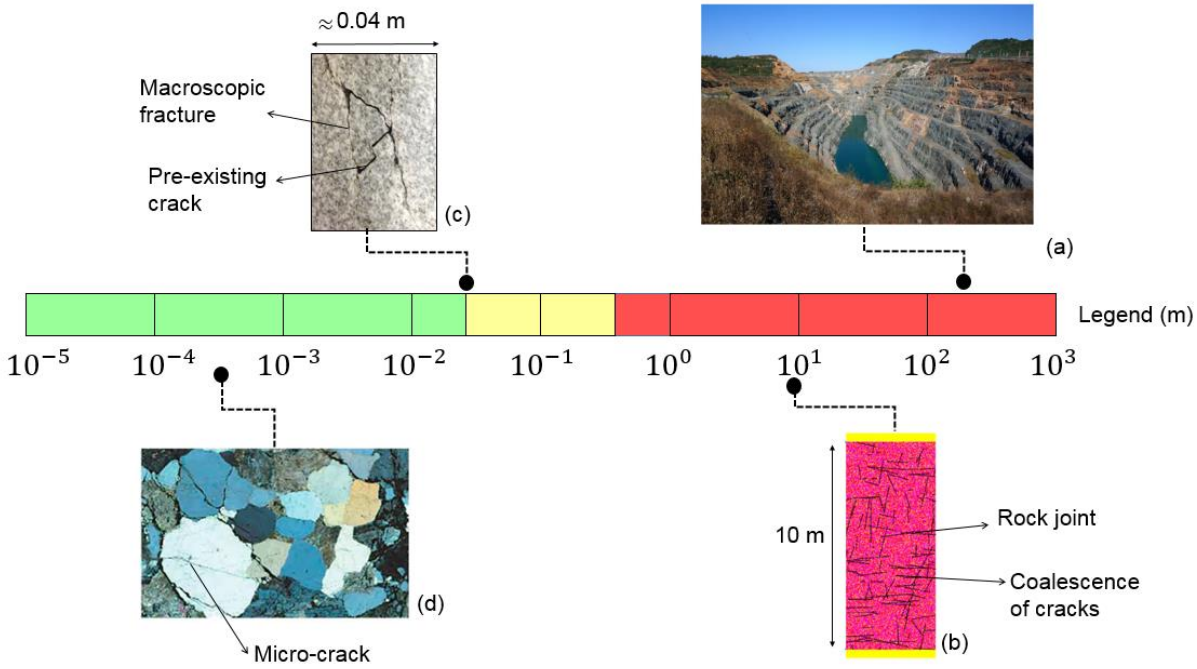

Figure 1.3 The rock mass characterisation at multiscale (inspired by Zhang et al. (2019)). (a) An open pit iron mine in China (Chen et al. 2015). (b) A numerical specimen including multiple joint sets (Farahmand et al. 2018). (c) The evolution of macroscopic fractures around pre-existing cracks in Barre granite (Moradian et al. 2016). (d) The distribution of micro-cracks at the grain scale (Zhang et al. 2019).

1.2 Research objectives

Figure 1.4 illustrates the aims and objectives of the present thesis. According to the problem statements which were briefly described in Section 1.2, the following research objectives are summarised for this PhD thesis:

1- To simulate the fracture behaviour of different materials (e.g. rock, grout, and mineral) and shear/tensile failure of various interfaces (e.g. bolt grout interface and grain boundary interface). To achieve this aim, the development of a DEM based cohesive model is required that can mimic the behaviour of DEM contacts in mode I (pure tension), II (pure shear), and mixed (combined tension and shear) mode.

2- To investigate the influence of pre-tension stress magnitude on the peak shear strength of bolted rock joints, and identify the optimum pre-tension stress at which the bolted rock joint demonstrates its ultimate shear performance. To achieve this aim, a novel stepwise pull-and-shear test (SPST) scheme is required to systematically analyse the effect of pre-tension stress magnitudes on the shear behaviour of bolted rock joints.

3- To study the influence of CNS boundary condition on the overall shear performance of bolted rock joint subjected to combined pull-shear load.
4- To understand the influence of bolt rib angle on the pre-tension behaviour of rock bolt.
5- To identify the optimum pre-tension stress magnitudes for various rib angles.
6- To investigate the potential of the DEM approach in reproducing the shear behaviour of infilled rock joints. To achieve this aim, a cohesive contact model is required.
7- To investigate the effect of inter- and intra-grain micro-cracking on the asperity damage response of rock joints with various surface roughness. To achieve this aim, development of a cohesive grain based model in DEM framework is required.
8- To study the influence of CNS condition on the micro-cracking response of polycrystalline rocks.
9- To investigate the potential of grain-based modelling in reproducing the macroscopic fracture and mechanical response of pre-cracked polycrystalline rock.
10- To investigate the influence of rock texture (i.e. grain size) on the damage and mechanical behaviour of pre-cracked polycrystalline rock. To achieve this aim, the generation of three different scenarios with various grain sizes is required.

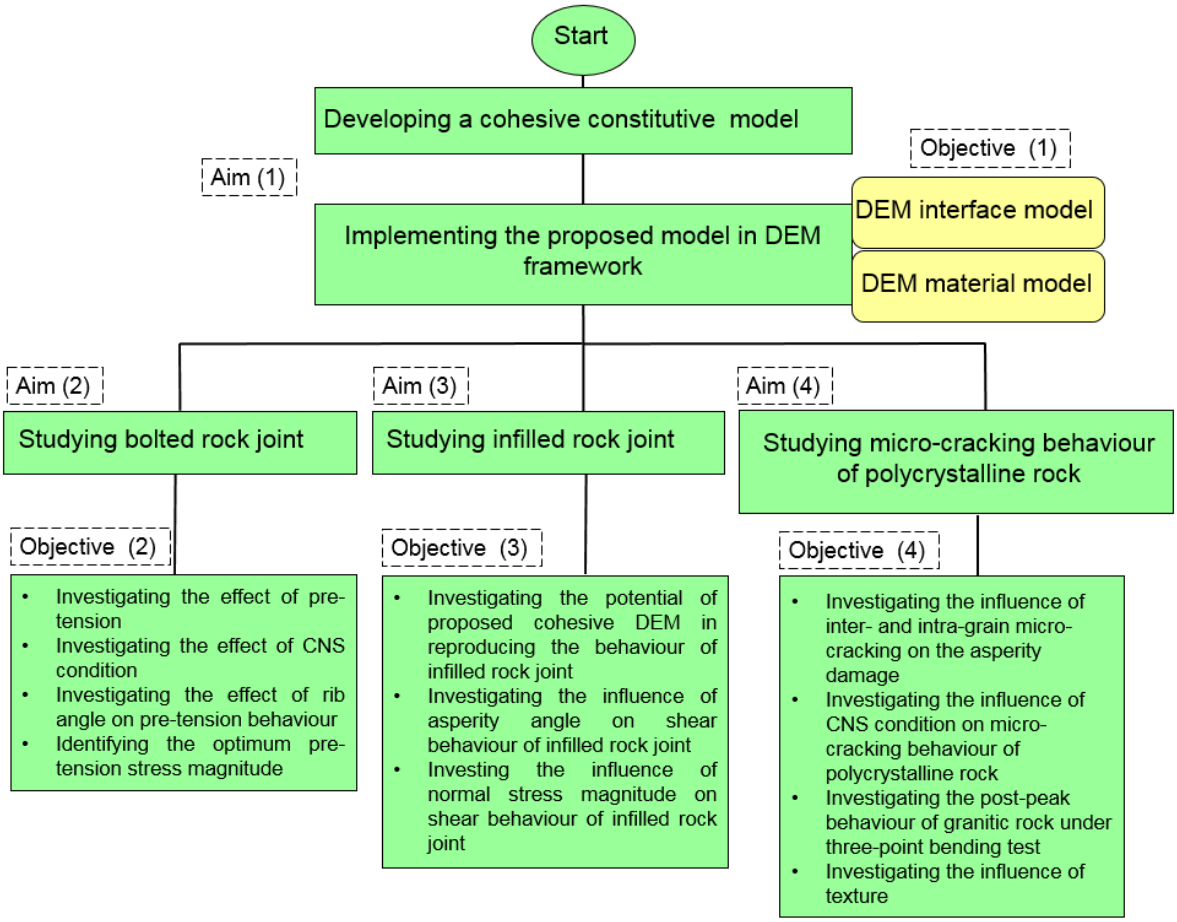

Figure 1.4 The aims and objectives of the present theses

1.3 Methodology

Although laboratory testing is the most common approach for rock failure investigation, setting up laboratory test (e.g. combined pull-shear test) take a considerable amount of resources. Alternatively, numerical tools have been widely applied to model the failure behaviour of rocks. Therefore, in this PhD thesis, numerical simulation has been selected as the research methodology.

The numerical developments related to shear behaviour of fully grouted rock bolt are not extensive. Most of the research studies have been performed by employing continuum models, which are basically incapable of simulating cracks explicitly. To overcome this shortcoming, discontinuum models were developed. The main advantage of discontinuum models is that they make it possible to explicitly demonstrate the fracture initiation and distribution over a particular computational time by monitoring consecutive bond-breakage of distinct elements.

As a discontinuum model, Discrete Element Method (DEM) (Cundall and Strack 1979) have been promising in terms of mimicking the failure behaviour of brittle rocks (Potyondy and Cundall 2004).

In this study, the commercial DEM code, Particle Flow Code (PFC2D) (Itasca 2016), is chosen as numerical tool. The particle assembly in PFC2D consists of random distribution of DEM particles with respect to the size and location of particles. In DEM simulations, the constitutive contact model and associated microproperties dictate the type of macroscopic response the model will exhibit upon failure (e.g. crack initiation due to compressive loading). Therefore, it is crucial to adopt an appropriate contact model to achieve a reliable numerical outcome. In this PhD thesis, a cohesive contact model was developed to firstly overcome the shortcomings of conventional material contact models (e.g. parallel bond, flat-joint, etc.) and secondly to enhance the modelling performance of the current interface contact model (e.g. the smooth joint model) (objective 1, Figure 1.4). The proposed model (Chapter 3) then was used to cover all the expected objectives described in Figure 1.4. The numerical methodologies designed to fulfil the objectives are described as follows:

1- A novel technique called stepwise pull-and-shear test (SPST) scheme was introduced to study the effect of pre-tension stress magnitude on the shear resistance of bolted rock joint. The capability of the cohesive model in reproducing the gradual softening response of bolt-grout interface and post-peak weakening behaviour of grout material was examined. The influence of the rib angle and CNS condition was numerically investigated (Chapter 4).

2- A series of numerical direct shear tests were generated to observe the ability of the cohesive model in mimicking the shear behaviour of clay-infilled rock joint. The influence of infill thickness to asperity height was studied (Chapter 5).

3- A cohesive grain-based model (GBM) was introduced to investigate the effect of surface roughness and CNS condition on the asperity damage mechanism of polycrystalline rock (Chapter 6).

4- The GBM framework was employed to reproduce the physical fracture and mechanical behaviour of pre-cracked granite. The influence of flaw inclination angle on the macroscopic fracture response was investigated (Chapter 7).

5- The GBM framework was employed to investigate the influence of rock texture on the damage and crack propagation of pre-cracked polycrystalline rock (Chapter 8).

1.4 Thesis structure

The thesis comprises of nine chapters. The key content of each chapter is briefly described as follows:

The first chapter (introduction) presents the research background, problem statement, and the key objective of the current PhD thesis.

Chapter 2 (Literature review) first provides a review of the field observations and the importance of CNS boundary condition in rock bolt studies. This is followed by the available experimental and numerical methods for characterisation of the shear performance of bolted rock joints. A review of laboratory, empirical, and numerical studies on clean and infilled rock joints is presented in the following section. Then, the existing GBM studies were reviewed, and the importance of developing a cohesive GBM framework is highlighted.

Chapter 3 (Discrete element based cohesive model) explains the principles of DEM approach specifically the concept of particle motion and interaction. Following this the formulation of the proposed cohesive model is provided. The stress return algorithm used to implement the model in PFC2D is explained in this chapter.

Chapter 4 (The performance of fully grouted rock bolts subjected to pull-shear load under CNS condition) introduces the DEM-based combined pull-shear load test on bolted rock joint. The DEM-based cohesive model was calibrated against standard experimental tests to identify the microproperties of rock, grout, and bolt-grout interface. A novel technique called stepwise pull-and-shear test (SPST) scheme was introduced to study the effect of pre-tension stress magnitude on the shear resistance of bolted rock joint. Both CNL and CNS direct shear tests were carried out to study the shear performance of bolted rock joints. In CNL tests, the influence of rib angle on pre-tension response was investigated. In each numerical test, the SPST scheme was employed to identify the optimum pre-tension stress magnitude at which the ultimate performance of bolting system was achieved.

Chapter 5 (DEM simulation of infilled rock joint) investigates the ability of the proposed cohesive model in reproducing the shear mechanism of infilled rock joints by a comparative study against the laboratory tests. A series of experimental CNL direct shear tests were undertaken to observe the shear behaviour of infilled rock joints. Idealised asperities were

generated to represent the surface roughness of rock joint, and kaolin was used as cohesive infill material. To assess the ability of the proposed cohesive model in reproducing the shear behaviour of clay-infilled rock joint, the numerical counterpart of the laboratory specimens were built in PFC2D. The microproperties of the numerical model was calibrated against the laboratory data. The influence of initial normal stress magnitude, asperity angle, and infill thickness on overall shear behaviour of infilled rock joints were investigated.

Chapter 6 (GBM simulation of jointed polycrystalline rock under CNL and CNS condition) presents the ability of the proposed cohesive GBM framework in reproducing the fracture behaviour of polycrystalline rock by a comparative study against the experimental observations. The calibrated model then was employed to investigate the influence of CNS condition and surface roughness on asperity damage mechanism of clean rock joints. The effect of grain crushing, which is the consequence of consecutive coalescence of inter- and intra-grain micro-cracks, on the shear mechanism of rock joints with natural roughness profiles is investigated. In particular, the shear strength and dilation of rock joints are examined. Finally, the process of asperity damage under CNS condition is presented.

Chapter 7 (GBM simulation of pre-cracked Barre granite) investigates the ability of the proposed GBM framework in reproducing the macroscopic fracture and mechanical behaviour of pre-cracked Barre granite. The experimental results of uniaxial compression and Brazilian tensile tests are used to calibrate the GBM. The calibrated GBM then is used to reproduce the initiation and distribution of macroscopic tensile fractures in pre-cracked specimens. A comparison is made between numerical fracture pattern and laboratory counterparts to ensure the reliability of numerical outcomes. Finally, the influence of random generation of grain distribution on the fracture pattern strength response is investigated.

Chapter 8 (Effect of mineral size on failure behaviour of pre-cracked Aue granite) investigates the effect of rock texture on damage and crack propagation of pre-cracked Aue granite. The proposed GBM approach is calibrated against the experimental data. Then, three different GBMs with fine, medium, and coarse grain size are generated. The calibrated model is used to investigate the effect of grain size on the fracture pattern distribution and macroscopic strength of the GBMs. The macroscopic crack distribution in both single- and double-flawed specimens are comprehensively studied.

Chapter 2: Literature review

2.1 Introduction

This comprehensive literature review allowed us to identify the possible gaps in the previous research, and come up with a clear plan to shed more light onto the hidden mechanisms of rock mass failure.

2.2 Rock bolt to stabilise rock mass

In the mining industry, rock bolting has been of interest to designers and engineers due to its effectiveness and low cost. In both surface and underground mining, rock bolts are an efficient means of reinforcement (Spang and Egger 1990). In mining practice, rock bolt or cable bolts install in a borehole that is drilled into the surrounding underground mining structure. The main function of rock bolting in the jointed rock mass is to augment the shear resistance of the rock joint surface and maximize the normal stress acting on the rock joint. This self-supporting mechanism significantly improves the integrity of jointed rock mass and allows effective arching and suspension of unstable rock blocks while the key blocks (Goodman 1995) remain connected together without unravelling (Li 2016). As unstable blocks move towards the tunnel face, rock bolt elongation may occur (Bobet and Einstein 2011). This elongation induces a tension force in the bolt surface, which is transferred to the surrounding rock mass as compression (He et al. 2015). Apart from tension forces, in bolted rock joints, shearing along the joint surface could be regarded as a major force component contributing to the failure of bolted rock joint (Li et al. 2016a; Li 2016; Srivastava and Singh 2015; Wu et al. 2018b). An extensive filed observations of Li (2010) in cut-and-fill mines revealed that both pull and shear loads contribute to the damage of rock bolts. The most recent experimental investigations of other scientists have also highlighted the importance of shear loading in the analysis of rock bolt performance (Wang et al. 2018; Wu et al. 2018b). Therefore, ignoring the importance of shear force may increase the uncertainty of reinforcement design, especially in areas where the unstable rock blocks have sliding potential.

Many studies have been devoted to the characterisation of pull and shear performance of rock bolts. A review of field observations, as well as experimental and numerical studies, are provided in the following sub-sections.

2.2.1 Field observations

The task of rock bolt in underground mining is to provide resistance for unstable block formed surrounding the excavation. An example of an unstable block reinforced using rock bolt is illustrated in Figure 2.1. According to block theory, the formation of such an unstable block is the consequence of rock excavation through a network of discontinuities (Goodman 1995). When the direction of rock block sliding is parallel to the rock bolt axis, only pull out force induces in the bolting system. However, it is often the case that the displacement direction of the rock block creates an angle with the rock bolt axis, which, in turn, subject the bolting system to a combined pull and shear load. Therefore, the total sliding displacement (δ_{tot}) is decomposed to an axial (δ_p), and shear (δ_s) displacements (Chen and Li 2015b). The tensile force induced along the rock bolt is due to axial displacement, while the shear displacement exert a shear force in the bolting system.

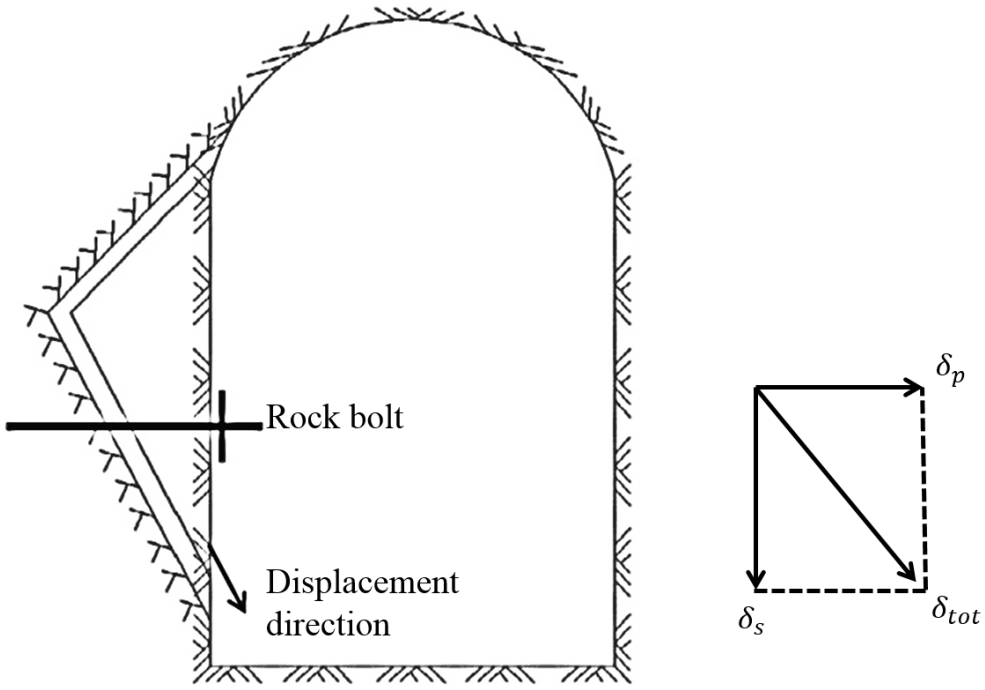

Figure 2.1 A sketch illustrating the loading behaviour of rock bolt due to rock joint displacement (modified from Chen and Li (2015b))

The performance of fully grouted rock bolts can be determined according to rock mass quality, in-situ stress condition, and excavation geometry (Li 2012). Presence of rock joints, in regions near the ground surface, form unstable rock blocks surrounding the underground opening. In low-stress state condition, the rock blocks would tend to collapse due to gravity (Li 2017). The role of rock bolt under such circumstance is to provide rock block stability and prevent any possible damage and catastrophe. Comparatively, in deep underground mines, due to high-

stress state, the quality of rock mass is improved as the number of geological defects is significantly reduced or, if exist, the rock joints are rarely open (Li 2010; Li 2012). Thus, in deep mining, the cause of roof collapse is no longer rock fall, but rather high in-situ stress condition. Therefore, the task of rock bolt at depth is to provide integrity for the rock mass to avoid mining collapse (Li 2017). Figure 2.2 depicts the failure of two rebar bolts in a metal mine in Sweden. This filed observation was carried out by Li (2012), and showed that the rock bolt failure was due to a combined pull and shear load. This failure mechanism is prevalent when the rock bolt crosses the rock joint and resist against the sliding of rock block as well as rockfall towards the excavation face. The sliding behaviour of the rock block depends highly on the geometrical surface configuration of the rock joint.

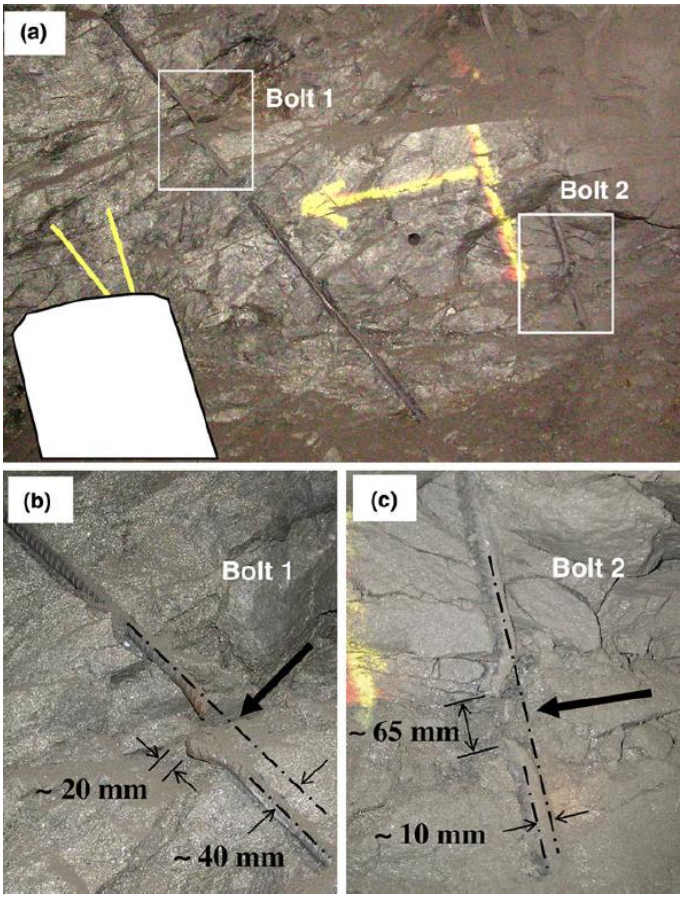

Figure 2.2 The failure of two fully grouted rock bolts in the roof of a mine tunnel (Li 2010). (a) The failure state of rock bolts in the rock mass. (b) The close-up view of Bolt 1. (c) The close-up view of Bolt 2.

2.2.2 Boundary condition in bolted rock joint

The natural discontinuities around orebodies can have a profound impact on the stability and safety of mining excavations. Any damage due to roof fall or rock slopes failure can hinder the mining activities and impose penalties to mining companies. In this regards, an appropriate

evaluation of rock joint shear behaviour is critical when designing the surface and underground mining structures. Conducting direct shear test is a common experimental methodology to evaluate the shear behaviour of rock joints. Constant normal load/stress (CNL) and constant normal stiffness (CNS) conditions are two different types of boundary condition that can be adopted during direct shear testing of rock joints (Indraratna et al. 2015; Park et al. 2013; Shrivastava and Rao 2018). In the slope stability analysis where the unstable rock block is sliding along the surface of discontinuity without any restriction, CNL boundary condition must be adopted. In contrast, in underground mining where the unstable rock block is restricted by neighbouring rock blocks, the applied normal stress is not constant and the analysis of the rock joint requires CNS condition (Bewick et al. 2014b; Indraranta et al. 2005; Indraratna and Welideniya 2003; Shang et al. 2018b; Thirukumaran and Indraratna 2016; Thirukumaran et al. 2016).

In Figure 2.3, the concept of CNL and CNS boundary condition is presented. Different rock stability cases are illustrated in Figure 2.3. A potential translational rockslide could be assumed for Case A. In such condition, the rock blocks could freely slide along the surface of rock joint. In Case B, however, the rock block is reinforced with rock bolt which induces an extra loading on the rock joint surface during shearing. This circumstance is regarded as one of the typical representative of CNS condition. Each rock block on the roof of underground excavations is constrained by its neighbouring rock blocks. The dilative response of the rock joint, which is the interface between two adjoining rock block, increases the normal stress during shearing process (Case 3).

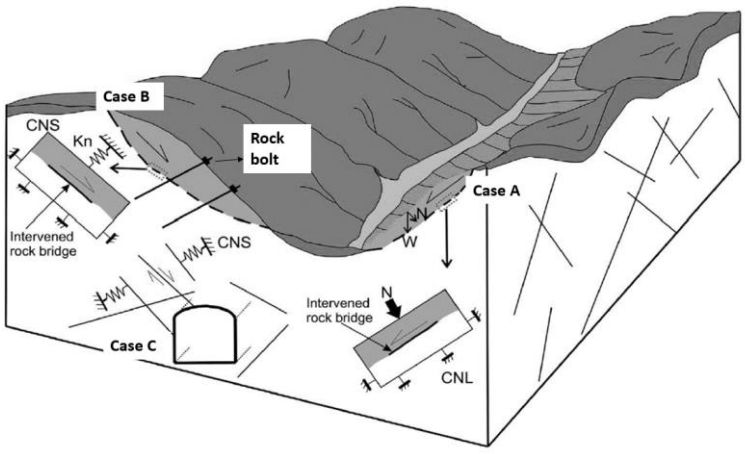

Figure 2.3 A schematic view of CNL and CNS boundary conditions (modified from Shang et al. (2018b))

Conducting laboratory direct shear test is a common technique to study the shear behaviour of rock joints both under CNL and CNS conditions. Under CNS condition the increment of normal stress is expressed as:

$$d\sigma_n = k^{cns} \times d\delta_n \tag{2.1}$$

where k^{cns} is the constant normal stiffness at an external boundary and $d\delta_n$ is the increment of normal displacement (Indraratna et al. 2015). Figure 2.4 illustrates a schematic view of CNS apparatus. In order to achieve CNS condition in the laboratory environment, a series of springs can be installed on the upper shear box to apply the initial normal stress on the specimen. The overall stiffness of the springs represent k^{cns} of rock joints.

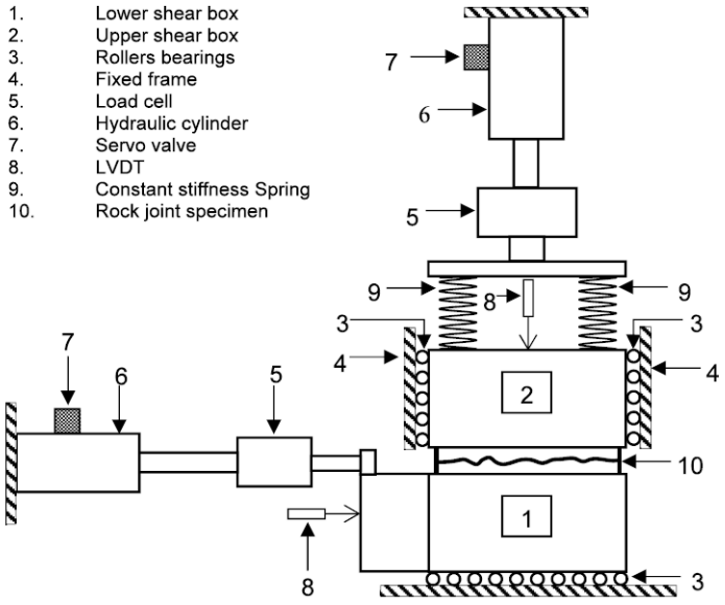

Figure 2.4 CNS direct shear test apparatus (Indraratna et al. 2015)

2.2.3 In-situ measurements

Fully-grouted rock bolts are the most common means of supporting in underground mining. Previous studies showed that in Australia, both stress corrosion cracking and bending contributes to rock bolt fracturing (Crosky et al. 2003). Therefore, filling the hollow space between the rock bolt and rock by grout material can extensively mitigate the corrosion issue (Song et al. 2017). An example of fully grouted rock bolt is shown in Figure 2.5. One of the methodologies that can be used to determine the performance of rock bolts is to carry out in-situ testing.

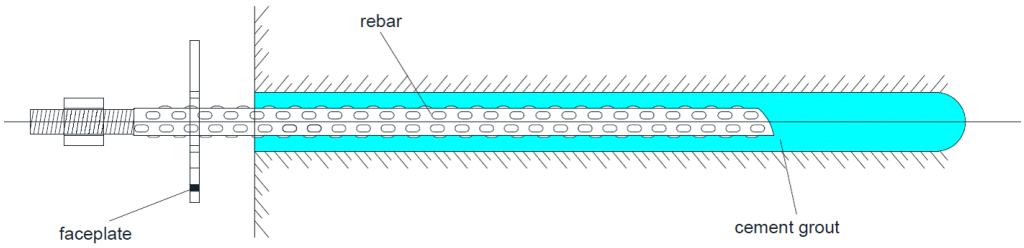

Figure 2.5 Fully grouted rock bolt placed in a borehole (Song et al. 2017)

Despite being complex and highly expensive, in-situ monitoring is an excellent technique for obtaining reliable results. In rock bolting, instrumentation involves strain measurement during loading procedure, which can be later converted into force according to Hooke relationships, or empirical formulas obtained from stress-strain response of bolting system (Li 2016). In Figure 2.6, the monitoring results measured by Li (2012) is illustrated that shows the axial tensile load in a D-bolt installed 1.5 m away from a mine stope. It can be seen that the load distribution is uniform at any section of the bolt, and its magnitude is very low at the proximity of the wall. This monitoring results show that yielding was occurred at the second innermost section of the rock bolt only 3 days after installation. After 15 days, the innermost section of the bolt failed at a stress level equal to 171 kN.

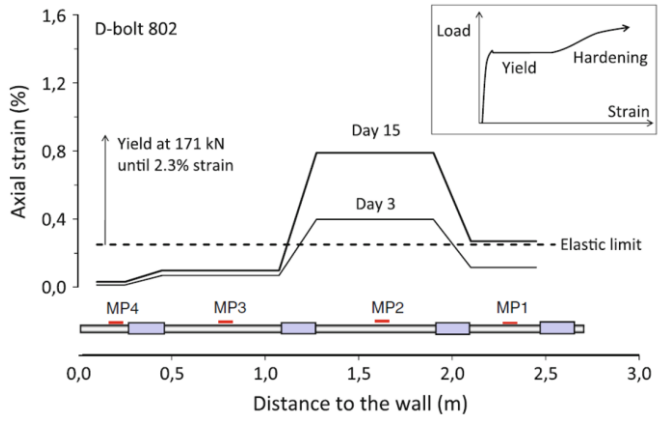

Figure 2.6 The field measurement of two D-bolt in an underground mine (Li 2012)

2.2.4 Experimental methods in rock bolting

Two types of loading can be measured in a bolting system, the axial tensile load, and the shear load. The focus of many studies in the literate has been to investigate either the tensile behaviour of the bolt (Hyett et al. 1995; Li et al. 2018a; Moosavi et al. 2002; Moosavi et al. 2005), or its shear behaviour (Li 2016; Li et al. 2016c; Wang et al. 2018; Wu et al. 2018b).

Very few researchers developed a laboratory apparatus to carry out combined pull and shear tests (Bawden et al. 1994; Chen and Li 2015b). More recently, Wu et al. (2018a) conducted a direct tensile test to investigate the tensile behaviour of fully grouted rock bolts. In order to better review the advantages and disadvantages of different testing techniques, the features of experimental methods and apparatus currently used in rock bolting research are listed in Table 2.1.

Table 2.1 Summery of rock bolt testing apparatus

Laboratory apparatus	Method	Advantages	Disadvantages
	Push test (Aziz et al. 2006)	Testing different encapsulation lengths	Neglecting shear behaviour of the bolt; influence of grout-rock interface was not considered; unable to examine surface roughness of the rock joint
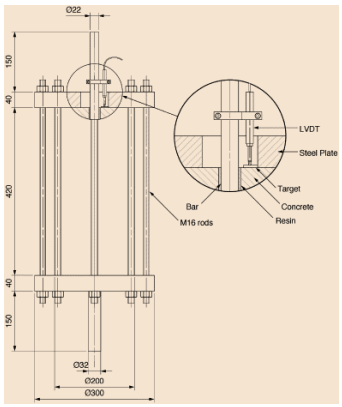	Pull out test (Ivanović and Neilson 2009)	Examining debonding characteristics of the bolt & similar to above	Similar to above
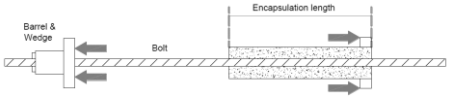	Unconstrained pull test* (Hutchinson and Diederichs 1996)	Similar to above	Similar to above

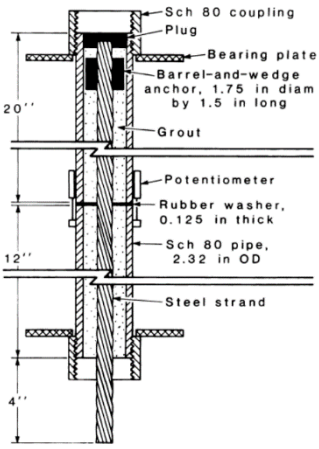	Long double encapsulation pull out test (Goris 1990)	Considering fully-grouted rock bolts; inducing confinement to both ends of the bolt	Similar to above
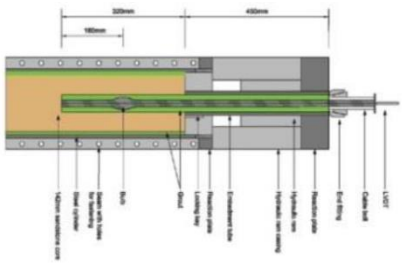	Short encapsulation pull out test (Thomas 2012)	Replicating bolt-grout and rock-grout interfaces; modified apparatus to avoid rock bolt rotation during pull out test; assigning constant confinement on the sample	Medium confining pressure; similar to above
	Direct shear testing (Yokota et al. 2018)	Replicating bolt-grout interface; resembling pull out test; considering interface configuration	Real rock bolt cannot be tested; scale dependency of debonding mechanism obtained from this method; similar to above
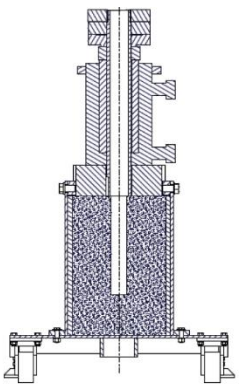	Laboratory Short Encapsulation Pull Test (Hagan et al. 2014)	New modifications to prevent rock bolt rotation; various failure modes of bolt-grout interface can be replicated; reusable mould	Neglecting shear behaviour of the bolt; influence of grout-rock interface was not considered; unable to examine surface roughness of the rock joint

	Single shear test apparatus* (Dulacka 1972)	Testing different bolt inclination angles	Combined pull and shear load is not possible; only CNL condition was applied; similar to above
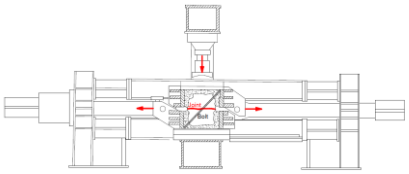	Single shear test apparatus* (Bjurstrom 1974)	Testing natural rock joint profiles; various bolt inclination angle is possible	Similar to above
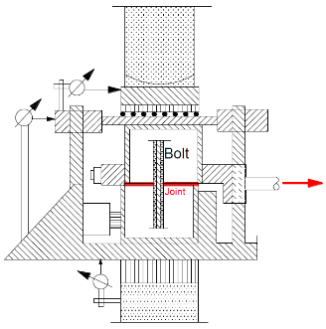	Single shear test apparatus* (Spang and Egger 1990)	Testing bolted rough joint; the influence of various parameters was examined; similar to above	Similar to above
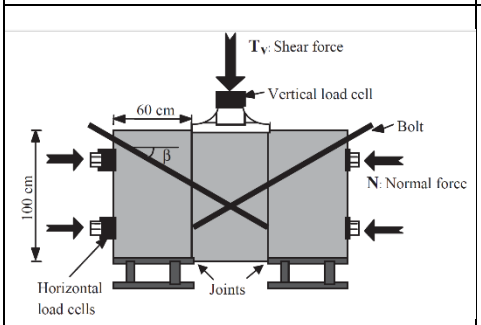	Double shear test apparatus (Grasselli 2005)	Multiple rock bolt testing is possible; different inclination angle of the bolt can be tested; rock bolts can be fully grouted	Joint roughness influence was neglected; only CNL condition was applied; combined pull and shear loading was not possible
	Single shear apparatus (McKenzie and King 2015)	Debonding is prevented during testing; apparatus is modified to consider compressive loading	Difficulty in preparing large specimens; bolt inclination cannot be adjusted; joint roughness cannot be replicated; combined pull and shear loads is neglected; CNS condition is not possible

	Single shear apparatus (Srivastava and Singh 2015)	Normal stress is adjustable; large size shear box allows studying complicated situations	Similar to above
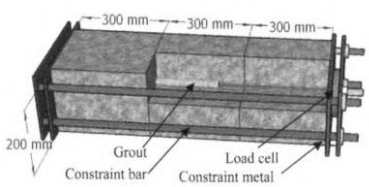	Double shear apparatus (Li et al. 2014)	Bolts can be pre-tensioned; Both shear and axial force can be recorded during testing	Similar to above
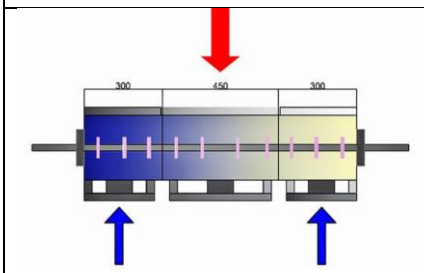	Double shear apparatus (Rasekh et al. 2017)	Contact between concrete blocks is prevented; Various pre-tension loads can be applied to the bolt	Similar to above
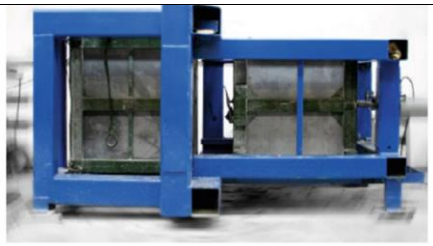	Single shear apparatus (Chen and Li 2015b)	Combined pull and shear loading is possible; Normal load can be adjusted	Blocks are separated so prevent studying frictional behaviour of the joint; CNS condition is not possible; Natural rock joint profiles cannot be tested
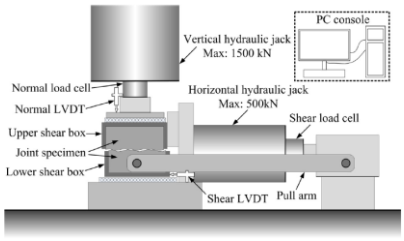	Single shear apparatus (Chen et al. 2018)	Constant normal load is adjustable; Natural rock joints can be tested; Testing fully grouted rock bolt is possible	CNS condition is not possible; Difficulty in testing various inclination angles; Combined pull-shear load is not possible

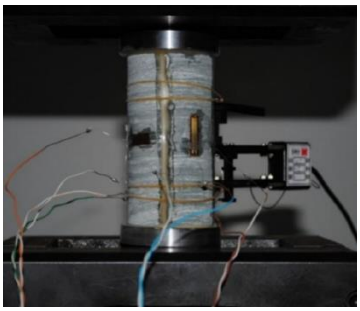	Direct tensile test (Wu et al. 2018a)	Evaluating the reinforced characteristics of rock; fully grouted rock bolt can be tested	Pull and shear load are not possible; Jointed rock bolt cannot be tested
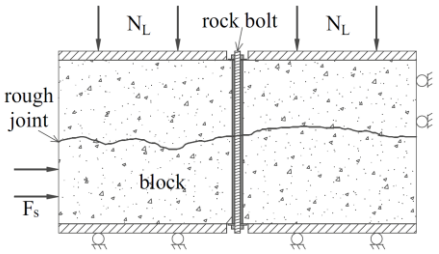	Single shear test apparatus (Wu et al. 2018b)	Influence of surface roughness can be examined; Normal force is adjustable	Combined pull-shear load is not possible; No CNS condition can be tested
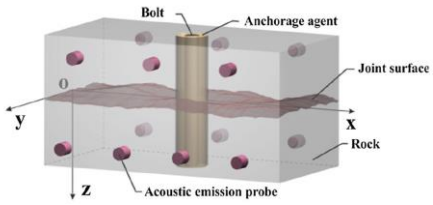	Single shear test apparatus (Wang et al. 2018)	Acoustic emission counts of bolted rock joints can be measured; Normal force is adjustable; Different natural rock joint profiles can be tested	Similar to above

2.2.5 The failure mechanism of bolted rock joint

Many scientists carried out laboratory investigation to study the mechanical shear resistance of bolted rock joints (Grasselli 2005; Haas 1976; Jalalifar and Aziz 2010; Jalalifar et al. 2006; Li et al. 2016b; McHugh and Signer 1999). Different researchers conducted a variety of laboratory investigations to study the influence of some essential factors on shear behaviour of bolted rock joints including bolt type (Chen and Li 2015a; Chen and Li 2015b; Grasselli 2005; Haas 1976; Li 2012; Rasekh et al. 2017), rock bolt diameter (Ferrero 1995; Spang and Egger 1990; Vlachopoulos et al. 2018), rock bolt surface profile (Jalalifar and Aziz 2010; Jalalifar et al. 2006), inclination angle of the bolt (Bjurstrom 1974; Chen and Li 2015a; Chen and Li 2015b; Dight and Chiu 1981; Feng et al. 2018; Haas 1976; Li et al. 2016b; Spang and Egger 1990; Yoshinaka et al. 1987), pretention force (Jalalifar and Aziz 2010; Jalalifar et al. 2006; Li et al. 2016c), grout properties (Kılıc et al. 2002; Zou et al. 2010), rock joint surface roughness (Wang

et al. 2018; Wu et al. 2018b; Yoshinaka et al. 1987), number of rock bolts (Srivastava and Singh 2015), CNS condition (Dey 2001), and combined pull-shear loading (Chen and Li 2015a; Chen and Li 2015b).

Dey (2001) carried out a series of laboratory tests to investigate the shear mechanism of bolted rock joints. His laboratory samples included saw-toothed idealised rock joint, and both clean and infilled rock joint were tested. In Figure 2.7, the experimental sample used in his study is illustrated. The result of his research revealed that the shear strength of both bolted and non-bolted rock joints experienced a significant drop with a thin layer of 1.5 mm. The CNS failure envelope showed a non-linear response, and in bolted rock joints, a significant increase was observed in the value of joint friction angle. The ratio of infill thickness to asperity height (t/a) was considered for more analysis. The results showed that by increasing the value of t/a, the role of rock bolting was less pronounced.

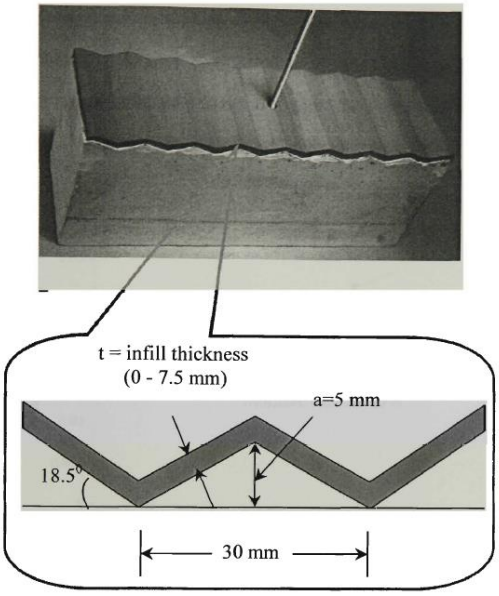

Figure 2.7 Experimental bolted infilled rock joint (Dey 2001)

For clean rock joint, the experimental investigation of Dey (2001) showed that the peak shear strength of the joint increased with increasing the magnitude of applied normal stress. His laboratory results also indicated that the stiffness of bolted rock joints significantly enhanced, however, at higher magnitude of normal stress the rock bolt contribution was functionally less important. The focus of Dey (2001) research was on idealized rock joint, without considering the effect of natural rock joint profiles. Recently, Wu et al. (2018b) conducted CNL direct shear tests to experimentally investigate the influence of joint roughness coefficient (JRC) on overall shear behaviour of bolted rock joints. They modified the following dimensionless values

proposed by Spang and Egger (1990) to characterize the shear behaviour of bolted rock joints with respect to JRC:

$$f_T = (T - T_n)/P \tag{2.2}$$

$$f_s = s/d_b \tag{2.3}$$

where T is the peak shear force obtained from laboratory results, T_n is the shear strength of natural unbolted rock joint, P is the tensile strength of the rock bolt, s is the shear displacement obtained from experiment, and d_b is the bolt diameter. Wu et al. (2018b) developed the following empirical formula that relates f_T and f_s to JRC for $0 \leq JRC \leq 20$:

$$f_T = y - (y - x)e^{-zJRC} \tag{2.4}$$

$$f_s = p \times JRC + q \tag{2.5}$$

where x, y, z, p, and q are fitting parameters that could be identified from laboratory results. Figure 2.8 shows the laboratory test results conducted on natural bolted rock joints obtained by Wu et al. (2018b). The results showed that the dimensionless parameter f_T exponentially increases with increasing the joint roughness, while a linear reduction is observable for f_s .

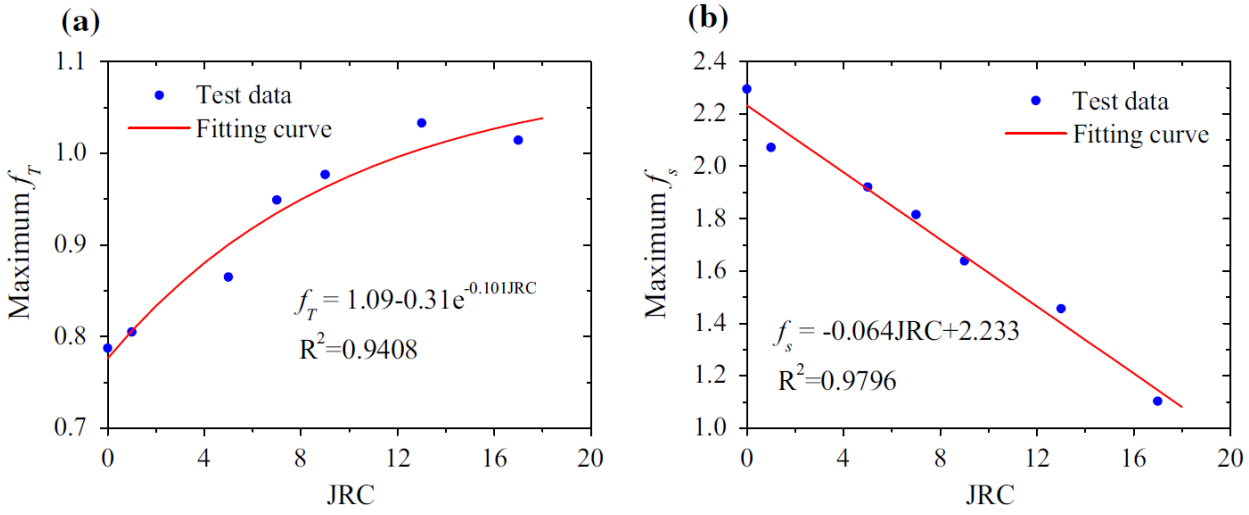

Figure 2.8 Evolution of maximum f_T (a) and f_s (b) with respect to JRC (Wu et al. 2018b)

Wang et al. (2018) conducted a series of CNL direct shear tests on natural rock joint profiles to characterise the shear mechanism of bolted rock joints using Acoustic Emission (AE) technique. They monitored the change in AE response during shearing process of different

anchorage systems and joint roughness. The following conclusions were derived from their research (Wang et al. 2018):

1- The shear strength of bolted rock joints, the peak shear strength gradually increased with increasing JRC. Rock bolt elongation significantly influenced the shear mechanism. A decrease in bolt elongation, significantly increased the effectiveness of the bolting system.
2- The unbolted rock joint experienced less damage compared to bolted counterparts. The macroscopic cracking response of unbolted rock joints showed a uniform distribution, while the cracks along bolted rock joints mainly distributed around the rock bolt. The cracking area around the rock bolt significantly decreased with increasing the rock bolt elongation.
3- The AE count curves obtained from direct shear test results were similar to those of uniaxial compression testing of rocks, as the curves could be divided to four various stages: initial emission, critical unstable damage, energy accumulation, and failure.
4- An increase in the JRC value significantly increased the peak energy ratio and the number of accumulative AE events.

Chen et al. (2018) studied the shear behaviour of bolted rock joints by conducting CNL direct shear tests on rock specimens including natural rock joint profiles. The diagram of deformed rock bolt as well as asperity damage in bolted specimens with different JRC values are illustrated in Figure 2.9. The laboratory investigation of Chen et al. (2018) showed that the shear stiffness of bolted rock joint, without exception, was higher than unbolted rock joints. They also found that the location of rock bolt deformation was adjacent to the rock joint interface. Two plastic hinges with the highest possible bending moment were observed in bolted samples. They concluded that the main cause for increasing the shear stiffness of bolted samples was restricting the shearing of the rock joint interface, and inducing an extra normal stress governed by tensile force resulted from dilatancy of the joint.

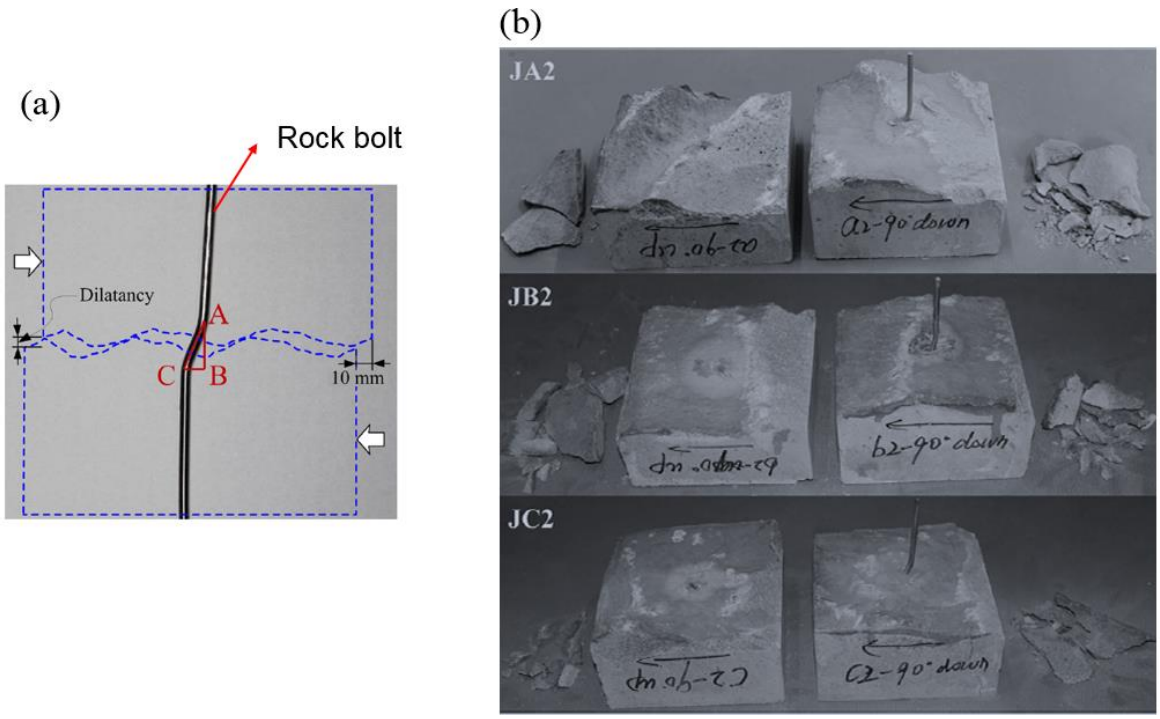

Figure 2.9 The laboratory results obtained by Chen et al. (2018). (a) Deformed rock bolt after CNL direct shear test. (b) Bolted specimens with different JRC after failure.

Although the above mentioned research highlighted the most important shear mechanisms of bolted rock joints, they suffer from some issues. Firstly, the influence of CNS boundary condition was neglected, that can restrict the application of these research to structures with CNL condition. Secondly, the influence of combined pull-shear loading was not studied that may increase the uncertainty in the results obtained. Chen and Li (2015b) designed a laboratory apparatus to study the shear behaviour of rock bolt by conducting combined pull-and shear loading on the bolting system. In their research, Chen and Li (2015b) suggested that, in order to better analyse the performance of fully grouted rock bolts subjected to combined pull and shear load, it is necessary to generate completely separated concrete blocks with zero friction. According to other laboratory investigations (Wang et al. 2018; Wu et al. 2018b), the roughness of rock joint plays an important role in the performance of bolted rock joints. Therefore, the approach followed by Chen and Li (2015b) suffers from uncertainty that originate from neglecting the influence of surface roughness. In addition, in the previous laboratory research the influence of pre-tension load (i.e. pull-out load) on the improvement of the shear resistance of bolted rock joint was neglected.

2.2.6 Numerical investigations on bolted rock joints

Although laboratory testing is the most common approach for investigating the shear mechanism of bolted as well as unbolted rock joints, setting up experiments takes a huge amount of resources. Experimental investigations require researchers to generate a wide range of specimens using various materials, to access advanced laboratory apparatus, and to dedicate time to the time-consuming nature of the experimental procedure. Consequently, many researchers have made their effort to develop numerical models to obtain more understanding about the shear mechanism of bolted rock joints. Numerical simulations are more time-efficient, repeatable, and financially beneficial. A summary of previous numerical investigations on bolted rock joint is given in Table 2.2.

Table 2.2 Summary of rock bolt numerical shear testing

The numerical test set up	Method	Advantages	Disadvantages
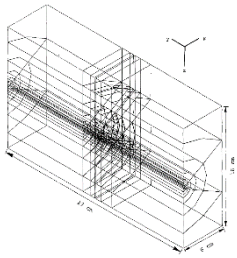	FEM (Spang and Egger 1990)	Simulating elasto-plastic behaviour of the rock bolt; Different bolt inclination angle was possible	Unable to simulate surface roughness of rock joint; CNS condition was neglected
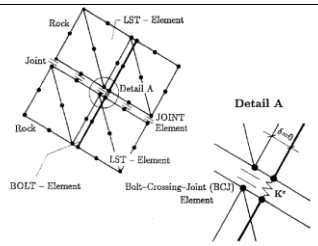	FEM (Marenče and Swoboda 1995)	Considering the influence of joint dilatancy and joint strength properties; Different bolt inclination angles were simulated	Similar to the above
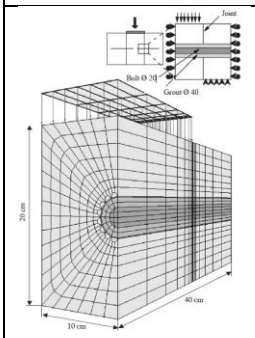	FEM (Grasselli 2005)	Simulating the zone of failure was carried out; Different bolt types could be tested	Similar to the above
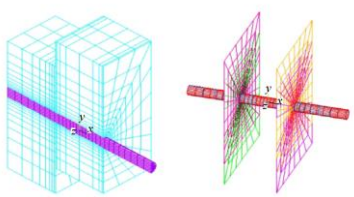	FEM (Song et al. 2010)	The double shear test is modelled including two joints; Fully grouted rock bolt was simulated	Surface roughness cannot be modelled; asperity damage cannot be reproduced; the Combined pull-shear load

			was neglected; CNS condition was not modelled
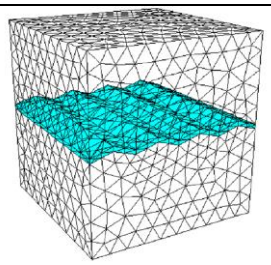	FDM (Lin et al. 2014)	Effect of asperity angles was considered; Different inclination angle of the bolt were simulated	The influence of pull out load was neglected; Asperity damage cannot be simulated; CNS condition was not considered
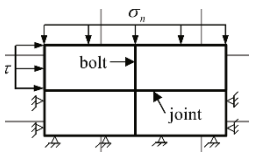	FEM (Deb and Das 2014)	The effect of rock joint was simulated; Various normal stress is possible to model	The surface roughness of the joint was neglected; Similar to above
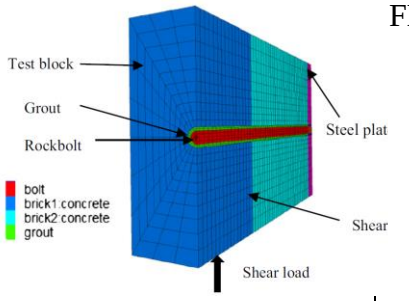	FDM (Li et al. 2016b)	Different bolt inclination angles were simulated; The joint effect could be simulated; Fully grouted rock bolt could be modelled	Asperity damage of rock joint cannot be modelled; CNS condition was neglected; Joint surface roughness is difficult to simulate; the Combined pull-shear load was neglected
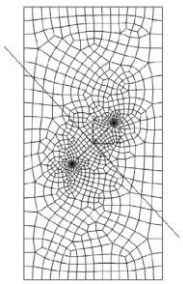	FEM (Zhang et al. 2016)	Different bolt inclination angle can be simulated; Change in rock strength can be modelled	Rock joint was neglected; CNS condition is not applicable in this approach; Pull-shear loading is not applicable in this approach
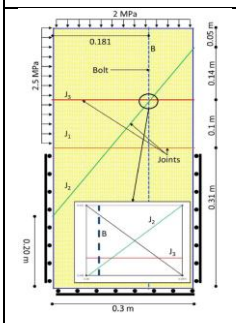	FEM (Deb and Gujjala 2018)	Multiple rock joint was simulated; Various bolt inclination angle was examined	Similar to the above

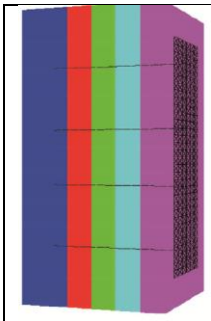	FEM (Zhu et al. 2018)	The reinforcement of bedding planes can be modelled; Applicable for large scale simulations	Similar to above
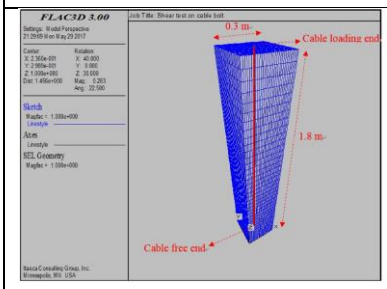	FDM (Li et al. 2019b)	Fully grouted rock bolt was simulated; Various anchorage length was modelled; Various bond-slip models were tested	The surface roughness of rock joints cannot be simulated; Asperity degradation cannot be modelled; Combined pull-shear load is difficult to simulate; CNS boundary condition is not applicable in this approach

In the numerical research mentioned in Table 2.2, the influence of surface roughness, CNS boundary condition, and combined pull-shear load were not considered. For a better understanding of the influence of these parameters, more investigations are required. In addition, there is no comprehensive numerical methodology to examine the effect of pre-tension load on the ultimate shear resistance of bolted rock joints. Such methodology is necessary for the field (e.g. underground coal mining) to find the optimum magnitude of pre-tension stress which can be used as a guideline to ensure roof stability.

It has been recognized that the debonding failure of the bolt-grout interface is the primary cause of damage in fully grouted rock bolts (Shang et al. 2018a). Understanding the bolt-grout interfacial debonding process and its subsequent bolt-grout shear behaviour, however, is not readily achievable in the laboratory environment.

Shang et al. (2018a) used DEM to mimic the debonding failure behaviour of bolt-grout interface and fracture response of grout material. An example of their numerical model and the experimental specimen is illustrated in Figure 2.10. Their numerical simulation revealed that at macroscopic scale, grout material demonstrated significant deformability and softening response (Shang et al. 2018a), which attributed to its micromechanical structure. The DEM

investigations of Shang et al. (2018a) showed that the Flat-Joint model (FJM), which is a DEM-based contact model (Potyondy 2012) available in commercial DEM codes (PFC2D) (Itasca 2016), is incapable of reproducing the softening behaviour of grout material during the post-peak stage of uniaxial compression tests. They concluded that the FJM suppressed the rotation of DEM particles after bond-break, which led to a sudden failure of DEM specimen. Besides, the FJM contacts return zero fracture energy response at the onset of failure, which in turn contributes to the sudden failure of DEM specimen. Thus a brittle macroscopic response will be observed during the post-peak stage, which is not inherently desirable compared to softening behaviour of experimental specimens. The laboratory results also showed that the samples, including smooth bolt-grout interface, exhibited gradual softening behaviour under shearing (Shang et al. 2018a). Therefore, the smooth-joint model (SJM), which is the widely used DEM interface model (Bahaaddini et al. 2013; Gutiérrez-Ch et al. 2018; Hofmann et al. 2015b; Shang et al. 2018a; Zhou et al. 2017), needs to be augmented by cohesive-damage formulation to characterise the failure mechanism of the bolt-grout interface adequately.

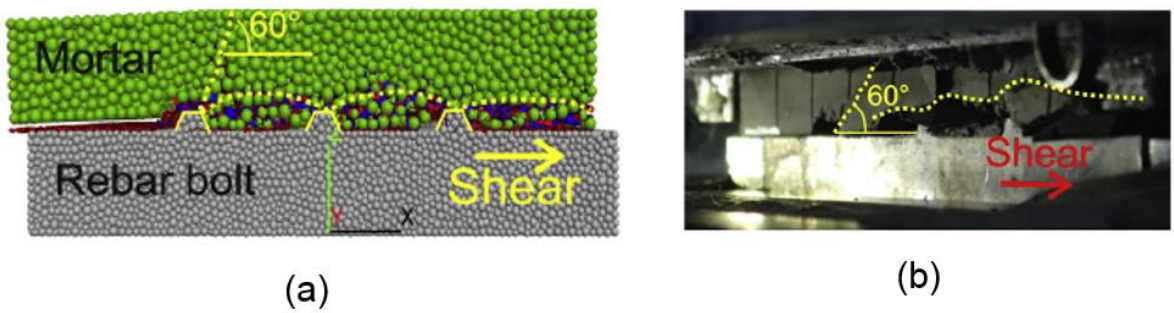

Figure 2.10The debonding failure of bolt-grout interface (Shang et al. 2018a). (a) DEM simulation results. (b) The experimental results.

2.3 Shear behaviour of clean and infilled rock joint

Understanding the failure mechanism of infilled rock joint has long been a subject of research because of its significant influence on rock block stability in underground excavations, mining operations and civil engineering projects. The presence of infill material within a joint can reduce its shear strength considerably. Infill thickness and rock joint roughness are the most important parameters controlling the shear behaviour of infilled rock joints (Mylvaganam 2007). The characterisation and prediction of the shear mechanism of infilled rock joints have received great concern in the research field of geotechnical engineering.

2.3.1 Laboratory investigations on infilled rock joint

A large number of studies have been conducted in the past few years in an effort to understand the shear behaviour of infilled rock joints (Barton 1974; Indraratna et al. 1999; Indraratna and Jayanathan 2005; Indraratna et al. 2010b; Indraratna and Welideniya 2003; Jahanian and Sadaghiani 2015; Ladanyi and Archambault 1977; Lama 1978; Papaliangas et al. 1990; Shrivastava and Rao 2013; Shrivastava and Rao 2018). Some researchers conducted triaxial testing to investigate the influence of the degree of saturation on shear behaviour of filled joint (Indraratna et al. 2014; Khosravi et al. 2016), other scientist used artificial and natural rock joints in their experiment to understand the effect of asperity angle and infill thickness on the shear performance of the joint (Jahanian and Sadaghiani 2015; Phien-Wej et al. 1990; Sinha and Singh 2000). The laboratory specimens used for infill study by different researchers are illustrated in Figure 2.11.

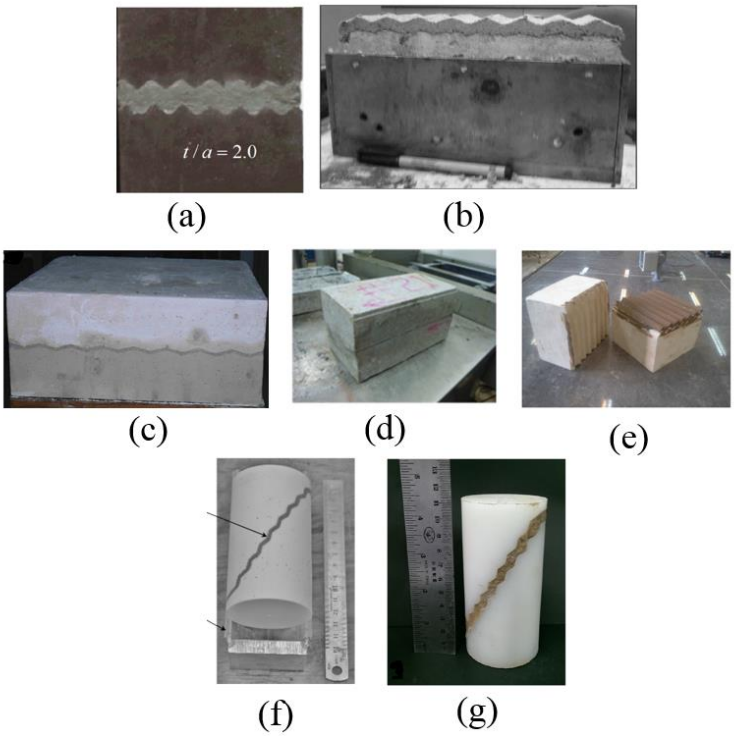

Figure 2.11 Different experimental specimens prepared for studying infilled rock joint behaviour after (a) Lu et al. (2017), (b) Oliveira et al. (2009), (c) Shrivastava and Rao (2018), (d) She and Sun (2018), (e) Jahanian and Sadaghiani (2015), (f) Indraratna and Jayanathan (2005) , and (g) Khosravi et al. (2016).

2.3.2 Empirical models to estimate the shear strength of infilled rock joints

Previous investigations have shed significant light on the impact of influential parameters on the shear strength of the infilled joints such as joint roughness, infill thickness, type of infill,

infill degree of saturation etc. Papaliangas et al. (1990) developed an empirical model to reproduce the shear behaviour of infill rock joints, which incorporated a predictor model suggested by Ladanyi and Archambault (1977). In Papaliangas et al. (1990) model, the peak shear stress of infilled rock joint varies between two strength limits, T_{max} (maximum shear strength of clean rock joint), and T_{min} (minimum possible shear strength of infilled rock joint). The controlling parameters in this model are infill thickness (t), infill type, asperity height (a), and the magnitude of normal stress. According to this empirical model, when the roughness of the joint is high (i.e. steep rock joint with high undulation), T_{min} can be regarded as the shear strength of infill material. In contrary, in the case of planar rock joint (i.e. smoothly polished rock joint surface), T_{min} can be calculated as the shear strength along with the interface bet ween rock joint surface and infill material, which often falls below the strength of infill material. The peak shear strength in Papaliangas et al. (1990) model is defined as follows:

$$G = G_{min} + (G_{max} - G_{min})^N \tag{2.6}$$

where $G = (\frac{T}{T_n}) \times 100$; $G_{min} = (\frac{T_{min}}{T_n}) \times 100$; $G_{max} = (\frac{T_{max}}{T_n}) \times 100$; $N = \left[1 - \frac{1}{H}(\frac{t}{a})\right]^M$; and H and M are empirical ratios that can be estimated from laboratory results. T_n is the normal stress and T is the shear stress. According to experimental observations of Papaliangas et al. (1990) the value of H can be considered for as 1.0 for cohesive infill (i.e. kaolin). The experimental results of Papaliangas et al. (1990) and Phien-Wej et al. (1990) showed that by increasing $\frac{t}{a}$ the peak shear strength of the system significantly decreases until reaching a constant residual value that is equal to the shear strength of infill.

Based on an extensive laboratory investigation on saw-toothed infilled rock joints, Mylvaganam (2007) proposed an empirical model that takes into account the overconsolidation ratio (OCR) of infill material, and t/a ratio. The experimental results showed that when t/a ratio is less than a critical value, rock joint asperities can contribute to shear failure, but when the t/a ratio exceeds the critical limit, the infill material controls the shear behaviour. According to Indraranta et al. (2005) experimental observations, at high normal stress magnitude, when the normal displacement of the rock joint is proportionally small, asperity degradation is inevitable. Mylvaganam (2007) defined the following ratio to incorporate the influence of OCR value in his model:

$$k_{oc,n} = \frac{(t/a)_{oc,n}}{(t/a)_{cr,n}} \tag{2.7}$$

where $(t/a)_{cr,n}$ is the critical ratio with OCR of n, and $(t/a)_{oc,n}$ is the critical ratio of a desired infill with OCR of n. On the basis of $k_{oc,n}$, the shear strength of infilled rock joint was classified 'interfering' and 'non-interfering' zones. For $k_{oc,n} > 1.0$, the shear mechanism is controlled by infill material. The observations of Indraranta et al. (2005) showed that when the critical t/a ratio is achieved for a normally consolidated cohesive infilled joint, the shear strength of the infilled rock joint can be approximated by infill friction ratio. An example of predicted values obtained by Mylvaganam (2007) is depicted in Figure 2.1. It can be seen that in 'non-interference' zone, the normalized shear strength of infilled rock joint remains constant.

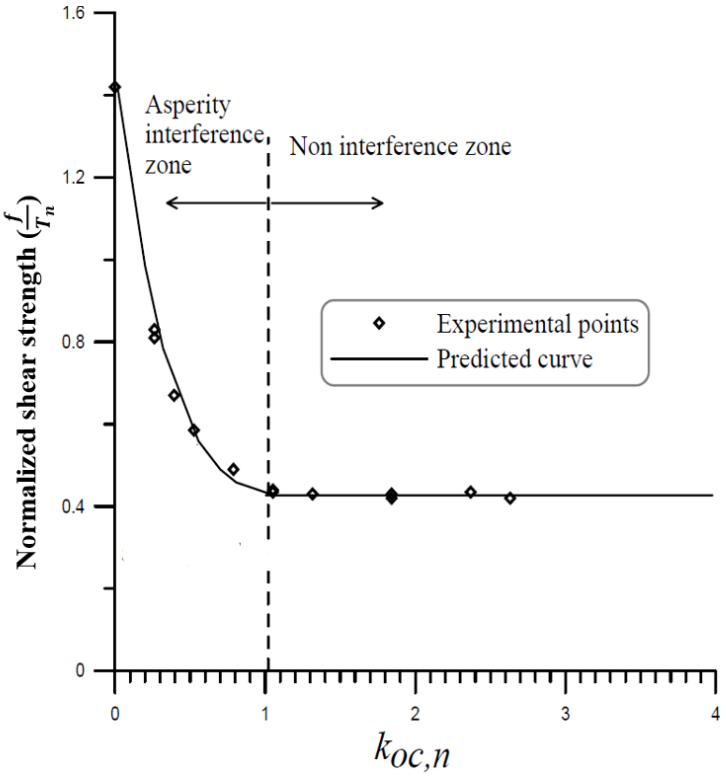

Figure 2.12 Prediction of infilled rock joint shear behaviour (modified from Mylvaganam (2007))

Indraratna et al. (2010b) defined three different stages to characterise the shear behaviour of infilled rock joints. This mechanism is illustrated in. The first phase is controlled by shear strength of infill material. The rock joint roughness provides a boundary for the infill in which the soil can fail. During the second stage, the infill material fills the void area generated be asperity. After some progress in shearing, the two wall sides of the rock joint will eventually

interact with each other increasing the shear strength of the infilled rock joint. From this stage until the end of the test, the shear strength of the system will be controlled by the surface roughness and the magnitude of the applied normal stress. Indraratna et al. (2010b) developed an empirical model based on the observed shear mechanism illustrated in Figure 2.13. They incorporated the influence of JRC, infill thickness, asperity height, and frictional behaviour of the infill material.

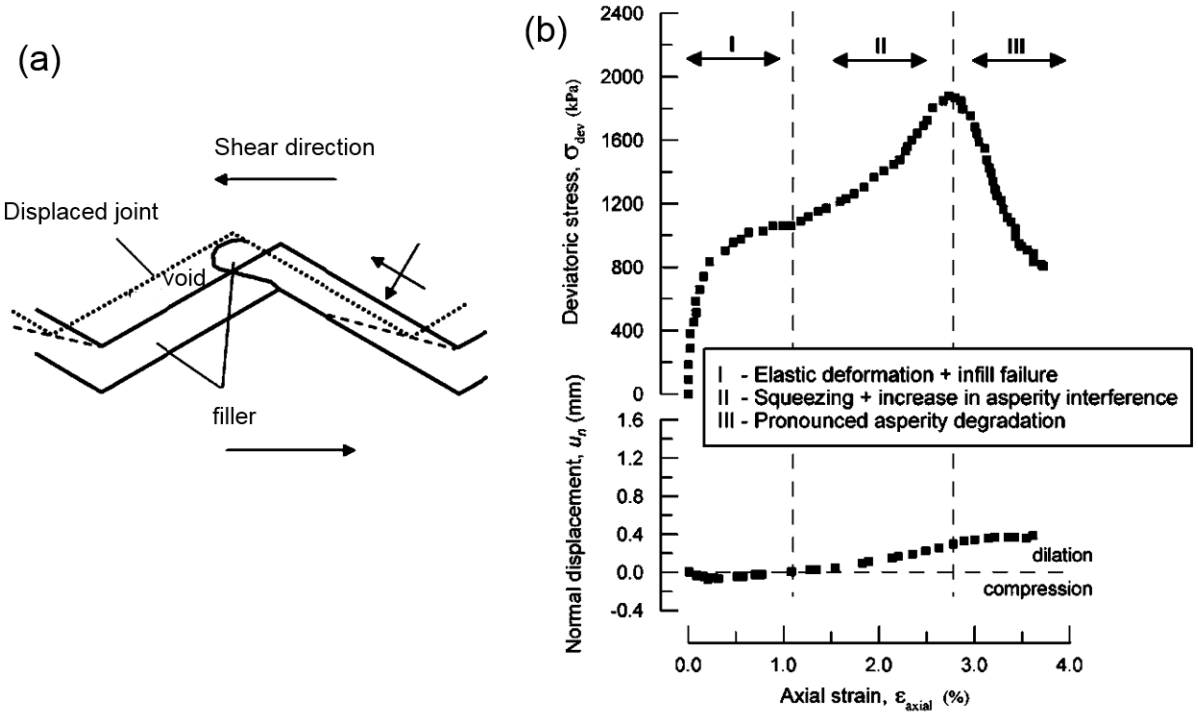

Figure 2.13 The empirical infilled rock joint model developed by Indraratna and Jayanathan (2005). (a) Interaction between infill material and asperities. (b) The three-phase mechanism for infilled rock joints.

Apart from asperity amplitude, which is one of the critical elements describing joint surface morphology, asperity wavelength also affects the shear behaviour of rock joints (Yang and Chiang 2000). The findings of Yang and Chiang (2000) showed that for a clean rock joint at a constant asperity amplitude when the asperity angle is reduced to 15° (or higher asperity wavelength) the peak shear stress drops significantly and asperity shear off is not highly significant compared to a rock joint with asperity angle of 30° (or lower asperity wavelength). Previous research of infilled rock joints attempted to link the peak shear strength to the ratio of infill thickness to asperity amplitude by varying the asperity angle (Jahanian and Sadaghiani 2015; Ladanyi and Archambault 1977). For instance in the study of Jahanian and Sadaghiani (2015) the asperity wavelength kept constant at 2 cm for 30° and 45° asperity angles.

Consequently, by following this approach the hidden mechanism behind the role of geometrical parameters of the joint cannot be observed.

2.3.3 Numerical simulation of infilled rock joint

Although laboratory observation is regarded as the gold standard to evaluate the influence of different parameters on overall shear performance of infilled rock joints, it is hampered by various restrictions. The experimental approach is expensive due to the requirement of sophisticated laboratory apparatus as well as huge amount of resources needed for sample generation. In addition, the laboratory investigation is highly time-consuming and increasingly onerous, especially when frequently repeated experiments are in demand. Using empirical predictors as a substitute on the other hand, suffers from some other difficulties. For instance, finding the fitting parameters from laboratory testing is a complicated challenge and may increase the uncertainty of these models in predicting the mechanical behaviour of infilled rock joints. In addition, empirical formulations are mainly based on very few experimental observations which cannot be generalised for a wide range of applications.

However, due to recent advancement in computer technology, computational methods have been increasingly adopted as an alternative tool in rock mechanics research. Amongst various numerical methods, discrete element method (DEM) (Cundall 1971) has been proved to be a propitious tool used by many scientists to overcome the financial risks and operating limitations of experimental approach in rock joint studies (Bahaaddini 2014; Bahaaddini et al. 2013; Kazerani et al. 2012; Kazerani and Zhao 2010; Park and Song 2009; Wang et al. 2019).

Duriez et al. (2011) used a DEM technique to simulate the mechanical behaviour of infilled rock joints. The model constructed by Duriez et al. (2011) in DEM codes is illustrated in Figure 2.14. 3D simulation was used in their study, and as it can be seen in Figure 2.14 only the infill layer was simulated. The rock joint considered in their study was assumed to have no JRC value, consequently, the rock joint was modelled as the area between two adjacent blocks. A simple frictional contact constitutive model was employed in their study, which restricts the application to only non-cohesive infills. The numerical results were verified against a simple theoretical model that was developed for predicting rock joint behaviour.

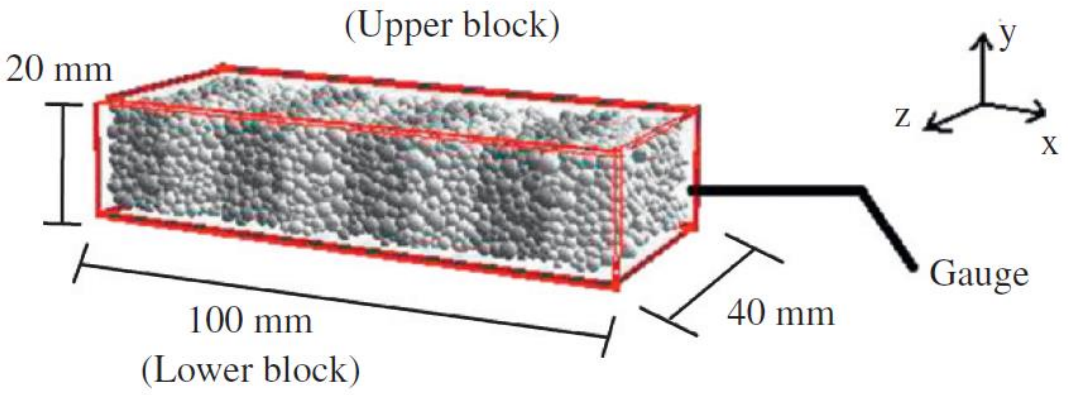

Figure 2.14 DEM specimen of infilled rock joint (Duriez et al. 2011)

It worth mentioning that neither in the theoretical model nor in DEM simulations was the influence of surface roughness considered (Duriez et al. 2011). Therefore, this approach cannot shed significant lights on the hidden mechanisms involved in the shearing process of infilled rock joint.

Furthermore, the presence of cohesive infill materials within rock joints is proportionately pervasive in nature (Indraratna and Jayanathan 2005), and it is essential to incorporate the phenomenological behaviour of such cohesive materials in DEM contact response. It is claimed in the current thesis that in order to enhance the results of DEM modelling of infilled rock joint, a cohesive constitutive model is required to be assigned on the contacts between infill particles. Such numerical framework enables us to better investigate the mechanical behaviour of infilled rock joint and obtain many reliable results from DEM simulations.

2.3.4 Empirical models to estimate the shear strength of clean rock joints

Rock joint shear strength is one of the most important parameters that should be taken into account in the design process of rock engineering structures. The presence of rock joint has an inevitable impact on shear and deformation behaviour of the rock mass. In natural rock joint, asperities control the mechanical behaviour of the joint. In this section, the advantages and disadvantages of current rock joint constitutive models are briefly discussed, and the available numerical techniques for rock joint simulation are compared. In Table 2.3 the advantages and disadvantages of the current empirical rock joint models are introduced.

Table 2.3 Advantages and disadvantages of current rock joint constitutive models

Model name	Advantages	Disadvantages
Mohr-Coulomb linear model	The model is very simple; Only two parameters are required for prediction	The effect of surface roughness is neglected; Asperity damage cannot be modelled
Model of Patton (1966)	Using the model is straightforward	Similar to the above
Model of Ladanyi and Archambault (1969)	The influence of asperity area was incorporated; The degree of rock joint interlocking can be predicted; The influence of initial joint opening could be considered; Taking advantage of its sounds theoretical background	High complexity in determining parameters; The model was developed based on idealized rock joint which restricts its application for natural rock joints
Model of Jaeger (1971)	The model is straightforward	It lacks theoretical background; Empirical parameters have no physical meaning
Model of Barton and Choubey (1977)	Incorporating the influence of surface roughness; The effect of rock joint strength could be considered	JRC is qualitative and may lead to subjectivity in results
Elastic-plastic model of Plesha (1987)	Asperity damage could be calculated; The model is straightforward	No direct method for obtaining the degradation parameter
Model of Grasselli and Egger (2003)	The model is able to capture anisotropy of rock joint; Three-dimensional surface roughness could be considered; The subjectivity in roughness estimation was highly reduced	Measuring model parameters in the laboratory is complicated; Using scanning techniques for obtaining model parameters is costly
Model of Cottrell et al. (2010)	Similar to the above	The model involves several empirical and fitting parameters restricting its generality
Model of Oh et al. (2015)	The influence of asperity degradation was incorporated in the model; Field-scale behaviour of rock joint could be estimated	Asperity degradation constant lacks comprehensive physical meaning; The relationship between rock joint parameters and damage coefficient was neglected
Model of Li et al. (2016d)	The influence of lab-scale unevenness and waviness were incorporated; The degradation parameters were related to rock joint parameters	The mechanical properties of asperities were neglected in predicting peak shear stress; The shear displacement at which peak shear stress occurs should be pre-

		defined that restrict the generality of the model

The literature review shows that the recent development in rock joint model suffers mainly from the lack of relationship between model parameters and physical properties of natural rock joints. The rock joint models reviewed in Table 2.3 are only applicable under the CNL condition. Thirukumaran and Indraratna (2016) provided a comprehensive literature review on the available CNS rock joint models. According to their review, the main objective of CNS models was to provide a reasonable approximation of rock joint normal displacement. However, the accuracy of a CNS model in reproducing rock joint dilation generally depends on how the influence of asperity damage and morphological properties of rock joint are involved in the constitutive relationships. This has been a long-lasting issue in the realm of rock mechanics.

2.3.5 Numerical models to simulate rock joint with asperity damage

The early efforts in rock joint studies were limited to the approximation of peak shear and residual strengths of the rock joint without considering the post-peak behaviour and asperity degradation response in the constitutive relationships (Ladanyi and Archambault 1977; Patton 1966). However, characterising the shear behaviour of rock joints as well as understanding the asperity damage mechanism is of critical importance in the design and construction procedure of many civil and mining structures (Tatone 2014). Since the 1980s, the widespread numerical techniques has provided this opportunity for the scientists to shed more light on the various shearing mechanisms involved in the failure process of rock joints. Several numerical tools to explicitly mimic the fracturing behaviour of idealized and natural rock joint has been developed, including: discrete element methods with rigid particles (e.g., parallel bond-smooth joint modelling in PFC2D (Bahaaddini et al. 2014, 2015; Bahaaddini et al. 2013)), discrete element method with Voronoi tessellations (e.g., Kazerani et al. (2012); Oh et al. (2017)), and hybrid methods (e.g., ELFEN (Tatone 2014); Y-Geo (Mahabadi et al. 2012)). A summary of previous numerical research using these methods is provided in this section, and their advantages and disadvantages are discussed. The potential research gaps are also identified.

- **Kazerani et al. (2012)**

Kazerani et al. (2012) simulated the degradation of idealized saw toothed asperities using UDEC (ITASCA Consulting Group 2008). The material heterogeneity and irregularity in fracturing pattern were achieved by constructing a particle assembly containing Constant-

Strain Triangular (CST) elements. The force-displacement law between DEM contacts was controlled by implementing an orthotropic cohesive model in the numerical framework, which allowed different shear and tensile behaviour for the contacts. A schematic view of their DEM simulation as well as shear stress-displacement results are illustrated in Figure 2.15. They established a statistical approach to accurately calibrate the micro-mechanical parameters of the contacts constitutive model. Standard laboratory tests (i.e. Brazilian tensile and uniaxial compression tests) were used in the calibration procedure. A Coulomb friction law was assigned on the interface to mimic the mechanical behaviour of rock joint. They examined the influence of asperity angle and normal stress magnitude on the macroscopic behaviour of the numerical specimens.

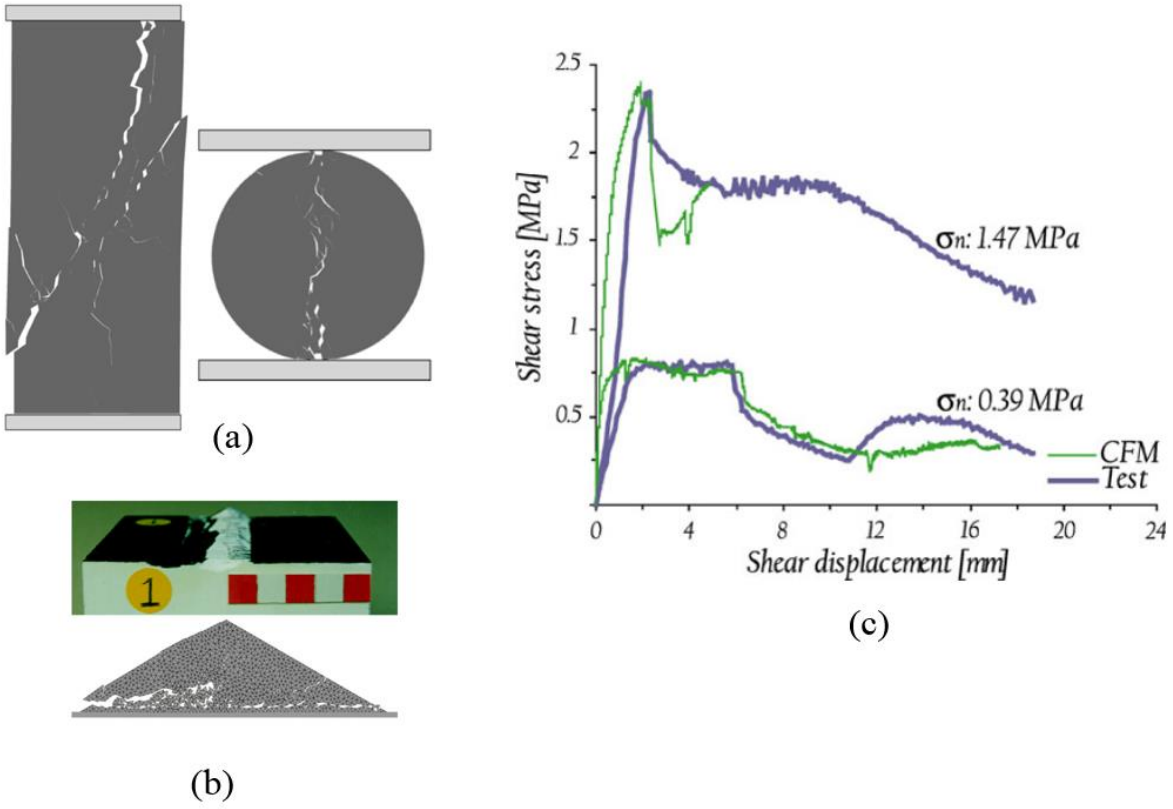

Figure 2.15 The DEM approach followed by Kazerani et al. (2012). (a) Uniaxial compression and Brazilian tensile test simulated for calibration purposes. (b) CNL direct shear test of idealized saw-toothed asperity. (c) typical shear stress-displacement response and its comparison with experimental results.

- **Bahaaddini et al. (2013)**

Bahaaddini et al. (2013) simulated the asperity degradation of idealised and natural rock joints in PFC2D. The PBM and SJM were employed to mimic the mechanical behaviour of asperities and rock joint interface, respectively. Figure 2.16 illustrates the result of CNL direct shear tests

obtained by Bahaaddini et al. (2013). In their study, they highlighted that assigning the SJM on the rock joint interface without considering some modification may lead to particle interlocking, which prevent the model to reproduce an accurate macroscopic behaviour throughout the shearing procedure. CNL testing was used to examine the shear behaviour of rock joint, and the influence of a variety of normal stress magnitudes was studied. As expected, their numerical simulations showed that the specimens with the highest normal stress experienced severe asperity damage and returned the least possible normal displacement. Bahaaddini et al. (2015) carried out a parametric study on micro-mechanical parameters of the smooth-joint model to study their influence on the macroscopic response of the numerical models. They employed two different rock joint, one natural rock joint with a known standard JRC value, and the other with an idealised saw-toothed profile. In the sliding model (i.e. low magnitude of normal stress), the results showed that normal and shear stiffness of the smooth-joint model has no significant influence on the shear behaviour of rock joint. However, an increase in the friction coefficient of the smooth-joint model resulted in an increase in the peak shear stress of the joints. In asperity damage mode, peak shear strength of the models was reduced with increasing the normal stiffness of the smooth-joint model, whereas, the same value was significantly reduced with increasing the shear stiffness and friction coefficient of the smooth-joint model.

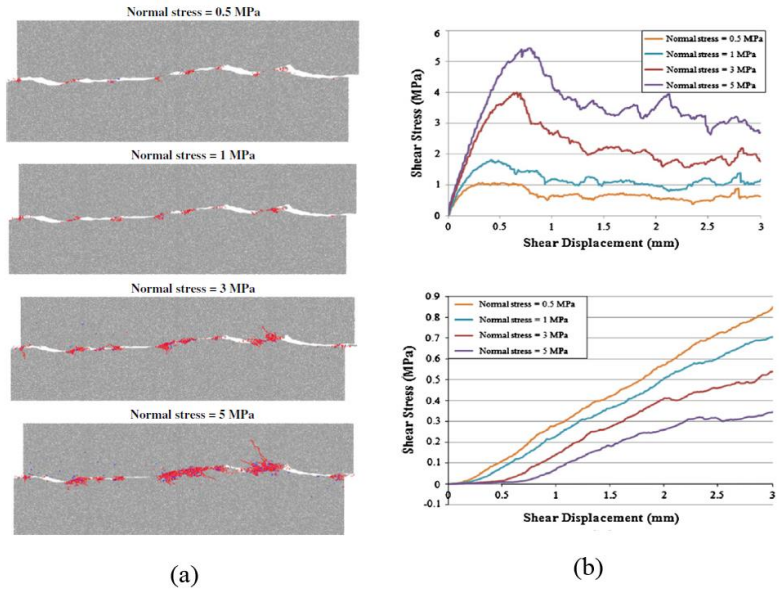

Figure 2.16 DEM simulation of natural rock joints conducted by Bahaaddini et al. (2013). (a) Explicit asperity degradation in numerical specimens. (b) Typical shear stress-displacement behaviour for natural rock joints with a JRC value of 16-18.

- **Tatone (2014)**

Tatone (2014) attempted to simulate CNL direct shear tests using hybrid methods. He employed FEM-DEM (Y-Geo) approach to simulate the shear behaviour of laboratory specimens. The model was calibrated against uniaxial compression and Brazilian tensile test results. Different rock joint profiles, including saw-toothed asperities as well as natural rock joints were simulated. A schematic view of his numerical specimens and stress-displacement response is depicted in Figure 2.17. One of the main issues with such numerical approach is unstable fracture propagation during post-peak stage (Figure 2.17b). When critical displacement is reached, contact failure starts in this model and micro-crack forms. Due to the consistent link between distinct elements, yielding of one element results in the failure of neighbouring elements, which is called "domino effect" (Tatone 2014). This uncontrolled fracturing response in the numerical system can result in rapid dissipation of contact energy and can cause an abrupt reduction in the value of shear stress during post-peak in a fluctuating manner (Figure 2.17b).

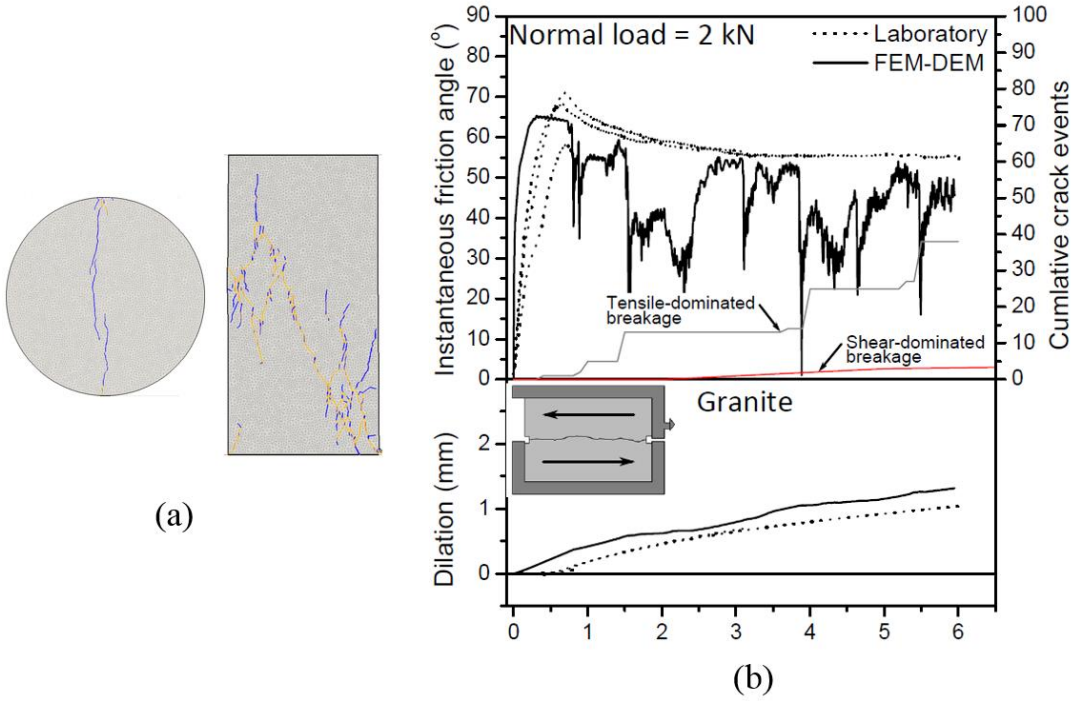

Figure 2.17The FEM-DEM approach followed by Tatone (2014). (a) Standard Brazilian tensile and uniaxial compression tests used for calibration. (b) The shear stress-displacement and dilation response of the model compared with the laboratory results.

- **Oh et al. (2017)**

Oh et al. (2017) conducted an experimental and numerical approach to study the dilative response of idealised saw-toothed asperities. The Voronoi logic available in UDEC software was used to characterise the fracturing behaviour of asperities. The Coulomb friction model was assigned on the rock joint, and a model counting for tensile and shear behaviour of contacts was considered for simulating the fracturing behaviour of particle assembly. Their DEM approach showed promising results compared to the laboratory data. Figure 2.18 shows an example of model failure, asperity damage, and shear stress-displacement and normal-shear displacement curves obtained by Oh et al. (2017). Their numerical parametric study showed that increasing the normal stress magnitude significantly reduces the dilation, and an increase in the asperity wavelength leads to higher dilation in all numerical specimens.

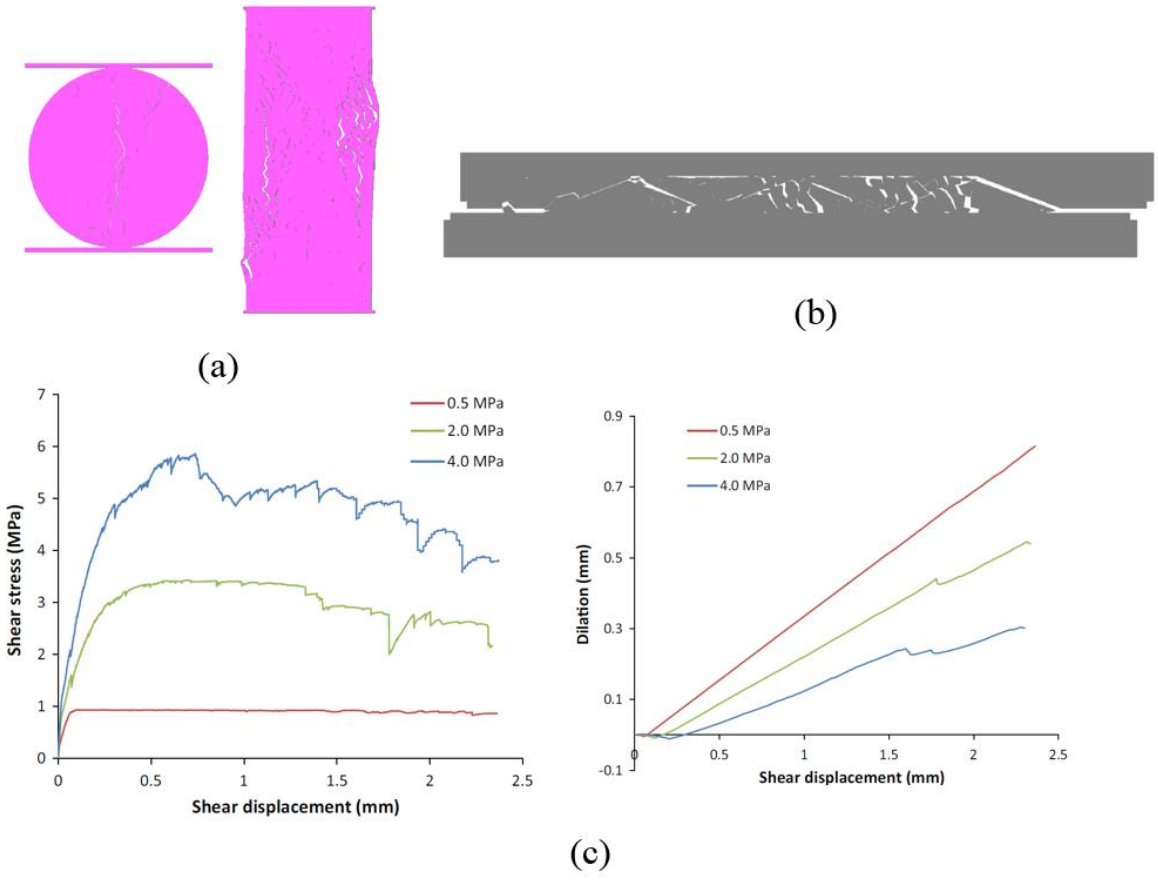

Figure 2.18 The DEM approach followed by Oh et al. (2017). (a) Standard Brazilian tensile and uniaxial compression tests used for calibration. (b) Asperity damage in idealised rock joint (c) Typical shear stress-displacement curves obtained from numerical simulations and the corresponding asperity degradation

Recently, some scientists used PFC-DEM approach to study the behaviour of jointed rock mass under CNS condition (Gutiérrez-Ch et al. 2018; Shang et al. 2018b). Gutiérrez-Ch et al. (2018)

used the flat-joint and smooth-joint models to simulate CNS direct shear tests of different rock joint profiles. Shang et al. (2018b) employed the parallel bond and the smooth-joint model to numerically study the mechanical and fracturing behaviour of incipient rock joints.

Although the above-mentioned research studies shed significant light on the rock joint shear mechanism, but there is no systematic numerical study in the literature to investigate the influence of various parameters such as boundary condition (both CNL and CNS), joint roughness coefficient, normal stress magnitude, and CNS stiffness on the overall shear behaviour of rock joints. In addition, the behaviour of bolted rock joints is required to be studied as the previous research mainly focused on unbolted rock joints.

The major issue in previous bonded particle model (PFC2D), which has been widely used in recent years, is that the bond failure and contact stress reduction are instantaneously leading to an abrupt energy release in DEM system. In reality, a gradual yielding of the bonds is involved in the process of fracture initiation and propagation (Khazaei et al. 2015). In order to make the bond breakage process in DEM more phenomenologically realistic, a softening constitutive model can be assigned on the DEM contacts. Such softening response at microscopic level enables us to control the overall energy dissipation of the system while maintaining a stable macroscopic fracturing growth.

On the other hand, the experimental observations revealed that, in polycrystalline rocks, the macroscopic shear behaviour of rock joint highly depends on the micro-texture of rock specimen (Meng et al. 2018). Thus, not only the surface roughness characteristics (Barton and Choubey 1977; Grasselli and Egger 2003; Kazerani et al. 2012), but also the microstructural properties of the host rock should be taken into account for evaluating the rock fall hazards caused by the shear failure of rock joints (Meng et al. 2018; Wang et al. 2019; Yang and Qiao 2018). In the previous numerical studies, the effect of rock texture on rock joint asperity damage was neglected. Therefore, the asperity damage behaviour in polycrystalline rocks needs further investigation.

2.4 DEM grain-based approach

The grain structure of crystalline rocks has an inevitable impact on the macroscopic failure behaviour, including strength, deformability, and cracking pattern. Phenomenologically, the brittle failure of polycrystalline rock is the results of cohesion degradation and frictional response at the microscopic level, which contributes to the strength of intact crystalline rock at the macroscopic scale (Hajiabdolmajid et al. 2002). The microstructure of polycrystalline rock,

and its effect on the microscopic damage mechanism and the macroscopic material response can be studied by using different experimental approach. Many scientists experimentally investigated the mechanisms involved in the brittle failure behaviour of crystalline rocks (Brace and Bombolakis 1963; Brace et al. 1966; Nicksiar and Martin 2014; Tapponnier and Brace 1976; Tuğrul and Zarif 1999). The laboratory techniques for failure characterisation of polycrystalline rocks are necessary; however, experimental approach requires sophisticated testing apparatus, careful sampling and material preparation, and complicated data processing, which is generally expensive and time-consuming.

A viable complement alternative to the experimental methods is offered by computational tools such as DEM. The DEM has received great attention in recent years as it has been augmented with a grain-based framework, which is capable of mimicking the mechanical behaviour of minerals. In order to accurately simulate the failure behaviour of brittle rock, a sufficient number of DEM particles at grain scale is required (Potyondy 2015). The grain-based model (GBM) has proved to be a promising tool to reproduce the fracture behaviour of polycrystalline rocks with a close agreement to the physical data (Bahrani and Kaiser 2016; Bahrani et al. 2014; Bahrani et al. 2011; Bewick et al. 2014c; Hofmann et al. 2015a; Hofmann et al. 2015b). The GBM refers to representing the grain microstructure of polycrystalline rock using a polygonal structure (Zhang and Wong 2018). The microstructure generation techniques such as Voronoi tessellation enabled GBM to reproduce polygonal elements as a counterpart of crystalline minerals, which facilitate the modelling of polycrystalline rocks. PFC2D offers a grain-based framework known as PFC-GBM that can realise the polycrystalline nature of rock specimen. The parallel-bond model (PBM) (Potyondy and Cundall 2004), and the smooth joint model (SJM) (Itasca 2016) are the most common contact models used in PFC-GBM research (Bahrani et al. 2014; Hofmann et al. 2015a; Potyondy 2010a) to simulate the fracture behaviour of crystalline rocks. Recently, Zhou et al. (2019) employed the flat-joint model (FJM) to mimic the cracking behaviour of intra-grain contacts.

The contact models used in the recent PFC-GBM studies are given Table 2.4. The FJM, PBM, and SJM are incapable of reproducing the gradual softening response at the contact level. In fact, in PBM and FJM, when the contact forces exceed the bond strength, bond-break occurs, which results in an abrupt reduction of contact forces to zero (Potyondy and Cundall 2004). Similarly in SJM, while the contact is broken in tension, both normal and shear forces reduce abruptly to zero (Itasca 2016). If SJM contact is in the shear state, a frictional force-displacement response with zero dilation is resulted (Itasca 2016). Therefore, neither PBM nor

SJM can exhibit a cohesive softening response after the yield limit. Notice that using PBM and SJM as GBM contact models may demonstrate satisfactory match with the physical specimen (e.g. Hofmann et al. (2015a), Bahrani et al. (2014), and Liu et al. (2018)), and can still be employed in GBM studies. However, augmenting the force-displacement laws of the PBM and SJM with a gradual softening response, which observed in the experimental tests (Hajiabdolmajid et al. 2002; Morgan et al. 2013), allows us to achieve a more realistic phenomenological constitutive model for simulating the cracking response of crystalline rocks.

To the best author's knowledge, no comprehensive GBM study considered the effect of rock joint on the fracture behaviour of polycrystalline rocks. It is, therefore, necessary to understand the influence of surface roughness and boundary condition on the asperity damage mechanism of brittle rock at mineralogical scale. The research on the influence of rock texture on the macroscopic behaviour of polycrystalline rocks is limited to intact rock (Hofmann et al. 2015a; Peng et al. 2017). Therefore, it is necessary to carry out a more comprehensive GBM study to investigate the influence of grain size on the macroscopic fracture and mechanical behaviour of pre-cracked polycrystalline rocks.

Table 2.4 The recent PFC-GBM studies

Author(s)	Research focus	Contact models
Hofmann et al. (2015a)	Investigating the influence of mineralogical factors on mechanical and fracture behaviour of Aue granite	PBM: intra-grain SJM: inter-grain
Bahrani et al. (2014)	Simulation of the laboratory response of both intact and granulated marble	PBM: intra-grain SJM: inter-grain
Bewick et al. (2014c)	Studying the rupture characteristics of non-jointed intact rock	PBM: intra-grain SJM: inter-grain
Liu et al. (2018)	Investigating the influence of heterogeneity on fracture behaviour of polycrystalline intact rock	PBM: intra-grain SJM: inter-grain
Peng et al. (2017)	Studying the influence of particle and grain size on the mechanical and fracture behaviour of polycrystalline intact rock	PBM: intra-grain SJM: inter-grain
Zhou et al. (2019)	Simulating the failure behaviour of Alxa porphyritic granite	FJM: intra-grain SJM: inter-grain

2.5 Summary

In summary, this chapter has reviewed the previous laboratory and numerical studied related to the following topics:

1- The shear performance of bolted rock joints subjected to shear load and combined pull-shear load.
2- The effect of CNL and CNS condition on the shear behaviour of bolted rock joints.
3- The shear behaviour of the bolt-grout interface.
4- The influence of surface roughness on the shear behaviour of rock joints.
5- The shear behaviour of infilled rock joint.
6- The simulation of polycrystalline rock using PFC-GBM approach.

A summary is given below:

1- The most common methods for studying the shear behaviour of bolted rock joints are reviewed and their shortcoming is discussed. It is mentioned that the understanding of the shearing mechanism of bolted rock joints under CNS condition requires further investigation.
2- It is highlighted that the current laboratory investigations on bolted rock joints ignore the combined pull-shear load. It is also discussed that the optimum pre-tension load at which the bolted rock joint exhibit its maximum shear strength should be identified during rock bolt testing. This is a critical parameter in the field, which allow the engineers to come up with an effective bolting design scheme and prevent the possible roof collapse.
3- The literature review revealed that the current DEM-based interface constitutive models require further improvement to reproduce the gradual softening response of the bolt-grout interface effectively. It is necessary to achieve an accurate pre-tension stress level during the pull-out test.
4- The current empirical rock joint models suffer from an accurate prediction of rock joint shear behaviour due to neglecting the asperity damage and geomorphological characteristics of rock joints. The review of numerical studies revealed that DEM approach is a promising tool for capturing the shear behaviour of rock joints. It is also concluded that the current DEM approach needs to be augmented with a softening model to prevent abrupt breakage of bonded contacts at the onset of failure.

5- In previous DEM modelling of rock joints, the effect of microstructural properties of polycrystalline rock was ignored. It is discussed that the asperity damage mechanism, which is controlled by grain crushing at mineralogical scale, can be captured by GBM approach. It is also concluded that the influence of surface roughness and CNL and CNS conditions on the asperity damage mechanism of jointed polycrystalline rocks require further investigation.

6- The review of current empirical models showed that they depend on many empirical ratios and parameters for predicting the shear behaviour of infilled rock joints. These empirical factors are hard to be accurately measured or even controlled in the laboratory, and thus increase the level of uncertainty during design. The previous DEM studies neglect the cohesive response of infill (e.g. in the case of clay-infilled rock joint). The applicability of the cohesive model in reproducing the shear behaviour of infilled rock joints has not been studied in the literature. As a result, further improvement and validation are still needed.

7- The previous studies highlighted the importance of discontinuities (e.g. defects, pre-existing cracks, and etc.) on the mechanical behaviour of polycrystalline rocks. The literature review also mentioned that the microstructural properties (e.g. grain size) play an essential role in the fracture behaviour of polycrystalline rocks. Therefore, a comprehensive study is required to further investigate the effect of rock texture on the macroscopic response of pre-cracked granite.

Chapter 3: Discrete element based cohesive model

3.1 Rock mass numerical modelling

Advanced numerical techniques have been widely employed by many scientists since the 1960s. Numerical simulations have the potential to augment our understanding of various failure mechanisms of rock. Once it is accurately calibrated, a numerical framework can perform as a virtual laboratory that can be applied to investigate the influence of various parameters on the mechanical behaviour of rock specimens. Numerical modelling has the capability to replicate an extremely arduous laboratory process, or it can be adapted to conduct numerical experiments, which are impossible in the laboratory environment (e.g. Zhao (2013)). In rock mechanics and mining engineering, the numerical approach can be used to modelling of rock mass failure response to engineering practices in various field environments, leading to an enhanced comprehension of damage process and hence enabling the mining engineers to come up with a coherent design procedure.

Rock mass is defined as a Discontinuous, Inhomogeneous, Anisotropic, and Non-Elastic (DIANE) (Harrison and Hudson 2000). "Material conceptualization" is the essential part of every computational method, which can explicitly or implicitly reproduce the mechanical behaviour of rock discontinuities (Jing 2003). There are two different categories of numerical methods defined in the literature based on conceptualization and simulation of the mechanical and deformation behaviour of jointed rock mass: continuous, and discontinuous models (Jing 2003). Hybrid continuum/discontinuum models also can be used as an alternative when the application of other method is restricted. The widespread numerical techniques that can be used in rock engineering problems can be classified as (Jing 2003):

- **Continuum methods**: finite element method (FEM), finite difference method (FDM) and boundary element method (BEM)
- **Discontinuum methods**: discrete element method (DEM), discontinuous deformation analysis (DDA) and discrete fracture network (DFN) methods
- **Hybrid methods**: hybrid FEM/BEM, hybrid BEM/DEM, hybrid FEM/DEM and other hybrid models.

The mechanical behaviour of discontinuities (e.g. rock joints, faults, etc.) can be simulated by discontinuous models, while the deformability and failure behaviour of rock can be considered as a continuous medium. The selection of appropriate methodology for simulating a rock engineering problem highly depends on the size and scale of the project (Bobet et al. 2009).

Fracture system geometry is another essential parameter that can influence the choice of numerical technique (Jing 2003). In Figure 3.1, the alternative methods for various fracturing condition in a typical rock mechanics problem is illustrated. When no fracture is involved in the problem or the rock mass is highly fractured, the continuum approach can be used for simulating purposes (Figure 3.1a). In the case of a highly fractured medium, a set of equivalent continuum properties obtained through homogenization process should be considered (Figure 3.1d). The continuum method can be adopted in the case of no fracture opening and no complete rock block formation (Figure 3.1b). The discontinuous models can be used when the separated rock blocks are observable, and the number of fracturing systems is too large to be modelled by a continuum approach (Figure 3.1c).

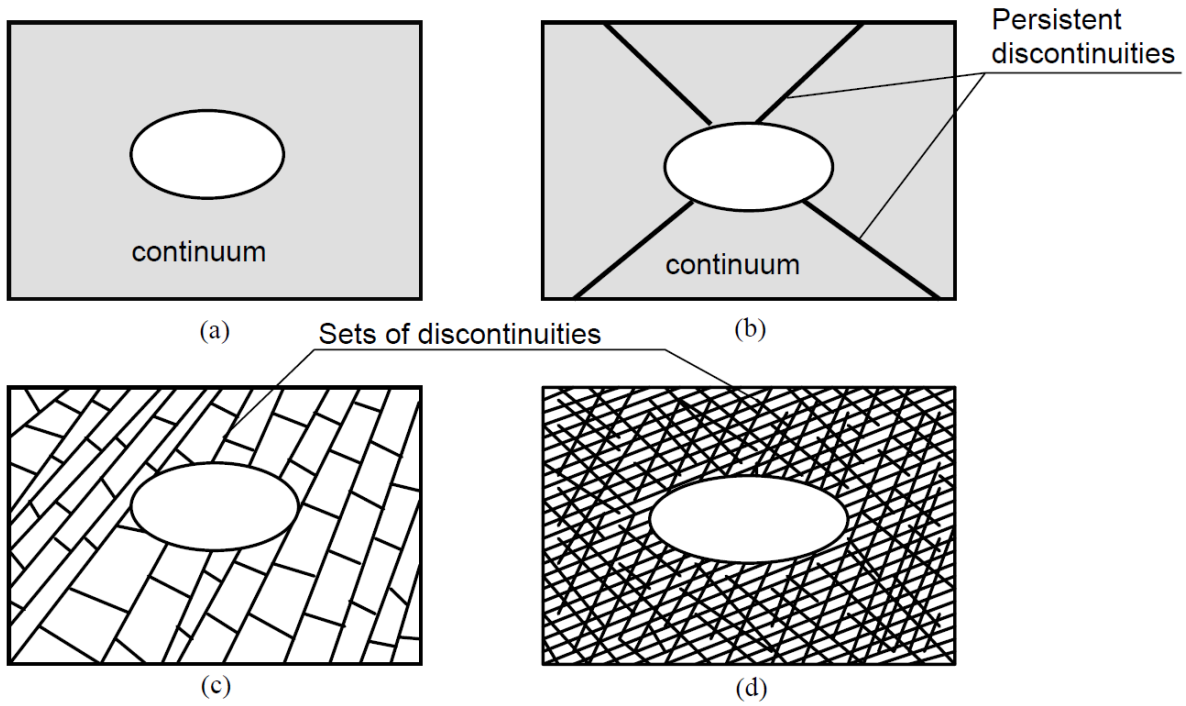

Figure 3.1 Various field circumstances that influence the selection of numerical models (Jing 2003). (a) Continuum model. (b) Either continuum model with fracturing system or discontinuous method. (c) Discontinuous method. (d) Continuum model with equivalent properties

It should be noted that modelling highly fractured rock mass requires high-performance computational system, as otherwise, the modelling process would be extremely time-consuming. While using a discontinuous approach in such circumstance may provide a reasonable outcome, it is somewhat restrictive to adopt a computationally demanding method for reproducing the rock mass behaviour in rock engineering design. The remedy, however, is to employ hybrid methods or multiple code processing techniques in practice. For instance,

Lorig and Brady (1984) proposed a numerical framework by which the far-field rock could be simulated using the BEM, and the near-field rock could be characterized by a series of discrete element blocks formed due to the interaction of rock joints. Their hybrid BEM-DEM is presented in Figure 3.2.

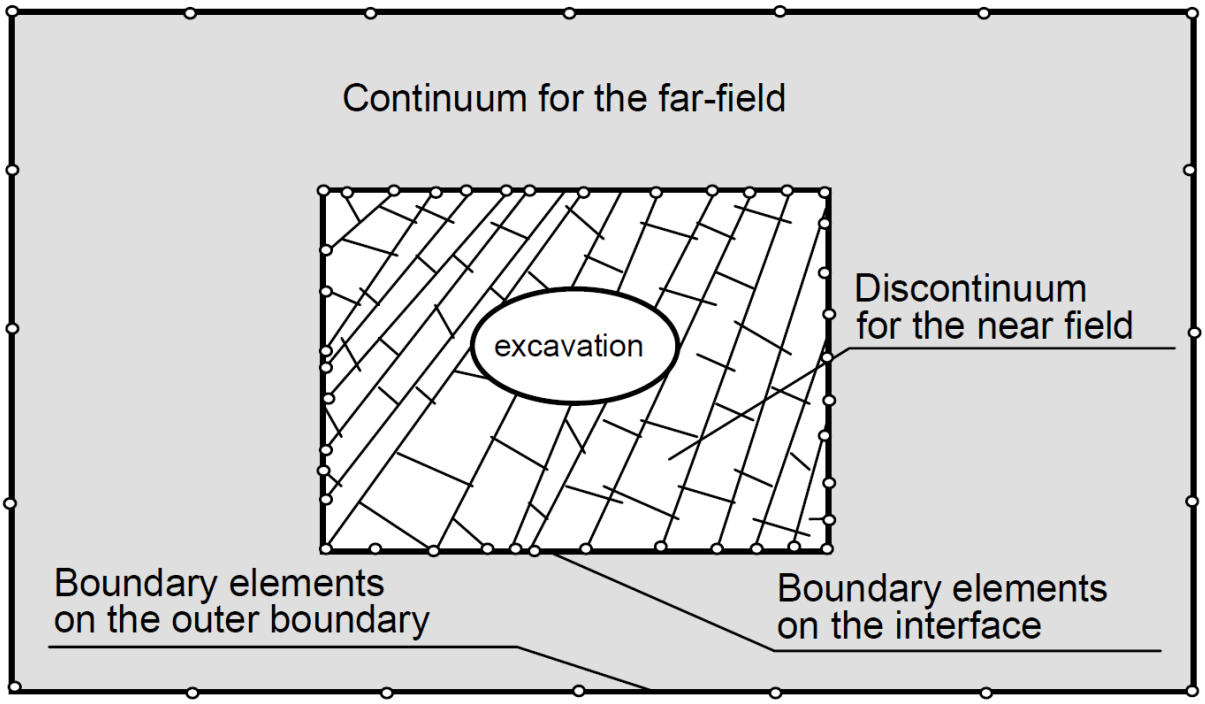

Figure 3.2 Hybrid method for simulating the stability of an underground opening excavated in a discontinuum media. DEM is used for the near-field zone, and BEM for the far-field area (Jing 2003).

3.2 Distinct element method

The distinct element method (DEM) has been a promising, widely used computational technique in rock mechanics for many years. Three main characteristics are considered in DEM simulations, namely: representation of contact between two DEM particle (or element), solid material representation, and detection of newly emerged contacts throughout the computational process (Cundall and Hart 1992). At every computational time-step, the mechanical properties of rigid DEM elements (e.g. position, velocity, and contact force) is updated according to Newton's second law as well as the force-displacement law (Zhao 2017).

Cundall (1971) developed the DEM to numerically simulate the progressive displacement of rock blocks in a 2D approach. In 2D modelling, PFC2D and UDEC and in 3D modelling PFC3D and 3DEC are the most popular computer codes. UDEC and 3DEC were originally developed to simulate the mechanical behaviour of discontinuities by improving the ability of

the original Cundall's work. An internal finite element analysis is implemented in these codes to account for the deformability of discrete elements (i.e. rock blocks).

3.2.1 Influence of scale in DEM

In general, DEM modelling can be employed to simulate both large scale structures (e.g. underground tunnels, mining roadways, etc.), and laboratory scale testings (e.g. direct shear test). In Figure 3.3, the numerical simulations using commercial DEM codes (UDEC and PFC2D) are depicted. In 2D, general concave or convex polygons can be constructed to represent discrete elements, with a finite number of straight edges (Jing 2003). The rock blocks in large scale simulations (i.e. Figure 3.3a), are formed due to the interaction between individual fractures. Fracture systems in large scale simulations can be either generated individually or by a random fracture generator that requires geometrical properties of rock joints (e.g. dip, dip direction, spacing, etc.). The deformation behaviour of rock blocks in large scale problem can be achieved by dividing the area of the polygons to zones. This process is known as mesh generation in DEM. An example of constant strain triangles in 2D is illustrated in Figure 3.4. A rock joint constitutive model is required to be assigned on the contacts between discrete elements to replicate the mechanical and shear behaviour of highly jointed medium. Therefore, in order for the numerical model to become realistic, the factors influencing the shear behaviour of rock joint should be incorporated in the constitutive relationships.

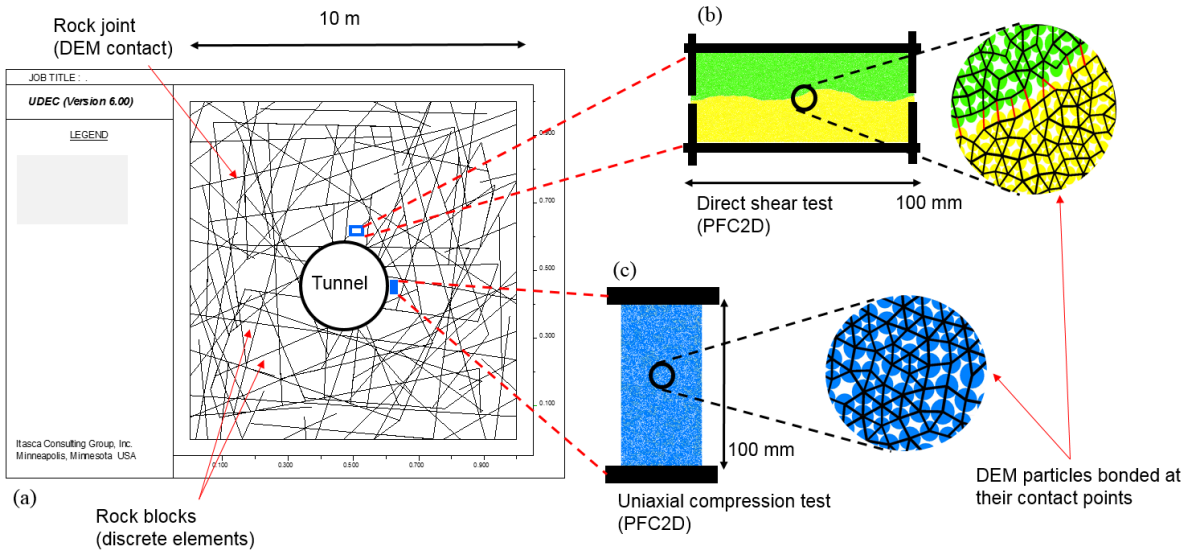

Figure 3.3 Influence of scale in DEM simulations a) A tunnel excavated in highly jointed rock mass simulated in UDEC, b) DEM direct shear test in PFC2D, c) DEM uniaxial compression test in PFC2D.

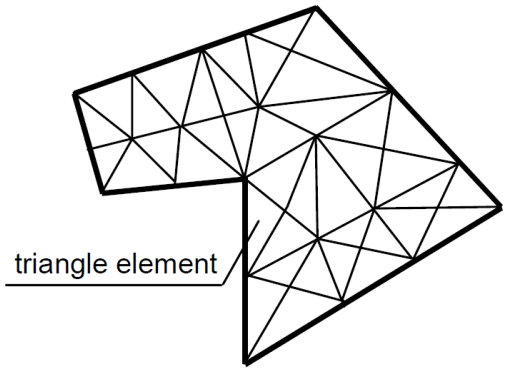

Figure 3.4 An example of mesh generation in DEM large scale simulation.

Simulating laboratory condition in DEM is rather different. PFC2D is a common DEM code that can be used to generate synthetic rock specimens for laboratory scale testing. Different boundary conditions can be assigned on the numerical specimens to simulate any desired experiment. In laboratory scale simulations, DEM particles should be bonded together via a system of spring with shear and normal stiffnesses, thus allowing transmission of force within DEM balls (Lisjak and Grasselli 2014). In Figure 3.3b and c, an example of a particle assembly generated in PFC2D is depicted. Each individual DEM particle can interact with its neighbouring counterpart via contacts. In such DEM framework, a contact constitutive model that accounts for the phenomenological response of the material should be assigned on the contacts. For instance, in Figure 3.3b and c parallel bond model (PBM) (Potyondy and Cundall 2004) is employed. Figure 3.5 illustrates a set of DEM particles bonded together using PBM. It can be seen from Figure 3.3b and c that surface roughness and irregularities of rock joint can be incorporated in DEM simulations. In such modelling, an additional constitutive model is required to mimic the mechanical behaviour of the interface between two rock blocks. This was achieved by developing the smooth-joint model (SJM) (Pierce et al. 2007) which performs as an interface contact constitutive model allowing the DEM particles to overlap and pass through each other instead of restricting them to move around one another (Bahaaddini et al. 2013).

Although there is no restriction in the model size for large scale simulations, an effective zone around the underground excavation is required to be defined to avoid extra computations. In small scale simulations, depending on the microstructural approach followed in model construction, the size of the model can be reduced as far as the macroscopic behaviour of the model is comparable with the laboratory counterparts.

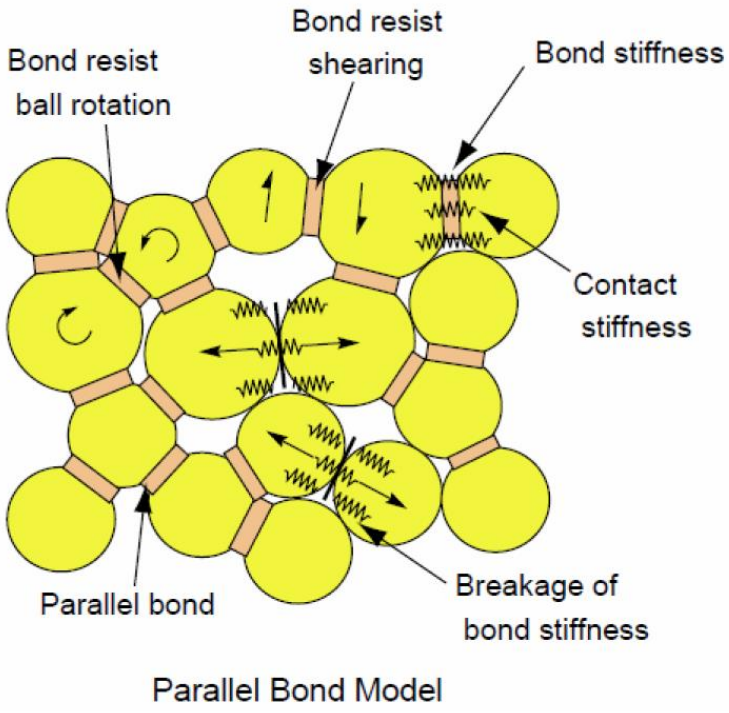

Figure 3.5 Illustration of DEM particles and their contacts: parallel bond constitutive model is assigned on the contacts (Cho et al. 2007).

3.3 DEM background for modelling cohesive materials

The DEM was firstly proposed by Cundall and Strack (1979) to study the mechanical behaviour of granular materials. The cohesive materials can be simulated as an assembly of rigid balls moving and interacting with each other at their contacts. A brief DEM background is presented in this section to show how a cohesive contact model can be incorporated in DEM to simulate the mechanical behaviour of the cohesive materials. The following sub-sections (1-1 and 1-2) can also be found in Potyondy and Cundall (2004), Nguyen et al. (2017a), and Nguyen et al. (2017b) and more comprehensively in Itasca (2016).

3.3.1 Law of motion

In DEM simulations, the governing equations are based on Newton's second law of motion. The resultant forces and moments acting upon a rigid particle can be described by two distinct components, the translational and rotational acceleration:

$$\vec{F}_i = m_i(\vec{u}_i - \vec{g}) \tag{3.1}$$

$$\vec{M}_i = \vec{\omega}_i I_i \tag{3.2}$$

where i denotes the order of particles in a particle assembly; $\vec{u}_i$ is particle acceleration, ω_i is the rotational velocity of particle; I_i is the inertia tensor; $\vec{g}$ is the body force acceleration vector (e.g., gravitational loading); and F_i and M_i are the resultant force and moment, respectively. The vectorial summation of all forces and moments acting upon a particle can be determined to calculate the resultant forces and moments as:

$$\vec{F}_i = \sum_j \vec{F}_{ij} + \vec{F}_i^{app} = \sum_j (\vec{F}_{ij}^n + \vec{F}_{ij}^s) + \vec{F}_i^{app} \tag{3.3}$$

$$\vec{M}_i = \sum_k \vec{F}_{ij}^s r_{ij} + \vec{M}_i^{app} \tag{3.4}$$

where r_{ij} is the distance from the centre of particle *i-th* and the contacting point of particle *i-th*. F_{ij}^n and F_{ij}^s are the normal and shear forces in the local coordinate system of the contact between particle i and j, respectively. $\vec{F}_i^{app}$ and $\vec{M}_i^{app}$ are the forces and moments applied on the particle i-th. The resultant forces and moments are illustrated in Figure 3.6a. Figure 3.6b illustrates the interactions between DEM particles in both force-displacement and stress-displacement forms.

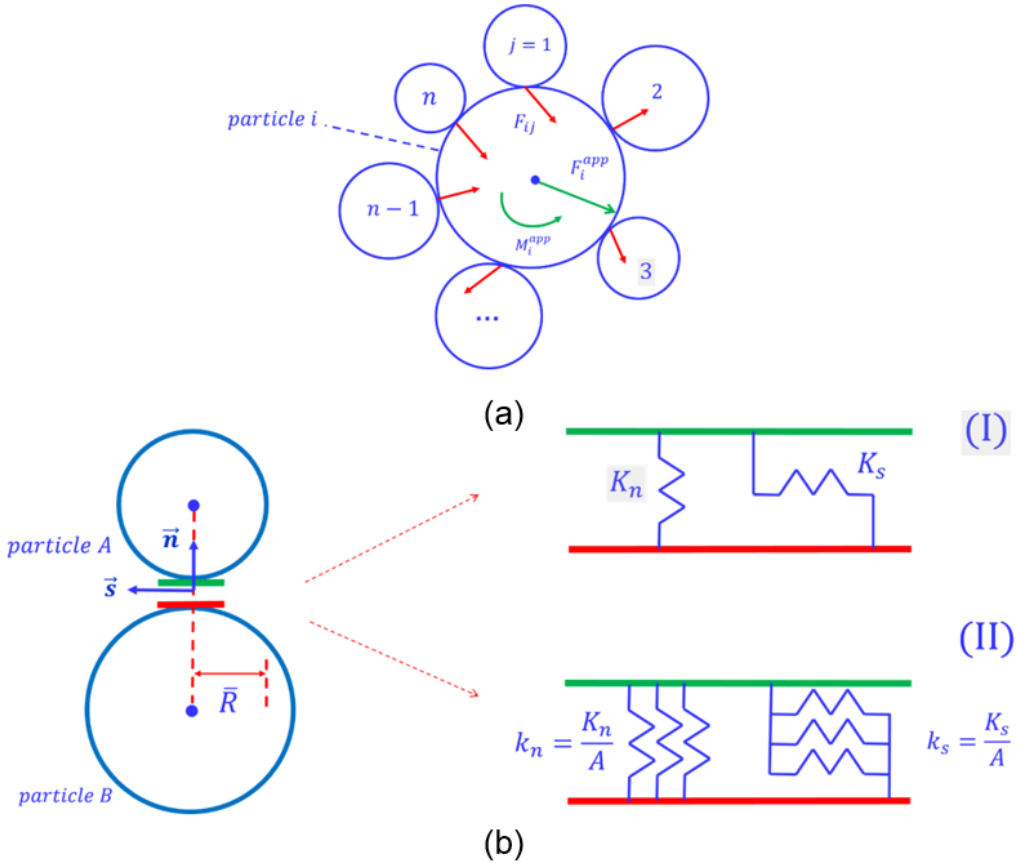

Figure 3.6 Graphical illustration of DEM. (a) Force and moments acting upon a DEM particle (Modified from Nguyen et al. (2017a)). (b) Interaction between bonded contact: (I) force-displacement form, and (II) stress-displacement form.

The equations of motions in DEM are dynamic-based accumulating kinetic energy in the system during the numerical simulation. In the DEM codes used in the present study (PFC2D) mechanical damping and local damping are considered to dissipate the dynamic energy. The same approach suggested by Potyondy and Cundall (2004) was adopted in this research to dissipate the kinetic energy and damp out the resulting acceleration of particles. The damping force and moment applied to each particle are proportional to the total forces and moments and can be added to the equation of motions such that the damped equations can be calculated as:

$$\vec{F}_i^{damp} = -\alpha(\vec{F}_i + m_i\vec{g})sign(\vec{u}_i) \tag{3.5}$$

$$\vec{M}_i^{damp} = -\alpha\vec{M}_i sign(\vec{\omega}_i) \tag{3.6}$$

where α is a nondimensional parameter known as global damping coefficient. A global damping of 0.7 is suggested to be sufficient in DEM (Potyondy and Cundall 2004) for

dissipating the kinetic energy and remaining under quasi-static equilibrium condition during the numerical simulation.

3.4 Constitutive relationships

In DEM simulation, the macroscopic failure behaviour is controlled by the contact constitutive models. Hence, the failure characteristics of the material, i.e. gradual softening, must be appropriately incorporated in the contact model.

We developed a new cohesive constitutive model for this study, for simulating the failure behaviour of intra-grain contacts in DEM codes. There are a number of cohesive models available in the literature (Le et al. 2017, 2018; Nguyen et al. 2017a; Nguyen et al. 2017b) that can be used as contact models in DEM. However, this study makes an effort to reduce the number of micro-mechanical parameters that need to be incorporated into the cohesive model. This allows its users to alleviate the complexity of calibration because fewer micro-mechanical parameters need to be calibrated. Additionally, by reducing the number of micro-mechanical parameters, and by increasing the simplicity of the computational algorithm, we made the numerical simulations more time-efficient.

The relative displacement $\boldsymbol{u}(u_n, u_s)$ of the contacts is decomposed into elastic and plastic components, to account for reversible and irreversible displacements in the contacts:

$$\boldsymbol{u} = \boldsymbol{u}^e + \boldsymbol{u}^p \tag{3.7}$$

The normal and shear stresses are linked to the relative displacements of the contacts between two particles, and can be calculated as follows:

$$\sigma_n = k_n^0(u_n - u_n^p) \tag{3.8}$$

$$\sigma_s = k_s^0(u_s - u_s^p) \tag{3.9}$$

where σ_n and σ_s are normal and shear stresses in the bonding contacts; u_n and u_n^p are the total and plastic normal displacements; u_s and u_s^p are the total and plastic shear displacements; k_n^0 and k_s^0 are the normal and shear stiffnesses, respectively.

3.4.1 Yield criterion and flow rule

In the cohesive mode, a yield criterion is necessary to determine the stress states under which the contact failures occur, and plastic displacement starts to accumulate. In order to model the

contact failure under mixed-mode conditions, a simple yield function that allows the strength and friction of the contacts to be chosen independently is considered. To satisfy this requirement, and keep the model as simple as possible, the following yield function is proposed:

$$F(\sigma_n, \sigma_s, C) = \sigma_s + \mu\sigma_n - C = 0 \tag{3.10}$$

where μ is the friction coefficient of the contact, and C is defined as follows:

$$C = C^0 e^{-\kappa u^p} \tag{3.11}$$

In Eq. 3.11, C^0 is the initial cohesion of the contacts, κ is the softening parameter, and u^p is the accumulated plastic displacement of the contact that can be calculated from its increments:

$$du^p = \sqrt{(du_n^p)^2 + (du_s^p)^2} \tag{3.12}$$

In this study, a damage parameter ($0 \leq D \leq 1$), used to measure the level of the contact's deterioration, is defined as:

$$D = \frac{C^0 - C}{C^0} = 1 - e^{-\kappa u^p} \tag{3.13}$$

Note that the softening parameter may not imply a physical meaning. The parameter must be incorporated in the relationships to simplify the model (Nguyen et al. 2017a; Nguyen et al. 2017b). Later, in DEM simulations, the damage parameter (D) can be monitored for each contact. It can be illustrated graphically to evaluate the state of damage in the numerical system. $D = 0$ shows that the contact is fully bonded, and $D = 1$ shows that the contact has completely failed. The model's behaviour in modes I and II is illustrated in Figure 3.7. The linear, elastic portion of the stress-displacement curves defines the contact behaviour before failure, followed by a non-linear stage that represents contact softening that occurs due to the progressive degradation of cohesion.

During DEM simulations based on particle sliding, the dilation effect can be achieved. However, the circular shape and microstructural features of the particles are not analogous to physical materials, so that obtaining the same physical dilative response at the contact level is an arduous task. Therefore, for DEM modelling, a dilatancy parameter is necessary to account for the dilation effect of the material at the mesoscale. Considering a flow rule including a

dilatancy parameter enables us to follow the rigorous procedure of developing the model using the framework of plasticity theory. In this regard, a non-associative flow rule was defined as follows:

$$G(\sigma_n, \sigma_s) = \sigma_s + \beta\sigma_n \tag{3.14}$$

where β is the dilation coefficient. Consequently, the flow rule of incremental displacement can be expressed as:

$$du_n^p = d\lambda \frac{\partial G}{\partial \sigma_n} \tag{3.15}$$

$$du_s^p = d\lambda \frac{\partial G}{\partial \sigma_s} \tag{3.16}$$

where $d\lambda \geq 0$ is the plastic multiplier.

A semi-implicit algorithm is used to update the stress in the case of the contact's inelastic behaviour. Following this algorithm, a trial stress state is used to check if inelastic behaviour takes place, indicated by $F^{trial} = F\left(\sigma_n^{trial}, \sigma_s^{trial}, C\right) > 0$, where the trial stresses are:

$$\sigma_n^{trial} = \sigma_n + d\sigma_n^{trial} \tag{3.17}$$

$$\sigma_s^{trial} = \sigma_s + d\sigma_s^{trial} \tag{3.18}$$

In which the trial stress increments are calculated as:

$$d\sigma_n^{trial} = k_n^0 du_n \tag{3.19}$$

$$d\sigma_s^{trial} = k_s^0 du_s \tag{3.20}$$

A Taylor expansion at the trial stress state gives:

$$F^{new} = F^{trial} + \frac{\partial F}{\partial \sigma_n} d\sigma_n^c + \frac{\partial F}{\partial \sigma_s} d\sigma_n^c + \frac{\partial F}{\partial C}\frac{\partial C}{\partial u^p} du^p \tag{3.21}$$

From Eqs. 3.11, 3.16, and 3.17, we will have:

$$\frac{\partial C}{\partial u^p} du^p = d\lambda\left(-\kappa C \sqrt{\left(\frac{\partial G}{\partial \sigma_n}\right)^2 + \left(\frac{\partial G}{\partial \sigma_s}\right)^2}\right) \tag{3.22}$$

Substituting Eq. 3.23 and $d\sigma_i^c = -k_i^0 du_i^p$ (with "i" standing for "n", or "s") in 3.22, we get:

$$F^{new} = F^{trial} - d\lambda \frac{\partial F}{\partial \sigma_n} k_n^0 \frac{\partial G}{\partial \sigma_n} - d\lambda \frac{\partial F}{\partial \sigma_s} k_s^0 \frac{\partial G}{\partial \sigma_s} - d\lambda \frac{\partial F}{\partial C} \kappa C \sqrt{\left(\frac{\partial G}{\partial \sigma_n}\right)^2 + \left(\frac{\partial G}{\partial \sigma_s}\right)^2} \tag{3.23}$$

the plastic multiplier $d\lambda$ can then be obtained as solution of the equation $F^{new} = 0$:

$$d\lambda = \frac{F^{trial}}{\frac{\partial F}{\partial \sigma_n} k_n^0 \frac{\partial G}{\partial \sigma_n} + \frac{\partial F}{\partial \sigma_s} k_s^0 \frac{\partial G}{\partial \sigma_s} + \frac{\partial F}{\partial C} \kappa C \sqrt{\left(\frac{\partial G}{\partial \sigma_n}\right)^2 + \left(\frac{\partial G}{\partial \sigma_s}\right)^2}} \tag{3.24}$$

The corrective stresses is determined as:

$$d\sigma_n^c = d\lambda(-k_n^0) \frac{\partial G}{\partial \sigma_n} \tag{3.25}$$

$$d\sigma_s^c = d\lambda(-k_s^0) \frac{\partial G}{\partial \sigma_n} \tag{3.26}$$

where $d\sigma_n^c$ and $d\sigma_s^c$ are corrective normal and shear stresses, respectively.

The total incremental stresses are finally obtained from:

$$d\sigma_n = d\sigma_n^{trial} + d\sigma_n^c \tag{3.27}$$

$$d\sigma_s = d\sigma_s^{trial} + d\sigma_s^c \tag{3.28}$$

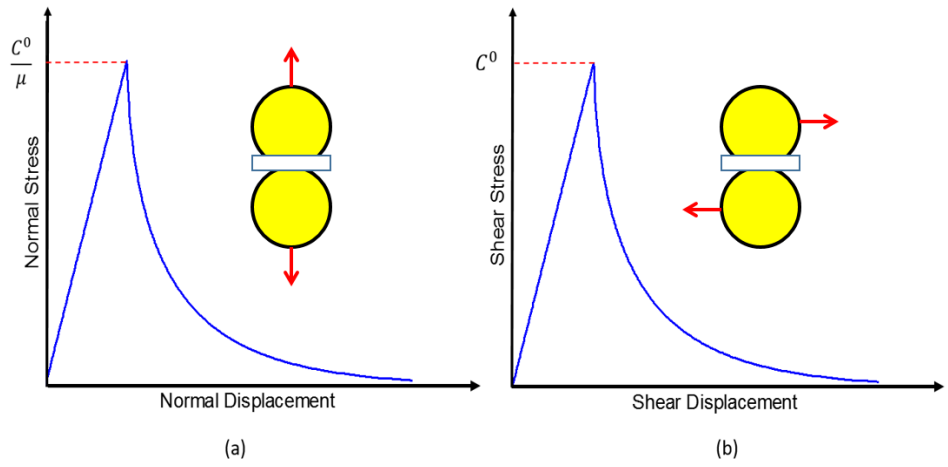

Figure 3.7 Stress-displacement behaviour of the proposed cohesive contact model in a) Mode I, and b) Mode II.

3.5 The smooth-joint model

The smooth-joint model simulates the micro-cracking behaviour of an interface in PFC software (Itasca 2016). The smooth-joint constitutive model is assigned to the DEM particles lying on the opposite side of the interface. The DEM particles intersected by this model are allowed to overlap and pass through one another. Figure 3.8 illustrates the performance of DEM particles intersected by the smooth-joint model. The orientation of the interface (Figure 3.8) in 2D is defined as the unit normal vector acting on the interface (Itasca 2016):

$$\hat{n}_j = (\sin\theta_p\,, \cos\theta_p) \tag{3.29}$$

where θ_p is the dip angle of the interface. $\hat{\boldsymbol{n}}_{\boldsymbol{c}}$ in Figure 3.8 is defined as the unit normal vector of the contact between two adjacent DEM particles. The smooth-joint interface consists of two coincident surfaces (shown as surface 1 and 2 in Figure 3.8). If and only if $\hat{\boldsymbol{n}}_{\boldsymbol{j}}.\hat{\boldsymbol{n}}_{\boldsymbol{c}} \geq 0$, then particle 2 lies in surface 2. The strength of smooth-joint contact mode is defined by the tensile strength, cohesion, and friction angle. When a smooth-joint contact fails (either in tension or shear), the contact maintain a residual strength defined by the smooth-joint friction coefficient. The details about updating the smooth-joint model force-displacement law for a bonded joint can be found in the manual of PFC2D (Itasca 2016). By employing the smooth-joint model, the existing bond between two DEM particles are removed and a set of elastic springs are assigned over a rectangular-shaped cross section. The cross sectional area of the smooth-joint model can be calculated as (Itasca 2016):

$$A^{sj} = 2\bar{R}^{sj}t \tag{3.30}$$

where t and $\bar{R}^{sj}$ are the thickness ($t = 1.0$) and radius of smooth-joint model cross-section, respectively. Note that $\bar{R}^{sj} = \lambda_r^{sj} min(R^1, R^2)$, where R^1 and R^2 are particles radii, and λ_r^{sj} is radius multiplier which is usually taken as 1.0.

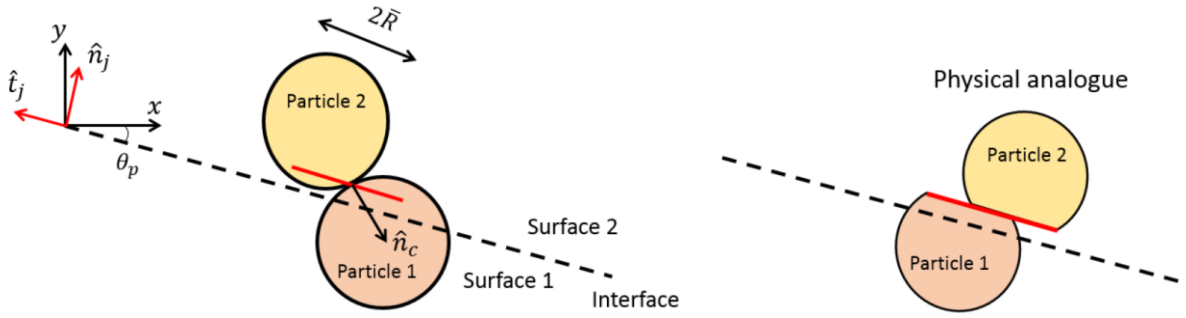

Figure 3.8 The smooth-joint model application in PFC2D (modified from (Itasca 2016)).

The constitutive relationships of the smooth-joint model was comprehensively described by Itasca (2016). A summary of the model behaviour can also be found in (Bahaaddini et al. 2013). The smooth-joint force is resolved into normal and shear forces as follows:

$$\mathrm{F}^t = -F_n\hat{n}_j + \mathrm{F_s} \tag{3.31}$$

The normal force is updated as follows:

$$F_n = (F_n)_0 + k_n^{sj} A^{sj} \Delta\delta_n^e \tag{3.32}$$

$(F_n)_0$ is the smooth-joint normal force at the beginning of the timestep, $k_n^{sj}$is the normal stiffness, A^{sj} is the bond cross-sectional area, and $\Delta\delta_n^e$ is the normal displacement increment. The trial shear force can be calculated as:

$$\mathbf{F_s^*} = (\mathbf{F_s})_\mathbf{0} - k_s^{sj} A^{sj} \Delta\delta_s^e \tag{3.33}$$

where $(\mathbf{F_s})_\mathbf{0}$ is the shear force at the beginning of the timestep, k_s^{sj} is the shear stiffness, and $\Delta\delta_s^e$ is the shear displacement increment. The shear strength of the contact can be considered as $F_s^\mu = -\mu^{sj} F_n$, where μ^{sj} is the friction coefficient of the contact. The micro-mechanical parameters that control the bond strength are tensile strength (σ_c^{sj}) and cohesion (c_0^{sj}). The shear strength of the contact is calculated from simple Mohr-Coulomb ($\tau_c^{sj} = \sigma_c^{sj} \tan\left(\varphi^{sj}\right) + c_0^{sj}$). The force-displacement law for a bonded contact is illustrated in Figure 3.9. When the bond is not in tension, the shear force is limited by:

$$\mathrm{F_s} = \begin{cases} \mathrm{F_s^*} & , \|\mathrm{F_s^*}\| < F_s^\mu \\ F_s^\mu \left(\mathrm{F_s^*} \Big/ \|\mathrm{F_s^*}\| \right), & otherwise \end{cases} \tag{3.34}$$

If $F_n \geq \sigma_c^{sj} A^{sj}$, then the contact fail in tension mode (Figure 3.9a) and $F_n = |\mathbf{F_s}| = 0.0$; otherwise if $|\mathbf{F_s^*}| \geq \tau_c^{sj} A^{sj}$ the contact is broken in shear mode, and the shear force of the contact is updated by Eq. 32 (Figure 3.9b).

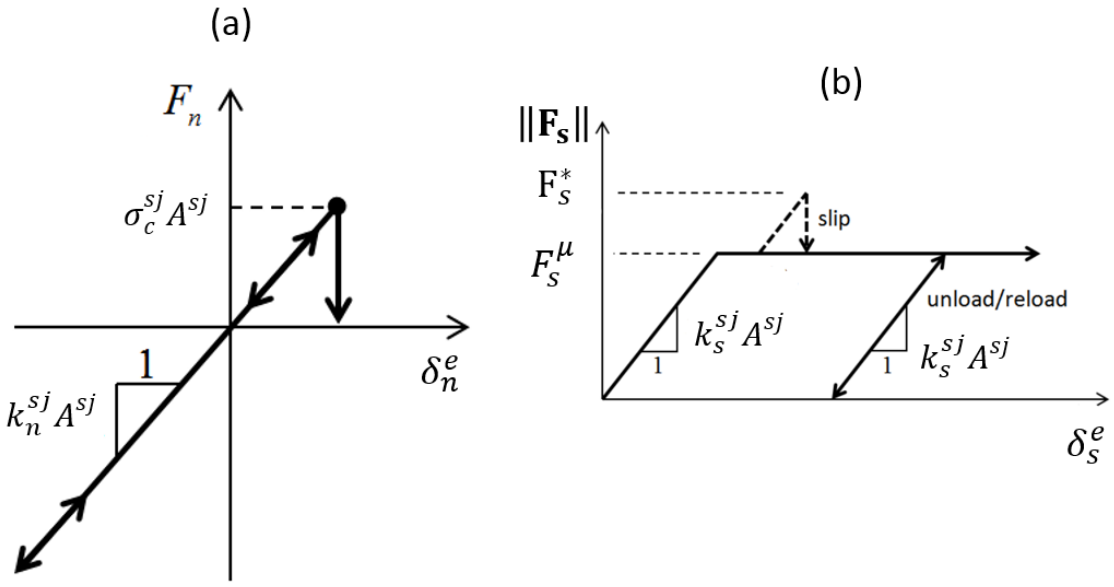

Figure 3.9 Force-displacement law in the smooth-joint model a) Normal force versus normal displacement, b) Shear force versus shear displacement (modified from (Itasca 2016)).

3.6 Implementation of the proposed model in DEM codes

The cohesive model in the present study was developed based on a generic plasticity framework. The constitutive relationships were developed based on stress and displacement of DEM contacts. The proposed cohesive model was implemented in C++ and compiled as a dynamic link library (DLL) files that could be loaded in PFC2D whenever needed. In the implementation algorithm developed in C++, the DEM forces were converted to stresses according to bond cross-sectional properties. This was necessary to measure the F^{trial} in every time-step. This implementation approach was successfully followed by other researchers (e.g. (Nguyen et al. 2017a; Nguyen et al. 2017b)).

The bond cross-sectional area ($\bar{A}$) in two dimensional space is defined as (Itasca 2016):

$$\bar{A} = 2\bar{R} \tag{3.35}$$

where $\bar{R}$ is defined as:

$$\bar{R} = \begin{cases} \min(R^1, R^2), ball - ball \\ R^1 \qquad\qquad , ball - facet \end{cases} \tag{3.36}$$

R^1 and R^2 are the radius of two adjoining particles that come into contact. Potyondy and Cundall (2004) proposed a deformability method, in which the normal stiffness of the contacts (k_n^0) can be related to the elastic modulus of the contact ($\bar{E}_c$) as follows (Itasca 2016):

$$k_n^0 = \frac{\bar{E}_c}{L} \tag{3.37}$$

where L can be determined as follows:

$$L = \begin{cases} R^1 + R^2, ball - ball \\ R^1 \quad\quad , ball - facet \end{cases} \tag{3.38}$$

During the calibration procedure normal to shear stiffness ratio k_n^0/k_n^0 was initiated to determine the shear stiffness of the contacts (k_n^0(Hofmann et al. 2015a; Liu et al. 2018). In C++ algorithm the contact deformability method was adopted to obtain shear and normal stiffness of the contacts which were necessary to calculate σ_n and σ_s from Eqs. 3.8 and 3.9, respectively.

The proposed cohesive model can be either employed as material contact model (e.g. rock and grout) or interface contact model (e.g. bolt-grout interface). The model was called a cohesive contact model (CCM) when it was used as a material model, and the microproperties of the model contained a subscript of CCM (e.g. C_{CCM}^0). We implemented the proposed model in the force-displacement law of the SJM to develop a cohesive interface model. The cohesive interface model was called cohesive smooth joint model (CSJM), and the microproperties of the model contained a subscript of CSJM (e.g. C_{CSJM}^0). Notice that the rock joint interface behaviour was simulated using the SJM.

The CCM and CSJM are separately solved in the simulations. In DEM modelling, the calculations alternate between the application of Newton's second law to the DEM balls and a force-displacement constitutive model at the contacts. The motion of DEM particles is determined by Newton's second law, while the constitutive model is used to update the contact forces arising from the relative motion of the balls at the contact locations (Itasca 2016). When updating the ball kinematics or when solving the constitutive laws at the contacts at a given time, each ball or each contact is processed independently, therefore any modification in the contact force, for instance, is not propagated instantaneously and does not affect neighbouring

contacts within the same iteration. Instead, any change in the system will potentially alter the model state for the next iteration. In the GBM framework, the forces arising from the relative motion of inter-grain contacts are updated via the CSJM, while the forces arising from the relative motion of intra-grain contacts are updated via the CCM.

In chapter 4, the CCM was employed to simulate the failure behaviour of the rock-like material and grout. The CSJM was used to mimic the shear behaviour of the bolt-grout interface. In chapter 5, the CCM was used to simulate the shear behaviour of infilled rock joints. In chapters 6, 7, and 8, the CCM was employed as the constitutive model of intra-grain contacts. In chapter 7 and 8, the SJM was used to simulate the cracking behaviour of inter-grain contacts. Notice that the aim of chapter 6 was to develop a cohesive GBM approach to reproduce the damage behaviour of polycrystalline rocks, thus the CSJM, as a cohesive interface model, was used to simulate the fracture behaviour of grain boundary contacts. In chapter 6, SJM was employed to simulate the shear behaviour of rock joint interface.

3.7 Summery

In this section, the mathematical formulation of the prosed cohesive contact model is introduced. The model is developed based on the principles of plasticity theory and damage mechanics. Only a single parameter is defined in the model (C^0) to control the contact strength, which reduces the complexity of the model formulation and hence makes the DEM simulations computationally efficient. A commercial DEM software package, PFC2D software, is used to implement the model. The common approach for implementing the use-defined contact models in PFC is to develop the stress-return algorithm in C++, and compile the codes as a Dynamic Link Library (DLL) file. The DLL file can be executed whenever required during the simulation process. Two model frameworks, CCM and CSJM are developed in PFC2D. CCM can be used as material model (e.g. rock, concrete, and grout) and CSJM can be used to simulate the interface between two materials such as bolt-grout interface or grain boundaries in crystalline rocks. The main advantage of the proposed cohesive model over current contact models (e.g. PBM) is that it reproduces the cohesive response of the contact when the maximum contact strength is reached. This feature allows us to correctly simulate the behaviour of geomaterials (e.g. crystalline rock and grout) at microscopic scale.

Chapter 4: The performance of fully grouted rock bolts subjected to pull-shear load under CNS condition

4.1 Introduction

Fully grouted rock bolt has been widely used as a reinforcement element in underground mining due to its economic benefits and advancement in the bolt system technology. The installation of rebar bolts can remarkably increase the inherent shear resistance of fractured rock mass (Ma et al. 2017). The load transfer capacity of fully grouted rock bolts is largely controlled by the shear strength of bolt-grout interface and the mechanical interlocking between the grout and rock bolt ribs (Cao et al. 2014; Li et al. 2019a; Ma et al. 2017; Shang et al. 2018a). The field observations revealed that the failure of rock bolt occurs due to a combination of both pull-out and shear forces (Li et al. 2016c). The main difficulty in the experimental study of bolted rock joints involves undertaking combined pull-shear loads tests. The frequency of combined pull-shear tests is limited due to difficulty in experimental test setup and cost and is limited to non-jointed specimens. The pull-out force can enhance the shear resistance of the bolted rock joint. However, finding an optimum value of pull-out force at which the bolting system exhibits its ultimate performance is still an issue in the field. In-situ tests are relatively expensive and are usually employed to measure the pull-out capacity of rock bolts.

Numerical modelling can provide a promising tool to investigate the shear behaviour of bolted rock joints. The DEM technique provides an opportunity for the user to incorporate the damage mechanisms into the force-displacement law of the contact to achieve a more realistic numerical framework. The actual surface roughness of rock joint can also be imported into DEM codes which allows the user to observe the asperity damage process numerically.

The objective of this chapter is to investigate the effect of contributing parameters on the behaviour of a bolted rock joint subjected to combined pull-and-shear loading using DEM approach. For simulating the fracture behaviour of grout material and bolt-grout interface in a better way, the proposed cohesive model introduced in chapter 3 was employed. The proposed contact model was incorporated in the force-displacement law of the SJM to handle the cohesive behaviour of the bolt-grout interface. The proposed model was also used as a cohesive contact model to model the fracture behaviour of rock and grout materials. The capability of the proposed model to capture the fracture behaviour of grout and bolt-grout interface was validated by uniaxial compression, and direct shear tests. In addition, the proposed modelling method was employed to simulate the asperity degradation of idealised saw-toothed rock joints.

A comparison was made between experimental and numerical results to observe the accuracy of DEM simulations. To further demonstrate the potential of the proposed cohesive DEM framework for characterising the mechanical behaviour of bolted rock joints subjected to combined pull-shear load, a stepwise pull-shear test (SPST) scheme was developed by which the influence of pretension load, rib angle, and CNS boundary condition on the ultimate shear resistance of rock joint was investigated. The proposed cohesive modelling method and SPST approach provided new insight into the shear behaviour of bolted rock joints, which was an extremely arduous task to achieve in the laboratory.

4.2 Calibration of the proposed cohesive DEM approach

The microproperties introduced in chapter 3 have to be calibrated prior to comparing the results of the cohesive DEM framework with the experimental counterparts. The selection of an appropriate set of micro-properties is a necessary step in DEM simulation. The typical method for calibrating the micro-parameters in PFC-DEM is to employ the results of a uniaxial compressive test of a physical specimen and reproduce the macroscopic behaviour of the physical specimen (Bahaaddini et al. 2013; Gutiérrez-Ch et al. 2018). In the present study, it was necessary to use the laboratory results of rock-like and grout materials for calibration purposes. The details of mortar content and its physical properties can be found in the studies conducted by Oh et al. (2017) and Li et al. (2016e). The macroscopic properties of grout were taken from the experimental work of Shang et al. (2018a). To calibrate the microproperties of SJM and CSJM, direct shear test and normal deformability tests on smooth interfaces were conducted in PFC2D. The model setup and boundary conditions in the calibration tests are illustrated in Figure 4.1.

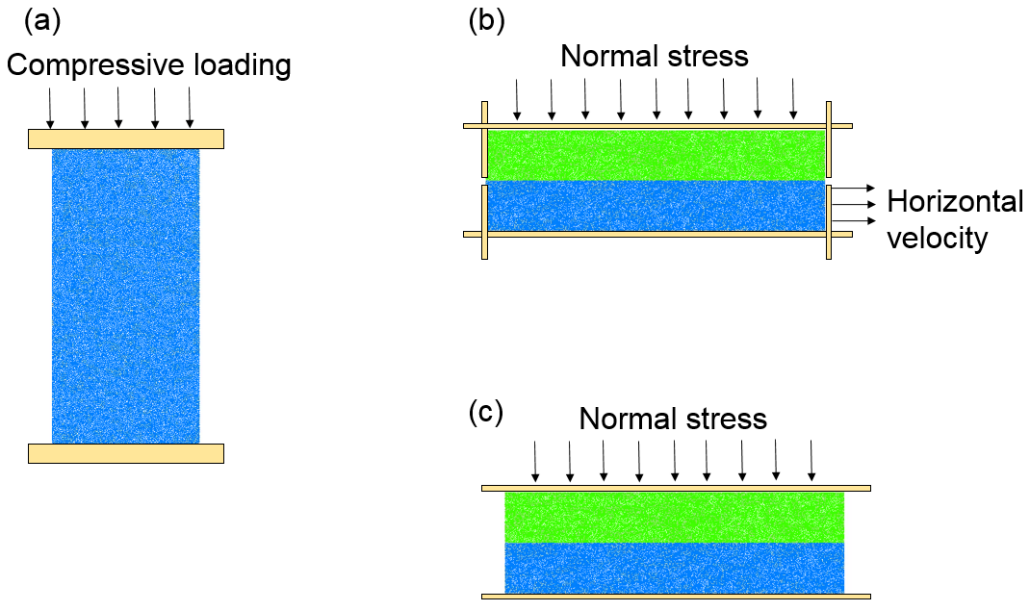

Figure 4.1 Numerical test setup for the calibration process. (a) Uniaxial compression test. (b) Direct shear test (planar rock joint). (c) Normal deformability test (planar rock joint).

4.2.1 Calibration of rock-like and grout-like materials

In this subsection, we present the calibration of micro-mechanical parameters for rock and grout. Since the calibration procedure for both materials was similar, only the calibration procedure for rock-like material is described in detail. The same approach was followed for calibrating the micro-properties of the grout material.

The dimension of a physical specimen for uniaxial compressive test was 100 in height and 40 mm in width. The same dimensions were created in PFC2D. The minimum particle radius (r_{min}) was chosen to be 0.25 mm, and the ratio of the maximum particle radius (r_{max}) to minimum particle radius (r_{min}) was considered to be 1.66. We employed the inverse calibration method to obtain the micro-mechanical properties of the cohesive model. These microproperties included C^0_{CCM}, μ_{CCM}, β_{CCM}, $\bar{E}_{c,CCM}$, k^*_{CCM}, and κ_{CCM}, which needed to be selected in an iterative process to reproduce a desired numerical response that matched the physical properties obtained from the laboratory testing.

In the present study, we employed the contact deformability method which is proposed by Potyondy and Cundall (2004) to calibrate $\bar{E}_{c,CCM}$. The first process involved matching the macroscopic Young's modulus with its experimental counterpart. The linear elastic behaviour of the DEM specimen is controlled by $\bar{E}_{c,CCM}$ and k^*_{CCM}. We altered these two parameters to match the macroscopic Young's modulus. Notice that, during the calibration of the linear

elastic stage the contact strength (C_{CCM}^{0}) was considered to be high enough to avoid any possible damage in the specimen. The next step is to calibrate the Poisson's ratio (υ) which is controlled by k_{CCM}^{*}. This parameter was calibrated in an iterative procedure with the first stage of calibration. Finally, the UCS of the model was reproduced by altering C_{CCM}^{0}, μ_{CCM}, β_{CCM}, and the softening parameter (κ_{CCM}). The strength of the cohesive contacts was controlled by C_{CCM}^{0}, and the softening parameter (κ_{CCM}) controls the softening behaviour of the contacts during post-peak stage. The friction coefficient of the contacts (μ_{CCM}) also influences the strength of the contacts, which in the macroscopic scale can control the UCS of the model. Thus, C_{CCM}^{0}, κ_{CCM}, and μ_{CCM} were chosen in to match the numerical UCS to the experimental observation.

It should be mentioned that the dilation coefficient of the cohesive contacts (β_{CCM}) is associated with the dilatancy angle of the bonds between cement bridges at the macroscopic scale, which is a local parameter and can only be measured using sophisticated laboratory observations. However, as an alternative approach proposed by Nguyen et al. (2017a), this micro-mechanical parameter can be calibrated by fitting it with the laboratory data (i.e. UCS test). We must emphasise that such local parameters are necessary to be incorporated in DEM based cohesive models to maintain the theoretical framework of plasticity theory (Nguyen et al. 2017a; Nguyen et al. 2017b). According to Nguyen et al. (2017a) such local parameters can be assumed equal to their macroscopic counterpart, but a parametric study is required to examine how sensitive is macroscopic behaviour to this micro-property. Unfortunately, the macroscopic dilation angle of the experimental specimen was not available for this study (Oh et al. 2017). Therefore, to calibrate β_{CCM}, we used a value of 0.2 was assumed and a parametric study was conducted in which this parameter was varied. The results of parametric study revealed that the change in β_{CCM} has a negligible influence on the macroscopic response (i.e. the value of UCS). This calibration approach was successfully adopted by Saadat and Taheri (2019b).

The calibrated micro-mechanical properties of the proposed cohesive model for rock-like material is given in Table 4.1, and the comparison between macroscopic numerical and physical response is provided in Table 4.2. The numerical simulation results are in an excellent agreement with the laboratory data, which means that the proposed DEM framework can reproduce the mechanical response of physical specimens.

Table 4.1 The calibrated micro-mechanical parameters used in the simulation of rock-like material

$\bar{E}_{c,CCM}$ (GPa)	k^*_{CCM}	C^0_{CCM}(MPa)	κ_{CCM} (m^{-1})	μ_{CCM}	β_{CCM}
9.2	1.82	23.2	2.5×10^6	0.58	0.2

Table 4.2 Comparison between macroscopic parameters obtained from the laboratory experiment (Oh et al. 2017) and DEM simulation

	UCS (MPa)	Young's modulus (GPa)	υ
Experiment (Oh et al. 2017)	46.3	14.9	0.2
Numerical	46.1	14.8	0.2

To calibrate the micro-mechanical properties of grout, we generate a DEM specimen with the size of 80 mm×40 mm, the same as the physical specimen used in the experiments. The r_{min} was set at 0.2 mm, and r_{max}/r_{min} was 1.66. We used the same procedure mentioned above to calibrate the micro-mechanical properties of the grout. The calibrated parameters are listed in Table 4.3. Figure 4.2a illustrates a comparison of the axial stress-strain curves from both the laboratory testing and the DEM simulation using the proposed cohesive model. You can seen that the simulation results matched well with its experimental counterparts. Figure 4.2c illustrates a close-up view of the damage state of the contacts in a localized damaged zone. The softening behaviour of these contacts allowed us to obtain the macroscopic responses of the model. In particular, the gradual softening response of the specimen during the post-peak stage showed a good agreement with the laboratory results. The gradual softening response of the stress-strain curve at the macroscopic scale was the intrinsic result of the collective behaviour of bonded-cohesive contacts in the DEM specimen. In the pre-peak stage of the stress-strain curve, the force state of several cohesive contacts reached their yield limit. These contacts then began to soften, yet still being capable of carrying force. The progressive compressive loading of the specimen resulted in an increase in the number of these softened contacts ($0.0 < D_{CCM} < 1.0$), which coalesced and linked together to form large macroscopic fractures. When the specimen reached its peak axial strength, the cohesion of several contacts was totally lost ($D_{CCM} = 1.0$), but there were still some contacts in the localised zones that had a softening response

(damaged contacts, $0.0 < D_{CCM} < 1.0$). The overall response of these failed and damaged contacts resulted in a softening response of the specimen at the macroscopic level (post-peak stage). Nevertheless, Shang et al. (2018a) reported that the current built-in contact constitutive model in PFC (Flat-Joint model) was not capable of capturing such softening behaviour. In fact, the Flat-Joint model exhibited brittle behaviour in the post-peak stage (Figure 4.2a), because the brittle bond-break occurred in the contacts after they lost their strength (i.e. cohesion or tensile strength). These differences in the macroscopic behaviour highlight the need to take into account softening behaviour in the constitutive relationships of DEM contacts.

The Poisson's ratio of the grout material was not provided by Shang et al. (2018a). Thus, we calibrated the numerical model k^*_{CCM} was calibrated in such a way to obtain the best fit with the laboratory results (stress-strain curve and fracture pattern). The numerical Poisson's ratio was measured to be 0.22. This calibration procedure was also followed by Shang et al. (2018a).

Table 4.3 The calibrated micro-mechanical parameters used in the simulation of grout-like material

	$\bar{E}_{c,CCM}$ (GPa)	k^*_{CCM}	C^0_{CCM}(MPa)	κ_{CCM} ($\mathbf{m^{-1}}$)	μ_{CCM}	β_{CCM}
Grout	4.35	1.9	18.0	2.5×10^6	0.48	0.22
Bolt	200	1.5	800	250×10^6	0.5	0.25

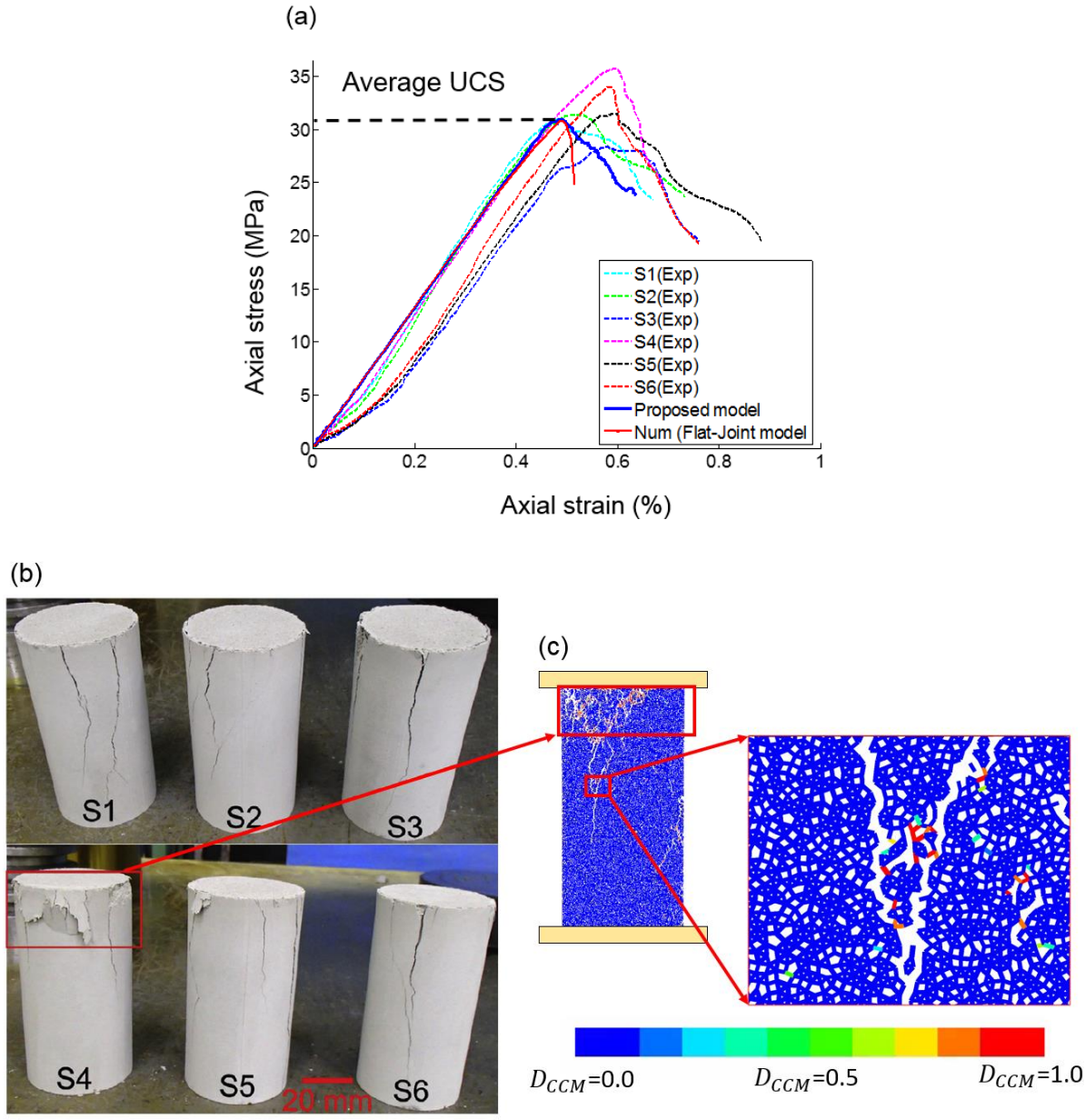

Figure 4.2 Calibration of the proposed model. (a) Comparison of the stress-strain curves from laboratory tests (Shang et al. 2018a) and DEM simulations. (b) Failure pattern of experimental specimens. (c) Macroscopic damage response of the numerical specimen with a close-up view of a localised damage zone.

4.2.2 Calibration of rock joint interface

To mimic the mechanical behaviour of rock joint interface, the SJM was used in the present study. The laboratory results of normal deformability and direct shear tests were used to calibrate the microproperties of SJM. The normal stiffness of SJM (k_n^{sj}) was calibrated against the results of an experimental normal deformability test, and the shear stiffness (k_s^{sj}) and

friction coefficient (μ^{sj}) of SJM were calibrated against the laboratory results of a direct shear test conducted on a planar rock joint. The experimental data provided by Oh et al. (2017) were used in the present study for the calibration purposes. Notice that the size of the specimen used in the laboratory investigation had a height of 100 mm and width of 100 mm. However, in the DEM simulations, the height of the specimens was reduced to 40 mm which had no significant effect on the macroscopic results but highly reduced the computational time. This approach was followed by others (e.g. Bahrani et al. (2014)), which made the DEM simulation more time efficient.

The laboratory data obtained from normal deformability test of a smooth rock joint were used. This test involved loading of a sample with a side length of 100 mm including smooth rock joint and another intact specimen (Oh et al. 2017). According to the experimental approach conducted by Bandis et al. (1983), the closure of rock joint can be measured by calculating the difference between the total deformation of the jointed specimen and the same value gained from an intact specimen. Figure 4.3a illustrates the comparison between DEM results and laboratory data. It can be observed that SJM reproduced both the non-linear and linear portion of the normal deformability test with a close agreement.

To calibrate k_s^{sj} and μ^{sj}values, the laboratory data obtained from the direct shear test of a planar rock joint under various normal stress magnitude were used. We set the calibration friction ratio (μ^{sj}) as 0.9, which was equal to the value obtained from laboratory testing (Oh et al. 2017). To obtain the macroscopic, numerical friction coefficient, we plotted the maximum shear strengths against their corresponding normal stress magnitudes. The results are illustrated in Figure 4.3b. You can see that the SJM successfully reproduced the same macroscopic friction coefficient obtained from laboratory testing. Unfortunately, the experimental stress-displacement curves were not available in the paper published by Oh et al. (2017). Gutiérrez-Ch et al. (2018) suggested that, in the absence of experimental data, the normal-to-shear stiffness ratio can be obtained by assuming a value between 1 to 10. We used this approach in the present study to specify k_s^{sj}. The numerical friction angle obtained from the numerical simulations (41°) (Figure 4.3c) showed a close agreement with the experimental counterpart achieved by Oh et al. (2017) (42°). The micro-mechanical parameters obtained during calibration of the smooth-joint model is given Table 4.4. The accuracy of the calibrated micro-mechanical parameters is further validated by DEM direct shear tests conducted on idealised

rock joints, and in our comparison of the results with their experimental counterparts (see Section 4).

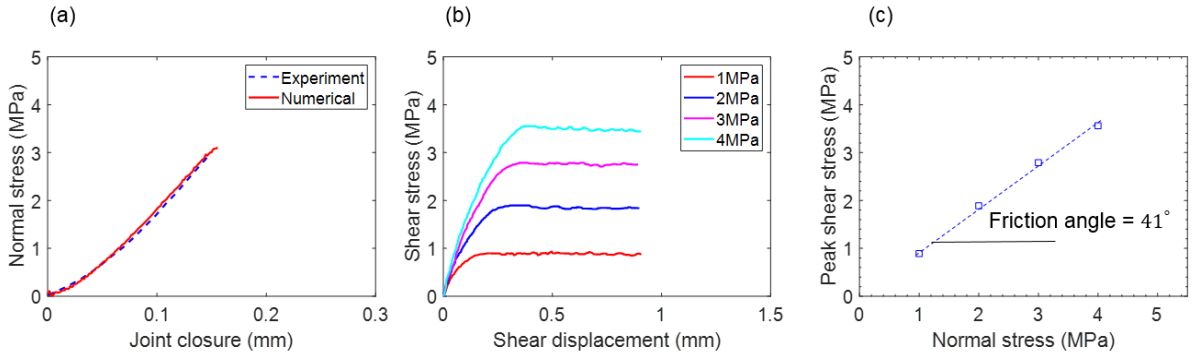

Figure 4.3 Calibration of the SJM. (a) Comparison of normal deformability test results from experiment (Oh et al. 2017) and numerical simulation; (b) direct shear test results of a planar rock joint under different constant normal stresses; (c) the friction angle obtained from numerical results.

Table 4.4 Calibrated SJM micro-properties.

k_n^{sj} (GPa/m)	k_s^{sj} (GPa/m)	μ^{sj}
480	55	0.9

4.2.3 Calibration of bolt-grout interface

In order to calibrate the micro-mechanical properties of the CSJM, we used the laboratory data obtained from direct shear and normal deformability tests. The numerical macroscopic shear and normal stiffnesses, and friction coefficient, were compared with their experimental counterparts. The laboratory data used for the CSJM calibration involved a rock bolt specimen without bolt ribs, which represents a planar interface (Shang et al. 2018a). The dimension of the numerical specimen was set to be the same as those of laboratory tests (80 mm × 24 mm). Notice that the r_{min} in CSJM calibration tests were the same as those of used for the calibration of the grout's micro-properties. The previously calibrated micro-properties (Table 4.3) obtained for the grout, were also used in direct shear tests. The assumption in the present study was to have no damage and deformation in the rebar bolt, since the uniaxial compressive strength and Young's modulus of the steel are much larger in compression compared to grout material. Therefore, a high value of bond strength to avoid bond-breakage is sufficient (Shang et al. 2018a). The micro-properties of the rebar bolt were selected based on previous literature (Shang et al. 2018a), and are listed in Table 4.5.

The calibration procedure of CSJM miro-properties is described as follows:

Firstly, a direct shear test under constant normal stress of 2 MPa was carried out, and the macroscopic shear stress-displacement curve of this numerical experiment was used as a basis for the calibration of the shear stiffness. The microscopic shear stiffness of the CSJM ($k^0_{s,CSJM}$) was altered at this step to reproduce the best fit with the experimental shear stress-displacement curve (i.e. elastic stage). Secondly, other direct shear tests were conducted but under higher normal stress magnitudes (4 MPa and 6 MPa), to calibrate C^0_{CSJM} and μ_{CSJM}. Notice that these two parameters control the peak shear strength in direct shear tests. At this stage, the softening parameter κ_{CSJM} was also altered to reproduce the best post-peak behaviour. Note that we had no direct laboratory method to calibrate β_{CSJM}. Therefore, we used a calibration similar to β_{CCM} (section 3-1), β_{CSJM} which was chosen because it reproduced the best fit with the experimental results.

Figure 4.4 illustrates a comparison of shear stress-displacement curves from DEM and laboratory tests under different normal stress magnitudes. Note that at higher normal stress magnitudes (i.e. 4 and 6 MPa), an initial stress fluctuation was observed in the experimental data (Figure 4.4), which was due to a disconnection between the shear box and the grout material (Shang et al. 2018a). However, the shear stress-displacement curves (Figure 4.4) show that the numerical results are in a good agreement with the experimental data. The softening behaviour in the shear stress-displacement curves demonstrates the necessity of incorporating an exponential softening response in the contact constitutive relationships. In fact, unlike the rock joint interface which showed no cohesive behaviour, the grout-bolt interface exhibited a gradual softening response due to a progressive bond cohesion degradation between the grout and the bolt (Shang et al. 2018a; Yokota et al. 2018). The macroscopic shear stress-displacement curves (Figure 4.4) show that by increasing the magnitude of the normal stress, the DEM specimens reproduced a more pronounced softening response, which we attributed to significant bond-break in the CSJM contacts. These numerical observations were in good agreement with the laboratory results.

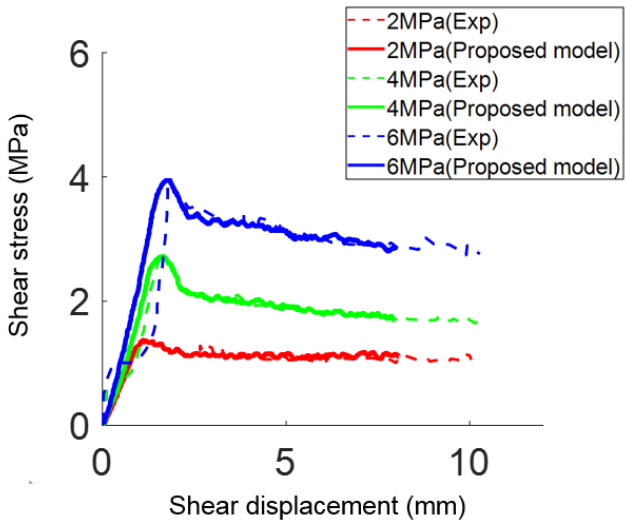

Figure 4.4 Comparison of the direct shear test results from the laboratory experiment (Shang et al. 2018a) and DEM simulations using the proposed CSJM.

As previously mentioned in section 3-2, it is common to calibrate the normal stiffness of the SJM against the results of normal deformability tests (Bahaaddini et al. 2013). We adopted the same approach for calibrating the normal stiffness of CSJM. To calibrate $k^0_{n,CSJM}$ a numerical deformability test was conducted on the planar grout-bolt interface and the outcome was compared with the laboratory results. Identical DEM specimens with and without a grout-bolt interface were generated, and tested uniaxially under compression. Notice that a horizontal velocity of 0.01 m/s, which was applied on the top of the specimens, was found to be sufficient for conducting the normal deformability test. The normal displacement and normal force of the numerical samples were recorded during the experiment. The normal deformation of the intact specimen (specimen without a grout-bolt interface) was subtracted from the normal deformation of the specimen that had a planar grout-bolt interface to estimate the macroscopic normal deformation of grout-bolt interface. The values of $k^0_{n,CSJM}$ were obtained by trial-and-error, to match the numerical normal stress-displacement curve with the laboratory data. Notice that the normal deformability test was conducted using an iterative process with the direct shear tests to reach a good match with the experimental results in both tests. The numerical simulation was compared with its experimental counterpart and the results are illustrated in Figure 4.5. You can see that the axial normal stress of the grout-bolt interface increased linearly when the normal displacement increased. The normal stress-displacement curve in the DEM simulation, using the proposed CSJM, excellently matches with the laboratory curve (Figure 4.5).

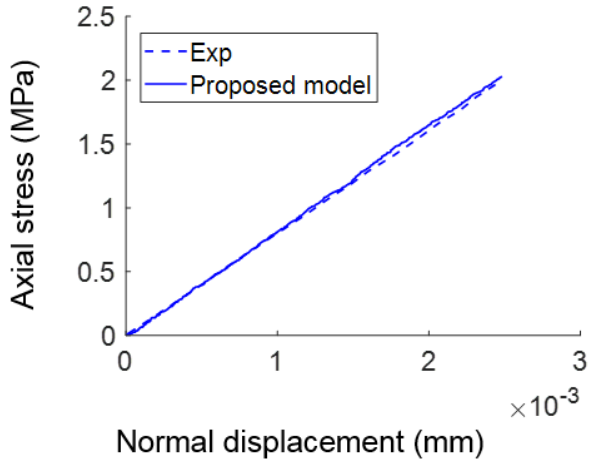

Figure 4.5 Axial stress against the normal displacement of the planar bolt-grout interface in normal deformability tests: Comparison of the experimental data (Shang et al. 2018a) with numerical results using the proposed model.

Table 4.5 The microproperties of the proposed CSJM used in the simulation of the bolt-grout interface

4.3 Validation of the proposed DEM framework

This section presents the simulation of idealised saw-toothed rock joints with different asperity angles, and bolt-grout interfaces with various rib angles, conducted to validate the calibrated DEM framework.

4.3.1 The shear behaviour of idealised rock joints

Oh et al. (2017) studied the dilative behaviour of idealised rock joints by conducting direct shear tests. The laboratory results obtained in their study were used in the present research to validate the numerical framework. Numerical specimens with base asperity angles of 20° and 30° and wavelengths of $\lambda^{RJ} = 25\,mm$ were generated in PFC2D, and tested under various normal stresses. The configuration of idealised rock joints can be found in Oh et al. (2017). The applied normal stress (σ_n^0) in the experimental observations (0.5, 2.0, 4.0 MPa) was based on the ratio of applied normal stress over the rock strength (i.e. $\sigma_n^0) \,/_{\sigma_c}$) that is $1\%, 5\%, 10\%$ ranging from low to high normal stress magnitudes (Oh et al. 2017). The servo-controlled mechanism was employed to apply the normal stress, and a horizontal velocity of 0.01 m/s was adopted in the direct shear tests.

Figure 4.6a and Figure 4.6b illustrate the shear stress-displacement and normal-shear displacement curves obtained from DEM simulations. The numerical and experimental

asperity damages after 2.5 mm of shear displacement are illustrated in Figure 4.6c. The red lines in Figure 4.6c represent the micro-cracks, which were the result of bond-break in the cohesive contacts. The accumulation of micro-cracks is plotted graphically to illustrate the associated asperity degradation. You can see that under low confining pressure, the dominant shear mechanism of rock joints was asperity sliding. For numerical specimens with asperity angles of both 20° and 30°, at a normal stress of 0.5 MPa, when the maximum shear strength of the joints was reached, the models showed plastic behaviour, and a gradual sliding along the surface of rock joints was observed. The corresponding DEM models (Figure 4.6c) verified this behaviour, when no significant asperity degradation occurred in the numerical specimens. By increasing the normal stress magnitude from 0.5 to 4 MPa, more micro-cracks were initiated in the asperity areas for both 20° and 30° of the asperity angle (Figure 4.6c). The shear stress-displacement curves (Figure 4.6a) show that after reaching peak shear strength, the numerical models produced a softening response, which was due to progressive asperity degradation. Under 4.0 MPa of normal stress, the asperity damage was more severe, which resulted in a more pronounced softening response. The numerical results also showed that the peak shear strength of the rock joints increased with an increasing inclination angle (Figure 4.6b). The DEM simulations show that at 30°, the numerical specimens' asperity degradation was more significant. We attributed this to its higher inclination angle because it increased the shear resistance of the rock joint (Figure 4.6c).

Figure 4.6d illustrates a comparison between the peak dilation angle of the DEM models and their laboratory counterparts. As aforementioned, rock joints under low normal stress magnitude remained nearly undamaged throughout the shearing procedure, allowing the sawtooth asperities of the top block to slide up over the opposite one, and resulting in a higher normal displacement of the joints. By increasing the normal stress magnitude, more severe asperity damage occurred in the models, resulting in a significant reduction of rock joint dilation. The comparison graph (Figure 4.6d) also showed that the specimens with a 30° inclination angle displayed a higher relative dilation response. Figure 4.6c indicates a good agreement between the experimental and numerical asperity damage using the proposed cohesive DEM framework. The comparison between the DEM and laboratory results (Figure 4.6c and Figure 4.6d) demonstrates that the proposed DEM framework can successfully reproduce the dilation behaviour of idealised asperities with different inclination angles.

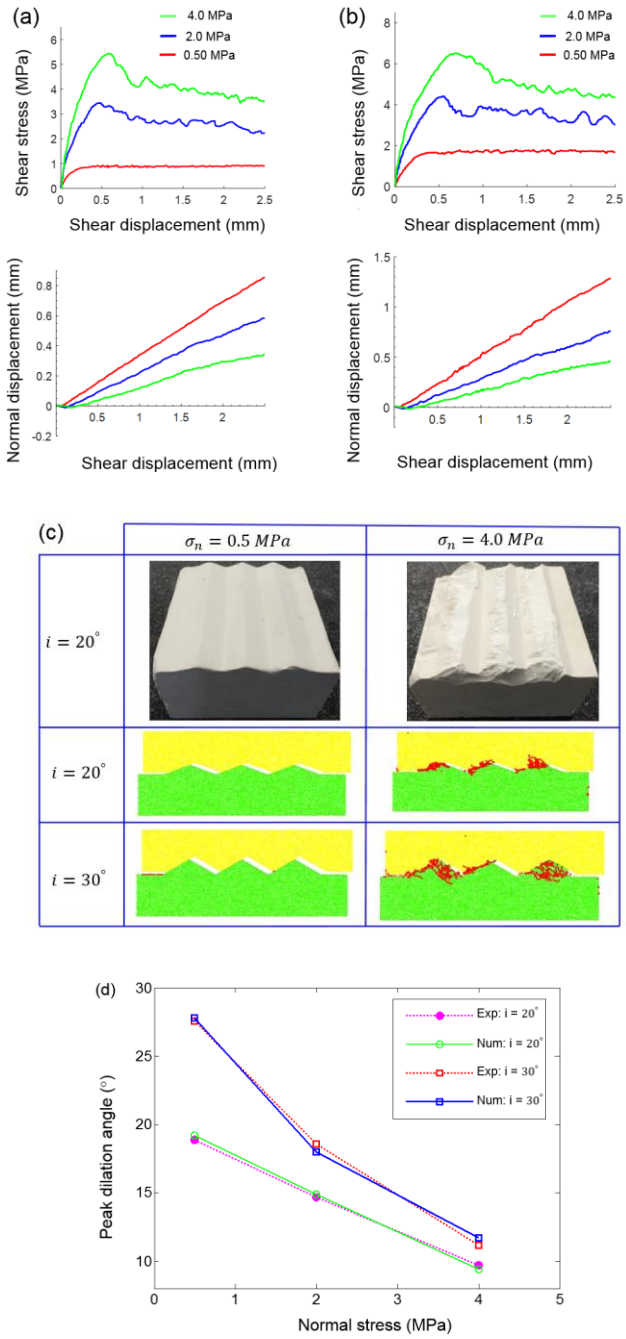

Figure 4.6 Direct shear test results from the laboratory experiment obtained by Oh et al. (2017) and DEM simulations using the proposed model: (a) and (b) Numerical shear stress-displacement and normal-shear displacement curves for 20° and 30° of asperity angles, respectively; (c) asperity degradation of the laboratory experiment and DEM simulation; (d) peak dilation angle of the laboratory experiment and the DEM simulation.

4.3.2 The shear behaviour of the bolt-grout interface

Figure 4.7 illustrates the DEM specimen generated in PFC2D that represents a rock bolting system with a rib angle (α) of 90°. The numerical specimen was comprised of two elements:

Mortar and rock bolt. The rock bolt was fixed, and we applied a horizontal velocity of 0.01 m/s to the edge of it during the direct shear test. We applied the normal stress on the top of the specimen (grout) using a servo-controlled mechanism.

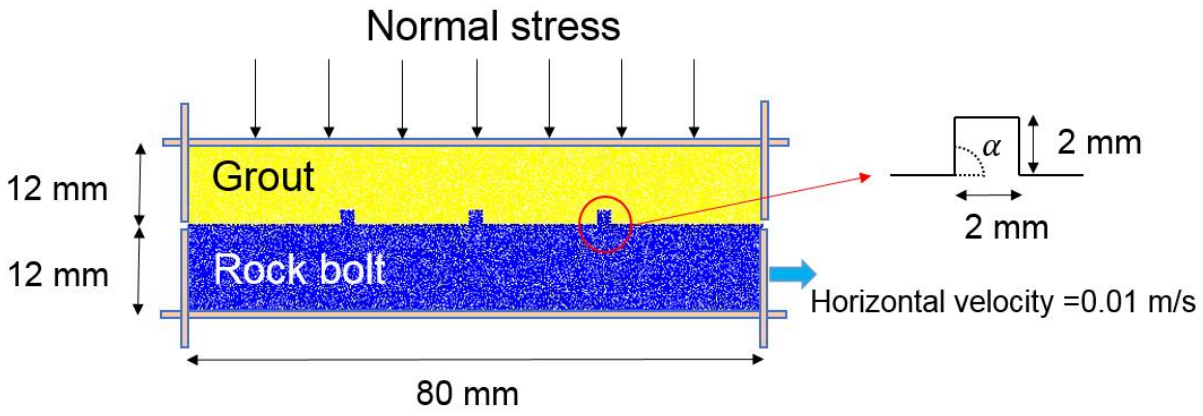

Figure 4.7 Numerical test setup for conducting a direct shear test on the bolt-grout interface (α= 90°).

Figure 4.8 illustrates the DEM simulation and experimental results. The numerical shear stress-displacement curve using the proposed DEM framework matches excellently with the laboratory curve (Figure 4.8a). During the shearing process, the numerical specimen was shown to undergo four different stages, including linear elastic at the beginning of the test, a non-linear response before reaching the peak shear strength, a gradual softening behaviour during which the specimen totally failed, and a residual stage, at which the shear stress plateaued.

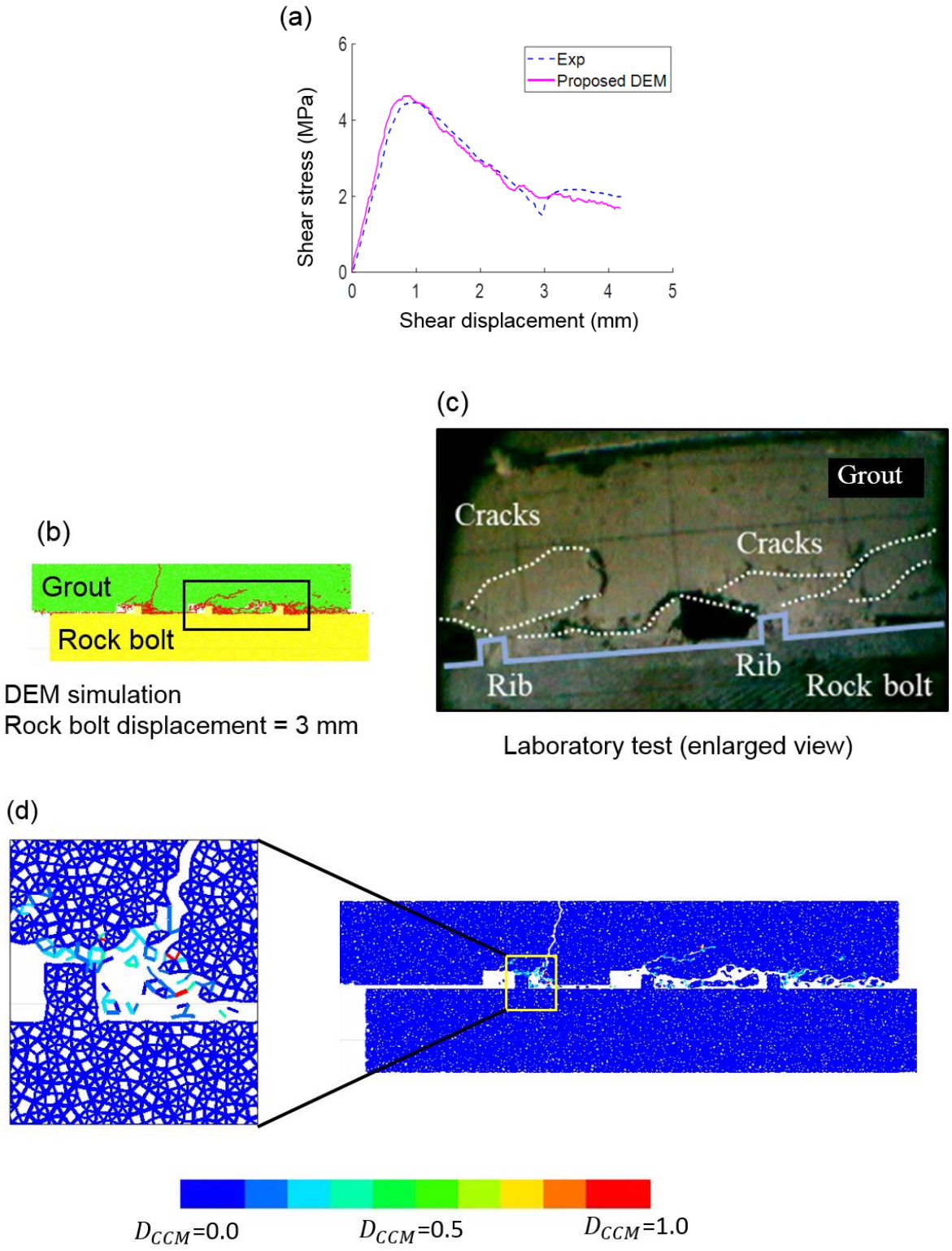

Figure 4.8 Comparison of the direct shear test results from the experiment (Shang et al. 2018a) and DEM simulation using the proposed model. (a) The shear stress-displacement curve. (b) and (c) The fracture pattern in the numerical and experimental specimen (Shang et al. 2018a), respectively. (d) The microscopic damage response of the DEM contacts at a localised failure zone.

Figure 4.8b and Figure 4.8c illustrate the fracture pattern in the numerical and experimental specimens, respectively. The comparison indicates a good agreement between the laboratory and the numerical cracking response using the proposed DEM framework. The numerical model demonstrates both inclined and sub-horizontal cracks. During the shearing process, the coalescence of micro-cracks, which were the result of bond-break in the cohesive contacts ($D_{CCM} = 1.0$), generated larger macroscopic cracks. Figure 4.8b shows that the accumulation of micro-cracks between two ribs led to the failure of the grout material. This failure mode was also observed during the experimental test (Yokota et al. 2019), which is shown in Figure 4.8c. The damage response of the cohesive contacts after 3 mm of shear displacement is depicted in Figure 4.8d. You can see that some of the contacts performed elastically ($D_{CCM} = 0.0$), while others demonstrated a softening response ($0.0 < D_{CCM} < 1.0$).

4.4 The simulation of bolted rock joints subjected to combined pull-shear load

This section presents an investigation of the influence of the combined pull and shear load. It employed the calibrated micro-properties, and studies the influence of pretension, the rib angle, and the CNS boundary condition. The setup of the numerical test explained in subsection 4.4.1. In subsection 4.4.2, the influence of the combined pull-shear load is described with a particular focus on the impact of the pretension load on the shear behaviour of the bolted rock joint. An investigation of the influence of the rib angle and the CNS condition is presented in subsections 4.4.3 and 4.4.4, respectively.

4.4.1 Numerical test setup

Figure 4.9 illustrates the DEM specimen for conducting the combined pull-shear load test using a fully grouted rock bolt. Figure 4.9a shows the boundary condition used in DEM modelling of a bolting system including rock joint, rock bolt, and grout. We assumed a diameter of 5 mm for the rock bolt, and a thickness of 4 mm for the grout. To generate the numerical specimen, the DEM particles were divided into three different groups: Rock, rock bolt, and grout. The particle size of the rock bolt and the grout groups were the same as those used for the calibration of micro-properties (section 4.2.1). Similarly, the particle size for the group of rock was similar to particle sizes that were used for the calibration of rock-like material micro-properties in section 3-1. Notice that in the verification process (section 4.3.2), half of the rock bolt profile was modelled. However, in the combined pull-shear load experiments the full rock bolt profile needed to be simulated. The width of the numerical specimen was 100 mm, which was similar

to that considered for the validation of rock joint shear behaviour (section 4.3.1). The height of the numerical specimen was 80 mm, which is equal to the length of the rock bolt simulated in the verification process (section 4.3.2). To carry out the pull-out test, a group of DEM particles (gear group in Figure 4.9a) was subjected to a vertical velocity of 0.01 m/s. This velocity was equal to that of used in the simulation of the grout-bolt shear behaviour in section 4-2. We conducted the direct shear test by applying a horizontal velocity of 0.01 m/s on the top rock block (Figure 4.9a). The pull-out load induces a normal stress on the rock joint profile. The axial stress along the bolt-grout interface and the induced normal stress on the rock joint interface (σ_n^i) were measured at different measurement circles, shown in Figure 4.9b and Figure 4.9c, respectively.

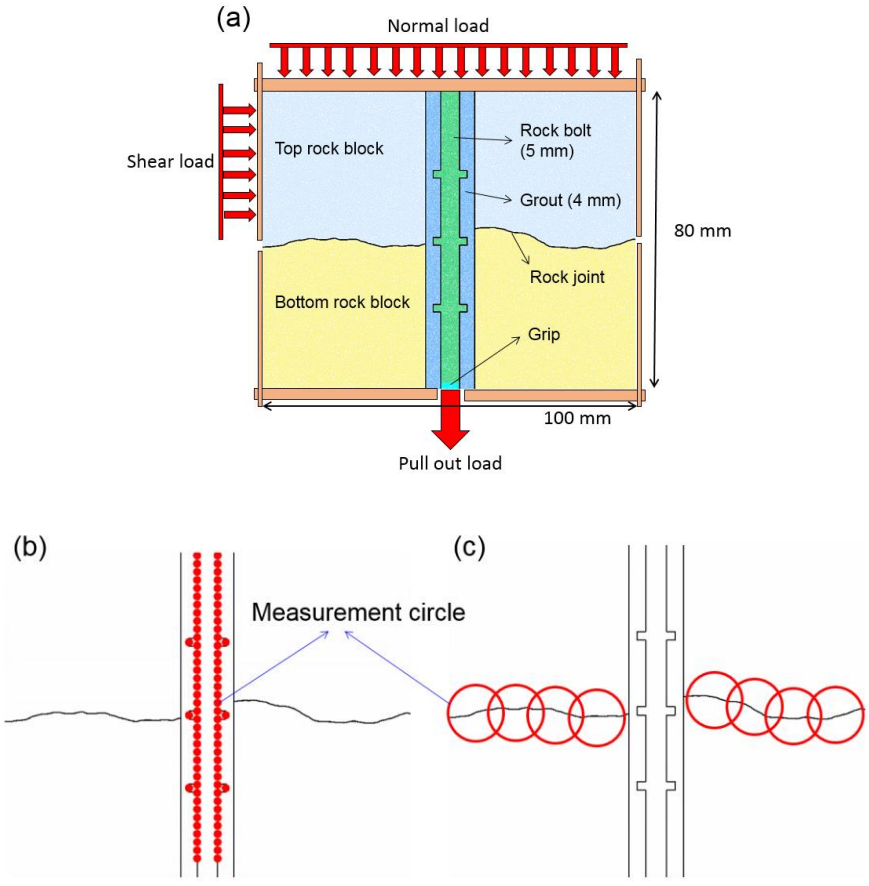

Figure 4.9 The DEM experiment for conducting combined pull-shear loading test: (a) DEM test setup and boundary condition; (b) and (c) measurement circles for monitoring axial stress-displacement of the bolt-grout interface and induced normal stress on rock joint interface, respectively.

4.4.2 The pull out and shear mechanisms

We established DEM simulations to investigate the influence of the combined pull-shear load on the shear behaviour of bolted rock joint. In the previous section (section 4.3.2), the interaction between the rock bolt and grout was studied using the proposed cohesive DEM.

Chen and Li (2015b) studied the performance of fully grouted rock bolts subjected to pull-shear loads. In their experimental research, the pull-out and shear loads were applied to the specimen at the same time, and the total force resulting from pull-and-shear loading was calculated to analyse the outcome of the laboratory tests. Notice that no rock joint was considered in their research. Following this approach, however, it is an immensely complicated task to understand the shear mechanism of bolted rock joints. The main reason for this is because the pull-out stress magnitude at which the highest normal stress is induced in the rock joint may or may not be reached using the method proposed by Chen and Li (2015b), which leads to an ambiguity in the results. We present an alternative, a stepwise pull-shear test (SPST) approach in this paper, in which the DEM direct shear tests are conducted at various pretension stress magnitudes. The proposed SPST approach enabled us to measure and compare the corresponding peak shear strength of the bolted rock joint at different pretension magnitudes. Thus, the performance of fully grouted rock bolts (i.e. the ultimate shear capacity of bolted rock joint) can be properly assessed.

The fully grouted rock bolt was subjected to a pull-out load, while the rock joint was sheared horizontally. The rock joint had an average joint roughness coefficient (JRC) of 10.2, which was digitised and imported in PFC2D. This rock joint profile was previously generated by Bahaaddini (2014). The rib angle of the rock bolt was set at90°. According to the experimental research available in the literature, the pull-out test can be conducted either under zero or non-zero confining pressure (Thenevin et al. 2017). In the present study, the numerical pull-out tests were conducted under zero confining pressure. This approach was followed by previous scholars investigating the influence of the surface configuration on the load transfer mechanism of fully grouted rock bolts (Aziz et al. 2006; Tao et al. 2017; Yazici and Kaiser 1992). The results of the numerical pull-out test are depicted in Figure 4.10. Figure 4.10a illustrates the axial stress-displacement response of the fully grouted rock bolt. The axial stress-displacement of the fully grouted rock bolt can be divided into four different stages (I to IV in Figure 4.10a). The σ_n^i was also measured during the pull-out process, and the results are illustrated in Figure 4.10b. The corresponding force chain and damage responses of the specimen at the end of each stage are shown in Figure 4.10c and Figure 4.10d, respectively. Notice that force chain

represents the compression and tension forces along arrays of DEM contacts. The thicker black lines in Figure 4.10c indicate a higher contact force value. The red lines in Figure 4.10c exhibit the DEM contacts with tension forces, which are influenced by the applied pull-out load.

Each stage in the stress-displacement curve (Figure 4.10a) is associated with a particular mechanism:

I-The initial linear elastic response from the beginning of the pull-out test to point "o" was observed in stage I. At different stress magnitudes in this stage, we monitored the force chain and damage responses of the grout and bolt-grout interface contacts ("m", "n", and "o" in Figure 4.10c, d and e). You can see in these results that the magnitude of compression forces gradually increased around the ribs (Figure 4.10c). At the end of this stage (point "o"), the compression forces developed towards the rock joint (Figure 4.10c), leading to a significant increase in the magnitude of σ_n^i (Figure 4.10a). During this stage, the number of yielding contacts increased, with a high concentration of damaged contacts observed in the bottom-half of the grout ("m", "n", and "o" in Figure 4.10d). You can see in Figure 4.10e that at points "m" and "n", there were some softening contacts ($0.0 < D_{CSJM} < 1.0$) along the bolt-grout interface. With an increase in the axial strength of the bolt to point "o" (Figure 4.10a and e), these contacts were completely damaged ($D_{CSJM} = 1.0$). However, there were still some contacts along the bolt-grout interface with $D_{CSJM} = 0.0$.

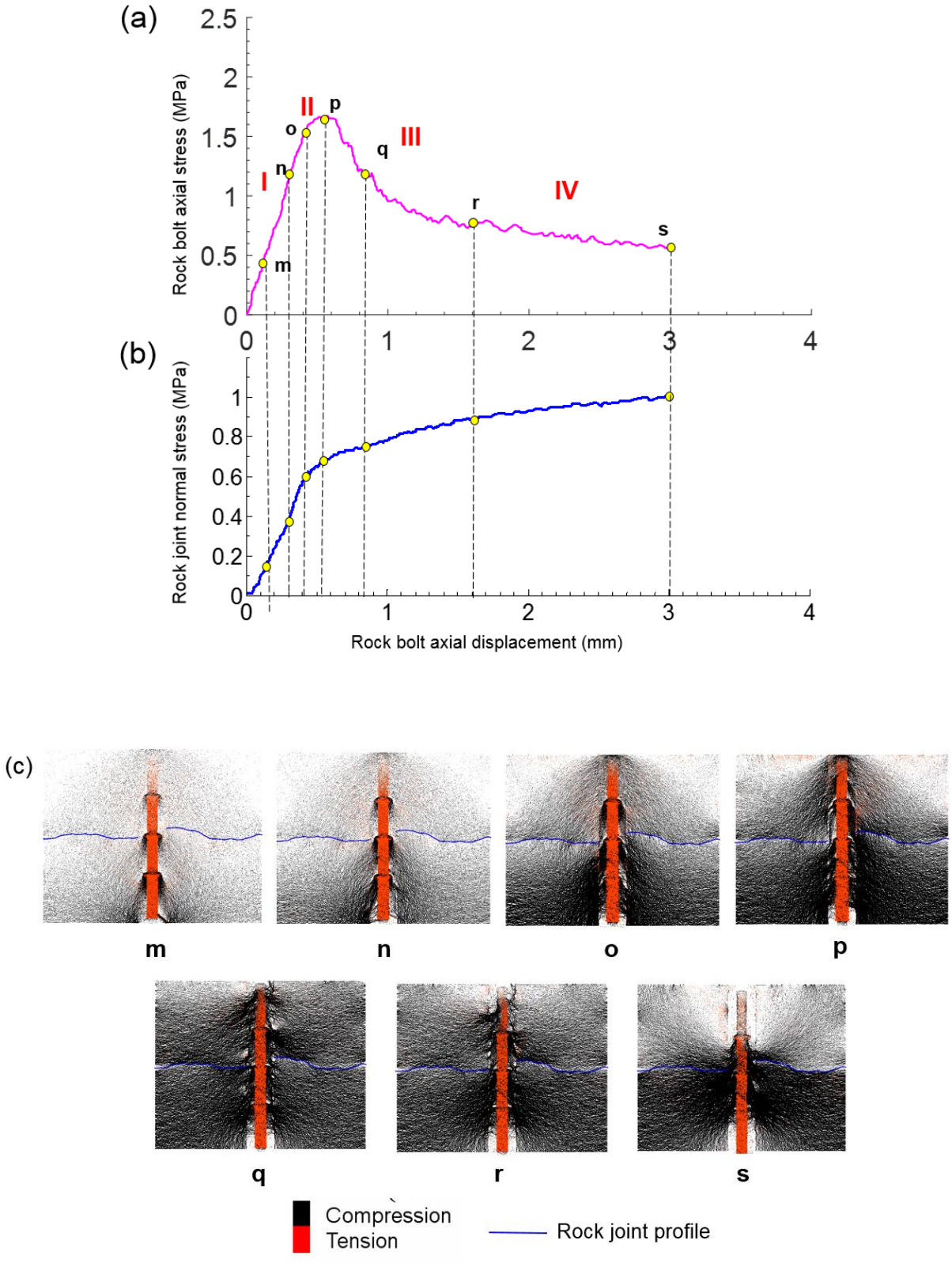
(a)
Rock bolt axial stress (MPa)
2.5
2
1.5
1
0.5
0
I
II
III
IV
m
n
o
p
q
r
s
0
1
2
3
4
(b)
Rock joint normal stress (MPa)
1
0.8
0.6
0.4
0.2
0
Rock bolt axial displacement (mm)
(c)
m
n
o
p
q
r
s
Compression
Tension
Rock joint profile

(Continue)

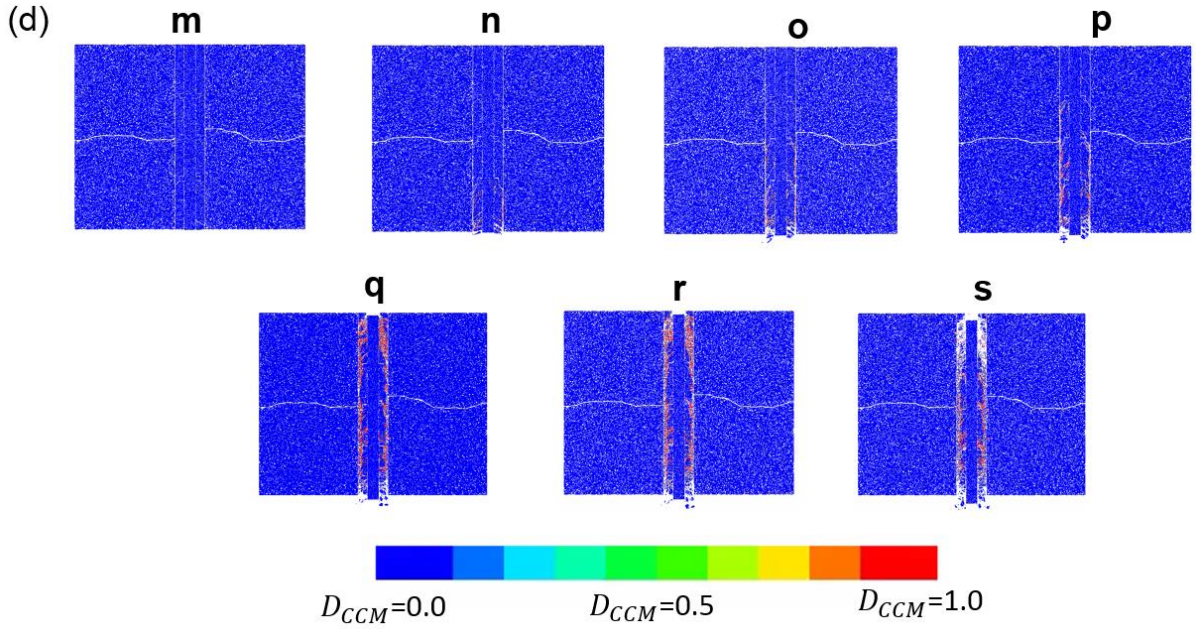
(d)
m
n
o
p
q
r
s
D_{CCM}=0.0
D_{CCM}=0.5
D_{CCM}=1.0

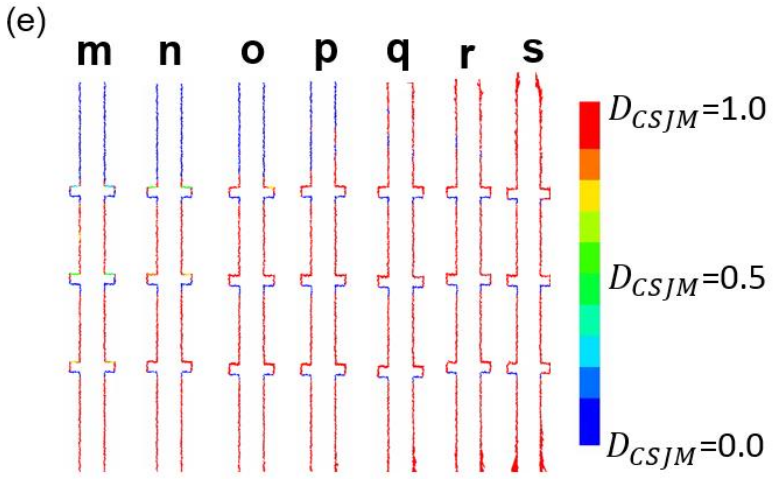
(e)
m
n
o
p
q
r
s
D_{CSJM}=1.0
D_{CSJM}=0.5
D_{CSJM}=0.0

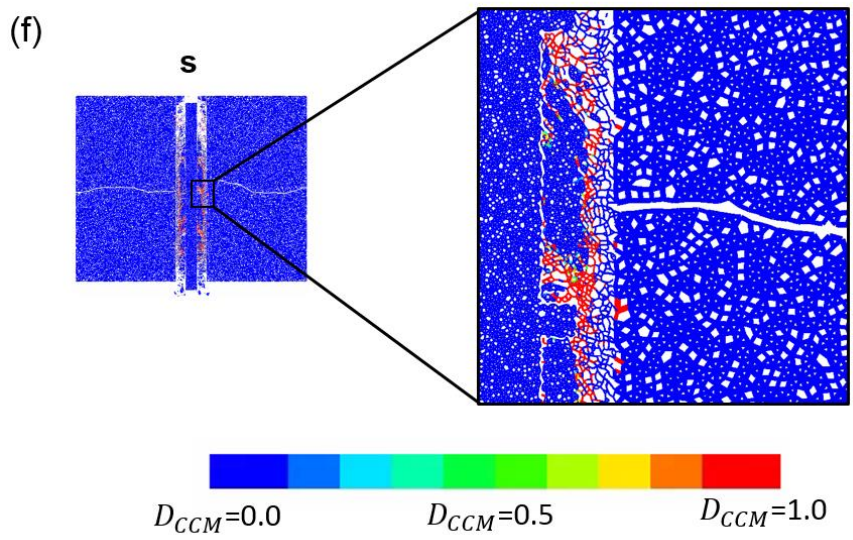

Figure 4.10 The numerical pull-out test results using the proposed model: (a) rock bolt axial strength versus rock bolt axial displacement; (b) induced normal stress on the rock joint interface versus axial displacement of the rock bolt; (c), (d), and (e) the force chain networks, the damage response of the cohesive contacts in the grout material, and the damage response in the bolt-grout interface contacts at various pull-out stress magnitudes, respectively; (f) a close up view of the damage state of the cohesive contacts in the grout material after completing the pullout process.

II-In this stage (from point "o" to point "p"), the axial stiffness dropped and the stress-displacement curve exhibited a nonlinear response before the peak axial strength was reached (point "p", Figure 4.10a). The rate of increase in the σ_n^i dropped during this stage (Figure 4.10b), which we attributed to the progressive development of damage in the grout material (Figure 4.10d). The compression forces around the ribs and rock joint profile showed a slight increase at the end of this stage (point "p", Figure 4.10c).

III- The axial stress decreased in this stage. Initially, the axial stress tended to reduce steeply, but the rate of stress reduction gradually decreased after point "q" (Figure 4.10a). The σ_n^i exhibited a gradual increase from peak axial strength (point "p") to the end of stage III (point "r") (Figure 4.10a). Although the damage response of the grout contacts showed a significant increase in the number of failed contacts (points "q" and "r" in Figure 4.10d; contact with colours other than blue), the σ_n^i exhibited a gradual increase during this stage. One possible reason for this is the mechanical interlock and frictional behaviour of the grout particles during

progressive pull-out loading, which may contribute to the increase of σ_n^i. You can see in Figure 4.10b that the rate of increase in the magnitude of σ_n^i during stage III was significantly lower than that in stage I. The compressive forces around the rock joint profile increased during this stage (points "q" and "r" in Figure 4.10c), which was consistent with the gradual increase in the σ_n^i (Figure 4.10b). The damage response of the bolt-grout interface contacts also exhibited a significant increase in the number of damaged contacts (Figure 4.10d). This behaviour continued until the end of the pull-out procedure (Figure 4.10e).

IV- During the residual phase, the rate of decrease in the axial strength was dramatically reduced (stage IV, Figure 4.10a). The rate of increase in the σ_n^i also declined gradually (Figure 4.10b). At the end of the pull-out test (point "s" in Figure 4.10c), the compressive forces in the specimen were mostly concentrated in the middle of the specimen, which we attributed to the severe bond-break at the upper and lower part of the grout (point "s" in Figure 4.10d). You can see from the damage response of the bolt-grout interface (point "s", Figure 4.10e) that the majority of the interface contacts were fully damaged ($D_{CSJM} = 1.0$) during this stage.

To better demonstrate the damaged and softening contacts in the grout material, a close-up view of the cohesive contacts at the end of the pull-out test (point "s") is depicted in Figure 4.10f. Observe that the majority of the contacts were fully damaged ($D_{CCM} = 1.0$), while very few contacts were in their softening stage ($0.0 < D_{CCM} < 1.0$).

After conducting the pull-out test, and obtaining the axial stress-displacement of the fully grouted rock bolt, the direct shear tests were carried out. The numerical observations (Figure 4.10a and b) showed that the pull-out force applied on the rock bolt induced a clamping effect on the rock joint's surface, which in turn increased the normal stress of the rock joint. It was expected that an increase in the σ_n^i would increase the shear strength of the rock joint. However, it is necessary when designing bolting systems to understand at which axial stress magnitude (shown in Figure 4.10a) the rock joint demonstrates the highest possible shear strength. To test this, we conducted a series of direct shear tests at each stress magnitude. The applied normal stress in the pull-and-shear test was set at$\sigma_n^{total} = \sigma_n^0 + \sigma_n^i$. The magnitude of σ_n^0 was 0.5 MPa. Therefore, the overall, applied normal stress on the rock joint interface was increased from point "m" (the minimum σ_n^i in the group) to point "s" (maximum σ_n^i in the group). The direct shear tests were conducted under CNL conditions; the influence of the CNS

condition is investigated in section 4.4.4. The numerical direct shear tests aimed to find the axial stress magnitude (i.e. pretension load) at which the rock joint produces the maximum shear strength. This helps to determine the optimum pretension loading during practical applications (i.e. in mining).

Figure 4.11 illustrates the results of the numerical direct shear tests conducted on the bolted rock joint. Figure 4.11a shows the shear stress-displacement graphs, and Figure 4.11b depicts the maximum shear stress of the bolted rock joint against the total applied normal stress magnitude (σ_n^{total}). The damage response of the numerical specimens at the end of the shearing process is also shown in Figure 4.11c.

The numerical specimens were named based on pretension stress magnitudes (e.g. "m", "n", and etc.) that were obtained during the pull-out test (see Figure 4.11a). It can be seen from Figure 4.11b that the specimen "o" reproduced the highest peak shear strength. The direct shear test results also showed that for the specimens with peak (specimen "p") and post-peak (specimens "q", "r", and "s") pretension stress magnitudes, the peak shear strength of the rock joint reduced, but it was higher than that obtained from the specimens in which the pretension stress magnitudes were in the linear elastic region (i.e. specimens "m" and "n") (see Figure 4.11b). The shear resistance of the rock joints for the peak and post-peak pretensions was associated with the presence of rock bolt element, and to some extent σ_n^i. These numerical observations can be interpreted according to the σ_n^i graph (Figure 4.10b) and force chain plots (Figure 4.10c). According to the pull-out test results, at point "o" the incremental rate of σ_n^i significantly decreased (Figure 4.10b), but point "o" had the highest σ_n^{total} compared to "m" and "n". Accordingly, the specimen "o" showed greater resistance against shearing, and reproduced the highest peak shear strength. Nonetheless, at peak (point "p") and post-peak (points "q", "r", and "s") stress magnitudes, the magnitude of compressive forces in the rock joint interface grew rapidly (Figure 4.10c), due to the frictional behaviour of the grout particles during progressive pull-out. This encouraged the rock contacts to come close to their yield limits (i.e. the onset of contact softening). Therefore, the weakened contacts in specimens "p", "q", "r", and "s" exhibited lower shear resistance, with severe asperity damage, when compared to specimen "o" (Figure 4.11c). These numerical observations revealed that the combined pull-and-shear load significantly influenced the shear resistance of the rock joint. There was also an axial tensile stress at which the fully grouted rock bolt demonstrated an optimum performance (i.e. optimum pretension stress).

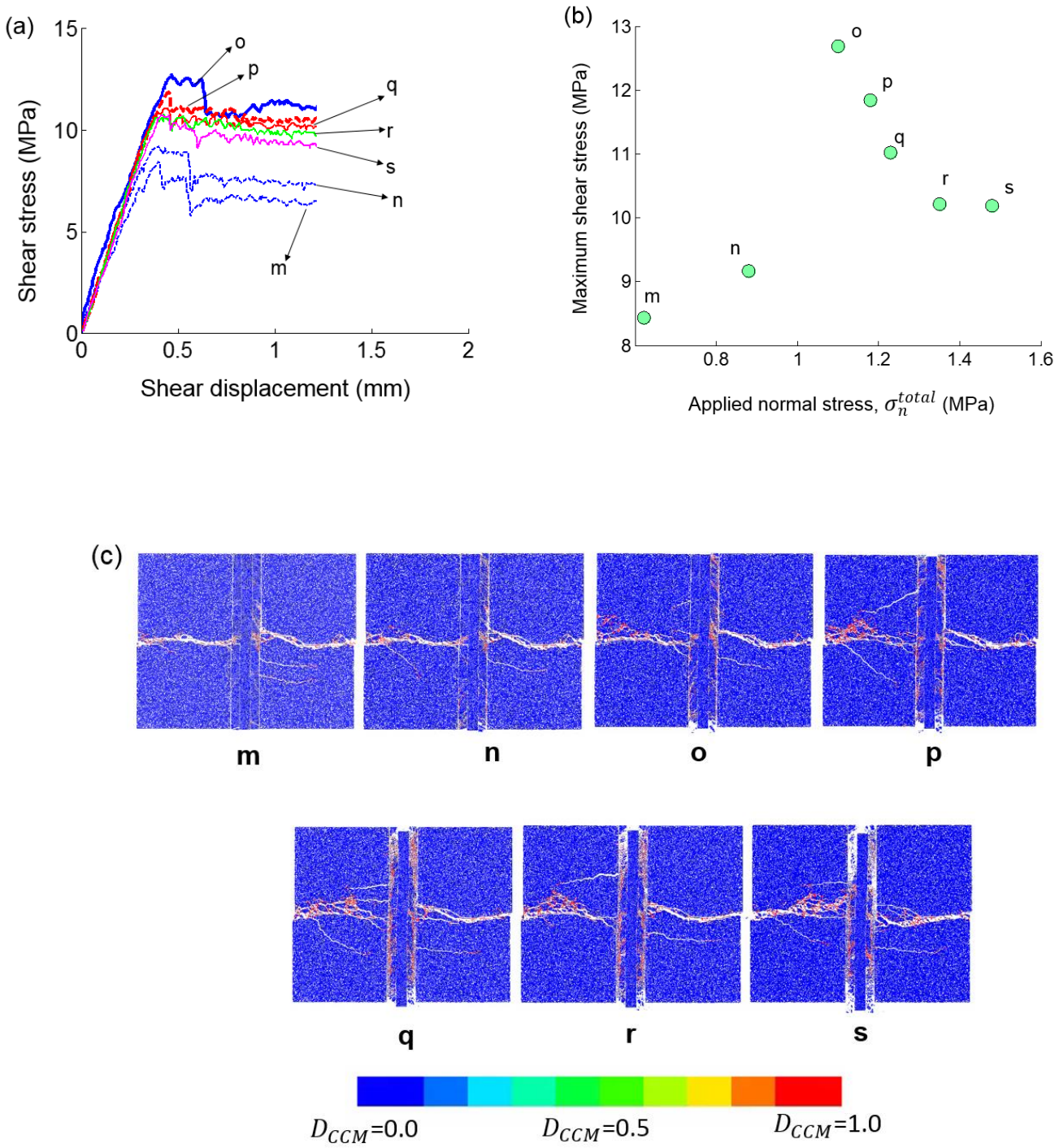

Figure 4.11 The numerical direct shear test results of a bolted rock joint with different pretension stress magnitude: (a) shear stress-displacement curves; (b) the maximum shear strength of the bolted rock joint at different pretension stress magnitudes; (c) the corresponding damage response of the cohesive contacts after completing the direct shear tests.

4.4.3 The influence of rib angle

In addition to the numerical specimens with rib angle of 90°, two other models with rib angles of 30° and 60° were simulated. Similar to the previous simulations, the pull-out tests were

conducted first; then, the direct shear tests were carried out to investigate the influence of α on the overall shear behaviour of bolted rock joints. Figure 4.12 illustrates the axial stress-displacement curves obtained from the pull-out tests. The corresponding σ_n^i against the axial displacement of the rock bolt is also demonstrated in each figure (Figure 4.12a and b).

The numerical simulations showed that the axial stress-displacement response $\alpha = 60^\circ$ (Figure 4.12a) was approximately similar to that with $\alpha = 90^\circ$ (Figure 4.12b). The σ_n^i was also consistent with the results obtained from the 90° rib angle. The axial stress-displacement curve with a 30° rib angle, however, exhibited slightly different results. When $\alpha = 30^\circ$, the peak axial strength was lower than that in the other numerical specimens, which was probably because of the slip behaviour along the bolt-grout interface, arising from insufficient mechanical interlocking. This meant that lower magnitudes of σ_n^i during the pull-out test (Figure 4.12b) resulted.

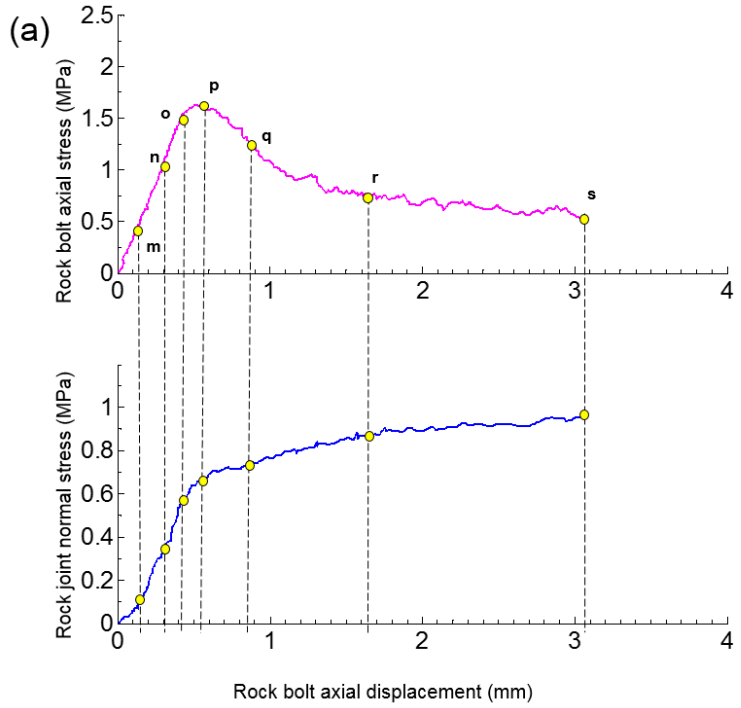

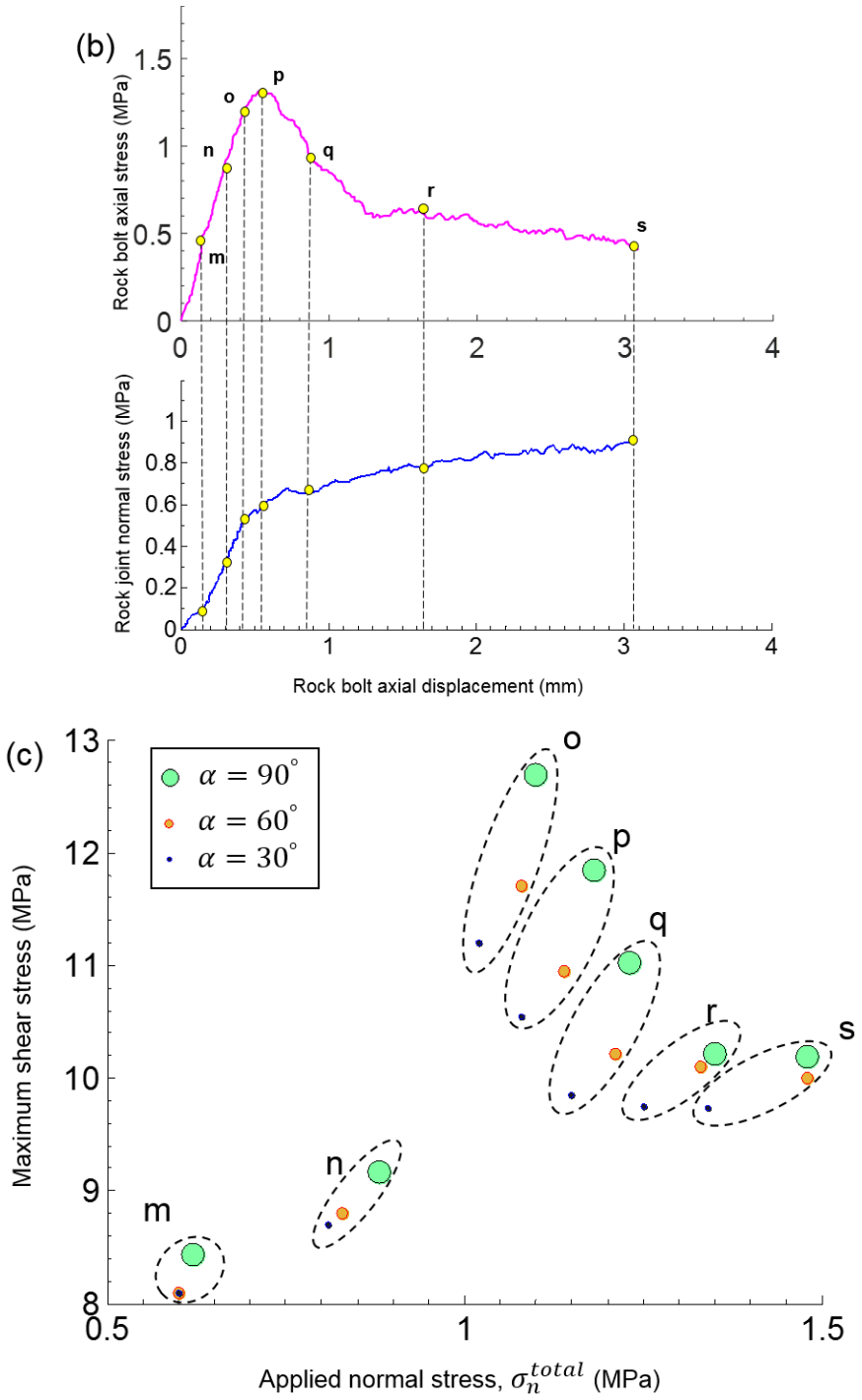

Figure 4.12 The numerical results of the combined pull-shear tests using different rib angles (α): (a) and (b) pull-out test results for rib angles of $60^{\circ}$and 30°, respectively; (c) maximum shear resistance of bolted rock joints versus applied normal stress at different pretension stress magnitudes for various rib angles.

The numerical observations obtained in the present study were consistent with the experimental results in the previous study (Yokota et al. 2019). Similar to the results presented in section

4.4.1, seven axial stress magnitudes were considered for examining the influence of the rib angle on the shear resistance of the bolted rock joint. We conducted fourteen numerical direct shear tests in total; the results are illustrated in Figure 4.12c. You can see that, as with the previous results, the ultimate performance of the fully grouted rock bolts was obtained when the axial stress of the rock bolt was at point "o". As with the 90° rib angle (section 4.4.1), in the numerical specimens with peak and post-peak stress magnitudes (specimens "p", "q", "r", and "s") the shear resistance of the bolted rock joints reduced, but it was higher than that obtained from the specimens with pretension in the linear elastic region.

4.4.4 The influence of CNS condition

It has been reported repeatedly in previous experimental research that the CNS boundary condition affects the shear resistance of bolted rock joints. In this section, the shear behaviour of the bolted rock joint (JRC=10.2, $\alpha = 90^{\circ}$) was studied under the CNS condition. The numerical setup under the CNS condition is illustrated in Figure 4.13.

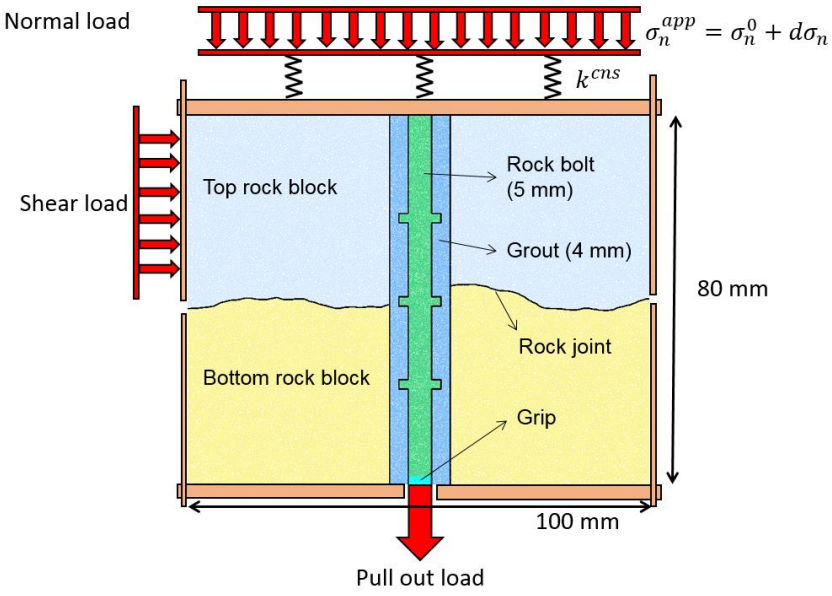

Figure 4.13 The numerical test setup for conducting a direct shear test on a bolted rock joint with a fully grouted rock bolt subjected to combined pull-shear loads under the CNS condition.

During CNS direct shear tests, the applied normal stress on the rock joint profile should be updated according to the normal displacement of the rock joint, and to the value of stiffness, as follows:

$$d\sigma_n = k^{cns} \times d\delta_n \tag{4.1}$$

$$\sigma_n^u = \sigma_{total}^n + d\sigma_n \quad (4.2)$$

where k^{cns} is the constant normal stiffness at an external boundary, and $d\delta_n$ is the increment of normal displacement (Indraratna et al. 2015). σ_n^u is the updated normal stress in the CNS direct shear test. σ_n^{total} was calculated as: $\sigma_n^{total} = \sigma_n^0 + \sigma_n^i$, and the magnitude of σ_n^0 was 0.5 MPa. In the numerical models, the normal displacement of the top wall was measured at each time-step, which represented the normal displacement of rock joint. The reaction force induced on the top wall was also measured, and was divided by the length of rock joints to calculate the normal stress.

We took the following steps to implement the CNS condition in PFC2D:

1- Apply a relatively small velocity on the top of the specimen, solve the model to equilibrium. At this step, the aim was to reach the initial normal stress magnitude (σ_n^0). The servo-controlled mechanism was activated during this step.

2- Begin the direct shear test by applying a horizontal velocity of 0.01 m/s on the top left wall after the specimen reaches the desired initial normal stress. Due to progressive shear displacement, the rock joint tended to dilate. This normal displacement was used to calculate the incremental normal stress magnitude ($d\sigma_n$ in Eq. 4.1). Before beginning this step, the applied normal stress was updated (σ_n^u) and, with the assistance of the servo-controlled mechanism, the newly defined target was achieved.

Seven different direct shear tests were conducted using the pretension stress magnitudes obtained in section 4.4.1. The maximum shear strength of the bolted rock joint with respect to the σ_n^{total} is shown in Figure 4.14a. Observe that the CNS condition resulted in an increase in the shear resistance of the bolted rock joint. However, the influence of the CNS condition was more significant at the pretension stress magnitudes obtained from the elastic response to the pull-out test (i.e. points "m" and "n" in Figure 4.14a). At point "o", which reproduced the highest possible shear resistance, the effect of the CNS condition starts to diminish. For the peak axial strength of the bolt-grout interface (point "p") and post-peak stress magnitudes, no outstanding difference was observed between the CNL and CNS test results.

The experimental results of Indraratna et al. (2015) on unbolted rock joints showed that when the initial normal stress is high, an increase in the normal stress occurs at a lower rate due to significant asperity degradation. Figure 4.14b illustrates the rate of increase in the normal stress

magnitude (σ_n^{total}) against the progressive shear displacement of the bolted rock joint. These results demonstrate that an increase in σ_n^{total} reached its highest rate for points "m" and "n", but it declined from point "o" to "s". We attributed the reduction in the shear resistance of the bolted rock joint to severe asperity damage at high σ_{total}^{n}.

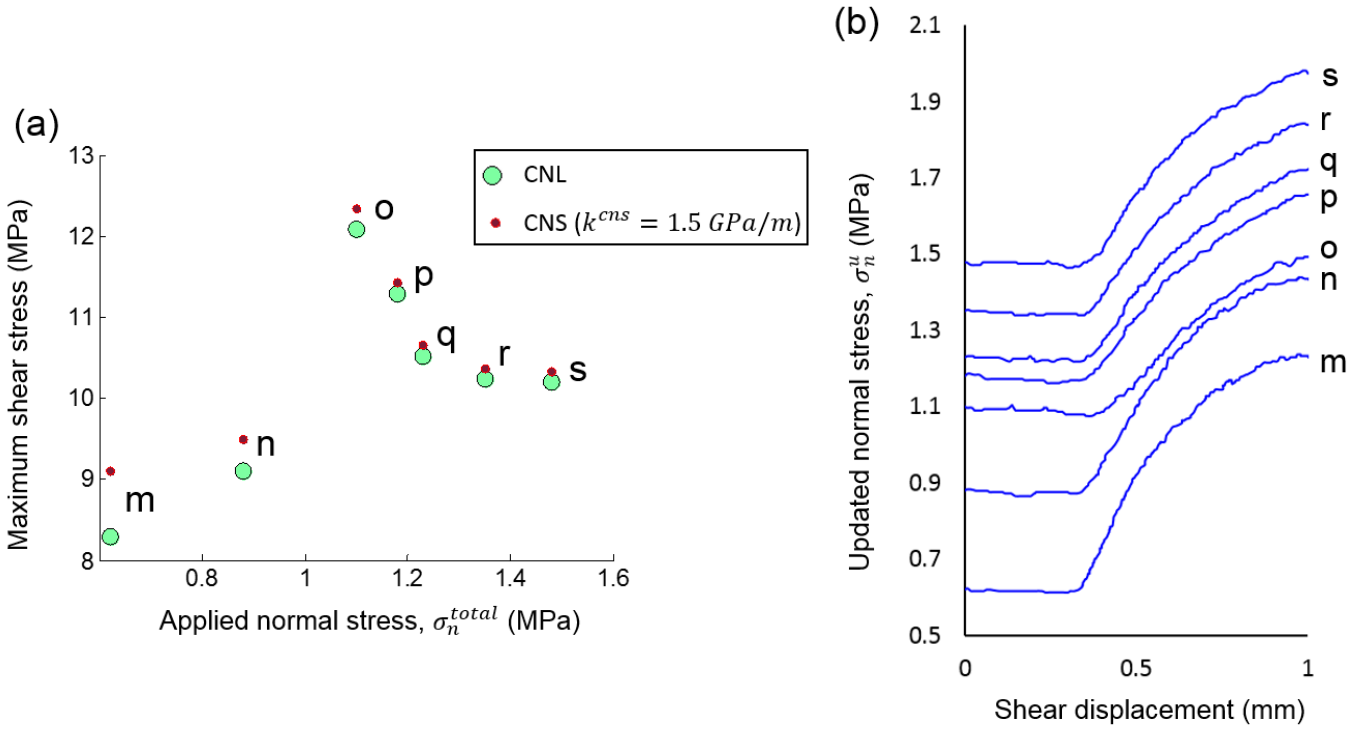

Figure 4.14 The result of combined pull-shear tests under CNS condition: (a) Comparison of maximum shear strength of bolted rock joints reinforced with fully grouted rock bolt under CNL and CNS conditions, (b) the applied normal stress (under CNS condition) versus shear displacement at various pretension stress magnitudes.

4.5 Conclusion

This chapter presented a new cohesive DEM framework for modelling rock joints reinforced with fully grouted rock bolts combining damage mechanics with a plasticity law.

The model was implemented as both a material and an interface contact law to mimic the progressive softening behaviour of cement bridges in both grout and rock material, as well as in a bolt-grout interface. Through various numerical simulations, we showed that the proposed modelling method was capable of reproducing the fracture behaviour of grout, bolt-grout interfaces, and rock joints, evidence for which were the excellent agreements of the stress-displacement and cracking patterns of the numerical simulations and their experimental

counterparts. Specifically, the proposed model demonstrated that it is able to capture the post-peak softening response of grout material during uniaxial compressive loading, which the current constitutive models in DEM codes (i.e. FJM in PFC2D) cannot accurately obtain.

This research also demonstrated through numerical experiments that the novel, stepwise pull-and-shear test (SPST) scheme, developed to conduct combined pull-and-shear loading tests, can identify the hidden mechanisms involved in the shear resistance behaviour of bolted rock joints. The idea was to apply pre-tension stress (i.e. pull-out load) on the rock bolt, and then perform direct shear tests on bolted rock joints. The numerical analyses of the pull-out experiment showed that four different stages (i.e. linear elastic, pre-peak hardening, post-peak softening, and residual stage) are involved in the failure of fully grouted rock bolts. During the pull-out test, we monitored the σ_n^i and its corresponding contact chain force network. Results showed that the σ_n^i increased and the contact compressive forces grew throughout the experiment, but the rate of increase significantly declined at the yield point, where the transition from a linear elastic to a pre-peak response occurred. The numerical direct shear tests also demonstrated that at yield pretension stress magnitude, the bolt delivered its ultimate performance; thus, maximum shear resistance was achieved at this point. The numerical observations revealed that the peak stress reduced with a decreasing rib angle of the rock bolt profile, and that this reduction was more pronounced for rib angles of 30°, which induced the lowest σ_n^i.

To better analyse the numerical results, the maximum shear stresses were plotted against their corresponding normal stresses, and a similar trend was observed for all rib angles, which gave rise to the fact that fully grouted rock bolts had the highest efficacy at the onset of the transition from linear elastic to pre-peak hardening behaviour. The numerical simulations showed that applying the CNS condition resulted in an increase in the peak resistance of rock joint, which was more pronounced at low pretension stress magnitudes in the elastic stage. During both the softening and the residual stages, however, the effect of the CNS condition was negligible.

The proposed modelling method, in conjunction with the SPST scheme, provided an efficient numerical framework that can be used by designers and geotechnical engineers for carrying out realistic experiments (i.e. combined pull-shear loads). Doing so will give them new insights into the mechanical performance of fully grouted rock bolts.

Chapter 5: DEM simulation of infilled rock joint

5.1 Introduction

The mechanical behaviour of the infilled rock joints is highly concerned in rock joint studies due to its involvement in a wide range of mining collapses. The presence of infill material within a joint can significantly influence its shear strength. Infill thickness and asperity angle are the most important parameters controlling the shear behaviour of infilled rock joints (Indraranta et al. 1999; Mylvaganam 2007; Oliveira et al. 2009). The characterisation and prediction of the shear mechanism of infilled rock joints is an significant problem in rock engineering projects. For instance, Indraratna et al. (2010a) reported that using an oversimplified constitutive model in the design process, which neglected the role of infill material, could have contributed to the collapse of São Paulo metro station. Thus, improving the understanding of the shear behaviour of infilled rock joints for better prediction of failure is crucial to practical applications in mining and geotechnical engineering.

The shear stress-deformation relationships of cohesive soils are characterised by a peak strength followed by a gradual reduction in strength to a residual strength (Kalteziotis 1981). At a molecular scale, the strength of cohesive soils is governed mainly by the forces between clay particles, which composed of cohesion and friction components (Wagner 2013). The shear failure of cohesive soils is associated with the gradual weakening of the bonds between clay particles (i.e. softening response at particle level). After peak shear strength is reached, strain localisation will occur, resulting in the development of a shear band (D'Ignazio and Länsivaara 2015). With the progressive shearing, microscopic frictional interaction between localised surfaces occurs, leading to a macroscopic residual response of the clay (Tembe et al. 2010). In this context, the gradual degradation of cohesion between soil particles can be described by damage mechanics, while plasticity theory can characterise the frictional interaction.

For cohesive soils, the PBM may still be employed to simulate their failure behaviour if DEM particles are generated at the molecular scale, which inhibits the practical application of DEM due to immense computational demand (Nguyen et al. 2017a). For making the numerical process time efficient, DEM particles are required to be created at granular scales. Therefore, the damage mechanism (e.g. cohesive softening response) have to be embodied in the constitutive contact model.

In this chapter, the proposed cohesive model was employed and used in the discrete element method (DEM) simulation to analyse the failure mechanism of infilled rock joints numerically. The exponential softening responses of the model in mixed mode loading conditions allow more realistic modelling of clay-infilled rock joints, which is more phenomenologically promising than the use of the current constitutive models in PFC2D such as the parallel bond model. Experimental works on shear behaviour of infilled materials and infilled rock joints under different normal loads are also carried out for the calibration of the cohesive model, and validation of the DEM based approach, respectively.

5.2 Experimental programme

5.2.1 Direct shear test on a cohesive soil

Before using the DEM-based cohesive model, the micro-parameters of the model should be calibrated against the macroscopic response of a cohesive soil in the laboratory. We used kaolin clay as infill material, which was commercially purchased from SIBELCO (2019). The details of infill properties are given in Table 5.1. A series of direct shear test was performed on the soil samples under different constant normal stresses (σ_n^0) of 100 kPa, 200 kPa, and 300 kPa. The soil was mixed with water and then cut into a specimen having a dimension of $60 \times 60 \times 20$ and inserted into the shear box for conducting the direct shear test. Two steel plates with the height of 20 mm were placed on the bottom and top part of the soil. Thus the total height was 60 mm. In the next stage, a vertical load was applied on the upper shear box. Axial loading was continued till stabilising the system, and then remained constant throughout the test. At the final stage, a constant horizontal velocity of 0.2 mm/min was applied on the lower shear box until reaching 8 mm of shear displacement while recording the shear stress and displacement. Three direct shear test under 100 kPa, 200 kPa, and 300 kPa were conducted, and the corresponding maximum shear stresses for each test were measured to identify the cohesion and friction angle of the cohesive soil (i.e. 21.3 kPa and 15.3°, respectively).

The results in terms of shear stress-shear displacement, normal-shear displacement, and peak shear stress – normal stress relations are presented in Figure 5.1. These macroscopic parameters will be used later on to calibrate the micro-mechanical parameters of the DEM-based cohesive model. Different stress stages were identified from laboratory observations (Figure 5.1a), namely: elastic (I), pre-peak (II), softening (III), and residual (IV) stages. Initially, the soil showed a constant shear stiffness stage (stage I). In stage I, the soil exhibited compressive response (negative normal displacement). After some shear displacement, the bond between

soil particles began to break leading to a non-linear shear behaviour before reaching the maximum strength. It can be seen that the shear displacement at which stage II started was increased by increasing the magnitude of confining pressure. At low confining pressure (100 kPa), the soil exhibited insignificant softening behaviour, while at high normal stress magnitudes (200 and 300 kPa) obvious softening response was observed (stage III, Figure 5.1a). The rate of compressive displacement was significantly reduced during stage II, and III (Figure 5.1a). During stage III, the specimen showed negligible change in the normal displacement (stage III, Figure 5.1a). The softening response was more pronounced when confining pressure is high, which was attributed to successive bond break at molecular level during this stage. With the progressive shear displacement of the specimens, a residual response was achieved (stage IV in Figure 5.1a), which attributed to the frictional behaviour of the soil particles (Tembe et al. 2010). The normal displacement of the soil remained in constant value during stage IV. These observations were consistent with the previous studies conducted on cohesive soil (e.g. Lin (2017)). The four different stages illustrated in Figure 5.1a will be used later on as guidelines to calibrate the proposed DEM framework.

Table 5.1 The basic properties of the infilled material

Property	
Unified soil classification system	CH
Specific gravity	2.58
Liquid limit, LL	58
Plastic limit, PL	28
Plasticity index	30
Optimum moisture content (%)	27
Maximum dry density ($\boldsymbol{kg/m^3}$)	1418

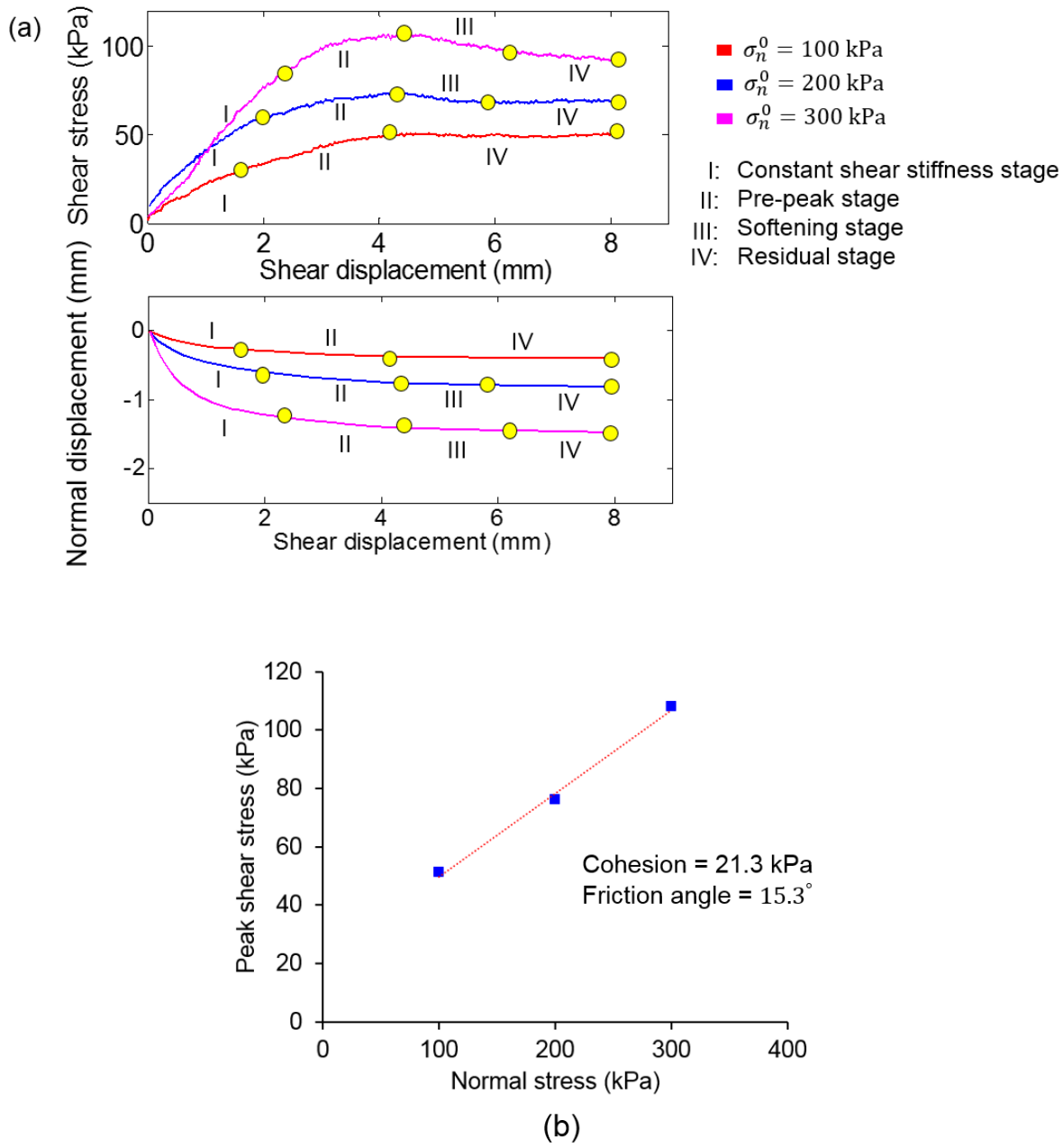

Figure 5.1 Results of the direct shear test on the cohesive soil. (a) Shear stress-displacement curves under different normal stresses (σ_n^0). (b) Calculating cohesion and friction angle of the soil based on direct shear test results.

In the next step of the experimental program, a series of direct shear tests were carried out on infilled single asperity rock joints. Conducting direct shear test on natural rock joints was not considered due to a large number of potential parameters involved in the shearing process (Tatone 2014), therefore, making calibration and validation process complicated.

5.2.2 Direct shear test on infilled rock joints under CNL condition

Dental plaster was used for generating replica rock joints as to produce rock joint with single asperity with high strength. Once this material is mixed with water at a ratio of 3:1, it can be moulded in any shape to produce a high strength replica after curing. Artificial rock samples that had a triangular joint profile with base angles of 20^{o} and 30^{o} were generated and cured at a temperature of $80^{\circ C}$ for 14 days. The previous experimental investigations on infilled rock joint showed that the ratio of infill thickness (t) to asperity height (a) has a significant influence on the shear behaviour of infilled rock joints (Jahanian and Sadaghiani 2015; Oliveira et al. 2009; Shrivastava and Rao 2018). In non-planer rock joints, as t/a increases, the overall shear strength of the rock joint decreases (Indraratna et al. 2010b). Rock joints with idealized saw-tooth asperities are suitable for studying the shear behaviour of infilled rock joints (Jahanian and Sadaghiani 2015; Lu et al. 2017; Shrivastava and Rao 2018), because they allow independent assessment of t/a. Thus, in the present study, we produced rock joints with different inclination angles to independently assess the shear behaviour of infilled rock joints. The geometrical configuration of rock joints is illustrated in Figure 5.2. The height of the top and bottom of the rock-like specimen was considered to be 12 mm, which gives a total height of 24 mm. Thus, the laboratory specimens with infill thickness of 12 mm had a total height of 12+12+12 = 36 mm. We placed steel plates with a height of 12 mm on the top and bottom part of the experimental specimens. Dental plaster was used to attach the steel plates to the rock-like material to avoid losing the connection between rock and steel plates during shear. Similarly, for 6 mm infill thickness, we placed steel plates with a height of 15 mm on the top and bottom part of the rock to obtain a total height of 60 mm. The dimension of infill specimens are illustrated in Figure 5.2b. As mentioned earlier, no asperity degradation was considered in the experimental program, and the test was conducted under 100 kPa and 300 kPa of constant normal stresses. The role of the replica was to provide a base restricted area for the infill material to shear after applying a normal stress and then a shear stress without occurring any asperity damage. The cohesive soil introduced in the previous section was used as the infill material.

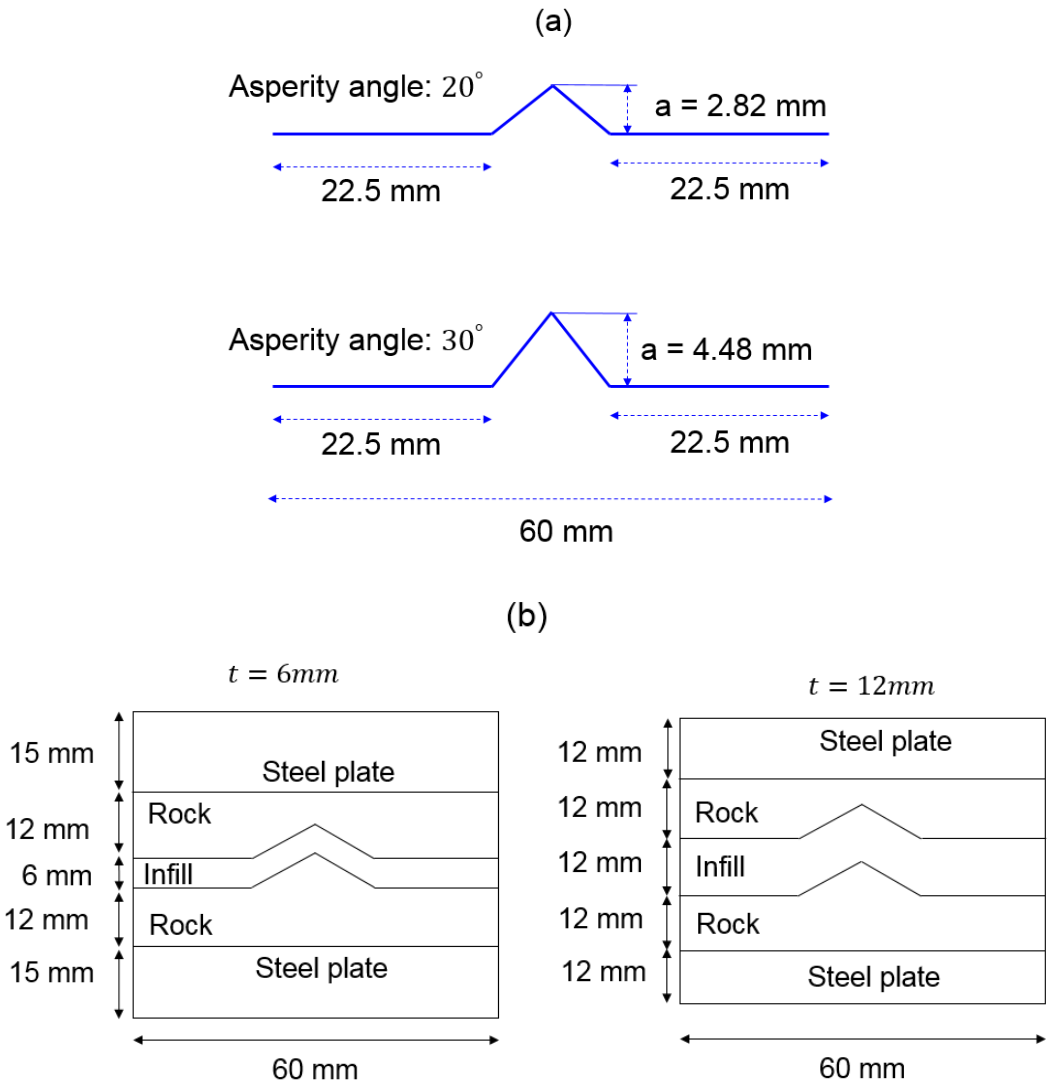

Figure 5.2 (a) The geometrical configuration of infilled rock joints. (b) The dimension of infill specimens.

The following procedure was followed for preparing the infilled rock joint specimens:

1- Plaster moulds were created to cast the synthetic rock samples. 3D printing technique was utilised to prepare the artificial joint surfaces with asperity angles of 20° and 30°. Both halves of the replica were created at the same session as two different negative moulds were in access for top and bottom half specimens.
2- The dental plaster was mixed with water at a ratio of 3:1 by mass to reach a low viscosity material that filled well into the moulds ensuring the escape of air bubbles. The casting procedure was completed in less than 10 minutes due to the fast curing rate of the dental plaster. The moulds then rested on a vibrating table for 10 minutes to eliminate any remaining air bubble as illustrated in Figure 5.3a.

3- The samples were de-moulded after one hour (Figure 5.3b). The rapid curing rate of the mixture accelerated this process. After that, the samples were left in the oven and cured for the next 14 days at 80℃.

4- The cohesive clay was prepared as per the procedure introduced in section 5-2. For creating the desired infill thickness (6 mm or 12 mm), different moulds were generated. The soil was conformed well to the moulds using a spatula. After that, a de-moulder was used to extrude the infill layer (Figure 5.3c).

5- The final stage included placing the infill layer on the rock joints surface. The infill layer was placed on the bottom block and trimmed to reach the same dimension of the replica (Figure 5.3d). After placing the top block on the infill layer, the whole sample was placed into the direct shear test machine to conduct experiment. (Figure 5.3e-f).

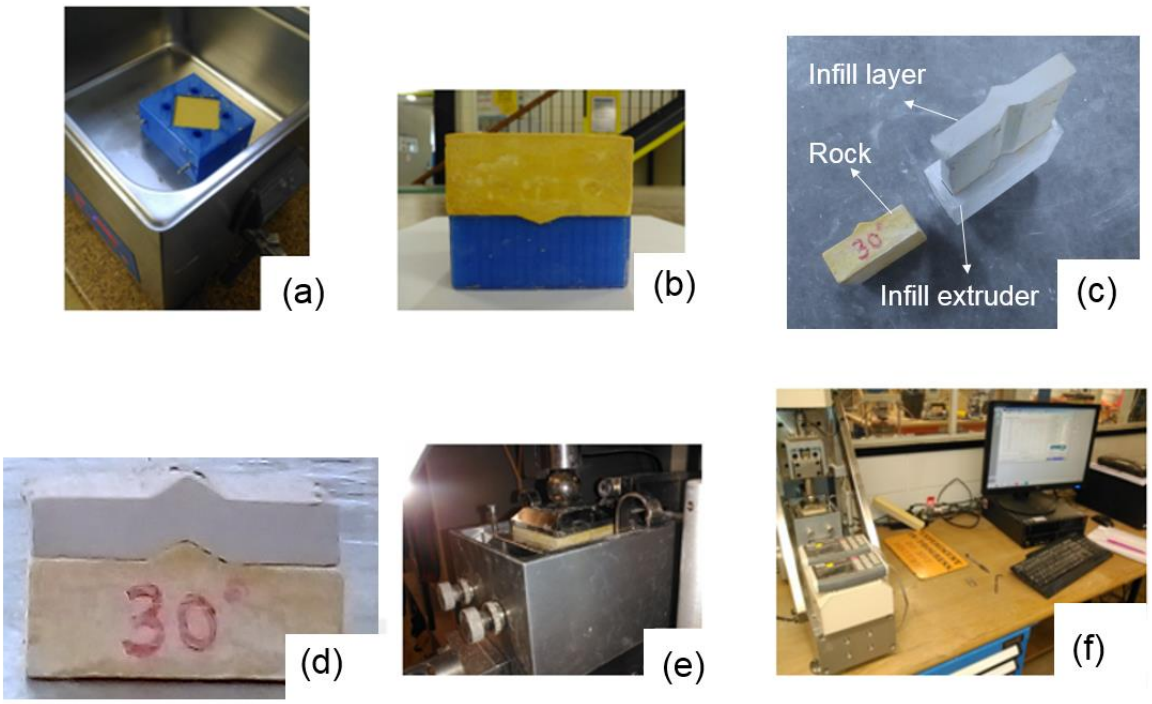

Figure 5.3 Different steps of direct shear test on infilled single asperity rock joints. (a) Pouring the dental plaster into the mould and vibrating the sample for 20 minutes. (b) Removing the sample from the mould. (c) Creating the desired infill thickness. (d) Placing the infill layer on rock joint surface. (e) Moving the specimen to the shear box. (f) Conducting the direct shear test and recording the data.

The direct shear tests were conducted using a GDS shear base system which is an electro-mechanical shear testing device. The shear box of this apparatus is made up of the top and bottom parts. A constant normal stress was applied on the upper shear box through a loading

frame. The upper box was remained stationary during the shearing procedure. A horizontal velocity with a rate of 0.2 mm/min was applied to the bottom part to achieve the shearing of the infilled rock joint. Both normal and shear forces were applied using GDS electro-mechanical force actuators. The data acquisition system was connected to a PC running GDSLAB data acquisition software for monitoring the shear stress and displacement throughout the shearing procedure. Six different direct shear tests were carried out on infilled rock joints. For rock joint with asperity inclination of 30°, an infill layer with 6 mm and 12 mm thickness was considered and for those with 20° asperity angle, an infill layer of 12 mm was prepared. Notice that no asperity damage was occured during our laboratory testing, which was necessary to understand the infill thickness and asperity characteristics on the shear mechanism of infilled rock joints (Jahanian and Sadaghiani 2015).

The results of direct shear test on infilled rock joints is illustrated in Figure 5.4. Figure 5.4a shows the shear stress-displacement, and normal-shear displacement curves. It can be seen that similar to cohesive soil shear behaviour (Figure 5.1a), the clay-infilled rock joints also exhibited four different stages which were previously introduced in section 5-2. However, higher peak and residual shear strengths were observed except for $t = 12\ mm$ and $\alpha = 20^{\circ}$, which attributed to the presence of asperities. The normal-shear displacement curves of infilled rock joints were also different from the soil. It can be seen that increasing the magnitude of the normal stress significantly enhanced the peak and residual strength of the infilled rock joints. In each graph, the ratio of infill thickness (t) to asperity height (a), t/a, is given. The stress stages, and normal displacement response obtained for infilled rock joints are demonstrated at shear-stress displacement graph obtained for the specimen with $t = 12\ mm$ and $\alpha = 20^{\circ}$, and the underlying shear mechanism is described as follows. At the initial stage of shearing (I), the shear stress is rapidly increased (constant shear stiffness), which is referred to here as the elastic stage. The initial compression was observed for all specimens in this stage. During this phase, the shear stiffness of the infilled rock joint was controlled by the applied normal stress. At stage II, nonlinear hardening was observed in the shear stress-displacement graph. There were two main reasons contributing to the nonlinear pre-peak behaviour of the infilled rock joint. Firstly, the progressive shear displacement weakened the bond between soil particles, causing a reduction in the shear stiffness and thus, a nonlinear response was observed during stage II, which was similar to the mechanism observed in Figure 5.1a. Secondly, due to infill squeezing between advancing asperities (Indraratna et al. 2010a), the asperity interfaces approached each other causing an enhancement of asperity interference that was represented by pre-hardening

behaviour at shear stress-displacement graph. This hardening behaviour, which was not the case in the specimens without rock joint (Figure 5.1a), significantly increased the peak shear strength of infilled rock joints. For the smaller t/a ratio of 1.3 and 2.7, the initial compression of infilled rock joints was followed by dilation. The dilative response for t/a ratio of 1.3 was more pronounced under both 100 and 300 kPa of normal stress, which was attributed to asperity interference when the infill thickness was relatively small. For t/a ratio of 4.25, however, the compression was continued, and the infilled rock joint only exhibited a similar behaviour of soil compression. After peak shear strength was reached, due to progressive degradation of cohesion, the infilled rock joints demonstrated a post-peak softening response (stage III). Unlike soil behaviour, at low confining stress (100 kPa), a slight softening response was observable in infilled rock joints. This was due to an increase in the stress level, which caused more bond break in the infill material during the post-peak response. The laboratory results showed that, in all infilled rock joints, the softening intensity increased significantly with increasing the confining pressure. For the smaller t/a ratio of 1.3 and 2.7, the rate of dilation was reduced during stage III, whereas for t/a ratio of 4.25 the compression continued with a lower rate. During stage IV, the infilled rock joint exhibited a residual behaviour, which was attributed to the frictional response between soil particles. Notice that, the shear stress characteristics of other specimens (with different asperity angle and infill thickness) can be similarly interpreted. Our experimental observations was consistent with the previous laboratory investigations (Indraratna et al. 2010a; Indraratna et al. 2013; Indraratna et al. 2014).

The laboratory results also showed that the geometrical configuration of rock joints influenced the peak and residual shear strengths. In order to better interpret the results based on rock joint geometrical properties, the peak and residual shear strengths of infilled rock joints were plotted against the t/a ratio, and the results are illustrated in Figure 5.4b. The experimental study of Ladanyi and Archambault (1977) demonstrated that higher shear strength will be achieved for infilled rock joints with steeper asperities, and the influence of infill thickness on peak shear strength is more pronounced for asperities with higher inclination angles. In the present study, we observed that by increasing the t/a ratio, the peak and residual shear strengths of the infilled rock joints exhibited a significant reduction (Figure 5.4b). For t/a of 1.3, the peak and residual strengths at both 100 and 300 kPa of normal stress showed the highest values, while for t/a of 4.25 the shear behaviour of rock joint was governed by infill material, and as expected, the value of peak and residual strengths of the rock joint approached to those of cohesive soil. The experimental results will be used to validate the proposed calibrated DEM framework.

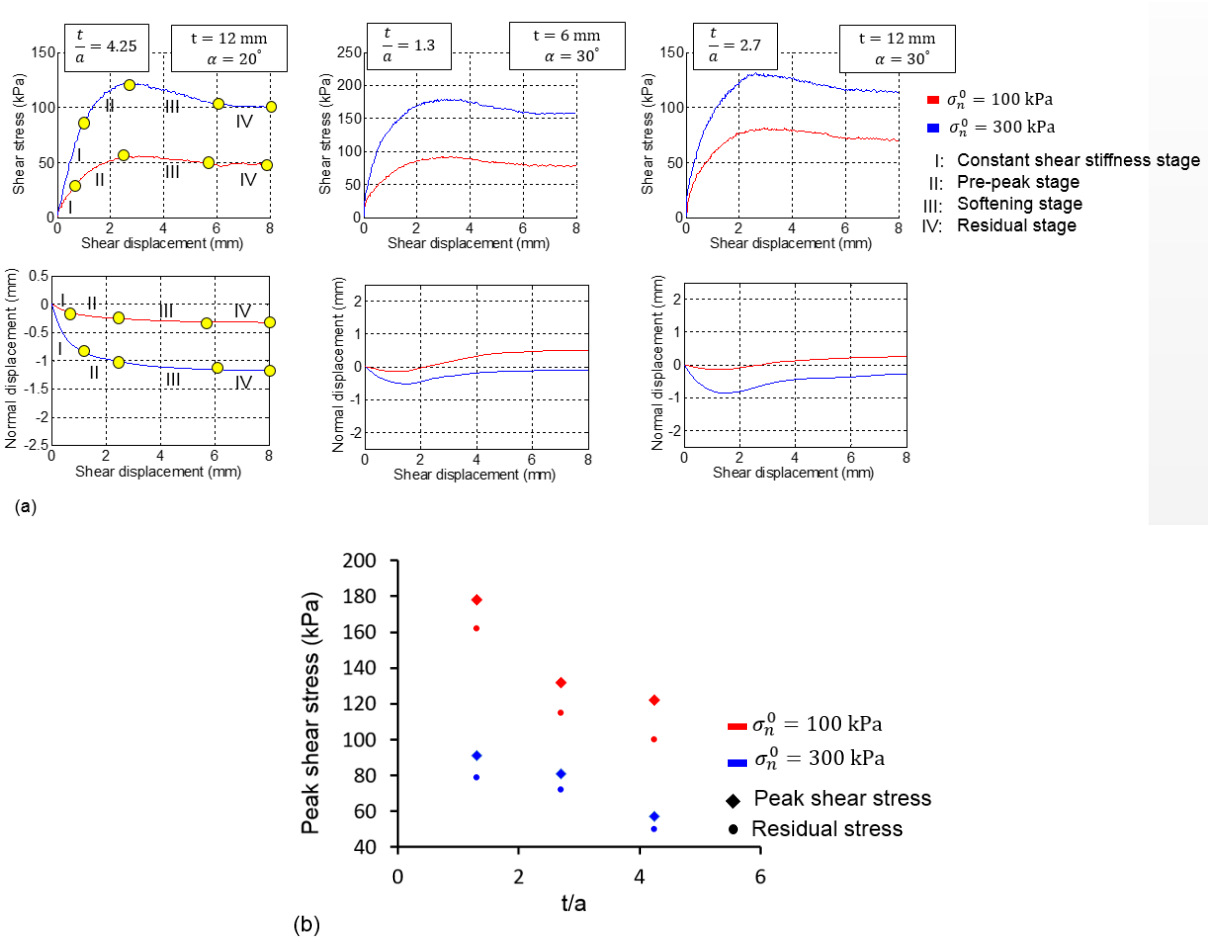

Figure 5.4 The results of the direct shear test on infilled rock joints with different asperity angles and infill thicknesses. (a) Shear stress-displacement and normal-shear displacement curves. (b) Variation of peak and residual shear strengths with the t/a ratio.

5.3 Establishment of the cohesive DEM

The proposed cohesive model (chapter 3) represent the properties of cohesive contacts at the granular scale so that it requires highly sophisticated experiments to achieve the micromechanical parameters of the cohesive soil. In general, the mechanical parameters obtained from the standard laboratory testing cannot be imported directly into the DEM model as the macro-mechanical behaviour is synthesised at mesoscale. The remedy, however, is to calibrate the micro parameters by matching the results of DEM simulation with experimental data. This procedure has been used in DEM studies for obtaining the micromechanical properties of constitutive models (Nguyen et al. 2017a; Potyondy and Cundall 2004; Shen et al. 2016). Here the results of direct shear tests on cohesive soil was used for calibrating the micro parameters. Firstly, a metrical vessel containing a dense pack of interlocked particles was generated. After that, the procedure was continued by calibration of normal and shear

stiffness of contacts ($k^0_{n,CCM}$ and $k^0_{s,CCM}$) through matching the DEM results in the elastic stage. Then the peak shear stress was approximated by altering cohesion (C^0_{CCM}). The next step was to calibrate the softening parameter (κ_{CCM}) based on the post-peak response of the cohesive soil. Finally, friction and dilation coefficients (μ_{CCM} and β_{CCM}) were calibrated by fitting DEM response with the experimental observations. After the calibration procedure, the micro parameters were adopted to validate the proposed cohesive model through simulating the shear behaviour of infilled rock joints.

5.3.1 Generation of DEM specimen

A two-dimensional model was created in PFC 2D for simulating the same laboratory direct shear tests introduced in subsection 5.2.1 and the micro-mechanical parameters of the cohesive constitutive model were calibrated by comparing the numerical simulation results with the physical response of the cohesive soil in direct shear testing. The height of laboratory specimen for the soil test was 60 mm out of which 20 mm was the height of soil sample, and 40 mm was the total height of steel plates placed on the top and bottom part of the soil (the height of each steel plate was 20 mm). A material vessel with a dimension of 60mm×50mm was created and a particle assembly including nearly 11,000 balls was generated in PFC 2D. The height of the soil specimen was 20 mm, which was equal to the laboratory counterpart. The height of steel plates in the numerical specimen was reduced by 5 mm to make the numerical simulations time efficient. Since no damage was expected in steel plates, reducing the size had no influence on the numerical results. The particle size was controlled by the uniform distribution with minimum and maximum diameters of $D_{min} = 0.48\,mm$ and $D_{max} = 0.64\,mm$ respectively. Using uniform grain size distribution is common practice in DEM simulations as simulating real grain size distribution is nearly impossible (Bahaaddini et al. 2013; Feng et al. 2018; Le et al. 2017; Nguyen et al. 2017a; Nguyen et al. 2017b). The reason is that creating a particle assembly with the exact porosity of physical material requires a huge number of particles leading to inefficient computation (Nguyen et al. 2017a). A comprehensive instructions for generating material-genesis in PFC has been described by Potyondy and Cundall (2004). According to their study, an overall porosity of 16% can ensure the generation of a dense particle assembly in DEM. The same approach was adopted in this study to generate samples. After producing the numerical samples, the particles were divided into two groups namely, soil and plate particles (Figure 5.5a). The steel plates used in the present study were assumed non-breakable and non-deformable as the strength and modulus of the steel plates were much larger in comparison with that of cohesive soil used. In the numerical setup, the height of the upper

and lower steel plates was assumed to be 15 mm to reduce the number of particles representing the steel plates. This minimised the simulation time and made the numerical approach computationally efficient. This assumption was acceptable as there was no damage in the steel plates. Furthermore, there was no gravity acting on the model so that the mass of particles had no influence on the mechanical response of the system. The PBM was applied on the contacts between steel plate particles (Figure 5.5b), and its microproperties were selected according to the literature (Shang et al. 2018a), which include Young's modulus (200 GPa), shear to stiffness ratio (1.5), cohesion (800 MPa), and tensile strength (400 MPa).

The proposed cohesive model was installed on soil-soil contacts and soil-steel contacts (Figure 5.5b). Figure 5.5c shows the boundary condition applied to the system. The calibration procedure involved matching the numerical results of direct shear test of the cohesive soil under 100 kPa of constant normal stress with experimental counterparts. Then micro-mechanical parameters related to the cohesive soil are obtained, and finally the same micro parameters on the model are adopted for reproducing the shear behaviour of the cohesive soil under 200 kPa and 300 kPa of constant normal stresses. In the numerical models, the walls created during particle assembly generation were removed and 8 new walls were created for applying the boundary condition and performing the direct shear test (Figure 5.5c). The upper block was kept stationary during the shearing procedure, and a constant horizontal velocity of 0.03 m/s was applied on wall 5. This velocity was chosen because it was observed through a series of numerical experiments that any value lower than this did not influence the overall stress-displacement curve and damage response of the models. The selected horizontal velocity allowed us to maintain the model in a quasi-static equilibrium condition while reducing the computational costs. The CNL condition was achieved by adopting a servo-controlled mechanism (Itasca 2016) and applying a desired constant normal stress on the wall 1. The reaction force in wall 5 was monitored and divided by the length of the specimen (60 mm) to calculate the shear stress, the horizontal displacement of wall 5 was measured during the shearing procedure to represent the shear displacement.

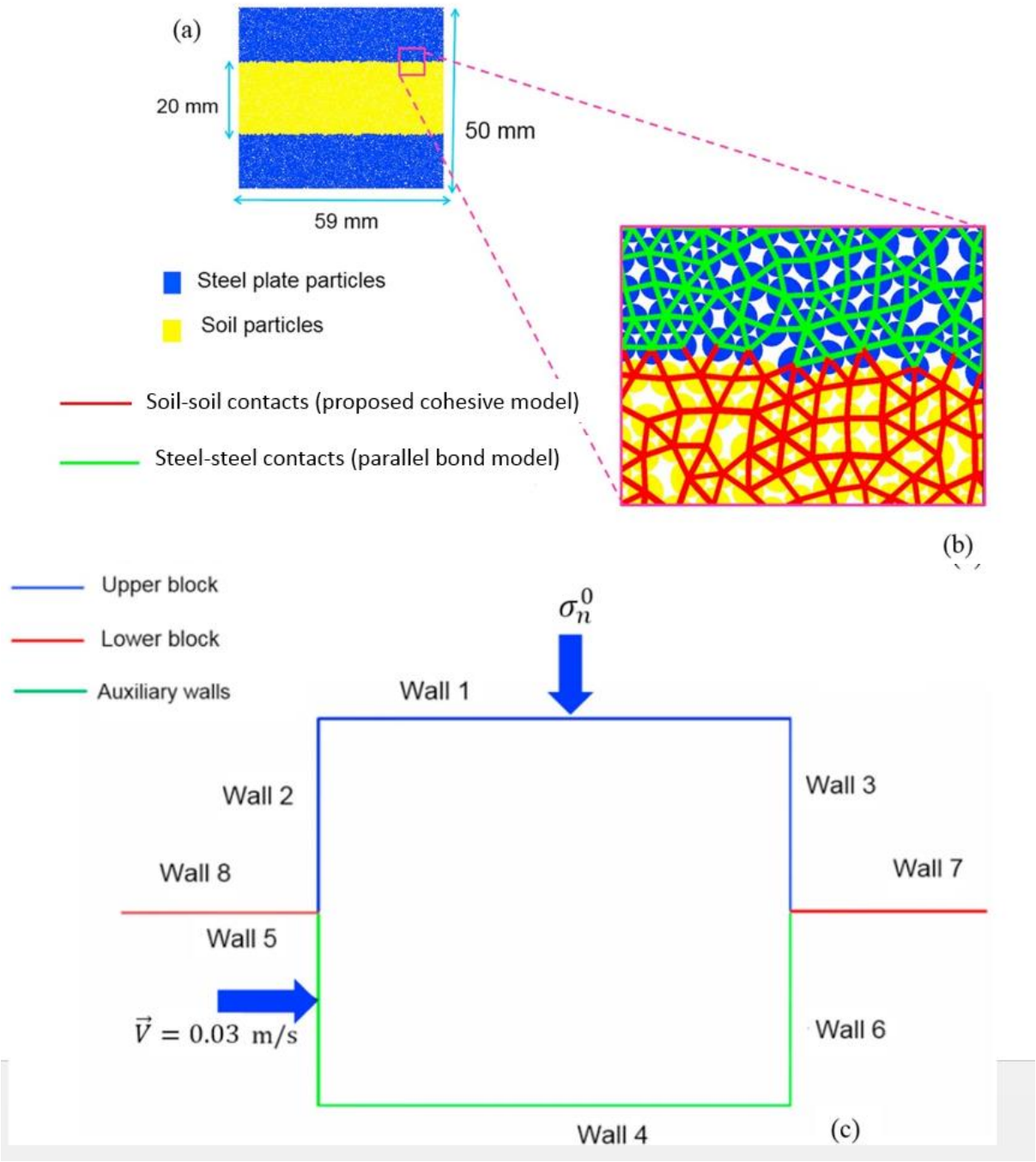

Figure 5.5 Numerical specimen for conducting a direct shear test on cohesive soil. (a) Material vessel dimension and particle assembly including soil and steel particles. (b) The constitutive contact models installed for each contact group. (c) The boundary condition applied on the material vessel for conducting the direct shear test.

5.3.2 Microproperties calibration and model validation

The micro parameters needed to be calibrated were $k_{n,CCM}^0$, $k_{s,CCM}^0$, C_{CCM}^0, μ_{CCM}, β_{CCM}, and κ_{CCM}. The PFC software also allows altering the value of $k_{n,CCM}^0$ and $k_{s,CCM}^0$ after sample generation procedure enabling the user to generate a single specimen and repeat the tests for

any desirable number of simulations. $k^0_{s,CCM}$ was calibrated through matching the simulation results with linear elastic part of the shear stress-displacement curve obtained from experiment. The $k^0_{n,CCM}/k^0_{s,CCM}$ ratio was assumed to be 1.8, and this assumption was further verified by obtaining the best fit from numerical simulations under various normal stress magnitudes. The desired peak shear stress was achieved by altering the cohesion of contacts (C^0_{CCM}). The friction coefficient (μ_{CCM}) was calibrated together with C^0_{CCM} in such a way to return the best match in terms of peak shear strength. The reliability of this microproperty was further verified by comparing the macroscopic numerical friction angle with the experimental counterpart. After achieving satisfactory macroscopic elastic response and peak shear strength, by varying the value of softening parameter (κ_{CCM}), the damage response of the cohesive soil throughout the post-peak stage was approximated. It should be noted that the softening parameter has a simultaneous influence on the pre-peak, the peak, and the post-peak responses. So that this parameter was calibrated in such a way to reproduce the best overall response in terms of pre-peak hardening, peak, and softening stages. The dilation ratio (β_{CCM}) is the local property of the cohesive soil, which can only be identified with more sophisticated laboratory techniques. However, as mentioned by Nguyen et al. (2017a), this parameter can be calibrated by fitting with the experimental observation. A parametric study of direct shear test was conducted in which β_{CCM} was varied in a range from 0.15 to 0.45. The numerical simulations exhibited that macroscopic response of the cohesive soil was virtually unaltered when varying the dilation coefficient in this range. The final set of microproperties obtained from calibration procedure are given in Table 5.2.

Table 5.2 The microproperties of the calibrated soil

$k^0_{s,CCM}$ (GPa/m)	$k^0_{n,CCM}/k^0_{s,CCM}$	C^0_{CCM} (kPa)	κ_{CCM} (1/m)	μ_{CCM}	β_{CCM}
0.7	1.8	23.5	18.0×10^3	0.32	0.2

For validating the proposed cohesive contact model, the same micro mechanical parameters obtained through calibration procedure under $\sigma_n^0 = 100$ kPa were adopted to reproduce the macroscopic response of the cohesive soil under 200 kPa and 300 kPa. The results of the validation process are given in Figure 5.6. Figure 5.6a indicates that the proposed model can approximate the macroscopic behaviour of the cohesive soil with an excellent agreement. As Figure 5.6a illustrates, an increase in the magnitude of normal stress showed higher shear stiffness and peak shear resistance.

In order to get a better insight regarding these observations, the damage evolution of cohesive soil was monitored during the shearing process, and the results are given in Figure 5.6b. Based on Eq. 3.13, the amount of damage was calculated for each cohesive contact during the shearing procedure and shown graphically to derive a better interpretation of shear zone evolution in the soil contacts. Completely damaged contacts are shown in red ($D_{CCM} = 1.0$) and bonded contacts are shown in blue ($D_{CCM} = 0.0$). It can be observed from Figure 5.6b that the number of bonded contacts (or contacts experienced linear elastic stage) was higher for a numerical specimen with σ_n^0 =100 kPa compared to higher normal stress magnitudes. In fact, as the magnitude of normal stress increased, the reaction force required for shearing the specimen was raised leading to a significant increase in the shear stiffness. Consequently, more contacts experienced their yielding limits.

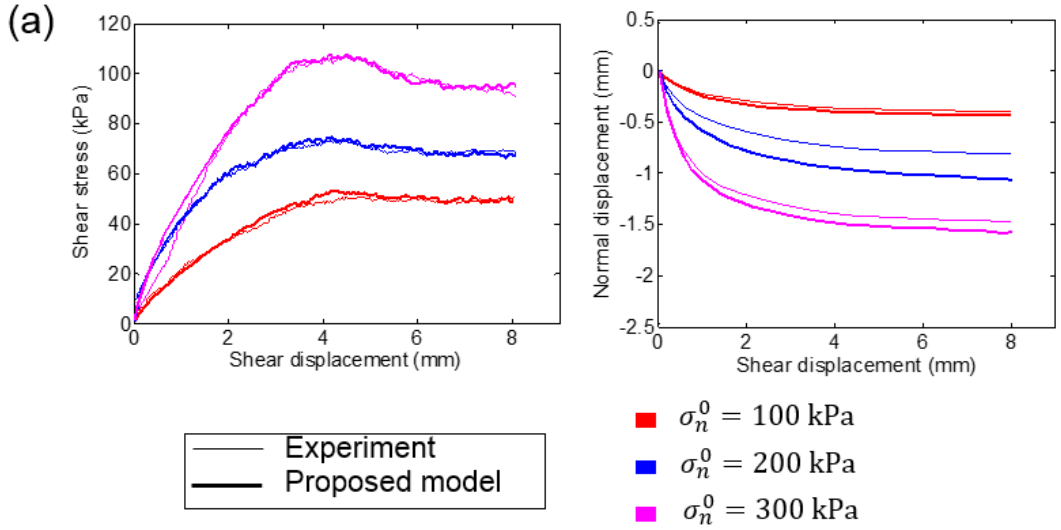

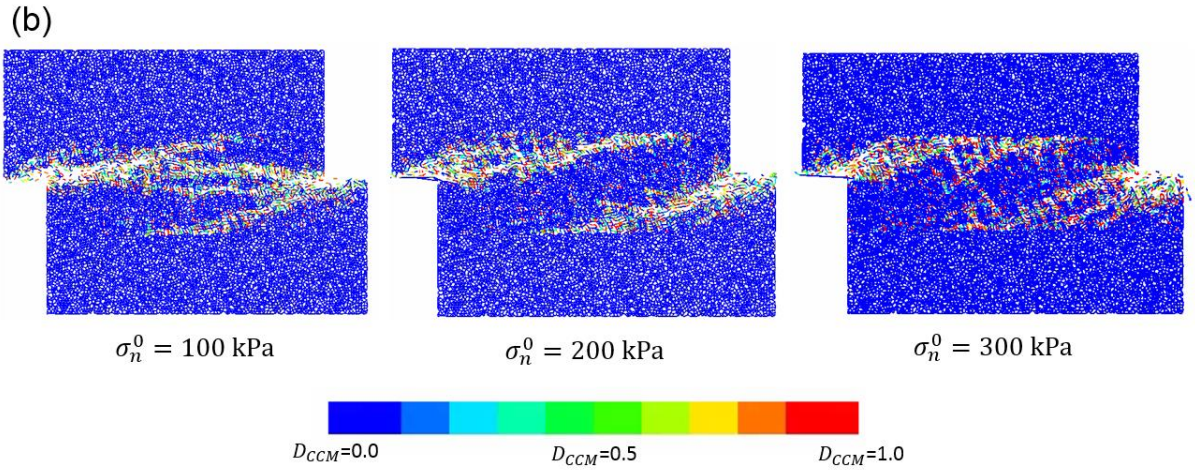

Figure 5.6 The results of experimental and numerical direct shear test on cohesive soil under various constant normal stresses. (a) The shear stress-displacement and normal-shear displacement results of calibration of micro-mechanical parameters. (b) Damage evolution pattern in numerical samples.

Figure 5.1a illustrates that in the physical specimens the shear stiffness increases by an increase in the normal stress, while the same material was used in all the tests. Similarly, the increase in the shear stiffness of the numerical specimen was due to an increase in the magnitude of normal stress (Figure 5.6a). In fact, the same material, which was represented by one set of microproperties, was used in all simulations to ensure that the calibrated model was able to mimic the macroscopic response of the cohesive soil under different normal stresses. Others also confirmed this approach in the previous DEM studies (Bahaaddini et al. 2013; Bewick et al. 2014c; Hofmann et al. 2015a; Oh et al. 2017).

To better interpret the damage evolution procedure in the material and to carefully observe the performance of the proposed cohesive model in reproducing the softening response at mesoscale, the value of damage in each contact was monitored at different stress stages introduced in section 5-2, and the results are illustrated in Figure 5.7. The points at which the damage evolution was monitored are marked with yellow circles on the graphs (Figure 5.7a). Similar to the laboratory observations (Figure 5.4a), the DEM shear mechanism of cohesive soil can be divided into four separate stages namely elastic, pre-peak, peak, and residual stages (Figure 5.7a). The shear mechanism observed during numerical modelling is described in the following paragraphs.

During constant shear stiffness phase (stage I in Figure 5.7a), the cohesive contacts returned their elastic response so that the reaction force measured from the wall 5 (Figure 5.5) only

showed an overall elastic behaviour of the cohesive contacts. With the progressive increase in shear displacement, the shear force needed to move the specimen horizontally was significantly increased, resulting in the yielding of the cohesive contacts. The normal-shear displacement curve (Figure 5.7a) showed initial compressive behaviour for all specimen, with the cohesive soil under 300 kPa exhibited the highest initial compression. From point "a" to point "b" of the shear stress-displacement graph (Figure 5.7a), the pre-peak stage (stage II) was observed for both 100 and 300 kPa of normal stress. At point "a" (Figure 5.7b, column a), the softening of cohesive contacts started, which mainly occurred at the upper left and lower right of the specimens. As expected, the number of yielding (softened) contacts ($0.0 < D_{CCM} < 1.0$) was higher at 300 kPa. Since in the yielding contacts $D_{CCM} < 1.0$, these contact therefore were still being able to carry stresses. On the other hand, a number of contacts at the central areas of the specimens were under elastic behaviour ($D_{CCM} = 0.0$), and could produce more stresses at grain level. Thus, the overall response of these softened and non-yielding bonds resulted in the pre-peak behaviour of the soil at the macroscopic scale. At the end of this stage (Figure 5.7b, column b), the localised shear zones were largely extended, and the maximum shear strength of the soil was achieved.

The numerical results showed that the damage response of the contacts was affected by the magnitude of applied normal stress. The numerical sample with $\sigma_n^0 = 300$ kPa produced more damaged contacts, while at $\sigma_n^0 =$100 kPa they were less pronounced. It can also be observed from Figure 5.7a that the shear stiffness of the specimens exhibited a gradual reduction (stage II), which attributed to the progressive contact softening and hence the growth of localised shear zones. The pre-peak phase (stage II), which regarded as a nonlinear elastic behaviour at macroscopic scale, was the natural consequence of the collective mechanical response of the DEM contacts, even though the nonlinear characteristics were not incorporated in the constitutive relationships of the proposed model. Notice that, phenomenologically, both yielding and non-yielding contacts are needed to capture the pre-peak nonlinear behaviour in the cohesive soil, which confirms the effectiveness and necessity of incorporating an exponential softening decay in the proposed DEM framework. During stage II, the rate of compression in the DEM particles reduced under both 100 and 300 kPa normal stress magnitude (stage II, Figure 5.7a), which could be attributed to the growth of localised damage zone in the specimens (column b, Figure 5.7b).

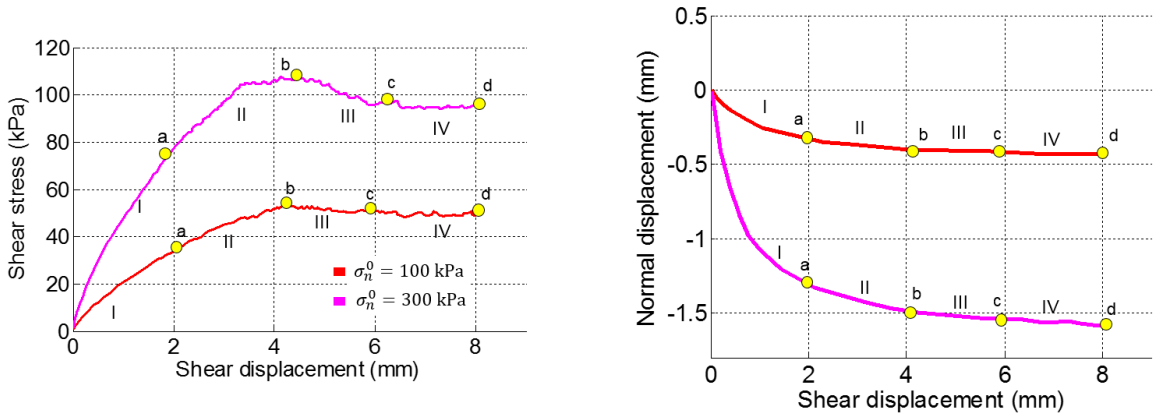

(a)

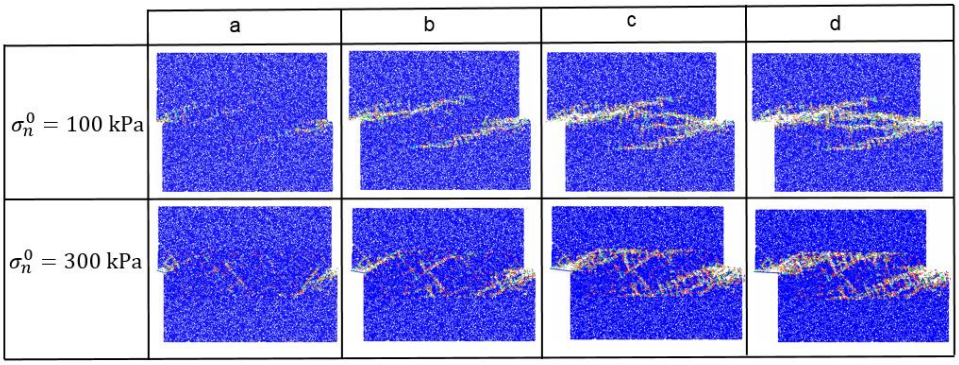

(b)

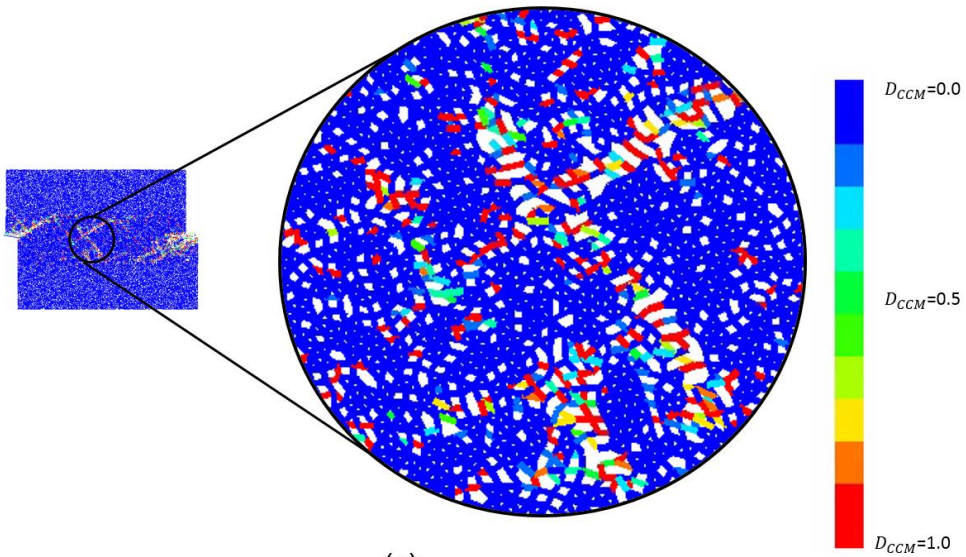

(c)

Figure 5.7 Results of a direct shear test on a numerical sample. (a) The shear stress-displacement graph. (b) The evolution of damage in the cohesive contacts at different stress level. (c) A close-up view of damage evolution under 300 kPa of normal stress at point “b”.

At peak shear strength (Figure 5.7a, point "b"), the numerical specimen with $\sigma_n^0 = 300$ kPa showed a higher number of damaged contacts ($D_{CCM} = 1.0$) at the centre than $\sigma_n^0 = 100$ kPa (Figure 5.7b, column b). This was due to the high magnitude of confining pressure, which caused the cohesive contacts in the middle of the specimen to come into their yielding limit, and display progressive damage behaviour. Figure 5.7c illustrates a close up view of the contacts in the central part of the specimen with 300 kPa. It can be seen that in this particular region, the contacts exhibited both softening ($0 < D_{CCM} < 1$) and damaged ($D_{CCM} = 1.0$) responses, which was hardly detected at low confining stress. After reaching the peak shear strength, the specimens entered to stage III at which the level of shear stress gradually declined. This macroscopic softening behaviour was mostly depended on the magnitude of applied normal stress which influenced the degree of contact resistance. Thus, it was observed that at the end of the softening stage (Figure 5.7b, $\sigma_n^0 = 300$ kPa, column c), substantial damage was incurred to the contacts, which in turn intensified the macroscopic softening response in the numerical specimen with $\sigma_n^0 = 300$ kPa (Figure 5.7a, stage III). In contrast, the mild softening stage under low confining pressure (Figure 5.7a, $\sigma_n^0 = 100$ kPa, stage III) was attributed to the behaviour of the contacts, which remained mainly at their softening phase ($0.0 < D < 1.0$) (Figure 5.7b, $\sigma_n^0 = 100$ kPa, column c). These numerical shear behaviour were reasonably consistent with the laboratory observations (Figure 5.1a). During stage III, an insignificant change in the compressive behaviour of the DEM model was observed, which was due to the extension of localised damage (stage III, Figure 5.7a). Finally, after nearly 6 mm of shear displacement, the residual shear strength was mobilized (Figure 5.7a stage IV). During this stage, the shearing process progressed along the localised shear zones (i.e. damaged contacts in Figure 5.7b, column c). It can be seen from Figure 5.7a that during stage IV the shear strength of the models remained unchanged, which was associated with the growth of insignificant number of softened or damaged contacts in the localised shear zones (Figure 5.7b, columns c and d). Similarly, the normal displacement of the models demonstrated a constant value (Figure 5.7a).

The above mentioned DEM results demonstrated the capability of the proposed cohesive DEM framework in capturing the mechanical and failure behaviour of cohesive soil tested under CNL direct shear tests.

Figure 5.8a and b illustrate the force-displacement law of PBM under tension and shear loading (Itasca 2016). It can be seen that when a DEM contact reaches its yielding limit (either tensile or shear strength), the contact forces abruptly reduce to zero (Itasca 2016). In fact, the PBM features no gradual degradation of contact strength after yield point. The force-displacement law depicted in Figure 5.8a and b, clearly illustrates that the PBM produce no gradual strength degradation. If the PBM is augmented with a cohesive post-peak behaviour, e.g. an exponential decay function, it will be able to reproduce a gradual softening response after yield point.

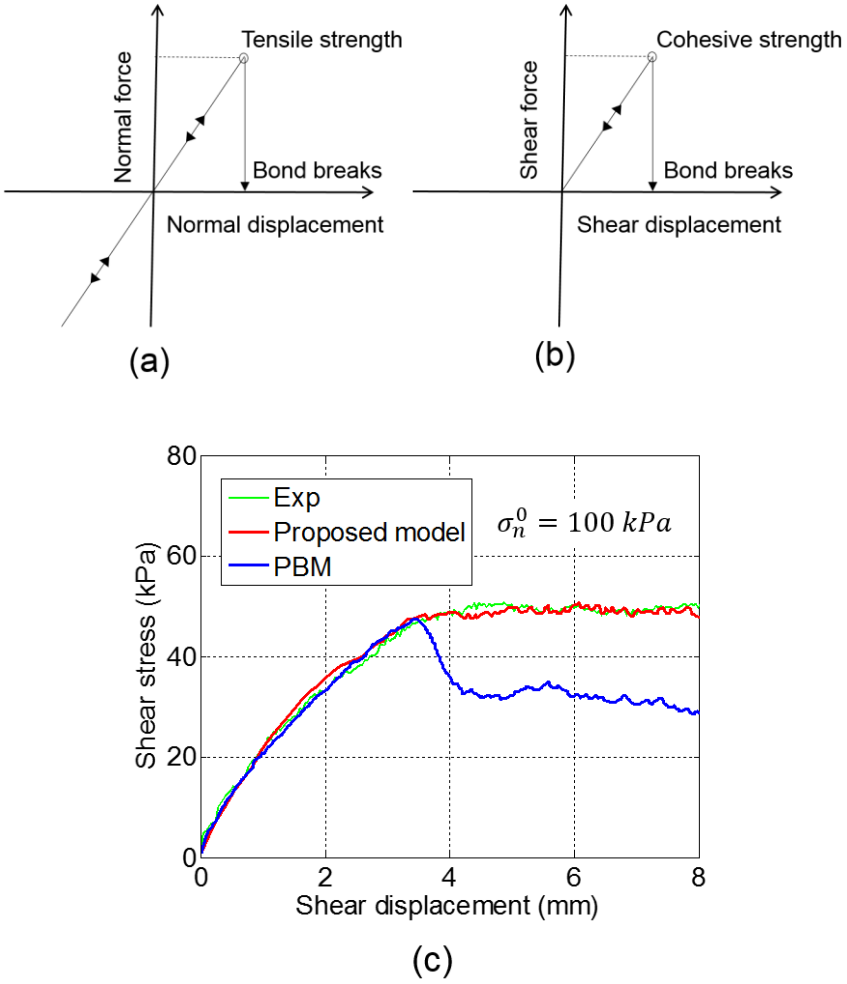

Figure 5.8 The simulation results using PBM. Force-displacement law of the PBM in (a) tension, and (b) shear. (c) The shear-stress displacement curves obtained from the direct shear test.

Another numerical direct shear test was carried out using the same DEM setup (Figure 5.5) and contact attribute. The only difference was that the cohesive model was replaced with the PBM. The PBM has four microproperties including normal and shear stiffness, tensile strength, and cohesion. The tensile strength and cohesion control the bond strength. The stiffness parameters of the PBM was kept the same as those of the cohesive model, and the cohesion of contacts was

assigned as the same C^0 obtained in the calibration procedure. There was no direct way to measure the tensile strength of the soil at microscopic level, therefore this parameter was assumed as equal to the contact cohesion. The macroscopic shear stress-displacement obtained from PBM is illustrated in Figure 5.8c. The PBM reproduced the same macroscopic elastic response as the proposed model. However, the peak and residual stresses could not be achieved by the PBM. The reason is that in the PBM when the contacts reached their yield limit (i.e. cohesive strength), the forces reduced abruptly to zero (Figure 5.8a and b). Hence, the PBM contacts could not resist against shearing. Thus, at macroscopic scale, the overall response was a peak shear strength followed by a residual behaviour. In the cohesive model, however, some of the cohesive contacts returned their softening response ($0.0 < D_{CCM} < 1.0$) after yield limit, and some other were still in the linear elastic stage ($D_{CCM} = 0.0$). As a result, the overall macroscopic response of the model was a pre-peak stage before the peak shear strength. Notice that, one can alter the microproperties of the PBM to obtain a good match with the experimental data (e.g. Tamás et al. (2013), Tamás et al. (2016), and Tamás (2018)). However, we believe that incorporating a softening response in the force-displacement law of the contacts allows us to achieve a more realistic phenomenological constitutive model for simulating the shear behaviour of clay-infilled rock joints.

5.3.3 Effect of shear rate on macroscopic response

In DEM modelling of the direct shear test, loading rate plays a significant role in macroscopic shear behaviour. A sufficiently small loading rate and a relatively high damping magnitude are required to ensure that the numerical specimen remains in quasi-static equilibrium, and there is no abrupt stress increase or unexpected macroscopic response within the DEM model (Kazerani and Zhao 2010). A damping coefficient of 0.7 suggested by Potyondy and Cundall (2004) was employed to approximate the quasi-static condition. The details of damping of particle motions can be found in (Potyondy and Cundall 2004). Notice that using the same experimental loading rate of 0.2 mm/min in numerical modelling is computationally inefficient. Alternatively, a sufficiently small shear loading rate can be selected to maintain the model in quasi-static equilibrium (Kazerani and Zhao 2010). In the present study, the direct shear test was repeated under different loading rates ranging from 0.01 to 0.2 m/s to identify the optimum shear loading rate. Figure 5.9 illustrates the influence of shear rate on the macroscopic behaviour of the numerical specimen. The numerical results showed that the shear loading rate less than 0.03 m/s had negligible influence on the macroscopic response of the specimen. Thus this shear rate was deemed to be sufficient to achieve quasi-static equilibrium and used in the

numerical model. This shear loading rate generated a mechanical timestep of roughly 1.2×10^{-7} s, which was automatically calculated by PFC software. Thus, the shear rate of 0.03 m/s can be interpreted to 36×10^{-7} mm/step. This means that 1 mm of shear displacement requires 360,000,000 computational steps. Others successfully followed this approach in previous DEM research (Bahaaddini et al. 2013; Kazerani and Zhao 2010).

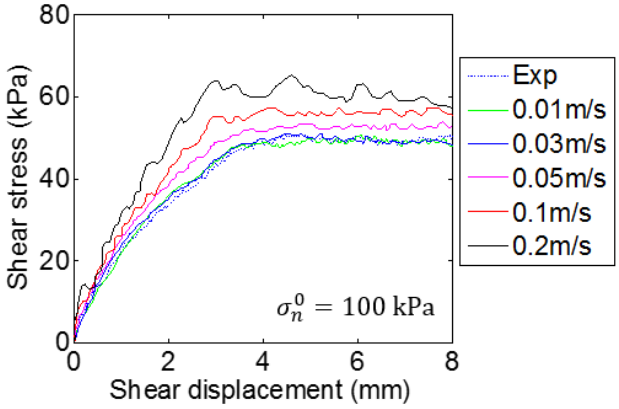

Figure 5.9 The shear stress-displacement curves using various shear rate

5.3.4 Particle size optimisation

The size of DEM particles highly influences the macroscopic response of DEM simulation. Potyondy and Cundall (2004) demonstrated that the size of DEM particles is an intrinsic parameter affecting the characterisation of the material. Thus it cannot be treated as a parameter that only controls the resolution of DEM simulation. They concluded that the particle size is the accurate representation of the effect of both packing and strength heterogeneity in DEM specimen. In fact, the number of DEM particles must be large enough to mimic the macroscopic physical response obtained from laboratory observation. Although increasing the number of particles is computationally inefficient, but an optimum particle size can be achieved by conducting a parametric study to ensure the convergence of the macroscopic results to the lowest possible size. Accordingly, four additional particle assemblies were generated and tested using the same micro parameters. Different models with various particle size were generated, and the ratio between the thickness of the soil (20 mm) and the average particle size was calculated (R_d). The results in Figure 5.10, which demonstrates shear stress-shear displacement relations, show that a convergence can be achieved by decreasing the particle size confirming that the numerical specimen with $R_d = 0.028$ was appropriate for calibration purposes as it generated a material vessel with the lowest possible number of balls leading to an efficient computational time. According to the results shown in Figure 5.10, the DEM specimens with

R_d of 0.047 and 0.038 failed to reproduce an appropriate macroscopic response, in terms of peak and residual behaviour. Models with R_d of 0.02 and 0.012 produced macroscopic results which were very close to the calibrated size ($R_d = 0.028$). Therefore, the model with minimum particle diameter (D_{min}) of 0.48 was chosen for the modelling purposes. Notice that the ratio between the maximum and minimum diameter ($^{D_{min}}/_{D_{max}}$) was considered to be 1.33 for all models.

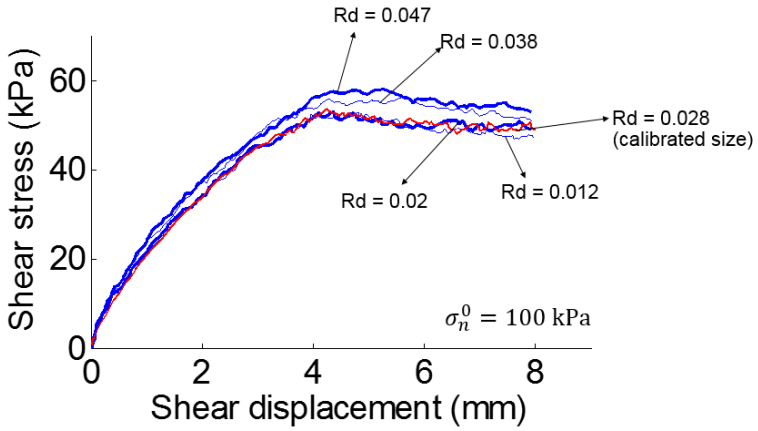

Figure 5.10 Shear behaviour of DEM specimen with various particle sizes

5.4 Generation of infilled rock joints in DEM

To further illustrate the performance of the proposed cohesive DEM framework, simulations of direct shear test on infilled rock joints were conducted using the calibrated microproprties. Notice that the maximum height of the laboratory specimens, including infill material ($t = 12\ mm$) and rock-like material, was 36 mm. In numerical models, the height was reduced to 30 mm to reduce the computational time. The dimension of numerical specimens are illustrated in Figure 5.11a. This assumption was numerically reasonable because no damage was considered to occur in the rock sample (Shang et al. 2018a). Therefore, material vessels with the dimension of 60×30 (mm) were generated and filled with the particles having a size of $D_{min} = 0.48\ mm$ and $D_{max} = 0.64\ mm$. The steps required for the generation of DEM specimen of infilled rock joint is demonstrated in the specimen of infilled rock joint is demonstrated in Figure 5.11b. Firstly, a material vessel with a dimension of 60×30 was generated. In the next step, the mode was solved to reach equilibrium.

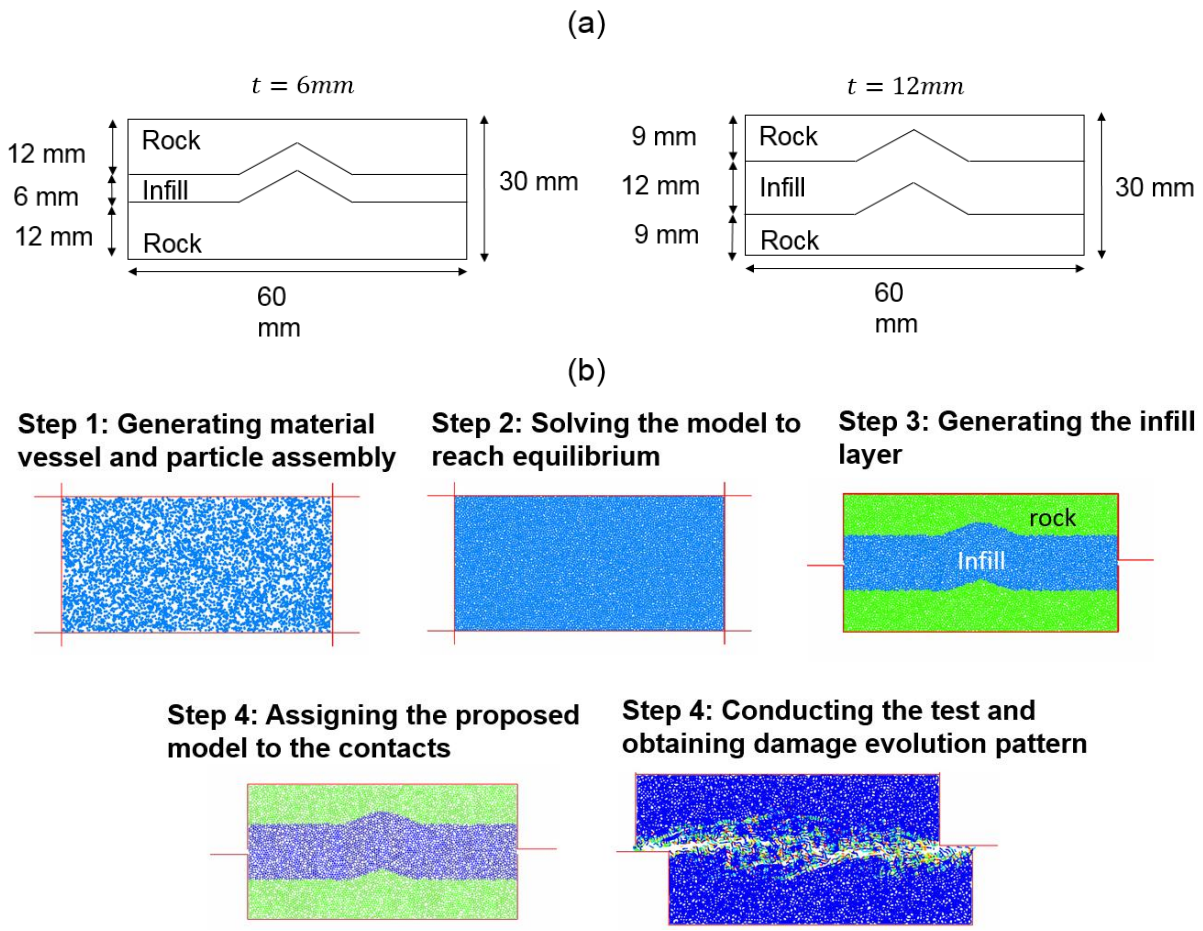

Figure 5.11 The dimension of numerical specimens. (b) Different steps for generation of particle assembly for conducting a numerical direct shear test on infilled rock joints.

The particle assembly was then divided into two separate groups, namely infill particle and rock particle groups. The geometry of rock joints asperity angles of 20° and 30° was imported into PFC 2D for producing a single asperity rock joint. Then, based on the infill thickness the required particles for generating the infill layer were selected, and the desired infill thickness was achieved. As demonstrated in Figure 5.12a, there were three different contact groups constructed in the system: rock-rock contacts, infill-infill contacts, and infill-rock contacts. The proposed cohesive model was installed on the infill-infill and infill-rock contact groups, and the PBM was installed on rock-rock contacts. The boundary condition of DEM specimen is illustrated in Figure 5.12b. The calibrated micro-mechanical parameters was employed to simulate the failure behaviour of infill-infill contacts. The microproperties of rock-rock contacts were selected according to the literature (Oh et al. 2017), which include Young's modulus (9.0 GPa), shear to normal stiffness ratio (1.85), cohesion (22.0 MPa), and tensile

strength (25.0 MPa). These contact properties allowed us to ensure the rock-rock contacts remained intact during simulations, without any asperity damage.

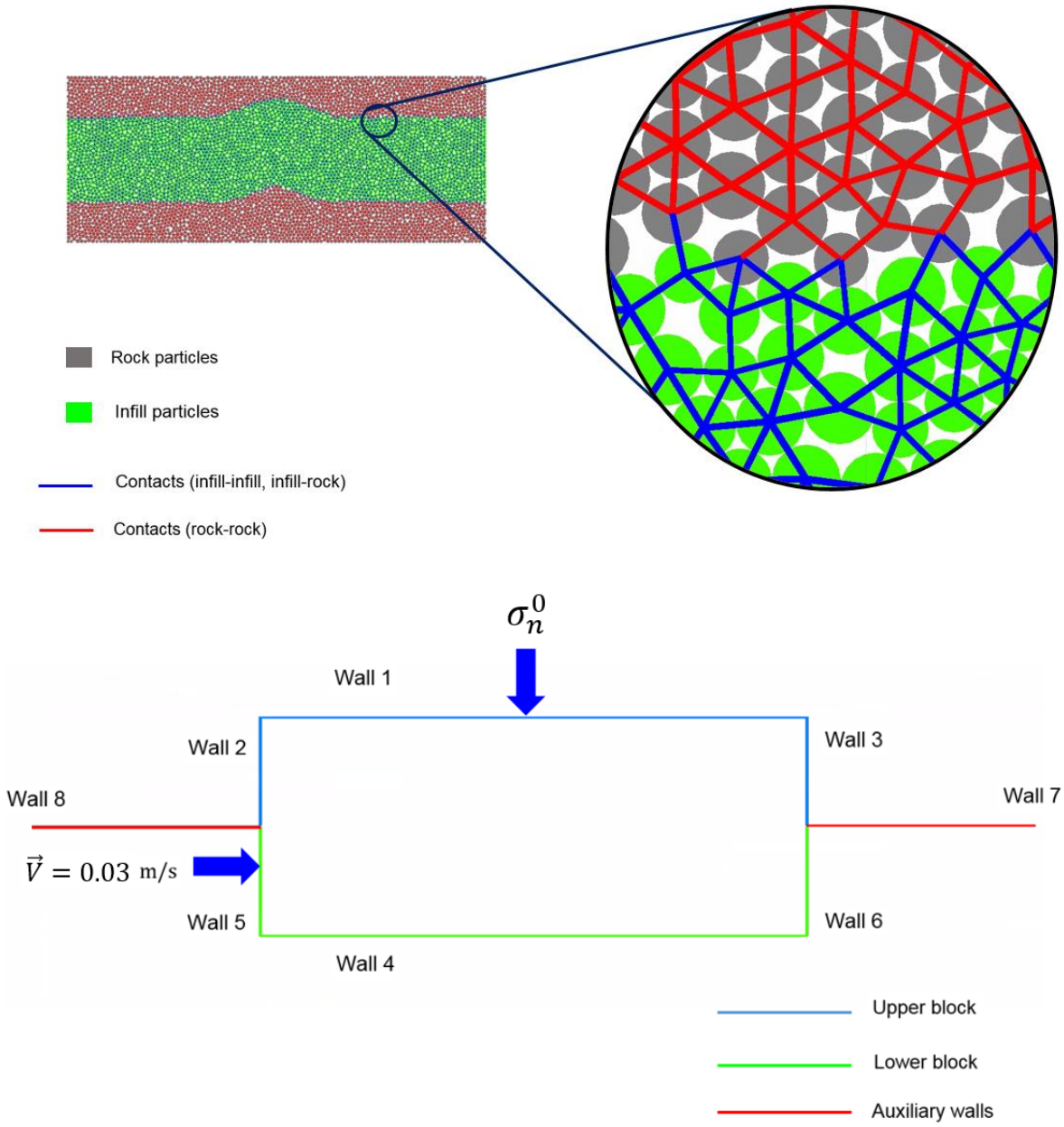

Figure 5.12 The numerical sample including an infill layer after contact installation; the proposed cohesive model was installed on infill-infill, and infill-rock contacts and PBM was used to characterise rock-rock contacts. (a) Particle assembly and assignment of constitutive models. (b) The boundary condition required for conducting the direct shear test on infilled rock joints.

After sample generation, particle configuration, and contact model installation (Figure 5.11b), all the walls in the sample were removed, and new walls were generated to apply the new

boundary condition and performing the direct shear test (Figure 5.12b). Using the servo-controlled mechanism, the constant normal stress was applied to the top wall of the upper block (wall 1, Figure 5.12b). The shearing procedure was achieved by applying a horizontal velocity of 0.03 m/s to the lower block (i.e. walls 4, 5, and 6, Figure 5.12b). The horizontal reaction force of wall 4 was monitored and divided by the joint length (60 mm) to calculate the shear stress during the test (Figure 5.12b). The horizontal displacement of the wall 4 was used to calculate shear displacement during shearing (Figure 5.12b). The synthetic numerical specimens were sheared at two normal stresses of 100 kPa and 300 kPa.

5.5 DEM simulation of the direct shear test of infilled joints

The shear behaviour of infilled rock joints simulated in DEM was compared with the experimental counterparts in Figure 5.13a, and excellent agreement was observed. As can be seen in Figure 5.13a, in all the numerical samples, the shear stress increased linearly from the beginning of the test, showed a pre-peak response before reaching the peak. Then the behaviour becomes strain softening with a gentle post-peak slope until the end of the shearing. Finally, the shear strength of the infilled rock joints remained at a constant residual level. Notice that the four stages observed in the laboratory specimens (subsection 5.2.2) were accurately identified by the proposed DEM framework, which will be described later in this section.

The numerical specimens with t/a ratio of 1.3 and 4.25 returned the highest and the lowest peak shear strength respectively (Figure 5.13a). For the specimen with 6 mm of infill thickness, the influence of asperity angle was more significant as it showed a higher peak shear stress. The macroscopic response in the laboratory investigation for 6 mm infill thickness was a combined asperity sliding and material softening. In the case of numerical samples with 12 mm of infill thickness, the greater number of cohesive contacts allowed them to have more control over the macroscopic shearing behaviour as the restriction provided by the asperity angle was reduced significantly. In fact, the wider space between joint surfaces enabled infilled particles to dominate the shear performance of the joint. This resulted in a dominating influence of infill contacts over asperity inclination, reducing the pre-peak hardening, and consequently a significant reduction in the peak shear stress. A detailed description of the shear mechanism of the infilled rock joint will be provided in the future in this section.

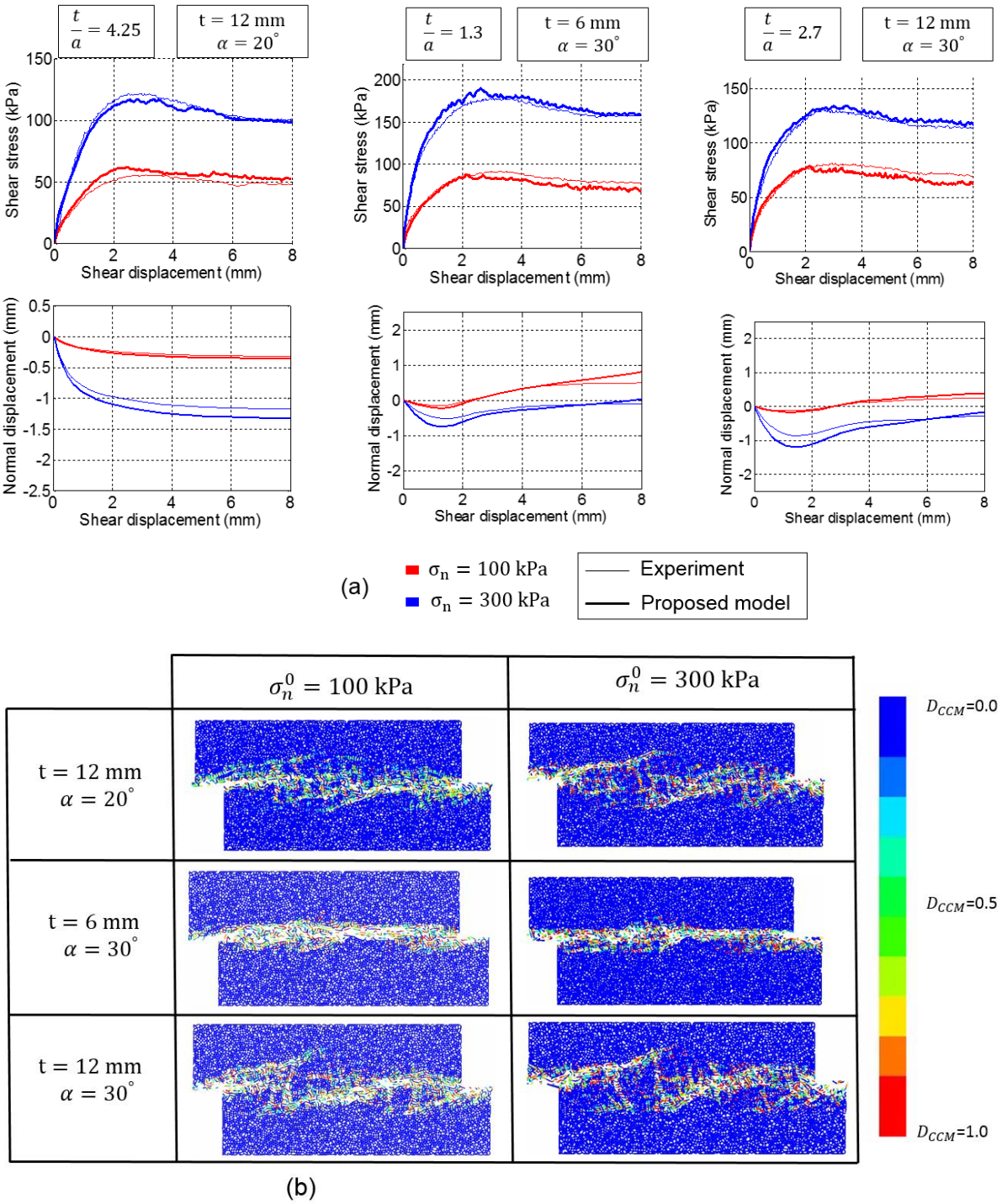

Figure 5.13 Comparison of direct shear test results from the laboratory experiment and DEM simulations using the proposed cohesive model. (a) Comparison of the shear stress-displacement and normal-shear displacement curves from laboratory tests and DEM simulations for infilled rock joints with asperity angle of 20° and 30° and infill thickness of 6 and 12 mm. (b) Damage evolution in the numerical specimens.

The normal-shear displacement curves (Figure 5.13a) show that the numerical specimen were subjected to an initial compression during the elastic stage. This initial compression was followed by a dilative response for t/a ratio of 1.3 and 2.7. However, the numerical results showed that the dilatational behaviour of infilled rock joint reduced when the t/a ratio was 4.25. This was an indication that the asperity inclination angle no longer had great effect on the overall dilation behaviour of the DEM specimen. For the smaller t/a ratio of 1.3 and 2.7, the initial compression was more significant under 300 kPa, which was attributed to the higher compressive response of DEM particles due to greater normal stress magnitude.

The damage evolution of cohesive infill was monitored during the shearing process and the final results are given in Figure 5.13b. Completely damaged contacts are shown in red ($D_{CCM} = 1.0$), bonded contacts are in blue ($D_{CCM} = 0.0$). It can be observed from Figure 5.13b that the number of softened contacts ($0.0 < D_{CCM} < 1.0$) was higher for numerical specimens with a normal stress of 100 kPa. In contrast, at 300 kPa confining pressure, the number of damaged contacts ($D_{CCM} = 1.0$) was significantly higher, indicating the greater resistance of the infill layer against shearing.

The peak and residual strengths obtained from DEM simulation are plotted against t/a, and the results are illustrated in Figure 5.14. The laboratory results are also included in Figure 5.14 to make a better comparison. It can be seen from Figure 5.14 that the peak and the residual strength of the infilled rock joints were very well captured by the proposed DEM framework. The numerical results showed that asperity interference highly influenced both the peak and residual strengths when $t/a < 2.67$, while at $t/a = 4.25$ the shear behaviour of the infilled rock joint was approximately governed by the infill material.

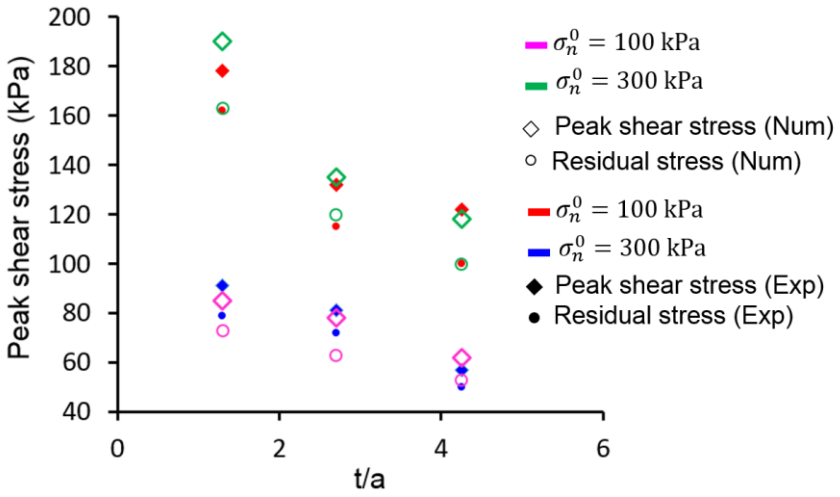

Figure 5.14 The comparison between numerical and experimental peak and residual strength of the infilled rock joints.

The value of damage in each infill contact was monitored at different shearing stages, and the results are illustrated in Figure 5.15. For demonstration purposes, only the results of the numerical specimen with $t = 6\ mm$ and $\alpha = 30^{\circ}$ are analysed. The points at which the damage evolution was monitored are marked with yellow circles on the graphs (Figure 5.15a), and their corresponding damage responses are illustrated in Figure 5.15b. Figure 5.15a illustrated the shear stress-displacement and normal-shear displacement curves of the DEM specimen. In the following paragraphs, the shear mechanism observed during numerical modelling of infilled rock joints is described.

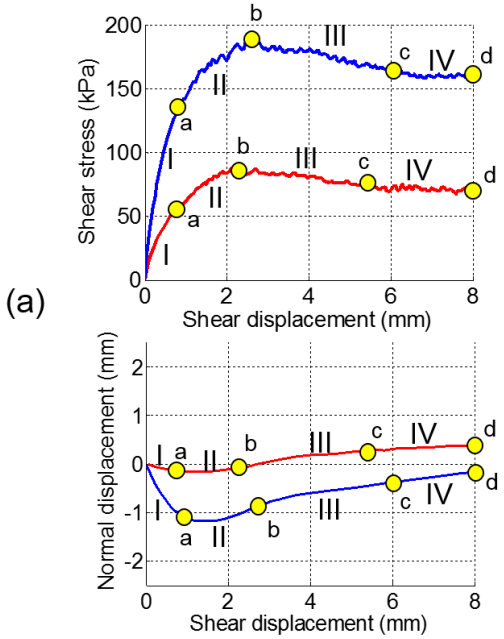

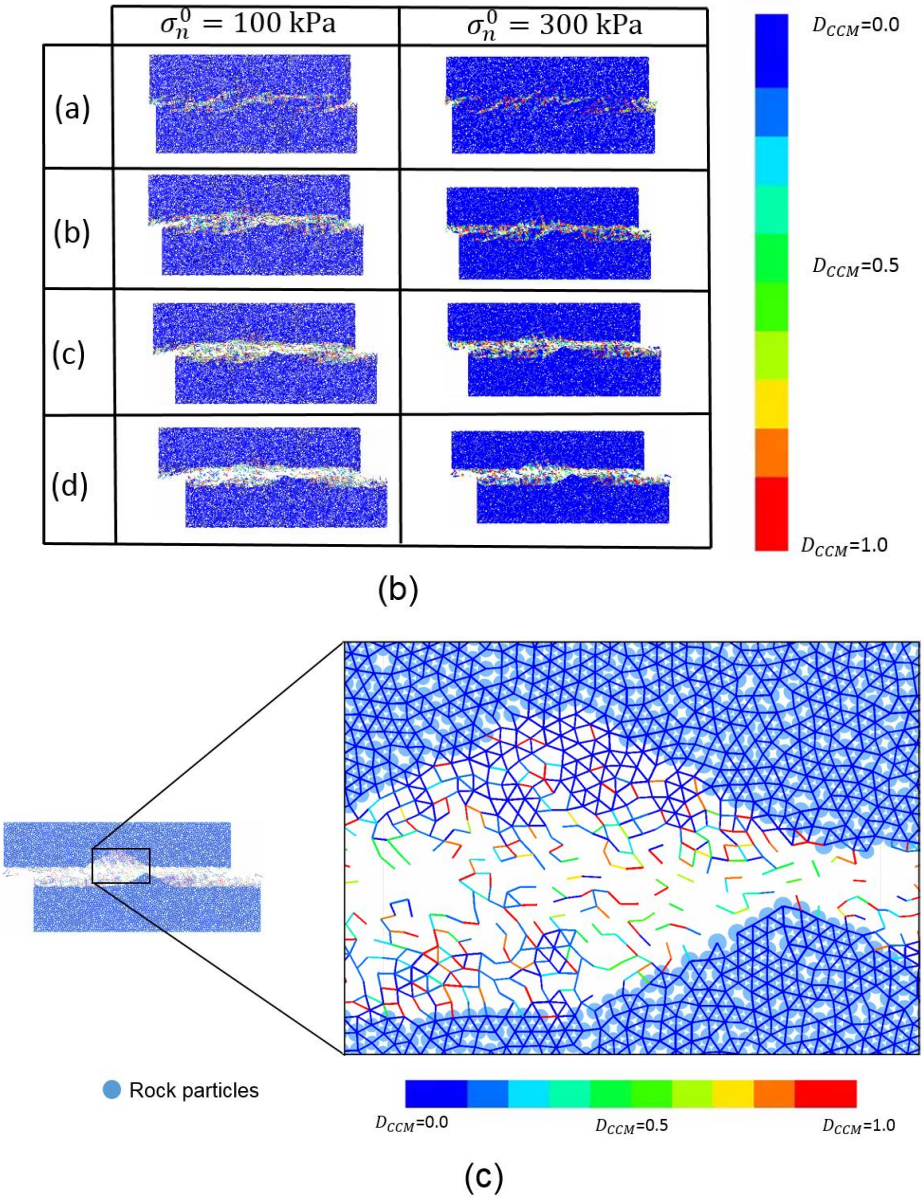

Figure 5.15 Damage evolution in the infill layer ($\alpha = 30^{\circ}$ and $t = 6\ mm$). (a) Shear stress-displacement curve for infilled rock joint. (b) Damage evolution pattern after different shear displacement. (c) Enlarged view of the damaged contacts in the infill layer ($\sigma_n^0 = 100$ kPa).

The constant shear stiffness phase (Figure 5.15a, stage I) in the numerical models with infilled rock joint was similar to that of achieved for DEM soil specimens. However, the infilled specimens presented a higher value of shear stiffness, which was attributed to the higher resistance of the infill layer against shear displacement due to the presence of idealised asperities. During the constant shear stiffness stage, the shear strength of the specimens was rapidly increased. Similar to the laboratory counterpart, the numerical specimen with 300 kPa confining pressure showed a higher value of shear stiffness. The normal-shear displacement

curve (Figure 5.15a) shows that the DEM specimens exhibited initial compression during stage I, which was due to the compressive response of DEM particles. This initial compression was higher under 300 kPa of normal stress magnitude. The corresponding damage evolution response of the numerical specimens at the end of the elastic stage (Figure 5.15a, point "a") was monitored and depicted in Figure 5.15b. It can be seen that under both 100 and 300 kPa of normal stress, some of the contacts at the upper left and lower right of the infill layer entered to their yielding limit ($0.0 < D_{CCM} < 1.0$) (Figure 5.15a, point "a"). As expected the numerical specimen with $\sigma_n^0 = 300$ kPa exhibited more softened contacts at this point. The accumulation of these softened contacts formed macroscopic localised shear zones. The numerical models displayed an overall nonlinear hardening response during stage II (Figure 5.15a), which akin to the experimental samples, had two leading factors. Firstly, the nonlinearity of the shear stress-displacement curve was associated with the reduction in the shear stiffness, which was the results of the rapid growth in the number of yielding contacts ($0.0 < D_{CCM} < 1.0$). Secondly, the continuous shear displacement of the rock joint intensified the degree of asperity interference, which improved the resistance of DEM contacts against shearing. This produced a pre-hardening behaviour at macroscopic scale leading to a higher peak shear strength in infilled rock joints than that of soil itself (Figure 5.15a, point "b"). It can be observed that in the numerical specimens with higher confining pressure, higher peak shear strength resulted at the end of stage II (Figure 5.15a, point "b"). The normal-shear displacement curve (Figure 5.15a, stage II) demonstrates that at point a, the dilative response of the infilled rock joints started, which was attributed to asperity interference as a result of progressive shear displacement of the rock joint. This occurred when the thickness of the infill layer was relatively thin.

During post peak stage (Figure 5.15a, stage III), the number of yielding contacts started to increase within the infill layer, which is evident by the softening response of the shear stress-displacement curves. In particular, the intensity of softening was less pronounced at lower confining pressure (Figure 5.15a, stage III, $\sigma_n^0 = 100$ kPa). This can be confirmed by the damage response of the contacts within the numerical specimens (Figure 5.15b, point "c"), where very few completely failed contacts ($D_{CCM} = 1.0$) were observed for $\sigma_n^0 = 100$ kPa, whereas specimen with $\sigma_n^0 = 300$ kPa exhibited a considerable number of damaged contacts. The growth in the localised shear zone evolution was accelerated from this stage because more cohesive contacts started to soften. Physically, the softening process is associated with the gradual degradation of the inter-particle bonding followed by frictional interaction of soil

particles in the localised shear zones. In this context, the micro-mechanical mechanism incorporated in the proposed DEM framework was able to very well capture the phenomenological aspects of cohesive soil failure at the macroscopic scale. The rate of dilation response of infilled rock joints reduced in stage III (Figure 5.15a, stage III), which could be attributed to growth in the number of softening contacts, and the extension of the localised shear zone. During stage IV, the frictional behaviour of DEM particles at grain scale produced a macroscopic residual response in the shear stress-displacement curves (Figure 5.15a, stage IV). The progressive shear displacement of the specimens during stage IV resulted in the extension of the localised shear zones, and accordingly the growth in the number of yielding contacts (Figure 5.15b, point "d").

The procedure described above was observed for all of the numerical models. As demonstrated in Figure 5.13a and b, the micro-mechanical behaviour of the cohesive contacts were affected by the magnitude of the normal stress thus the macroscopic response of the numerical samples in terms of both damage evolution and the peak and the residual shear stresses were changed. In the present research, we assumed no asperity damage. It can be observed from Figure 5.15c that the damage only occurred in the infill layer. The DEM particles of the infill layer are not given in this plot to better demonstrate the cohesive contacts.

5.6 Conclusion

This chapter presents a combined experimental-numerical investigation for the characterisation of the shear behaviour of clay-infilled rock joints. A series of laboratory direct shear tests were carried out on infilled rock joints filled with a cohesive soil. Idealised single asperity rock joints with a base angle of 20° and 30° were created and tested under CNL condition with 100 and 300 kPa of normal stress magnitude. The macroscopic properties of cohesive soil were also obtained from direct shear test results carried out on the soil. The experimental approach provided the macroscopic response of various infilled rock joints, while a proposed DEM framework supplied further insights into the failure mechanism and microscopic damage response of the cohesive soil. The microproperties of the proposed DEM framework were calibrated against the outcome of laboratory direct shear tests of cohesive soil. In particular, the cohesion and friction angle of the physical soil were numerically obtained similar to the experimental results. The calibrated DEM framework was then employed to reproduce the mechanical and failure behaviour of the infilled rock joints. The DEM results demonstrated a good agreement with the experimental counterparts. Based on the laboratory and DEM results, the following conclusions can be drawn:

1- The shear stress-displacement curves of the clay-infilled rock joints exhibited four different stages in both experimental and numerical observations. During stage I, the shear stress of the infilled rock joints was rapidly increased. A nonlinear hardening response was observed during stage II, which was associated with the progressive bond-break in the infill layer, and enhancement of asperity interference. Then the peak shear strength of the rock joint was achieved, following with a gradual softening response (stage III). Finally, due to frictional behaviour between infill particles, a macroscopic residual response was achieved.

2- The normal-shear displacement curves showed that the infilled rock joint exhibited an initial compression. A dilative behaviour for t/a ratio of 1.3 and 2.7 followed this initial compression. For the highest t/a ratio, however, the normal displacement of infilled rock joint approached to that of the soil itself.

3- The observations showed that the intensity of the softening response increased significantly with increasing the magnitude of normal stress. The numerical damage response showed that under high confining pressure the number of completely failed contacts ($D_{CCM} = 1.0$) was proportionally higher than that of low confining stress.

4- The DEM results showed that localised shear zones at the point in which a transition from elastic behaviour to nonlinear elastic behaviour occurred. These localised shear zones largely extended during the shearing procedure, with a progressive increase in the number of yielding contacts ($0.0 < D_{CCM} < 1.0$). It was observed that, the DEM specimen with high confining pressure reproduced more completely damaged contacts compared to specimens with low normal stress magnitude.

5- The macroscopic behaviour of the numerical and experimental specimens in terms of peak and residual shear strengths were also interpreted based on t/a. Both numerical and laboratory results showed that the asperity interference was the major contributing factor for specimens with $t/a < 2.67$. However, when $t/a = 4.25$, the mechanical behaviour of the infilled rock joint was approximately governed by the infill layer.

Chapter 6: GBM simulation of jointed polycrystalline rock under CNL and CNS condition

6.1 Introduction

The focus of this study is on the brittle failure of polycrystalline rocks (i.e. granite) using cohesive based distinct element method (DEM). Various parameters control the mechanical and damage response of crystalline rocks, such as microstructural properties of grains (i.e. shape and size), mineral constituents, pre-existing defects, cavities, etc (Gao et al. 2016; Li et al. 2019c; Liu et al. 2018; Wang and Cai 2018).

The macroscopic fracture process is the dominant damage mechanism controlling the mechanical response and the integrity of crystalline rocks (Morgan et al. 2013). It has been repeatedly observed in the experimental and numerical studies that the microstructural characteristics of crystalline rocks control the micro-cracking process of the mineral itself, and hence the overall macroscopic response of rock including strength, deformability, and fracture pattern (Bahrani and Kaiser 2016; Hajiabdolmajid et al. 2002; Hofmann et al. 2015a; Li et al. 2019c; Nicksiar and Martin 2014; Tuğrul and Zarif 1999; Wang and Cai 2018).

The presence of natural discontinuities around orebodies can have a profound influence on the stability and safety of mining structures (Taheri and Tani 2010). Therefore, an appropriate assessment of rock joint shear behaviour is necessary for the design and construction procedure of mining excavations. The experimental observations revealed that, in polycrystalline rocks, the macroscopic shear behaviour of rock joint highly depends on the micro-texture of rock specimen (Meng et al. 2018). Thus, not only the surface roughness characteristics (Barton and Choubey 1977; Grasselli and Egger 2003; Kazerani et al. 2012), but also the microstructural properties of the host rock should be taken into account for evaluating the rock fall hazards caused by the shear failure of rock joints (Meng et al. 2018; Wang et al. 2019; Yang and Qiao 2018).

In the present chapter, we employed the proposed cohesive GBM to numerically investigate the shear behaviour of rock joints with a focus on the micro-texture of asperities. To do so, we imported the geometrical characteristics of three different rock joints with different joint roughness coefficients (JRC) into the numerical models. After that, numerical direct shear tests under constant normal load (CNL), and constant normal stiffness (CNS) were conducted.

6.2 Validation of cohesive GBM

In GBM approach, a random generation algorithm is required to construct the polygonal microstructure of the model. In this section, the microstructural properties of three different granitic rocks were incorporated into the GBM to generate different numerical specimens. We used an algorithm proposed by Potyondy (2010a) for random generation of polycrystalline microstructures, which has been extensively used in the previous GBM studies (e.g. Saadat and Taheri (2019b), Hofmann et al. (2015a)). The complete details of this algorithm can be found in (Potyondy 2010a). In section 6.2.1, we will introduce a comprehensive calibration procedure to analyse the significance of cohesive modelling. We will also demonstrate in section 6.2.1 that non-cohesive GBM (e.g. PBM-SJM) is unable to reproduce the macroscopic behaviour (i.e. load-displacement curve) of brittle rock (e.g. granite). In section 6.2.2, the ability of the model in reproducing the macroscopic behaviour of Eibenstock II granite in UCS, Brazilian, and triaxial tests with different confining pressures (σ_3) will be investigated. In section 6.2.3, we will compare the numerical fracture pattern of Aue granite under asymmetric uniaxial and confining tests with their experimental counterparts.

6.2.1 Simulation of Adelaide black granite

According to the previous experimental and numerical investigations the polycrystalline rocks exhibit a gradual cohesive-frictional damage response during failure (Hajiabdolmajid et al. 2002; Khazaei et al. 2015). This gradual damage development in polycrystalline rock is more pronounced under three-point bending tests on single-edge-notched beam in which the global load-displacement curve exhibits obvious softening response (Parisio et al. 2019). There are experimental evidences from three-point bending (TPB) tests on the single-edge-notched beam that the development of fracture process zone (FPZ) in polycrystalline rock (e.g. granite) is attributed to propagation of macroscopic tensile cracks, which in turn is the result of the progressive coalescence of micro-cracks along cleavage planes in minerals (Parisio et al. 2019). Therefore, it is needed to incorporate a softening response in the constitutive relationships of DEM contacts to achieve a more realistic numerical outcome. Notice that non-cohesive contact models (e.g. PBM) are incapable of reproducing the gradual softening behaviour of soft rock in three-point bending test of rock (Nguyen et al. 2017a). In this section, we demonstrate a process for calibration of Adelaide black granite using three experimental tests: uniaxial compression test, Brazilian tensile strength test, and three-point bending test.

The thin section analysis of experimental specimen showed that Adelaide black granite consists of 45-50% plagioclase, 20-25% pyroxene, 10% biotite, 5% amphibole, 5% magnetite, and 1-

2% quartz (Parisio et al. 2019). The average grain size of Adelaide black granite reported in the literature is 2.5 mm, with a minimum and maximum grain size of 0.02 mm and 6.5 mm, respectively (Parisio et al. 2019). Due to the small percentage of amphibole, magnetite, and quartz, each was categorised as "other minerals" during specimen generation procedure, and a unique set of micro-properties (CCM) were assigned on its DEM contacts. These simplifications were needed to reduce the complexity of numerical simulation process and was also adopted in our previous GBM research (Saadat and Taheri 2019a). These data were used to build the GBM models and calibrate the model's micro-properties. A systematic calibration procedure, as outlined in the flowchart presented in Figure 6.1, was followed in order to determine a set of appropriate micro-properties that was able to reproduce the macroscopic mechanical behaviour (e.g. UCS) and the global load-displacement of three-point bending test of a physical specimen. The calibration aimed to achieve a set of microproperties which could reproduce the similar macroscopic behaviour of the experimental specimens (e.g. Young's modulus, Poisson's ratio, etc.). The CCM and CSJM were assigned as intra- and inter-grain contact models, respectively. The following points were considered during the calibration process:

1- The CSJM was assigned to the contacts representing mineral interfaces such that the mechanical behaviour of grain boundary at the contact level is defined by contact strength (i.e. C^0_{CSJM}). When the contact reaches its yield limit, the mechanical behaviour of the contact is controlled by the softening parameter (κ_{CSJM}) until bond-break occurs. After bond-break, the contact behaviour is controlled by the friction coefficient (μ_{CSJM}).
2- The peak strength envelop of the intra-grain contact (i.e. the contact inside a mineral) are defined by C^0_{CCM} , μ_{CCM}, β_{CCM}, and κ_{CCM}. Different microproperties (e.g. C^0_{CCM}) were assigned to the four minerals, including quartz, plagioclase, orthoclase, and mica.
3- We employed the contact deformability method (Potyondy and Cundall 2004) to calibrate the Young's modulus of intra-grain contacts ($\bar{E}_{CCM}$). The normal and shear stiffness of CSJM ($k^0_{n,CSJM}$, $k^0_{s,CSJM}$) were assigned explicitly.

The details of the calibration procedure can be found in our previous GBM study (Saadat and Taheri 2019b). Here, we briefly described the calibration steps:

1- The macroscopic Young's modulus of the specimen was mainly controlled by $\bar{E}_{CCM}$, and $k^0_{n,CSJM}$, $k^0_{s,CSJM}$. We only needed to obtain the linear elastic response of the

specimen (i.e. macroscopic Young's modulus), therefore we assigned a high value for the strength microproperties (e.g. C^0_{CCM}).

2- The Poisson's ratio of the model was calibrated by altering $k^0_{n,CSJM}/k^0_{s,CSJM}$ and $k^0_{n,CCM}/k^0_{s,CCM}$ ratios. It was necessary to repeat this step in an iterative process with step 1.

3- The macroscopic Brazilian tensile strength (BTS) of the model was calibrated by carrying out the Brazilian tensile test (Figure 6.2). In this step, an appropriate value for the inter-grain cohesion (C^0_{CSJM}) was identified. Notice that in the GBM approach the macroscopic tensile strength is characterised by the strength of inter-grain contacts (Hofmann et al. 2015a; Saadat and Taheri 2019b). The relative inter-grain microproperties that control the macroscopic tensile behaviour of Brazilian disk was also calibrated at this stage (i.e. μ_{CSJM}, and β_{CSJM}). We altered these micro-mechanical properties until achieving a good agreement between the numerical results and experimental counterparts.

4- The uniaxial compressive strength (UCS) was calibrated by choosing appropriate intra-grain properties (i.e. C^0_{CCM}, μ_{CCM}, and β_{CCM}). The inter-grain microproperties obtained from step 3 were assigned to the inter-grain contact in this step. As microproperties influence different macroscopic properties, several iterations were undertaken between step 1 and 4 to identify a satisfying set of microproperties.

Notice that the above mentioned steps were used to calibrate the deformability parameters of the model (e.g. Young's modulus, UCS), but κ_{CCM} and κ_{CSJM} were selected by fitting the post-peak response of numerical TPB test with its laboratory counterpart. The results of TPB test on notched sample of Adelaide black granite carried out by Parisio et al. (2019) were chose for this purpose. The laboratory setup and loading condition are illustrated in Figure 6.2. The rock beam was supported by two roller at the bottom, and the specimen was loaded by a roller located at the mid-span of the rock beam at the top (Parisio et al. 2019). The same test setup was used in PFC2D to support and load the beam. The uniaxial compression test was carried out by applying a vertical load on the upper wall. In order to prevent ball-facet overlap, a relatively high stiffness was assigned to the walls (10 % higher than the average ball-ball stiffness). The ball-wall contacts were considered to be frictionless, which prevents the loading plates from inhibiting the rock bulging (Saadat and Taheri 2019b).

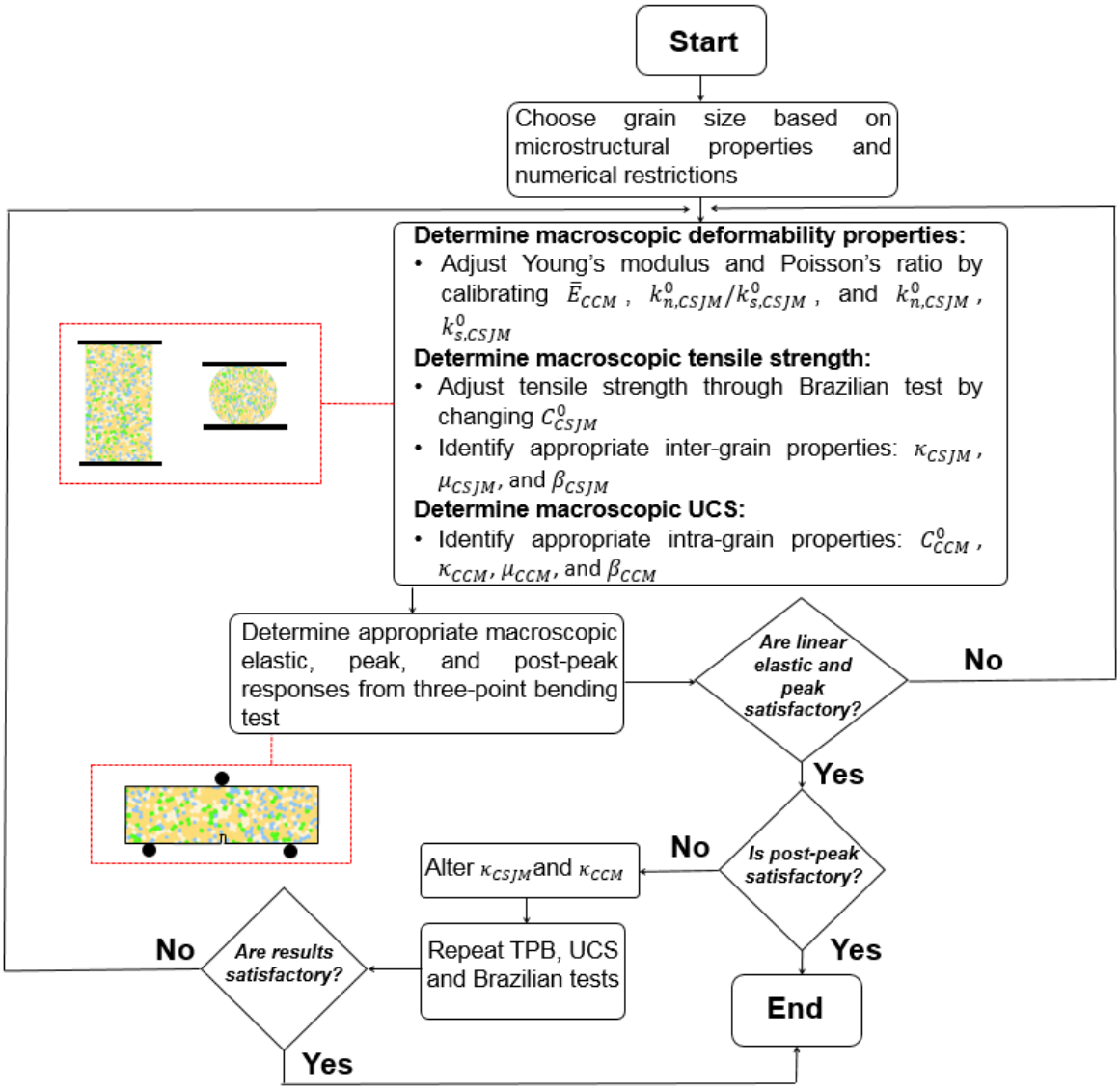

Figure 6.1 Flowchart illustrating the calibration procedure of the proposed cohesive GBM

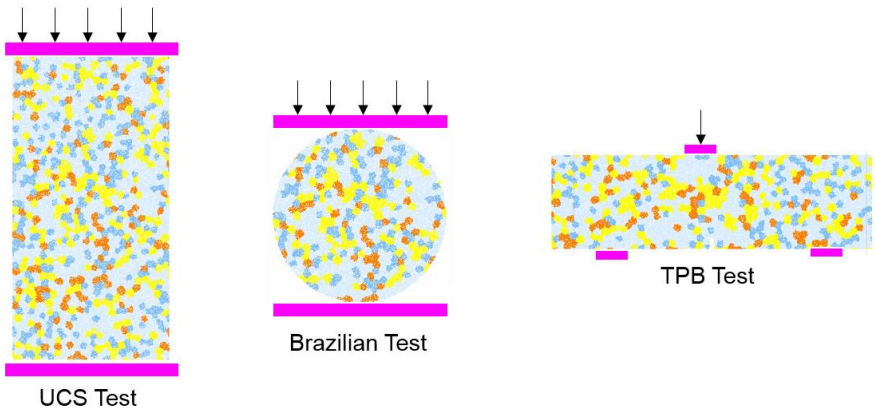

Figure 6.2 Numerical setups of different calibration tests

The calibrated micro-properties and a comparison between numerical and experimental macroscopic data are given in Table 6.1 and Table 6.2, respectively. Notice that in GBM approach we approximate the heterogeneity of the rock by adopting a random scheme to generate the minerals in 2D (Potyondy 2010a). You can see that the calibrated GBM model was able to reproduce the laboratory data with a good match. Another GBM simulation of TPB test was performed using the same numerical setup, boundary condition, and microstructural characteristic. The only difference was that the cohesive contact constitutive models were replaced by PBM (intra-grain contacts) and SJM (inter-grain contacts). The elastic properties and deformation characteristics of PBM and SJM contacts were kept the same as those of the CCM and CSJM, while the tensile strength and cohesive micro-parameters were calibrated to produce the best fit with the peak load of the laboratory specimen.

Table 6.1 Micro-mechanical parameters obtained from the calibration procedure of Adelaide black granite

Element	Parameter	Grain 1 Pyroxene	Grain 2 Plagioclase	Grain 3 Biotite	Grain 4 Others
Particles forming grains	Minimum particle radius forming grain, R_{min} (mm)	0.15	0.15	0.15	0.15
	Maximum to minimum radius ratio, R_{max}/R_{min}	1.66	1.66	1.66	1.66
Cohesive model	Young's Modulus, $\bar{E}_{CCM}$ (GPa)	120	105	105	85
	Normal to shear stiffness ratio, ($k^0_{n,CCM}/k^0_{s,CCM}$)	1.0	2.0	2.0	1.5
	Cohesion, (C^0_{CCM}) (MPa)	160	145	110	145
	Friction ratio, (μ_{CCM})	0.50	0.55	0.50	0.55
	Dilation ratio, (β_{CCM})	0.25	0.25	0.20	0.25
	Softening parameter, κ_{CCM} (1/m)	15,000,000	8,000,000	5,000,000	8,000,000

Micro-mechanical parameters of the grain boundaries (the smooth joint contacts)

Smooth-joint model	Normal stiffness, ($k^0_{n,CSJM}$) (GPa/m)	250,000
	Shear stiffness, ($k^0_{n,CSJM}$) (GPa/m)	130,000
	Cohesion, (C^0_{CSJM}) (MPa)	8.7
	Friction ratio, (μ_{CSJM})	0.45
	Dilation ratio, (β_{CSJM})	0.25
	Softening parameter, κ_{CSJM} (1/m)	1,000,000

Table 6.2 Macroscopic properties of Adelaide black granite (Parisio et al. 2019) and GBM approach

Property	Adelaide black granite granite (Experimental)	Adelaide black granite (Numerical)
Uniaxial compressive strength (MPa)	180	185
Young's modulus (GPa)	102	105
Poisson's ratio	0.24	0.28
Brazilian tensile strength (MPa)	10.9	11.5

The comparison between experiment and GBM simulation for the applied load magnitude against the crack mouth opening displacement (CMOD) curves is illustrated in Figure 6.3. Figure 6.3a illustrates the global load-displacement curves and Figure 6.3b shows the macroscopic fracture patterns. The load-CMOD curve in the numerical simulation using the proposed cohesive GBM framework satisfactorily matches with the experimental counterpart (Figure 6.3a). During the loading procedure, the GBM specimen was exhibited to undergo three distinct stages including initial linear elastic, hardening before reaching the peak, and finally gradual softening until the specimen was completely failed. The macroscopic hardening behaviour of the load-CMOD curve was the direct consequence of the collective response of cohesive inter- and intra-grain contacts, even though the proposed cohesive contact model

featured no hardening characteristics at the contact level. During the softening stage, the inter-grain contacts the surrounding the crack tip area gradually softened, resulting in a softening response in the macroscopic load-CMOD curve, which exhibited a good match with the experimental counterpart. Nevertheless, the GBM with PBM and SJM contact models could not capture a promising hardening response as the tensile strength of inter-grain contacts were totally damaged at the moment the bond strength was reached. Therefore, the specimen reached its peak load and entered to softening stage. As it can be seen, the softening response of the GBM with PBM and SJM was not perfectly matched with the experimental results, which was due to lack of microscopic strain-softening behaviour. Notice that one can alter the micro-properties of PBM and SJM to achieve a satisfactory peak load, but it is obvious that macroscopic softening behaviour will not be captured as PBM and SJM has no micro-parameter that controls the contact's post-peak behaviour. The inability of PBM in reproducing the post-peak softening behaviour in TPB test was also investigated by Nguyen et al. (2017a) and Nguyen et al. (2017b). In Figure 6.3b a comparison between the fracture distribution in the numerical specimen and the distribution of acoustic emission (AE) events from the laboratory analysis is depicted. Notice that the damage contour plots of the numerical analysis of Parisio et al. (2019) are also shown in Figure 6.3b. The proposed cohesive GBM is able to capture the FPZ very well.

We simulated two more TPB test with different softening parameter (κ_{CSJM}) to demonstrate how this micro-property influences the overall post-peak response of the specimen (Figure 6.3c). You can see from Figure 6.3c that the specimen with higher κ_{CSJM} (i.e. lower softening behaviour at contact level) exhibited less macroscopic softening during post-peak, while the specimen with lower κ_{CSJM} (i.e. higher softening behaviour at contact level) could reproduce a relatively higher peak load and hence a more pronounce macroscopic softening behaviour.

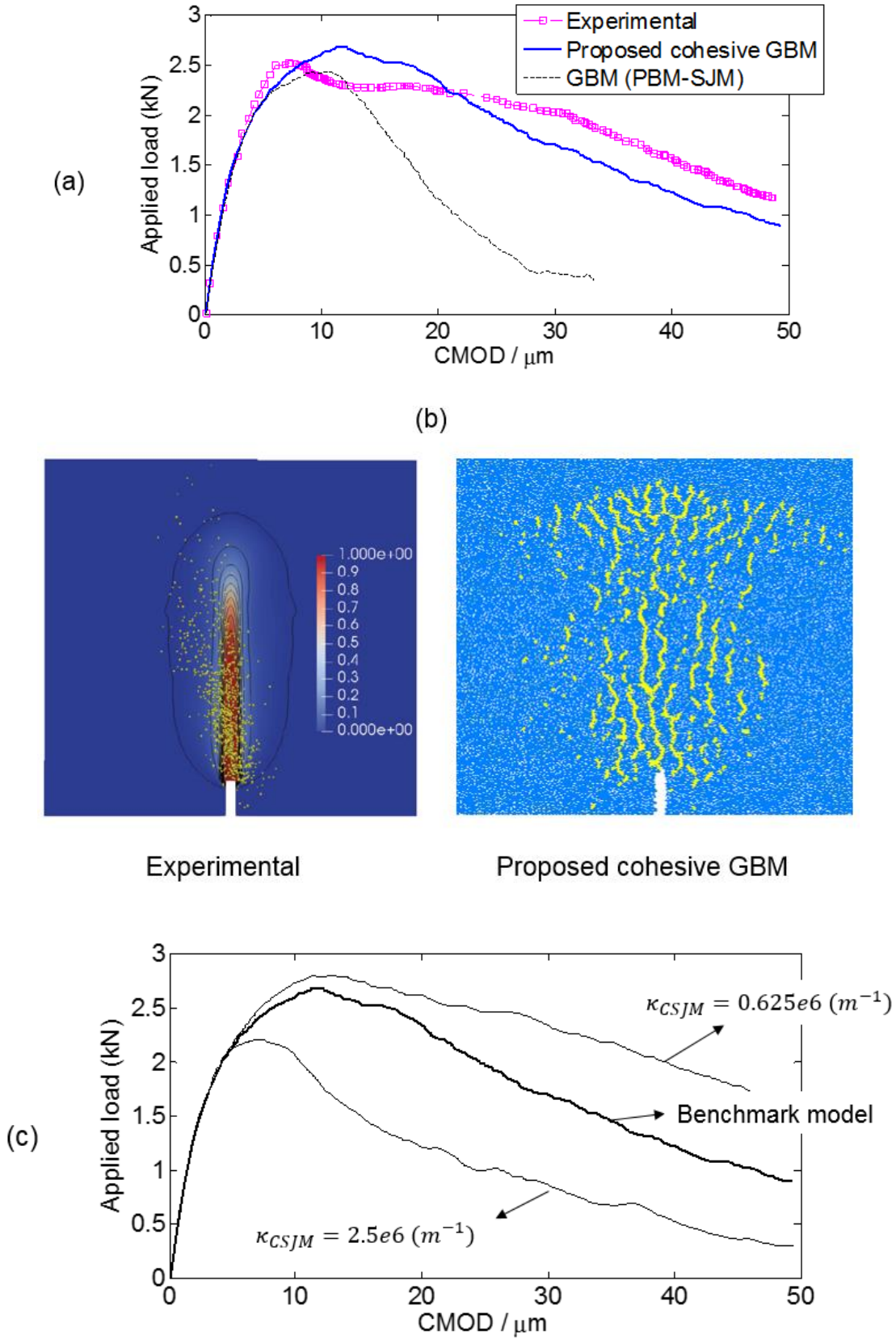

Figure 6.3 The results of TPB tests. (a) and (b) Comparison of experimental (Parisio et al. 2019) and numerical results; the yellow lines in (b) show the distribution of micro-cracks in the GBM specimen. (c) The results of the parametric study on the softening parameter of CSJM.

6.2.2 Simulation of Eibenstock II granite

Eibenstock II granite consists of 44% quartz, 24% plagioclase, 21% orthoclase, and 11% mica (Hofmann et al. 2015a). The minimum and maximum grain size of this granite are 0.49 mm and 1.79 mm, respectively, with an average grain size of 1.14 mm (Hofmann et al. 2015a). The same procedure (steps 1-4) introduced in section 6.2.1 was used to calibrate the model. The microproperteis of Eibenstock II granite is given in Table 6.3. The simulation and experimental results are illustrated in Figure 6.4. You can see from stress-strain curves in Figure 6.4a that the simulation results agree with the experimental counterparts. Notice that we typically perform a confined biaxial test in PFC2D, and compare the response with what is obtained from triaxial tests on the physical rock. One needs to take care when getting the elastic constants from the 2D model. This assumption is valid because $\sigma_2 = \sigma_3$ in the laboratory environment. Thus, in each confined experiment, we ensured that the macroscopic elastic response of the specimens were in good agreement with the physical counterparts. This approach was also adopted in the previous GBM research (e.g. Hofmann et al. 2015a). Figure 6.4b shows the distribution of macroscopic cracks in GBM specimens including inter- and intra-grain micro-cracks. The numerical results revealed that even under uniaxial loading condition, obvious grain crushing occurred, which is consistent with the laboratory observations. Figure 6.4b shows that with increasing confining pressure (σ_3), the induced inter- and intra-grain micro-cracks formed macroscopic fracture zones, which are similar to those of experimental specimens. Figure 6.4c shows a relation between indirect tensile strength versus strain of the Brazilian test. The average tensile strength of Eibenstock II granite was 7.0 MPa (Tan 2013), which was very well reproduced by the proposed cohesive GBM (Figure 6.4c). You can also see that the macroscopic fracture response of the numerical specimen agrees with the laboratory observation (Figure 6.4d). Notice that in Brazilian tensile strength test, only inter-grain micro-cracks (small black lines in Figure 6.4d) appeared in the GBM specimen, which was due to the small microscopic tensile strength of inter-grain contacts (C^0_{CSJM}) required to match the numerical results with experimental observations. These results were consistent with the previous GBM investigations (e.g. (Hofmann et al. 2015a; Hofmann et al. 2015b; Liu et al. 2018; Saadat and Taheri 2019a, 2019b)).

Table 6.3 Micro-mechanical parameters obtained from the calibration procedure of Eibenstock II granite

Element	Parameter	Grain 1	Grain 2	Grain 3	Grain 4
		Quartz	Plagioclase	Orthoclase	Mica

Particles forming grains	Minimum particle radius forming grain, R_{min} (mm)	0.15	0.15	0.15	0.15
	Maximum to minimum radius ratio, R_{max}/R_{min}	1.66	1.66	1.66	1.66
Cohesive model	Young's Modulus, $\bar{E}_{CCM}$ (GPa)	45	35	30	25
	Normal to shear stiffness ratio, ($k^0_{n,CCM}/k^0_{s,CCM}$)	1.0	2.0	2.0	1.5
	Cohesion, (C^0_{CCM}) (MPa)	105	82	82	45
	Friction ratio, (μ_{CCM})	0.50	0.55	0.55	0.50
	Dilation ratio, (β_{CCM})	0.22	0.25	0.25	0.2
	Softening parameter, κ_{CCM} (1/m)	15,000,000	8,000,000	8,000,000	5,000,000

Micro-mechanical parameters of the grain boundaries (the smooth joint contacts)

Smooth-joint model	Normal stiffness, ($k^0_{n,CSJM}$) (GPa/m)	85,000
	Shear stiffness, ($k^0_{n,CSJM}$) (GPa/m)	12,500
	Cohesion, (C^0_{CSJM}) (MPa)	5.7
	Friction ratio, (μ_{CSJM})	0.40
	Dilation ratio, (β_{CSJM})	0.25
	Softening parameter, κ_{CSJM} (1/m)	1,200,000

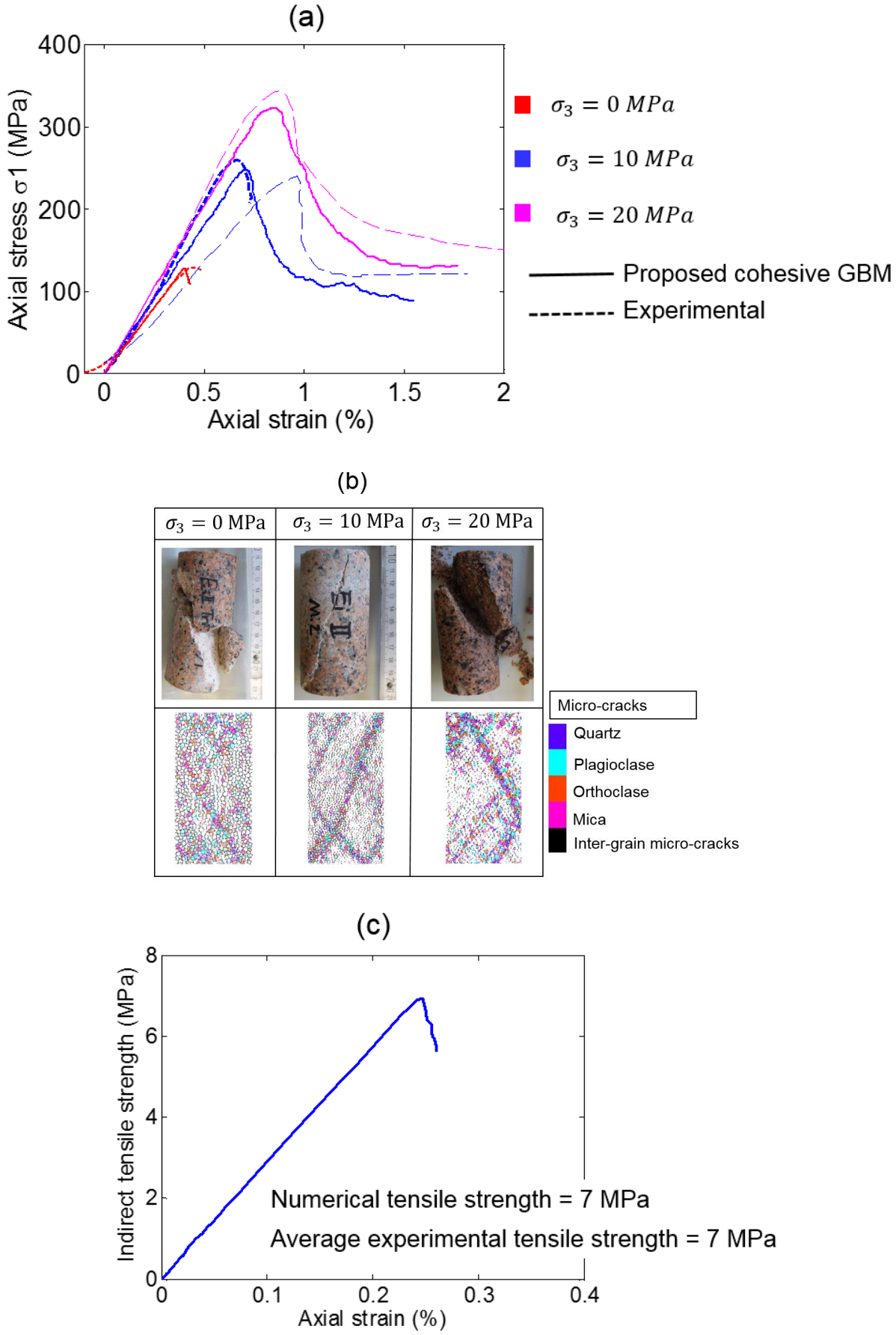
(a)
Axial stress σ1 (MPa)
Axial strain (%)
$\sigma_3 = 0\ MPa$
$\sigma_3 = 10\ MPa$
$\sigma_3 = 20\ MPa$
Proposed cohesive GBM
Experimental
(b)
$\sigma_3 = 0$ MPa
$\sigma_3 = 10$ MPa
$\sigma_3 = 20$ MPa
Micro-cracks
Quartz
Plagioclase
Orthoclase
Mica
Inter-grain micro-cracks
(c)
Indirect tensile strength (MPa)
Axial strain (%)
Numerical tensile strength = 7 MPa
Average experimental tensile strength = 7 MPa

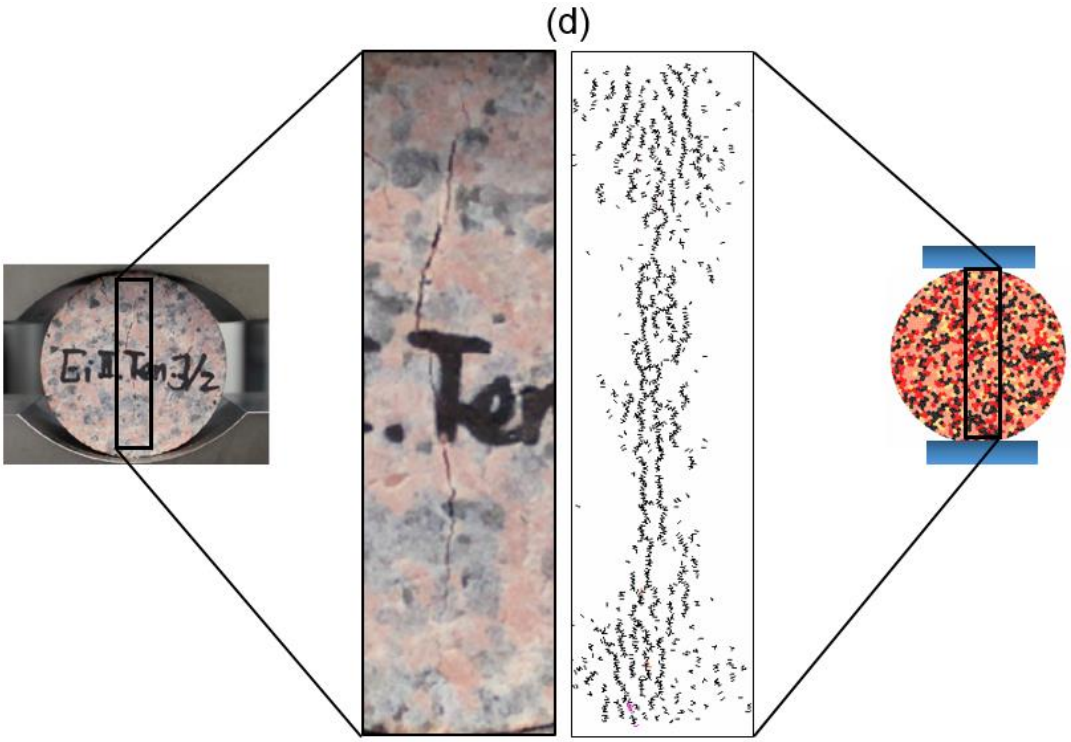

Figure 6.4 Simulation of Eibenstock II granite using the proposed cohesive GBM. (Experimental results from Tan (2013)) (a) Stress-strain curves after compressive tests under various confining pressures (Notice that there are two experimental tests with $\sigma_3 = 10\ MPa$ and one of them is depicted by dashed thick blue lines and the other by dashed think blue line). (b) Macroscopic crack distribution in GBMs and their experimental counterparts. (c) The results of numerical Brazilian test. (d) Macroscopic tensile crack distribution in the GBM specimen and its experimental counterpart.

6.2.3 Simulation of Aue granite

The red Aue granite from Blauenthal/Germany (syeno–monzo-granite) (Hofmann et al. 2015a) was simulated in this section. The mineral size and content are given in Table 6.4. According to Hofmann et al. (2015a) the grain size varies from 0.9 to 1.8 mm; hence, the grain size standard deviation within this given range was used to generate GBM specimens. The dimension of the laboratory specimen for the unconfined compressive test was 100 mm (height) × 50 mm (diameter), and the diameter of the Brazilian disk was 50 mm. The GBM specimens with the same dimensions were generated in the present research.

Table 6.4 Mineral content and size for Aue granite (Yoon et al. 2012; Zang 1997; Zang et al. 2000)

	Quartz	Plagioclase	Orthoclase	Mica
Mineral content (%)	30	40	20	10
Avg. mineral diameter (mm)	1.45±0.35	1.35±0.45	1.35±0.45	1.2±0.3

The experimental results from unconfined and confined compressive and Brazilian tensile tests of Aue granite were used for calibration purposes.

The microproperties of calibrated Aue granite is listed in Table 6.5, and the macroscopic parameters of both numerical and experimental observations are given in Table 6.6. Figure 6.5 illustrates the numerical stress-strain graph and corresponding failure state of the specimen at peak. The numerical results show that the macroscopic cracks were formed in the specimen as a result of interaction between inter- and intra-grain micro-cracks.

Table 6.5 Micro-mechanical parameters obtained from the calibration procedure of Aue granite

Element	Parameter	Grain 1 Quartz	Grain 2 Plagioclase	Grain 3 Orthoclase	Grain 4 Mica
Particles forming grains	Minimum particle radius forming grain, R_{min} (mm)	0.15	0.15	0.15	0.15
	Maximum to minimum radius ratio, R_{max}/R_{min}	1.66	1.66	1.66	1.66
Cohesive model	Young's Modulus, $\bar{E}_{CCM}$ (GPa)	62	52	42	32
	Normal to shear stiffness ratio, ($k^0_{n,CCM}/k^0_{s,CCM}$)	1.0	2.0	2.0	1.5
	Cohesion, (C^0_{CCM}) (MPa)	118	95	95	60
	Friction ratio, (μ_{CCM})	0.58	0.6	0.6	0.55
	Dilation ratio, (β_{CCM})	0.22	0.25	0.25	0.2

	Average normal stiffness (GPa)	245,000	210,000	185,000	163,000
	Average shear stiffness, (GPa)	245,000	119,000	121,000	136,000
	Softening parameter, κ_{CCM} (1/m)	25,000,000	18,000,000	18,000,000	15,000,000

Micro-mechanical parameters of the grain boundaries (the smooth joint contacts)

Smooth-joint model	Normal stiffness, ($k^0_{n,CSJM}$) (GPa/m)	106,000
	Shear stiffness, ($k^0_{n,CSJM}$) (GPa/m)	28,500
	Cohesion, (C^0_{CSJM}) (MPa)	7.0
	Friction ratio, (μ_{CSJM})	0.45
	Dilation ratio, (β_{CSJM})	0.25
	Softening parameter, κ_{CSJM} (1/m)	1,500,000

Table 6.6 Macroscopic properties of Aue granite (Yoon et al. 2012) and GBM approach

Property	Aue granite (Experimental)	Aue granite (Numerical)
Uniaxial compressive strength (MPa)	134±7	138
$\boldsymbol{\sigma_{1@10MPa}}$	256	248
$\boldsymbol{\sigma_{1@40MPa}}$	456	436
Young's modulus (GPa)	48±8	50
Poisson's ratio	0.19	0.22
Brazilian tensile strength (MPa)	8±1	8.3

Figure 6.6 illustrates the results of the Brazilian tensile test and the corresponding damage response of inter-grain contacts at different tensile stress magnitudes. In GBM approach, the macroscopic tensile strength of the model is controlled by the microscopic tensile strength of the inter-grain contacts (Potyondy 2010a). In the previous PFC-GBM studies, SJM has been extensively employed to simulate the micro-cracking behaviour of inter-grain contacts. In the present study, CSJM was proposed and assigned to inter-grain contact, which modelled the gradual softening of grain boundaries. In CSJM, when the contact reaches its yield limit, the softening response of the contact begins. D_{CSJM} demonstrates the degree of damage in the inter-grain contacts, and can be plotted graphically to depict the localized damage response of inter-grain contacts. We monitored the damage state of grain boundaries at different stress magnitudes to observe the effectiveness of CSJM in reproducing the mechanical behaviour of Aue granite. In Figure 6.6b, an enlarged view of the inter-grain contacts is illustrated below each specimen to better exhibit the softening response of grain-boundary contacts. It can be seen that from point "a" to point "c" the number of soften contacts ($0.0 < D_{CSJM} < 1.0$) significantly increased, with the majority of the damage occurred in the middle portion of the Brazilian disk, point "b", and extended towards the loading plates, point "c" (Figure 6.6b).

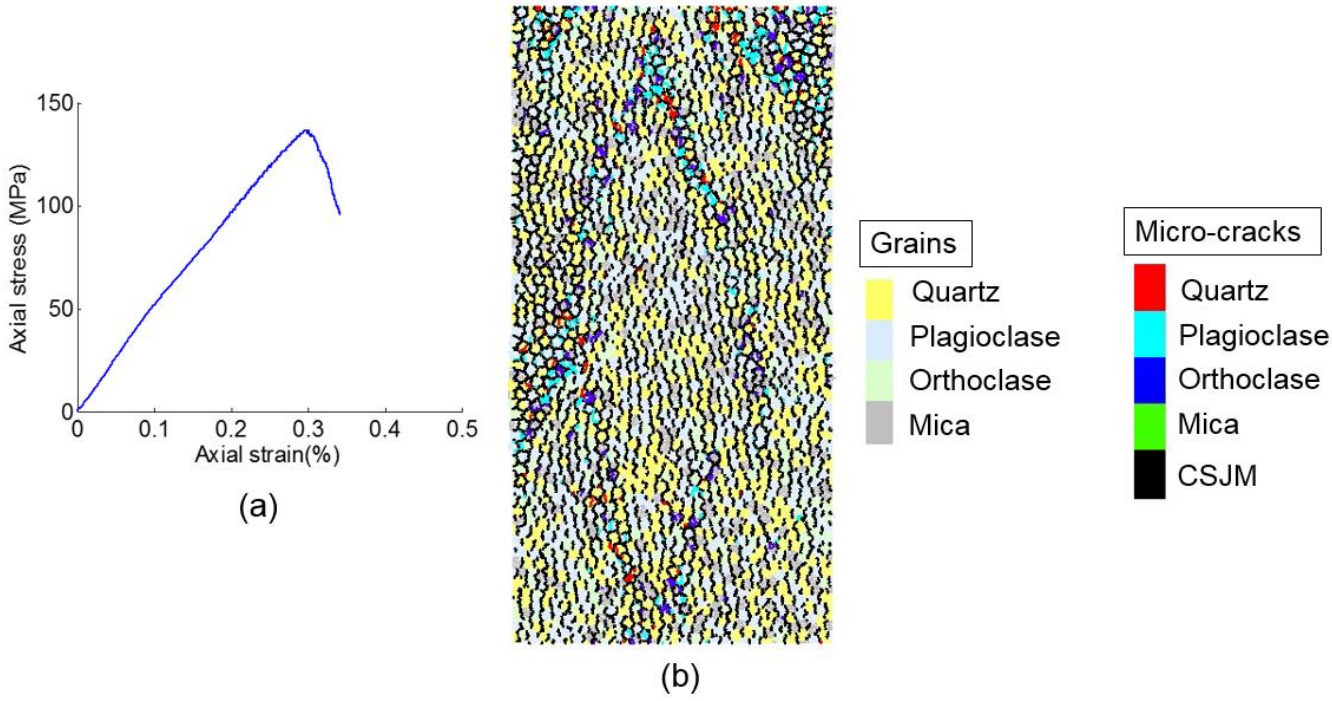

Figure 6.5 The numerical behaviour of Aue granite under uniaxial compression loading. (a) Axial stress-strain curve. (b) Fracture distribution at peak axial stress.

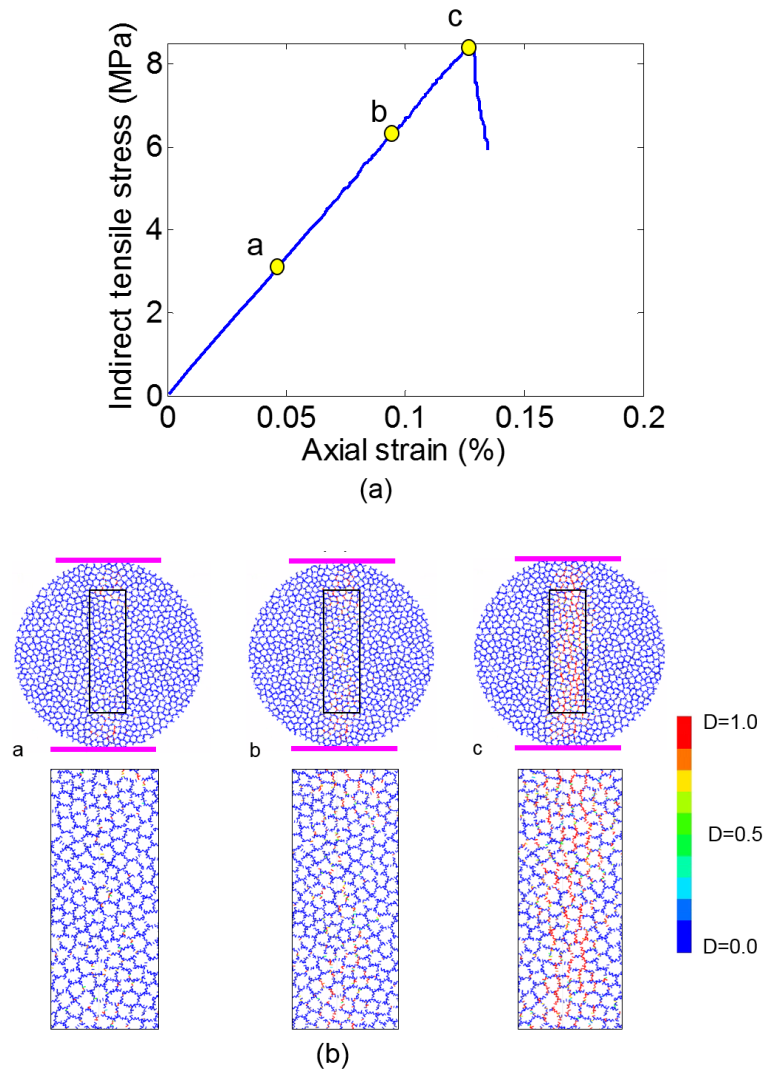

Figure 6.6 The Brazilian tensile test. (a) Axial stress-strain curve. (b) Microscopic damage response in the cohesive inter-grain contacts.

To further validate the abilities of the proposed cohesive model, a series of uniaxial and triaxial asymmetric tests were simulated using the cohesive GBM framework. Figure 6.7 illustrates the experimental (Figure 6.7a) and numerical (Figure 6.7a) setup of the asymmetric test. The length of top loading wall was shortened to 30 mm (specimen diameter was 50 mm), leaving the upper left portion of the specimen (20 mm) free of compressive loading (Yoon et al. 2012). As stated by Yoon et al. (2012), I asymmetric testing aims to observe the development of shear rupture zone in the specimens, which is an important failure mechanism in deep mining structures (Bewick et al. 2014a). Figure 6.8 illustrates a comparison between fracture behaviour of laboratory uniaxial and triaxial asymmetric tests and the micro-cracking response of the proposed cohesive GBM. The laboratory observations showed that at atmospheric pressure, the cracks initiated at the edge (3D) or point (2D) of the asymmetric steel loading platen, and

developed sub-vertically towards the stationary steel platen (Figure 6.8 a and b, $\sigma_3 = 0\ MPa$) (Stanchits and Dresen 2003; Yoon et al. 2012). You can see that in the proposed GBM framework very well captured this failure pattern, with the sub-vertical macroscopic cracks were formed due to the progressive coalescence of inter- and intra-grain micro-cracks. At 10 and 40 MPa confining pressure, cracks were initiated at the edge of loading platen and propagated towards the loaded portion of the specimens (Figure 6.8 a and b, $\sigma_3 = 10$ and $40\ MPa$) (Stanchits and Dresen 2003; Yoon et al. 2012). You can see from Figure 6.8c ($\sigma_3 = 10$ and $40\ MPa$) that the GBM specimen exhibited a close failure pattern to its laboratory counterparts. Notice that in the numerical specimen more unconnected inter-grain micro-cracks developed away from the major fracture. This is because a very small tensile strength is required to match the Brazilian tensile strength results (Hofmann et al. 2015a; Saadat and Taheri 2019a, 2019b). The micro-cracks that may have developed away from the major fracture could not be observed in the physical specimens. However this does not mean that these micro-cracks do not exist (Hofmann et al. 2015a). Therefore, the GBM results seem to fit the laboratory observations reasonably well, and the macroscopic behaviour can be reproduced.

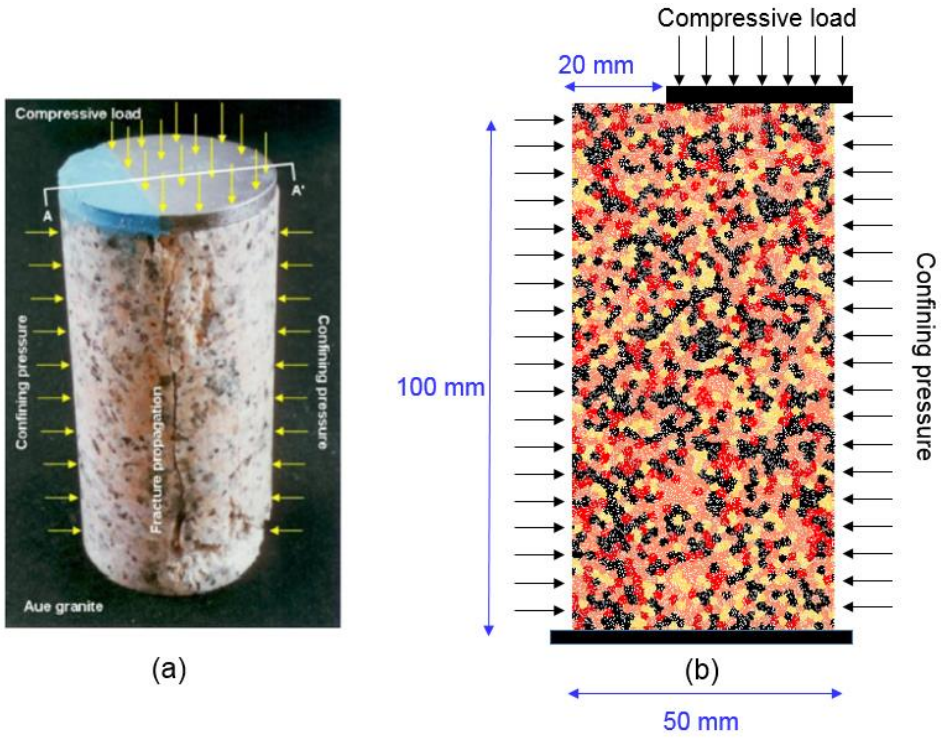

Figure 6.7 The specimen setup for the asymmetric test. (a) Laboratory setup (Yoon et al. 2012). (b) Numerical setup.

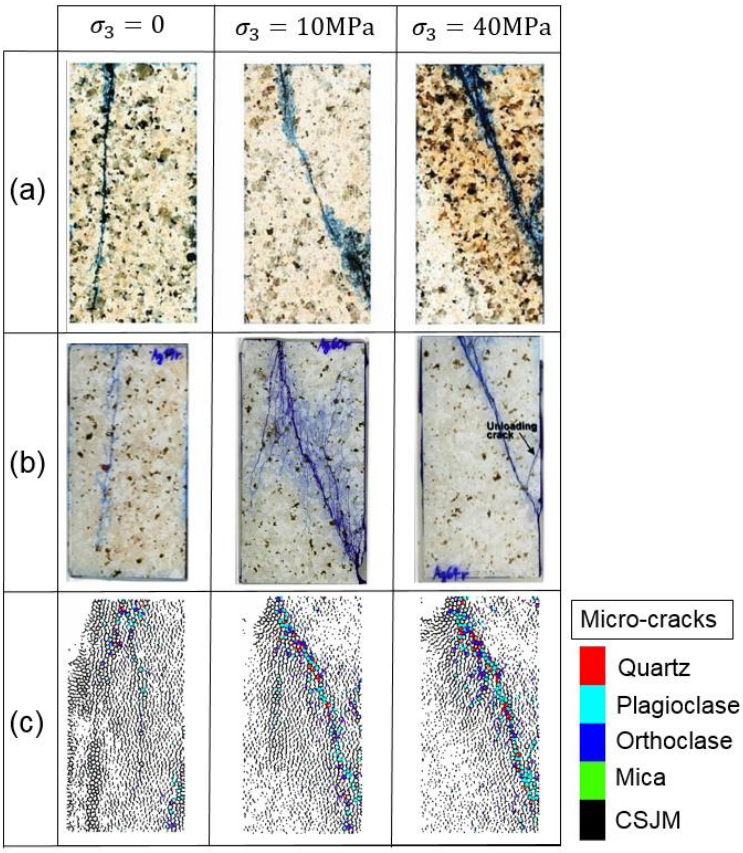

Figure 6.8 Comparison of the crack distribution of asymmetric uniaxial and triaxial tests at 10 and 40 MPa confining pressure with the micro-cracking response of the GBM specimens. (a) Experimental results from Stanchits and Dresen (2003). (b) Experimental results from Yoon et al. (2012). (c) The macroscopic fracture behaviour and micro-crack distribution in GBM specimens.

In Figure 6.9 the numerical observations of Hofmann et al. (2015a) and Yoon et al. (2012) are illustrated. Hofmann et al. (2015a) used GBM modelling with PBM-SJM constitutive models and Yoon et al. (2012) employed clumped particle model to simulate Aue granite. You can see from Figure 6.8 that, unlike GBM simulation of Hofmann et al. (2015a) (Figure 6.9a) and Yoon et al. (2012) (Figure 6.9b), in the present GBM specimen obvious grain crushing was observed with an intense concentration along the major fracture, which was closer to the physical behaviour.

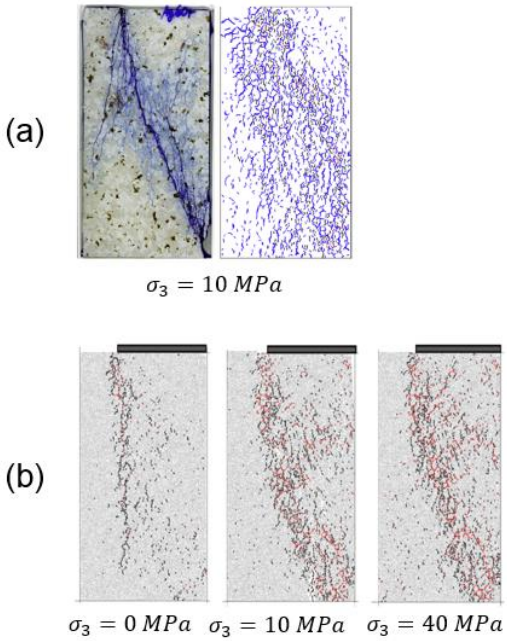

Figure 6.9 Numerical crack pattern observed in asymmetric tests of Aue granite by (a) Hofmann et al. (2015a) and (b) Yoon et al. (2012).

6.3 Rock joint shear behaviour using cohesive GBM

6.3.1 Influence of JRC and CNS condition on rock joint behaviour

In order to study the impact of surface roughness of rock joints and microstructural characteristic of polycrystalline rock on the overall shear behaviour GBM specimens, we selected three different natural rock joint profiles with known JRC values of 4.6 (smooth), 10.2 (rough), and 17.5 (very rough), which were measured by Bahaaddini (2014). The surface configuration of rock joint profiles is depicted in Figure 6.10. Hereafter, the GBM specimens with JRC values of 4.6, 10.2, and 17.5 are called JP1, JP2, and JP3, respectively. The direct shear tests performed under both CNL and CNS conditions. The numerical setup under CNL and CNS conditions are illustrated in Figure 6.11. The increment of initial normal stress magnitudes (σ_n^0) under CNS condition is calculated according to Eq. 4.1 and Eq. 4.2.

Different researchers used various CNS stiffness values in DEM studies. For instance, Bewick et al. (2014b) suggested CNS stiffnesses of 10, 30, and 100 GPa/m for GBM simulations of intact sandstone with average UCS and Young's modulus of 140 MPa, and 44 GPa, respectively. Shang et al. (2018b) assumed CNS stiffness values of 1, 10, and 30 GPa/m to numerically study the shear behaviour of incipient rock joints of Horton Formation Siltstone under CNS condition. The average UCS and Young's modulus of their specimen, respectively,

were approximately 140 MPa, and 35 GPa. In the present study, a k^{cns} of 15GPa/m was considered for Aue granite to carry out CNS direct shear tests.

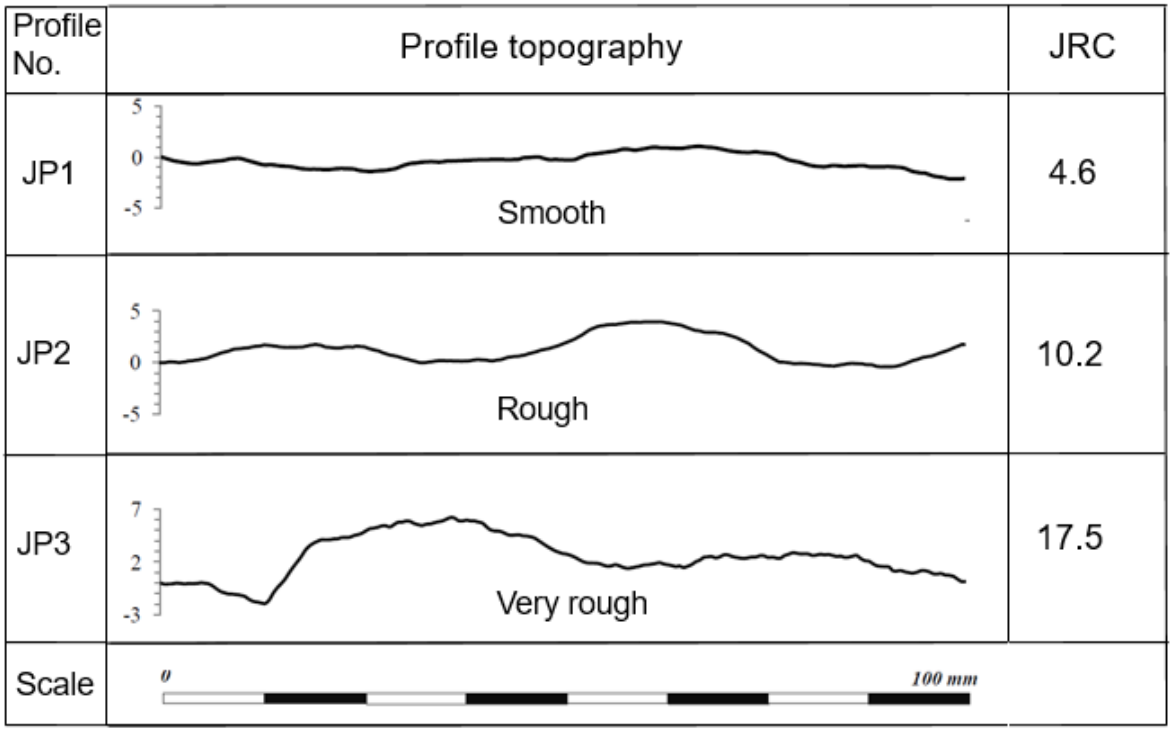

Figure 6.10 Natural rock joint profiles used in the GBM approach (modified from (Bahaaddini 2014))

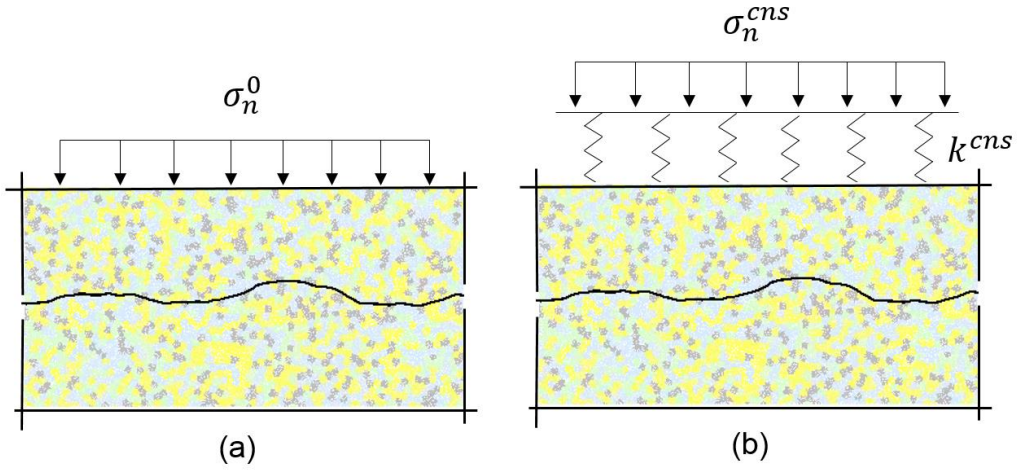

Figure 6.11 Direct shear test setup of GBM specimen under (a) CNL, and (b) CNS conditions.

The SJM was applied to the DEM particles forming the rock joint interface. The macroscopic data for calibrating SJM microproperties were not available. However, it often the case in numerical investigations that one set of microproperties can be assumed to represent the mechanical behaviour of rock joint (Bahrani and Kaiser 2016; Zhou et al. 2017). Gutiérrez-

Ch et al. (2018) suggested a value between 1 and 10 for k_n^{SJM}/k_s^{SJM} to simulate direct shear tests using SJM. The microproperties of SJM include normal stiffness (k_n^{SJM}), shear stiffness (k_s^{SJM}), and friction ratio (μ^{SJM}). In the present study, a set of microproperties representing the mechanical behaviour of rock joint was assumed for investigating the influence of surface roughness and CNS condition on rock joint shear behaviour. The value of k_n^{SJM} and k_s^{SJM} were considered to be 10,000 and 2,500 GPa/m, respectively. The friction ratio (μ^{SJM}) was assumed to be 0.75.

The results of the numerical direct shear test for JP2 under different initial normal stress magnitudes (σ_n^0) are presented in Figure 6.12. We have used three different terms suggested by Bahaaddini et al. (2013) for describing the shear mechanism of rock joints: 'asperity sliding', 'asperity wear', and 'asperity shear-off'. 'Asperity damage' is a term used by the authors by which the degradation of asperities was described. When the degradation of asperities was high, we used descriptive terms such as 'sever asperity damage' and 'pronounced asperity damage'. We also used the term 'minor asperity damage' to describe low-intensity asperity degradation, and 'grain crushing' to refer to the development of intra-grain micro-cracks (Morgan et al. 2013; Saadat and Taheri 2019a). Asperity sliding occurs under low normal stress where the walls of rock joint slide freely over each other (Bahaaddini et al. 2013). This may be followed by minor asperity damage which is evident by very few intra-grain contacts and slight concentration of inter-grain contacts around the critical asperity areas (see CNL specimen with $\sigma_n^0 = 2\ MPa$, Figure 6.12b). Asperity wear takes place under medium normal stress magnitude (Bahaaddini et al. 2013), and causes higher asperity damage in the forms of grain crushing. This shear mechanism exhibits a higher concentration of inter-grain micro-cracks, which cancan be seen in CNL specimen with $\sigma_n^0 = 7\ MPa$, Figure 6.12b. Finally, when the applied normal stress magnitude is high, the rock joint tends to demonstrate the asperity shear-off mechanism (Bahaaddini et al. 2013). This shear behaviour is usually followed by pronounced asperity damage which is the direct consequence of severe grain crushing and high concentration of inter-grain micro-cracks around the critical asperity areas. Figure 6.12b shows an instance of asperity shear-off in CNL specimen with $\sigma_n^0 = 7\ MPa$.

The shear stress-displacement graphs (Figure 6.12a) showed that the slope of the linear elastic stage of the GBMs increased with increasing σ_n^0. The results demonstrated that all GBMs, under CNS condition, exhibited a higher peak shear strength. For $\sigma_n^0 = 2\ MPa$ a distinct peak shear strength could not be recognized, which was due to a progressive increase of applied normal stress. For medium and high σ_n^0 (i.e. 7 and 14 MPa), a distinct peak shear strength

could be observed under CNS, but there was still a slight increase in the shear strength during post peak. The CNL models exhibited a higher dilative response compared to CNS models (Figure 6.12a). The fracture response of GBMs showed that the asperity degradation in CNS models was more pronounced than those undertaken under CNL condition (Figure 6.12b). These behaviours were attributed to an increase in the magnitude of normal stress in the CNS condition. The CNL models showed a transition from asperity sliding mode ($\sigma_n^0 = 2\ MPa$) to asperity wear ($\sigma_n^0 = 7\ MPa$) and asperity shear off ($\sigma_n^0 = 14\ MPa$) modes by increasing σ_n^0 (Figure 6.12a and b).

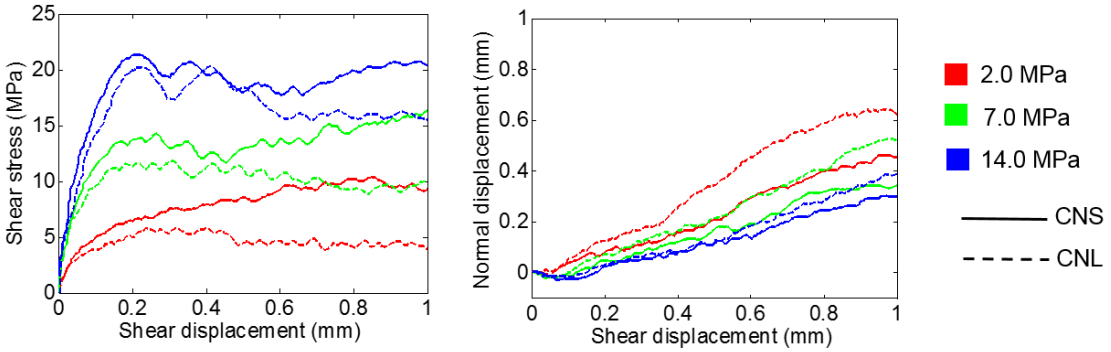

(a)

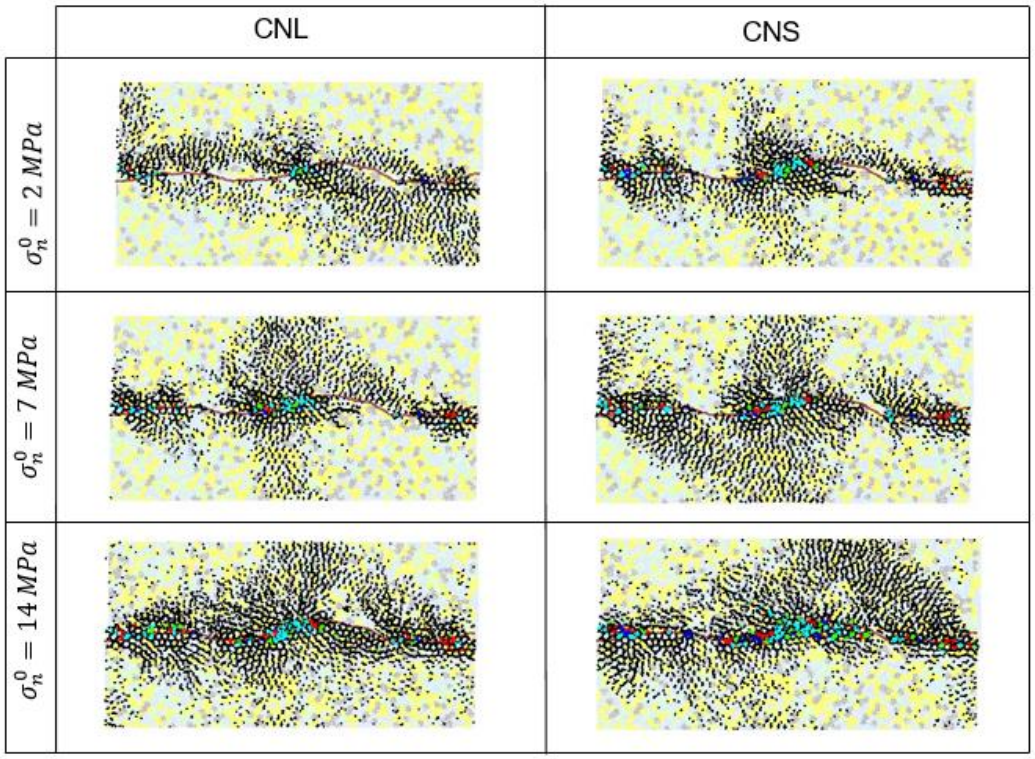

(b)

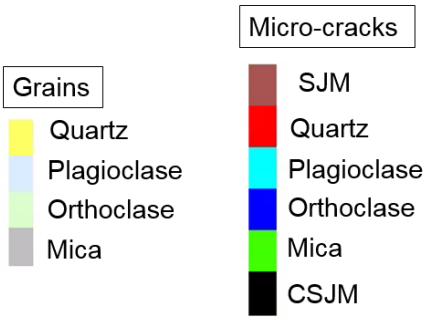

Figure 6.12 The result of the direct shear test on GBM specimen under CNL and CNS conditions: (a) shear stress-displacement and normal-shear displacement graphs; (b) distribution of inter- and intra-grain micro-cracks.

The macroscopic fracture behaviour of GBMs in Figure 6.12b shows that in all GBMs, asperity damage occurred due to bond-break in the intra-grain contact, which resulted in grain crushing in critical asperities. The experimental investigations of Morgan et al. (2013) showed that mineral strength highly controls the degree of grain crushing in polycrystalline rocks. The GBM results (Figure 6.12b) revealed that when the shear mechanism was asperity sliding (i.e. $\sigma_n^0 = 2\ MPa$), the grain crushing was not significant. In contrast, in GBMs with higher σ_n^0 more intra-grain cracks were promoted resulting in a more pronounced localized asperity degradation. The distribution pattern of inter-grain micro-cracks (black lines in Figure 6.12b) showed that by increasing σ_n^0, the inter-grain micro-cracks tended to develop vertically towards the top loading wall. The numerical simulations revealed that grain crushing (i.e. localized asperity damage) was more pronounced under CNS condition. This may be attributed to asperity interlocking as a result of an increase in the applied normal stress under CNS condition, which prevented the rock joint surface from slipping along the irregularities. As a results, the critical asperities exhibited more resistance against shearing leading to more grain crushing.

In order to better analyse the asperity degradation of rock joints under CNS condition during the shear procedure, the fracture distribution pattern of GBM (JP2) with 2.0 and 14.0 MPa of σ_n^0 was monitored at four different shear stress magnitudes, and the results are illustrated in Figure 6.13. In the pre-peak stage (point "a", Figure 6.13), both GBMs demonstrated the formation of inter-grain micro-crack around the critical asperity areas. When $\sigma_n^0 = 14.0\ MPa$ a slight grain crushing is observed. With further shear displacement, the number of inter- and intra-grain micro-cracks enhanced in the GBMs (point "b", Figure 6.13). The peak shear

strength occurred in GBM with $\sigma_n^0 = 14.0\ MPa$ at point "b", while no recognizable peak was observed for the test at $\sigma_n^0 = 2.0\ MPa$. Then, the GBM with $\sigma_n^0 = 14.0\ MPa$ experienced a softening stage during which a high degree of bond-break occurred in inter-grain contacts (point "c", Figure 6.13). A pronounced localized asperity damage (i.e. grain crushing) was also observed at this point. In comparison, the GBM with $\sigma_n^0 = 2.0\ MPa$ showed minor asperity damage, and the inter-grain micro-cracks developed around the rock joint surface (point "c", Figure 6.13). At the end of the shearing stage (point d), severe asperity damage occurred in the GBM with $\sigma_n^0 = 14.0\ MPa$, and inter-grain micro-cracks coalesced to form larger grain boundary fractures apart from the rock joint interface. In contract at point "d", the GBM with $\sigma_n^0 = 2.0\ MPa$ exhibited a low intensity of asperity damage, and the formation of tensile fractures was less severe. Notice that the extension of tensile fractures was the result of progressive coalescence of inter-grain micro-cracks, which are demonstrated by accumulation of fractures in grain bountries (i.e. black lines) demonstrated in Figure 6.13. The extension of tensile fractures along grain boundaries was the results of assigning small contact strength (C_{CSJM}^0) to the inter-grain contacts in order to match the experimental Brazilian tensile strength. This is the pivotal aspect of GBM simulation (Hofmann et al. 2015a; Saadat and Taheri 2019b). These numerical observations are consistent with the fracture behaviour of physical specimens. For instance, the experimental results of Meng et al. (2018) on granite with irregular rock joints showed that apart from asperity damage, several tensile fractures were initiated and distributed into the rock specimen away from rock joint profile.

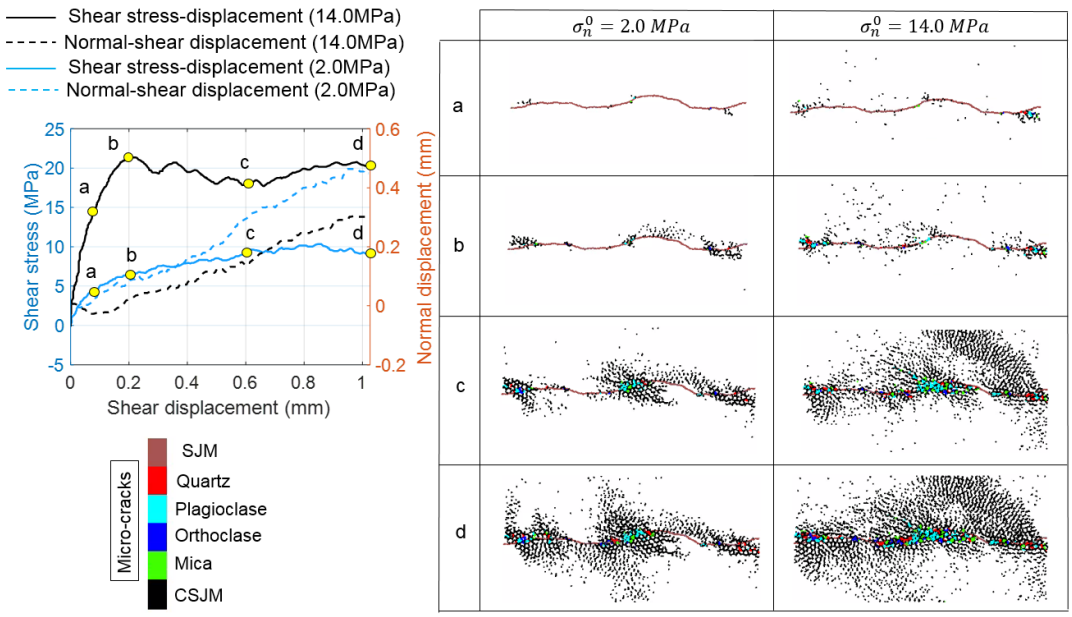

Figure 6.13 Asperity degradation of GBMs with different σ_n^0 under CNS condition (JP2).

In order to assess the influence of JRC on the shear mechanism and fracture behaviour of GBM specimen under CNS condition, the numerical direct shear tests were carried out using JP1, JP2, and JP3 (Figure 6.10) with $\sigma_n^0 = 2.0\ MPa$. Figure 6.14 illustrates the shear stress-displacement and normal-shear displacement relations, and the fracture distribution in GBMs. As expected, by increasing the value of JRC, the peak shear strength and normal displacement seincrease (Figure 6.14a). The GBM with JP2 and JP3 showed severe asperity damage, whereas JP1 exhibited dominant asperity sliding (Figure 6.14a) with slight asperity damage (Figure 6.14b). The results showed that the shear stress in JP2 gradually increased after 0.2 mm of shear displacement, which was due to the effect of CNS condition. This behaviour was not observed in JP1 and JP3. These numerical results were consistent with the experimental observations of Indraratna et al. (2015).

In the present research, we employed 2D numerical simulation to generate various morphologies of rock joint. This simplification was required in order to reduce the computational costs. It is true that more details can be incorporated into the numerical specimen in 3D, which can give us a more comprehensive understanding of rock joint shear behaviour. However, 2D assumption is valid because the macroscopic response of the GBM specimens are consistent with the laboratory observations (Meng et al. 2018). Also, this has been a common approach in DEM studies to adopt 2D simulations (e.g. Bahaaddini (2014)).

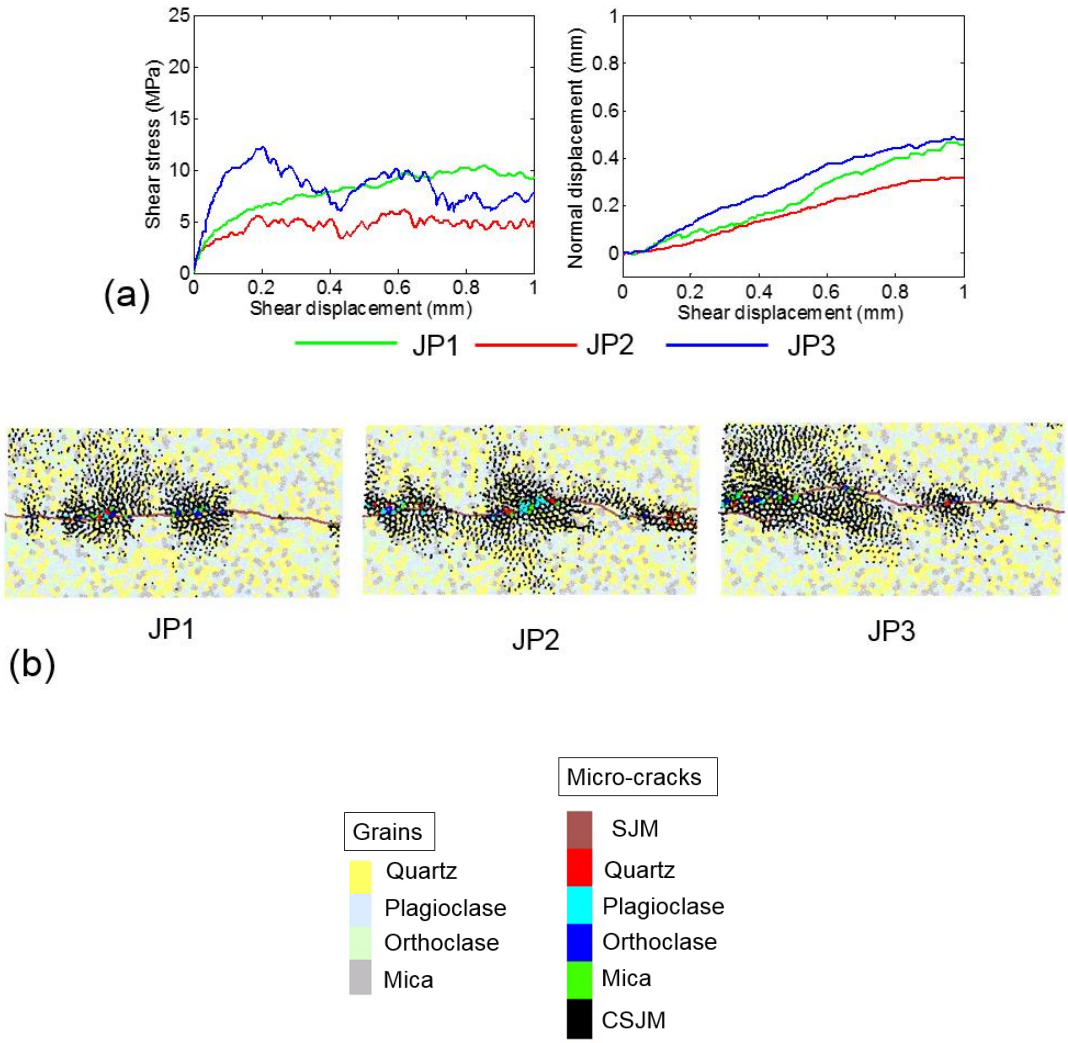

Figure 6.14 The numerical direct shear test results on rock joints with different surface roughness under CNS condition. (a) The shear stress-displacement and normal-shear displacement curves (b) The fracture distribution and asperity damage in GBM specimens.

6.3.2 Influence of grain size on the shear behaviour of rock joint

We generated three distinct grain size scenarios given in Table 6.7, which are similar to our previous research studying the effect of rock texture on macroscopic behaviour of pre-cracked polycrystalline rocks (Saadat and Taheri 2019b). This enables us to investigate the influence of grain size on macroscopic behaviour of rock joint (JP2). To do so, we have conducted 18 numerical direct shear tests in PFC2D to examine the effect of rock texture on macroscopic shear behaviour of rock joints under both CNL and CNS conditions. The peak shear stress and peak dilation angle of the numerical specimens were measured, and the results of this parametric study are illustrated in Figure 6.15.

Table 6.7 Overview of various grain size scenarios for investigating the influence of grain size heterogeneity on the shear mechanism of rock joint

	Average mineral diameter (mm)			
	Quartz	Plagioclase	Orthoclase	Mica
Fine grain	1.45±0.35	1.35±0.45	1.35±0.45	1.2±0.3
Medium grain	3.2	1.6	1.6	1.6
Coarse grain	4.3	3.0	3.0	3.0

You may see that at $\sigma_n^0 = 2\ MPa$ the grain size has a negligible influence on the peak shear stress and peak dilation angle of rock joint under both CNL and CNS conditions. At σ_n^0 of 7 and 14 MPa, the effect of grain size was more pronounced .The highest peak shear stresses and the lowest peak dilation angles are observed at σ_n^0 = 14 MPa , respectively (Figure 6.15) . The increase in the shear stress of rock joints was attributed to the higher asperity strength because an increase in the grain size relatively rises the UCS of GBMs (Hofmann et al. 2015a; Peng et al. 2017; Saadat and Taheri 2019b). The reduction in peak dilation angle might be due to severe asperity damage. As it can be seen in Figure 6.15a, the influence of CNS condition on peak shear strength was more pronounced under $\sigma_n^0 = 2\ MPa$, which was due to the predominant asperity sliding mechanism resulting from low confining stress (Indraratna et al. 2015). Nonetheless, the peak dilation angle of CNS specimens showed lower values compared to their

CNL counterparts regardless of σ_n^0 magnitude, which was attributed to a progressive increase of applied normal stress under CNS condition.

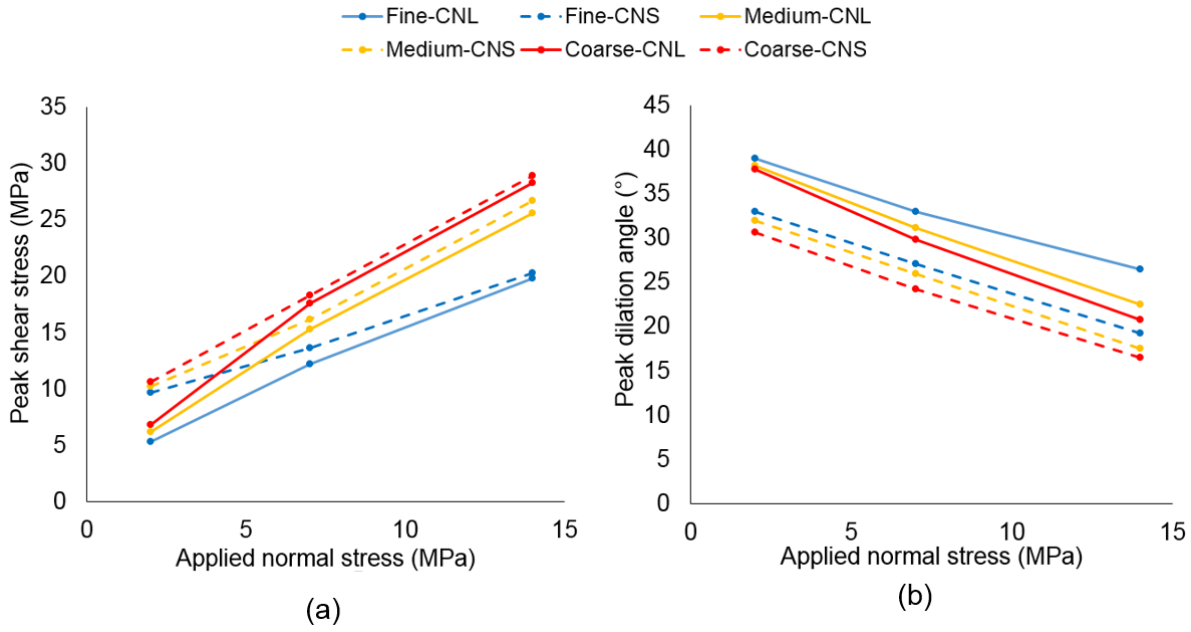

Figure 6.15 The effect of grain size on the (a) peak shear stress, and (b) peak dilation angle of rock joint (JP2)

6.4 Conclusion

The proposed cohesive model was used to develop a cohesive GBM framework to simulate the fracture behaviour of polycrystalline rocks. The gradual softening response of inter- and intra-grain contacts was simulated by incorporating an exponential damage evolution function to the force-displacement laws. The damage response of the contacts controlled using a softening parameter, which defined as a microproperty in the constitutive relationships. The model was validated with the experimental results of three types of granites namely Adelaide black granite, Eibenstock II granite, and Aue granite. The model exhibited good capability in reproducing the macroscopic behaviour of granitic specimens. The following conclusions were derived from validation procedure:

- The numerical results obtained from TPB tests conducted on Adelaide black granite revealed that it is absolutely necessary to incorporate a cohesive response in the constitutive relationships of DEM contacts since PBM was incapable of reproducing a promising post-peak response.

- The lower value of softening parameter showed a more softening response during post-peak stage of TPB test, which was attributed to a high magnitude of fracture energy at microscopic scale.
- The proposed model exhibited a promising capability in reproducing the fracture pattern of polycrystalline rocks under confining pressure.
- Under high confining pressure, the experimental results showed a more pronounced grain crushing, which could be very well identified by the proposed GBM via significant development of intra-grain micro-cracks.
- The proposed GBM framework showed a promising ability in reproducing the fracture behaviour of granitic rock under unconfined and confined asymmetric tests.

Therefore, the proposed GBM framework could be regarded as an alternative tool to an experimental approach, which can be employed to obtain new insight regarding the fracture behaviour of polycrystalline rocks.

The calibrated model was employed for investigating the asperity damage mechanism of rock joints with various surface roughness under both CNL and CNS conditions. Three rock joint profiles were digitized and imported into PFC2D to produce jointed polycrystalline specimens. The numerical results indicated that the response of rock joints under CNS was greatly controlled by asperity damage (i.e. grain crushing), the extent of which increased with increasing σ_n^0 and surface roughness. The normal displacement of rock joints increased with increasing JRC, and reduced with increasing σ_n^0. The asperity damage was occurred in GBMs as a result of grain crushing which was due to bond-break in the intra-grain contacts, an effect that was more severe in rough rock joints.

Chapter 7: GBM simulation of pre-cracked Barre granite

7.1 Introduction

The determination of rock mass strength and damage mechanism of granitic rocks is critical at design and construction stages of mining projects. Mining excavation at great depth generates severe challenges in the development of mining structures such as pillars and tunnels (Bahrani et al. 2011). As planes of weaknesses, discontinuities (e.g. joints) can control and affect the strength, deformation, and failure behaviour of rock masses (Brady and Brown 2004). Conducting laboratory tests on pre-cracked specimens enhances our understating about the cracking processes and damage behaviour of rocks. The results of such experimental testing can serve as a basis for the development of constitutive models (i.e. in continuum methods) that can be used for the simulation of field scale problems (Bobet and Einstein 1998). The macroscopic cracking response, however, is highly influenced by the microstructure of the rock at the grain scale (Wu et al. 2000). In this respect, studying the underlying mechanism of the initiation of inter- and intra-grain micro-cracks is crucial.

The development of macroscopic fractures due to the initiation and coalescence of inter-and intra-grain micro-cracks is the dominant damage mechanism influencing the mechanical behaviour and integrity of brittle rocks (Moradian et al. 2016; Morgan et al. 2013). Different parameters, such as grain shape and size, the type of minerals, and the presence of pre-existing cracks, affect the mechanical and failure responses of rock as a heterogeneous material. The mechanical behaviour of the rock mass is controlled by intact rock blocks and defects (i.e. joints, fractures, and cracks) (Taheri and Tani 2010). One of the main reasons for rock mass failure is the coalescence of pre-existing flaws (Yin et al. 2014; Zhou et al. 2018).

Many scientists have concluded that the mechanical and failure behaviours of crystalline rocks are highly influenced by inter- and intra-grain crack initiation and crack propagation at the mineral scale (Diaz et al. 2016; Rodríguez et al. 2016; Tavallali and Vervoort 2010; Tuğrul and Zarif 1999). Therefore, studying the macroscopic failure and mechanical behaviour of pre-crack rock specimens is highly relevant during the process of rock mass characterisation, especially for the evaluation of rock mass strength (Bahrani and Kaiser 2016; Cao et al. 2016; Liu et al. 2018; Mayer and Stead 2017; Morgan et al. 2013).

The focus of this chapter is to employ the proposed model to mimic the mechanical and failure behaviour of pre-cracked crystalline rocks. The proposed GBM framework was calibrated against the experimental uniaxial compressive and Brazilian split-tensile-testing results using

Barre granite. The calibrated model was then used for simulating the macroscopic mechanical and fracturing behaviour of physical pre-cracked Barre granite, and a good agreement was obtained. We found that using the proposed GBM framework, both inter- and intra-grain micro-cracking behaviour can be simulated. These capabilities allow us to obtain a better insight into the influence of the microstructural features of the pre-cracked granite's failure mechanisms.

7.2 Modelling polycrystalline rock using GBM

In general, the different minerals, pores, and defects in intact rocks control the rocks' mechanical and deformation behaviours (Liu et al. 2018). Better insight into the damage process and failure behaviour of brittle materials can be obtained by studying the processes of the propagation and coalescence of macroscopic cracks that initiate from pre-existing flaws. In the GBM approach, micro-cracks initiate and propagate in the numerical specimen due to bond failures in the inter- and intra-grain contacts. In the presence of pre-existing cracks, the macroscopic failure pattern, and the material strength, are highly influenced by the initiation and propagation of micro-cracks that form around the inner- and outer- flaw-tip regions of the pre-existing flaws. Prior experimental observations have revealed that the flaw inclination angle affects granite's fracturing processes (Miller and Einstein 2008; Morgan et al. 2013). In the following sub-sections, the calibration procedure of the GBM approach against laboratory data of Barre granite is described first. Then, the micro-parameters obtained during the calibration process are used to simulate the mechanical and cracking behaviours of Barre granite under uniaxial compression.

7.2.1 Model setup and calibration procedure

The micro-mechanical parameters incorporated in the constitutive relationships of the cohesive and smooth-joint models are different from the macroscopic parameters measured in the laboratory. Therefore, the micro-mechanical parameters must be obtained in a calibration procedure (Bahrani et al. 2014; Farahmand et al. 2018; Liu et al. 2018). In the present study, the mechanical properties of Barre granite given by Miller (2008) and Morgan et al. (2013) were used to calibrate the proposed GBM framework. The calibration procedure involved altering the microproperties of the model until reaching a good match between simulated macroscopic parameters and the laboratory test results. We used the results of the uniaxial compressive and Brazilian tensile tests of Barre granite to calibrate the GBM. The macroscopic parameters used in the calibration procedure included Young's modulus, the uniaxial compressive strength (UCS), Poisson's ratio, the Brazilian tensile strength (BTS), and the ratio of UCS/BTS.

Barre granite is approximately comprised of 36% plagioclase, 32% quartz, 18% K-feldspar, 8% biotite, 3% muscovite, and 3% granophyre minerals (Morgan et al. 2013). The average grain size of Barre granite reported in the literature is 1.7 mm, with a minimum and maximum grain size of 0.87 mm and of 2.54 mm, respectively (Morgan et al. 2013). These data were used for generating the synthetic specimens illustrated in Figure 7.1. Due to the small percentage of muscovite and granophyre minerals, each was categorised as "other minerals", together with biotite, during the sample generation procedure. A unique set of micro-mechanical parameters were assigned to the DEM contacts that formed the "other minerals" group. In this research, the average grain size was slightly increased to 1.9 mm, which is still in the range of 0.87-2.54 mm, to make the numerical simulations computationally efficient. Increasing the average grain size to reduce computation time has also been adopted in previous GBM studies (Bewick et al. 2014c; Liu et al. 2018). These assumptions were required to reduce the complexity of numerical simulations and were verified by comparing them with the laboratory results.

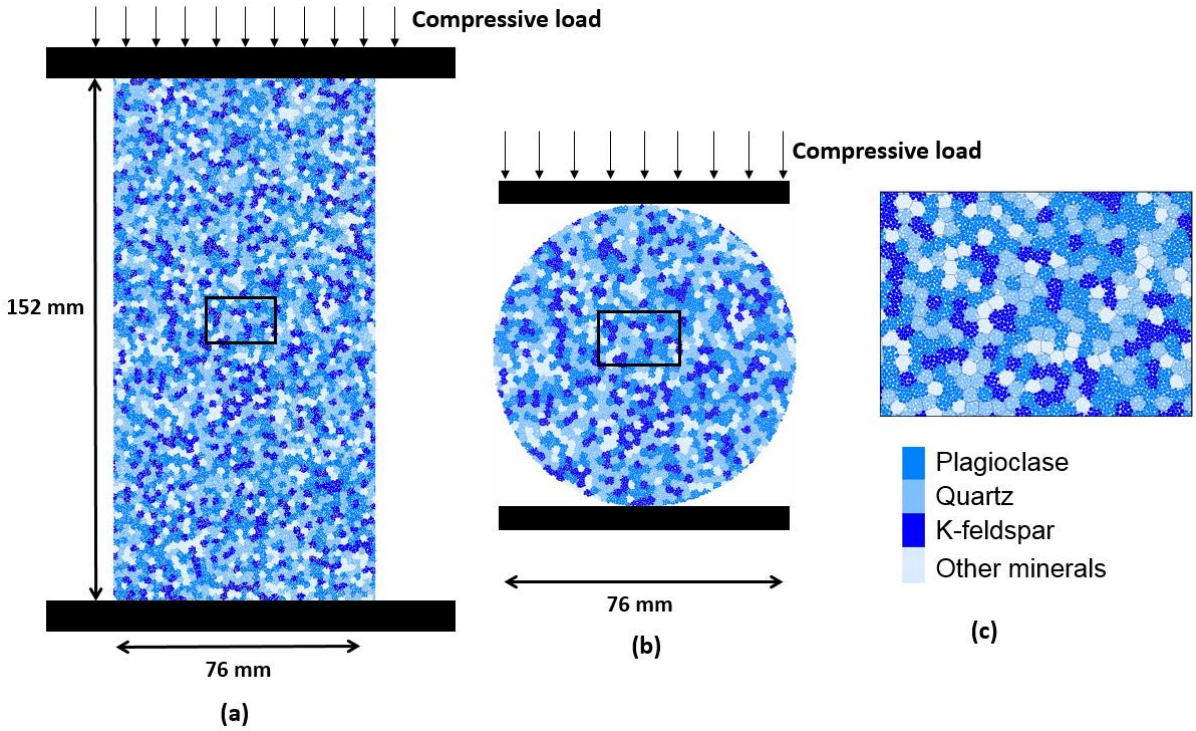

Figure 7.1 Schematic of numerical test setups. *(*a) *U*niaxial compression test. *(b) Brazilian tensile test. (*c) *A* close-up view of grain structure in synthetic Barre granite.

We generated a rectangular specimen with a height of 152 mm and a width of 76 mm to simulate the uniaxial compression test (Fig. 6a). To produce reliable UCS results, particle sizes

should be relatively small compared to the dimensions of the specimen (Munoz et al. 2016; Potyondy and Cundall 2004). Bahrani et al. (2014) and Hofmann et al. (2015a) suggested that at least five minerals are needed along the shorter dimension of the model to simulate a uniaxial test in PFC-GBM. In this research, a minimum particle radius of 0.2 mm was used, to ensure that each mineral was made of at least ten DEM particles. This increase in the number of DEM particles inside the grain allows for more realistic micro-cracking behaviour of the GBM. The numerical UCS specimen contains approximately 47,000 DEM particles.

ISRM (Ulusay 2015) suggested that the specimen diameter in the Brazilian tensile test ought to be at least ten times the average grain size. Accordingly, for simulating the Brazilian tensile test, a circular specimen with a diameter of 75 mm, containing approximately 18,000 DEM particles, was generated in PFC2D (Figure 7.1b). A close-up view of the polygonal grain structure generated by GBM approach is illustrated in Fig.5c.

The calibration procedure is performed by considering a set of micro-mechanical parameters and conducting uniaxial compression and Brazilian tensile tests until the macroscopic properties captured by the proposed GBM framework match the corresponding properties gained from the experimental tests. A summary of the GBM calibration can be found in Bahrani et al. (2014), in which the process was explained by reproducing the mechanical and fracturing behavior of experimental intact and granulated Wombeyan marble. This process was also confirmed by Hofmann et al. (2015a) and Liu et al. (2018). The calibration procedure of GBM approach is comprehensively discussed in chapter 6.

The stress-strain curves of the uniaxial compressive test and the Brazilian tensile test are depicted in Figure 7.2. The micro-mechanical parameters obtained from the calibration procedure are listed in Table 7.1, and the macroscopic results of both the experimental and numerical tests are given in Table 7.2. Note that there is a discrepancy between the stress-strain results (Figure 7.2a) from the beginning of loading until axial stress equal to 40 MPa, even the overall stiffnesses of the stress-strain results obtained from the numerical modelling and the experimental study are similar. The discrepancy is mainly due to a bedding error measurement (Munoz et al. 2016; Taheri and Tani 2008), and to the closure of existing micro-cracks in the experimental measurement at the beginning of loading, during the crack-closure stage (Taheri et al. 2016; Zeng et al. 2018). These two phenomena create a curvature at the beginning of loading in the experimental measurement, which cannot be captured by the numerical model. Since a constant value for the stiffness of inter- and intra-grain contacts needed in the GBM

approach, a linear elastic response was reproduced by the model, even at the beginning of the numerical test. Therefore, no curvature of numerical stress-strain curve (i.e. crack closure) was observed. The linear portion of the stress-strain graph (Figure 7.2a) was used to calibrate the Young's modulus of the rock (Potyondy 2010a). In general, in the current numerical studies, crack closure is not regarded as a macroscopic parameter that should be identified during the calibration procedure. Instead, the reliability of the numerical models can be validated by comparing the numerical results with the Young's modulus, UCS, tensile strength, and Poisson's ratio of the rock (Farahmand et al. 2018; Li et al. 2018b; Potyondy 2010a; Potyondy and Cundall 2004). In the present study, the mechanical parameters of Barre granite were well captured by the proposed GBM framework. We, therefore, assumed that the underestimation of the initial crack closure had negligible implications on the outcome of the present study, because the model well captured the macroscopic mechanical parameters. This assumption was verified in the early attempts of PFC-GBM approach (Potyondy 2010a, 2010b), which is widely adopted in the current GBM investigations (Farahmand et al. 2018; Li et al. 2018b; Liu et al. 2018; Peng et al. 2017).

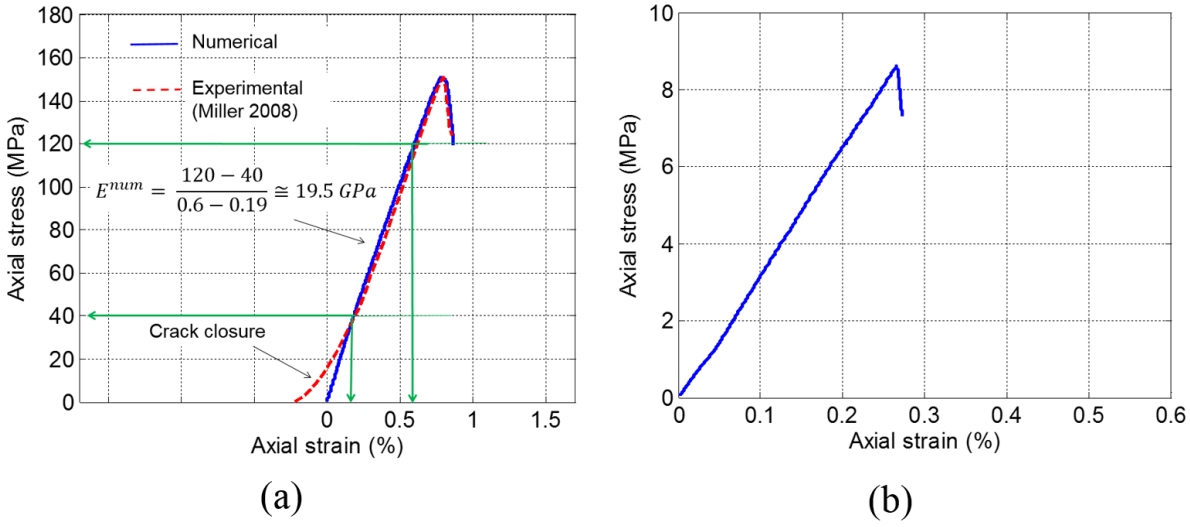

Figure 7.2 Stress-strain curves obtained from numerical simulations. (a) The uniaxial compression tests. (b) The Brazilian tensile test.

Table 7.1 Calibrated microproperties for simulating the macroscopic behaviour of Barre granite.

Micro-mechanical parameters of the grains (the cohesive contacts)

Element	Parameter	Grain 1 Plagioclase	Grain 2 Quartz	Grain 3 K-feldspar	Grain 4 Other
Particles forming grains	Minimum particle radius forming grain, R_{min} (mm)	0.2	0.2	0.2	0.2
	Maximum to minimum radius ratio, r_{max}/r_{min}	1.66	1.66	1.66	1.66
Cohesive model	Young's Modulus, $\bar{E}_{c,CCM}$ (GPa)	12.5	14.0	10.5	5.8
	Normal to shear stiffness ratio, $(k^0_{n,CCM}/k^0_{s,CCM})$	2.0	1.0	2.0	1.5
	Cohesion, (C^0_{CCM}) (MPa)	125	165	125	90
	Friction ratio, (μ_{CCM})	0.55	0.55	0.55	0.55
	Dilation ratio, (β_{CCM})	0.22	0.22	0.22	0.22
	Softening parameter κ_{CCM} (1/m)	12×10^6	15×10^6	12×10^6	10×10^6

Micro-mechanical parameters of the grain boundaries (the smooth joint contacts)

Smooth-joint model	Normal stiffness, (k_n^{sj}) (GPa)	87,000
	Shear stiffness, (k_s^{sj}) (GPa)	47,000
	Tensile strength, (σ_c^{sj}) (MPa)	9.0

Cohesion, (c_0^{sj}) (MPa)	150
Friction angle, (φ^{sj}) $(^{\circ})$	82
Friction coefficient, (μ^{sj})	0.92

Table 7.2 Laboratory test results (Miller 2008) compared to numerically observed results for calibrated Barre granite.

Property	(Experimental)	Numerical
Uniaxial compressive strength (MPa)	151	150
Young's modulus (GPa)	19.2	19.9
Poisson's ratio	0.16	0.19
Brazilian tensile strength (MPa)	5.08-10.65	8.4

Figure 7.2b depicts the stress-strain curve of the Brazilian tensile test. It shows a linear elastic phase, a peak tensile strength, and an abrupt reduction of axial loading. Note that the stress-strain curve related to the Brazilian tensile test is not provided by Miller (2008). Therefore, only the peak tensile strength obtained from the numerical simulation was compared with experimental observations. This calibration approach was also followed in a number of previous numerical studies (Bahrani et al. 2014; Bewick et al. 2014c; Hofmann et al. 2015a; Liu et al. 2018).

The final macroscopic fracturing responses observed in the uniaxial compressive and Brazilian tensile tests are illustrated in Figure 7.3 and Figure 7.4, respectively. The macroscopic fracturing response of the specimen under uniaxial compression is illustrated in Figure 7.3a. For more clarity, the micro-cracking pattern of the uniaxial test is shown separately.

It can be seen from Figure 7.3b that the grain boundary micro-cracks dominated the specimen. This observation is in agreement with Mosher et al. (1975) who experimentally studied the fracturing characteristics of granite and found that the macroscopic tensile cracks that formed sub-parallel to the direction of compressive loading dominate the failure of brittle rocks. At

pre-peak, the intra-grain contacts entered to their yielding limit (softening behaviour). After cohesion degradation ($D_{CCM} = 1.0$), bond-break occurred and intra-grain micro-cracks initiated. At some locations in the specimen (Figure 7.3b), the interaction between inter- and intra-grain micro-cracks formed the macroscopic shear cracks, which was consistent with the macroscopic shear failure observed in brittle crystalline rocks (Hofmann et al. 2015a; Li et al. 2018b). The majority of micro-cracks propagated and developed along the axial direction. Macroscopic fractures generated in brittle crystalline rocks under uniaxial compression are often dominated by cracks at the micro level, in a direction approximately perpendicular to the loading plates. The failure mode observed in the present study's numerical simulation is called "axial splitting", which is in agreement with previous observations (Potyondy 2010a). Figure 7.4 shows that no intra-grain micro-cracks were observed during the Brazilian tensile test and only inter-grain micro-cracks presented during simulation. This was attributed to the low tensile strength assigned on the grain interface contacts, which resulted in the early initiation of inter-grain micro-cracks and the failure of the GBM specimen (Hofmann et al. 2015a; Hofmann et al. 2015b; Liu et al. 2018; Saadat and Taheri 2019b). The progressive coalescence of these tensile micro-cracks formed macroscopic tensile fractures, which extended towards the loading plates.

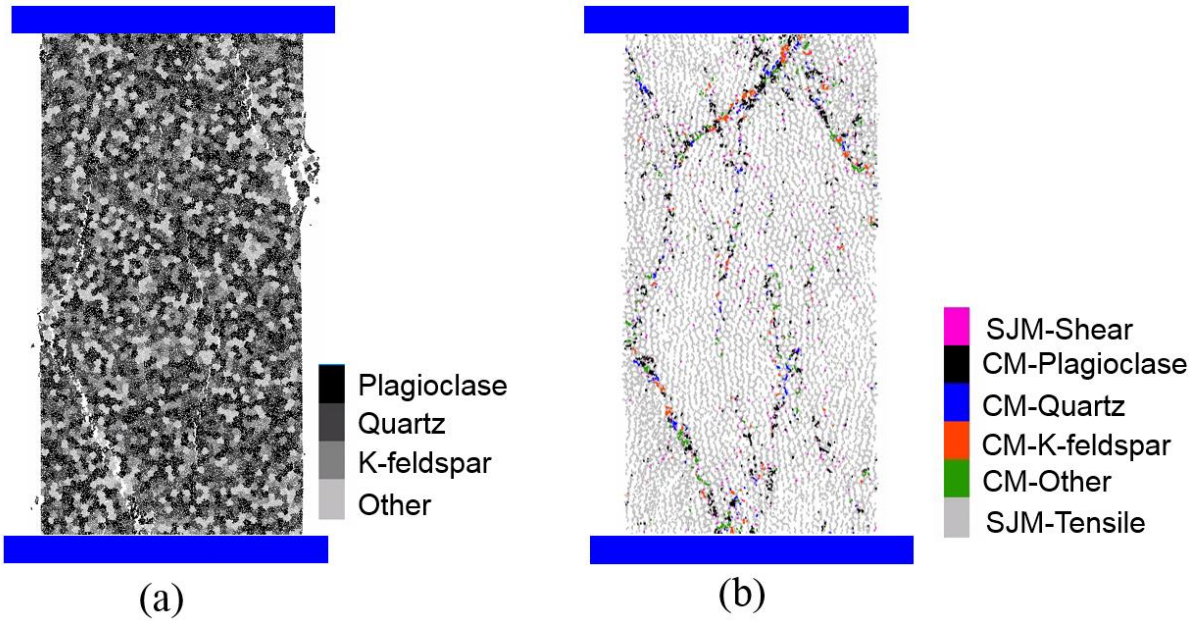

Figure 7.3 The final numerical results obtained from uniaxial compression test. (a) The macroscopic fractures developed during axial loading. (b) The distribution of inter- and intra-grain micro-cracks in the specimen (SJM: smooth-joint model, and CM: cohesive model).

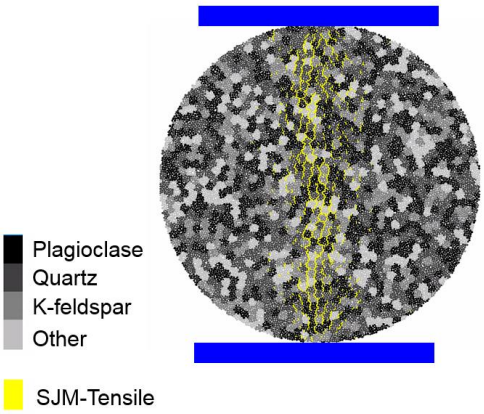

Figure 7.4 Distribution of macroscopic tensile cracks in Brazilian specimen after failure.

7.2.2 Random distribution of mineral grains

Ideally, the topological and statistical properties of the GBM specimens should be similar to those of the physical rock (Potyondy 2010a). Voronoi tessellation is widely used, but the topological and statistical properties of the crystalline rock cannot be realistically generated by this method (Potyondy 2010a). The PFC's two-dimensional disk-packing scheme has been used by many scholars to generate polycrystalline microstructure (Bahrani et al. 2014; Hofmann et al. 2015a; Potyondy 2010a), which gives an appropriate match between synthetic and real grain microstructure (Potyondy 2010a). However, the sensitivity of the calibrated model to the random distribution of the grains should be examined by considering several distributions for the minerals. To do so, five seed numbers were considered to generate various GBM specimens with a different random distribution of the minerals. The results showed that the Young's modulus varied only between 19.5 to 20.5 GPa, and the Poisson's ratio varied between 0.17 to 0.19. The UCS varied between 148 to 153 MPa, and the Brazilian tensile strength varied between 8.2 to 8.8 MPa. The GBM investigation of Saadat and Taheri (2019b) also revealed that the mechanical parameters of Aue granite showed insignificant variation with random distribution of minerals. However, we will demonstrate in section 5.3.2 that the crack distribution pattern can be influenced by the random distribution of grains. Hofmann et al. (2015a) also emphasized that the change in the distribution of grain had significant influence on the fracture pattern as a result of inhomogeneities. The variation in the numerical results is very well within the variation of the mechanical parameters of the physical Barre granite. Therefore, it was meaningful to employ the calibrated parameters for conducting uniaxial compression test on pre-cracked specimens.

7.3 Modelling pre-cracked Barre granite

7.3.1 Numerical model setup for pre-cracked specimens

The GBM approach was used to carry out a numerical simulation of pre-cracked granite, to validate the proposed GBM framework and evaluate its potential in reproducing the macroscopic fracturing behaviour and strength responses of physical specimens. We adopted the micro-mechanical parameters obtained during the calibration procedure, and the macroscopic responses of the pre-cracked granite were simulated. The specimen dimension for the experimental UCS test was 152 mm (height) × 76 mm (width), and the same specimen size was used for conducting compression tests on pre-cracked specimens Miller (2008). The same specimen size was used for generating the GBM specimens in PFC2D. The geometries of pre-existing flaws were generated in PFC2D as per the information provided in the experimental study conducted by Miller (2008) (illustrated in Figure 7.5). The pre-existing flaws were created in the physical Barre granite using an OMAX waterjet, which produced a crack with a thickness of 1.5 mm (Miller 2008; Morgan et al. 2013). The same thickness size was imported into PFC2D for generating the pre-cracked GBM specimens. After importing the geometries into the software, the pre-existing cracks were developed by removing the DEM particles.

In the specimens tested in the current study, the ligament length (L) and bridging angle (α) were considered to be constant, but the inclination angle (θ) was varied. The flaw length ($2b$) was equal to 13 mm and, the ligament length was equal to a for all specimens. The bridging angle was equal to 60°, and the flaw inclination angles of 0°, 30°, 30°, and 75° were simulated. The crack initiation, coalescence, and peak axial stresses were monitored during testing, and the crack propagation pattern and failure modes of the numerical specimens were compared with the experimental data. The values of crack initiation, coalescence, and peak axial stresses were obtained during numerical testing, using the definitions given by Miller and Einstein (2008), and Morgan et al. (2013). The crack initiation stress refers to the stress at which the first macroscopic crack initiates from the tips or the surface of the pre-existing flaw. The coalescence stress refers to the stress magnitude at which the pre-existing flaws link together and coalesce due to the expansion of macroscopic fractures in the bridging area. The peak axial stress is the stress at which the maximum axial strength of the specimens is achieved.

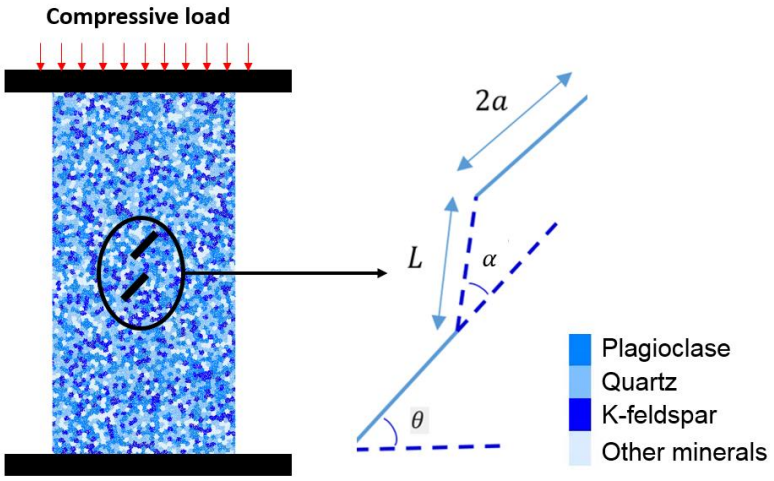

Figure 7.5 Grain-based pre-cracked Barre granite in PFC2D and geometrical configuration of pre-existing cracks.

7.3.2 Fracture behaviour of pre-cracked granite ($\theta = 30^{\circ}$)

The results of the uniaxial compression loading tests for the numerical and experimental specimens are illustrated in Figure 7.6. The complete stress-strain curves of the numerical specimens, with a flaw inclination angle of 30°, and three different experimental counterparts, are illustrated in Figure 7.6a. The numerical results were compared with the average values obtained from the experimental results. The micro-cracking behaviour, and the development of macroscopic cracks in the flaw zone at different stages of loading are illustrated in Figure 7.6b, c, and d. In Miller's (2008) study, for each experimental test, a simplified sketch of the final fracture pattern was provided including macroscopic cracks, white patching, and crushing zone (see laboratory fracturing patterns in Figure 7.6b, c, and d). It can be seen from Figure 7.6 that there was a discrepancy between the experimental results in terms of stress-strain curve and fracturing pattern, which may be attributed to the meandering path defined by the mineral boundaries (Morgan et al. 2013). Since the microstructure and the meandering paths in each specimen were different, the macroscopic fracturing responses and hence the stress-strain curves in the physical specimens (Figure 7.6a) showed some variations.

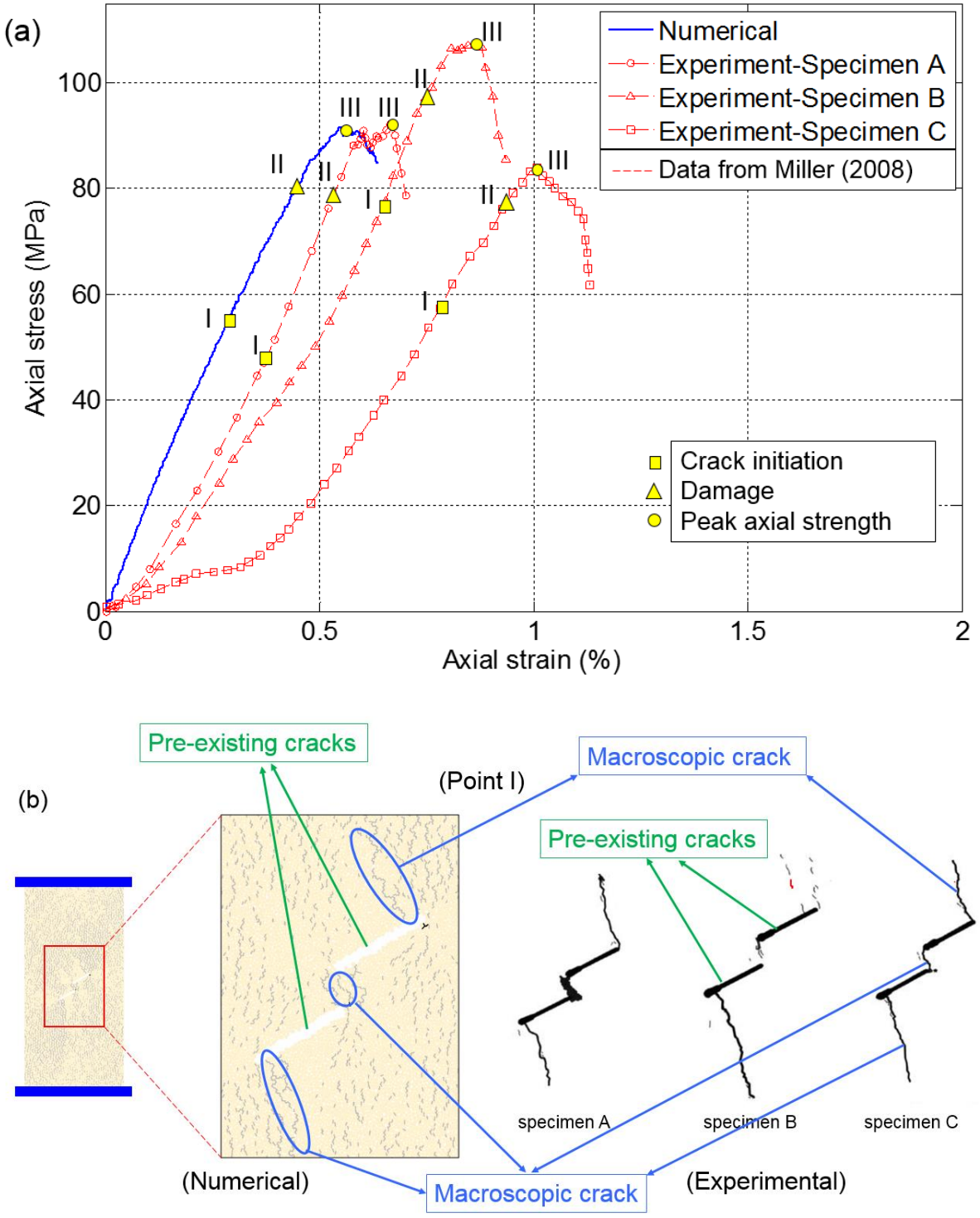
(a)
Numerical
Experiment-Specimen A
Experiment-Specimen B
Experiment-Specimen C
Data from Miller (2008)
Crack initiation
Damage
Peak axial strength
Axial stress (MPa)
Axial strain (%)
0
20
40
60
80
100
0
0.5
1
1.5
2
I
II
III
(b)
Pre-existing cracks
(Point I)
Macroscopic crack
Pre-existing cracks
specimen A
specimen B
specimen C
(Numerical)
Macroscopic crack
(Experimental)

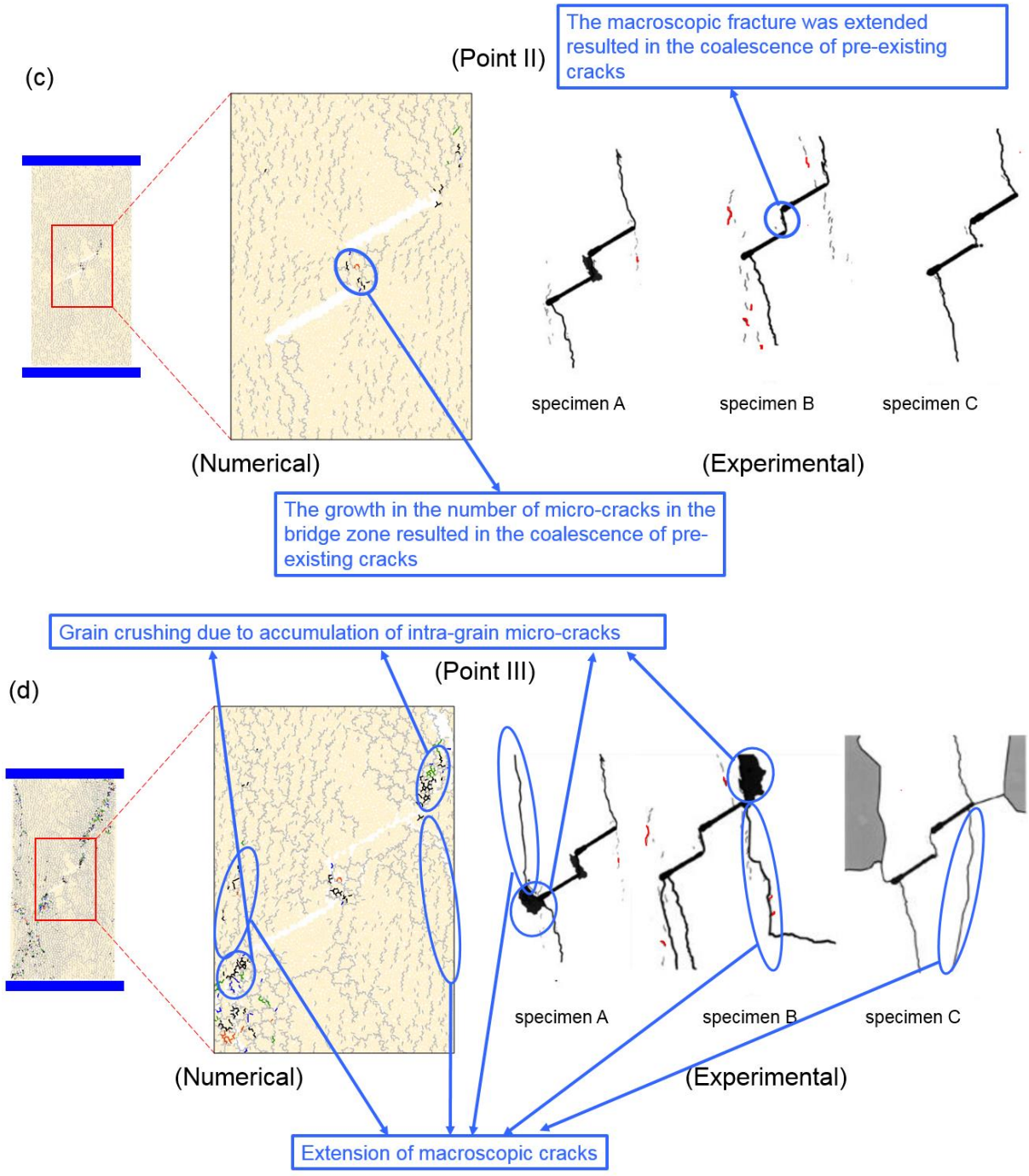
(c)
(Point II)
The macroscopic fracture was extended resulted in the coalescence of pre-existing cracks
specimen A
specimen B
specimen C
(Numerical)
(Experimental)
The growth in the number of micro-cracks in the bridge zone resulted in the coalescence of pre-existing cracks
Grain crushing due to accumulation of intra-grain micro-cracks
(Point III)
(d)
specimen A
specimen B
specimen C
(Numerical)
(Experimental)
Extension of macroscopic cracks

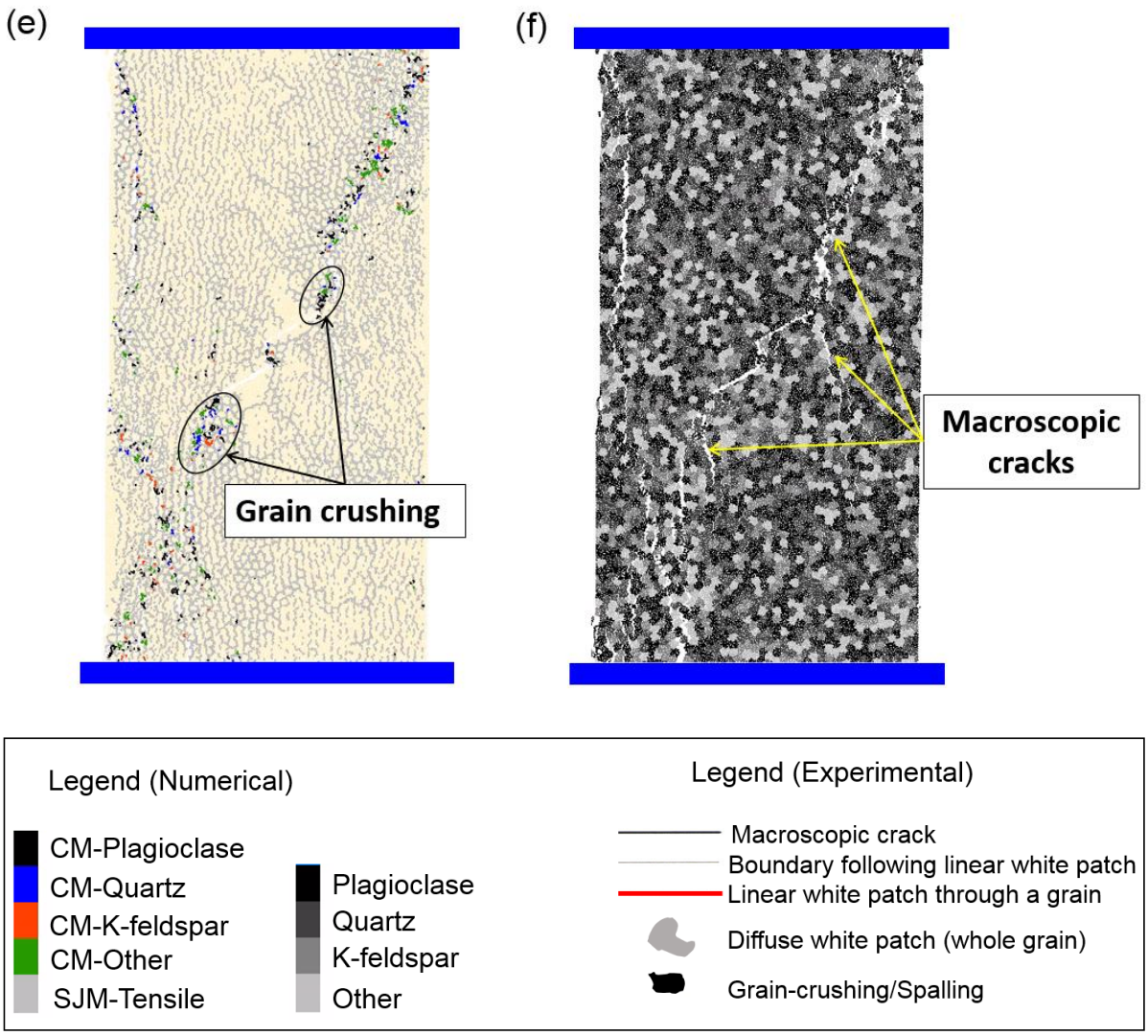

Figure 7.6 Numerical and experimental results for a specimen with $\theta = 30^{\circ}$. (a) The numerical and experimental stress-strain curves, the crack initiation, crack damage , and peak axial stresses are marked at each graph. (b) The numerical and experimental macro-cracks at point I. (c) The numerical and experimental macro-cracks at point II. (d) The numerical and experimental macro-cracks at point III. (e) The distribution of inter- and intra-grain micro-cracks, and grain crushing around the flaw tips. (f) The pattern of macroscopic cracks in the GBM specimen at failure. (Experimental results were modified from Miller 2008).

According to Morgan et al. (2013), in Barre granite, visible regions of mineral lightning occurred on the surface of the specimen before fracturing, which was called “white patching”. There are two types of white patching were observed in Barre granite: linear and diffusive white patching (Miller 2008). Figure 7.7 illustrates different types of white patching in Barre granite. Linear white patching can travel along the grain boundary to form grain boundary

white patching, or travel through a mineral to create an intragranular white patching (Figure 7.7a). Grain boundary white patches appear in the specimen before crack initiation along the grain boundaries. In diffusive white pathing, multiple minerals lightened entirely with no preferential direction (Figure 7.7b). Diffusive white patching is mostly associated with the shear cracking, but in some specimens, it can appear before both tensile and shear cracking (Morgan et al. 2013). In the GBM specimens, the inter- and intra-grain micro-cracks were monitored to compare the numerical cracking behaviour with the experimental counterparts.

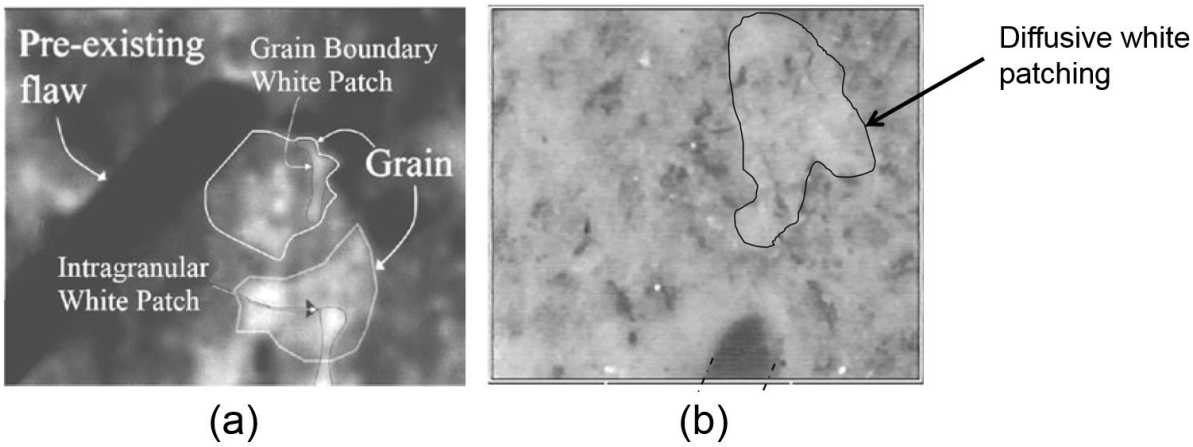

Figure 7.7 Different types of white patching observed in Barre granite. (a) Linear white patching (grain boundary & intragranular). (b) Diffusive white patching. (modified from Morgan et al. (2013)).

The numerical results exhibited a linear-elastic behaviour from the beginning of the test until the simulation reached crack initiation stress (point I in Figure 7.6a). Unlike the pre-cracked numerical specimen, the laboratory specimens showed an initial non-linear behaviour similar to intact rock. The reason is that at the crack initiation stress magnitude (Figure 7.6b), initial macroscopic cracks appeared in the flaw areas due to bond-breakage in the inter-grain contacts. As a result of the low tensile strength of the inter-grain micro-cracks, the contact boundaries initially failed in the linear elastic stage. The progressive coalescence of the inter-grain micro-cracks formed large, sub-vertical cracks, and when the density of the inter-grain micro-cracks was sufficiently high, macroscopic fractures developed that were nearly parallel to the direction of the axial loading (Figure 7.6b).

The experimental observations of Morgan et al. (2013) on pre-cracked Barre granite revealed that macroscopic tensile cracks typically follow the grain boundaries and are "jagged" in shape. Figure 7.8 illustrates a schematic representation of the grain boundary tensile crack observed in Barre granite by Morgan et al. (2013) and Moradian et al. (2016). In our numerical

simulations, we observed the same failure pattern during the propagation of macroscopic tensile cracks.

In GBM, due to the random, polygonal shape of Voronoi elements that were generated to mimic the minerals, the grain boundaries were jagged in shape. Thus, the inter-grain micro-cracks were propagated in a meandering, jagged path that was dictated by the grain interfaces (Figure 7.6b). The simulations revealed that the tensile wing cracks initiated near flaw tips, and they propagated vertically towards the loading walls (Figure 7.6b). This was similar to the pattern observed in the experiments. Figure 7.6b shows that, at the crack initiation stress, some inter-grain micro-cracks appeared in the bridging area. However, according to the laboratory observations, the coalescence of the pre-existing crack did not occur at crack initiation stress magnitude, because further loading was needed in order to widen the tensile cracks in the bridging zone and fully link the flaws (Miller 2008). At crack initiation stress either grain breakage (specimen A), or tensile cracks (specimen B and C) presented in the bridging area (Figure 7.6b). However, it was not until reaching the crack coalescence stress level that the macroscopic fractures fully developed and the coalescence of the pre-existing cracks occurred. Similarly, in the numerical specimens, after macroscopic crack initiation further loading was needed to cause the coalescence of the pre-existing cracks (Figure 7.6c).

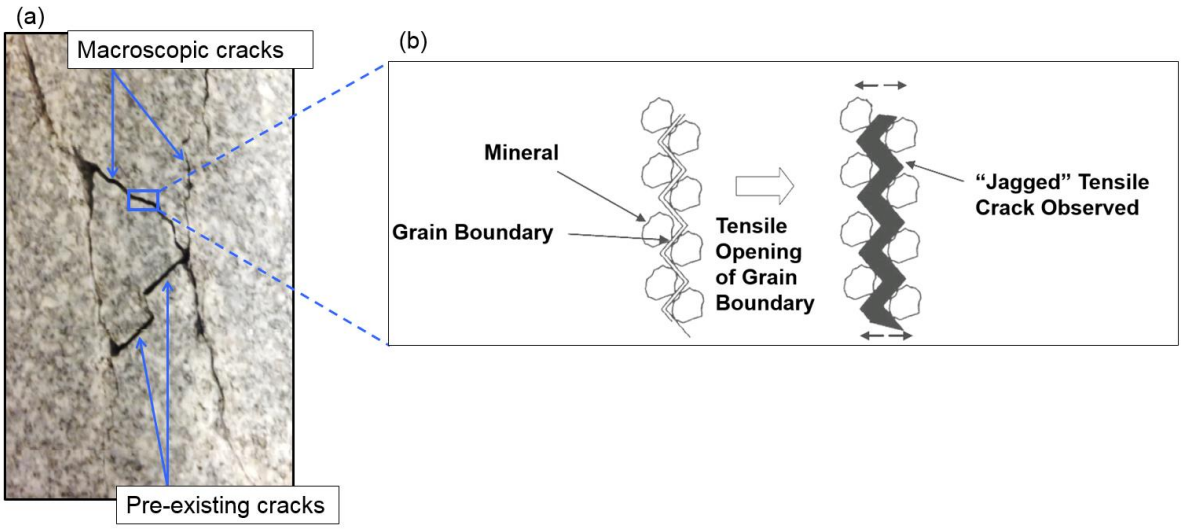

Figure 7.8 (a) Macroscopic cracks in pre-cracked Barre granite (modified from Moradian et al. 2016). (b) The jagged shape tensile cracks developed along the meandering path defined by the mineral boundaries (modified from Morgan et al. 2013).

The stress magnitude at which the coalescence of pre-existing cracks occurred was defined as the coalescence stress by Miller (2008). In the current study, this stress level is called *damage*

stress. At the crack damage stress level (Fig. 10c), a sufficiently high number of inter- and intra-grain micro-cracks initiated from the inner- and outer-tip regions. The macroscopic tensile cracks formed at point I expanded, and larger macroscopic cracks around the flaw tips were formed. In the GBM simulation, the extension of the macroscopic crack inside the bridging area resulted in crack coalescence.

From point II until the peak axial stress (point III), a non-linear behaviour was observed in the numerical stress-strain curve (Figure 7.6a), which was the result of a progressive macroscopic crack extension around the flaw tips and other areas of the specimen. Finally, at a stress magnitude of 92.8 MPa (point III in Figure 7.6a), the maximum numerical axial strength was achieved, the specimen completely failed, and the axial stress dropped accordingly. It can be seen that, at point III (Figure 7.6d), the simulated macroscopic fractures expanded and developed in a direction parallel to the compressive loading. A localised, macroscopic fracture path was exhibited near the flaw tips, which was the consequence of inter- and intra-grain micro-crack coalescence. In the laboratory specimens (A and B), this behaviour was identified as grain crushing. Our numerical observations presented in Figure 7.6, confirm that the proposed GBM framework has the capability to reproduce the macroscopic stress-strain response and fracturing behaviour of pre-cracked Barre granite.

One of the factors that effectively controls the degree of grain crushing in the physical Barre granite is the mineral strength. Increasing the mineral strength reduces the grain breakage, therefore less intra-grain micro-cracks appear during the failure of Barre granite. The experimental observations showed that the Barre granite has strong minerals (e.g. quartz) which inhibits the severe breakage of the minerals under uniaxial compressive loading (Morgan et al. 2013). However, in the experimental pre-cracked specimens, some localised grain crushing was evident around the tips of the pre-existing flaws, which in turn was associated with the large sliding displacement along the surface of macroscopic fractures (Morgan et al. 2013). Similarly, in the GBM specimen, we explored that the bond breakage occurred in the minerals existed at the vicinity of macroscopic fracture interfaces (Figure 7.6e and f). Numerical simulations show that the large sliding displacement of the minerals along the surfaces of macroscopic fractures caused failure of intra-grain contacts, which resulted in the localised grain crushing.

In the numerical specimens, a relatively high number of unconnected grain boundary micro-cracks appeared away from the major macroscopic fractures (i.e. point III in Figure 7.6d). This

was due to the low value of the microscopic tensile strength assigned to the grain boundary contacts. In the experimental specimens, however, the unconnected micro-cracks may not be visible, but this does not mean that they are not present in the specimen (Hofmann et al. 2015a).

7.3.3 The effect of flaw inclination angle

In order to further validate the sensitivity of the proposed GBM framework to the orientation of pre-existing cracks, different numerical specimens with various flaw inclination angles were generated in PFC2D, and the results were compared with the laboratory data (Miller 2008).

Figure 7.9 illustrates the results of comparing the fracture pattern obtained from the GBM simulations at peak axial stress. The results revealed that the GBM model can successfully reproduce the experimental, macroscopic fracturing response. The numerical results showed that the macroscopic fractures initiated from the tips and surfaces of pre-existing flaws, and developed in an upward direction. The orientation of macroscopic cracks that are parallel to the applied stress also support the notion that tensile cracking is the dominant failure mode in GBM specimens. Both the inter- and intra-grain micro-cracks contributed to the process of fracture development in the numerical specimens. However, the majority of micro-cracks initiated due to the failure of boundary contacts.

It can be seen in Figure 7.9 that the coalescence pattern observed in the GBM simulations was slightly different from those gained from the experimental observations. This is mainly due to the fact that, during sample generation in PFC2D, the minerals were randomly produced. This meant that the paths generated by the grain boundaries were slightly different from those of laboratory specimens, and resulted in a modest variation in the coalescence pattern. However, the fracturing responses obtained from modelling were in agreement with those observed in the laboratory specimens.

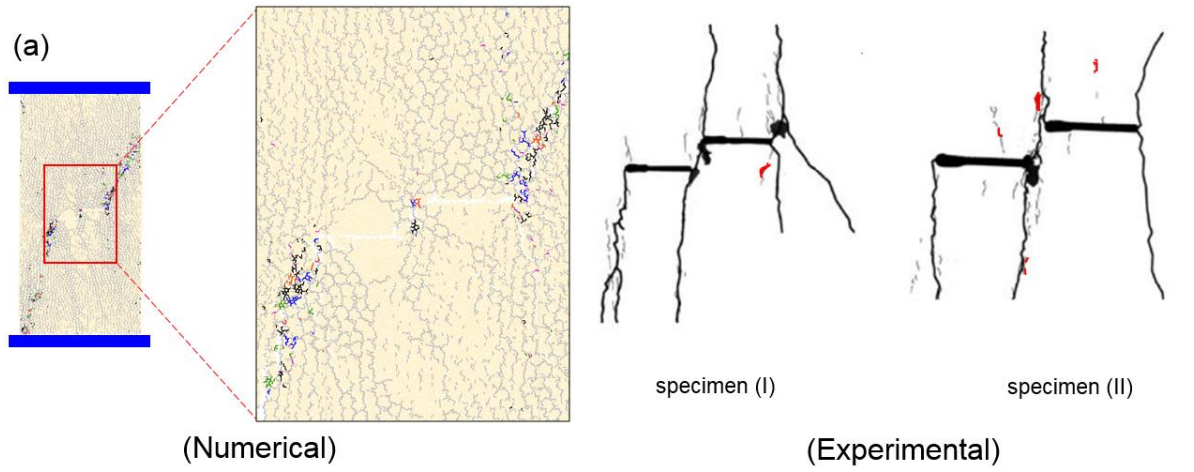
(a)
specimen (I)
specimen (II)
(Numerical)
(Experimental)

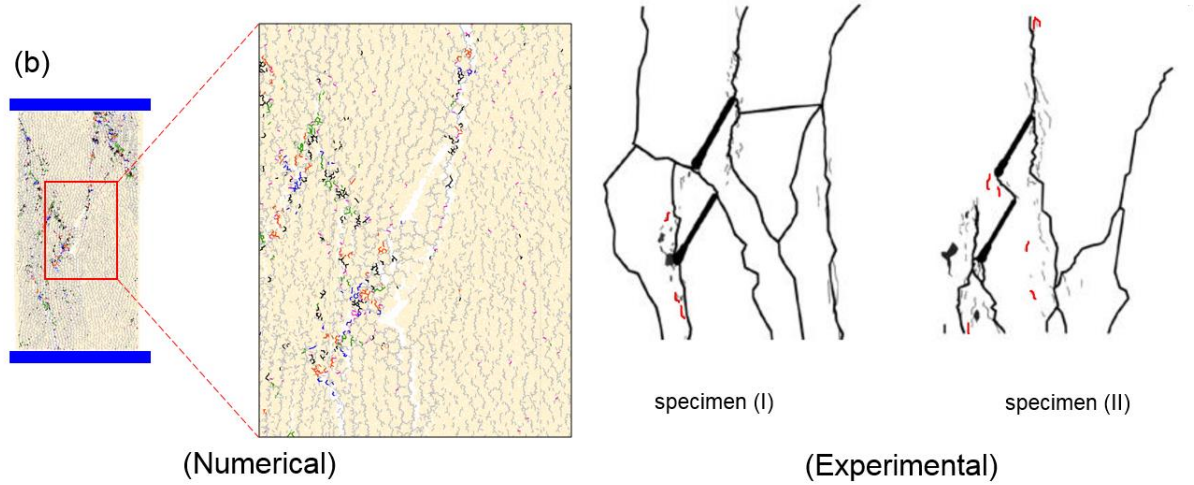
(b)
specimen (I)
specimen (II)
(Numerical)
(Experimental)

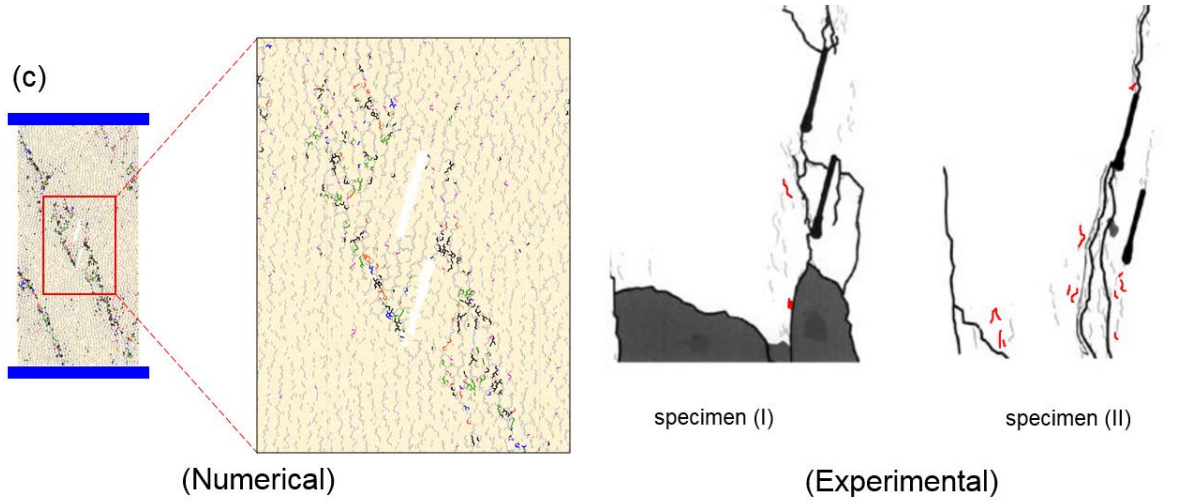
(c)
specimen (I)
specimen (II)
(Numerical)
(Experimental)

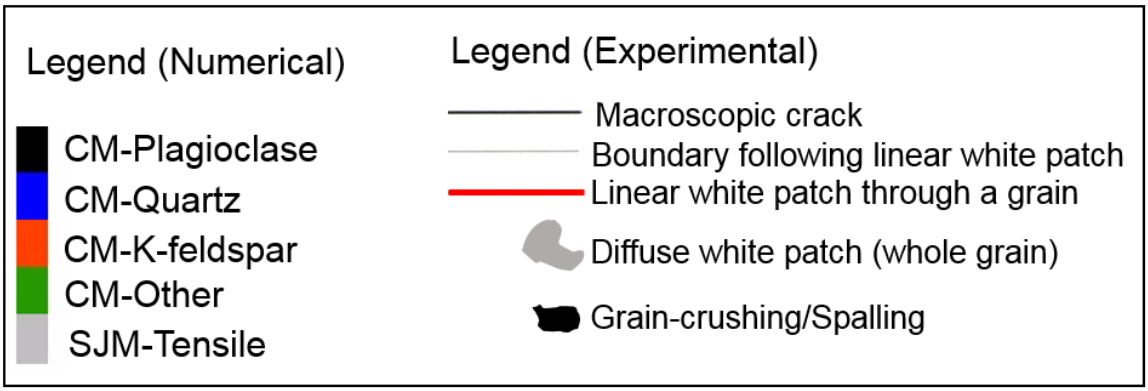

Figure 7.9 Fracture pattern obtained from proposed GBM approach at peak axial strength level versus experimental observations (after Miller 2008): (a) $\theta = 0^{\circ}$, (b) $\theta = 60^{\circ}$, (c) $\theta = 75^{\circ}$.

7.4 The influence of grain microstructure on macroscopic response

The calibrated model was run three more times with different random seed numbers, which allowed us to investigate the influence of the grain microstructure on the mechanical and fracture behaviour of the GBM specimens. In the following subsections, the stress analysis of the models, and the variation in the macroscopic fracture pattern are presented.

7.4.1 Stress analysis

Figure 7.10 depicts the average crack initiation, coalescence, and peak axial stresses for both numerical and experimental specimens. It can be seen from igure 7.10 that different random distribution of minerals leads to a slight variation in the stress results. However, the numerical results are in agreement with the experimental data. In intact rock specimens (e.g. specimens without pre-existing cracks), the crack initiation stress can be defined as a point where the Poisson's ratio starts to increase (Zhang and Wong 2013). The crack initiation stress of intact specimen is generally about 0.3-0.5 times of the peak strength (Brace et al. 1966; Martin 1993; Zhang and Wong 2012). However, in the physical pre-cracked Barre granite specimens, the crack initiation stress was defined as the stress magnitude corresponding to the appearance of the initial macroscopic cracks around the tips or on the surface of the pre-existing flaw (Miller 2008; Morgan et al. 2013). Wong and Einstein (2009a) measured the stress corresponding to the initial observable macroscopic crack in the flaw region as the crack initiation stress of pre-cracked Gypsum and Carrara marble. Zhang and Wong (2012) also adopted the same approach in their numerical study to obtain crack initiation stress of single-flawed rock-like specimens. Similarly, we monitored the crack initiation stress corresponding to the appearance of the first macroscopic cracks around the tips or on the surface of the pre-existing flaws. This enabled us

to make a better comparison with the same values obtained from laboratory counterparts (Miller 2008). Hence, the crack initiation stresses obtained from this approach are much higher than those of intact specimens, especially for flaw inclination angles of 60° and 75° (Miller 2008; Morgan et al. 2013; Zhang and Wong 2012).

From Figure 7.10a, the numerical crack initiation stress decreased with a low slope when the flaw inclination angle increased from 0° to 30°. In comparison, when the flaw inclination angle increased from 30° to 75° the crack initiation stress increased with a high slope. We believe that the stress concentration and random distribution of minerals are the possible reasons for the variation of the crack initiation stress in the GBM specimens. At $\theta = 0^{\circ}$, since the loading direction was perpendicular to the flaw surface, the stress concentration in the flaw region was significantly high, which caused the failure of the inter-grain contacts at a stress magnitude of approximately 70% of the peak axial strength. The slight decrease in the crack initiation stress at $\theta = 30^{\circ}$ could be attributed to the randomness of the distribution of the grains. As it mentioned by Morgan et al. (2013), the macroscopic tensile cracks in Barre granite followed a meandering path created by the grain boundaries. In the GBM specimens, this meandering paths are defined by the random generation of polygons representing the grains. For the GBM specimen with $\theta = 30^{\circ}$ the bond breakage of the inter-grain contacts initiated at a slightly lower stress level, which caused a rapid growth of the macroscopic tensile crack along the meandering paths. It can be seen from Figure 7.9a that the macroscopic tensile cracks were initially perpendicular to the surface of the pre-existing crack, which was attributed to the creation of the weakest possible meandering paths along this direction. Due to progressive compression, the macroscopic tensile cracks extended rapidly and aligned parallel with the loading direction (Figure 7.9a). For $\theta > 30^{\circ}$, the influence of the pre-existing crack was gradually reduced, therefore, the bond-break in the inter-grain contacts occurred at higher crack initiation stresses. In fact, they required more loading to initiate the primary macroscopic tensile cracks.

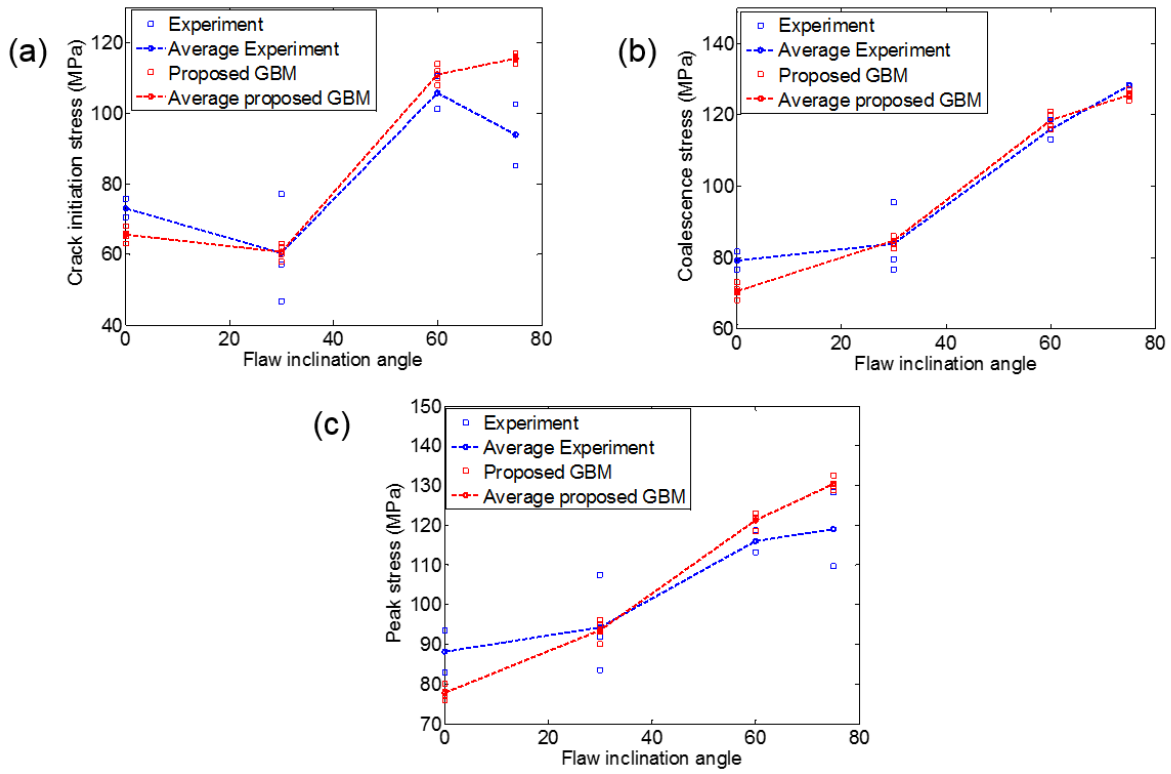

Figure 7.10 The influence of flaw inclination angle on the mechanical response of pre-cracked Barre granite (numerical results versus experimental observations). (a) The crack initiation stress. (b) The coalescence stress. (b) The peak stress.

By increasing the flaw inclination angle, the value of the numerical peak axial strength was increased with the highest magnitude achieved at an inclination angle of 75° (Figure 7.10c). The same trend was observed during experimental tests. At 75° of the inclination in one of the laboratory specimens, the coalescence between pre-existing flaws did not occur (Miller 2008). As a result, only one value of crack damage stress is presented in Figure 7.10b for this test. Ideally, if the exact topological and statistical properties of the physical specimen were incorporated in the numerical modelling, the simulation response would be more realistic. However, the aim of numerical simulations is not to incorporate the exact statistical and topological properties in the model, but rather to provide the best possible match with the real specimens (Saadat and Taheri 2019b). According to Potyondy (2010a), using disk-packing scheme for sample generation, which was also used in the present research, can provide a good match with the physical microstructure. Nonetheless, it can be seen in Figure 7.9 that the coalescence pattern observed in the GBM simulations was slightly different from those gained from the experimental observations. This is mainly because, during sample generation in PFC2D, the minerals were randomly produced. This means that the paths generated by the

grain boundaries are slightly different from those of laboratory specimens, and resulted in a modest variation in the coalescence pattern. This difference between crack distribution of GBM and laboratory results was also highlighted by the previous researchers such as Hofmann et al. (2015a) and Bahrani et al. (2014). However, they concluded that these differences were inevitable, and thus they considered the outcome of their GBM simulations as the best possible match. Similarly, the fracturing responses obtained from modelling are regarded to be in agreement with those observed in the laboratory specimens.

7.4.2 Fracture pattern analysis

Figure 7.11 shows the distribution of inter- and intra-grain micro-cracks (I), and the development of macroscopic fractures (II) in the GBM specimens with different seed number. As expected, change in the randomness of the distribution of grains resulted in the inhomogeneous spatial distribution of the micro-cracks. It was observed that, for the flaw inclination angles investigated, the change in the distribution pattern of intra-grain micro-cracks was more pronounced than inter-grain micro-cracks, which was attributed to the inhomogeneity in the mineral grains (Hofmann et al. 2015a). For instance, in Seed 2 (Figure 7.11b-I) the accumulation of intra-grain micro-cracks (grain crushing) at the outer tips of the pre-existing cracks was more conspicuous than Seed 1 and 3. The random distribution of minerals also impacted the development of macroscopic fractures. It can be seen from Figure 7.11b-II that for Seed 1, an anti-wing crack developed above the left tip of the lower flaw, which was not the case in Seed 2 and 3 (the anti-wing crack is circled for emphasis). The same behaviour was also observed for $\theta = 60^{\circ}$, where anti-wing cracks formed in Seed 1 and 2, but Seed 3 only exhibited wing crack growth. Macroscopic cracks often originate at the tips of flaws, but in Seed 1 ($\theta = 0^{\circ}$), one macroscopic fracture initiated from the flaw surface and extended vertically towards the loading plate (Figure 7.11a-II, Seed 1). The results also showed that the coalescence pattern of the pre-existing cracks was influenced by the grain microstructure. For example, for $\theta = 75^{\circ}$ (Figure 7.11d-II), different coalescence patterns were observed. In Seed 1 and 2, the outer flaw tips were connected with macroscopic fractures, whereas in Seed 3 the right tips of two flaws coalesced. Miller (2008) also observed that the coalescence pattern in the pre-cracked Barre granite was highly influenced by the grain microstructure. Although fracture pattern was influenced by the inhomogeneity of minerals, but in the GBM specimens simulated, the fractures were formed subparallel to the loading direction, which is the common failure mode in the brittle rocks (Liu et al. 2018; Potyondy 2010a; Tang et al. 2000).

The growth of macroscopic fractures in pre-cracked Barre granite is the direct consequence of the failure of grain boundaries and the grain breakage. The laboratory observations of Morgan et al. (2013) and Miller (2008) showed that the distribution of macroscopic fractures in the pre-cracked Barre granite was influenced by the topological and statistical properties of the minerals.

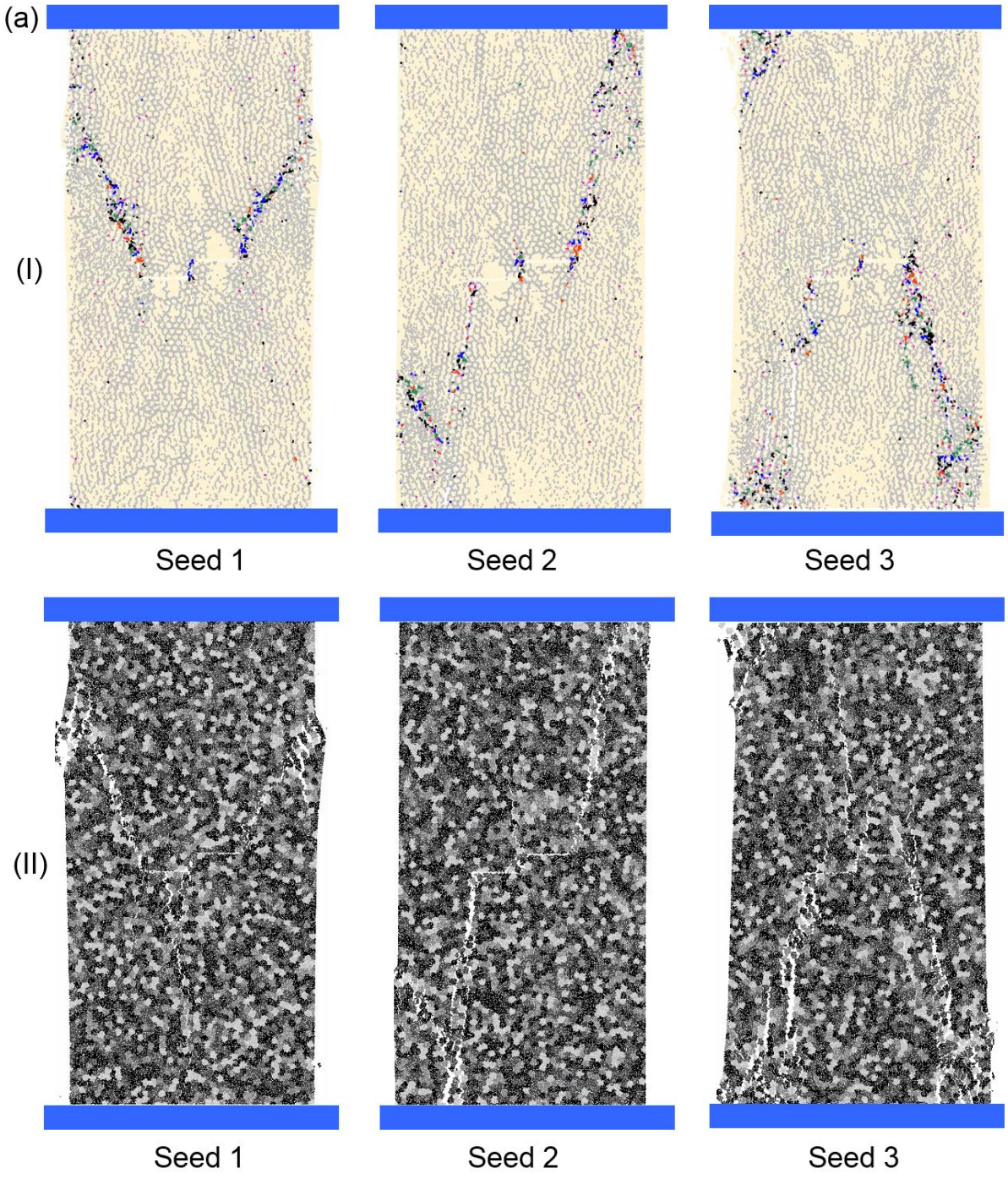

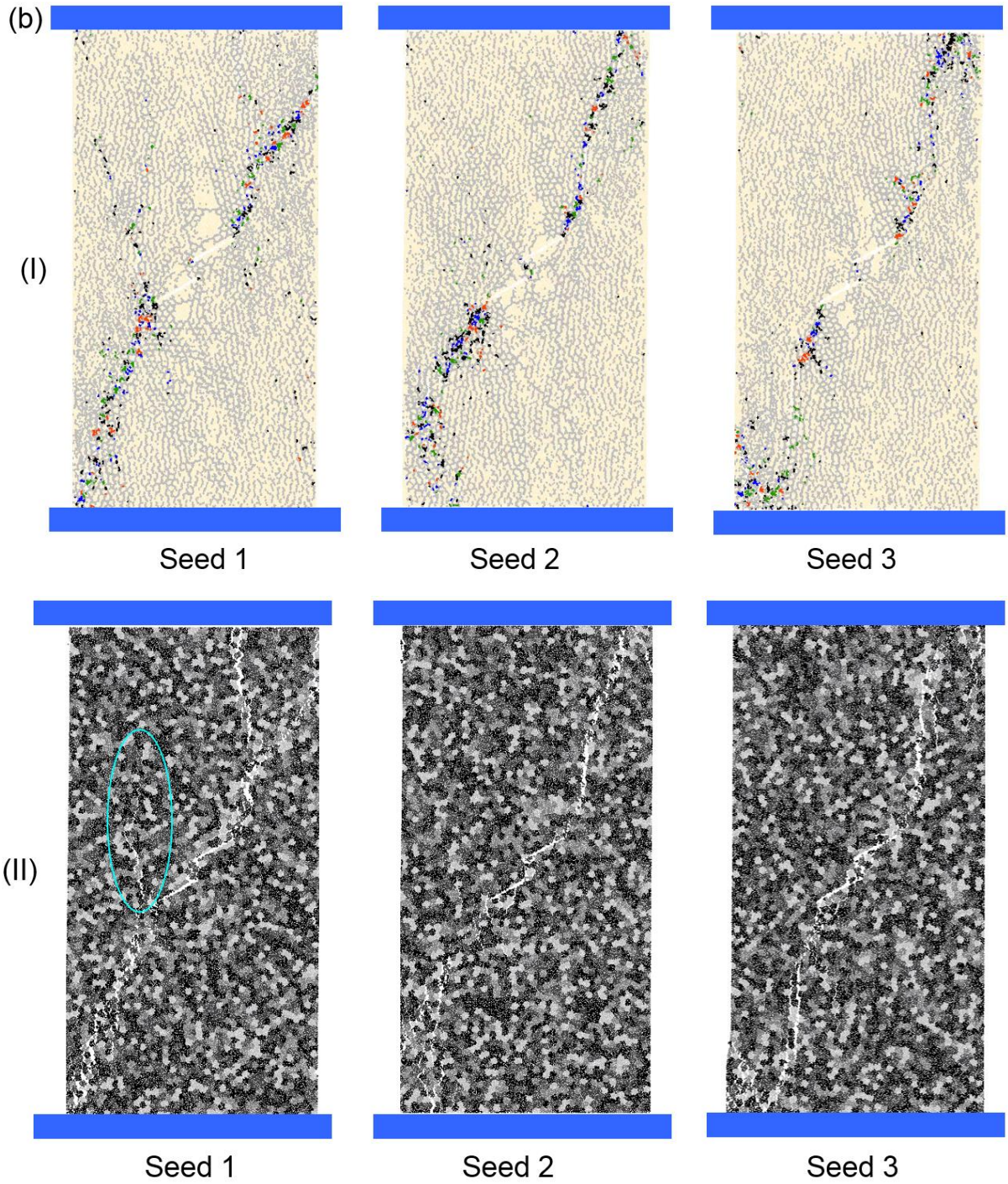
(b)
(I)
Seed 1
Seed 2
Seed 3
(II)
Seed 1
Seed 2
Seed 3

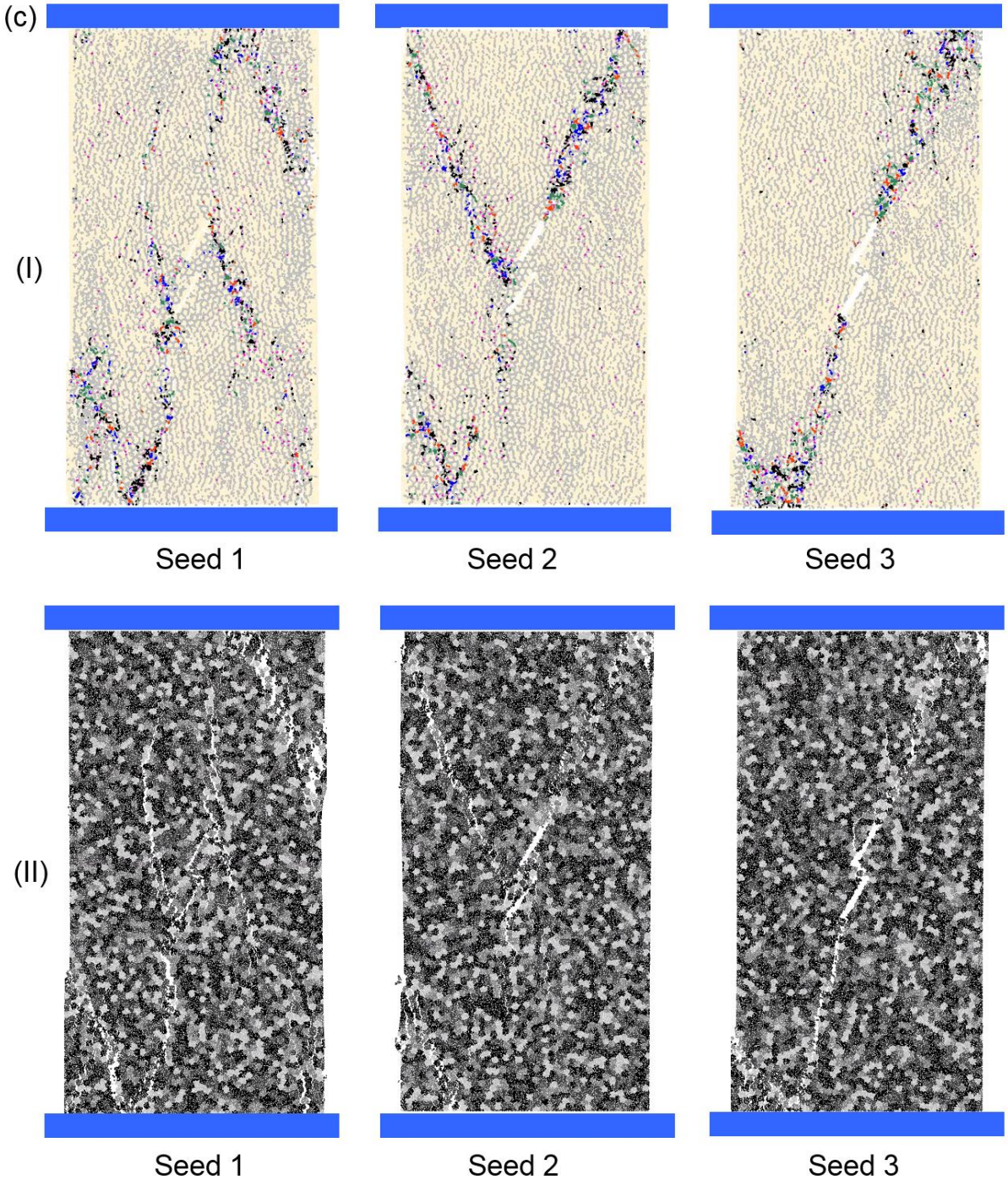
(c)
(I)
Seed 1
Seed 2
Seed 3
(II)
Seed 1
Seed 2
Seed 3

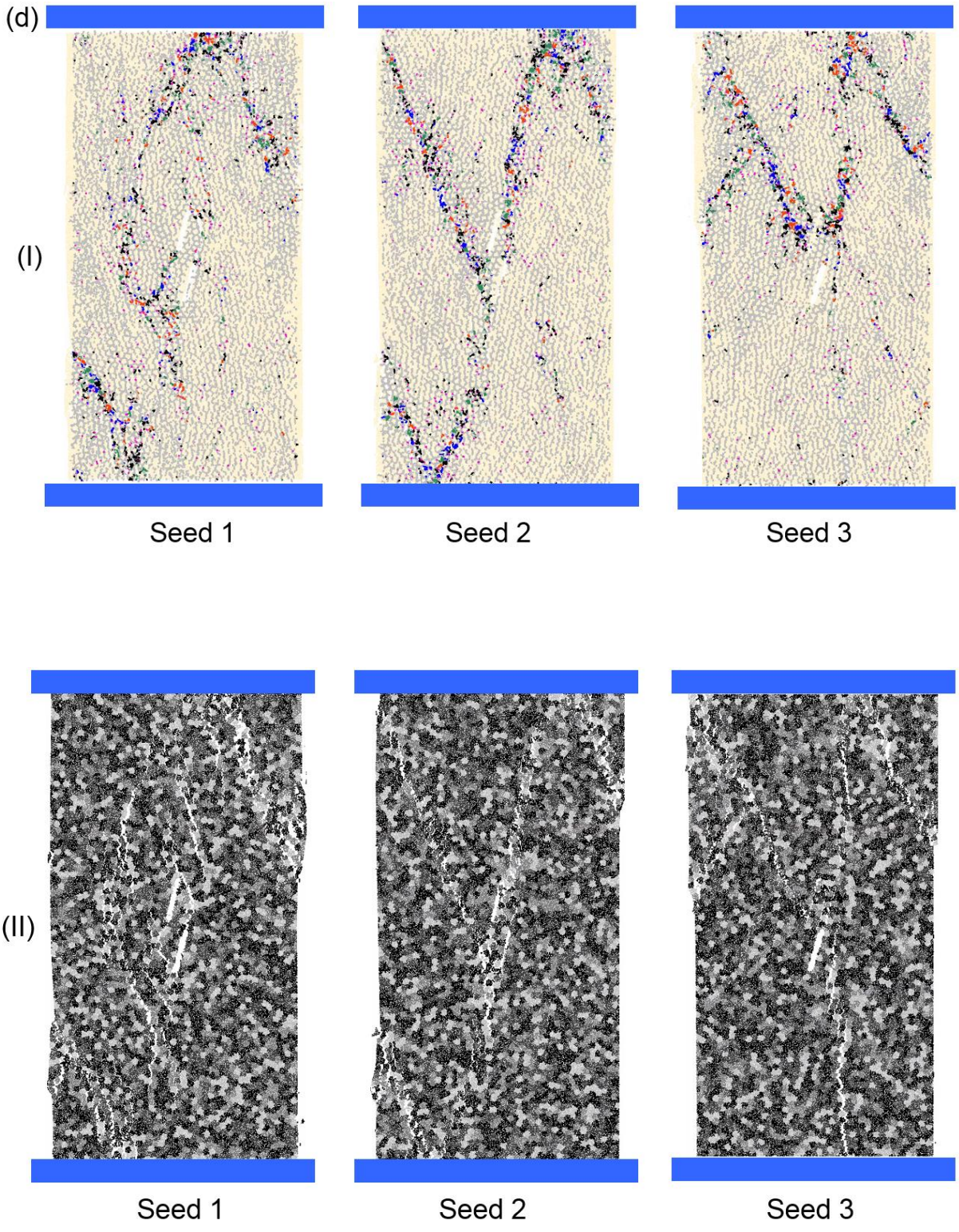
(d)
(I)
Seed 1
Seed 2
Seed 3
(II)
Seed 1
Seed 2
Seed 3

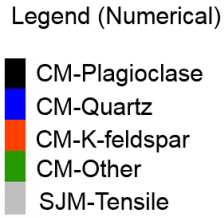

Figure 7.11 Distribution of micro-cracks (I) and macroscopic fractures (II) in the pre-cracked GBM specimens. a) $\theta = 0^{\circ}$. b) $\theta = 30^{\circ}$. c) $\theta = 60^{\circ}$. d) $\theta = 75^{\circ}$.

7.5 Conclusion

From the analysis of the stress-strain curves obtained from numerical simulations, we observed that the macroscopic crack pattern at the crack initiation, damage, and peak axial stresses of double-flawed Barre granite can be reproduced by the proposed GBM framework with an acceptable level of accuracy. The numerical simulations showed that, by increasing the flaw inclination angle, the peak axial stress increases. Increasing the inclination angle of pre-existing cracks also showed the same incremental effect on crack initiation and the crack's damage stresses. The macroscopic fracturing patterns achieved in the numerical simulations also suggest that the modes of macroscopic crack initiation and propagation observed in the laboratory specimens, at least phenomenologically, can be identified by the proposed GBM framework. The numerical modelling revealed that the first macroscopic tensile cracks initiated from the tips and surfaces of the pre-existing cracks, and that they propagated upward towards the loading plates. It was also found that the formation of macroscopic fractures in the flaw region can be attributed to the initiation and coalescence of the inter-grain micro-cracks that formed due to the failure of the smooth joint model contacts. The GBM simulations showed that the intra-grain micro-cracks begin to initiate and develop in the model before reaching the crack damage stress. The coalescence of pre-existing flaws occurred due to the combined interactions of the inter- and intra-grain micro-cracks.

This numerical modelling approach can be used for further investigations, such as studying the effects of grain size, mineralogy, and contact strength on the failure mechanism of crystalline rocks. The micro-cracking features, based on the current GBM approach, such as the extension and development of macroscopic cracks due to the progressive coalescence of inter- and intra-grain micro-cracks, which eventually led to the formation of macroscopic fracturing zones around the flaw tips and the coalescence of pre-existing cracks, will serve as guidelines for future experimental tests. The proposed GBM framework provided a cost-effective approach

that helps in the determination of crack initiation, damage, and peak axial stresses of crystalline rocks, which are essential in the development of constitutive models (i.e. continuum models) that can be used for large scale simulation of mining structures.

Chapter 8: Effect of mineral size on failure behaviour of pre-cracked Aue granite

8.1 Introduction

The mechanical and failure behaviour of rock as a heterogeneous material is controlled by various parameters, such as grain shape and size, the type of minerals, and the existence of pre-existing flaws. Rock masses contain discontinuities (i.e. joints, fractures, and cracks), and their various geometrical patterns determine the strength of the material (Taheri and Tani 2010). The coalescence of two pre-existing cracks is the primary cause of rock mass failure (Yin et al. 2014). In underground and surface mining structures, rock mass stability is profoundly affected by the propagation and coalescence of macroscopic cracks initiating from the pre-existing flaws, on various rock mass scales. The macroscopic cracking process is the dominant damage mechanism controlling the mechanical behaviour and the integrity of brittle rocks (Morgan et al. 2013).

The focus of this chapter is on the failure and mechanical behaviour of single- and double-flawed rock specimens under uniaxial compression. We investigated the effect of the grain size distribution on micro- and macro-cracking behaviour, and the damage mechanism of single- and double-flawed numerical specimens. To do so, we generated models with three different size distribution scenarios, and conducted uniaxial compression tests. Lastly, the damage response and micro-crack propagation in intra-grain contacts are discussed ahead of the conclusions.

8.2 Modelling procedure

Since the micro-mechanical parameters incorporated in the proposed cohesive model represent the cement bridges of minerals at grain level, it may require advanced laboratory techniques to identify the local parameters of the material. Alternatively, the model parameters can be calibrated against the results of standard experimental tests such as unconfined compression and Brazilian tensile tests. This calibration approach has been extensively used in current DEM investigations due to lack of laboratory techniques to measure the properties of crystalline rocks at mineralogical scale (Bahrani and Kaiser 2016; Bahrani et al. 2014; Bewick et al. 2014c; Hofmann et al. 2015b; Lan et al. 2010; Liu et al. 2018; Nicksiar and Martin 2014). Thus, the same approach was adopted in the present study. The procedure for calibrating the micro-mechanical parameters of GBM against laboratory results of Aue granite is also described in chapter 6. After calibration of micro-mechanical parameters, three different scenarios were

generated to numerically investigate the influence of rock texture on the behaviour of pre-cracked Aue granite.

To set up and calibrate the proposed cohesive model by adopting the GBM approach in PFC2D, we used experimental results from unconfined compressive tests, and a Brazilian tensile test. The micro-mechanical properties of the cohesive GBM approach were achieved, such that the macroscopic behaviour of the numerical simulation matches the observed, experimental macroscopic properties (i.e. uniaxial compressive strength, tensile strength, Young's modulus) of Aue granite. The cohesive and smooth-joint models were assigned as intra- and inter-grain constitutive models, respectively. The cohesive and smooth-joint models are solved separately in the simulations. The yield limit of each model functions separately, which means if the yield limit is reached in one model, it will not affect the other model simulation.

The mineral sizes and mineral content of Aue granite were taken from (Hofmann et al. 2015a). The data related to the average grain size and mineral content is given in **Error! Reference ource not found.**. According to Hofmann et al. (2015a) the mineral size of Aue granite varies from 0.9 to 1.8 mm; hence, the standard deviation of grain size for each mineral was considered within this range to build the necessary polygons in GBM. In GBM approach, the distribution of minerals is generated randomly. Note that there are an infinite number of seeds that can be generated by the algorithm available in PFC-GBM. However, it has been a common approach in PFC-GBM investigations to generate one seed for each mineral size (i.e. each scenario) and investigate the influence of grain size on the behaviour of crystalline rocks (Hofmann et al. 2015a; Lan et al. 2010; Liu et al. 2018; Peng et al. 2017). This parametric study approach is significant, because by altering only one parameter and fixing the others, the influence of particular parameters can be revealed (i.e. grain size).

The dimensions of the experimental samples for the UCS test were 100 mm (height) × 50 mm (diameter), and the Brazilian test's physical disk had a diameter of 50 mm. To make the numerical approach computationally efficient, we generated a numerical specimen of 50 mm (height) × 25 mm (diameter). Figure 8.1 shows the synthetic rock samples generated for the Brazilian tensile and uniaxial compressive tests. The black mesh lines in Figure 8.1 show the mineral structure. We reduced the sample size to obtain time-efficient simulations as has also been done by other researchers in GBM studies (e.g. Bahrani et al. (2014) and Hofmann et al. (2015a)). The effect of scale is not significant, according to Potyondy and Cundall (2004) and Hofmann et al. (2015a), provided the particle sizes are relatively small compared to the

dimensions of the specimen. The uniaxial compression test was conducted by applying a vertical load on the upper wall. In order to avoid any ball-facet overlap, a relatively high normal stiffness (10% higher than the ball-ball average stiffness) was assigned to the walls (Bahaaddini et al. 2013). The same set up was considered for the Brazilian tensile test. Note that the uniaxial compression and the Brazilian tensile tests were setup in a way to have frictionless ball-wall contacts. With this arrangement, an ideal rock-platen condition can be achieved which prevents the loading plates from inhibiting the rock bulging (Itasca 2016).

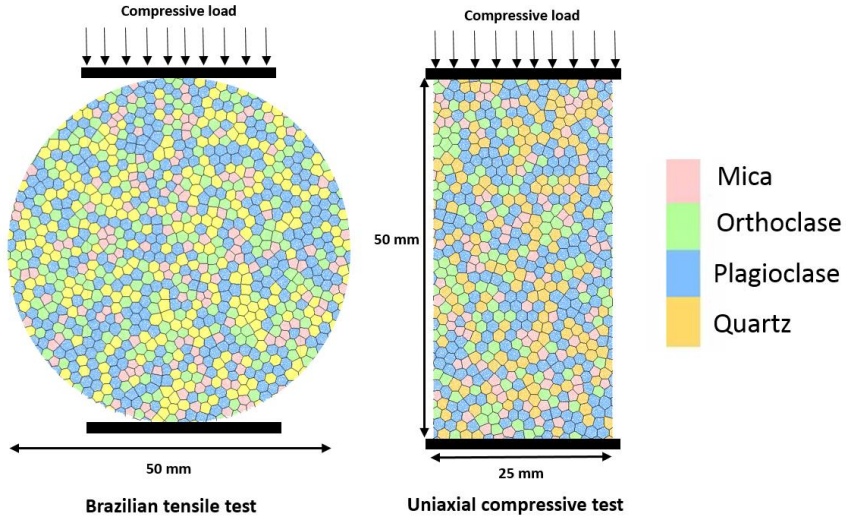

Figure 8.1 Schematic of numerical test setups. The black lines indicate the grain boundary.

The micro-parameters for Aue granite are listed in Table 8.1, and the macroscopic properties of Aue granite from the laboratory testing and numerical simulations are compared in Table 8.2.

Table 8.2 shows that the strength properties of intact rock determined by the numerical model, such as tensile strength, and uniaxial compressive strength, are in good agreement with the experimental results. The inter-grain micro-cracks developed during uniaxial testing were parallel to the direction of axial loading. The failed specimen in Figure 8.2a shows that macroscopic fractures were formed in the specimen due to the interaction of the inter- and intra-grain micro-cracks. In the case of the Brazilian test however (Figure 8.2b), the failure of the specimen was due to development of macroscopic tensile fractures formed as a result of bond-break in the inter-grain contacts (SJM).

As shown in Table 8.2, the cohesive GBM approach successfully captures the macroscopic properties, especially the tensile strength derived from the Brazilian test. The ratio of the

uniaxial compressive strength to the tensile strength derived from the Brazilian test is 17.9, which is within the range of the experimental counterpart (15.6-18.1). This reveals that the cohesive GBM approach developed in this study is capable of simulating the macroscopic mechanical properties of rock by replicating the microstructure of rock at a granular level. As the macro-mechanical properties obtained from the numerical simulations (Table 8.2) match the experimental counterpart, the micro-mechanical properties given in Table 2 can be used to model the mechanical behaviour of Aue granite.

Table 8.1 Micro-mechanical parameters obtained from calibration procedure of Aue granite

Element	Parameter	Grain 1 Quartz	Grain 2 Plagioclase	Grain 3 Orthoclase	Grain 4 Mica
Particles forming grains	Minimum particle radius forming grain, Rmin (mm)	0.1	0.1	0.1	0.1
	Maximum to minimum radius ratio, R_{max}/R_{min}	1.66	1.66	1.66	1.66
Cohesive model	Young's Modulus, $\bar{E}_{c,CCM}$ (GPa)	62	52	42	32
	Normal to shear stiffness ratio, $(k^0_{n,CCM}/k^0_{s,CCM})$	1.0	2.0	2.0	1.5
	Cohesion, (C^0_{CCM}) (MPa)	118	95	95	60
	Friction ratio, (μ_{CCM})	0.58	0.6	0.6	0.55
	Dilation ratio, (β_{CCM})	0.22	0.25	0.25	0.2
	Softening parameter, κ_{CCM} (1/m)	25,000,000	18,000,000	18,000,000	15,000,000

Micro-mechanical parameters of the grain boundaries (the smooth joint contacts)

Smooth-joint model	Normal stiffness, (k_n^{sj}) (GPa/m)	106,000

Shear stiffness, (k_s^{sj}) (GPa/m)	28,500
Tensile strength, (σ_c^{sj}) (MPa)	8
Cohesion, (c^{sj}) (MPa)	150
Friction angle, (φ^{sj}) ($^{\circ}$)	80
Friction coefficient, (μ^{sj})	0.95

Table 8.2 Macroscopic properties of Aue granite (Yoon et al.(Yoon et al. 2012)) and GBM approach.

Property	Aue granite (Experimental)	Aue granite (Numerical)
Uniaxial compressive strength (MPa)	134±7	135
Young's modulus (GPa)	48±8	49
Poisson's ratio	0.19	0.2
Brazilian tensile strength (MPa)	8±1	7.54

The random distribution of the grains and DEM particles are essential in GBM study, and the sensitivity of the calibrated model to these factors should be evaluated before using the calibrated GBM for performing parametric study (Hofmann et al. 2015a). To investigate the effect of the randomness of the distribution of the grains having the same grain size and mineral content, the calibrated model was run seven more times with a variety of seed numbers for the grain distribution and the DEM particle distribution. The results showed that the Young's modulus varied only between 48 to 50 GPa, and the Poisson's ratio varied between 0.19 0.21. The UCS and Brazilian tensile strength varied between 133.4 to 136.8 MPa, and 7.2 to 8.5 MPa, respectively. Similarly, with the various seed number for the distribution of DEM particles in the model, the Young's modulus varied between 47 to 49, and the Poison's ratio varied between 0.18 to 0.22. The results also showed that the UCS and Brazilian tensile strength varied between 132.8 to 135.2 MPa, and 7.1 to 8.2 MPa, respectively. The variation in the numerical results is very well within the variation of the mechanical parameters of the

physical Aue granite. Therefore, it was meaningful to employ the calibrated parameters for conducting more investigations.

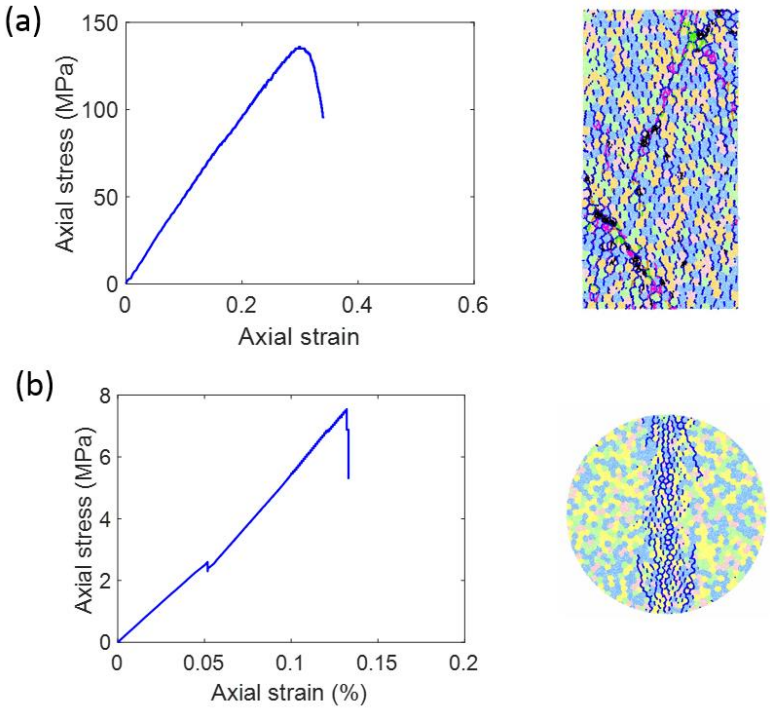

Figure 8.2 The numerical response of the intact granite under. (a) The uniaxial compression, and (b) Brazilian tensile tests.

8.3 Generating pre-cracked granite with different grain sizes

In mineralogy, grain size is a parameter that can be used for classifying crystalline rocks. A widely used method for measuring the grain size in a physical rock is to analyse a thin section of the specimen using a polarized microscope. Generally, the shape of minerals is not spherical and a particular grain approaches the shape of a polygon. In nature, we may find a specific rock with various grain sizes. For instance, Figure 8.3 illustrates three thin sections of an Australian sandstone with various grain sizes (i.e. fine, medium, and coarse grained sandstone).

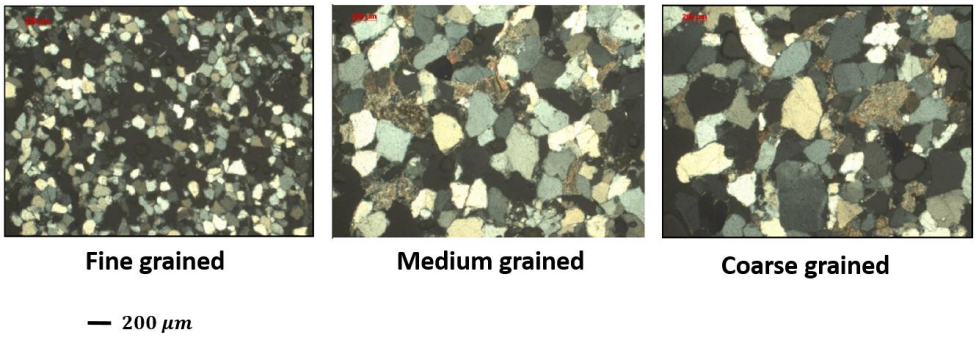

Figure 8.3 Various grain sizes observed in three types of Australian sandstones (Wasantha et al. 2015).

We considered three different grain size scenarios to investigate the influence of grain size on the strength, cracking, and damage responses of single- and double-flawed specimens. The average grain diameter considered in each scenario is given in Table 8.3. The grain size for scenario 1 is equal to the grain size of the experimental Aue granite (calibrated model). The size of quartz for scenario 1 was also different from the other minerals (1.45±0.35 mm). For scenario 2 and 3, the average size of quartz was considered to be 3.2 mm and 4.3 mm, respectively. The average size for other minerals (plagioclase, orthoclase, and mica) was assumed to be 1.6 mm and 3.0 mm for scenario 2 and 3, respectively. For scenario 2 and 3, the average grain size of quartz was considered to be different from other minerals to achieve a heterogeneous mineral size distribution. Hence, the average grain size increased with scenario number which allowed us to have different grain size categories for comparison purposes. Note that the grain sizes presented in Table 8.3 indicate the average size of each mineral. The grain-based single- and double-flawed synthetic specimens, as well as the geometry of the double-flawed samples, are illustrated in Figure 8.4a,b and Figure 8.4c, respectively. The ligament length in double-flawed specimens was always equal to the length of the flaw. The flaw length was considered to be 4 mm, and the inclination angle was varied ($\theta = 0^{\circ}$, 15°, 30°, 45°, 60°, 75°). The pre-existing cracks in the double-flawed specimens were generated to be left-stepping flaws, with bridging angles of 60°. The specimen dimensions were equal to the models generated during the calibration process (50 mm high and 25 mm wide).

The scenarios considered in the present study had a grain size almost equivalent to that of the physical specimen. An ideal grain-generation algorithm should be able to produce a mineral microstructure which is similar to the statistical and topological properties of the physical specimen. However, the aim of numerical simulations is not to incorporate the exact grain microstructure in the model, but rather to provide the best possible match with the real

specimens. In the present study, a grain-based disk-packing scheme proposed by Potyondy (2010a) was employed to generate the polycrystalline structure of Aue granite. It has been observed in the previous investigations that disk-packing scheme, which is available in PFC2D (Itasca 2016), gives a perfect match with the physical specimens in terms of microstructural properties (Hofmann et al. 2015a; Li et al. 2018b; Liu et al. 2018; Potyondy 2010a, 2010b), compared to other grain-generation algorithms available in UDEC and 3DEC software packages (Potyondy 2010a).

In previous GBM research conducted by Hofmann et al. (Hofmann et al. 2015a) on the same granite, the average grain size adopted in the parametric study ranged from 0.5 to 5 mm. According to Hofmann et al. (2015a), if there are less than five minerals along the shorter dimension of the model, you need to increase the size of the specimens. In our study, however, the average mineral size was slightly reduced in the large-grain-size specimens (scenario 3) to 4.3 mm for quartz, and 3 mm for the rest of minerals. This resulted in approximately 5-7 minerals along the shorter dimension of the specimen, which maintained the same dimensions and made the simulations more time-efficient.

It should be mentioned that all the numerical models for the pre-cracked granite were constructed with the same distribution of minerals (i.e. the same seed number was used to generate the randomness of the distribution of the minerals). In order to generate the GBM specimens for performing parametric study on mineral size, the algorithm proposed by Potyondy (2010b) was used which is capable of generating a specimen with the desired polygon size. This approach for generating a random distribution of minerals has been practised in many PFC-GBM studies (Bahrani and Kaiser 2016; Bahrani et al. 2014; Bewick et al. 2014b; Bewick et al. 2014c; Hofmann et al. 2015a; Liu et al. 2018). It has been a common approach in PFC-GBM to generate one seed for each mineral size (i.e. each scenario) and investigate the influence of grain size on the behavior of crystalline rocks (Hofmann et al. 2015a; Lan et al. 2010; Liu et al. 2018; Peng et al. 2017).

The micro-mechanical properties of the calibrated Aue granite model were employed to investigate the influence of mineral size (see Table 8.3) on the mechanical and fracturing behavior of pre-cracked GBM specimens. Notice that, since the micro-mechanical parameters in the present study were calibrated against a physical Aue granite specimen, it was meaningful to employ the same set of calibrated parameters for conducting parametric study on grain size. By considering the micro-mechanical parameters (e.g. C_{CCM}^{0} and etc.) to be constant, and

varying the grain size, we would be able to recognize the influence of mineral size on the mechanical and fracturing behavior of pre-cracked specimens. The benefit of this approach is that once the micro-mechanical parameters representing a physical granite sample with known grain size are gained, they can be employed for conducting a further parametric study on various influential parameters such as grain size, mineral content, etc. It should be mentioned that this methodology has been used by other researchers and demonstrated promising ability to shed more light on the mechanical behavior of crystalline rocks (Hofmann et al. 2015a; Hofmann et al. 2015b; Lan et al. 2010; Liu et al. 2018; Nicksiar and Martin 2014; Peng et al. 2017; Wong et al. 2018). Accordingly, in the present study, the same approach was adopted for investigating the influence of rock texture on the macroscopic behavior of pre-cracked Aue granite.

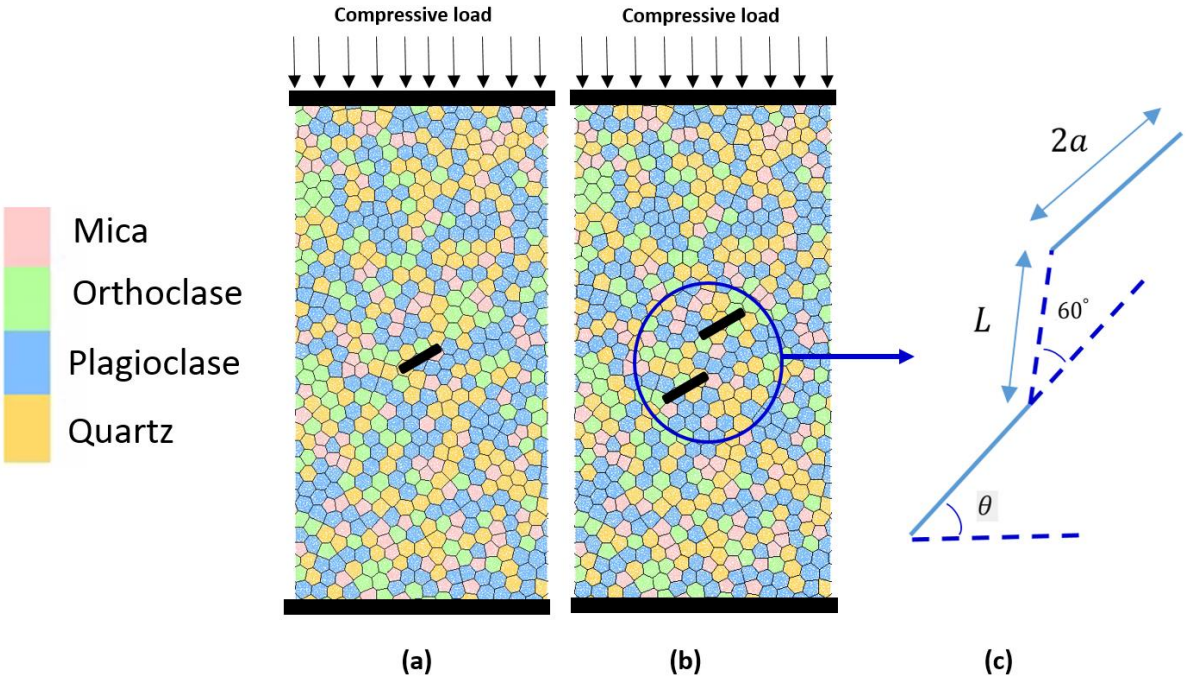

Figure 8.4 The grain-based numerical model of a) single-flawed and b) double-flawed specimens. The black lines indicate the grain boundary. c) The geometry of pre-existing cracks in double-flawed specimen defined by flaw inclination angle (θ), bridge angle (60°), bridge length (L), and flaw length (2a).

Table 8.3 An overview of various scenarios with different mineral size distribution considered to investigate the influence of grain size heterogeneity on the simulation results of single- and double-flawed specimens.

	Avg. mineral diameter (mm)			
	Quartz	Plagioclase	Orthoclase	Mica
Scenario 1	1.45±0.35	1.35±0.45	1.35±0.45	1.2±0.3
Scenario 2	3.2	1.60	1.6	1.6
Scenario 3	4.3	3.0	3.0	3.0

8.4 The results of numerical simulations

In this section, we investigate the influence of the grain size distribution on crack initiation and propagation, and the failure mechanism of single- and double-flawed specimens. We obtain the micro-cracking pattern from the failure of inter- and intra-grain contacts, and monitor the damage evolution patterns in the mineral contacts by tracking the damage parameter (D_{CCM}) defined in the cohesive constitutive model (Eq. 3.13).

The micro-cracking process in brittle rocks is closely related to mineral grains, pores, and pre-existing flaws. By characterising the micro-cracking process concerning the mineral size distribution, we can enhance our understanding of the macroscopic damage behaviour of brittle rocks. As mentioned in section 3, the mineral composition and the distribution of the grain size of various minerals can be simulated using the PFC-GBM approach. One of the merits of this numerical tool is that the influence of the grain size distribution on the mechanical behaviour and cracking responses of the minerals can be captured.

We generated different numerical specimens with a small grain size (Scenario 1), medium grain size (Scenario 2), and large grain size (Scenario 3) to assess the fracturing and failure behaviour of single flaw specimens under uniaxial compression. The mineral content assigned for these numerical specimens was similar to the calibrated specimen. We observed that the grain size profoundly affected the number of both inter- and intra-grain micro-cracks, and the mechanical responses of the numerical specimens.

8.4.1 Monitoring micro-cracks in GBM

In DEM modelling, the breakage of inter- and intra-grain contacts can simulate the nucleation of a micro-crack. In the current numerical study, an inter-grain micro-crack formed when the smooth joint contact between adjacent boundary particles was broken. Each micro-crack was

represented as a single straight line, with a length equal to the average diameter of its particles. The accumulation of certain number of micro-cracks forms a macroscopic crack. Figure 8.5 illustrates a schematic view of micro-crack initiation in DEM. According to Diederichs (2000), the centroid of the micro-crack lies along the line connecting the centres of adjacent particles (Figure 8.5a,b). Zhang and Wong (2012) defined the centroid of two adjacent micro-cracks as a_m, and the length of the longest micro-crack as c_m (Figure 8.5c). When $a_m/c_m \leq 1$, the two micro-cracks were treated as single micro-crack (Zhang and Wong 2012). A macroscopic crack was formed in the model when three or more micro-cracks initiated. Figure 8.6 illustrates the initiation of micro-cracks in a pre-cracked specimen ($\theta = 0^{\circ}$). It can be seen that the breakage of inter-grain contacts resulted in the formation of macroscopic cracks on the surface of pre-existing flaw (Figure 8.6a). A close-up view of the flaw region is presented in Figure 8.6b, which shows how the accumulation of a number of inter-grain micro-cracks could form a macroscopic crack. In the current study, the inter- and intra-grain micro-cracks were graphically monitored; different colours were assigned to different types of micro-cracks. The approach suggested by Zhang and Wong (2012) to measure the crack initiation stress was adopted in this research, which is the stress at which the first macroscopic tensile cracks form in the flaw regions (either at the tips or on the surface). The same method was used to monitor the macroscopic cracks that formed due to the coalescence of inter- and intra-grain micro-cracks. To trace the macroscopic tensile cracks (ie. at the level of crack initiation stress), we graphically plotted the micro-cracks that formed along the grain boundaries.

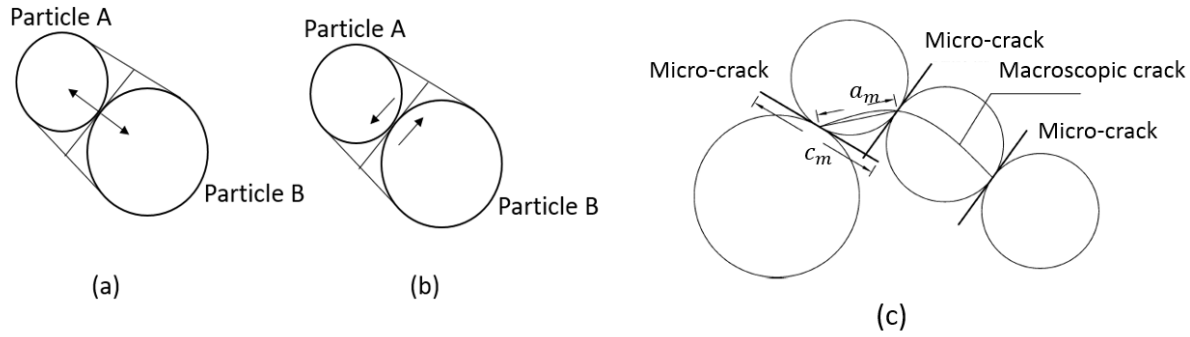

Figure 8.5 Definition of micro-cracks and macroscopic crack in PFC software: (a) tensile crack; (b) shear crack (adopted from Diederichs (2000)); (c) construction of macroscopic cracks (adopted from Zhang and Wong (2012))

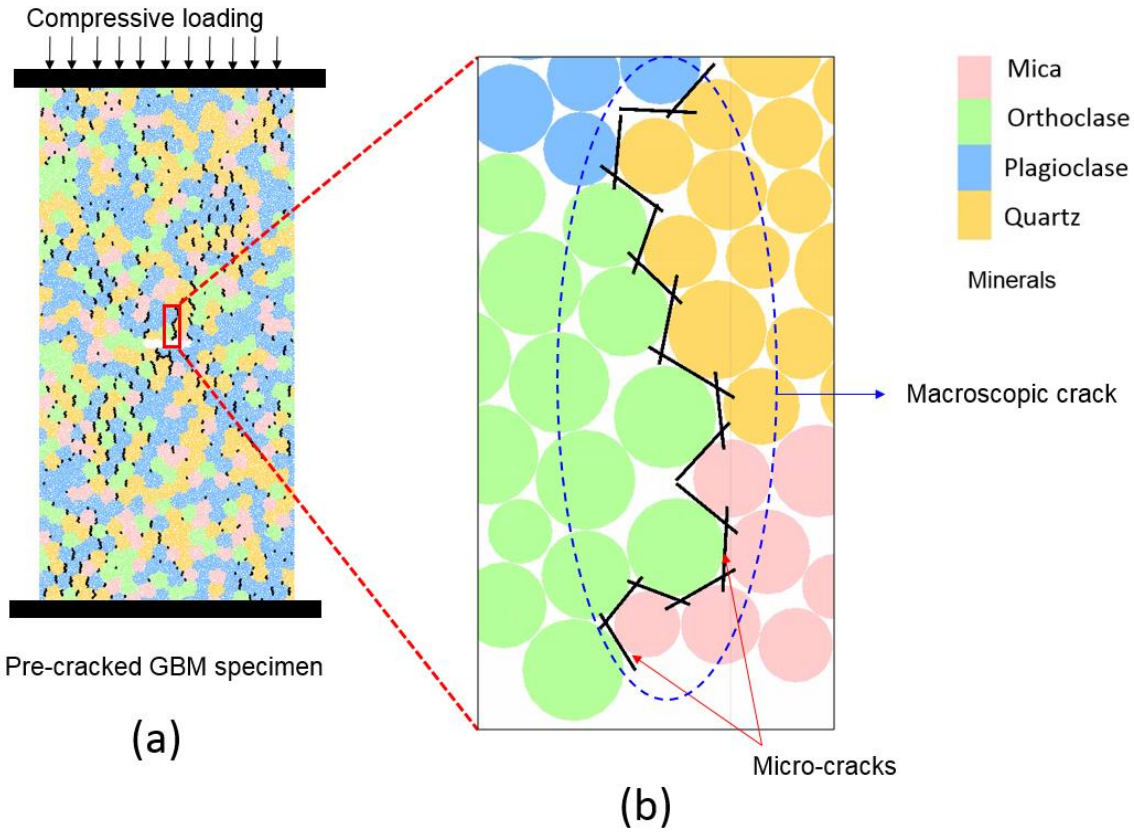

Figure 8.6 Nucleation of micro-cracks in GBM, and development of macroscopic cracks. (a) Development of macroscopic cracks in a pre-cracked numerical specimen ($\theta = 0^{\circ}$), the black lines indicate macroscopic cracks (b) A close-up view of the formation of a macroscopic crack on the surface of pre-existing flaw. The black lines represent micro-cracks.

8.4.2 PFC-GBM modelling of brittle rocks including a single flaw

Three different numerical specimens with various grain size distribution were generated. The specimens had the same mineral type (quartz, plagioclase, orthoclase, and mica). Numerical specimens with single and double pre-existing cracks were generated by removing the DEM particles according to the aperture, length, and inclination angle of the flaws. It has frequently been observed in the experimental studies that tensile wing cracks are the most common form of cracks that initiate in single and double flawed specimens (Jin et al. 2017; Wong and Einstein 2009b; Zhang and Wong 2012). The experimental observations of Wong and Einstein (2009b), for instance, showed that the tensile wing cracks were always the first cracks initiated during uniaxial compression testing.

In order to provide a comprehensive analysis of PFC-GBM modelling of the macroscopic and microscopic fracturing behaviour of brittle rocks including pre-existing cracks, we monitored the initiation, development, and coalescence of inter- and intra-grain micro-cracks and linked them with the axial stress-strain curves. To make this paper more concise, only the macroscopic axial stress-strain curves of specimens with $\theta = 30^{\circ}$ and their corresponding micro-cracking behaviour at different loading points are presented as a typical example showing the failure mechanism.

One of the important factors affecting the potential of spalling around underground mining excavations is the crack initiation stress (Diederichs 2007; Nicksiar and Martin 2014; Zhang and Wong 2012). The initiation of cracks from pre-existing flaws controls the dominant failure mechanisms and mechanical behaviour of brittle rocks on a variety of scales (Morgan et al. 2013). Therefore, in the following sub-sections, the crack initiation stress and its corresponding micro-cracking responses are presented. Additionally, the final failure mode of the models is provided, and we discuss the influence of grain size and flaw inclination angles on the distribution of inter-and intra-grain micro-cracks.

8.4.2.1 The failure mechanism of single-flawed specimens (example from $\theta = 30^{\circ}$)

The axial stress-strain curves and the micro-cracking behaviour of the specimens that included a single, pre-existing crack with an inclination angle of 30° is illustrated in Figure 8.7. Different stress levels were considered in this graph as points I, II, and III. The point I showed the stress level at which the initiation of macroscopic cracks on the surface or at the tips of the pre-existing cracks was observed. The stress level at which the coalescence between inter- and intra-grain micro-cracks was occurred is marked as point II. The point III corresponds to the peak axial strength of the GBM specimens. It can be seen that the grain size profoundly influenced the micro-cracking and macroscopic behaviour of the numerical specimens with a single flaw. For single-flawed specimens, the numerical behaviour was monitored in three distinct points: Initiation of primary cracks (I), extension of macroscopic cracks (II), failure of the model and peak axial strength (III). The crack initiation stress (I) increased from 39.6 MPa for scenario 1, to 49.6 MPa for scenario 2, but reduced to 36.9 for scenario 3. The initiation of tensile cracks at point I in all of the specimens was found to be due to the failure of the inter-grain contacts (SJM). It is clear in Figure 8.7 that the grain boundaries control the crack initiation pattern (I in Figure 8.7b, c, and d), and that the mineral size can highly influence the pattern of tensile crack initiation as inter-grain micro-cracks grow. We also found that, apart from the tip area, other inter-grain micro-cracks are formed in the different parts of the

specimens (I). However, the length of the macroscopic tensile cracks was longer around the flaw tips compared to other regions, especially for scenario 1 and 2 (I in Figure 8.7b and c). During compressive loading of the specimens, intra-grain contacts started to enter to their yielding limit. At this point, the stress-displacement of intra-grain contacts appeared as a softening response. After complete degradation of cohesion (C_{CCM}^{0}) and reaching the final stage of softening behaviour ($D_{CCM} = 1.0$), the intra-grain micro-cracks were initiated. These intra-grain micro-cracks mostly tended to initiate from macroscopic tensile fractures that were previously formed from the flaw tips due to bond-breakage in inter-grain contacts. Accordingly, a progressive coalescence between inter- and intra-grain micro-cracks occurred, which resulted in the formation of a much larger macroscopic fractures. The corresponding point where the interaction between inter- and intra-grain micro-cracks was observed, is marked as point II in stress-strain graphs (II in Figure 8.7b, c, and d). It can also be observed that from point I to point II, all numerical specimens experienced a significant growth in inter-grain micro-cracks in the direction parallel to the applied compressive loading, leading to the extension of macroscopic tensile cracks.

The progressive failure of intra-grain contact leads to peak axial strength (III). The corresponding peak axial stresses for scenarios 1, 2, and 3 are 103, 132, and 231 MPa, respectively; they show a significant increase in the intra-grain micro-crack initiation stress with increasing the grain size (Figure 8.7a)., which is consistent with the observations of Hofmann et al. (2015a), Gui et al. (2016), and Peng et al. (2017). According to Hofmann et al. (2015a), bond-breaks occur faster in the parallel bond model, since the stress on the bond is higher in smaller grains, and they result in a significant reduction in the axial strength. Similarly, since the cohesion (C_{CCM}^{0}) for all three scenarios in the current cohesive model are equal, the intra-grain contacts in the minerals with higher stress concentrations reach their complete damage state ($D_{CCM} = 1.0$) much earlier, leading to a significant reduction in the strength of the material. In scenario 3, only one grain boundary was formed around the pre-existing crack, which was connected to the flaw tips. Consequently, this weak inter-grain interface could easily fail at a lower axial stress to form a primary, macroscopic tensile crack. However, in scenario 3, despite it having the lowest crack initiation stress, the grains showed a higher resistance against compressive loading. This is because the stress concentration in the minerals was lower, leading to a much higher peak axial strength. The possible reason for having the lowest crack initiation stress in scenario 3 might be attributed to the dimension of the grains surrounded the pre-existing crack. Due to the large dimension of the grains in

scenario 3, the macroscopic crack could initiate along one interface (which was straight), while in scenario 1 and 2, due to smaller grain sizes, the same sized macroscopic crack had to be initiated along multiple grain boundaries (i.e. jagged shape interface). It was believed that the jagged interfaces in scenario 1 and 2 acted as rough interfaces (i.e. interfaces with irregular asperities), but in the contrary, the straight interfaces in scenario 3 acted as planar interfaces (i.e. smooth interfaces). Accordingly, in scenario 3 when $\theta \leq 30^{\circ}$, the inter-grain micro-crack could rapidly grow along the straight grain interfaces to form macroscopic cracks at the early stages of compressive loading. In scenario 1 and 2, however, more time stepping was required to initiate the micro-cracks along with the jagged shaped grain interfaces and develop a macroscopic crack. However, in scenario 3 when $\theta > 30^{\circ}$, as the angle between the loading direction and the pre-existing crack was reduced, the contribution of low stress concentration in the flaw zone was more pronounced leading to relatively higher crack initiation stresses.

The graphical representation of intra-grain micro-cracks in Figure 8.7b, c, and d revealed that the propagation of intra-grain micro-cracks at peak (III) was more pronounced for scenario 3 compared to other grain sizes, which was due to a larger number of DEM particles inside the minerals. It can be seen that at the onset of failure (III), the density of both inter- and intra-grain micro-cracks increased, and smaller grain size in specimens showed a higher number of micro-cracks. The macroscopic cracks formed in all scenarios as a direct consequence of progressive coalescence between inter- and intra-grain micro-cracks that initiated from the pre-existing flaws at the centre of the specimen.

The localized macroscopic shear fractures also formed in the specimens (Figure 8.7b, c, and d; III), which were the result of interaction between inter- and intra-grain micro-cracks. Notice that the macroscopic shear fractures began to generate when the intra-grain micro-cracks appeared in the specimens, which initiated due to grain sliding. This fracture mechanism was previously observed by Morgan et al. (2013). According to their experimental research, in crystalline rocks such as granite, the localized shear cracking is associated with the relative sliding along the fracture interfaces that are already developed in the specimen (Morgan et al. 2013). This numerical simulations were also consistent with the macroscopic shear fractures observed in the GBM study of brittle rocks (Hofmann et al. 2015a; Liu et al. 2018).

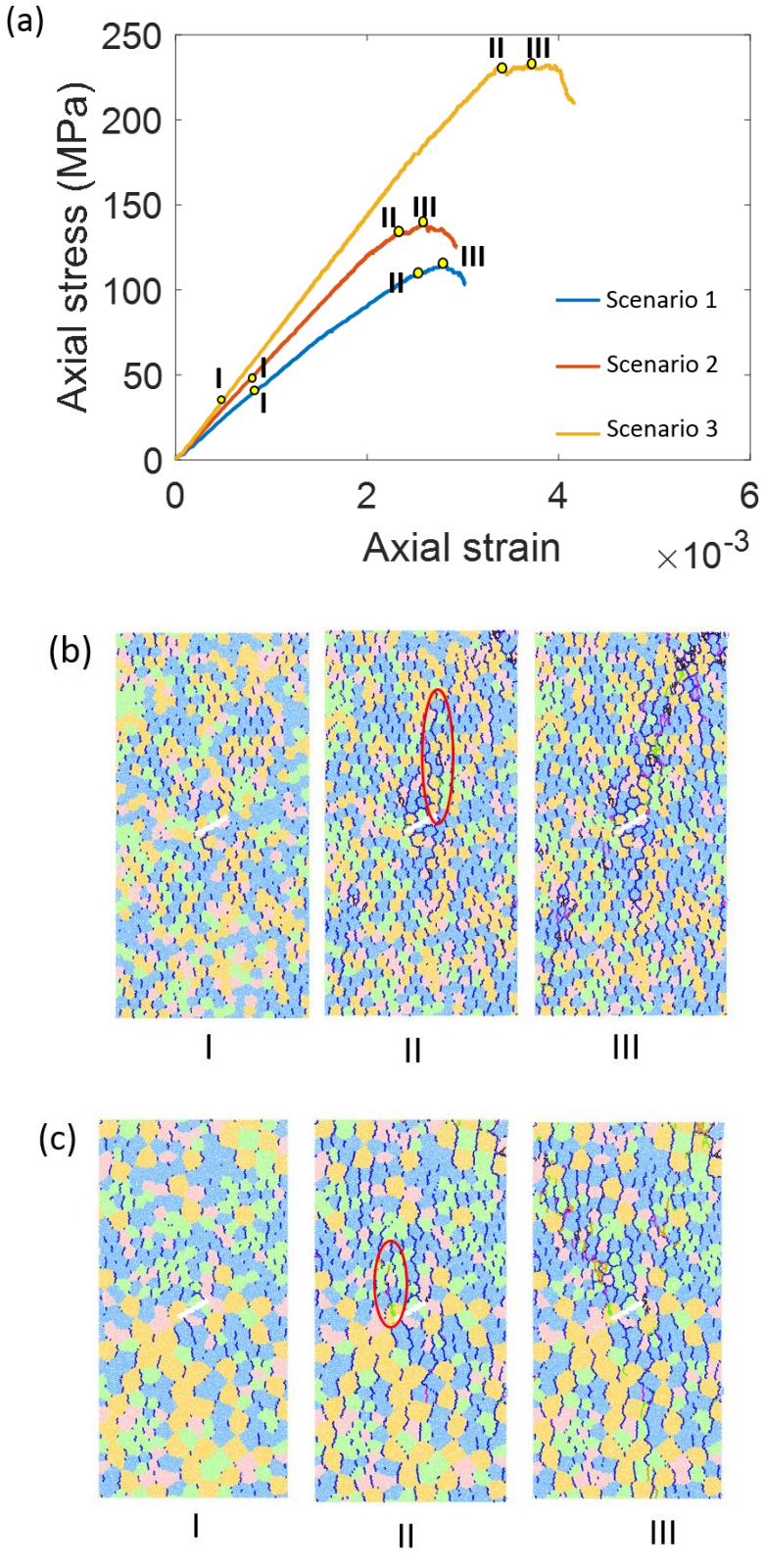
(a)
Axial stress (MPa)
250
200
150
100
50
0
0
2
4
6
Axial strain
×10-3
I
II
III
Scenario 1
Scenario 2
Scenario 3
(b)
I
II
III
(c)
I
II
III

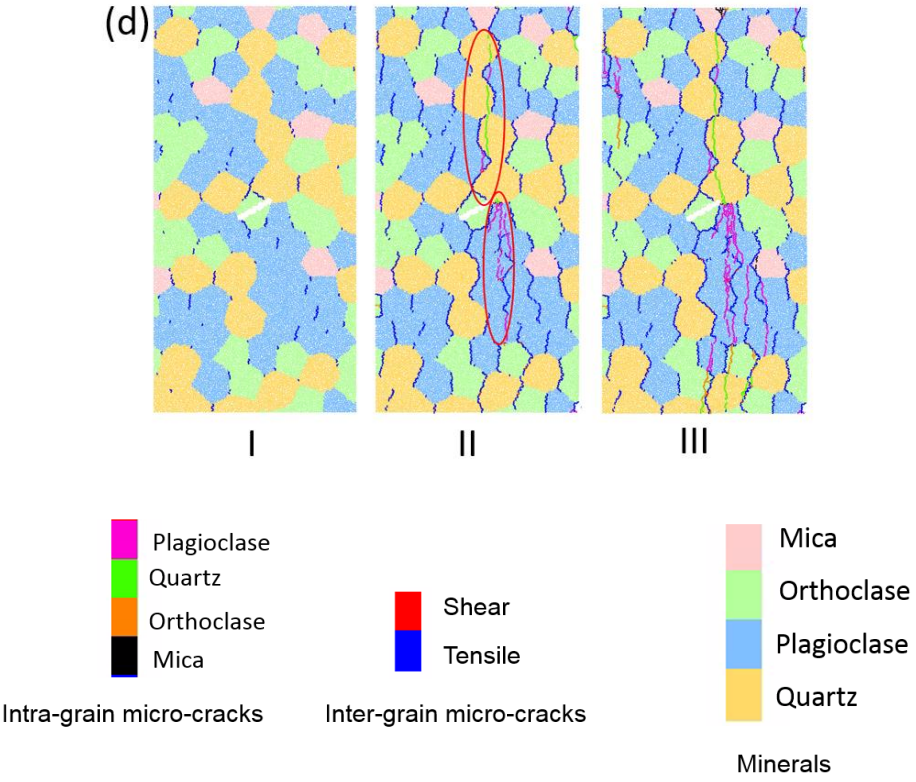

Figure 8.7 The macroscopic failure behaviour of numerical specimens with $\theta = 30^{\circ}$ a) the complete axial stress-strain curves b) scenario 1 c) scenario 2 d) scenario 3.

8.4.2.2 Initial cracks in the single-flaw specimens

The initial macroscopic cracks that developed around the flaw tip are illustrated in Figure 8.8. The blue lines depicted in the figures are tensile inter-grain micro-cracks formed as a result of bond-break in SJ contacts, in tensile mode. The laboratory observations of Morgan et al. (2013) showed that tensile cracks typically propagated along a meandering path created by the grain boundaries. Therefore, the shape of tensile cracks around pre-existing cracks is always "jagged" rather than smooth. The numerical observations in the current study also showed the same jagged pattern in the development of propagated macroscopic cracks. The jagged pattern in the development of macroscopic tensile cracks in the numerical simulations is associated with the shape of the Voronoi tessellations that were created during the sample generation procedure.

The crack initiation stress is given under each specimen (Figure 8.8). We can see that, for all grain sizes, the crack initiation increased with an increasing flaw inclination angle. For scenario 2, when $\theta > 0^{\circ}$ the crack initiation stress was approximately 10 MPa higher than scenario 1. Monitoring inter-grain micro-cracks for scenarios 1 and 2 (Figure 8.8a-c and Figure 8.8a′-c′)

revealed that for θ equal to 0° , 15°, and 30°, the first tensile cracks were relatively close to the middle surface of the flaw. In comparison, when θ was equal to 45° , 60°, and 75° , the first crack growth occurred in the inter-granular boundaries, away from the centre and close to the flaw tip (Figure 8.8d-f and Figure 8.8d′-f′). In scenario 3, for $\theta \leq 30^{\circ}$, the crack initiation stress was lower than for scenarios 1 and 2, but it raised significantly to a peak axial strength for 60° and 75°, leading to the presence of a few intra-grain micro-cracks (Figure 8.8e″-f″). In scenario 3, specimens with high flaw inclination angles (i.e. $\theta > 30^{\circ}$) were significantly influenced by the low stress concentration, which resulted in a higher crack initiation stresses. At 60° and 75°, the low stress concentration was more effective resulting in a higher axial stress to fully grow the macroscopic cracks around the flaw.

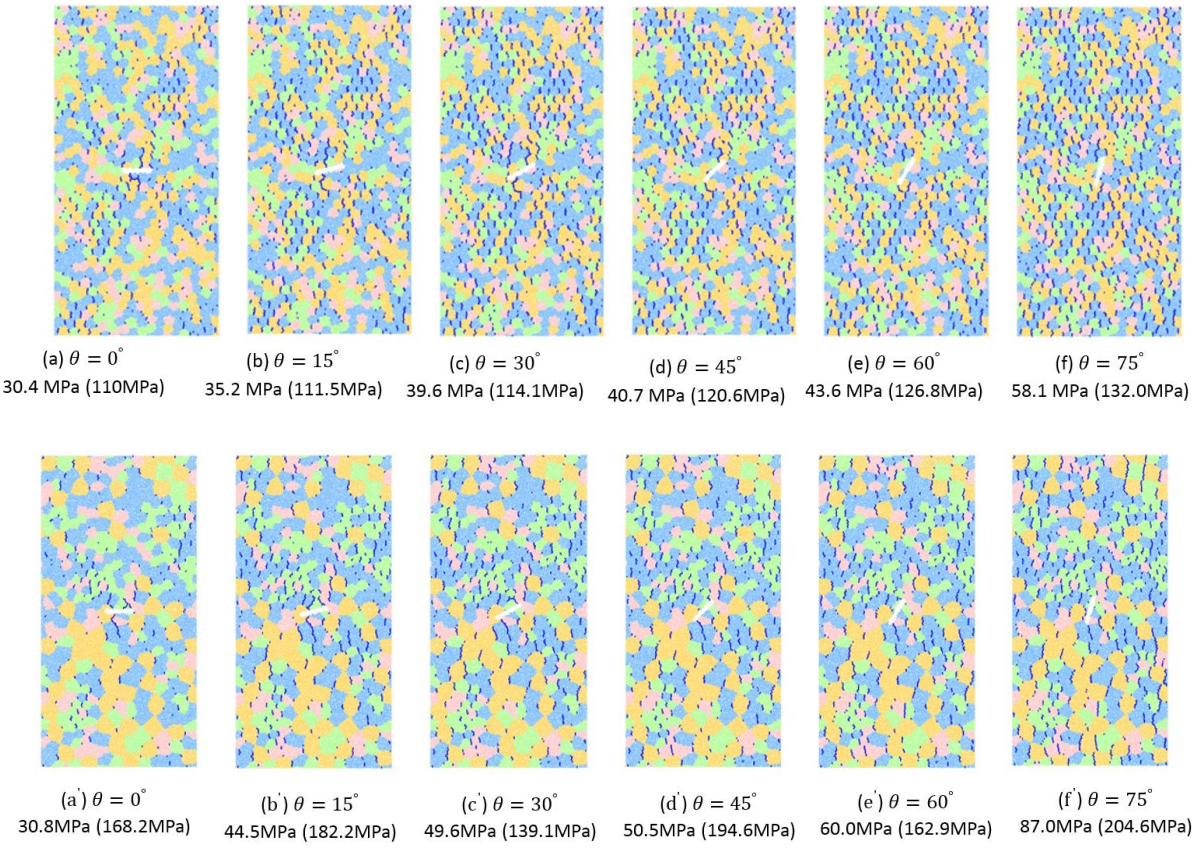

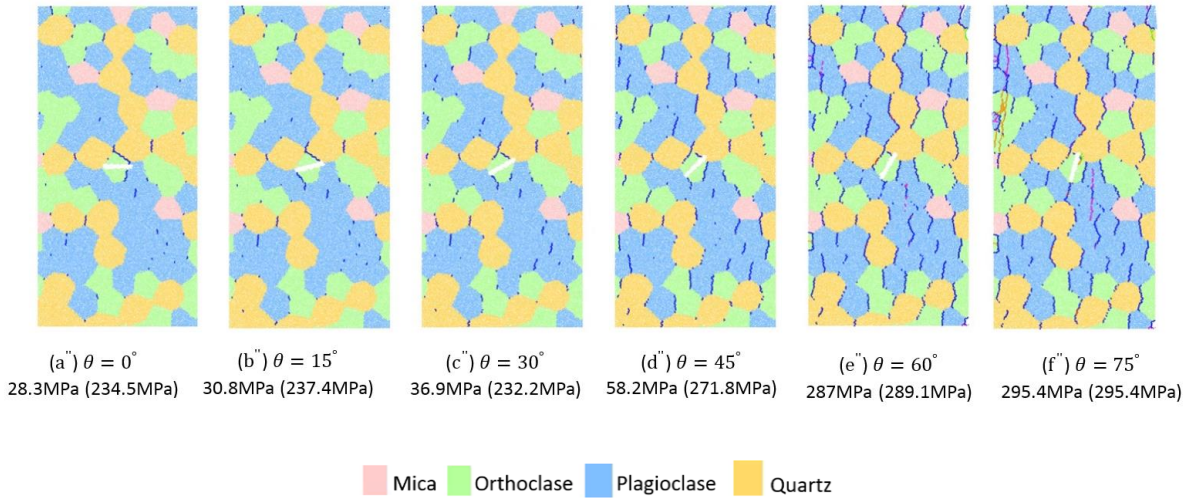

Figure 8.8 Initiation of primary macroscopic cracks for the specimens with different inclination angles and grain sizes. The crack initiation stress and the peak stress (in parentheses) are given below each numerical specimen. The blue lines indicate the inter-grain micro-cracks. The first row (a-f) shows scenario 1, the second row (a′-f′) shows scenario 2, and the third raw (a″-f″) shows scenario 3.

8.4.2.3 Failure behaviour of single-flaw specimens

A progressive increase in uniaxial compressive loading leads to the development of secondary macroscopic cracks and failure of the specimens at peak stress. The complete stress-strain curves for all numerical samples are illustrated in Figure 8.9, and the fracture patterns at peak axial strength are shown in Figure 8.10. It is clear from Figure 8.9 that the maximum axial stress for scenario 1 was the lowest when the inclination angle was equal to 15°. For $\theta > 15^{\circ}$, there was an increase in the maximum axial strength of the material. For scenario 3 (the largest grain size), the lowest possible maximum axial strength occurred at $\theta = 30^{\circ}$, and for $\theta > 30^{\circ}$ there was an increase in the strength of the specimens. The results for scenario 2 (medium grain size), however, were significantly different. At $\theta = 30^{\circ}$ and $\theta = 60^{\circ}$, the lowest axial strengths were reached. We believe this is due to different mineral distributions around the flaw region when the inclination angle changes. For this scenario, the weakest mineral (mica) was present around the right side of the flaw's tip. Since the cohesion of mica was the lowest value (i.e. 60 MPa) compared to other minerals, it predominantly influenced the evolution of intra-grain micro-cracks around the tip region. Figure 8.9 also shows that all specimens in each scenario underwent the same elastic behaviour before macroscopic cracks propagated.

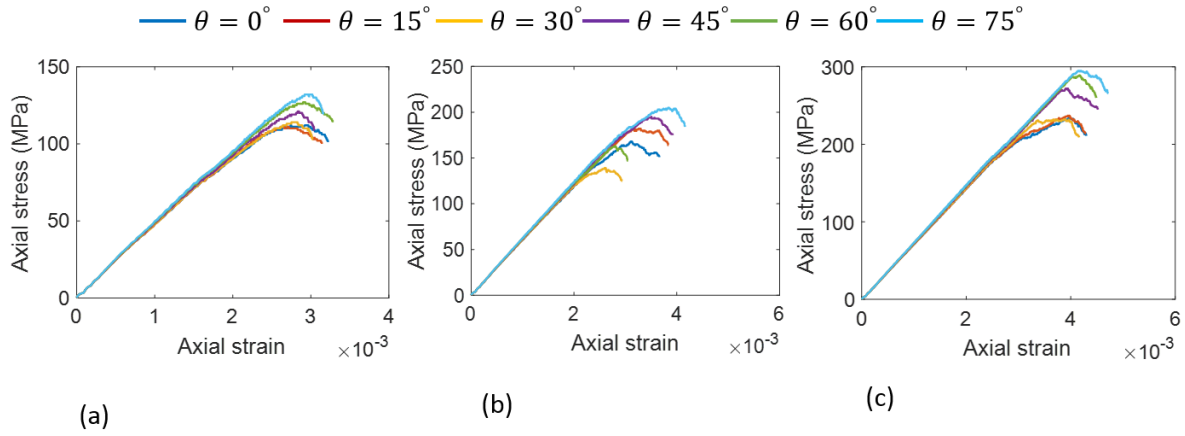

Figure 8.9 Complete axial stress-strain curves for single-flawed specimens: a) scenario 1 b) scenario 2 c) scenario 3.

Figure 8.10 shows that an increase in compressive loading resulted in a dramatic rise in the number of both inter- and intra-grain micro-cracks. The secondary macroscopic cracks around the flaw's tip propagated due to the bond-break in the intra-grain contacts, and the progressive coalescence between the inter- and intra-grain micro-cracks. The laboratory observations of Morgan et al. (2013) showed that the secondary macroscopic cracks had a powdery residue, indicating grain breakage. According to Morgan et al. (2013), mineral breakage was associated with a sizeable sliding displacement along the surface of the crack. Other laboratory investigations (e.g. Akesson et al. (2004), Kranz (1983), and Tapponnier and Brace (1976)) also found that micro-cracks generally initiate from the grain interfaces, and that the intra-grain micro-cracks will be formed at high applied stress. In the present study's GBM numerical simulations, the initiation of micro-cracks was mostly caused by stress concentration at the inter-grain contacts (grain boundaries), and the intra-grain micro-cracks initiated when the applied stress was high. The majority of micro-cracks in the numerical specimens propagated and extended in a direction parallel to the maximum axial stress. This failure mechanism at the microscopic level is known as axial splitting (Potyondy 2010a; Tang et al. 2000), and it was observed in all numerical specimens regardless of their grain size. We can see in Figure 8.10e-f, Figure 8.10e′-f′, and Figure 8.10e″-f″ that numerical specimens with $\theta \geq 60^{\circ}$ produced fewer intra-grain micro-cracks, and the failure of these specimens occurred due to the progressive coalescence between the inter-grain micro-cracks. This can be attributed to the fact that, as the flaw inclination angle increased, the behaviour of the numerical specimens came closer to intact rock, which lead to a reduction in the number of intra-grain micro-cracks (Liu et al. 2018). It was observed that for $\theta < 45^{\circ}$, the number of intra-grain micro-cracks around the tip

region was increased by increasing the grain size (Figure 8.10a-c, Figure 8.10a′-c′, and Figure 8.10a″-c″). One possible reason is that an increase in the grain size leads to an overall increase in the strength of the specimens, so that more damaged contacts (intra-grain micro-cracks) are produced to reach the failure state.

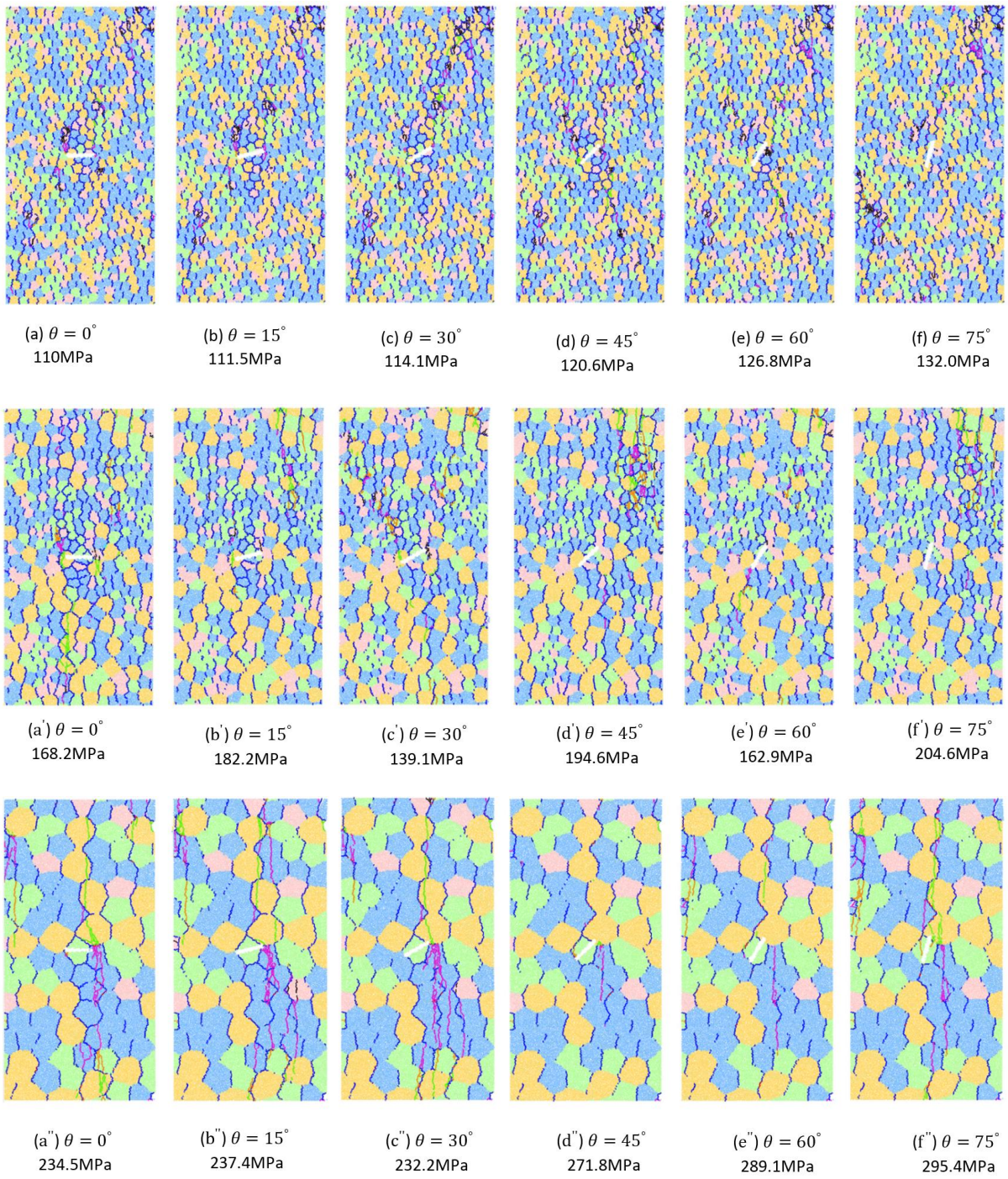

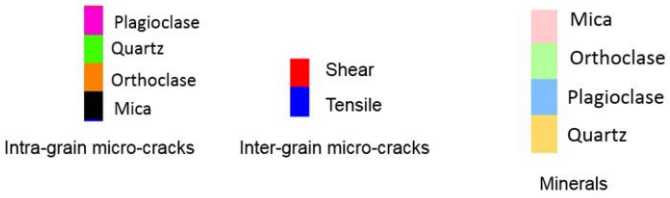

Figure 8.10 Final fracture pattern including inter- and intra-grain micro-cracks. The first row (a-f) shows scenario 1, the second row (a′-f′) shows scenario 2, and the third raw (a″-f″) shows scenario 3.

8.4.3 PFC-GBM modelling of brittle rocks including a double flaw

The linkage of pre-existing flaws (crack coalescence) is an important phenomenon in nature (Miller and Einstein 2008), as it controls the failure mechanism of materials (Morgan et al. 2013). In this regard, numerical specimens containing double flaws were generated and tested under uniaxial compressive loading.

8.4.3.1 The failure mechanism of double-flaw specimens (example from $\theta = 30^{\circ}$)

Figure 8.11 illustrates the stress-strain curves for numerical specimens with $\theta = 30^{\circ}$, and their corresponding micro-cracking behaviour. Different stress levels were considered in this graph as points I, II, III, and IV. The point I showed the stress level at which the initiation of macroscopic cracks on the surface or at the tips of the pre-existing flaws was observed. The stress level at which the development of macroscopic tensile cracks inside the bridging area occurred was presented by point II. For double-flaw specimens, a coalescence stress (point III) was considered in the stress-strain curves to monitor the onset of flaw coalescence. The peak axial strength of the GBM specimens was indicated by point IV. The micro-cracks developed at various points of loading are also monitored during the simulations, and are shown in Figure 8.11b-d. According to Figure 8.11, the increase in the grain size resulted in an increase in the peak axial strength. At point I, for all numerical specimens, the inter-grain micro-cracks were initiated in the bridging area of the flaw system. It can be seen in Figure 8.11b-d that the inter-grain micro-cracks were only initiated in this particular area because the stress concentration was relatively high. The crack initiation stress was slightly raised by increasing the grain size.

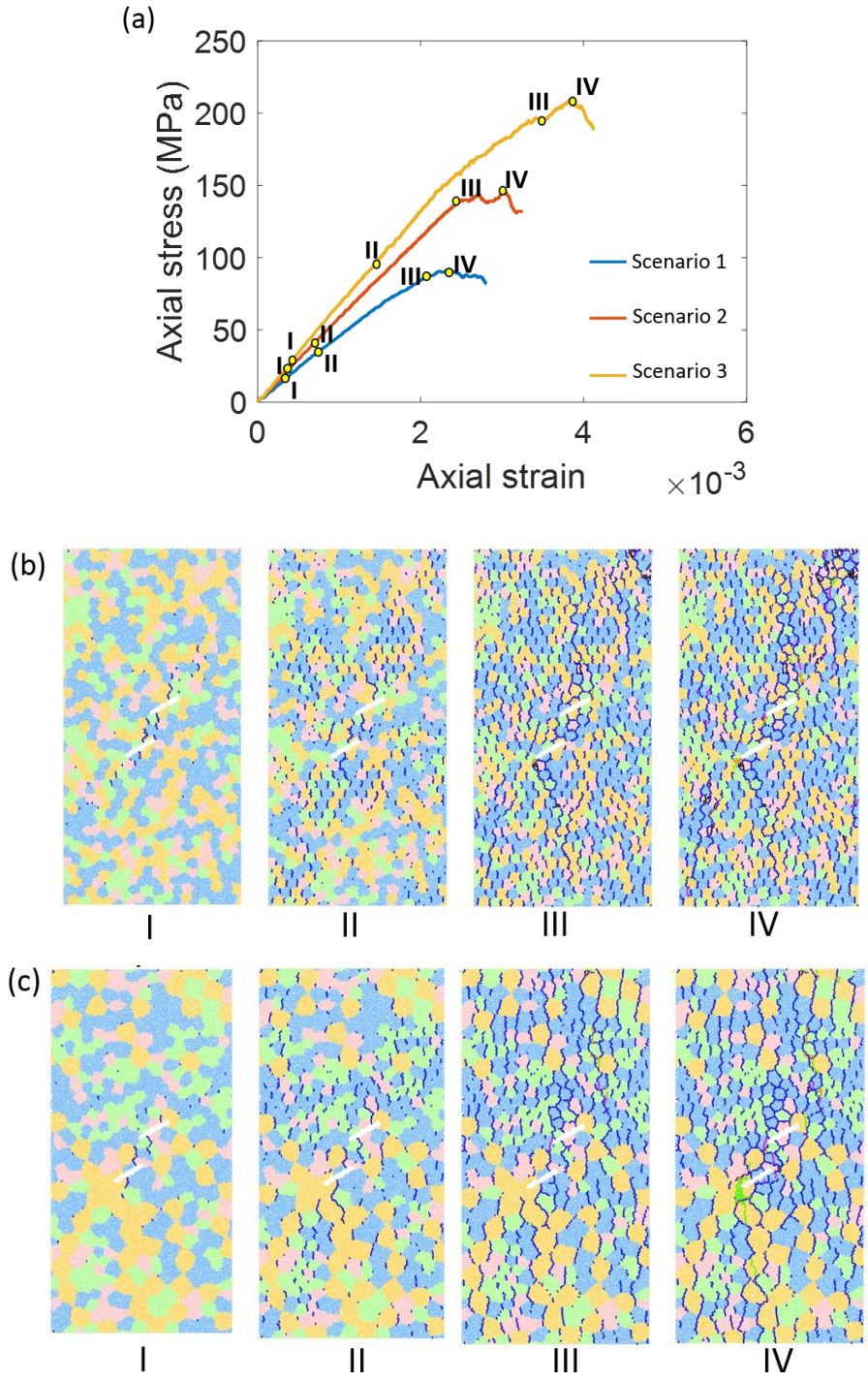
(a)
Axial stress (MPa)
250
200
150
100
50
0
0
2
4
6
Axial strain
×10-3
Scenario 1
Scenario 2
Scenario 3
I
II
III
IV
(b)
(c)

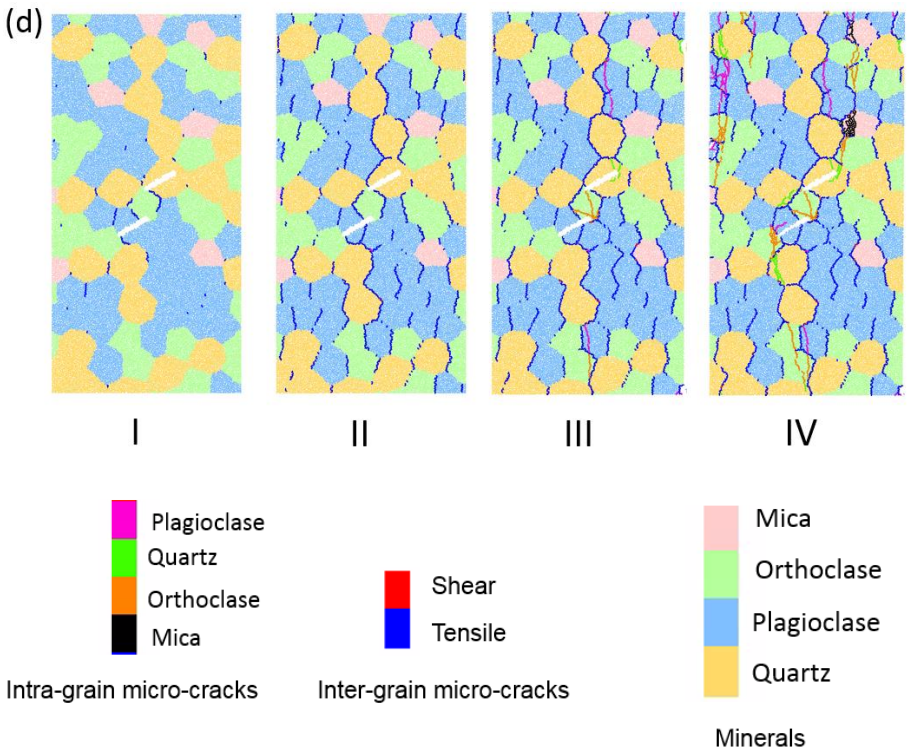

Figure 8.11 The macroscopic failure behaviour of double-flawed specimens with $\theta = 30^{\circ}$a) complete axial stress-strain curves b) scenario 1 c) scenario 2 d) scenario 3

The macroscopic tensile cracks propagated in the bridging zone at point II. At point III, the coalescence of pre-existing cracks was observed in all scenarios; it occurred due to the rapid extension and development of macroscopic cracks in the bridging area. In all numerical specimens, the macroscopic tensile cracks that were the result of progressive linkage of inter-grain micro-cracks, were formed from the flaw tips. The micro-cracks developed until point II are grain boundary tensile cracks, which initiated as a result of bond-break in the SJM. A small tensile strength needed to be assigned to the inter-grain contacts during the calibration procedure in order to match the Brazillian tensile test results. This early coalescence of pre-existing cracks due to the initiation of inter-grain micro-cracks may not be observable during experimental testing. However, it does not mean that they are not present in the physical specimens (Hofmann et al. 2015a). In the numerical simulations, the macroscopic cracks fully developed in the bridging zone due to progressive compressive loading, leading to flaw coalescence at point III. The axial stress-strain curve in Figure 8.11a shows that the large grain size specimens required a higher axial stress to reach point II. This may contribute to the longer length of the grain boundaries in this specimen, as the inter-grain contacts required more time-stepping and, consequently, more axial stress to fully develop and form the macroscopic tensile crack.

At point III, intra-grain micro-cracks started to initiate. In all three scenarios, more inter-grain micro-cracks initiated and formed macroscopic tensile cracks, which propagated in the loading direction. The progressive coalescence between the inter- and intra-grain micro-cracks caused non-linear behaviour in the axial stress-strain curves before reaching the peak axial strength. The intra-grain micro-cracks tended to initiate from the flaw tips in scenarios 1 and 2. However, in scenario 3 the intra-grain micro-cracks appeared in the bridging area and at the flaw tips. This was mainly because of the presence of larger minerals in the bridging area. In fact, only one mineral was generated in the bridging area in scenario 3, and due to a higher number of DEM particles, it tended to produce more intra-grain micro-cracks. By the continuous loading of the numerical specimens, more intra-grain contacts (with the cohesive model) reached their yielding limit, generating intra-grain micro-cracks. The interaction between inter- and intra-grain micro-cracks formed macroscopic fractures in a direction parallel to the maximum axial stress. This leads to the failure of the specimens at point IV, where the peak axial strength was achieved. As shown in Figure 8.11b-d, , the number of intra-grain micro-cracks increased significantly at peak axial strength, and the macroscopic cracks were fully propagated, extending parallel to the direction of axial loading.

8.4.3.2 Initial cracks in the double-flaw specimens

To gain a better insight into the crack initiation pattern and coalescence of primary macroscopic cracks, we monitored the state of the numerical specimens at the time the primary macroscopic cracks initiated. The results are illustrated in Figure 8.12. This figure shows that the macroscopic cracks in all numerical specimens initiated from the surface of pre-existing flaws and propagated vertically towards the loading DEM walls. Similar to single-flawed specimens, the inter-grain micro-cracks were initiated due to the bond-failure in SJM contacts. Figure 8.12 shows that the macroscopic cracks initiated from the middle portion of the flaws, and that they shifted towards the tips with an increase in the inclination angle. In scenario 3, the macroscopic cracks only followed the grain boundary provided by orthoclase in the inner tip area due to the large diameter of the grains. In fact, for this specimen, the bridging zone was dominated by this mineral, a meandering path defined the propagation of the inter-grain micro-cracks as a result. Note that the calibrated contact strength (C_{CCM}^{0}) for orthoclase and plagioclase are equal, while the same value is different for quartz and mica. This difference between the mineral strength may change the cracking response in the bridging zone. For instance, the weakest mineral (mica) has the potential to develop more micro-cracks leading to grain crushing in the inner tip area. However, in such circumstance, many other factors (i.e. stress concentration, flaw

inclination angle, and etc.) may influence the results. Scenario 3 showed that, for $\theta \geq 60^{\circ}$ (Figure 8.12e″-f″), since the angle between pre-existing crack and loading direction was relatively small compared to other specimens, the influence of pre-existing flaw was less pronounced leading to a relatively higher crack initiation stress. In fact, for $\theta \geq 60^{\circ}$ more time stepping was needed for the initiation of the micro-cracks and the formation of macroscopic crack. This resulted in the initiation of fewer micro-cracks in the bridging area compared to other specimens. This shows that both inclination angle and grain size can influence the initiation of primary tensile cracks. The stress at which the initial tensile cracks formed in the flaw system was monitored, and is given below each specimen in Figure 8.12. The results revealed that crack initiation stress was increased when the inclination angle of the flaw was increased, and when the rate of increase was higher for scenario 3. These numerical findings were consistent with the laboratory observations of Barre granite (Miller and Einstein 2008) containing left-stepping pre-existing cracks.

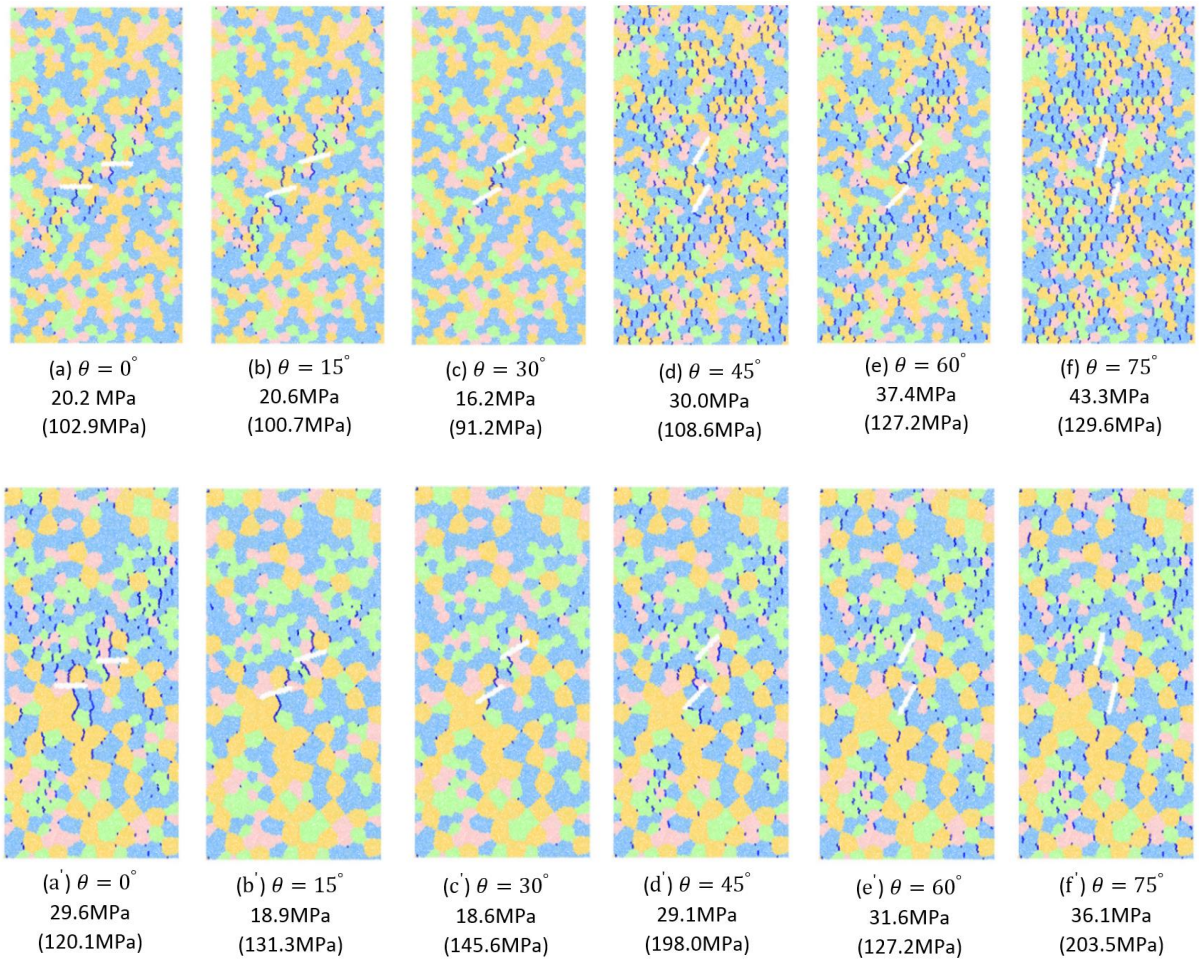

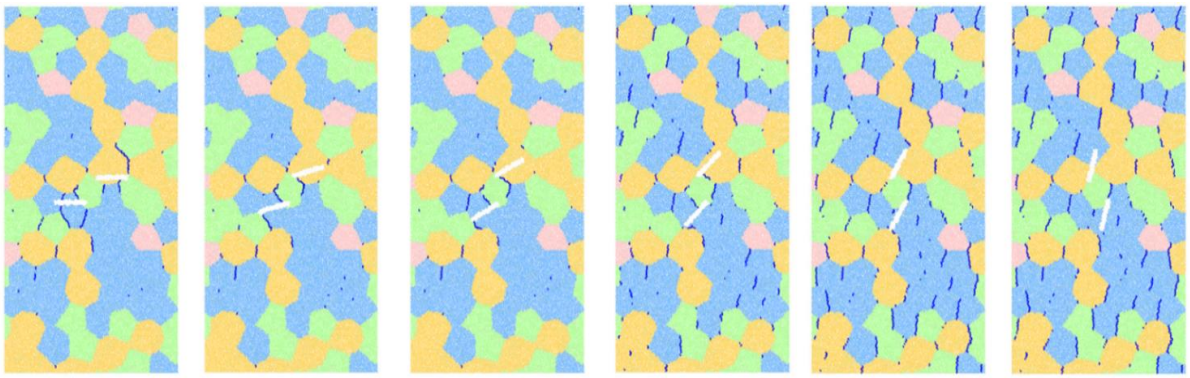

Figure 8.12 Initiation of primary macroscopic cracks for the specimens with different inclination angles and grain sizes. The crack initiation stress and the peak stress (in parentheses) are given below each numerical specimen. The blue lines indicate the inter-grain micro-cracks. The first row (a-f) shows scenario 1, the second row (a′-f′) shows scenario 2, and the third raw (a″-f″) shows scenario 3.

8.4.3.3 Failure behaviour of double-flaw specimens

A progressive increase in uniaxial compressive loading leads to the development of secondary macroscopic cracks and the failure of the specimens at peak stress. The complete stress-strain curves for all numerical samples are illustrated in Figure 8.13, and the fracture patterns at peak levels are shown in Figure 8.14.

The axial stress-strain curves in Figure 8.13 show that almost all specimens in the same scenario underwent the same elastic behaviour before macroscopic cracks propagated. The results revealed that the specimens exhibited a more brittle failure response with an increase in the flaw inclination angle. As indicated in Figure 8.13, the peak strength gradually increased following an increase in the grain size. The flaw inclination angle was also found to influence the peak strength in each scenario. For relatively low inclination angles ($\theta \leq 30^{\circ}$), the peak strength decreased, but increased when θ increased from 45° to 75°. At $\theta \leq 30^{\circ}$ pre-hardening and post-peak softening behaviours were observed that showed the influence of the flaw inclination angle on the overall macroscopic response of the specimens.

During the design procedure of underground structures, pre-hardening and post-peak softening is of great importance because such behaviour can control the stability or instability of the rock blocks surrounding the tunnel. A more comprehensive understanding of the mechanical and failure behaviours of rock can help designers to better predict the residual behaviour of failed

rock blocks. In underground mining for instance, the residual and deformation characteristics of rock are more important than its peak axial strength, because it is crucial in achieving both the stability and optimal support of the tunnel (Gao and Kang 2017).

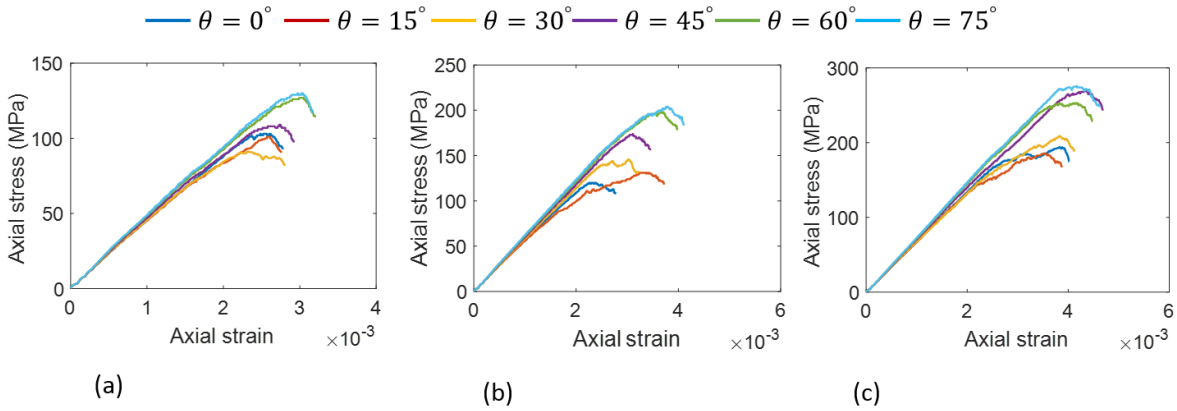

Figure 8.13 Complete axial stress-strain curves for double-flawed specimens: a) scenario 1 b) scenario 2 c) scenario 3.

The results presented in Figure 8.14 indicate the coalescence behaviour observed in double-flaw specimens. Both inter- and intra-grain micro-cracks evolved at the onset of failure. As mentioned in section 3, the inter-grain micro-cracks propagate due to a low tensile strength assigned to the SJM contacts. The linkage of these inter-grain micro-cracks generates macroscopic tensile cracks that exist in both the inner and outer flaw regions. According to Morgan et al. (2013), the main reason for shear cracking is the size and shear strength of the grains. Increasing the shear strength of the minerals reduces the number of shear cracks. The strength of the minerals (intra-grain contacts) in the current study's GBM simulations were controlled by the cohesion (C^0_{CCM}) obtained during the calibration procedure. The growth of intra-grain micro-cracks was the result of the gradual degradation of bond cohesion, and finally of the bond-break in the contacts inside the minerals.

At failure point, macroscopic cracks extended from the outer flaws' tips as a result of the combined inter- and intra-grain micro-crack growth. However, different coalescence patterns of pre-existing cracks were obtained when the grain size changed. Figure 8.14 shows that scenarios 1 and 2 produced almost identical coalescence patterns. For scenarios 1 and 2, the inter-grain micro-cracks in the bridging zone formed macroscopic cracks leading to the coalescence of pre-existing cracks. The primary macroscopic cracks were fully grown from the tips and surface of the flaws, towards the direction parallel to the maximum axial stress. In scenario 3, at $\theta \leq 30^{\circ}$ the inter-grain micro-cracks developed in orthoclase caused the

coalescence of pre-existing cracks. In contrast, at 45° and 60° relatively few intra-grain micro-cracks were developed in the orthoclase, but the number of micro-cracks increased significantly in the plagioclase and quartz. For specimens with an inclination angel of 75°, however, a combination of plagioclase and orthoclase micro-cracks resulted in the coalescence of pre-existing cracks. Overall, it was observed that compared to scenarios 1 and 2, the large grain size specimens (scenario 3) produced a higher number of intra-grain micro-cracks in the bridging area.

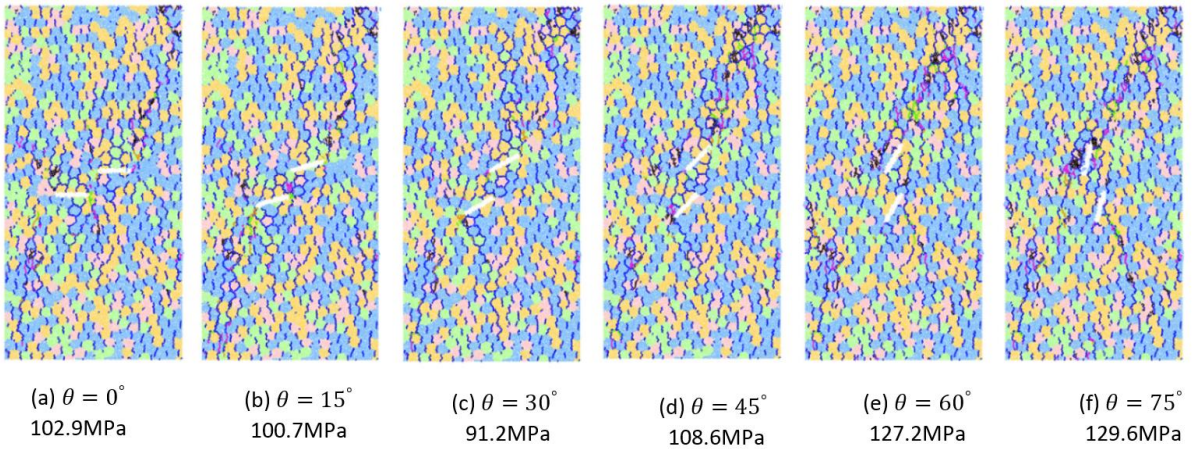

(a) $\theta = 0^{\circ}$ 102.9MPa
(b) $\theta = 15^{\circ}$ 100.7MPa
(c) $\theta = 30^{\circ}$ 91.2MPa
(d) $\theta = 45^{\circ}$ 108.6MPa
(e) $\theta = 60^{\circ}$ 127.2MPa
(f) $\theta = 75^{\circ}$ 129.6MPa

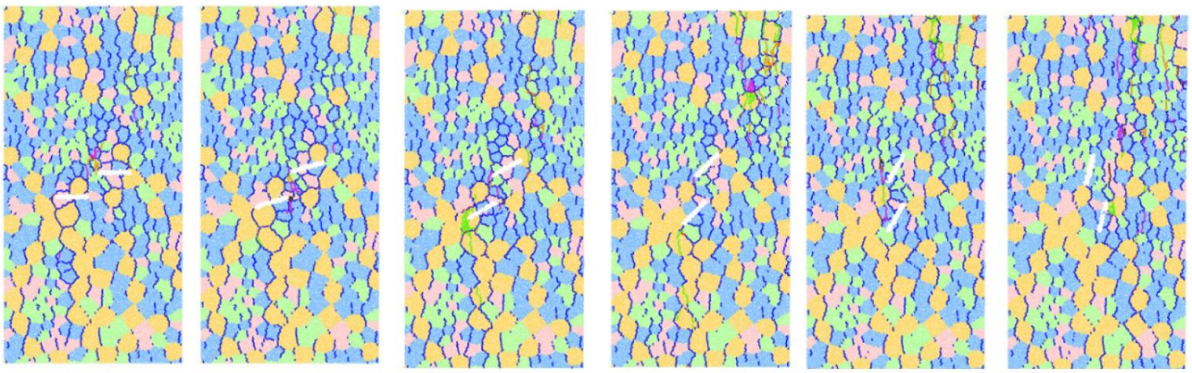

(a') $\theta = 0^{\circ}$ 120.1MPa
(b') $\theta = 15^{\circ}$ 131.3MPa
(c') $\theta = 30^{\circ}$ 145.6MPa
(d') $\theta = 45^{\circ}$ 173.8MPa
(e') $\theta = 60^{\circ}$ 198MPa
(f') $\theta = 75^{\circ}$ 203.5MPa

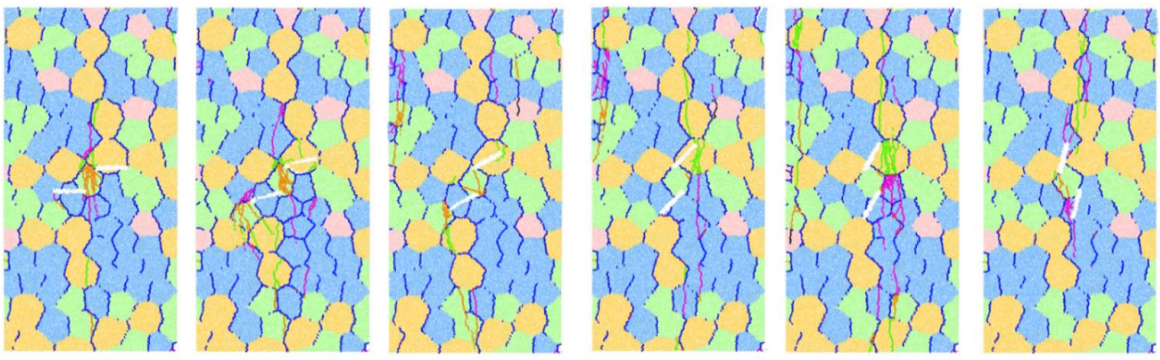

(a'') $\theta = 0^{\circ}$ 234.5MPa
(b'') $\theta = 15^{\circ}$ 237.4MPa
(c'') $\theta = 30^{\circ}$ 232.2MPa
(d'') $\theta = 45^{\circ}$ 271.8MPa
(e'') $\theta = 60^{\circ}$ 289.1MPa
(f'') $\theta = 75^{\circ}$ 295.4MPa

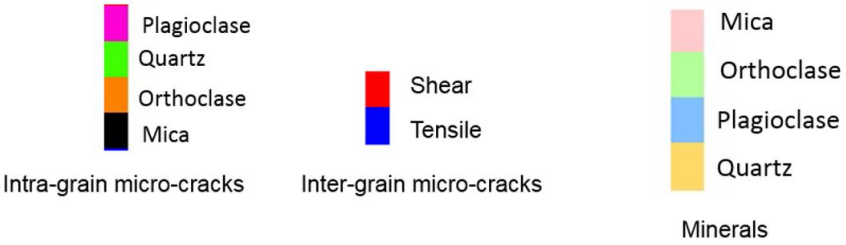

Figure 8.14 Final fracture pattern including inter- and intra-grain micro-cracks. The first row (a-f) shows scenario 1, the second row (a′-f′) shows scenario 2, and the third raw (a″-f″) shows scenario 3.

8.5 Axial strength and damage evolution

In general, intact rock contains various mineral grains that produce different micro-cracking responses when the sample is loaded. The pre-existing flaws and pores may also alter the failure behaviour as well as the axial strength and mechanical properties of intact rocks. In dense, brittle rocks, the boundaries between the minerals' grains are the weakest elements and can be regarded as the major source of micro-crack initiation and propagation. In the GBM approach, these inter-grain contacts are well simulated using the smooth-joint model. However, the micro-cracking response inside the mineral grains is also of great importance as the coalescence and interaction between the inter- and intra-grain contacts control the overall mechanical behaviours of rock. This part analyses the maximum axial strength of the numerical specimens, and their damage evolution responses after complete failure.

8.5.1 Maximum axial strength of the specimens

The peak axial stresses obtained from uniaxial compressive tests are depicted in Figure 8.15. The peak axial strength in scenario 3 (Figure 8.15c) is the highest compared to the other scenarios. The results show that the single-flaw specimens returned a significantly higher peak axial strength compared to the double-flaw specimens, in all scenarios. However, as the flaw inclination angle (θ) increased, the peak axial strength of the double-flaw samples gradually approached that of the single-flaw specimens. For single-flaw specimens, in scenario 1 and 3 the peak axial strength experienced a gradual increase by an increase in θ. In scenario 2, however, we observed a fluctuation in the value of maximum strength, which was attributed to the grain size and the distribution of minerals around the pre-existing crack. The results also revealed that the mineral size changed the inclination angle at which the lowest possible axial strength occurred. For instance, in scenario 1, the lowest axial strength was achieved at $\theta = 30^{\circ}$; in scenarios 2 and 3 the same value was obtained at $\theta = 0^{\circ}$ and $\theta = 15^{\circ}$, respectively.

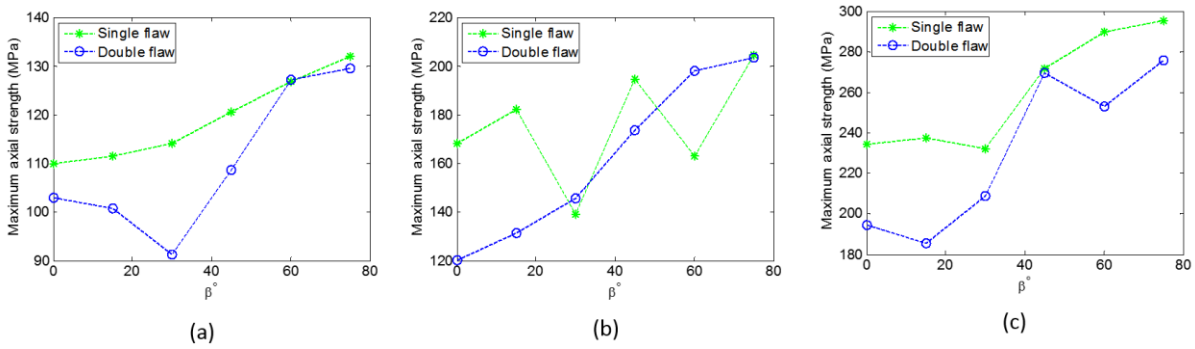

Figure 8.15 Maximum axial strength of the single- and double-flawed specimens with different mineral size a) scenario 1, b) scenario 2, c) scenario 3.

8.5.2 Damage evolution inside the minerals

In this study, a proposed cohesive model was assigned to the intra-grain contacts to study the micro-cracking response and the microscopic and macroscopic damage evolution mechanisms in the minerals. When the intra-grain contact reached their yielding regions, they exhibited softening behaviours before being completely broken. By monitoring the damage parameter (D_{CCM}) defined in the cohesive model (Eq. 3.13), the damage state of the intra-grain contacts could be numerically evaluated. This lets us investigate the influence of the grain size on the microscopic softening responses of the intra-grain contacts in their post-peak regions, for both single- and double-flaw specimens. The evolution of damage in single- and double-flaw specimens at failure point, with various grain sizes, is illustrated in Figure 8.16 and Figure 8.17, respectively.

The results showed that the grain size had a significant influence on the damage mechanisms and softening responses of the intra-grain contacts. For the both single- and double-flaw specimens, the numerical models with calibrated grain sizes showed almost no softening intra-grain contacts (Figure 8.16a and Figure 8.17a). In fact, the contacts, coming to their failure point, reproduced their softening behaviour very quickly, and broke more quickly. In comparison, the numerical specimens with medium and large grain sizes showed more softening contacts (Figure 8.16b,c and Figure 8.17b,c).

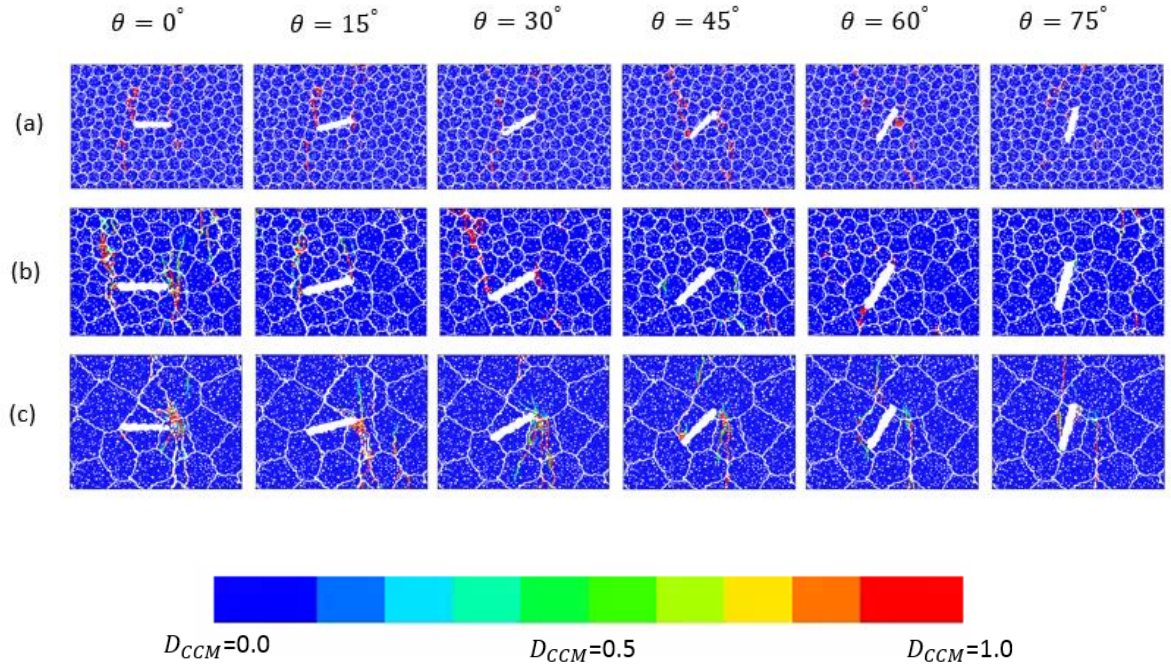

Figure 8.16 Damage evolution of intra-grain contacts at peak stress for single-flawed specimens a) scenario 1 b) scenario 2 c) scenario 3.

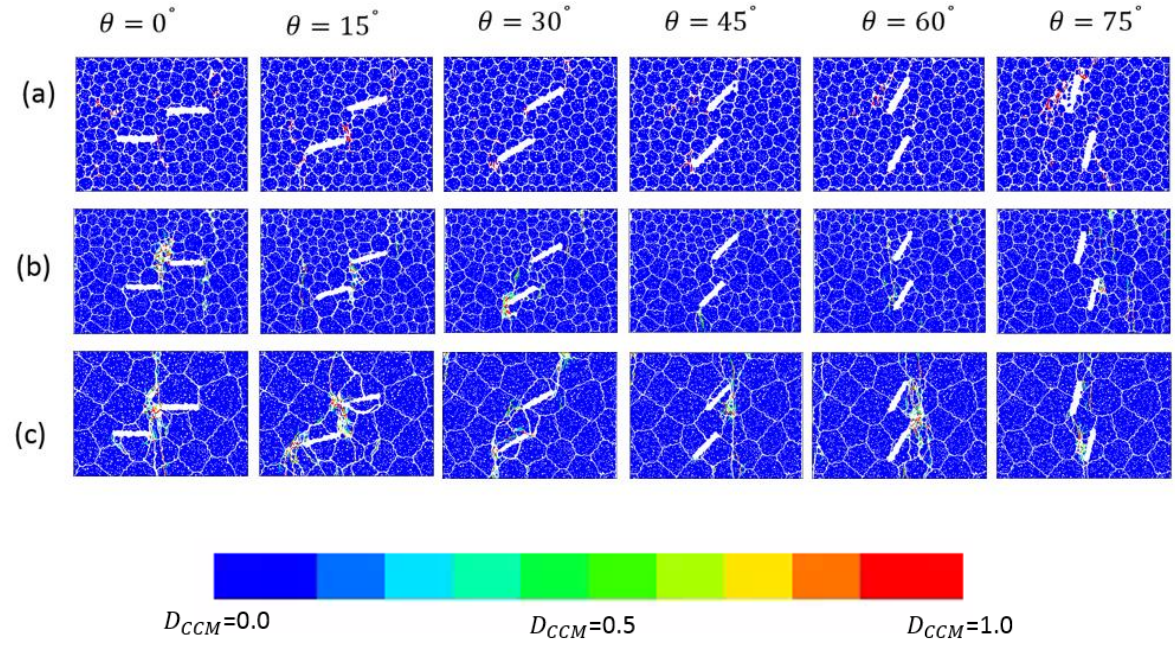

Figure 8.17 Damage evolution of intra-grain contacts at peak stress for double-flawed specimens a) scenario 1 b) scenario 2 c) scenario 3.

Moreover, we observed that, for all grain sizes, the macroscopic cracks passed through a mineral and initiated the intra-grain micro-cracks in the stress concentration zone. For scenarios 2 and 3, the number of particles and consequently the number of contacts forming a mineral is

higher than the number of particles and contacts in scenario 1. A higher number of particles in the grains increased the possibility that the intra-grain contacts would display their softening responses ($0 < D_{CCM} < 1.0$) without being completely damaged. In the softening contacts, the stress was gradually reduced, allowing the contacts to show more resistance against failure. By increasing the number of softening contacts within the grains (or increasing the grain size), the maximum strength of the numerical specimen was significantly increased. As mentioned in section 4, the specimens tend to produce intact (or flaw-less) rock behaviour at high inclination angles. Consequently, the failure behaviour of the specimens is dominated by the bond-break in the inter-grain contacts. The same behaviour was also observed for scenario 1 and scenario 2 at $\theta \geq 60^{\circ}$ where the number of either damaged or softening contacts experienced a significant reduction. In double-flaw specimens, both softening ($0.0 < D_{CCM} < 1.0$) and failed contacts ($D_{CCM} = 1.0$) contribute to the coalescence of pre-existing cracks.

8.6 Conclusion

For both single-and double-flaw specimens, the strength of the material increased significantly with an increase in mineral size. The numerical simulation showed that the primary macroscopic cracks initiated from the surface or tip of a flaw, as a direct consequence of bond-break in the inter-grain contacts. These macroscopic cracks developed along a meandering path created by the boundaries between the grains, leading to a jagged-shaped macroscopic crack around the pre-existing cracks. For low-flaw inclination angles, the inter-grain micro-cracks initiated from the middle portion of the flaw. In the samples with high inclination angles, the inter-grain micro-cracks shifted towards the tips of the flaws. This was not the case for the samples with large grain sizes, as the location of flaw tips was highly controlled by the size of minerals. This leads to the initiation of inter-grain micro-cracks around the tip area for all inclination angles. For double-flaw specimens with large grain size distributions (scenario 3), the bridging zone was generated inside orthoclase. This mineral had a dominant influence on the micro-cracking and coalescence responses in the inner tip region.

This study showed that two major factors are important in the macroscopic responses of the material: The grain size and the inclination angle of pre-existing cracks. In double-flaw specimens, the coalescence of pre-existing cracks occurred due to the linkage of inter- and intra-grain micro-cracks and production of softening contacts when the flaws have low inclination angles. By increasing the inclination angle, the number of intra-grain micro-cracks and softening contacts in the bridging area reduced significantly, and the coalescence occurred as a result of inter-grain micro-crack propagation.

Chapter 9: Conclusions and recommendations

9.1 Conclusions

This thesis presented the application of a new cohesive contact model in characterising the fracture behaviour of fully grouted rock bolt, bolted rock joint, infilled rock joint, and jointed and pre-cracked polycrystalline rock. The model was implemented in PFC2D, which is a distinct element code in which the rock joint and bolt-grout interface are simulated explicitly.

The formulation of the proposed cohesive model was presented in Chapter 3. A generic cohesive framework was employed which coupled plasticity theory with damage mechanics. The model features the bond-break of DEM contacts in mode I, II and mixed mode. To reduce the complexity of the calibration procedure, only one parameter was defined in the model to control the contact strength limit. If either of the normal or shear stresses acting on the two contacting DEM particles exceeds their corresponding bond strength limit, the contact enters to its softening stage. An exponential damage function was considered in the model to facilitate the gradual softening degradation of contact strength, which is controlled by a softening parameter. If the contact strength is completely damaged, the cohesive bond breaks and the contact is removed from the model along with its associated stress, moment, and stiffnesses. At the onset of bond-break, the location of the damaged contact can be traced by a micro-crack which is marked in the model by a line segment. The accumulation of micro-cracks can be displayed as macroscopic fracture response or localised damage of the material (e.g. macroscopic tensile fracture, asperity damage, etc.). If the contact is still in its softening stage, the damage state of contacts can be monitored at each computational time-step using the graphical interface of PFC2D, which enhances the interpretation of model damage response.

In chapter 4 the proposed cohesive DEM framework was employed for modelling the shear behaviour bolted rock joints. The new findings and critical contributions of this chapter are described as follows:

- The proposed model successfully reproduced the failure and mechanical behaviour of bolt-grout interface and grout material. In particular, the softening post-peak response of the grout material, which was an issue in previous studies, was very well captured. The calibrated model was also able to reproduce the asperity damage of rock joint with idealised saw toothed asperities. This chapter introduced a novel numerical technique called stepwise pull-and-shear test (SPST) scheme, which facilitated the

accomplishment of combined pull-and-shear loading tests. The SPST technique provided further insight into the performance of fully grouted rock bolts subjected to pull-shear loads, given the fact that the field observations indicated that the bolt failure is due to a combination of pull-out and shear loading.

- The idea of SPST technique was to apply pre-tension stress (i.e. pull out load) on the rock bolt, and then undertake direct shear test on bolted rock joint. Four different stages (i.e. linear elastic, pre-peak hardening, post-peak softening, and residual stage) characterised the failure mechanism of fully grouted rock bolt during pull out experiment. The monitoring of contact chain force networks showed that the contact compressive forces and their associated induced normal stress in the rock joint interface (σ_n^i) enhanced throughout the pull out process. The numerical results indicated that the rate of increase for σ_n^i significantly declined at the yield point, where the transition from linear elastic to pre-peak response occurred. The ultimate shear resistance of rock bolt was achieved at yield pretension stress magnitude.
- The rib angle of rock bolt profile influenced both σ_n^i and peak shear stress. The bolted rock joints exhibited less shear resistance by reducing the rib angle, and the reduction was more pronounced for rib angle of 30°.
- The numerical results showed that all rib angles displayed a similar trend when the peak shear strength was plotted against the corresponding normal stress. This lead to the conclusion that regardless of rib angle, the fully grouted rock bolts demonstrated their highest performance at the onset of transition from linear elastic to pre-peak hardening behaviour.
- The CNS condition led to an increase in the peak shear resistance of rock joint, which was more pronounced at low pretension stress magnitude in linear elastic stage. During softening and the residual stages, however, the effect of CNS condition was negligible.
- The proposed DEM-based cohesive model in conjunction with the SPST technique provided an efficient numerical tool that can be employed by designers and geotechnical engineers to carry out realistic combined pull-shear experiments, to obtain new insight into the mechanical performance of fully grouted rock bolts under both CNL and CNS conditions.

In chapter 5 a combined experimental-numerical investigation was presented for the characterisation of the shear behaviour of clay-infilled rock joints. A series of laboratory direct shear test on rock joint with idealised single asperity rock joints with a base angle of 20° and

30° were carried out. A cohesive soil (i.e kaolin) with the thickness of 6 and 12 mm was used as infill layer. The test was undertaken under CNL condition with 100 and 300 kPa of normal stress magnitudes. The microproperties of the proposed cohesive model were calibrated against the outcome of laboratory direct shear tests of cohesive soil, and the ability of the model in simulating the shear behaviour of infilled rock joints was examined. The experimental approach provided the macroscopic response of various infilled rock joints, while the proposed numerical framework supplied further insights into the shear mechanism and damage behaviour of cohesive contacts. The DEM simulations demonstrated a good agreement with the experimental counterparts. The following conclusions are drawn from the numerical simulations and experimental results presented in this chapter:

- The shear mechanism of clay-infilled rock joints demonstrated four distinct stages in the laboratory which could be successfully reproduced by the proposed cohesive model. Stage I characterised the linear elastic behaviour of the soil in which the shear stress of the infilled rock joint was rapidly increased. During stage II, the rock joint exhibited a nonlinear hardening response, which was due to softening response and/or damage of the cohesive contacts. It is believed that the enhancement of asperity interference also contributed to this nonlinear hardening behaviour. The infilled rock joint then demonstrated its peak shear strength, following with a gradual softening response (stage III). Finally, the progressive frictional response of DEM particles gave rise to a residual shear stress of the infilled rock joint.
- The infilled rock joints with t/a ratio of 1.3 and 2.7 exhibited a dilative response after an initial compression. For higher t/a ratio this behaviour was not seen, and the rock joint presented a normal displacement similar to soil.
- A more pronounced softening response was achieved for specimens with high normal stress magnitudes. The bond-break in these specimens was also severe.
- The localised shear zones started to grow when the transition from elastic behaviour to nonlinear elastic response occurred, which largely extended during the shearing process as a result of contact damage.
- The laboratory and numerical observations of infilled rock joints revealed that the asperity interference was the dominant contributing factor in governing the shear mechanism of specimens with $t/a < 2.67$. The results showed that for $t/a = 4.25$ the shear mechanism was mainly controlled by infill material.

In chapter 6, the proposed cohesive model was used to develop a cohesive GBM framework to simulate the fracture behaviour of polycrystalline rocks. The model was calibrated with the experimental results of uniaxial compression, and Brazilian tensile tests carried out on Aue granite. The cohesive GBM showed good capability in reproducing the macroscopic behaviour of polycrystalline rock. The numerical framework then was used to simulate the shear behaviour of rock joints with different surface roughness under both CNL and CNS condition. The following conclusions are drawn from the numerical experiments carried out in this chapter:

- The numerical results showed that it is necessary to incorporate the softening response in the force-displacement law of DEM contacts since PBM and SJM are not capable of reproducing the post-peak response in TPB test of Adelaide black granite.
- The numerical results indicated that the main reason for asperity damage was the formation of intra-grain micro-cracks leading to grain crushing in critical asperity areas. This grain crushing was believed to be the consequence of large shear displacement along the fracture surface.
- The CNS direct shear tests revealed that the behaviour of rock joint was mainly controlled by grain crushing, the extent of which increased with increasing the applied initial stress magnitude and JRC.
- The dilative response of rock joints increased with increasing JRC and reduced with increasing the initial stress magnitude.
- The GBMs exhibited a higher peak shear strength under CNS condition which was due to a progressive increase in the value of applied normal stress.
- The grain crushing was more severe in rough rock joints (i.e. high JRC), which was attributed to higher resistance of these rock joints against the shear process.

In chapter 7, the proposed cohesive model was employed to simulate the fracture and mechanical behaviour of pre-cracked Barre granite using GBM framework. The microstructural properties of Barre granite were incorporated in the GBM algorithm to build the synthetic polycrystalline rocks. The geometrical configuration of pre-existing flaws was imported into PFC2D to generate pre-cracked GBM specimens. The proposed GBM framework provided a cost-effective approach that helps in the determination of crack initiation, damage, and peak axial stresses of crystalline rocks, which are essential in the development of constitutive models (i.e. continuum models) that can be used for large scale

simulation of mining structures. The new findings and key observations of this chapter are as follows:

- The stress-strain curves and fracture patterns obtained from numerical simulations showed that the proposed GBM has the ability to mimic the fracture and mechanical properties of pre-cracked polycrystalline rock. In particular, crack initiation, damage, and the numerical framework very well captured peak axial stresses. The fracture patterns also showed a close agreement with the experimental counterparts.
- The GBM simulations showed that by increasing the inclination angle of pre-existing cracks the peak axial stress increases. The similar trend was also exhibited for crack initiation and crack damage stresses.
- The numerical modelling revealed that the initial macroscopic tensile cracks initiated from the tips and surfaces of flaws and that they extended upwards towards the loading plates.
- The numerical results showed that the formation of macroscopic tensile fractures in the flaw region was the consequence of bond-break in the smooth joint model contacts (i.e. inter-grain contacts).
- The initiation of intra-grain micro-crack started before reaching the crack damage stress.
- The accumulation and linkage of inter- and intra-grain micro-cracks resulted in the coalescence of pre-existing flaws.
- The micro-cracking features, based on the current GBM approach, such as the extension and development of macroscopic cracks due to the progressive coalescence of inter- and intra-grain micro-cracks, which eventually led to the formation of macroscopic fracturing zones around the flaw tips and the coalescence of pre-existing cracks, will serve as guidelines for future experimental tests.

In chapter 8, the proposed GBM framework was employed to investigate the influence of grain size on the damage and fracture behaviour of pre-cracked polycrystalline rock. The GBM is able to handle any number of mineral types with different range of grain sizes. Three different grain size scenarios namely fine, medium, and coarse, were selected to generate the GBM specimens. The new findings and key contributions obtained from this investigation are as follows:

- The strength of GBMs increased significantly with an increase in mineral size for both single- and double-flawed specimens.
- The first macroscopic tensile fracture initiated from the tip or surface of the pre-existing cracks, which attributed to bond-break in SJM contacts.
- The pattern of fracture distribution was controlled by the meandering path created by the random distribution of minerals in the GBM, which generated a jagged-shaped tensile crack around the flaws.
- The micro-cracks initiated from the middle portion of the flaw in GBMs with low-flaw inclination angle. However, for GBMs with higher inclinations angles, the tensile cracks shifted towards the flaw tips.
- In coarse grain size, GBMs mineral size controlled the location of flaw tip leading to initiation of tensile cracks around the tip area.
- The bridging zone in large grain size GBMs was generated inside orthoclase which gave rise to the dominant effect of this mineral on the macroscopic fracture pattern in the inner tip areas.
- The numerical observations revealed that both grain size and flaw inclination angle influence the macroscopic response of pre-cracked polycrystalline rocks.
- Monitoring the damage evolution of the GBM showed that by increasing the inclination angle, the number of intra-grain micro-cracks and softening contacts in the bridging area reduced significantly, and the coalescence occurred as a result of inter-grain micro-crack propagation.

9.2 Recommendations for future work

Based on the results obtained in the present thesis, the recommendation for future numerical simulations are outlined as follows:

- The shear behaviour of bolted rock joints subjected to pull-shear load should be investigated using a range of JRC values.
- The presented SPST technique emphasised the pretension behaviour of fully grouted rock bolt under zero confining stress. The pretension response of fully grouted rock bolt subjected to confining pressure should be investigated in future research.
- One of the main factors that influence the increment of normal stress under CNS condition is CNS stiffness. The shear behaviour of bolted rock joints under various ranges of CNS stiffness should be considered.

- In this thesis, the failure of rock bolt was neglected and only the failure response of rock joint, grout, and bolt-grout interface were emphasised. It is required, however, to take into account the effect of bolt rupture on the shear behaviour of bolted rock joints.
- In the numerical investigations of infilled rock joints under direct shear, rock joint profiles were idealised as triangular saw-toothed asperities. In future work, natural rock joint profiles with different waviness and unevenness should be considered.
- Only a single peak shear mechanism was observed for infilled rock joints, without asperity damage. The cohesive DEM framework should be modified in future numerical research to observe more shear mechanisms (e.g. double peak shear mechanism, asperity damage mechanism, and etc.).
- In cohesive GBM approach, a random generation scheme was used to generate the microstructure of polycrystalline rock. In future research, advanced technologies such as digital image processing techniques should be employed to incorporate the realistic microstructural properties into the numerical specimens.
- In present numerical simulations rock bolts installed in rock-like material, which may limit the application of the proposed approach to certain rock types. In future studies, the cohesive GBM approach should be used to investigate the effect of rock bolt on asperity damage and shear behaviour of polycrystalline rocks.
- Application of the proposed cohesive GBM to study the scale effect on different rock joint profiles and different polycrystalline rock is recommended for future study.
- The application of 2D GBM approach in understanding complicated 3D phenomena (e.g. the effect of grain geometry on the micro-cracking response, the influence of the 3D distribution of mineral on macroscopic fracture pattern, and etc.) is limited. Developing an extended 3D GBM approach is recommended in future research for analysis of the failure mechanism of polycrystalline rocks.
- In polycrystalline rock, there is a decline in axial strength once the peak strength is achieved, and the magnitude of this strength reduction depends highly on the level of lateral confining pressure. In future research, the effect of confining pressure should be taken into account to investigate the fracture behaviour of polycrystalline rock more accurately.

References

Akesson U, Hansson J, Stigh J. (2004) Characterisation of microcracks in the Bohus granite, western Sweden, caused by uniaxial cyclic loading. *Engineering Geology 72*: 131-142. doi: https://doi.org/10.1016/j.enggeo.2003.07.001

Aziz N, Jalalifar H, Concalves J. (2006) Bolt surface configurations and load transfer mechanism. *In: Proceedings of the 7th Coal Operators' Conference, Wollongong, NSW, Australia, 236-244. URL: http://ro.uow.edu.au/coal/51/*.

Bahaaddini M (2014). *Numerical study of the mechanical behaviour of rock joints and non-persistent jointed rock masses.* Ph.D. thesis, The University of New South Wales, Sydney, Australia.

Bahaaddini M, Hagan PC, Mitra R, Hebblewhite BK. (2014) Scale effect on the shear behaviour of rock joints based on a numerical study. *Engineering Geology 181*: 212-223. doi: https://doi.org/10.1016/j.enggeo.2014.07.018

Bahaaddini M, Hagan PC, Mitra R, Hebblewhite BK. (2015) Parametric Study of Smooth Joint Parameters on the Shear Behaviour of Rock Joints. *Rock Mechanics and Rock Engineering 48*: 923-940. doi: 10.1007/s00603-014-0641-6

Bahaaddini M, Sharrock G, Hebblewhite B. (2013) Numerical direct shear tests to model the shear behaviour of rock joints. *Computers and Geotechnics 51*: 101-115.

Bahrani N, Kaiser PK. (2016) Numerical investigation of the influence of specimen size on the unconfined strength of defected rocks. *Computers and Geotechnics 77*: 56-67. doi: https://doi.org/10.1016/j.compgeo.2016.04.004

Bahrani N, Kaiser PK, Valley B. (2014) Distinct element method simulation of an analogue for a highly interlocked, non-persistently jointed rockmass. *International Journal of Rock Mechanics and Mining Sciences 71*: 117-130. doi: https://doi.org/10.1016/j.ijrmms.2014.07.005

Bahrani N, Valley B, Kaiser PK, Pierce M (2011). *Evaluation of PFC2D Grain-Based Model For Simulation of Confinement-Dependent Rock Strength Degradation And Failure Processes*. Paper presented at the 45th U.S. Rock Mechanics / Geomechanics Symposium, San Francisco, California. https://doi.org/

Bandis SC, Lumsden AC, Barton NR. (1983) Fundamentals of rock joint deformation. *International Journal of Rock Mechanics and Mining Sciences & Geomechanics Abstracts 20*: 249-268. doi: https://doi.org/10.1016/0148-9062(83)90595-8

Barton N. (1974) A review of the shear strength of filled discontinuities in rock.

Barton N, Choubey V. (1977) The shear strength of rock joints in theory and practice. *Rock mechanics 10*: 1-54. doi: 10.1007/BF01261801

Bawden W, Dube S, Hyett A. (1994) A laboratory study on the capacity of fully grouted cable bolts subjected to combined axial and lateral loads. *Report to URIF, Kingston, Ontario, Canada, pp 1-11.*

Bewick RP, Kaiser PK, Bawden WF (2014a). *Shear rupture – two case studies from a deep mine*. Paper presented at the Seventh International Conference on Deep and High Stress Mining, Perth. https://papers.acg.uwa.edu.au/p/1410_45_Bewick/

Bewick RP, Kaiser PK, Bawden WF. (2014b) Shear rupture under constant normal stiffness boundary conditions. *Tectonophysics 634*: 76-90. doi: https://doi.org/10.1016/j.tecto.2014.07.016

Bewick RP, Kaiser PK, Bawden WF, Bahrani N. (2014c) DEM Simulation of Direct Shear: 1. Rupture Under Constant Normal Stress Boundary Conditions. *Rock Mechanics and Rock Engineering 47*: 1647-1671. doi: 10.1007/s00603-013-0490-8

Bjurstrom S (1974). *Shear strength of hard rock joint reinforced by grouted untensioned bolts.* In: Proceedings of the International Congress of Rock Mechanics, Denver, pp 1194-1199.

Bobet A, Einstein HH. (1998) Fracture coalescence in rock-type materials under uniaxial and biaxial compression. *International Journal of Rock Mechanics and Mining Sciences 35*: 863-888. doi: https://doi.org/10.1016/S0148-9062(98)00005-9

Bobet A, Einstein HH. (2011) Tunnel reinforcement with rockbolts. *Tunnelling and Underground Space Technology 26*: 100-123. doi: https://doi.org/10.1016/j.tust.2010.06.006

Bobet A, Fakhimi A, Johnson S, Morris J, Tonon F, Yeung MR. (2009) Numerical Models in Discontinuous Media: Review of Advances for Rock Mechanics Applications. *Journal of Geotechnical and Geoenvironmental Engineering 135*: 1547-1561. doi: 10.1061/(ASCE)GT.1943-5606.0000133

Brace WF, Bombolakis EG. (1963) A note on brittle crack growth in compression. *Journal of Geophysical Research 68*: 3709-3713. doi: 10.1029/JZ068i012p03709

Brace WF, Paulding BW, Scholz C. (1966) Dilatancy in the fracture of crystalline rocks. *Journal of Geophysical Research 71*: 3939-3953. doi: doi:10.1029/JZ071i016p03939

Brady BHG, Brown ET. (2004) Rock Mechanics for Underground Mining. *3rd ed. Netherlands: Kluwer Academic Publishers.*

Cao C, Ren T, Cook C, Cao Y. (2014) Analytical approach in optimising selection of rebar bolts in preventing rock bolting failure. *International Journal of Rock Mechanics and Mining Sciences 72*: 16-25. doi: https://doi.org/10.1016/j.ijrmms.2014.04.026

Cao R-h, Cao P, Lin H, Pu C-z, Ou K. (2016) Mechanical Behavior of Brittle Rock-Like Specimens with Pre-existing Fissures Under Uniaxial Loading: Experimental Studies and Particle Mechanics Approach. *Rock Mechanics and Rock Engineering 49*: 763-783. doi: 10.1007/s00603-015-0779-x

Chen J, Li K, Chang K-J, Sofia G, Tarolli P. (2015) Open-pit mining geomorphic feature characterisation. *International Journal of Applied Earth Observation and Geoinformation 42*: 76-86. doi: https://doi.org/10.1016/j.jag.2015.05.001

Chen N, Zhang X, Jiang Q, Feng X, Wei W, Yi B. (2018) Shear Behavior of Rough Rock Joints Reinforced by Bolts. *International Journal of Geomechanics 18*: 04017130. doi: 10.1061/(ASCE)GM.1943-5622.0001048

Chen Y, Li C. (2015a) Influences of Loading Condition and Rock Strength to the Performance of Rock Bolts. *Geotechnical Testing Journal 38*: 208-218. doi: https://doi.org/10.1520/GTJ20140033

Chen Y, Li CC. (2015b) Performance of fully encapsulated rebar bolts and D-Bolts under combined pull-and-shear loading. *Tunnelling and Underground Space Technology 45*: 99-106. doi: https://doi.org/10.1016/j.tust.2014.09.008

Cho N, Martin CD, Sego DC. (2007) A clumped particle model for rock. *International Journal of Rock Mechanics and Mining Sciences 44*: 997-1010. doi: https://doi.org/10.1016/j.ijrmms.2007.02.002

Cottrell B, Tatone BSA, Grasselli G (2010). *Joint Replica Shear Testing And Roughness Degradation Measurement*. Paper presented at the ISRM International Symposium - EUROCK 2010, Lausanne, Switzerland. https://doi.org/

Crosky A, Smith B, Hebblewhite B. (2003) Failure of rockbolts in underground mines in Australia. *Practical Failure Analysis 3*: 70-78. doi: 10.1007/BF02717427

Cundall P. (1971) A computer model for simulating progressive, large scale movements in blocky rock systems. International Symposium on Rock Fracture. Nancy, France.

Cundall P, Strack O. (1979) A discrete numerical model for granular assemblies *Geotechnique 29*: 47-65.

Cundall PA, Hart RD. (1992) Numerical modeling of discontinua. *Engineering Computations 9*: 101-113. doi: 10.1108/eb023851

D'Ignazio M, Länsivaara T. (2015) Shear bands in soft clays: strain-softening behavior in finite element method. *Rakenteiden mekaniikka 48*: 83-98.

Deb D, Das KC. (2014) A new doubly enriched finite element for modelling grouted bolt crossed by rock joint. *International Journal of Rock Mechanics and Mining Sciences 70*: 47-58. doi: https://doi.org/10.1016/j.ijrmms.2014.04.004

Deb D, Gujjala YK. (2018) Extended finite element procedures for analysis of bolt crossing multiple intersecting rock joints. *International Journal of Rock Mechanics and Mining Sciences 107*: 249-260. doi: https://doi.org/10.1016/j.ijrmms.2018.04.052

Dey A (2001). *Shear behaviour of fully grouted bolts under constant normal stiffness condition.* Ph.D. thesis, University of Wollongong, NSW, Australia

Diaz MB, Jung SG, Zhuang L, Kim KY, Yeom S, Shin HS (2016). *Effect of Cleavage Anisotropy on Hydraulic Fracturing Behavior of Pocheon Granite*. Paper presented at the 50th U.S. Rock Mechanics/Geomechanics Symposium, Houston, Texas.

Diederichs MS (2000). *Instability of hard rockmasses, the role of tensile damage and relaxation.* UWSpace. Retrieved from http://hdl.handle.net/10012/480

Diederichs MS. (2007) The 2003 Canadian Geotechnical Colloquium: Mechanistic interpretation and practical application of damage and spalling prediction criteria for deep tunnelling. *Canadian Geotechnical Journal 44*: 1082-1116. doi: 10.1139/T07-033

Dight PM, Chiu HK. (1981) Prediction of shear behaviour of joints using profiles. *International Journal of Rock Mechanics and Mining Sciences & Geomechanics Abstracts 18*: 369-386. doi: https://doi.org/10.1016/0148-9062(81)90002-4

Dulacka H. (1972) Dowel action of reinforcing crossing cracks in concrete. *American Concrete Institute Journal*: 754-757.

Duriez J, Darve F, Donzé F. (2011) A discrete modeling-based constitutive relation for infilled rock joints. *Int J Rock Mech Min Sci 48*: 458-468.

Farahmand K, Vazaios I, Diederichs MS, Vlachopoulos N. (2018) Investigating the scale-dependency of the geometrical and mechanical properties of a moderately jointed rock using a synthetic rock mass (SRM) approach. *Computers and Geotechnics 95*: 162-179. doi: https://doi.org/10.1016/j.compgeo.2017.10.002

Feng S, Liu X, Chen H, Zhao T. (2018) Micro-mechanical analysis of geomembrane-sand interactions using DEM. *Computers and Geotechnics 94*: 58-71.

Ferrero AM. (1995) The shear strength of reinforced rock joints. *International Journal of Rock Mechanics and Mining Sciences & Geomechanics Abstracts 32*: 595-605. doi: https://doi.org/10.1016/0148-9062(95)00002-X

Gao F, Kang H. (2017) Experimental Study on the Residual Strength of Coal Under Low Confinement. *Rock Mechanics and Rock Engineering 50*: 285-296. doi: 10.1007/s00603-016-1120-z

Gao F, Stead D, Elmo D. (2016) Numerical simulation of microstructure of brittle rock using a grain-breakable distinct element grain-based model. *Computers and Geotechnics 78*: 203-217. doi: https://doi.org/10.1016/j.compgeo.2016.05.019

Goodman RE. (1995) Block theory and its application. *Géotechnique 45*: 383-423. doi: 10.1680/geot.1995.45.3.383

Goris J. (1990) Laboratory evaluation of cable bolt supports: evaluation of supports using conventional cables (RI9308). Report of investigations, Bureau of Mines, USA, pp 1-23.

Grasselli G. (2005) 3D Behaviour of bolted rock joints: experimental and numerical study. *International Journal of Rock Mechanics and Mining Sciences 42*: 13-24. doi: https://doi.org/10.1016/j.ijrmms.2004.06.003

Grasselli G, Egger P. (2003) Constitutive law for the shear strength of rock joints based on three-dimensional surface parameters. *International Journal of Rock Mechanics and Mining Sciences 40*: 25-40. doi: https://doi.org/10.1016/S1365-1609(02)00101-6

Gui YL, Zhao ZY, Ji J, Wang XM, Zhou KP, Ma SQ. (2016) The grain effect of intact rock modelling using discrete element method with Voronoi grains. *Géotechnique Letters 6*: 136-143. doi: 10.1680/jgele.16.00005

Gutiérrez-Ch JG, Senent S, Melentijevic S, Jimenez R. (2018) Distinct element method simulations of rock-concrete interfaces under different boundary conditions. *Engineering Geology 240*: 123-139. doi: https://doi.org/10.1016/j.enggeo.2018.04.017

Haas C. (1976) Shear resistance of rock bolts. Soc Min Eng 260: pp 32–41.

Hagan P, Chen J, Saydam S (2014). *The load transfer mechanism of fully grouted cable bolts under laboratory tests.* In: Proceedings of the 14th Coal Operators' Conference, Wollongong, NSW, Australia, pp 137-146.

Hajiabdolmajid V, Kaiser P. (2003) Brittleness of rock and stability assessment in hard rock tunneling. *Tunnelling and Underground Space Technology 18*: 35-48. doi: https://doi.org/10.1016/S0886-7798(02)00100-1

Hajiabdolmajid V, Kaiser PK, Martin CD. (2002) Modelling brittle failure of rock. *International Journal of Rock Mechanics and Mining Sciences 39*: 731-741. doi: https://doi.org/10.1016/S1365-1609(02)00051-5

Harrison J, Hudson J. (2000) Part 2: illustrative workable examples. In: S.arkk.a P, Eloranta P, editors. Oxford: Pergamon.

Harrison JP, Hudson JA. (1977) Engineering rock mechanics: An introduction to the principles, Oxford: Pergamon.

He L, An XM, Zhao XB, Zhao ZY, Zhao J. (2018) Development of a Unified Rock Bolt Model in Discontinuous Deformation Analysis. *Rock Mechanics and Rock Engineering 51*: 827-847. doi: 10.1007/s00603-017-1341-9

He L, An XM, Zhao ZY. (2015) Fully Grouted Rock Bolts: An Analytical Investigation. *Rock Mechanics and Rock Engineering 48*: 1181-1196. doi: 10.1007/s00603-014-0610-0

Hofmann H, Babadagli T, Yoon JS, Zang A, Zimmermann G. (2015a) A grain based modeling study of mineralogical factors affecting strength, elastic behavior and micro fracture development during compression tests in granites. *Engineering Fracture Mechanics 147*: 261-275. doi: 10.1016/j.engfracmech.2015.09.008

Hofmann H, Babadagli T, Zimmermann G. (2015b) A grain based modeling study of fracture branching during compression tests in granites. *International Journal of Rock Mechanics and Mining Sciences 77*: 152-162. doi: https://doi.org/10.1016/j.ijrmms.2015.04.008

Huang Z, Broch E, Lu M. (2002) Cavern roof stability—mechanism of arching and stabilization by rockbolting. *Tunnelling and Underground Space Technology 17*: 249-261. doi: https://doi.org/10.1016/S0886-7798(02)00010-X

Hutchinson D, Diederichs M. (1996) Cable bolting in underground mines. Richmond, British Columbia: BiTech Publishers.

Hyett AJ, Bawden WF, Macsporran GR, Moosavi M. (1995) A constitutive law for bond failure of fully-grouted cable bolts using a modified hoek cell. *International Journal of Rock*

Mechanics and Mining Sciences & Geomechanics Abstracts 32: 11-36. doi: https://doi.org/10.1016/0148-9062(94)00018-X
Indraranta B, Welideniya H, Brown E. (2005) A shear strength model for idealised infilled joints under constant normal stiffness *Géotechnique 55*: 215-226.
Indraratna B, Haque A. (2000) Shear behaviour of rock joints. *Rotterdam: A.A. Balkema*.
Indraratna B, Haque A, Aziz N. (1999) Shear behaviour of idealized infilled joints under constant normal stiffness. *Géotechnique 49*: 331-355. doi: 10.1680/geot.1999.49.3.331
Indraratna B, Jayanathan M. (2005) Measurement of pore water pressure of clay-infilled rock joints during triaxial shearing. *Géotechnique 55*: 759-764. doi: 10.1680/geot.2005.55.10.759
Indraratna B, Oliveira D, Brown E, Assis A. (2010a) Effect of soil-infilled joints on the stability of rock wedges formed in a tunnel roof. *International Journal of Rock Mechanics and Mining Sciences 47*: 739-751.
Indraratna B, Oliveira DAF, Brown ET, de Assis AP. (2010b) Effect of soil–infilled joints on the stability of rock wedges formed in a tunnel roof. *International Journal of Rock Mechanics and Mining Sciences 47*: 739-751. doi: https://doi.org/10.1016/j.ijrmms.2010.05.006
Indraratna B, Premadasa W, Brown ET. (2013) Shear behaviour of rock joints with unsaturated infill. *Géotechnique 63*: 1356-1360. doi: 10.1680/geot.12.P.065
Indraratna B, Premadasa W, Brown ET, Gens A, Heitor A. (2014) Shear strength of rock joints influenced by compacted infill. *International Journal of Rock Mechanics and Mining Sciences 70*: 296-307. doi: https://doi.org/10.1016/j.ijrmms.2014.04.019
Indraratna B, Thirukumaran S, Brown ET, Zhu S-P. (2015) Modelling the Shear Behaviour of Rock Joints with Asperity Damage Under Constant Normal Stiffness. *Rock Mechanics and Rock Engineering 48*: 179-195. doi: 10.1007/s00603-014-0556-2
Indraratna B, Welideniya HS (2003). *Shear Behaviour of Graphite Infilled Joints Based On Constant Normal Stiffness (CNS) Test Conditions*. Paper presented at the 10th ISRM Congress, Sandton, South Africa. https://doi.org/
Itasca. (2016) PFC manual, version 5.0, Minneapolis.
ITASCA Consulting Group I. (2008) UDEC and 3DEC manual.
Ivanović A, Neilson RD. (2009) Modelling of debonding along the fixed anchor length. *International Journal of Rock Mechanics and Mining Sciences 46*: 699-707. doi: https://doi.org/10.1016/j.ijrmms.2008.09.008
Jaeger JC. (1971) Friction of Rocks and Stability of Rock Slopes. *Géotechnique 21*: 97-134. doi: 10.1680/geot.1971.21.2.97
Jahanian H, Sadaghiani MH. (2015) Experimental Study on the Shear Strength of Sandy Clay Infilled Regular Rough Rock Joints. *Rock Mechanics and Rock Engineering 48*: 907-922. doi: 10.1007/s00603-014-0643-4
Jalalifar H, Aziz N. (2010) Experimental and 3D Numerical Simulation of Reinforced Shear Joints. *Rock Mechanics and Rock Engineering 43*: 95-103. doi: 10.1007/s00603-009-0031-7
Jalalifar H, Aziz N, Hadi M. (2006) The effect of surface profile, rock strength and pretension load on bending behaviour of fully grouted bolts. *Geotechnical & Geological Engineering 24*: 1203-1227. doi: 10.1007/s10706-005-1340-6
Jin-feng Z, Peng-hao Z. (2019) Analytical model of fully grouted bolts in pull-out tests and in situ rock masses. *International Journal of Rock Mechanics and Mining Sciences 113*: 278-294. doi: https://doi.org/10.1016/j.ijrmms.2018.11.015
Jin J, Cao P, Chen Y, Pu C, Mao D, Fan X. (2017) Influence of single flaw on the failure process and energy mechanics of rock-like material. *Computers and Geotechnics 86*: 150-162. doi: https://doi.org/10.1016/j.compgeo.2017.01.011

Jing L. (2003) A review of techniques, advances and outstanding issues in numerical modelling for rock mechanics and rock engineering. *International Journal of Rock Mechanics and Mining Sciences 40*: 283-353. doi: https://doi.org/10.1016/S1365-1609(03)00013-3

Kalteziotis N (1981). *Progressive instability in strain-softening soil with particular reference to undrained bearing capacity*. Ph.D. thesis, University of Surrey, United Kingdom.

Kazerani T, Yang ZY, Zhao J. (2012) A Discrete Element Model for Predicting Shear Strength and Degradation of Rock Joint by Using Compressive and Tensile Test Data. *Rock Mechanics and Rock Engineering 45*: 695-709. doi: 10.1007/s00603-011-0153-6

Kazerani T, Zhao J. (2010) Micromechanical parameters in bonded particle method for modelling of brittle material failure. *International Journal for Numerical and Analytical Methods in Geomechanics 34*: 1877-1895. doi: 10.1002/nag.884

Khazaei C, Hazzard J, Chalaturnyk R. (2015) Damage quantification of intact rocks using acoustic emission energies recorded during uniaxial compression test and discrete element modeling. *Computers and Geotechnics 67*: 94-102. doi: https://doi.org/10.1016/j.compgeo.2015.02.012

Khosravi A, Serej AD, Mousavi SM, Haeri SM. (2016) Effect of hydraulic hysteresis and degree of saturation of infill materials on the behavior of an infilled rock fracture. *International Journal of Rock Mechanics and Mining Sciences 88*: 105-114. doi: https://doi.org/10.1016/j.ijrmms.2016.07.001

Kılıc A, Yasar E, Celik AG. (2002) Effect of grout properties on the pull-out load capacity of fully grouted rock bolt. *Tunnelling and Underground Space Technology 17*: 355-362. doi: https://doi.org/10.1016/S0886-7798(02)00038-X

Kranz RL. (1983) Microcracks in rocks: A review. *Tectonophysics 100*: 449-480. doi: https://doi.org/10.1016/0040-1951(83)90198-1

Ladanyi B, Archambault G (1969). *Simulation Of Shear Behavior Of A Jointed Rock Mass*. Paper presented at the The 11th U.S. Symposium on Rock Mechanics (USRMS), Berkeley, California.

Ladanyi B, Archambault G. (1977) Shear strength and Deformability of Filled Indented Joints. In: Proceedings of the 1st International Symposium on the Geotechnics of Structurally Complex Formations, Capri, Italy, September 1977, pp 317–326.

Lama R (1978). *Influence of clay infillings on shear behaviour of joints*. Paper presented at the 3rd Congress of Int. Assoc. Eng. Geol, Madrid.

Lan H, Martin CD, Hu B. (2010) Effect of heterogeneity of brittle rock on micromechanical extensile behavior during compression loading. *Journal of Geophysical Research: Solid Earth 115*. doi: doi:10.1029/2009JB006496

Le LA, Nguyen GD, Bui HH, Sheikh AH, Kotousov A, Khanna A. (2017) Modelling jointed rock mass as a continuum with an embedded cohesive-frictional model. *Engineering Geology 228*: 107-120. doi: https://doi.org/10.1016/j.enggeo.2017.07.011

Le LA, Nguyen GD, Bui HH, Sheikh AH, Kotousov A, Khanna A. (2018) Localised failure mechanism as the basis for constitutive modelling of geomaterials. *International Journal of Engineering Science accepted & in press.*

Li CC. (2010) Field Observations of Rock Bolts in High Stress Rock Masses. *Rock Mechanics and Rock Engineering 43*: 491-496. doi: 10.1007/s00603-009-0067-8

Li CC. (2012) Performance of D-bolts Under Static Loading. *Rock Mechanics and Rock Engineering 45*: 183-192. doi: 10.1007/s00603-011-0198-6

Li CC. (2017) Principles of rockbolting design. *Journal of Rock Mechanics and Geotechnical Engineering 9*: 396-414. doi: https://doi.org/10.1016/j.jrmge.2017.04.002

Li D, Masoumi H, Hagan PC, Saydam S. (2019a) Experimental and analytical study on the mechanical behaviour of cable bolts subjected to axial loading and constant normal

stiffness. *International Journal of Rock Mechanics and Mining Sciences 113*: 83-91. doi: https://doi.org/10.1016/j.ijrmms.2018.11.011

Li D, Masoumi H, Saydam S, Hagan PC. (2018a) Mechanical Characterisation of Modified Cable Bolts Under Axial Loading: An Extensive Parametric Study. *Rock Mechanics and Rock Engineering 51*: 2895-2910. doi: 10.1007/s00603-018-1475-4

Li L, Hagan PC, Saydam S (2014). *Tensile Stress Mobilization Along a Rock Bolt Under Shear Load*. Paper presented at the 3rd ISRM Young Scholars Symposium on Rock Mechanics, Xi'an, China. https://doi.org/

Li L, Hagan PC, Saydam S, Hebblewhite B. (2016a) Shear resistance contribution of support systems in double shear test. *Tunnelling and Underground Space Technology 56*: 168-175. doi: https://doi.org/10.1016/j.tust.2016.03.011

Li L, Hagan PC, Saydam S, Hebblewhite B, Li Y. (2016b) Parametric Study of Rockbolt Shear Behaviour by Double Shear Test. *Rock Mechanics and Rock Engineering 49*: 4787-4797. doi: 10.1007/s00603-016-1063-4

Li X (2016). *Study of cable bolt shear strength characteristics for ground reinforcement in mines.* Ph.D. thesis, University of Wollongong, Australia.

Li X, Aziz N, Mirzaghorbanali A, Nemcik J. (2016c) Behavior of Fiber Glass Bolts, Rock Bolts and Cable Bolts in Shear. *Rock Mechanics and Rock Engineering 49*: 2723-2735. doi: 10.1007/s00603-015-0907-7

Li X, Yang G, Nemcik J, Mirzaghorbanali A, Aziz N. (2019b) Numerical investigation of the shear behaviour of a cable bolt in single shear test. *Tunnelling and Underground Space Technology 84*: 227-236. doi: https://doi.org/10.1016/j.tust.2018.11.016

Li XF, Li HB, Zhao J. (2019c) The role of transgranular capability in grain-based modelling of crystalline rocks. *Computers and Geotechnics 110*: 161-183. doi: https://doi.org/10.1016/j.compgeo.2019.02.018

Li XF, Zhang QB, Li HB, Zhao J. (2018b) Grain-Based Discrete Element Method (GB-DEM) Modelling of Multi-scale Fracturing in Rocks Under Dynamic Loading. *Rock Mechanics and Rock Engineering 51*: 3785-3817. doi: 10.1007/s00603-018-1566-2

Li Y, Oh J, Mitra R, Hebblewhite B. (2016d) A constitutive model for a laboratory rock joint with multi-scale asperity degradation. *Computers and Geotechnics 72*: 143-151. doi: https://doi.org/10.1016/j.compgeo.2015.10.008

Li Y, Oh J, Mitra R, Hebblewhite B. (2016e) Experimental Studies on the Mechanical Behaviour of Rock Joints with Various Openings. *Rock Mechanics and Rock Engineering 49*: 837-853. doi: 10.1007/s00603-015-0781-3

Lin C (2017). *Investigation of shear stress behaviour of compacted Kaolin clay mixed with salt solution.* M.Sc Thesis, The University of Queensland, Australia.

Lin H, Xiong Z, Liu T, Cao R, Cao P. (2014) Numerical simulations of the effect of bolt inclination on the shear strength of rock joints. *International Journal of Rock Mechanics and Mining Sciences 66*: 49-56. doi: https://doi.org/10.1016/j.ijrmms.2013.12.010

Lisjak A, Grasselli G. (2014) A review of discrete modeling techniques for fracturing processes in discontinuous rock masses. *Journal of Rock Mechanics and Geotechnical Engineering 6*: 301-314. doi: https://doi.org/10.1016/j.jrmge.2013.12.007

Liu G, Cai M, Huang M. (2018) Mechanical properties of brittle rock governed by micro-geometric heterogeneity. *Computers and Geotechnics*. doi: https://doi.org/10.1016/j.compgeo.2017.11.013

Lorig L, Brady B (1984, 1984). *A hybrid computational scheme for excavation and support design in jointed rock media.* In: Proceeding of the Symposium Design and Performance of Underground Excavations, Cambridge, pp 105-112.

Lu Y, Wang L, Li Z, Sun H. (2017) Experimental Study on the Shear Behavior of Regular Sandstone Joints Filled with Cement Grout. *Rock Mechanics and Rock Engineering 50*: 1321-1336. doi: 10.1007/s00603-016-1154-2

Ma S, Aziz N, Nemcik J, Mirzaghorbanali A. (2017) The Effects of Installation Procedure on Bond Characteristics of Fully Grouted Rock Bolts. *Geotechnical Testing Journal 40*: 846-857. doi: https://doi.org/10.1520/GTJ20160239

Mahabadi OK, Lisjak A, Munjiza A, Grasselli G. (2012) Y-Geo: New Combined Finite-Discrete Element Numerical Code for Geomechanical Applications. *International Journal of Geomechanics 12*: 676-688. doi: 10.1061/(ASCE)GM.1943-5622.0000216

Marenče M, Swoboda G. (1995) Numerical model for rock bolts with consideration of rock joint movements. *Rock Mechanics and Rock Engineering 28*: 145-165. doi: 10.1007/BF01020149

Martin CD. (1993) The strength of massive Lac du Bonnet granite around underground openings. *Ph.D. thesis, University of Manitoba, Winnipeg, Canada*.

Mayer JM, Stead D. (2017) Exploration into the causes of uncertainty in UDEC Grain Boundary Models. *Computers and Geotechnics 82*: 110-123. doi: https://doi.org/10.1016/j.compgeo.2016.10.003

McHugh E, Signer S. (1999) Roof bolt response to shear stress: laboratory analysis. https://www.cdc.gov/niosh/mining/userfiles/works/pdfs/rbrss.pdf.

McKenzie R, King B. (2015) Megabolt shear testing program. Presented at the NSW Underground Geotechnical Society Preliminary Program, Sydney, NSW, Australia.

Meng F, Wong LNY, Zhou H, Wang Z. (2018) Comparative study on dynamic shear behavior and failure mechanism of two types of granite joint. *Engineering Geology 245*: 356-369. doi: https://doi.org/10.1016/j.enggeo.2018.09.005

Miller JT (2008). *Crack Coalescence in Granite.* MSc Thesis, Massachusetts Institute of Technology.

Miller JT, Einstein HH (2008). *Crack Coalescence Tests on Granite*. Paper presented at the The 42nd U.S. Rock Mechanics Symposium (USRMS), San Francisco, California.

Moosavi M, Bawden WF, Hyett AJ. (2002) Mechanism of bond failure and load distribution along fully grouted cable-bolts. *Mining Technology 111*: 1-12. doi: 10.1179/mnt.2002.111.1.1

Moosavi M, Jafari A, Khosravi A. (2005) Bond of cement grouted reinforcing bars under constant radial pressure. *Cement and Concrete Composites 27*: 103-109. doi: https://doi.org/10.1016/j.cemconcomp.2003.12.002

Moradian Z, Einstein HH, Ballivy G. (2016) Detection of Cracking Levels in Brittle Rocks by Parametric Analysis of the Acoustic Emission Signals. *Rock Mechanics and Rock Engineering 49*: 785-800. doi: 10.1007/s00603-015-0775-1

Morgan SP, Johnson CA, Einstein HH. (2013) Cracking processes in Barre granite: fracture process zones and crack coalescence. *International Journal of Fracture 180*: 177-204. doi: 10.1007/s10704-013-9810-y

Mosher S, Berger RL, Anderson DE. (1975) Fracturing characteristics of two granites. *Rock mechanics 7*: 167-176. doi: 10.1007/BF01246723

Munoz H, Taheri A, Chanda EK. (2016) Pre-Peak and Post-Peak Rock Strain Characteristics During Uniaxial Compression by 3D Digital Image Correlation. *Rock Mechanics and Rock Engineering 49*: 2541-2554. doi: 10.1007/s00603-016-0935-y

Mylvaganam J (2007). *Shear behaviour of normally consolidated and overconsolidated infilled rock joints under undrained triaxial conditions.* Ph.D. thesis, University of Wollongong, Australia.

Nguyen NHT, Bui HH, Nguyen GD, Kodikara J. (2017a) A cohesive damage-plasticity model for DEM and its application for numerical investigation of soft rock fracture properties.

International Journal of Plasticity 98: 175-196. doi: https://doi.org/10.1016/j.ijplas.2017.07.008

Nguyen NHT, Bui HH, Nguyen GD, Kodikara J, Arooran S, Jitsangiam P. (2017b) A thermodynamics-based cohesive model for discrete element modelling of fracture in cemented materials. *International Journal of Solids and Structures 117*: 159-176. doi: https://doi.org/10.1016/j.ijsolstr.2017.03.027

Nicksiar M, Martin CD. (2014) Factors Affecting Crack Initiation in Low Porosity Crystalline Rocks. *Rock Mechanics and Rock Engineering 47*: 1165-1181. doi: 10.1007/s00603-013-0451-2

Oh J, Cording EJ, Moon T. (2015) A joint shear model incorporating small-scale and large-scale irregularities. *International Journal of Rock Mechanics and Mining Sciences 76*: 78-87. doi: https://doi.org/10.1016/j.ijrmms.2015.02.011

Oh J, Li Y, Mitra R, Canbulat I. (2017) A numerical study on dilation of a saw-toothed rock joint under direct shear. *Rock Mech Rock Eng 50*: 913–925.

Oliveira DAF, Indraratna B, Nemcik J. (2009) Critical review on shear strength models for soil-infilled joints. *Geomechanics and Geoengineering 4*: 237-244. doi: 10.1080/17486020903128564

Papaliangas T, Lumsden A, Hencher S, Manolopoulou S. (1990) Shear strength of modelled filled rock joints. *In: Proceedings of the International Symposium on Rock Joints, Loen, Norway, June 1990, pp 275–282*.

Parisio F, Tarokh A, Makhnenko R, Naumov D, Miao X-Y, Kolditz O, Nagel T. (2019) Experimental characterization and numerical modelling of fracture processes in granite. *International Journal of Solids and Structures 163*: 102-116. doi: https://doi.org/10.1016/j.ijsolstr.2018.12.019

Park J-W, Lee Y-K, Song J-J, Choi B-H. (2013) A Constitutive Model for Shear Behavior of Rock Joints Based on Three-Dimensional Quantification of Joint Roughness. *Rock Mechanics and Rock Engineering 46*: 1513-1537. doi: 10.1007/s00603-012-0365-4

Park J-W, Song J-J. (2009) Numerical simulation of a direct shear test on a rock joint using a bonded-particle model. *International Journal of Rock Mechanics and Mining Sciences 46*: 1315-1328. doi: https://doi.org/10.1016/j.ijrmms.2009.03.007

Patton FD (1966). *Multiple Modes of Shear Failure In Rock*. Paper presented at the 1st ISRM Congress, Lisbon, Portugal.

Peng J, Wong LNY, Teh CI. (2017) Effects of grain size-to-particle size ratio on micro-cracking behavior using a bonded-particle grain-based model. *International Journal of Rock Mechanics and Mining Sciences 100*: 207-217. doi: https://doi.org/10.1016/j.ijrmms.2017.10.004

Phien-Wej N, Shrestha U, Rantucci G. (1990) Effect of infill thickness on shear behaviour of rock joints. *In: Proceedings of the International Symposium on Rock Joints, Loen, Norway, June 1990, pp 289–294*.

Pierce M, Cundall P, Potyondy D, Mas I (2007). *A synthetic rock mass model for jointed rock.* In: Rock mechanics: meeting society's challenges and demands. 1st Canada–US rock mechanics symposium, London: Vancouver, pp.

Plesha ME. (1987) Constitutive models for rock discontinuities with dilatancy and surface degradation. *International Journal for Numerical and Analytical Methods in Geomechanics 11*: 345-362. doi: doi:10.1002/nag.1610110404

Potyondy D. (2010a) A grain-based model for rock: Approaching the true microstructure. *In: Proc. Rock Mech. in the Nordic Countries, 10p*.

Potyondy D. (2010b) PFC2D Grain-Structure Generator. *PFC2D Example on Itasca website, Itasca Consulting Group, Inc., Minneapolis, MN, May 28.*

Potyondy D. (2012) FC2D flat-joint contact model. *Itasca Consulting Group Inc, Minneapolis*.

Potyondy D, Cundall P. (2004) A bonded-particle model for rock. *Int J Rock Mech Min Sci 41*: 1329-1364.
Potyondy DO. (2015) The bonded-particle model as a tool for rock mechanics research and application: current trends and future directions. *Geosystem Engineering 18*: 1-28. doi: 10.1080/12269328.2014.998346
Rasekh H, Aziz N, Mirza A, Nemcik J, Li X, Yang G, Khaleghparast S. (2017) Double Shear Testing of Cable Bolts with No Concrete Face Contacts. *Procedia Engineering 191*: 1169-1177. doi: https://doi.org/10.1016/j.proeng.2017.05.292
Rodríguez P, Arab PB, Celestino TB. (2016) Characterization of rock cracking patterns in diametral compression tests by acoustic emission and petrographic analysis. *International Journal of Rock Mechanics and Mining Sciences 83*: 73-85. doi: https://doi.org/10.1016/j.ijrmms.2015.12.017
Saadat M, Taheri A. (2019a) Modelling Micro-cracking Behaviour of Pre-cracked Granite Using Grain-Based Distinct Element Model. *Rock Mechanics and Rock Engineering*. doi: 10.1007/s00603-019-01862-0
Saadat M, Taheri A. (2019b) A numerical approach to investigate the effects of rock texture on the damage and crack propagation of a pre-cracked granite. *Computers and Geotechnics 111*: 89-111. doi: https://doi.org/10.1016/j.compgeo.2019.03.009
Shang J, Yokota Y, Zhao Z, Dang W. (2018a) DEM simulation of mortar-bolt interface behaviour subjected to shearing. *Construction and Building Materials 185*: 120-137. doi: https://doi.org/10.1016/j.conbuildmat.2018.07.044
Shang J, Zhao Z, Ma S. (2018b) On the shear failure of incipient rock discontinuities under CNL and CNS boundary conditions: Insights from DEM modelling. *Engineering Geology 234*: 153-166. doi: https://doi.org/10.1016/j.enggeo.2018.01.012
She C-X, Sun F-T. (2018) Study of the Peak Shear Strength of a Cement-Filled Hard Rock Joint. *Rock Mechanics and Rock Engineering 51*: 713-728. doi: 10.1007/s00603-017-1358-0
Shen Z, Jiang M, Thornton C. (2016) DEM simulation of bonded granular material. Part I: Contact model and application to cemented sand. *Computers and Geotechnics 75*: 192-209.
Shrivastava A, Rao K. (2013) Development of a Large-Scale Direct Shear Testing Machine for Unfilled and Infilled Rock Joints Under Constant Normal Stiffness Conditions. *Geotechnical Testing Journal 36*: 670-679. doi: https://doi.org/10.1520/GTJ20120155
Shrivastava AK, Rao KS. (2018) Physical Modeling of Shear Behavior of Infilled Rock Joints Under CNL and CNS Boundary Conditions. *Rock Mechanics and Rock Engineering 51*: 101-118. doi: 10.1007/s00603-017-1318-8
SIBELCO. (2019) Clay&Kaolin ,https://www.sibelco.com/materials/clay-kaolin/; 2019 [accessed 11 April 2019].
Sinha UN, Singh B. (2000) Testing of rock joints filled with gouge using a triaxial apparatus. *International Journal of Rock Mechanics and Mining Sciences 37*: 963-981. doi: https://doi.org/10.1016/S1365-1609(00)00030-7
Song G, Li W, Wang B, Ho SCM. (2017) A Review of Rock Bolt Monitoring Using Smart Sensors. *Sensors (Basel, Switzerland) 17*: 776. doi: 10.3390/s17040776
Song H, Duan Y, Yang J. (2010) Numerical simulation on bolted rock joint shearing performance. *Mining Science and Technology (China) 20*: 460-465. doi: https://doi.org/10.1016/S1674-5264(09)60226-X
Spang K, Egger P. (1990) Action of fully-grouted bolts in jointed rock and factors of influence. *Rock Mechanics and Rock Engineering 23*: 201-229. doi: 10.1007/BF01022954

Srivastava LP, Singh M. (2015) Effect of Fully Grouted Passive Bolts on Joint Shear Strength Parameters in a Blocky Mass. *Rock Mechanics and Rock Engineering 48*: 1197-1206. doi: 10.1007/s00603-014-0615-8

Stanchits S, Dresen G (2003). *Separation of Tensile and Shear Cracks Based on Acoustic Emission Analysis of Rock Fracture*. Paper presented at the In: Non-Destructive Testing in Civil Engineering (NDT-CE), International Symposium, Berlin; .

Taheri A, Tani K. (2008) Developing of an apparatus for down-hole triaxial tests in a rock mass. *Int J Rock Mech Min Sci 45*: 800-806.

Taheri A, Tani K. (2010) Assessment of the Stability of Rock Slopes by the Slope Stability Rating Classification System. *Rock Mechanics and Rock Engineering 43*: 321-333. doi: 10.1007/s00603-009-0050-4

Taheri A, Yfantidis N, Olivares C, Connelly B, Bastian T. (2016) Experimental Study on Degradation of Mechanical Properties of Sandstone Under Different Cyclic Loadings. *Geotechnical Testing Journal 39*: 673-687. doi: 10.1520/GTJ20150231

Tamás K. (2018) The role of bond and damping in the discrete element model of soil-sweep interaction. *Biosystems Engineering 169*: 57-70. doi: https://doi.org/10.1016/j.biosystemseng.2018.02.001

Tamás K, Jóri IJ, Mouazen AM. (2013) Modelling soil–sweep interaction with discrete element method. *Soil and Tillage Research 134*: 223-231. doi: https://doi.org/10.1016/j.still.2013.09.001

Tamás K, Kovács Á, Jóri IJ. (2016) The Evaluation of the Parallel Bond's Properties in DEM Modeling of Soils. *Periodica Polytechnica Mechanical Engineering 60*: 21-31. doi: https://doi.org/10.3311/PPme.8427

Tan X (2013). *Hydro-Mechanical Coupled Behavior of Brittle Rocks - Laboratory Experiments and Numerical Simulations.* Ph.D. thesis, Universität Bergakademie Freiberg, Germany.

Tang CA, Liu H, Lee PKK, Tsui Y, Tham LG. (2000) Numerical studies of the influence of microstructure on rock failure in uniaxial compression — Part I: effect of heterogeneity. *International Journal of Rock Mechanics and Mining Sciences 37*: 555-569. doi: https://doi.org/10.1016/S1365-1609(99)00121-5

Tao W, Chen C, Jun H, Ting R. (2017) Effect of bolt rib spacing on load transfer mechanism. *International Journal of Mining Science and Technology 27*: 431-434. doi: https://doi.org/10.1016/j.ijmst.2017.03.009

Tapponnier P, Brace WF. (1976) Development of stress-induced microcracks in Westerly Granite. *International Journal of Rock Mechanics and Mining Sciences & Geomechanics Abstracts 13*: 103-112. doi: https://doi.org/10.1016/0148-9062(76)91937-9

Tatone B (2014). *Investigating the evolution of rock discontinuity asperity degradation and void space morphology under direct shear test.* Ph.D. thesis, University of Toronto, Toronto, Canada.

Tavallali A, Vervoort A. (2010) Failure of Layered Sandstone under Brazilian Test Conditions: Effect of Micro-Scale Parameters on Macro-Scale Behaviour. *Rock Mechanics and Rock Engineering 43*: 641-653. doi: 10.1007/s00603-010-0084-7

Tembe S, Lockner DA, Wong T-F. (2010) Effect of clay content and mineralogy on frictional sliding behavior of simulated gouges: Binary and ternary mixtures of quartz, illite, and montmorillonite. *Journal of Geophysical Research: Solid Earth 115*. doi: doi:10.1029/2009JB006383

Thenevin I, Blanco-Martín L, Hadj-Hassen F, Schleifer J, Lubosik Z, Wrana A. (2017) Laboratory pull-out tests on fully grouted rock bolts and cable bolts: Results and lessons

learned. *Journal of Rock Mechanics and Geotechnical Engineering 9*: 843-855. doi: https://doi.org/10.1016/j.jrmge.2017.04.005

Thirukumaran S, Indraratna B. (2016) A review of shear strength models for rock joints subjected to constant normal stiffness. *Journal of Rock Mechanics and Geotechnical Engineering 8*: 405-414. doi: https://doi.org/10.1016/j.jrmge.2015.10.006

Thirukumaran S, Indraratna B, Brown ET, Kaiser PK. (2016) Stability of a Rock Block in a Tunnel Roof Under Constant Normal Stiffness Conditions. *Rock Mechanics and Rock Engineering 49*: 1587-1593. doi: 10.1007/s00603-015-0770-6

Thomas R. (2012) The load transfer properties of post–groutable cable bolts used in Australia coal industry. *In: Proceedings of the 31st International Conference on Ground Control in Mining, Morgantown, WV, 1-10*.

Tuğrul A, Zarif IH. (1999) Correlation of mineralogical and textural characteristics with engineering properties of selected granitic rocks from Turkey. *Engineering Geology 51*: 303-317. doi: https://doi.org/10.1016/S0013-7952(98)00071-4

Ulusay R. (2015) The ISRM suggested methods for rock characterization, testing and monitoring: 2007-2014. *15*: 47–48.

Vlachopoulos N, Cruz D, Forbes B. (2018) Utilizing a novel fiber optic technology to capture the axial responses of fully grouted rock bolts. *Journal of Rock Mechanics and Geotechnical Engineering 10*: 222-235. doi: https://doi.org/10.1016/j.jrmge.2017.11.007

Wagner JF. (2013). Chapter 9 - Mechanical Properties of Clays and Clay Minerals. In F. Bergaya & G. Lagaly (Eds.), *Developments in Clay Science* (Vol. 5, pp. 347-381): Elsevier.

Wang G, Zhang Y, Jiang Y, Liu P, Guo Y, Liu J, Ma M, Wang K, Wang S. (2018) Shear Behaviour and Acoustic Emission Characteristics of Bolted Rock Joints with Different Roughnesses. *Rock Mechanics and Rock Engineering*. doi: 10.1007/s00603-018-1438-9

Wang X, Cai M. (2018) Modeling of brittle rock failure considering inter- and intra-grain contact failures. *Computers and Geotechnics 101*: 224-244. doi: https://doi.org/10.1016/j.compgeo.2018.04.016

Wang X, Kang H, Gao F. (2019) Numerical investigation on the shear behavior of jointed coal mass. *Computers and Geotechnics 106*: 274-285. doi: https://doi.org/10.1016/j.compgeo.2018.11.005

Wasantha PLP, Ranjith PG, Zhao J, Shao SS, Permata G. (2015) Strain Rate Effect on the Mechanical Behaviour of Sandstones with Different Grain Sizes. *Rock Mechanics and Rock Engineering 48*: 1883-1895. doi: 10.1007/s00603-014-0688-4

Wong LNY, Einstein HH. (2009a) Crack Coalescence in Molded Gypsum and Carrara Marble: Part 1. Macroscopic Observations and Interpretation. *Rock Mechanics and Rock Engineering 42*: 475-511. doi: 10.1007/s00603-008-0002-4

Wong LNY, Einstein HH. (2009b) Systematic evaluation of cracking behavior in specimens containing single flaws under uniaxial compression. *International Journal of Rock Mechanics and Mining Sciences 46*: 239-249. doi: https://doi.org/10.1016/j.ijrmms.2008.03.006

Wong LNY, Peng J, Teh CI. (2018) Numerical investigation of mineralogical composition effect on strength and micro-cracking behavior of crystalline rocks. *Journal of Natural Gas Science and Engineering 53*: 191-203. doi: https://doi.org/10.1016/j.jngse.2018.03.004

Wu C, Chen X, Hong Y, Xu R, Yu D. (2018a) Experimental Investigation of the Tensile Behavior of Rock with Fully Grouted Bolts by the Direct Tensile Test. *Rock Mechanics and Rock Engineering 51*: 351-357. doi: 10.1007/s00603-017-1307-y

Wu X, Jiang Y, Li B. (2018b) Influence of Joint Roughness on the Shear Behaviour of Fully Encapsulated Rock Bolt. *Rock Mechanics and Rock Engineering 51*: 953-959. doi: 10.1007/s00603-017-1365-1

Wu XY, Baud P, Wong T-f. (2000) Micromechanics of compressive failure and spatial evolution of anisotropic damage in Darley Dale sandstone. *International Journal of Rock Mechanics and Mining Sciences 37*: 143-160. doi: https://doi.org/10.1016/S1365-1609(99)00093-3

Yang X-X, Qiao W-G. (2018) Numerical investigation of the shear behavior of granite materials containing discontinuous joints by utilizing the flat-joint model. *Computers and Geotechnics 104*: 69-80. doi: https://doi.org/10.1016/j.compgeo.2018.08.014

Yang ZY, Chiang DY. (2000) An experimental study on the progressive shear behavior of rock joints with tooth-shaped asperities. *International Journal of Rock Mechanics and Mining Sciences 37*: 1247-1259. doi: https://doi.org/10.1016/S1365-1609(00)00055-1

Yazici S, Kaiser PK. (1992) Bond strength of grouted cable bolts. *International Journal of Rock Mechanics and Mining Sciences & Geomechanics Abstracts 29*: 279-292. doi: https://doi.org/10.1016/0148-9062(92)93661-3

Yin P, Wong RHC, Chau KT. (2014) Coalescence of two parallel pre-existing surface cracks in granite. *International Journal of Rock Mechanics and Mining Sciences 68*: 66-84. doi: https://doi.org/10.1016/j.ijrmms.2014.02.011

Yokota Y, Zhao Z, Nie W, Date K, Iwano K, Okada Y. (2018) Experimental and Numerical Study on the Interface Behaviour Between the Rock Bolt and Bond Material. *Rock Mechanics and Rock Engineering*. doi: 10.1007/s00603-018-1629-4

Yokota Y, Zhao Z, Shang J, Nie W, Date K, Iwano K, Okada Y. (2019) Effect of bolt configuration on the interface behaviour between a rock bolt and bond material: A comprehensive DDA investigation. *Computers and Geotechnics 105*: 116-128. doi: https://doi.org/10.1016/j.compgeo.2018.09.017

Yoon JS, Zang A, Stephansson O. (2012) Simulating fracture and friction of Aue granite under confined asymmetric compressive test using clumped particle model. *International Journal of Rock Mechanics and Mining Sciences 49*: 68-83. doi: https://doi.org/10.1016/j.ijrmms.2011.11.004

Yoshinaka R, Sakaguchi S, Shimizu T, Arai H, Kato E (1987). *Experimental Study On the Rock Bolt Reinforcement In Discontinuous Rocks*. Paper presented at the 6th ISRM Congress, Montreal, Canada. https://doi.org/

Zang A. (1997) Akustische Emissionen beim Sprödbruch von Gestein. *Habilitationsschrift, Scientific Technical Report STR97/19.*

Zang A, Wagner FC, Stanchits S, Janssen C, Dresen G. (2000) Fracture process zone in granite. *Journal of Geophysical Research: Solid Earth 105*: 23651-23661. doi: 10.1029/2000JB900239

Zeng W, Yang S-Q, Tian W-L. (2018) Experimental and numerical investigation of brittle sandstone specimens containing different shapes of holes under uniaxial compression. *Engineering Fracture Mechanics 200*: 430-450. doi: https://doi.org/10.1016/j.engfracmech.2018.08.016

Zhang B, Li S, Xia K, Yang X, Zhang D, Wang S, Zhu J. (2016) Reinforcement of rock mass with cross-flaws using rock bolt. *Tunnelling and Underground Space Technology 51*: 346-353. doi: https://doi.org/10.1016/j.tust.2015.10.007

Zhang X-P, Wong LNY. (2012) Cracking Processes in Rock-Like Material Containing a Single Flaw Under Uniaxial Compression: A Numerical Study Based on Parallel Bonded-Particle Model Approach. *Rock Mechanics and Rock Engineering 45*: 711-737. doi: 10.1007/s00603-011-0176-z

Zhang X-P, Wong LNY. (2013) Crack Initiation, Propagation and Coalescence in Rock-Like Material Containing Two Flaws: a Numerical Study Based on Bonded-Particle Model Approach. *Rock Mechanics and Rock Engineering 46*: 1001-1021. doi: 10.1007/s00603-012-0323-1

Zhang Y, Wong LNY. (2018) A review of numerical techniques approaching microstructures of crystalline rocks. *Computers & Geosciences 115*: 167-187. doi: https://doi.org/10.1016/j.cageo.2018.03.012

Zhang Y, Wong LNY, Chan KK. (2019) An Extended Grain-Based Model Accounting for Microstructures in Rock Deformation. *Journal of Geophysical Research: Solid Earth 124*: 125-148. doi: 10.1029/2018jb016165

Zhao T. (2017) Introduction to Discrete Element Method. In: Coupled DEM-CFD Analyses of Landslide-Induced Debris Flows. Springer, Singapore

Zhao Z. (2013) Gouge Particle Evolution in a Rock Fracture Undergoing Shear: a Microscopic DEM Study. *Rock Mechanics and Rock Engineering 46*: 1461-1479. doi: 10.1007/s00603-013-0373-z

Zhou J, Lan H, Zhang L, Yang D, Song J, Wang S. (2019) Novel grain-based model for simulation of brittle failure of Alxa porphyritic granite. *Engineering Geology 251*: 100-114. doi: https://doi.org/10.1016/j.enggeo.2019.02.005

Zhou J, Zhang L, Pan Z, Han Z. (2017) Numerical studies of interactions between hydraulic and natural fractures by Smooth Joint Model. *Journal of Natural Gas Science and Engineering 46*: 592-602. doi: https://doi.org/10.1016/j.jngse.2017.07.030

Zhou X-P, Zhang J-Z, Wong LNY. (2018) Experimental Study on the Growth, Coalescence and Wrapping Behaviors of 3D Cross-Embedded Flaws Under Uniaxial Compression. *Rock Mechanics and Rock Engineering 51*: 1379-1400. doi: 10.1007/s00603-018-1406-4

Zhu W, Jing H, Yang L, Pan B, Su H. (2018) Strength and deformation behaviors of bedded rock mass under bolt reinforcement. *International Journal of Mining Science and Technology 28*: 593-599. doi: https://doi.org/10.1016/j.ijmst.2018.03.006

Zou DHS, Cheng J, Yue R, Sun X. (2010) Grout quality and its impact on guided ultrasonic waves in grouted rock bolts. *Journal of Applied Geophysics 72*: 102-106. doi: https://doi.org/10.1016/j.jappgeo.2010.07.006

Appendix A (Paper 1)

Effect of contributing parameters on the behaviour of a bolted rock joint subjected to combined pull-and-shear loading: A DEM approach

Saadat M, Taheri A. (2019) Effect of Contributing Parameters on the Behaviour of a Bolted Rock Joint Subjected to Combined Pull-and-Shear Loading: A DEM Approach. *Rock Mechanics and Rock Engineering*. https://doi: 10.1007/s00603-019-01921-6

Statement of Authorship

Title of Paper	Effect of contributing parameters on the behaviour of a bolted rock joint subjected to combined pull-and-shear loading
Publication Status	✓ Published ☐ Accepted for Publication ☐ Submitted for Publication ☐ Unpublished and Unsubmitted work written in manuscript style
Publication Details	Saadat M, Taheri A. (2019) Effect of contributing parameters on the behaviour of a bolted rock joint subjected to combined pull-and-shear loading: A DEM approach Rock Mechanics and Rock Engineering doi: 10.1007/s00603-019-01921-6

Principal Author

Name of Principal Author (Candidate)	Mahdi Saadat		
Contribution to the Paper	Developed the cohesive DEM framework Developed the numerical SPST scheme Conducted the numerical modelling of bolted rock joints Analysed the experimental and numerical results Wrote the entire manuscript		
Overall percentage (%)	80%		
Certification:	This paper reports on original research I conducted during the period of my Higher Degree by Research candidature and is not subject to any obligations or contractual agreements with a third party that would constrain its inclusion in this thesis. I am the primary author of this paper.		
Signature		Date	07 August 2019

Co-Author Contributions

By signing the Statement of Authorship, each author certifies that:

i. the candidate's stated contribution to the publication is accurate (as detailed above);
ii. permission is granted for the candidate in include the publication in the thesis; and

iii. the sum of all co-author contributions is equal to 100% less the candidate's stated contribution.

Name of Co-Author	Dr Abbas Taheri		
Contribution to the Paper	Supervision of the technical work and SPTS scheme, revision of the manuscript		
Signature		Date	07 August 2019

End of the document

Rock Mechanics and Rock Engineering
https://doi.org/10.1007/s00603-019-01921-6

ORIGINAL PAPER

Effect of Contributing Parameters on the Behaviour of a Bolted Rock Joint Subjected to Combined Pull-and-Shear Loading: A DEM Approach

Mahdi Saadat[1] · **Abbas Taheri**[1]

Received: 31 March 2019 / Accepted: 17 July 2019

Abstract

The mechanical performance of fully grouted rock bolts is essential in the stability of underground excavations in jointed rock masses. This research implements a new cohesive contact model in distinct element codes (PFC2D) to investigate the fracturing response of rock-like and grout material, as well as the bolt–grout interface. The results are compared in detail with experimental observations. The proposed modelling approach, used in conjunction with the distinct element method (DEM), successfully predicted the behaviour of grout failure and the bolt–grout interface's shear response. We then developed a novel numerical, stepwise pull-and-shear test (SPST) scheme to further analyse the mechanical behaviour of bolted rock joints subjected to simultaneous pull–shear loading. The cohesive DEM framework proposed in this paper was used to carry out the SPST scheme numerically. The mechanism involved in enhancing the shear strength of bolted rock joint was determined by monitoring the $\sigma_{\mathrm{n}}^{\mathrm{i}}$ and its corresponding contact chain force network during the pull-out test. The influence of pretension stress, the rig angle of the bolt profile, and the constant normal stiffness (CNS) condition are assessed systematically. In particular, the pretension stress magnitude at which the synthetic rock bolting system exhibits the highest shear resistance is identified. The findings from this research highlight the sensitivity of bolted rock joints to the simultaneous pull-and-shear loading, boundary conditions, and bolt–grout interface configurations.

Keywords Bolted rock joint · Combined pull-and-shear load · DEM approach · Cohesive contact model · CNS condition

Abbreviations

CCM	Cohesive contact model
CNL	Constant normal load
CNS	Constant normal stiffness
CSJM	Cohesive smooth-joint model
DEM	Distinct element method
DLL	Dynamic link library
JRC	Joint roughness coefficient
SJM	Smooth joint model
SPST	Stepwise pull-and-shear test

List of Symbols

$\boldsymbol{u}^{\mathrm{p}}$	Relative displacement
$\boldsymbol{u}^{\mathrm{e}}$	Relative elastic displacement
$\boldsymbol{u}^{\mathrm{p}}$	Relative plastic displacement
σ_{n}	Contact normal stress
σ_{s}	Contact shear stress
k_{n}^{0}	Contact normal stiffness
k_{s}^{0}	Contact shear stiffness
$u_{\mathrm{n}}^{\mathrm{p}}$	Total normal plastic displacement
$u_{\mathrm{s}}^{\mathrm{p}}$	Total shear plastic displacement
F	Yield function
C	Cohesion of contact
C^{0}	Initial cohesive of contact
μ	Friction coefficient of contact
κ	Softening parameter
u^{p}	Accumulated plastic displacement of contact
D	Damage parameter
G	Plastic potential
β	Dilation coefficient of contact
$d\lambda$	Plastic multiplier
$\sigma_{\mathrm{n}}^{\mathrm{trial}}$	Trial normal stress of contact
$\sigma_{\mathrm{s}}^{\mathrm{trial}}$	Trial shear stress of contact
F^{trial}	Trial yield function
$\bar{A}$	Cross-sectional area of contact
$\bar{R}$	Radius of DEM particle
$\overline{E_{\mathrm{c}}}$	Elastic modulus of contact

✉ Mahdi Saadat
mahdi.saadat@adelaide.edu.au

[1] School of Civil, Environmental and Mining Engineering, The University of Adelaide, Adelaide, Australia

Published online: 26 July 2019

L	Contact length
k^*	Normal-to-shear stiffness ratio of contact
υ	Poisson's ratio
$r_{\max}$	Maximum radius of DEM particle
$r_{\min}$	Minimum radius of DEM particle
α	Rib angle
$\bar{E}_{c,CCM}$	CCM elastic modulus
C^0_{CCM}	CCM initial cohesion
μ_{CCM}	CCM friction coefficient
β_{CCM}	CCM dilation coefficient
k^*_{CCM}	CCM normal-to-shear stiffness ratio
κ_{CCM}	CCM-softening parameter
D_{CCM}	CCM damage parameter
$k^{\mathrm{sj}}_{\mathrm{n}}$	Normal stiffness of SJM contact
$k^{\mathrm{sj}}_{\mathrm{s}}$	Shear stiffness of SJM contact
μ^{sj}	Friction coefficient of SJM contact
$k^0_{\mathrm{s,CSJM}}$	CSJM shear stiffness
$k^0_{\mathrm{n,CSJM}}$	CSJM normal stiffness
C^0_{CSJM}	CSJM initial cohesion
μ_{CSJM}	CSJM friction coefficient
β_{CSJM}	CSJM dilation coefficient
κ_{CSJM}	CSJM-softening parameter
D_{CSJM}	CSJM damage parameter
λ	Wavelength of idealised rock joint
σ^0_{n}	Applied normal stress in CNL direct shear test
σ_{c}	Rock compressive strength
$\sigma^{\mathrm{i}}_{\mathrm{n}}$	Induced normal stress on rock joint interface
$\mathrm{d}\sigma_{\mathrm{n}}$	Change in the normal stress during CNS direct shear test
k^{cns}	CNS stiffness
$\mathrm{d}\delta_{\mathrm{n}}$	Change in the normal displacement of rock joint
$\sigma^{\mathrm{u}}_{\mathrm{n}}$	Updated normal stress in CNS direct shear test
$\sigma^{\mathrm{total}}_{\mathrm{n}}$	Applied normal stress in pull-and-shear test

1 Introduction

The natural discontinuities in rock masses have a profound impact on the stability and safety of underground excavations. Any damage due to roof fall or the failure of rock slopes can hinder mining activities, and result in penalties being imposed on mining companies. In this regard, an appropriate evaluation of rock joint shear behaviour is critical when designing both surface and underground mining structures.

Fully grouted rock bolt has been widely used as a reinforcement element in underground mining due to its economic benefits and advancement in the bolt system technology (He et al. 2018; Huang et al. 2002; Jin-feng and Peng-hao 2019). The fully grouted rock bolt also fully utilises the bolt strength (He et al. 2018). Rock bolting system forms a self-supporting structure in rock mass through supporting loosened rock blocks, improving shear resistance of rock joints (He et al. 2018; Ma et al. 2017), and restraining rock mass deformation (Chen and Li 2015b). The load transfer capacity of fully grouted rock bolts is largely controlled by the shear strength of the bolt–grout interface and the mechanical interlocking between the grout and the rock bolt ribs (Cao et al. 2014; Li et al. 2019; Ma et al. 2017; Shang et al. 2018a). Pull-out testing is commonly used to study the load transfer mechanism of fully grouted rock bolt (Jin-feng and Peng-hao 2019). However, in field conditions, the failure of rock bolts occurs due to a combination of both pull-out and shear forces (Li et al. 2016b). Therefore, understanding the failure mechanism of bolted rock joint under such a mixing loading condition is useful for rock support system design (Chen and Li 2015b; Li 2010). The behaviour of a bolted rock joint subjected to combined pull–shear load is depicted in Fig. 1.

Several parameters can influence the mechanical behaviour of bolted rock joints. These include boundary conditions imposed by the surrounding rock block, the rib angle of the rebar bolt, the surface roughness of the rock joint, the confining pressure applied on the rock joint profile, the presence of infill material inside the rock joint, and so on. In conventional laboratory investigations, the mechanical behaviour of rock joints is usually investigated under a constant normal load/stress (CNL) boundary condition, where the applied normal stress on the rock joint profile is constant. However, in underground mining, the unstable rock block is restricted by neighbouring rock blocks; the applied normal stress is not constant, and the analysis of the rock joint requires a constant normal stiffness (CNS) condition (Bewick et al. 2014a; Indraranta et al. 2005; Indraratna and Welideniya 2003; Shang et al. 2018b; Thirukumaran and Indraratna 2016; Thirukumaran et al. 2016).

Many scientists have carried out laboratory investigations to study the mechanical shear resistance of bolted rock joints (Grasselli 2005; Haas 1976; Jalalifar and Aziz 2010b; Jalalifar et al. 2006; Li et al. 2016a; McHugh and Signer 1999). Different researchers have conducted a variety of laboratory investigations to study the influence of some important factors on the shear behaviour of bolted rock joints, including bolt type (Chen and Li 2015a, b; Grasselli 2005; Haas 1976; Li 2012; Rasekh et al. 2017), rock bolt diameter (Ferrero 1995; Spang and Egger 1990; Vlachopoulos et al. 2018), rock bolt surface profile (Jalalifar and Aziz 2010b; Jalalifar et al. 2006), inclination angle of the bolt (Bjurstrom 1974; Chen and Li 2015a, b; Dight and Chiu 1981; Feng et al. 2018; Haas 1976; Li et al. 2016a; Spang and Egger 1990; Yoshinaka et al. 1987), pretention force (Jalalifar and Aziz 2010b; Jalalifar et al. 2006; Li et al. 2016b), grout properties (Kılıc et al. 2002; Zou et al. 2010), rock joint surface roughness (Wang et al. 2018; Wu et al. 2018; Yoshinaka et al. 1987), number of rock bolts (Srivastava and Singh 2015), CNS condition (Dey 2001), and combined pull-and-shear

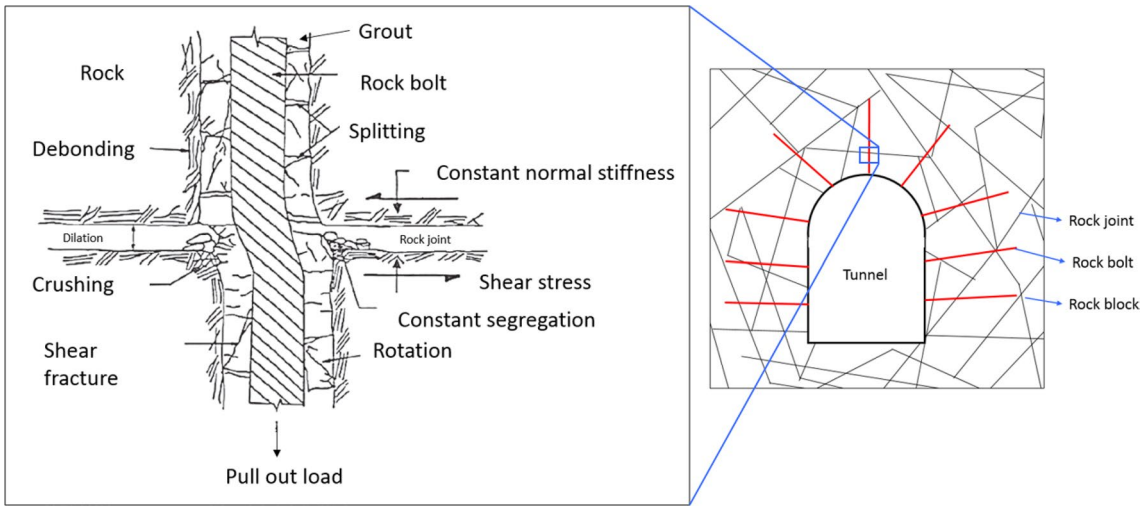

Fig. 1 Mechanical behaviour of bolted rock joint subjected to a combined pull–shear load [inspired after Indraratna and Haque (2000)]

loading (Chen and Li 2015a, b). Recently, Wu et al. (2018), Wang et al. (2018), and Chen et al. (2018) conducted a laboratory experiment to study the behaviour of bolted rock joints, including natural rock joint profiles. Despite the fact that the above-mentioned research highlighted the most important shear mechanisms of bolted rock joints, it suffers from some issues. First, the influence of the CNS boundary condition was neglected in the majority of the above-mentioned studies, which can restrict the application of those researches to structures with CNL conditions. Second, the influence of combined pull–shear loading was not studied, which may increase the uncertainty in the results obtained. Chen and Li (2015b) designed a laboratory apparatus to study the shear behaviour of rock bolt by conducting combined pull-and shear loading on the bolting system, but they neglected the influence of pretension and surface roughness.

It has been recognized that the debonding failure of the bolt–grout interface is the primary cause of damage in fully grouted rock bolts (Shang et al. 2018a). Understanding the bolt–grout interfacial debonding process and its subsequent bolt–grout shear behaviour, however, is not readily achievable in the laboratory environment. Previous experimental investigations revealed that pretension load (i.e., pull-out load) influences the shear resistance of the rock bolt (Gilbert et al. 2015; Jalalifar and Aziz 2010a, b). Mirzaghorbanali et al. (2017) studied the influence of pretension load on the shear strength of cable bolts, and concluded that the shear strength of the bolts at peak shear load increased by increasing the pretension load. Their laboratory apparatus, however, could not consider the effects of surface roughness and boundary conditions (e.g., CNS). The laboratory experiments of Jalalifar et al. (2006) showed that the pretension load contributed to the enhancement of the shear resistance of the bolted joint. Various investigations have been carried out to determine the influence of pretension on the overall shear performance of bolted rock joints (e.g., Mirzaghorbanali et al. (2017)), but the role of rib angles and CNS conditions is still unclear. From the perspective of practical applications (Fig. 1), more research is required to understand the shear mechanism of rock joints subjected to a combined pull–shear load. It is necessary for practical designers in mining projects to understand the point at which the magnitude of the pretension stress exhibits the bolted rock joint's ultimate shear performance.

Although laboratory testing is the most common approach for rock bolting investigation, setting up combined pull–shear load tests take a considerable amount of resources. This is why numerical tools have been widely applied to model the failure behaviour of rock joints. Recently, some scholars conducted experimental and numerical direct shear tests to investigate the debonding failure mechanism of the bolt–grout interface (Shang et al. 2018a; Yokota et al. 2018, 2019), and highlighted the influence of the rib angle on the shear strength of the bolt–grout interface. Discrete-based numerical methods such as discrete element method (DEM) (Cundall and Strack 1979) are promising in terms of mimicking the failure behaviour of brittle rocks (Bewick et al. 2014b; Gao and Kang 2017; Hofmann et al. 2015b; Lisjak and Grasselli 2014) and rock mass (Bahaaddini et al. 2013; Gutiérrez-Ch et al. 2018). Shang et al. (2018a) used DEM to mimic the debonding failure behaviour of the bolt–grout interface and the fracture response of grout material. In this study, grout material demonstrated significant deformability and softening response at the macroscopic scale (Shang et al. 2018a), which was attributed to its micromechanical structure. The DEM investigations of Shang et al. (2018a) revealed that the flat-joint model (FJM),

which is a DEM-based contact model (Potyondy 2012) available in commercial DEM codes (PFC2D) (Itasca Consulting Group Inc 2016), is incapable of reproducing the softening behaviour of grout material during the post-peak stage of uniaxial compression tests. They concluded that the FJM suppressed the rotation of DEM particles after bond break, which led to an abrupt failure of the DEM specimen. In addition, the FJM contacts return zero fracture energy responses at the onset of failure, which in turn contributes to the sudden failure of the DEM specimen. Thus, a brittle macroscopic response will be observed during the post-peak stage, which is not inherently desirable compared to the softening behaviour of experimental specimens. The laboratory results also showed that the samples including smooth bolt–grout interfaces exhibited a gradual softening behaviour under shearing (Shang et al. 2018a). Therefore, the smooth-joint model (SJM), which is a widely used DEM interface model (Bahaaddini et al. 2013; Gutiérrez-Ch et al. 2018; Hofmann et al. 2015b; Shang et al. 2018a; Zhou et al. 2017), needs to be augmented by cohesive-damage formulation to characterise effectively the failure mechanism of the bolt–grout interface.

This study employs a novel DEM-based cohesive contact model proposed by Saadat and Taheri (2019) that couples damage mechanics and plasticity theory in both modes I and II to simulate fracture behaviour of grout material and the bolt–grout interface in a better way. The proposed cohesive DEM framework features an exponential decay damage function that considers the influence of both normal and shear stresses. Thus, it inhibits the abrupt contact failure that enhances the macroscopic softening response of the DEM model. The proposed contact model was also incorporated in the numerical framework of the SJM to handle the cohesive behaviour of the bolt–grout interface. The newly proposed interface model is called cohesive SJM (CSJM). This study validates the proposed model's ability to capture the fracture behaviour of grout and the bolt–grout interface by uniaxial compression and direct shear tests. In addition, the proposed modelling method was employed to simulate the asperity degradation of idealised saw-toothed rock joints. This paper compares the experimental and numerical results to observe the accuracy of DEM simulations. To further demonstrate the potential of the proposed cohesive DEM framework for characterising the mechanical behaviour of bolted rock joints subjected to a combined pull–shear load, we developed a stepwise pull–shear test (SPST) scheme. This scheme investigates the influence of pretension load, rib angle, and CNS boundary condition on the ultimate shear resistance of rock joints. The proposed cohesive modelling method and SPST approach provides new insights into the shear behaviour of bolted rock joints, which is an extremely arduous task to achieve in laboratory.

2 Distinct Element-Based Cohesive Model

In the present study, a new cohesive, contact model (CCM) developed by Saadat and Taheri (2019) was employed for simulating the fracture behaviour of rock-like and grout-like materials as well as the shear behaviour of bolt–grout interface contacts. There are various DEM-based cohesive models available in the literature (e.g., Le et al. 2017, 2018; Nguyen et al. 2017a; b) that can be used for simulating cohesive contact behaviour. However, in the new cohesive DEM framework, we reduced the number of micro-mechanical properties, because it allows us to make the calibration procedure more straightforward. In addition, a simple cohesive contact model reduces the computational demand.

In the proposed contact model (Saadat and Taheri 2019), the relative displacement $\boldsymbol{u}\ (u_{\mathrm{n}}, u_{\mathrm{s}})$ of the DEM contacts is decomposed into elastic and plastic components, to account for reversible and irreversible displacements:

$$\boldsymbol{u} = \boldsymbol{u}^{\mathrm{e}} + \boldsymbol{u}^{\mathrm{p}}. \tag{1}$$

The contact normal and shear stresses are linked to their corresponding relative displacements. They can be calculated by

$$\sigma_{\mathrm{n}} = k_{\mathrm{n}}^{0}\left(u_{\mathrm{n}} - u_{\mathrm{n}}^{\mathrm{p}}\right) \tag{2}$$

$$\sigma_{\mathrm{s}} = k_{\mathrm{s}}^{0}\left(u_{\mathrm{s}} - u_{\mathrm{s}}^{\mathrm{p}}\right), \tag{3}$$

where σ_{n} and σ_{s} are normal and shear stresses in the bonding contacts; u_{n} and $u_{\mathrm{n}}^{\mathrm{p}}$ are the total and plastic normal displacements; u_{s} and $u_{\mathrm{s}}^{\mathrm{p}}$ are the total and plastic shear displacements; and k_{n}^{0} and k_{s}^{0} are the normal and shear stiffnesses, respectively.

The following yield function that takes into account the mixed-mode failure of DEM contacts is proposed to identify the yield point at which the contacts enter their softening stage:

$$F\left(\sigma_{\mathrm{n}}, \sigma_{\mathrm{s}}, C\right) = \sigma_{\mathrm{s}} + \mu\sigma_{\mathrm{n}} - C = 0, \tag{4}$$

where μ is the friction coefficient of the contact and C is defined as

$$C = C^{0}\mathrm{e}^{-\kappa u^{\mathrm{p}}}. \tag{5}$$

In Eq. 5, C^{0} is the initial bond cohesion, κ is the softening parameter, and u^{p} is the contact's accumulated plastic displacement, which can be calculated from its increments, defined as

$$\mathrm{d}u^{\mathrm{p}} = \sqrt{\left(\mathrm{d}u_{\mathrm{n}}^{\mathrm{p}}\right)^{2} + \left(\mathrm{d}u_{\mathrm{s}}^{\mathrm{p}}\right)^{2}}. \tag{6}$$

A damage parameter ($0 \le D \le 1$) can be defined to measure the degree of damage in the cohesive contacts:

$$D = \frac{C^{0} - C}{C^{0}} = 1 - \mathrm{e}^{-\kappa u^{\mathrm{p}}}. \tag{7}$$

The damage parameter introduced in Eq. 7 is included in the implementation algorithm, which enabled PFC2D to demonstrate the damage response of the model as a graphical output feature. When the contact exhibits no failure, the damage parameter takes a value of $D = 0.0$; a completely damaged contact returns $D = 1.0$. During the softening stage, the associative damage response of the contact will be $0 < D < 1$..

Simulating the dilation response at the microscopic level in DEM modelling requires the microstructural features of the physical material in the model to be incorporated, which is a difficult task to achieve (Nguyen et al. 2017a). Instead of this, we propose a dilatancy parameter that accounts for the dilation effect of the cohesive bonds, using the following non-associative flow rule:

$$G(\sigma_n, \sigma_s) = \sigma_s + \beta\sigma_n, \tag{8}$$

where β is the dilation coefficient. Consequently, the flow rule of incremental displacement can be expressed as

$$du_n^p = d\lambda \frac{\partial G}{\partial \sigma_n} \tag{9}$$

$$du_s^p = d\lambda \frac{\partial G}{\partial \sigma_s}, \tag{10}$$

where $d\lambda \geq 0$ is the plastic multiplier. Figure 2 illustrates the behaviour of the DEM contact in modes I and II. The linear elastic portion of the stress–displacement curves defines the contact behaviour before failure ($D = 0.0$). They are followed by a non-linear stage that represents contact softening due to the progressive degradation of cohesion ($0 < D < 1$).

A common approach for implementing the user-defined contact models in PFC is to develop the stress-return algorithm in C++, and compile the code as dynamic link library (DLL) files (Itasca Consulting Group Inc 2016). The DLL files can be executed whenever needed during modelling. When the cohesive contacts enter their softening stage, their inelastic behaviour is determined by calculating the trial stress state as follows:

$$\sigma_n^{trial} = \sigma_n + k_n^0 du_n \tag{11}$$

$$\sigma_s^{trial} = \sigma_s + k_s^0 du_s. \tag{12}$$

The value of the yield function is then updated according to Eq. 4. The cohesive contact exhibits softening behaviour if $F > 0$, and the normal and shear plastic displacements will be updated based on the flow rule, with $d\lambda$ calculated from Taylor's expansion of the yield function as follows:

$$d\lambda = \frac{F^{trial}}{\frac{\partial F}{\partial \sigma_n} k_n^0 \frac{\partial G}{\partial \sigma_n} + \frac{\partial F}{\partial \sigma_s} k_s^0 \frac{\partial G}{\partial \sigma_s} + \frac{\partial F}{\partial C} \kappa C \sqrt{\left(\frac{\partial G}{\partial \sigma_n}\right)^2 + \left(\frac{\partial G}{\partial \sigma_s}\right)^2}}. \tag{13}$$

Finally, the corrected normal and shear stresses are calculated as follows:

$$d\sigma_n = d\sigma_n^{trial} + d\lambda\left(-k_n^0\right)\frac{\partial G}{\partial \sigma_n} \tag{14}$$

$$d\sigma_s = d\sigma_s^{trial} + d\lambda\left(-k_s^0\right)\frac{\partial G}{\partial \sigma_n}. \tag{15}$$

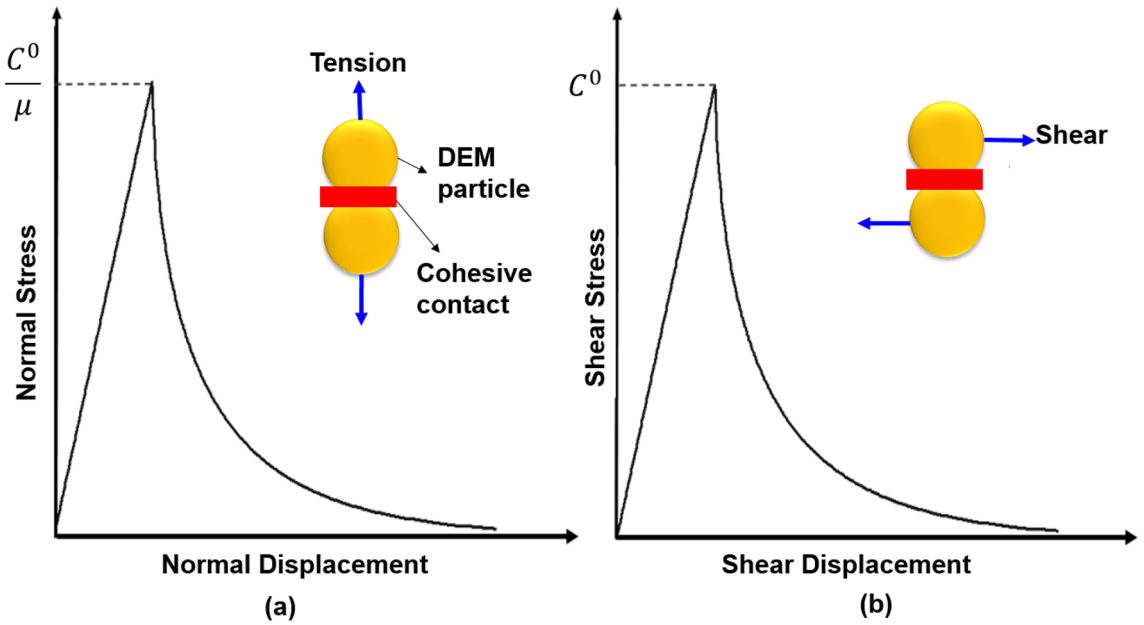

Fig. 2 Stress–displacement behaviour of the proposed cohesive model: **a** mode I and **b** mode II [after (Saadat and Taheri 2019)]

The stress-return algorithm mentioned above operates on the contacts that enter their yield limits with $F^{\text{trial}} > 0$ until 99.99% of their cohesion is damaged. After the complete degradation of cohesion, the cohesive bond between two particles is broken ($D = 1.0$). In C++codes, the bond cross-sectional properties are calculated, because they are needed to compute the DEM stresses and their corresponding F^{trial}. This implementation approach has been successfully followed by other researchers (e.g., Nguyen et al. 2017a, b). The cross-sectional area ($\bar{A}$) of DEM contact in two-dimensional space is defined as (Itasca Consulting Group Inc 2016)

$$\bar{A} = 2\bar{R}, \tag{16}$$

where $\bar{R}$ is defined as

$$\bar{R} = \begin{cases} \min\left(R^1, R^2\right), & \text{ball} - \text{ball} \\ R^1, & \text{ball} - \text{facet} \end{cases} \tag{17}$$

where R^1 and R^2 are the radiuses of two adjoining DEM particles that are bonded together. Potyondy and Cundall (2004) proposed a deformability method, in which the normal stiffness of the contacts ($\bar{k}^{\text{n}}$) can be related to the elastic modulus of the contact ($\bar{E}_{\text{c}}$) as follows (Itasca Consulting Group Inc 2016):

$$k_{\text{n}}^0 = \frac{\bar{E}_{\text{c}}}{L}, \tag{18}$$

where L can be determined as follows:

$$L = \begin{cases} R^1 + R^2, & \text{ball} - \text{ball} \\ R^1, & \text{ball} - \text{facet} \end{cases} \tag{19}$$

During the calibration procedure, the normal-to-shear stiffness ratio $k^* = {k_{\text{n}}^0}/{k_{\text{s}}^0}$ was initiated to determine the shear stiffness of the contacts (k_{s}^0) (Hofmann et al. 2015a; Liu et al. 2018).

We implemented the algorithm above in PFC2D to simulate the fracture behaviour of rock, grout, and bolt–grout interfaces. The proposed cohesive model can be employed as either a material contact model (e.g., rock and grout) or an interface contact model (e.g., bolt–grout interface). Throughout this paper, we use CCM to refer to the cohesive contact model, and the micro-properties of the model contained a subscript of CCM (e.g., C_{CCM}^0). We implemented the proposed cohesive model in the force–displacement law of SJM to achieve a cohesive interface model, which we denote as cohesive SJM (CSJM). The micro-properties of the cohesive interface model contained a subscript of CSJM (e.g., C_{CSJM}^0). Notice that the rock joint interface behaviour was simulated using the SJM. The details of the SJM can be found in (Itasca Consulting Group Inc 2016) and (Bahaaddini et al. 2013).

3 Calibration of the Proposed Cohesive DEM Approach

The micro-properties introduced in Sect. 2 have to be calibrated before comparing the results of the cohesive DEM framework with their experimental counterparts. The selection of an appropriate set of micro-properties is a necessary step in DEM simulation (Bahaaddini et al. 2013). The typical method for calibrating micro-parameters in PFC–DEM is to employ the results of a uniaxial compressive test of a physical specimen for reproducing the macroscopic behaviour of physical specimens (Bahaaddini et al. 2013; Gutiérrez-Ch et al. 2018). In the present study, it was necessary to use the laboratory results of rock-like and grout materials for calibration purposes. The details of mortar content and its physical properties can be found in the studies conducted by Oh et al. (2017) and Li et al. (2016c). The macroscopic properties of grout were taken from the experimental work of Shang et al. (2018a). To calibrate the micro-properties of SJM and CSJM, we conducted direct shear tests and normal deformability tests on smooth interfaces using PFC2D. The model's setup and boundary conditions in the calibration tests are illustrated in Fig. 3. In Sect. 3.1, we provide the calibration of the proposed cohesive model for rock-like and grout-like materials. The calibration of CSJM for the rock joint and bolt–grout interfaces is given in Sects. 3.2 and 3.3, respectively.

3.1 Calibration of Rock-Like and Grout-Like Materials

In this subsection, we present the calibration of micro-mechanical parameters for rock and grout. Since the calibration procedure for both materials was similar, only the calibration procedure for rock-like material is described in detail. The same approach was followed for calibrating the micro-properties of the grout material.

The dimension of a physical specimen for the uniaxial compressive test was 100 mm in height and 40 mm in width. The same dimensions were created in PFC2D. The minimum particle radius (r_{min}) was chosen to be 0.25 mm, and the ratio of the maximum particle radius (r_{max}) to minimum particle radius (r_{min}) was set as 1.66. We employed the inverse calibration method to obtain the micro-mechanical properties of the cohesive model. These micro-properties included C_{CCM}^0, μ_{CCM}, β_{CCM}, $\bar{E}_{\text{c, CCM}}$, k_{CCM}^*, and κ_{CCM}, which needed to be selected in an iterative process to reproduce a numerical response that matched the physical properties obtained from the laboratory testing.

In the present study, we employed the contact deformability method which is proposed by Potyondy and Cundall

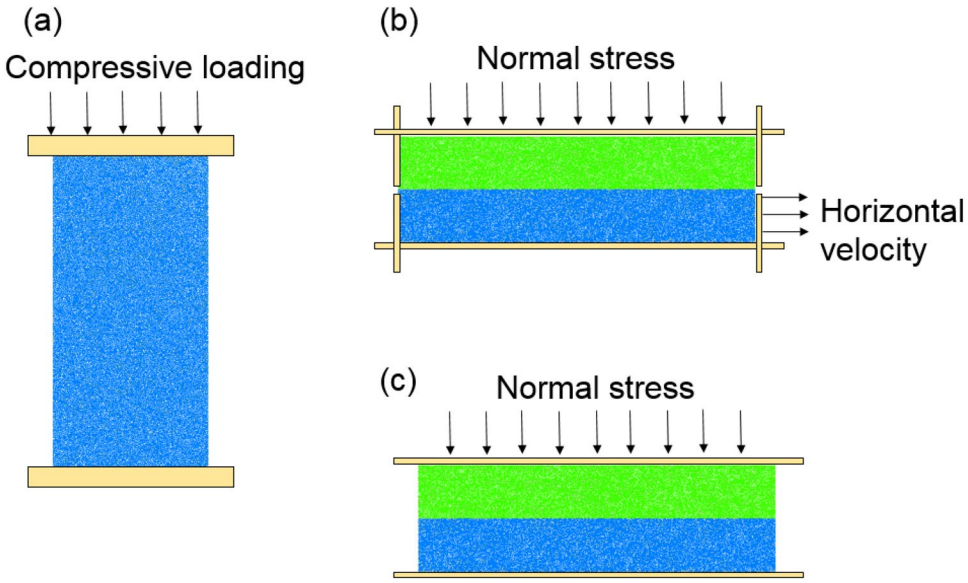

Fig. 3 Numerical test setup for the calibration process. **a** Uniaxial compression test, **b** direct shear test (planar rock joint), **c** normal deformability test (planar rock joint)

(2004) to calibrate $\bar{E}_{c,CCM}$. The first process involved matching the macroscopic Young's modulus with its experimental counterpart. The linear elastic behaviour of the DEM specimen is controlled by $\bar{E}_{c,CCM}$ and k^*_{CCM}. We altered these two parameters to match the macroscopic Young's modulus. Notice that, during the calibration of the linear elastic stage, the contact strength (C^0_{CCM}) was considered to be high enough to avoid any possible damage in the specimen. The next step is to calibrate the Poisson's ratio (), which is controlled by k^*_{CCM}. This parameter was calibrated in an iterative procedure with the first stage of calibration. Finally, the UCS of the model was reproduced by altering C^0_{CCM}, μ_{CCM}, β_{CCM}, and the softening parameter (κ_{CCM}). The strength of the cohesive contacts was controlled by C^0_{CCM}; the softening parameter (κ_{CCM}) controls the softening behaviour of the DEM contacts during post-peak stage. The friction coefficient of the contacts (μ_{CCM}) also influences the strength of the contacts, which in the macroscopic scale can control the UCS of the model. Thus, C^0_{CCM}, κ_{CCM}, and μ_{CCM} were chosen to match the numerical UCS to the experimental observation.

It should be mentioned that the dilation coefficient of the cohesive contacts (β_{CCM}) is associated with the dilatancy angle of the bonds between cement bridges at the macroscopic scale, which is a local parameter and can only be measured using sophisticated laboratory observations. However, as an alternative approach, proposed by Nguyen et al. (2017a), this micro-mechanical parameter can be calibrated by fitting it with the laboratory data (i.e., UCS test). We must emphasise that such local parameters toned to be incorporated in DEM-based cohesive models to maintain the theoretical framework of plasticity theory (Nguyen et al. 2017a, b). According to Nguyen et al. (2017a), such local parameters can be assumed equal to their macroscopic counterparts, but a parametric study is required to examine how sensitive is macroscopic behaviour to this micro-property. Unfortunately, the macroscopic dilation angle of the experimental specimen was not available for this study (Oh et al. 2017). Therefore, to calibrate β_{CCM}, we used a value of 0.2, and conducted a parametric study in which this parameter varied. The results of the parametric study revealed that the change in β_{CCM} has a negligible influence on the macroscopic response (i.e., the value of UCS). This calibration approach was successfully adopted in our previous research (Saadat and Taheri 2019).

The calibrated micro-mechanical properties of the proposed cohesive model for rock-like material is given in Table 1, and the comparison between macroscopic numerical and physical response is provided in Table 2. The numerical simulation results are in excellent agreement with the laboratory data, which means that the proposed

Table 1 Calibrated micro-mechanical parameters used in the simulation of rock-like material

$\bar{E}_{c,CCM}$ (GPa)	k^*_{CCM}	C^0_{CCM}(MPa)	κ_{CCM} (m^{-1})	μ_{CCM}	β_{CCM}
9.2	1.82	23.2	2.5×10^6	0.58	0.2

Table 2 Comparison between macroscopic parameters obtained from the laboratory experiment (Oh et al. 2017) and DEM simulation

	UCS (MPa)	Young's modulus (GPa)	υ
Experiment (Oh et al. 2017)	46.3	14.9	0.2
Numerical	46.1	14.8	0.2

DEM framework can reproduce the mechanical response of physical specimens.

To calibrate the micro-mechanical properties of grout, we generated a DEM specimen with the size of 80 mm × 40 mm, the same as the physical specimen used in the experiments. $r_{\min}$ was set at 0.2 mm, and ${}^{r\max}/_{r_{\min}}$ was 1.66. We used the same procedure mentioned above to calibrate the micro-mechanical properties of the grout. The calibrated parameters are listed in Table 3. Figure 4a illustrates a comparison of the axial stress–strain curves from both the laboratory testing and the DEM simulation using the proposed cohesive model. You can see that the simulation results matched well with its experimental

Table 3 Calibrated micro-mechanical parameters used in the simulation of grout-like material

	$\bar{E}_{c,CCM}$ (GPa)	k^*_{CCM}	C^0_{CCM}(MPa)	κ_{CCM} (m^{-1})	μ_{CCM}	β_{CCM}
Grout	4.35	1.9	18.0	2.5×10^6	0.48	0.22
Bolt	200	1.5	800	250×10^6	0.5	0.25

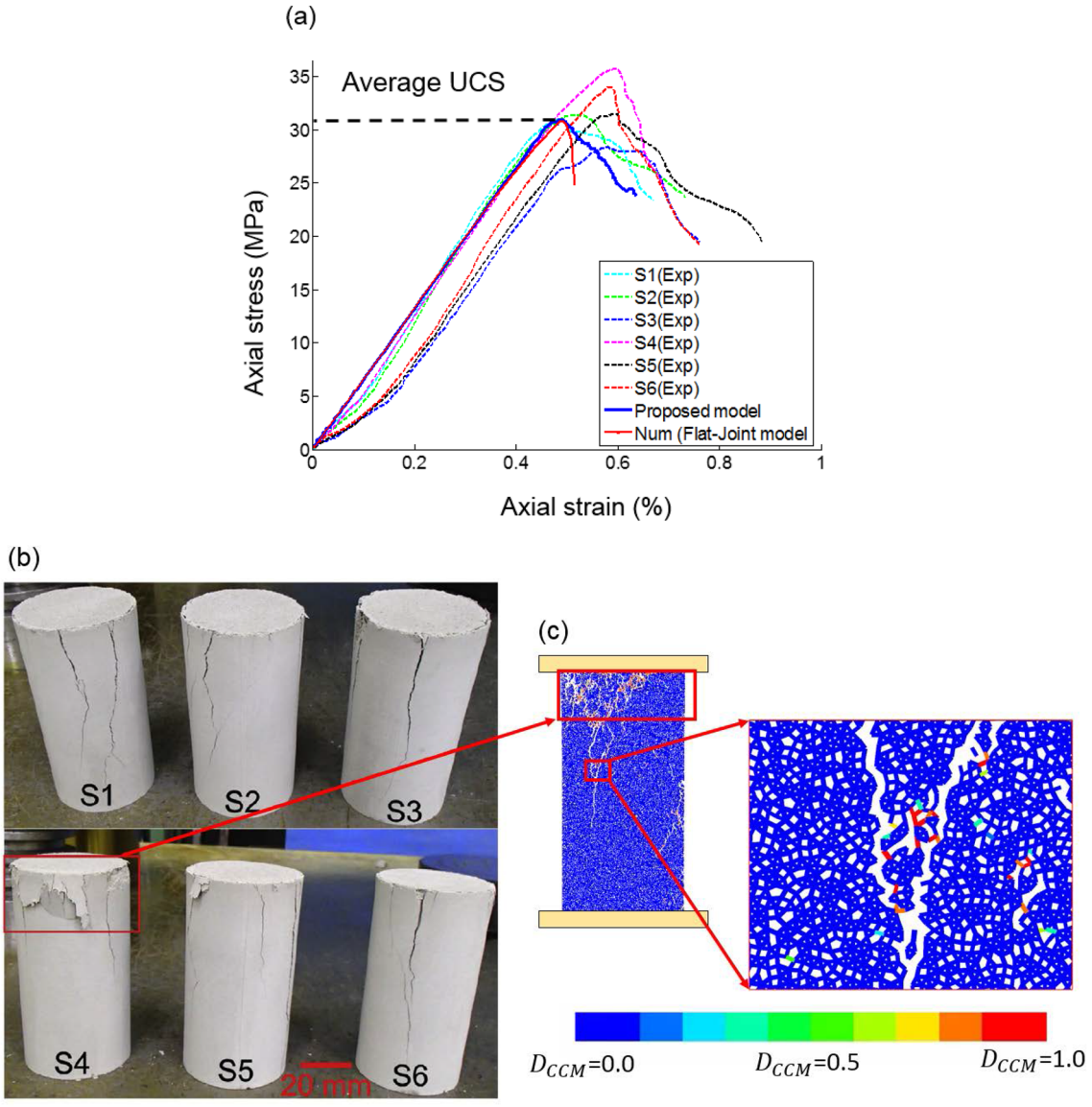

Fig. 4 Calibration of the proposed model. **a** Comparison of the stress–strain curves from laboratory tests (Shang et al. 2018a) and DEM simulations; **b** failure pattern of experimental specimens; and **c** macroscopic damage response of the numerical specimen with a close-up view of a localized damage zone

counterparts. Figure 4c illustrates a close-up view of the damage state of the contacts in a localized damaged zone. The softening behaviour of these contacts allowed us to obtain the macroscopic responses of the model. In particular, the gradual softening response of the specimen during the post-peak stage showed good agreement with the laboratory results. The gradual softening response of the stress–strain curve at the macroscopic scale was the intrinsic result of the collective behaviour of bonded-cohesive contacts in the DEM specimen. In the pre-peak stage of the stress–strain curve, several cohesive contacts reached their yield limit. These contacts then began to soften, yet were capable of carrying force. The progressive compressive loading of the specimen resulted in an increase in the number of these softened contacts ($0.0 < D_{CCM} < 1.0$), which coalesced and linked together to form large macroscopic fractures. When the specimen reached its peak axial strength, the cohesion of several contacts was totally lost ($D_{CCM} = 1.0$), but there were still some contacts in the localized zones that had a softening response (damaged contacts, $0.0 < D_{CCM} < 1.0$). The overall response of these failed and damaged contacts resulted in a softening response of the specimen at the macroscopic level (post-peak stage). Nevertheless, Shang et al. (2018a) reported that the current built-in contact constitutive model in PFC (flat-joint model) was not capable of capturing such softening behaviour. In fact, the flat-joint model exhibited brittle behaviour in the post-peak stage (Fig. 4a), because the brittle bond break occurred in the contacts after they lost their strength (i.e., cohesion or tensile strength). These differences in the macroscopic behaviour highlight the need to take into account softening behaviour (Fig. 2) in the constitutive relationships of DEM contacts.

The Poisson's ratio of the grout material was not provided by Shang et al. (2018a). Thus, we calibrated the numerical model k^*_{CCM} to obtain the best fit with the laboratory results (stress–strain curve and fracture pattern). The numerical Poisson's ratio was measured to be 0.22. This calibration procedure was also followed by Shang et al. (2018a).

3.2 Calibration of Rock Joint Interface

We used the SJM in the present study to mimic the mechanical behaviour of rock joint interfaces. The laboratory results of normal deformability and direct shear tests were used to calibrate the micro-properties of SJM. The normal stiffness of SJM (k_n^{sj}) was calibrated against the results of an experimental normal deformability test, and the shear stiffness (k_s^{sj}) and friction coefficient (μ^{sj}) of SJM were calibrated against the laboratory results of a direct shear test conducted on a planar rock joint. The experimental data provided by Oh et al. (2017) were used in the present study for the calibration purposes. Notice that the size of the specimen used in the laboratory investigation had a height of 100 mm and width of 100 mm. However, in the DEM simulations, the height of the specimens was reduced to 40 mm. It had no significant effect on the macroscopic results, but highly reduced the computational time. This approach was followed by others (e.g., Bahrani et al. (2014)), and made the DEM simulation more time efficient.

The laboratory data obtained from the normal deformability test of a smooth rock joint were used to calibrate k_n^{sj}. This test involved loading a sample with a side length of 100 mm, including a smooth rock joint and another intact specimen (Oh et al. 2017). According to the experimental approach conducted by Bandis et al. (1983), the closure of the rock joint can be measured by calculating the difference between the total deformation of the jointed specimen and the same value gained from an intact specimen. Figure 5a illustrates the comparison between the DEM results and laboratory data. Observe that SJM reproduced both the non-linear and linear portion of the normal deformability test with close agreement.

To calibrate k_s^{sj} and μ^{sj} values, the laboratory data obtained from the direct shear test of a planar rock joint under various normal stress magnitude were used. We set the calibration friction ratio (μ^{sj}) as 0.9, which was equal to the value obtained from laboratory testing (Oh et al. 2017). To obtain the macroscopic, numerical friction coefficient, we plotted

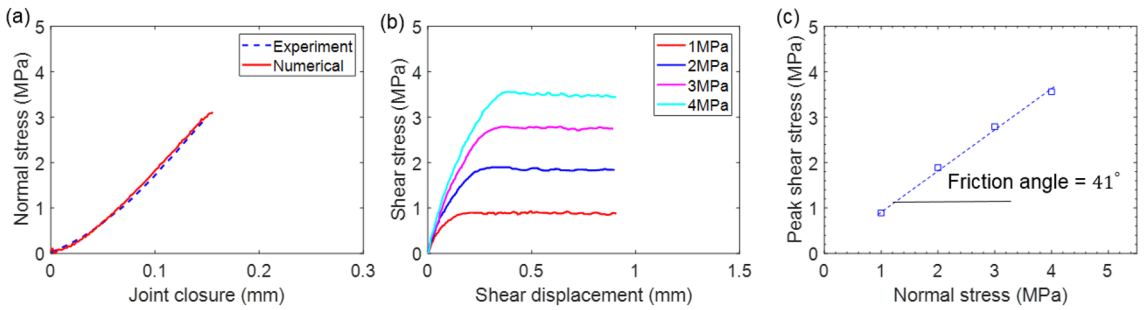

Fig. 5 Calibration of the SJM. **a** Comparison of normal deformability test results from experiment (Oh et al. 2017) and numerical simulation; **b** direct shear test results of a planar rock joint under different constant normal stresses; **c** friction angle obtained from numerical results

Table 4 Calibrated SJM micro-properties

k_n^{sj} (GPa/m)	k_s^{sj} (GPa/m)	μ^{sj}
480	55	0.9

the maximum shear strengths against their corresponding normal stress magnitudes. The results are illustrated in Fig. 5b. You can see that the SJM successfully reproduced the same macroscopic friction coefficient obtained from laboratory testing. Unfortunately, the experimental stress–displacement curves were not available in the paper published by Oh et al. (2017). Gutiérrez-Ch et al. (2018) suggested that, in the absence of experimental data, the normal-to-shear stiffness ratio can be obtained by assuming a value between 1 and 10. We used this approach in the present study to specify k_s^{sj}. The numerical friction angle obtained from the numerical simulations (41°) (Fig. 5c) showed close agreement with the experimental counterpart achieved by Oh et al. (2017) (42°). The micro-mechanical parameters obtained during calibration of the smooth-joint model is given Table 4. The accuracy of the calibrated micro-mechanical parameters is further validated by DEM direct shear tests conducted on idealised rock joints, and in our comparison of the results with their experimental counterparts (see Sect. 4).

3.3 Calibration of the Bolt–Grout Interface

To calibrate the micro-mechanical properties of the CSJM, we used the laboratory data obtained from direct shear and normal deformability tests. The numerical macroscopic shear and normal stiffnesses, and friction coefficient, were compared with their experimental counterparts. The laboratory data used for the CSJM calibration involved a rock bolt specimen without bolt ribs, which represents a planar interface (Shang et al. 2018a). The dimension of the numerical specimen was set to be the same as those of laboratory tests (80 mm × 24 mm). Notice that r_{min} in CSJM calibration tests were the same as those of used for the calibration of the grout's micro-properties. The previously calibrated micro-properties (Table 3) obtained for the grout were also used in direct shear tests. An assumption we made for the present study was to have no damage and deformation in the rebar bolt, since the uniaxial compressive strength and Young's modulus of the steel are much larger in compression compared to grout material. Therefore, a high value of bond strength to avoid bond breakage is sufficient (Shang et al. 2018a). The micro-properties of the rebar bolt were selected based on the previous literature (Shang et al. 2018a), and are listed in the experimental data (Shang et al. 2018a) with numerical results using the proposed model.

The calibration procedure of CSJM micro-properties was carried out as follows.

First, a direct shear test under constant normal stress of 2 MPa was carried out, and the macroscopic shear stress–displacement curve of this numerical experiment was used as a basis for the calibration of the shear stiffness. The microscopic shear stiffness of the CSJM ($k^0_{s,CSJM}$) was altered at this step to reproduce the best fit with the experimental shear stress–displacement curve (i.e., elastic stage).

Second, further direct shear tests were conducted but under higher normal stress magnitudes (4 MPa and 6 MPa), to calibrate C^0_{CSJM} and μ_{CSJM}. Notice that these two parameters control the peak shear strength in direct shear tests. At this stage, the softening parameter κ_{CSJM} was also altered to reproduce the best post-peak behaviour. Note that we had no direct laboratory method with which to calibrate β_{CSJM}. Therefore, we used a calibration similar to β_{CCM} (Sect. 3.1), which was chosen, because it reproduced the best fit with the experimental results.

Figure 6 illustrates a comparison of shear stress–displacement curves from DEM and laboratory tests under different normal stress magnitudes. Note that at higher normal stress magnitudes (i.e., 4 and 6 MPa), an initial stress fluctuation was observed in the experimental data (Fig. 6), which was due to a disconnection between the shear box and the grout material (Shang et al. 2018a). However, from the shear stress–displacement curves (Fig. 6) show that the numerical results are in good agreement with the experimental data. The softening behaviour in the shear stress–displacement curves demonstrates the necessity of incorporating an exponential softening response in the contact constitutive relationships. In fact, unlike the rock joint interface, which showed no cohesive behaviour, the grout–bolt interface exhibited a gradual softening response

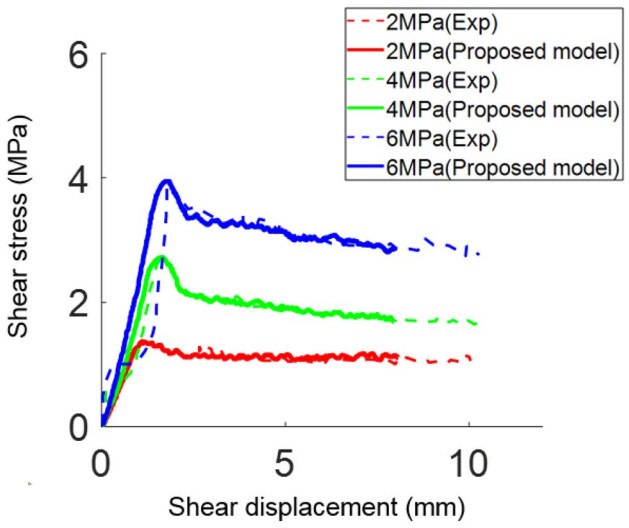

Fig. 6 Comparison of the direct shear test results from the laboratory experiment (Shang et al. 2018a) and DEM simulations using the proposed CSJM

due to a progressive bond cohesion degradation between the grout and the bolt (Shang et al. 2018a; Yokota et al. 2018). The macroscopic shear stress–displacement curves (Fig. 6) show that by increasing the magnitude of the normal stress, the DEM specimens reproduced a more pronounced softening response, which we attributed to significant bond break in the CSJM contacts. These numerical observations were in good agreement with the laboratory results.

As previously mentioned (Sect. 3.2), it is common to calibrate the normal stiffness of the SJM against the results of normal deformability tests (Bahaaddini et al. 2013). We adopted the same approach for calibrating the normal stiffness of CSJM. To calibrate $k^0_{n,CSJM}$, a numerical deformability test was conducted on the planar grout–bolt interface, and the outcome was compared with the laboratory results. Identical DEM specimens with and without a grout–bolt interface were generated, and tested uniaxially under compression. Notice that a horizontal velocity of 0.01 m/s, which was applied on the top of the specimens, was found to be sufficient for conducting the normal deformability test. The normal displacement and normal force of the numerical samples were recorded during the experiment. The normal deformation of the intact specimen (specimen without a grout–bolt interface) was subtracted from the normal deformation of the specimen that had a planar grout–bolt interface to estimate the macroscopic normal deformation of the grout–bolt interface. The values of $k^0_{n,CSJM}$ were obtained by trial-and-error, to match the numerical normal stress–displacement curve with the laboratory data. Notice that the normal deformability test was conducted using an iterative process with the direct shear tests to reach a good match with the experimental results in both tests. The numerical simulation was compared with its experimental counterpart and the results are illustrated in Fig. 7. You can see that the axial normal stress of the grout–bolt interface increased linearly when the normal displacement increased. The normal stress–displacement curve in the DEM simulation, using the proposed CSJM, excellently matches with the laboratory curve (Fig. 7). In Table 5, the micro-properties of the proposed CSJM are used in the simulation of the bolt–grout interface.

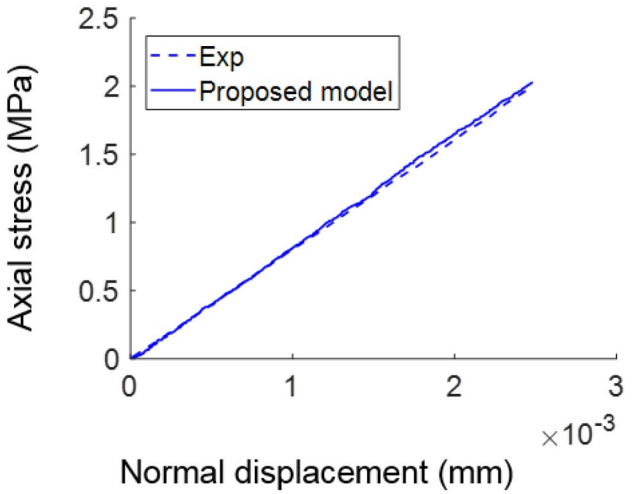

Fig. 7 Axial stress against the normal displacement of the planar bolt–grout interface in normal deformability tests: comparison of the experimental data (Shang et al. 2018a) with numerical results using the proposed model

Table 5 Calibrated CSJM micro-properties

$k^0_{n,CSJM}$ (GPa/m)	$k^0_{s,CSJM}$ (GPa/m)	μ_{CSJM}	C^0_{CSJM} (MPa)	κ_{CSJM} (m^{-1})	β_{CSJM}
1500	75	0.62	2.8	0.55×10^6	0.25

4 Validation of the Proposed DEM Framework

This section presents the simulation of idealised, saw-toothed rock joints with different asperity angles, and bolt–grout interfaces with various rib angles, conducted to validate the calibrated DEM framework.

4.1 The Shear Behaviour of Idealised Rock Joints

Oh et al. (2017) studied the dilative behaviour of idealised rock joints by conducting direct shear tests. The laboratory results obtained in their study were used in the present research to validate the numerical framework. Numerical specimens with base asperity angles of 20° and 30° and wavelengths of $\lambda = 25$ mm were generated in PFC2D, and tested under various normal stresses. The configuration of idealised rock joints can be found in Oh et al. (2017). The applied normal stress (σ^0_n) in the experimental observations (0.5, 2.0, and 4.0 MPa) was based on the ratio of applied normal stress over the rock strength (i.e., σ^0_n/σ_c); that is, 1%, 5%, 10% ranging from low to high normal stress magnitudes (Oh et al. 2017). The servo-controlled mechanism was employed to apply the normal stress, and a horizontal velocity of 0.01 m/s was adopted in the direct shear tests.

Figure 8a, b illustrates the shear stress–displacement and normal–shear displacement curves obtained from DEM simulations. The numerical and experimental asperity damages after 2.5 mm of shear displacement are illustrated in Fig. 8c. The red lines in Fig. 8c represent the micro-cracks, which were the result of bond break in the cohesive contacts. The accumulation of micro-cracks is

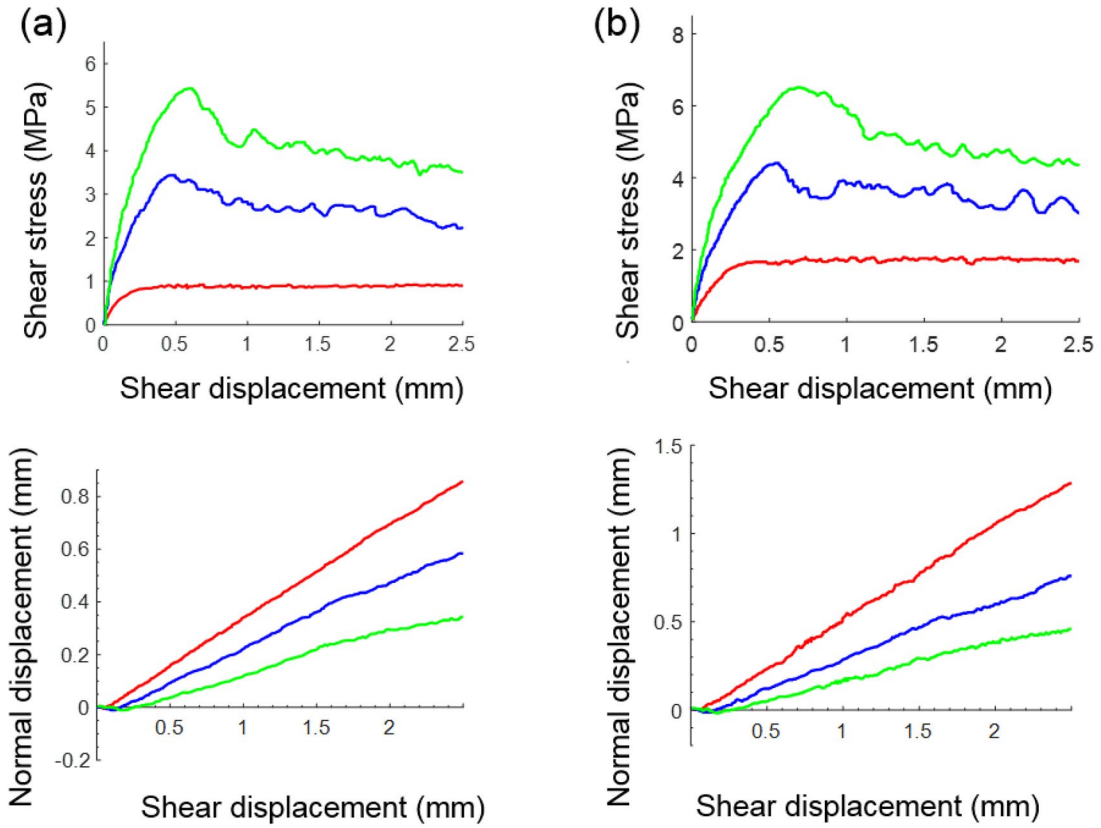
(a)
Shear stress (MPa)
Shear displacement (mm)
Normal displacement (mm)
Shear displacement (mm)
(b)
Shear stress (MPa)
Shear displacement (mm)
Normal displacement (mm)
Shear displacement (mm)

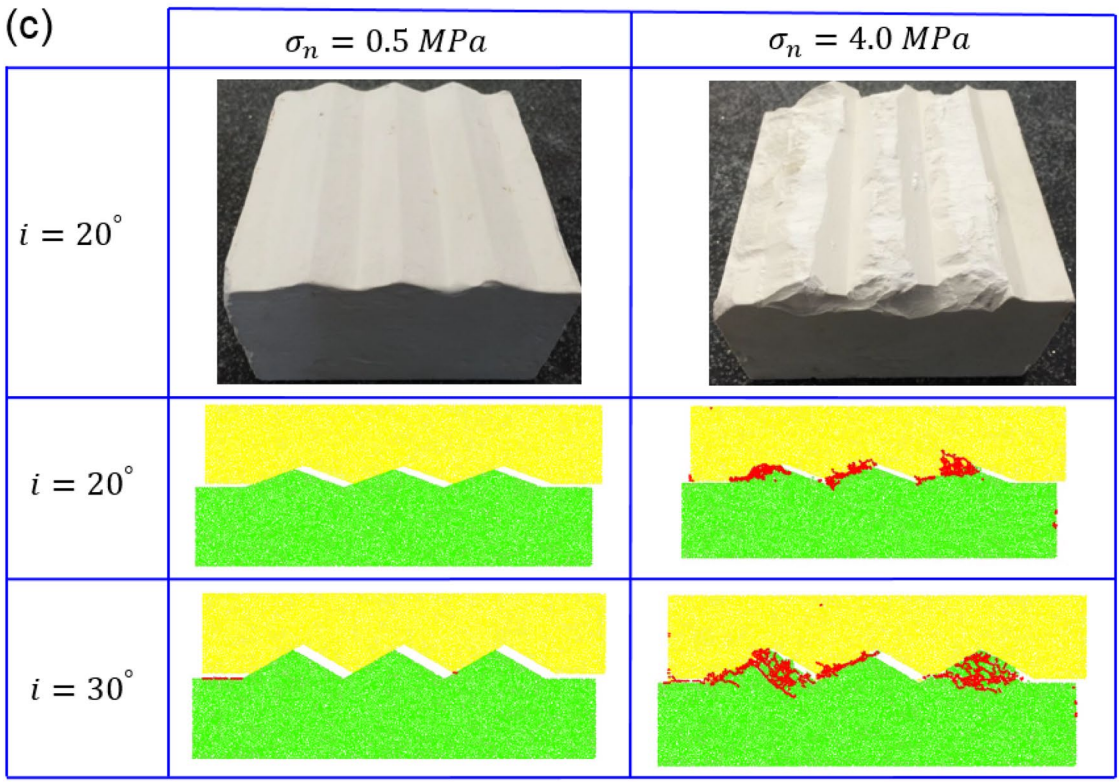
(c)
$\sigma_n = 0.5\ MPa$
$\sigma_n = 4.0\ MPa$
$i = 20^\circ$
$i = 20^\circ$
$i = 30^\circ$

◀**Fig. 8** Direct shear test results from the laboratory experiment obtained by Oh et al. (2017) and DEM simulations using the proposed model: **a** numerical shear stress–displacement and normal–shear displacement curves for 20° and 30° of asperity angles, respectively; **b** asperity degradation of the laboratory experiment and DEM simulation; **c** peak dilation angle of the laboratory experiment and the DEM simulation (colour figure online)

plotted graphically to illustrate the associated asperity degradation. You can see that under low confining pressure, the dominant shear mechanism of rock joints was asperity sliding. For numerical specimens with asperity angles of both 20° and 30°, at a normal stress of 0.5 MPa, when the maximum shear strength of the joints was reached, the models showed plastic behaviour, and a gradual sliding along the surface of rock joints was observed. The corresponding DEM models (Fig. 8c) verified this behaviour when no significant asperity degradation occurred in the numerical specimens. By increasing the normal stress magnitude from 0.5 to 4 MPa, more micro-cracks were initiated in the asperity areas for both 20° and 30° of the asperity angle (Fig. 8c). The shear stress–displacement curves (Fig. 8a) show that after reaching peak shear strength, the numerical models produced a softening response, which was due to progressive asperity degradation. Under 4.0 MPa of normal stress, the asperity damage was more severe, which resulted in a more pronounced softening response. The numerical results also showed that the peak shear strength of the rock joints increased with an increasing inclination angle (Fig. 8b). The DEM simulations show that at 30°, the numerical specimens' asperity degradation was more significant. We attributed this to its higher inclination angle, because it increased the shear resistance of the rock joint (Fig. 8c).

Figure 8d illustrates a comparison between the peak dilation angle of the DEM models and their laboratory counterparts. As aforementioned, rock joints under low normal stress magnitude remained nearly undamaged throughout the shearing procedure, allowing the sawtooth asperities of the top block to slide up over the opposite one, and resulting in a higher normal displacement of the joints. By increasing the normal stress magnitude, more severe asperity damage occurred in the models, resulting in a significant reduction of rock joint dilation. The comparison graph (Fig. 8d) also showed that the specimens with a 30° inclination angle displayed a higher relative dilation response. Figure 8c indicates good agreement

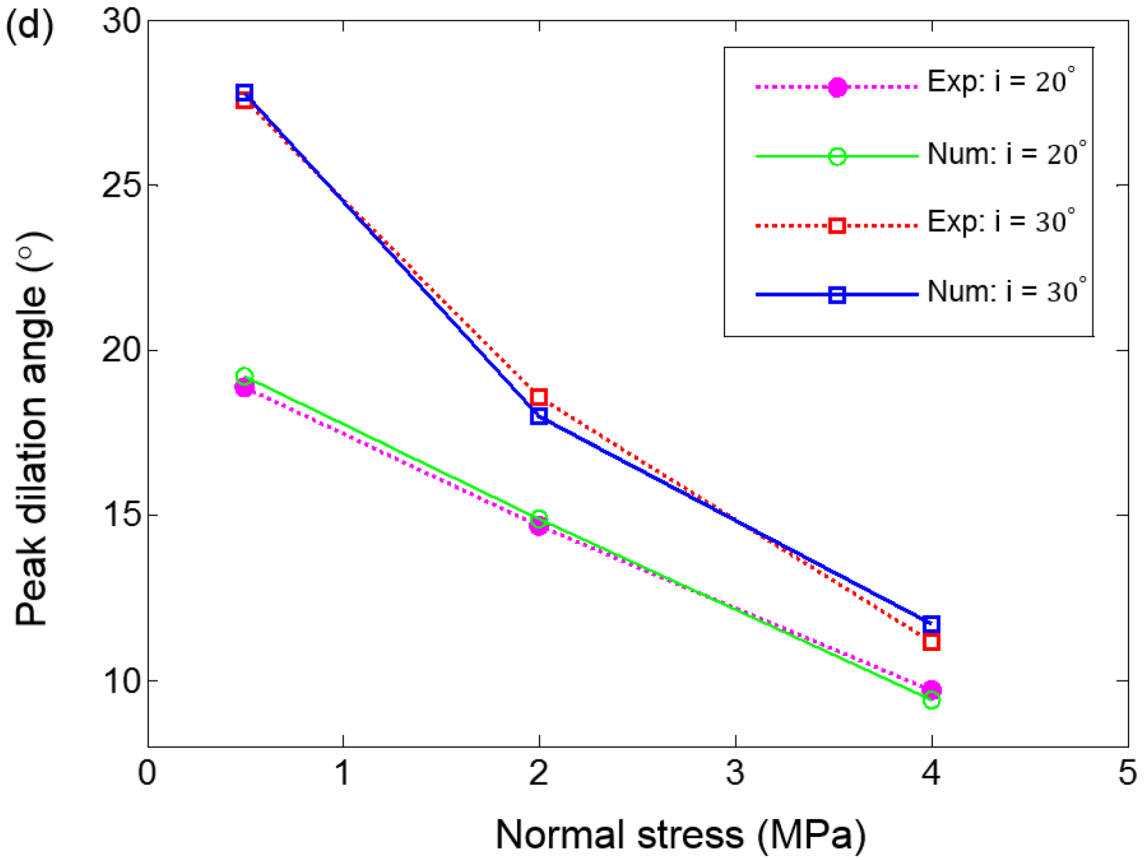

Fig. 8 (continued)

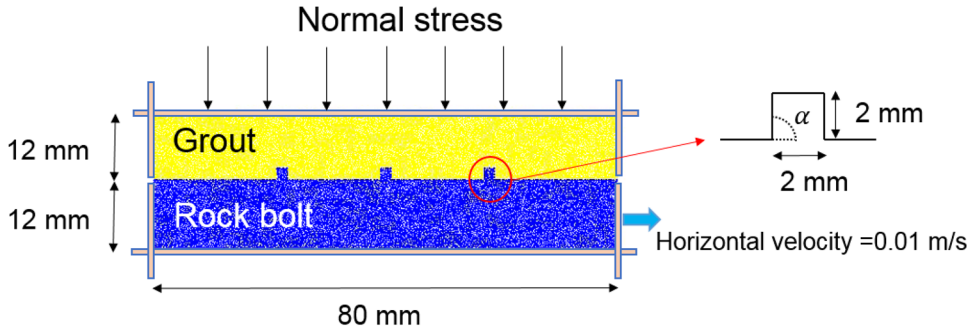

Fig. 9 Numerical test setup for conducting a direct shear test on the bolt–grout interface ($\alpha = 90°$)

between the experimental and numerical asperity damage using the proposed cohesive DEM framework. The comparison between the DEM and laboratory results (Fig. 8c, d) demonstrates that the proposed DEM framework can successfully reproduce the dilation behaviour of idealised asperities with different inclination angles.

4.2 The Shear Behaviour of the Grout–Bolt Interface

Figure 9 illustrates the DEM specimen generated in PFC2D that represents a rock bolting system with a rib angle (α) of 90°. The numerical specimen was comprised of two elements: Mortar and rock bolt. The rock bolt was fixed, and we applied a horizontal velocity of 0.01 m/s to the edge of it during the direct shear test. We applied the normal stress on the top of the specimen (grout) using a servo-controlled mechanism. The calibrated parameters obtained in Sect. 3.1 were assigned to the mortar and rock bolt, and the micro-properties achieved in Sect. 3.3 were used to simulate the shear behaviour of the bolt–grout interface.

Figure 10 illustrates the DEM simulation and experimental results. The numerical shear stress–displacement curve using the proposed DEM framework matches excellently with the laboratory curve (Fig. 10a). During the shearing process, the numerical specimen was shown to undergo four different stages, including linear elastic at the beginning of the test, a non-linear response before reaching the peak shear strength, a gradual softening behaviour during which the specimen totally failed, and a residual stage, at which the shear stress plateaued. The details related to these four stages will be discussed in Sect. 5.1.

Figure 10b, c illustrates the fracture pattern in the numerical and experimental specimens, respectively. The comparison indicates good agreement between the laboratory and the numerical cracking response using the proposed DEM framework. The numerical model demonstrates both inclined and sub-horizontal cracks. During the shearing process, the coalescence of micro-cracks, which were the result of bond break in the cohesive contacts ($D_{CCM} = 1.0$), generated larger macroscopic cracks. Figure 10b shows that the accumulation of micro-cracks between two ribs led to the failure of the grout material. This failure mode was also observed during the experimental test (Yokota et al. 2019), which is shown in Fig. 10c. The damage response of the cohesive contacts after 3 mm of shear displacement is depicted in Fig. 10d. You can see that some of the contacts performed elastically ($D_{CCM} = 0.0$), while others demonstrated a softening response ($0.0 < D_{CCM} < 1.0$).

5 The Simulation of Bolted Rock Joints Subjected to Combined Pull–Shear Load

This section presents an investigation of the influence of the combined pull-and-shear load. It employed the calibrated micro-properties, and studies the influence of pretension, the rib angle, and the CNS boundary condition. The setup of the numerical test is explained in Sect. 5.1. In Sect. 5.2, the influence of the combined pull–shear load is described with a particular focus on the impact of the pretension load on the shear behaviour of the bolted rock joint. An investigation of the influence of the rib angle and the CNS condition is presented in Sects. 5.3 and 5.4, respectively.

5.1 Numerical Test Setup

Figure 11 illustrates the DEM specimen for conducting the combined pull–shear load test using a fully grouted rock bolt. Figure 11a shows the boundary condition used in DEM modelling of a bolting system including rock joint, rock bolt, and grout. We assumed a diameter of 5 mm for the rock bolt, and a thickness of 4 mm for the grout. To generate the numerical specimen, the DEM particles were divided into three different groups: rock, rock bolt, and grout. The particle size of the rock bolt and the grout groups was the same as those used for the calibration of micro-properties (Sect. 3.1). Similarly, the particle size for the group of rock was similar to particle sizes that were used for the calibration of rock-like material micro-properties in Sect. 3.1.

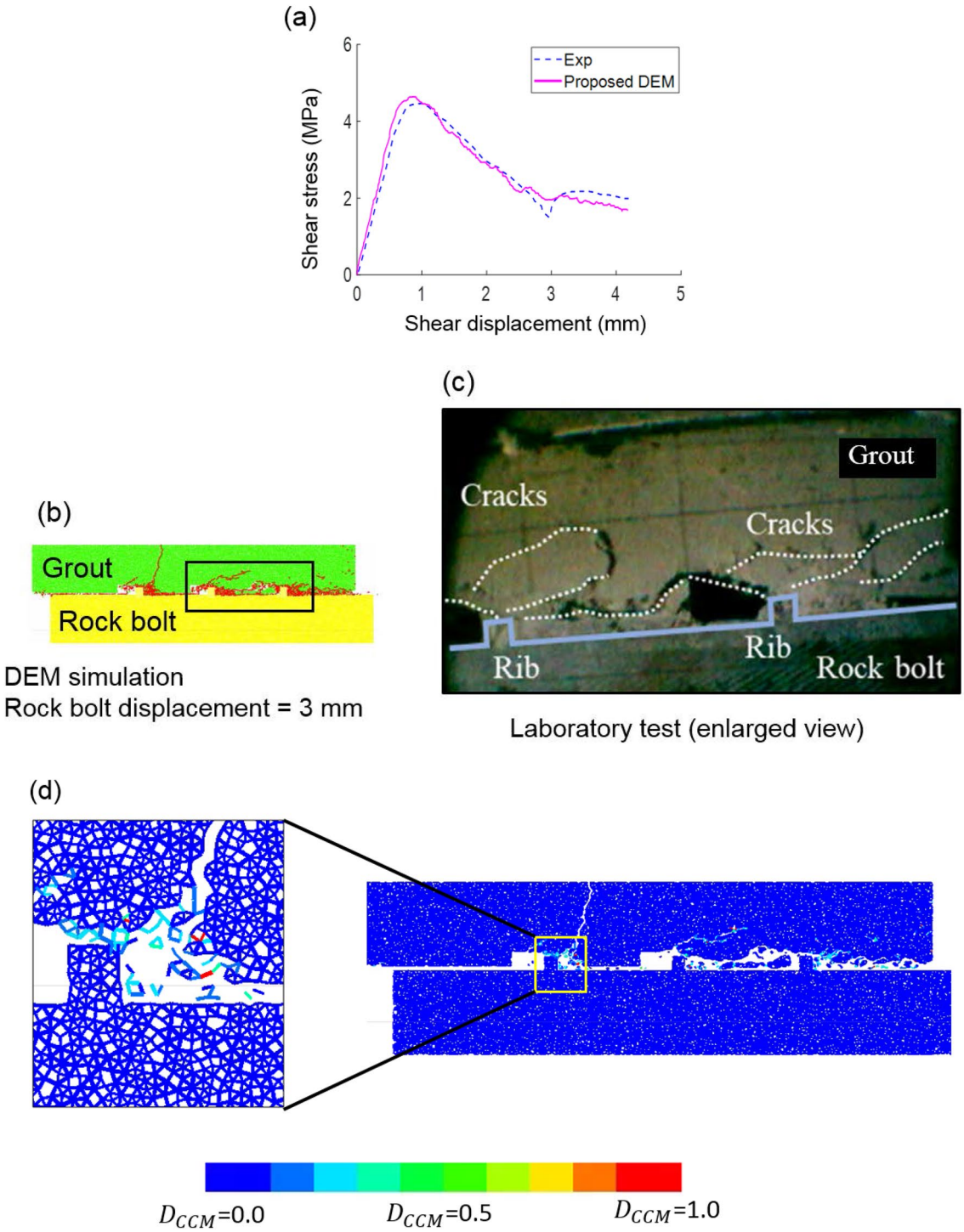

Fig. 10 Comparison of the direct shear test results from the experiment (Shang et al. 2018a) and DEM simulation using the proposed model: **a** shear stress–displacement curve; **b**, **c** fracture pattern in the numerical and experimental specimen (Shang et al. 2018a), respectively; **d** microscopic damage response of the DEM contacts at a localized failure zone

Notice that in the verification process (Sect. 4.2), half of the rock bolt profile was modelled. However, in the combined pull–shear load experiments, the full rock bolt profile needed to be simulated. The width of the numerical specimen was 100 mm, which was similar to that considered for the validation of rock joint shear behaviour (Sect. 4.1). The height of the numerical specimen was 80 mm, which is equal to the length of the rock bolt simulated in the verification process

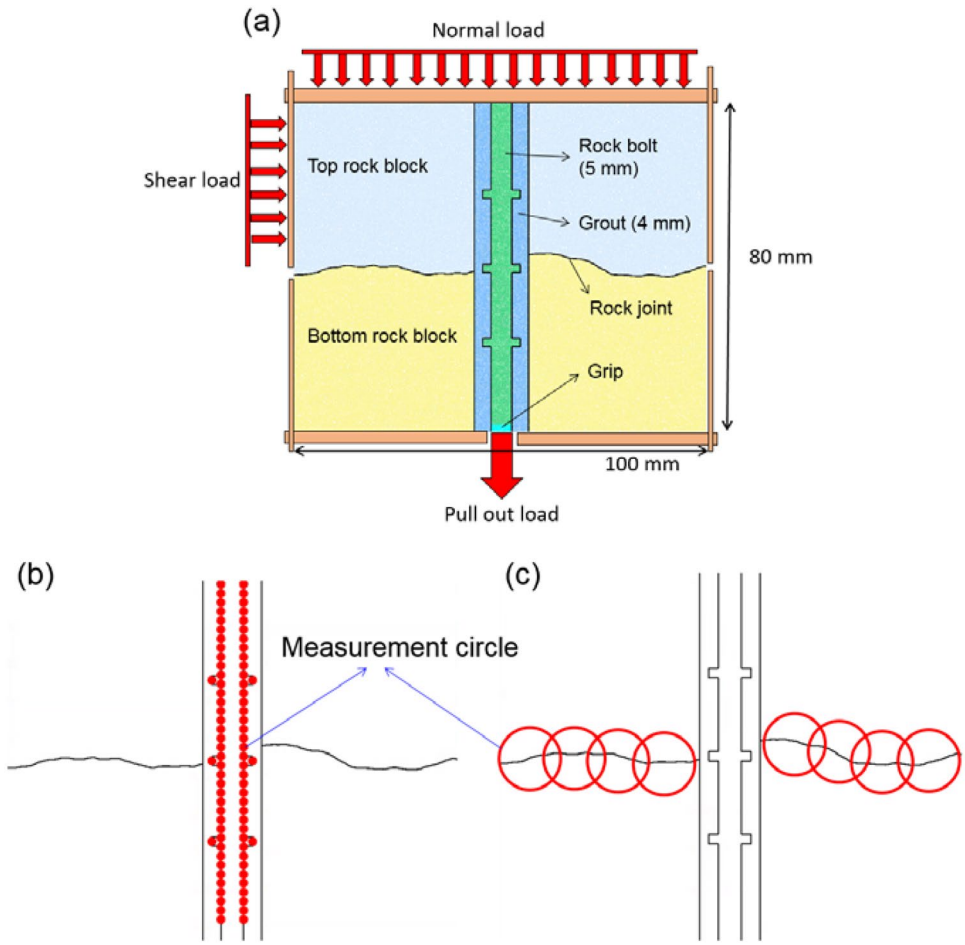

Fig. 11 DEM experiment for conducting combined pull–shear loading test: **a** DEM test setup and boundary condition; **b**, **c** measurement circles for monitoring axial stress–displacement of the bolt–grout interface and induced normal stress on rock joint interface, respectively

(Sect. 4.2). To carry out the pull-out test, a group of DEM particles (gear group in Fig. 11a) was subjected to a vertical velocity of 0.01 m/s. This velocity was equal to that of used in the simulation of the grout–bolt shear behaviour in Sect. 4.2. We conducted the direct shear test by applying a horizontal velocity of 0.01 m/s on the top rock block (Fig. 11a). The pull-out load induces a normal stress on the rock joint profile. The axial stress along the bolt–grout interface and the induced normal stress on the rock joint interface (σ_n^i) were measured at different measurement circles, as shown in Fig. 11b, c, respectively.

5.2 The Pull-Out and Shear Mechanisms

We established DEM simulations to investigate the influence of the combined pull–shear load on the shear behaviour of bolted rock joint. In the previous section (Sect. 4.2), the interaction between the rock bolt and grout was studied using the proposed cohesive DEM.

Chen and Li (2015b) studied the performance of fully grouted rock bolts subjected to pull–shear loads. In their experimental research, the pull-out and shear loads were applied to the specimen at the same time, and the total force resulting from pull-and-shear loading was calculated to analyse the outcome of the laboratory tests. Notice that no rock joint was considered in their research. Following this approach, however, it is an immensely complicated task to understand the shear mechanism of bolted rock joints. The main reason for this is because the pull-out stress magnitude at which the highest normal stress is induced in the rock joint may or may not be reached using the method proposed by Chen and Li (2015b), which leads to an ambiguity in the results. We present an alternative, a stepwise pull–shear test (SPST) approach in this paper, in which the DEM direct shear tests are conducted at various pretension stress magnitudes. The proposed SPST approach enabled us to measure and compare the corresponding peak shear strength of the bolted rock joint at different pretension magnitudes. Thus, the performance of fully grouted rock bolts (i.e., the ultimate shear capacity of bolted rock joint) can be properly assessed.

The fully grouted rock bolt was subjected to a pull-out load, while the rock joint was sheared horizontally. The rock joint had an average joint roughness coefficient (JRC) of 10.2, which was digitised and imported in PFC2D. This rock joint profile was previously generated by Bahaaddini (2014). The rib angle of the rock bolt was set at 90°. According to

the experimental research available in the literature, the pull-out test can be conducted either under zero- or non-zero-confining pressure (Thenevin et al. 2017). In the present study, the numerical pull-out tests were conducted under zero-confining pressure. This approach was followed by the previous scholars investigating the influence of the surface configuration on the load transfer mechanism of fully grouted rock bolts (Aziz et al. 2006; Tao et al. 2017; Yazici

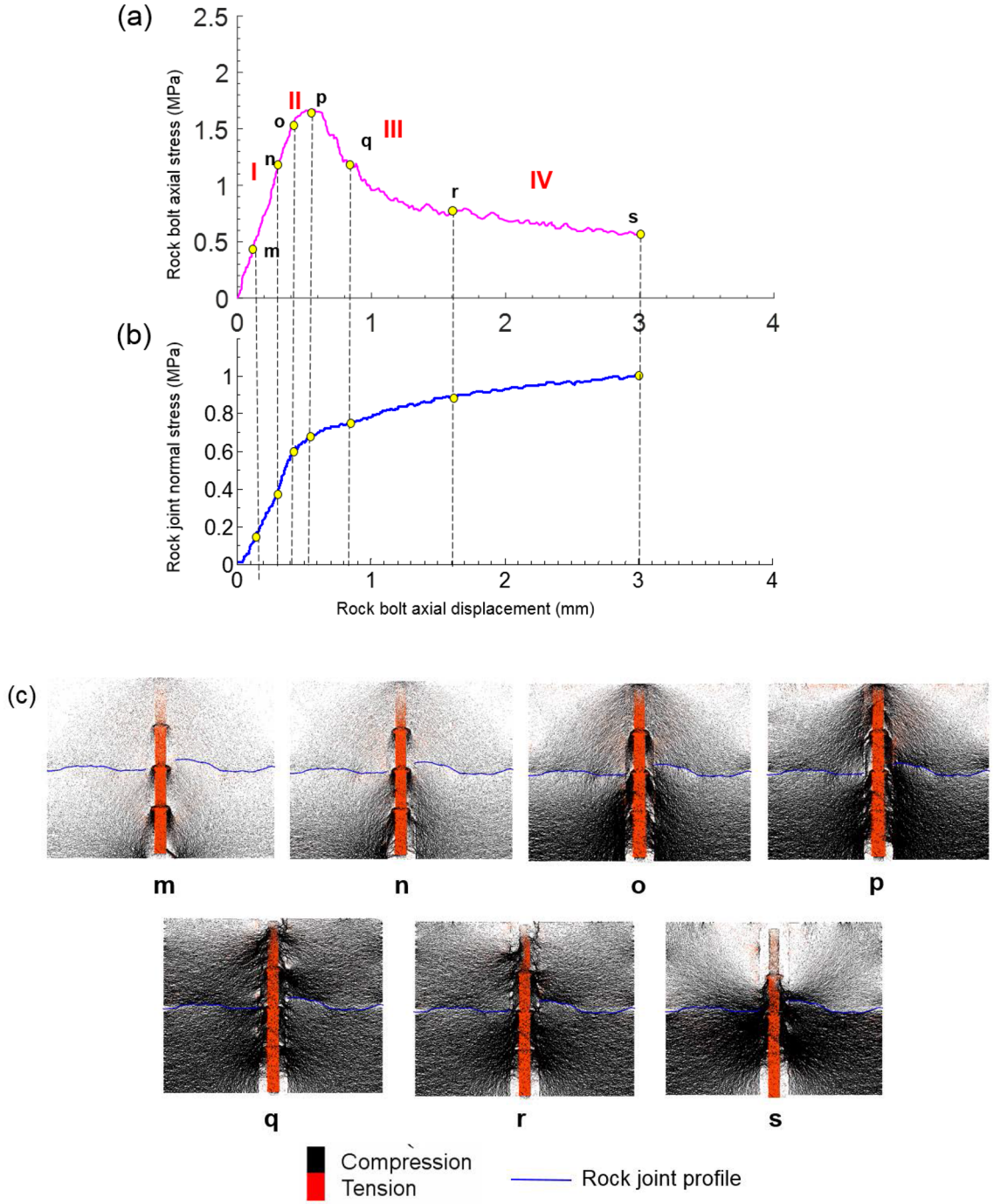

Fig. 12 Numerical pull-out test results using the proposed model: **a** rock bolt axial strength versus rock bolt axial displacement; **b** induced normal stress on the rock joint interface versus axial displacement of the rock bolt; **c**–**e** force chain networks, the damage response of the cohesive contacts in the grout material, and the damage response in the bolt–grout interface contacts at various pull-out stress magnitudes, respectively; **f** close-up view of the damage state of the cohesive contacts in the grout material after completing the pull-out process (colour figure online)

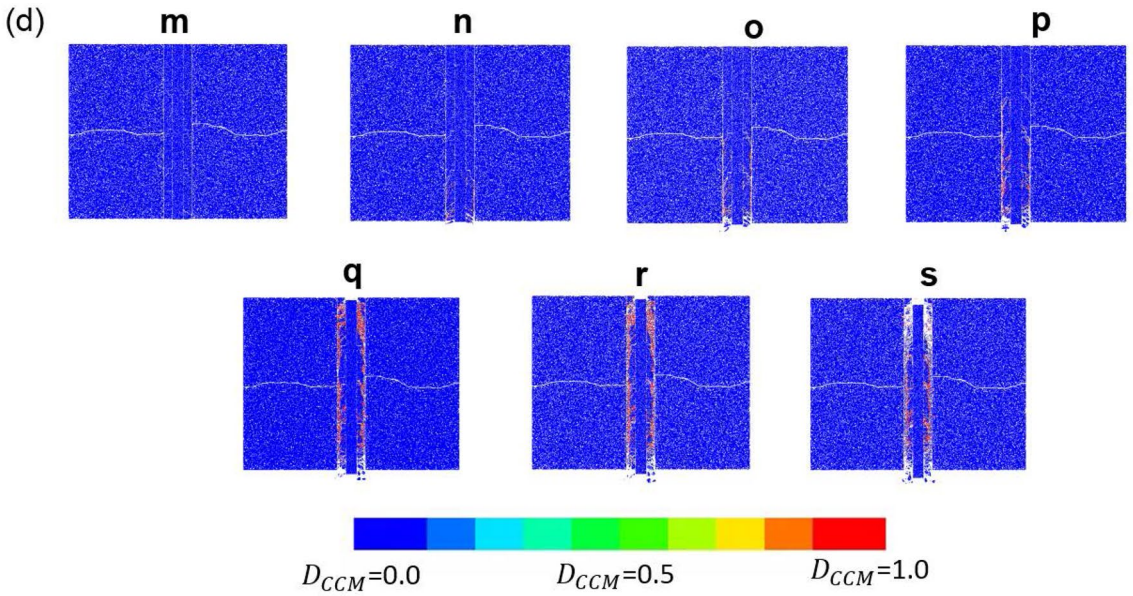

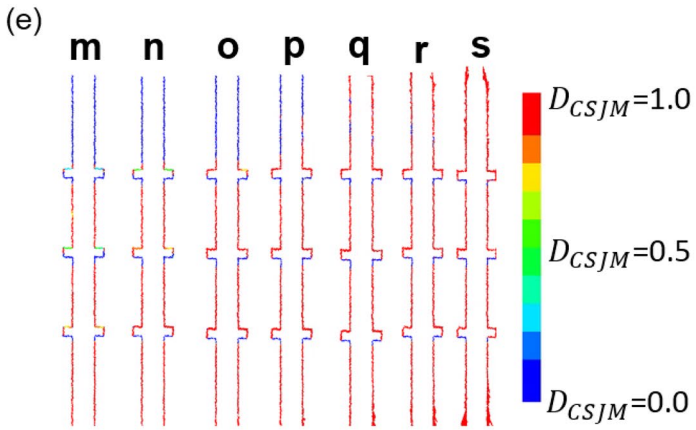

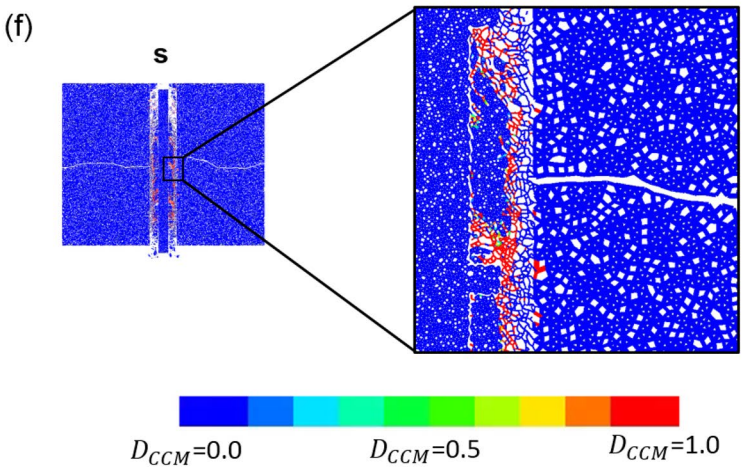

Fig. 12 (continued)

and Kaiser 1992). The results of the numerical pull-out test are depicted in Fig. 12. Figure 12a illustrates the axial stress–displacement response of the fully grouted rock bolt. The axial stress–displacement of the fully grouted rock bolt can be divided into four different stages (I–IV in Fig. 12a). σ_n^i was also measured during the pull-out process, and the results are illustrated in Fig. 12b. The corresponding force chain and damage responses of the specimen at the end of each stage are shown in Fig. 12c, d, respectively. Notice that force chain represents the compression and tension forces along arrays of DEM contacts. The thicker black lines in Fig. 12c indicate a higher contact force value. The red lines in Fig. 12c exhibit the DEM contacts with tension forces, which are influenced by the applied pull-out load.

Each stage in the stress–displacement curve (Fig. 12a) is associated with a particular mechanism:

1. The initial linear elastic response from the beginning of the pull-out test to point "o" was observed in stage I. At different stress magnitudes in this stage, we monitored the force chain and damage responses of the grout and bolt–grout interface contacts ("m", "n", and "o" in Fig. 12c–e). You can see in these results that the magnitude of compression forces gradually increased around the ribs (Fig. 12c). At the end of this stage (point "o"), the compression forces developed towards the rock joint (Fig. 12c), leading to a significant increase in the magnitude of σ_n^i (Fig. 12a). During this stage, the number of yielding contacts increased, with a high concentration of damaged contacts observed in the bottom-half of the grout ("m", "n", and "o" in Fig. 12d). You can see in Fig. 12e that at points "m" and "n", there were some softening contacts ($0.0 < D_{CSJM} < 1.0$) along the bolt–grout interface. With an increase in the axial strength of the bolt to point "o" (Fig. 12a, e), these contacts were completely damaged ($D_{CSJM} = 1.0$). However, there were still some contacts along the bolt–grout interface with $D_{CSJM} = 0.0$..
2. In this stage (from point "o" to point "p"), the axial stiffness dropped and the stress–displacement curve exhibited a non-linear response before the peak axial strength was reached (point "p", Fig. 12a). The rate of increase in the σ_n^i dropped during this stage (Fig. 12b), which we attributed to the progressive development of damage in the grout material (Fig. 12d). The compression forces around the ribs and rock joint profile showed a slight increase at the end of this stage (point "p", Fig. 12c).
3. The axial stress decreased in this stage. Initially, the axial stress tended to reduce steeply, but the rate of stress reduction gradually decreased after point "q" (Fig. 12a). σ_n^i exhibited a gradual increase from peak axial strength (point "p") to the end of stage III (point "r") (Fig. 12a). Although the damage response of the grout contacts showed a significant increase in the number of failed contacts (points "q" and "r" in Fig. 12d; contact with colours other than blue), the σ_n^i exhibited a gradual increase during this stage. One possible reason for this is the mechanical interlock and frictional behaviour of the grout particles during progressive pull-out loading, which may contribute to the increase of σ_n^i. You can see in Fig. 12b that the rate of increase in the magnitude of σ_n^i during stage III was significantly lower than that in stage I. The compressive forces around the rock joint profile increased during this stage (points "q" and "r" in Fig. 12c), which was consistent with the gradual increase in σ_n^i (Fig. 12b). The damage response of the bolt–grout interface contacts also exhibited a significant increase in the number of damaged contacts (Fig. 12d). This behaviour continued until the end of the pull-out procedure (Fig. 12e).
4. During the residual phase, the rate of decrease in the axial strength was dramatically reduced (stage IV, Fig. 12a). The rate of increase in the σ_n^i also declined gradually (Fig. 12b). At the end of the pull-out test (point "s" in Fig. 12c), the compressive forces in the specimen were mostly concentrated in the middle of the specimen, which we attributed to the severe bond break at the upper and lower parts of the grout (point "s" in Fig. 12d). You can see from the damage response of the bolt–grout interface (point "s", Fig. 12e) that the majority of the interface contacts were fully damaged ($D_{CSJM} = 1.0$) during this stage.

To better demonstrate the damaged and softening contacts in the grout material, a close-up view of the cohesive contacts at the end of the pull-out test (point "s") is depicted in Fig. 12f. Observe that the majority of the contacts were fully damaged ($D_{CCM} = 1.0$), while very few contacts were in their softening stage ($0.0 < D_{CCM} < 1.0$.).

After conducting the pull-out test, and obtaining the axial stress–displacement of the fully grouted rock bolt, the direct shear tests were carried out. The numerical observations (Fig. 12a, b) showed that the pull-out force applied on the rock bolt induced a clamping effect on the rock joint's surface, which in turn increased the normal stress of the rock joint. It was expected that an increase in σ_n^i would increase the shear strength of the rock joint. However, it is necessary when designing bolting systems to understand at which axial stress magnitude (shown in Fig. 12a), the rock joint demonstrates the highest possible shear strength. To test this, we conducted a series of direct shear tests at each stress magnitude. The applied normal stress in the pull-and-shear test was set at $\sigma_n^{total} = \sigma_n^0 + \sigma_n^i$. The magnitude of σ_n^0 was 0.5 MPa. Therefore, the overall, applied normal stress on the rock joint interface was increased from point "m" (the minimum σ_n^i in the group) to

point "s" (maximum σ_n^i in the group). The direct shear tests were conducted under CNL conditions; the influence of the CNS condition is investigated in Sect. 5.3. The numerical direct shear tests aimed to find the axial stress magnitude (i.e., pretension load) at which the rock joint produces the maximum shear strength. This helps to determine the optimum pretension loading during practical applications (i.e., in mining).

Figure 13 illustrates the results of the numerical direct shear tests conducted on the bolted rock joint. Figure 13a shows the shear stress–displacement graphs, and Fig. 13b depicts the maximum shear stress of the bolted rock joint against the total applied normal stress magnitude (σ_n^{total}). The damage response of the numerical specimens at the end of the shearing process is also shown in Fig. 13c.

The numerical specimens were named based on pretension stress magnitudes (e.g., "m", "n", etc.) that were obtained during the pull-out test (see Fig. 13a). It can be seen from Fig. 13b that the specimen "o" reproduced the highest peak shear strength. The direct shear test results also showed that for the specimens with peak (specimen "p") and post-peak (specimens "q", "r", and "s") pretension stress magnitudes, the peak shear strength of the rock joint reduced, but it was higher than that obtained from the specimens in which the pretension stress magnitudes were in the linear elastic region (i.e., specimens "m" and "n") (see Fig. 13b). The shear resistance of the rock joints for the peak and post-peak pretensions was associated with the presence of rock bolt element, and to some extent σ_n^i. These numerical observations can be interpreted according to the σ_n^i graph (Fig. 12b) and force chain plots (Fig. 12c). According to the pull-out test results, at point "o" the incremental rate of σ_n^i significantly decreased (Fig. 12b), but point "o" had the highest σ_n^{total} compared to "m" and "n". Accordingly, the specimen "o" showed greater resistance against shearing, and reproduced the highest peak shear strength. Nonetheless, at peak (point "p") and post-peak (points "q", "r", and "s") stress magnitudes, the magnitude of compressive forces in the rock joint interface grew rapidly (Fig. 12c), due to the frictional behaviour of the grout particles during progressive pull-out. This encouraged the rock contacts to come close to their yield limits (i.e., the onset of contact softening). Therefore, the weakened contacts in specimens "p", "q", "r", and "s" exhibited lower shear resistance, with severe asperity damage, when compared to specimen "o" (Fig. 13c). These numerical observations revealed that the combined pull-and-shear load significantly influenced the shear resistance of the rock joint. There was also an axial tensile stress at which the fully grouted rock bolt demonstrated an optimum performance (i.e., optimum pretension stress).

5.3 The Influence of Rib Angle

In addition to the numerical specimens with rib angle of 90°, two other models with rib angles of 30° and 60° were simulated. Similar to the previous simulations, the pull-out tests were conducted first; then, the direct shear tests were carried out to investigate the influence of α on the overall shear behaviour of bolted rock joints. Figure 14 illustrates the axial stress–displacement curves obtained from the pull-out tests. The corresponding σ_n^i against the axial displacement of the rock bolt is also demonstrated in each figure (Fig. 14a, b).

The numerical simulations showed that the axial stress–displacement response $\alpha = 60°$ (Fig. 14a) was approximately similar to that with $\alpha = 90°$ (Fig. 14b). σ_n^i was also consistent with the results obtained from the 90° rib angle. The axial stress–displacement curve with a 30° rib angle, however, exhibited slightly different results. When $\alpha = 30°$, the peak axial strength was lower than that in the other numerical specimens, which was probably because of the slip behaviour along the bolt–grout interface, arising from insufficient mechanical interlocking. This meant that lower magnitudes of σ_n^i during the pull-out test (Fig. 14b) resulted.

The numerical observations obtained in the present study were consistent with the experimental results in the previous study (Yokota et al. 2019). Similar to the results presented in Sect. 5.1, seven axial stress magnitudes were considered for examining the influence of the rib angle on the shear resistance of the bolted rock joint. We conducted fourteen numerical direct shear tests in total; the results are illustrated in Fig. 14c. You can see that, as with the previous results, the ultimate performance of the fully grouted rock bolts was obtained when the axial stress of the rock bolt was at point "o". As with the 90° rib angle (Sect. 5.1), in the numerical specimens with peak and post-peak stress magnitudes (specimens "p", "q", "r", and "s"), the shear resistance of the bolted rock joints reduced, but it was higher than that obtained from the specimens with pretension in the linear elastic region.

5.4 The Influence of the CNS Condition

It has been reported repeatedly in the previous experimental research that the CNS boundary condition affects the shear resistance of bolted rock joints. In this section, the shear behaviour of the bolted rock joint (JRC = 10.2, $\alpha = 90°$) was studied under the CNS condition. The numerical setup under the CNS condition is illustrated in Fig. 15.

During CNS direct shear tests, the applied normal stress on the rock joint profile should be updated according to the normal displacement of the rock joint, and to the value of stiffness, as follows:

$$d\sigma_n = k^{cns} \times d\delta_n \tag{20}$$

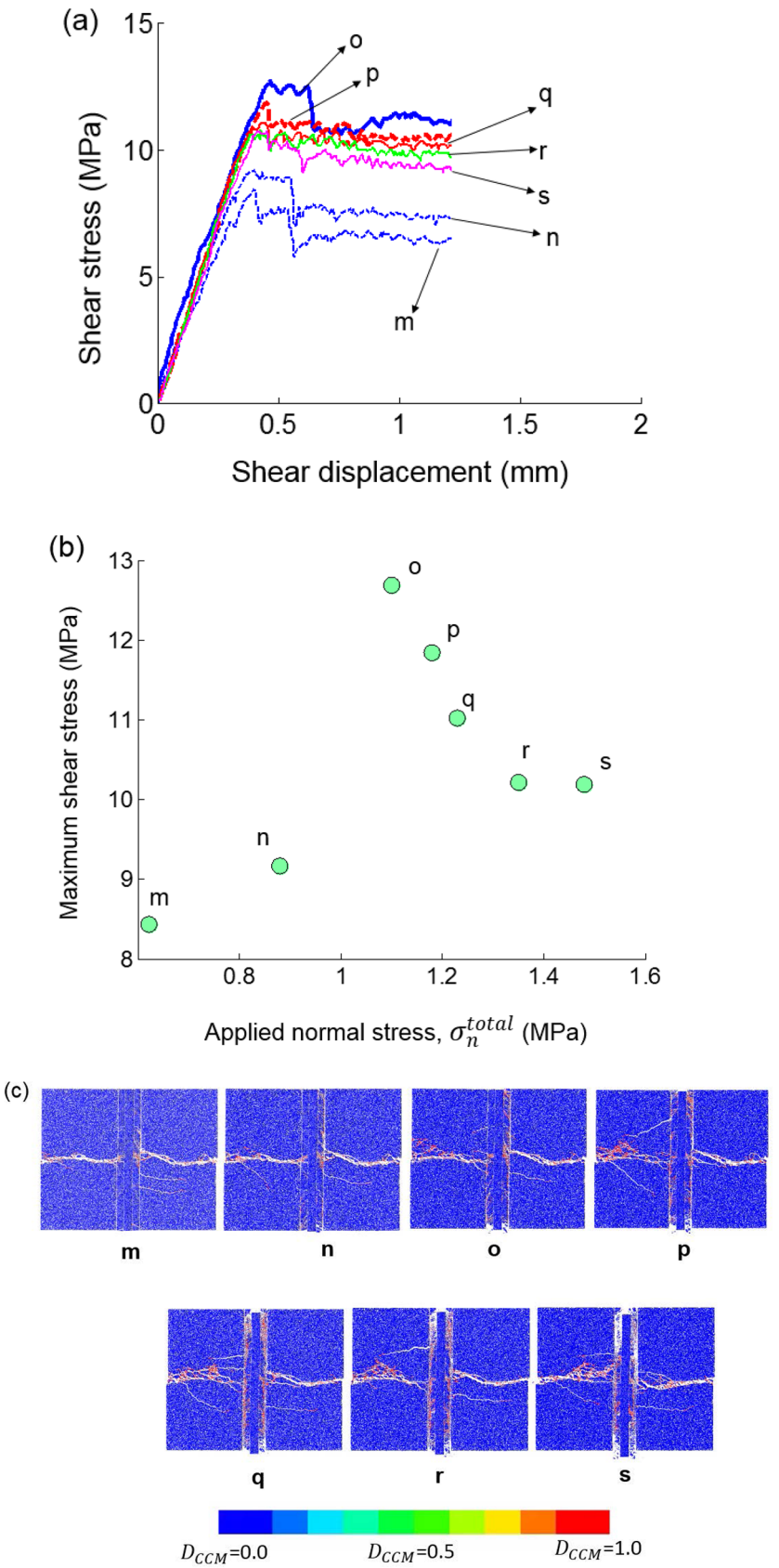

Fig. 13 Numerical direct shear test results of a bolted rock joint with different pretension stress magnitude: **a** shear stress–displacement curves; **b** maximum shear strength of the bolted rock joint at different pretension stress magnitudes; **c** corresponding damage response of the cohesive contacts after completing the direct shear tests

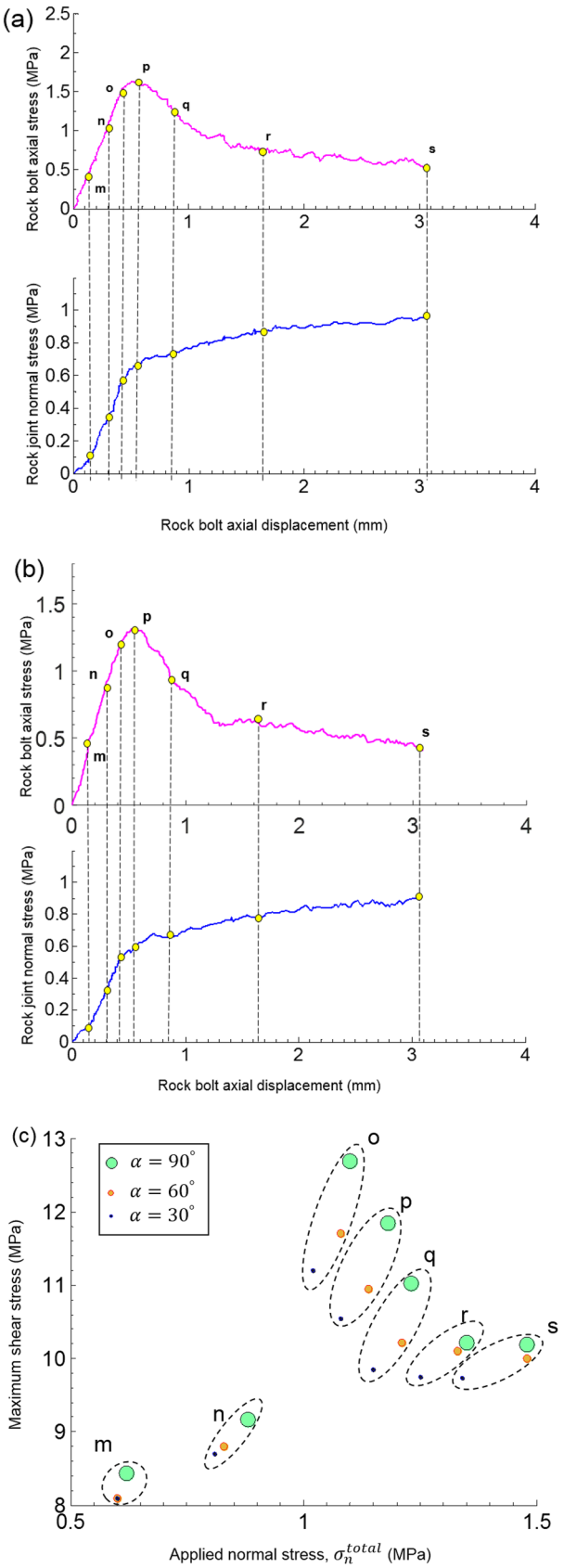

Fig. 14 Numerical results of the combined pull–shear tests using different rib angles (α): **a**, **b** pull-out test results for rib angles of 60° and 30°, respectively; **c** maximum shear resistance of bolted rock joints versus applied normal stress at different pretension stress magnitudes for various rib angles

$$\sigma_{\mathrm{n}}^{\mathrm{u}} = \sigma_{\mathrm{total}}^{\mathrm{n}} + \mathrm{d}\sigma_{\mathrm{n}}, \tag{21}$$

where k^{cns} is the constant normal stiffness at an external boundary, and $\mathrm{d}\delta_{\mathrm{n}}$ is the increment of normal displacement (Indraratna et al. 2015). $\sigma_{\mathrm{n}}^{\mathrm{u}}$ is the updated normal stress in the CNS direct shear test. $\sigma_{\mathrm{n}}^{\mathrm{total}}$ was calculated as: $\sigma_{\mathrm{n}}^{\mathrm{total}} = \sigma_{\mathrm{n}}^{0} + \sigma_{\mathrm{n}}^{\mathrm{i}}$, and the magnitude of σ_{n}^{0} was 0.5 MPa. In the numerical models, the normal displacement of the top wall was measured at each time step, which represented the normal displacement of rock joint. The reaction force induced on the top wall was also measured, and was divided by the length of rock joints to calculate the normal stress.

We took the following steps to implement the CNS condition in PFC2D:

1. Apply a relatively small velocity on the top of the specimen, solve the model to equilibrium. At this step, the aim was to reach the initial normal stress magnitude (σ_{n}^{0}). The servo-controlled mechanism was activated during this step.
2. Begin the direct shear test by applying a horizontal velocity of 0.01 m/s on the top left wall after the specimen reaches the desired initial normal stress. Due to progressive shear displacement, the rock joint tended to dilate. This normal displacement was used to calculate the incremental normal stress magnitude ($\mathrm{d}\sigma_{\mathrm{n}}$ in Eq. 20). Before beginning this step, the applied normal stress was updated ($\sigma_{\mathrm{n}}^{\mathrm{u}}$), and with the assistance of the servo-controlled mechanism, the newly defined target was achieved.

Seven different direct shear tests were conducted using the pretension stress magnitudes, as obtained in Sect. 5.1. The maximum shear strength of the bolted rock joint with respect to $\sigma_{\mathrm{n}}^{\mathrm{total}}$ is shown in Fig. 16a. Observe that the CNS condition resulted in an increase in the shear resistance of the bolted rock joint. However, the influence of the CNS condition was more significant at the pretension stress magnitudes obtained from the elastic response to the pull-out test (i.e., points "m" and "n" in Fig. 16a). At point "o", which reproduced the highest possible shear resistance, the effect of the CNS condition starts to diminish. For the peak axial strength of the bolt–grout interface (point "p") and post-peak stress magnitudes, no outstanding difference was observed between the CNL and CNS test results.

The experimental results of Indraratna et al. (2015) on unbolted rock joints showed that when the initial normal

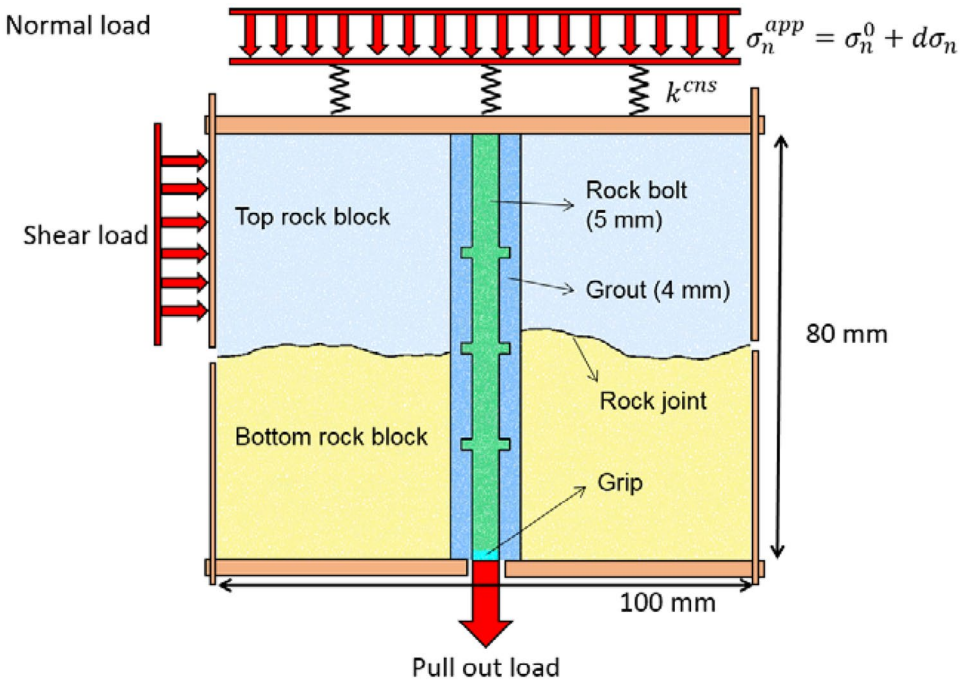

Fig. 15 Numerical test setup for conducting a direct shear test on a bolted rock joint with a fully grouted rock bolt subjected to combined pull–shear loads under the CNS condition

stress is high, an increase in the normal stress occurs at a lower rate due to significant asperity degradation. Figure 16b illustrates the rate of increase in the normal stress magnitude (σ_n^{total}) against the progressive shear displacement of the bolted rock joint. These results demonstrate that an increase in σ_n^{total} reached its highest rate for points "m" and "n", but it declined from point "o" to "s". We attributed the reduction in the shear resistance of the bolted rock joint to severe asperity damage at high σ_{total}^{n}.

These findings are consistent with the laboratory observation of Indraratna et al. (2015), in which they concluded that when the initial normal stress is high, an increase in the normal stress occurs at a lower rate due to significant asperity degradation.

6 Conclusion

This paper presented a new cohesive DEM framework, employed for modelling rock joints reinforced with fully grouted rock bolts combining damage mechanics with a plasticity law.

The model was implemented as both a material and an interface contact law to mimic the progressive softening behaviour of cement bridges in both grout and rock material, as well as in a bolt–grout interface. Through various numerical simulations, we showed that the proposed modelling method was capable of reproducing the fracture behaviour of grout, bolt–grout interfaces, and rock joints, evidence for which were the excellent agreement of the stress–displacement and cracking patterns of the numerical simulations and their experimental counterparts. Specifically, the proposed model demonstrated that it is able to capture the post-peak softening response of grout material during uniaxial compressive loading, which the current constitutive models in DEM codes (i.e., FJM in PFC2D) cannot accurately obtain.

This paper also demonstrated through numerical experiments that the novel, stepwise pull-and-shear test (SPST) scheme, developed to conduct combined pull-and-shear loading tests, can identify the hidden mechanisms involved in the shear resistance behaviour of bolted rock joints. The idea was to apply pretension stress (i.e., pull-out load) on the rock bolt, and then perform direct shear tests on bolted rock joints. The numerical analyses of the pull-out experiment showed that four different stages (i.e., linear elastic, pre-peak hardening, post-peak softening, and residual stage) are involved in the failure of fully grouted rock bolts. During the pull-out test, we monitored the σ_n^i and its corresponding contact chain force network. Results showed that σ_n^i increased and the contact compressive forces grew throughout the experiment, but the rate of increase significantly declined at the yield point, where the transition from a linear elastic to a pre-peak response occurred. The numerical direct shear tests also demonstrated that at yield pretension stress magnitude, the bolt delivered its ultimate performance; thus, maximum shear resistance was achieved at this point. The numerical observations revealed that the peak stress reduced with a decreasing rib angle of the rock bolt profile and that this reduction was more pronounced for rib angles of 30°, which induced the lowest σ_n^i.

To better analyse the numerical results, the maximum shear stresses were plotted against their corresponding

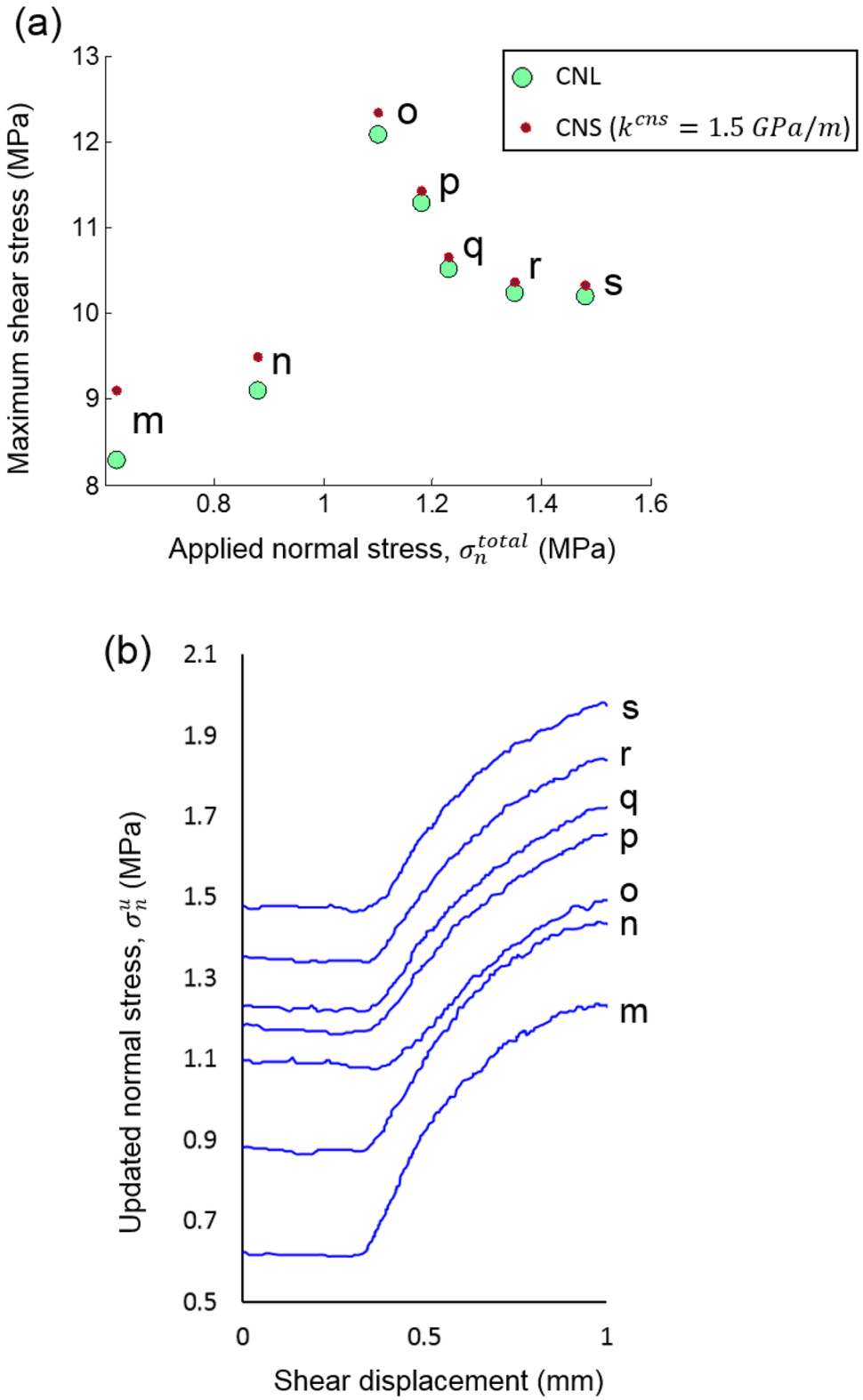

Fig. 16 Result of combined pull–shear tests under CNS condition: **a** comparison of maximum shear strength of bolted rock joints reinforced with fully grouted rock bolt under CNL and CNS conditions, **b** applied normal stress (under CNS condition) versus shear displacement at various pretension stress magnitudes

normal stresses, and a similar trend was observed for all rib angles, which gave rise to the fact that fully grouted rock bolts had the highest efficacy at the onset of the transition from linear elastic to pre-peak hardening behaviour. The numerical simulations showed that applying the CNS condition resulted in an increase in the peak resistance of rock joint, which was more pronounced at low pretension stress magnitudes in the elastic stage. During both the

softening and the residual stages, however, the effect of the CNS condition was negligible.

The proposed modelling method, in conjunction with the SPST scheme, provided an efficient numerical framework that can be used by designers and geotechnical engineers for carrying out realistic experiments (i.e., combined pull–shear loads). Doing so will give them new insights into the mechanical performance of fully grouted rock bolts.

Acknowledgements The cohesive model employed in this study was formulated based on a generic framework by Giang D. Nguyen (University of Adelaide) and Ha H. Bui (Monash University), with Giang D. Nguyen's help in the development and revision of the model. The first author thanks Mr Sacha Emam from Itasca Consulting group for his invaluable help and comments during implementation and verification of the model in PFC software. The comments from Dr. David O. Potyondy from Itasca Consulting group are highly appreciated. The authors also acknowledge the assistance of professional editor Leticia Mooney in preparation of this paper.

Compliance with Ethical Standards

Conflict of interest The first author declares that he has no conflict of interest. The second author declares that he has no conflict of interest.

References

Aziz N, Jalalifar H, Concalves J (2006) Bolt surface configurations and load transfer mechanism. In: Aziz, Keilich (eds) Proceedings of 7th underground coal operators conference, coal 2006. Wollongong, 5–7 July, pp 236–244. http://www.ro.uow.edu.au/coal/51/

Bahaaddini M (2014) Numerical study of the mechanical behaviour of rock joints and non-persistent jointed rock masses. PhD thesis, The University of New South Wales, Sydney, Australia

Bahaaddini M, Sharrock G, Hebblewhite B (2013) Numerical direct shear tests to model the shear behaviour of rock joints. Comput Geotech 51:101–115

Bahrani N, Kaiser PK, Valley B (2014) Distinct element method simulation of an analogue for a highly interlocked, non-persistently jointed rockmass. Int J Rock Mech Min Sci 71:117–130. https://doi.org/10.1016/j.ijrmms.2014.07.005

Bandis SC, Lumsden AC, Barton NR (1983) Fundamentals of rock joint deformation. Int J Rock Mech Min Sci Geomech Abstr 20:249–268. https://doi.org/10.1016/0148-9062(83)90595-8

Bewick RP, Kaiser PK, Bawden WF (2014a) Shear rupture under constant normal stiffness boundary conditions. Tectonophysics 634:76–90. https://doi.org/10.1016/j.tecto.2014.07.016

Bewick RP, Kaiser PK, Bawden WF, Bahrani N (2014b) DEM simulation of direct shear: 1. rupture under constant normal stress boundary conditions. Rock Mech Rock Eng 47:1647–1671. https://doi.org/10.1007/s00603-013-0490-8

Bjurstrom S (1974) Shear strength of hard rock joint reinforced by grouted untensioned bolts. In: Proceedings of the International Congress of Rock Mechanics, Denver, pp 1194–1199

Cao C, Ren T, Cook C, Cao Y (2014) Analytical approach in optimising selection of rebar bolts in preventing rock bolting failure. Int J Rock Mech Min Sci 72:16–25. https://doi.org/10.1016/j.ijrmms.2014.04.026

Chen Y, Li C (2015a) Influences of loading condition and rock strength to the performance of rock bolts. Geotech Test J 38:208–218. https://doi.org/10.1520/GTJ20140033

Chen Y, Li CC (2015b) Performance of fully encapsulated rebar bolts and D-Bolts under combined pull-and-shear loading. Tunn Undergr Space Technol 45:99–106. https://doi.org/10.1016/j.tust.2014.09.008

Chen N, Zhang X, Jiang Q, Feng X, Wei W, Yi B (2018) Shear behavior of rough rock joints reinforced by bolts. Int J Geomech 18:04017130. https://doi.org/10.1061/(ASCE)GM.1943-5622.0001048

Cundall P, Strack O (1979) A discrete numerical model for granular assemblies. Geotechnique 29:47–65

Dey A (2001) Shear behaviour of fully grouted bolts under constant normal stiffness condition. PhD thesis, University of Wollongong, NSW, Australia

Dight PM, Chiu HK (1981) Prediction of shear behaviour of joints using profiles. Int J Rock Mech Min Sci Geomech Abstr 18:369–386. https://doi.org/10.1016/0148-9062(81)90002-4

Feng S, Liu X, Chen H, Zhao T (2018) Micro-mechanical analysis of geomembrane-sand interactions using DEM. Comput Geotech 94:58–71

Ferrero AM (1995) The shear strength of reinforced rock joints. Int J Rock Mech Min Sci Geomech Abstr 32:595–605. https://doi.org/10.1016/0148-9062(95)00002-X

Gao F, Kang H (2017) Experimental study on the residual strength of coal under low confinement. Rock Mech Rock Eng 50:285–296. https://doi.org/10.1007/s00603-016-1120-z

Gilbert D, Mirzaghorbanali A, Li X, Rasekh H, Aziz N, Nemcik J (2015) Strength properties of fibre glass and other polymer based dowels for strata reinforcement in coal mines. In: Coal operators' conference. University of Wollongong, Wollongong, pp 365–375. https://ro.uow.edu.au/coal/586/

Grasselli G (2005) 3D Behaviour of bolted rock joints: experimental and numerical study. Int J Rock Mech Min Sci 42:13–24. https://doi.org/10.1016/j.ijrmms.2004.06.003

Gutiérrez-Ch JG, Senent S, Melentijevic S, Jimenez R (2018) Distinct element method simulations of rock-concrete interfaces under different boundary conditions. Eng Geol 240:123–139. https://doi.org/10.1016/j.enggeo.2018.04.017

Haas C (1976) Shear resistance of rock bolts. Soc Min Eng 260:32–41

He L, An XM, Zhao XB, Zhao ZY, Zhao J (2018) Development of a unified rock bolt model in discontinuous deformation analysis. Rock Mech Rock Eng 51:827–847. https://doi.org/10.1007/s00603-017-1341-9

Hofmann H, Babadagli T, Yoon JS, Zang A, Zimmermann G (2015a) A grain based modeling study of mineralogical factors affecting strength, elastic behavior and micro fracture development during compression tests in granites. Eng Fract Mech 147:261–275. https://doi.org/10.1016/j.engfracmech.2015.09.008

Hofmann H, Babadagli T, Zimmermann G (2015b) A grain based modeling study of fracture branching during compression tests in granites. Int J Rock Mech Min Sci 77:152–162. https://doi.org/10.1016/j.ijrmms.2015.04.008

Huang Z, Broch E, Lu M (2002) Cavern roof stability—mechanism of arching and stabilization by rockbolting. Tunn Undergr Space Technol 17:249–261. https://doi.org/10.1016/S0886-7798(02)00010-X

Indraranta B, Welideniya H, Brown E (2005) A shear strength model for idealised infilled joints under constant normal stiffness. Géotechnique 55:215–226

Indraratna B, Haque A (2000) Shear behaviour of rock joints. A.A. Balkema, Rotterdam

Indraratna B, Welideniya HS (2003) Shear Behaviour of Graphite Infilled Joints Based On Constant Normal Stiffness (CNS) Test Conditions. In: Paper presented at the 10th ISRM Congress, Sandton, South Africa

Indraratna B, Thirukumaran S, Brown ET, Zhu S-P (2015) Modelling the shear behaviour of rock joints with asperity damage under constant normal stiffness. Rock Mech Rock Eng 48:179–195. https://doi.org/10.1007/s00603-014-0556-2

Itasca Consulting Group Inc (2016) PFC manual, version 5.0, Minneapolis

Jalalifar H, Aziz N (2010a) Analytical behaviour of bolt-joint intersection under lateral loading conditions. Rock Mech Rock Eng 43:89–94. https://doi.org/10.1007/s00603-009-0032-6

Jalalifar H, Aziz N (2010b) Experimental and 3D numerical simulation of reinforced shear joints. Rock Mech Rock Eng 43:95–103. https://doi.org/10.1007/s00603-009-0031-7

Jalalifar H, Aziz N, Hadi M (2006) The effect of surface profile, rock strength and pretension load on bending behaviour of fully grouted bolts. Geotech Geol Eng 24:1203–1227. https://doi.org/10.1007/s10706-005-1340-6

Jin-feng Z, Peng-hao Z (2019) Analytical model of fully grouted bolts in pull-out tests and in situ rock masses. Int J Rock Mech Min Sci 113:278–294. https://doi.org/10.1016/j.ijrmms.2018.11.015

Kılıc A, Yasar E, Celik AG (2002) Effect of grout properties on the pull-out load capacity of fully grouted rock bolt. Tunn Undergr Space Technol 17:355–362. https://doi.org/10.1016/S0886-7798(02)00038-X

Le LA, Nguyen GD, Bui HH, Sheikh AH, Kotousov A, Khanna A (2017) Modelling jointed rock mass as a continuum with an embedded cohesive-frictional model. Eng Geol 228:107–120. https://doi.org/10.1016/j.enggeo.2017.07.011

Le LA, Nguyen GD, Bui HH, Sheikh AH, Kotousov A (2018) Localised failure mechanism as the basis for constitutive modelling of geomaterials. Int J Eng Sci 133:284–310. https://doi.org/10.1016/j.ijengsci.2018.09.004

Li CC (2010) Field observations of rock bolts in high stress rock masses. Rock Mech Rock Eng 43:491–496. https://doi.org/10.1007/s00603-009-0067-8

Li CC (2012) Performance of D-bolts under static loading. Rock Mech Rock Eng 45:183–192. https://doi.org/10.1007/s00603-011-0198-6

Li L, Hagan PC, Saydam S, Hebblewhite B, Li Y (2016a) Parametric study of rockbolt shear behaviour by double shear test. Rock Mech Rock Eng 49:4787–4797. https://doi.org/10.1007/s00603-016-1063-4

Li X, Aziz N, Mirzaghorbanali A, Nemcik J (2016b) Behavior of fiber glass bolts, rock bolts and cable bolts in shear. Rock Mech Rock Eng 49:2723–2735. https://doi.org/10.1007/s00603-015-0907-7

Li Y, Oh J, Mitra R, Hebblewhite B (2016c) Experimental studies on the mechanical behaviour of rock joints with various openings. Rock Mech Rock Eng 49:837–853. https://doi.org/10.1007/s00603-015-0781-3

Li D, Masoumi H, Hagan PC, Saydam S (2019) Experimental and analytical study on the mechanical behaviour of cable bolts subjected to axial loading and constant normal stiffness. Int J Rock Mech Min Sci 113:83–91. https://doi.org/10.1016/j.ijrmms.2018.11.011

Lisjak A, Grasselli G (2014) A review of discrete modeling techniques for fracturing processes in discontinuous rock masses. J Rock Mech Geotech Eng 6:301–314. https://doi.org/10.1016/j.jrmge.2013.12.007

Liu G, Cai M, Huang M (2018) Mechanical properties of brittle rock governed by micro-geometric heterogeneity. Comput Geotech. https://doi.org/10.1016/j.compgeo.2017.11.013

Ma S, Aziz N, Nemcik J, Mirzaghorbanali A (2017) The effects of installation procedure on bond characteristics of fully grouted rock bolts. Geotech Test J 40:846–857. https://doi.org/10.1520/GTJ20160239

McHugh E, Signer S (1999) Roof bolt response to shear stress: laboratory analysis. In: Peng and C. Mark (eds) Proceedings of 18th International Conference on Ground Control in Mining. WV University, Morgantown, 3–5 Aug, pp 232–238. https://www.cdc.gov/niosh/mining/works/coversheet573.html

Mirzaghorbanali A, Rasekh H, Aziz N, Yang G, Khaleghparast S, Nemcik J (2017) Shear strength properties of cable bolts using a new double shear instrument, experimental study, and numerical simulation. Tunn Undergr Space Technol 70:240–253. https://doi.org/10.1016/j.tust.2017.07.018

Nguyen NHT, Bui HH, Nguyen GD, Kodikara J (2017a) A cohesive damage-plasticity model for DEM and its application for numerical investigation of soft rock fracture properties. Int J Plast 98:175–196. https://doi.org/10.1016/j.ijplas.2017.07.008

Nguyen NHT, Bui HH, Nguyen GD, Kodikara J, Arooran S, Jitsangiam P (2017b) A thermodynamics-based cohesive model for discrete element modelling of fracture in cemented materials. Int J Solids Struct 117:159–176. https://doi.org/10.1016/j.ijsolstr.2017.03.027

Oh J, Li Y, Mitra R, Canbulat I (2017) A numerical study on dilation of a saw-toothed rock joint under direct shear. Rock Mech Rock Eng 50:913–925

Potyondy D (2012) FC2D flat-joint contact model. Itasca Consulting Group Inc, Minneapolis

Potyondy D, Cundall P (2004) A bonded-particle model for rock. Int J Rock Mech Min Sci 41:1329–1364

Rasekh H, Aziz N, Mirza A, Nemcik J, Li X, Yang G, Khaleghparast S (2017) Double shear testing of cable bolts with no concrete face contacts. Procedia Eng 191:1169–1177. https://doi.org/10.1016/j.proeng.2017.05.292

Saadat M, Taheri A (2019) A numerical approach to investigate the effects of rock texture on the damage and crack propagation of a pre-cracked granite. Comput Geotech 111:89–111. https://doi.org/10.1016/j.compgeo.2019.03.009

Shang J, Yokota Y, Zhao Z, Dang W (2018a) DEM simulation of mortar-bolt interface behaviour subjected to shearing. Constr Build Mater 185:120–137. https://doi.org/10.1016/j.conbuildmat.2018.07.044

Shang J, Zhao Z, Ma S (2018b) On the shear failure of incipient rock discontinuities under CNL and CNS boundary conditions: insights from DEM modelling. Eng Geol 234:153–166. https://doi.org/10.1016/j.enggeo.2018.01.012

Spang K, Egger P (1990) Action of fully-grouted bolts in jointed rock and factors of influence. Rock Mech Rock Eng 23:201–229. https://doi.org/10.1007/BF01022954

Srivastava LP, Singh M (2015) Effect of fully grouted passive bolts on joint shear strength parameters in a blocky mass. Rock Mech Rock Eng 48:1197–1206. https://doi.org/10.1007/s00603-014-0615-8

Tao W, Chen C, Jun H, Ting R (2017) Effect of bolt rib spacing on load transfer mechanism. Int J Min Sci Tech 27:431–434. https://doi.org/10.1016/j.ijmst.2017.03.009

Thenevin I, Blanco-Martín L, Hadj-Hassen F, Schleifer J, Lubosik Z, Wrana A (2017) Laboratory pull-out tests on fully grouted rock bolts and cable bolts: results and lessons learned. J Rock Mech Geotech Eng 9:843–855. https://doi.org/10.1016/j.jrmge.2017.04.005

Thirukumaran S, Indraratna B (2016) A review of shear strength models for rock joints subjected to constant normal stiffness. J Rock Mech Geotech Eng 8:405–414. https://doi.org/10.1016/j.jrmge.2015.10.006

Thirukumaran S, Indraratna B, Brown ET, Kaiser PK (2016) Stability of a rock block in a tunnel roof under constant normal stiffness conditions. Rock Mech Rock Eng 49:1587–1593. https://doi.org/10.1007/s00603-015-0770-6

Vlachopoulos N, Cruz D, Forbes B (2018) Utilizing a novel fiber optic technology to capture the axial responses of fully grouted rock bolts. J Rock Mech Geotech Eng 10:222–235. https://doi.org/10.1016/j.jrmge.2017.11.007

Wang G, Zhang Y, Jiang Y, Liu P, Guo Y, Liu J, Ma M, Wang K, Wang S (2018) Shear behaviour and acoustic emission characteristics of bolted rock joints with different roughnesses. Rock Mech Rock Eng. https://doi.org/10.1007/s00603-018-1438-9

Wu X, Jiang Y, Li B (2018) Influence of joint roughness on the shear behaviour of fully encapsulated rock bolt. Rock Mech Rock Eng 51:953–959. https://doi.org/10.1007/s00603-017-1365-1

Yazici S, Kaiser PK (1992) Bond strength of grouted cable bolts. Int J Rock Mech Min Sci Geomech Abstr 29:279–292. https://doi.org/10.1016/0148-9062(92)93661-3

Yokota Y, Zhao Z, Nie W, Date K, Iwano K, Okada Y (2018) Experimental and numerical study on the interface behaviour between the rock bolt and bond material. Rock Mech Rock Eng. https://doi.org/10.1007/s00603-018-1629-4

Yokota Y, Zhao Z, Shang J, Nie W, Date K, Iwano K, Okada Y (2019) Effect of bolt configuration on the interface behaviour between a rock bolt and bond material: a comprehensive DDA investigation. Comput Geotech 105:116–128. https://doi.org/10.1016/j.compgeo.2018.09.017

Yoshinaka R, Sakaguchi S, Shimizu T, Arai H, Kato E (1987) Experimental study on the rock bolt reinforcement in discontinuous rocks. In: Paper presented at the 6th ISRM congress, Montreal, Canada

Zhou J, Zhang L, Pan Z, Han Z (2017) Numerical studies of interactions between hydraulic and natural fractures by smooth joint model. J Nat Gas Sci Eng 46:592–602. https://doi.org/10.1016/j.jngse.2017.07.030

Zou DHS, Cheng J, Yue R, Sun X (2010) Grout quality and its impact on guided ultrasonic waves in grouted rock bolts. J Appl Geophys 72:102–106. https://doi.org/10.1016/j.jappgeo.2010.07.006

Appendix B (Paper 2)

A cohesive discrete element based approach to characterizing the shear behaviour of cohesive soil and clay-infilled rock joints

Saadat M, Taheri A. (2019) A cohesive discrete element based approach to characterizing the shear behavior of cohesive soil and clay-infilled rock joints. *Computers and Geotechnics 114*: 103109. doi: https://doi.org/10.1016/j.compgeo.2019.103109

Statement of Authorship

Title of Paper	A cohesive discrete element based approach to characterizing the shear behaviour of cohesive soil and clay-infilled rock joints
Publication Status	✓ Published ☐ Accepted for Publication ☐ Submitted for Publication ☐ Unpublished and Unsubmitted work written in manuscript style
Publication Details	Saadat M, Taheri A. (2019) A cohesive discrete element based approach to characterizing the shear behavior of cohesive soil and clay-infilled rock joints. Computers and Geotechnics 114: 103109. doi: https://doi.org/10.1016/j.compgeo.2019.103109

Principal Author

Name of Principal Author (Candidate)	Mahdi Saadat
Contribution to the Paper	Developed the cohesive DEM framework Conducted the experimental testing on infilled rock joints Conducted the numerical modelling of infilled rock joints Analysed the experimental and numerical results Wrote the entire manuscript
Overall percentage (%)	80%
Certification:	This paper reports on original research I conducted during the period of my Higher Degree by Research candidature and is not subject to any obligations or contractual agreements with a third party that would constrain its inclusion in this thesis. I am the primary author of this paper.
Signature	Date: 07 August 2019

Co-Author Contributions

By signing the Statement of Authorship, each author certifies that:

i. the candidate's stated contribution to the publication is accurate (as detailed above);

ii. permission is granted for the candidate in include the publication in the thesis; and

iii. the sum of all co-author contributions is equal to 100% less the candidate's stated contribution.

Name of Co-Author	Dr Abbas Taheri		
Contribution to the Paper	Supervision of the technical work, revision of the manuscript		
Signature		Date	07 August 2019

End of the document

Computers and Geotechnics 114 (2019) 103109

Contents lists available at ScienceDirect

Computers and Geotechnics

journal homepage: www.elsevier.com/locate/compgeo

Research Paper

A cohesive discrete element based approach to characterizing the shear behavior of cohesive soil and clay-infilled rock joints

Mahdi Saadat*, Abbas Taheri

School of Civil, Environmental and Mining Engineering, The University of Adelaide, Australia

ARTICLE INFO

Keywords:
Infilled rock joint
Plasticity theory
Cohesive contact model
Discrete element method
Damage mechanics

ABSTRACT

The mechanical behaviour of the infilled rock joints is highly concerned in rock joint studies due to its involvement in a wide range of mining collapses. In this study, a new cohesive constitutive model was employed and used in discrete element method (DEM) simulation to analyse the failure mechanism of infilled rock joints numerically. The exponential softening responses of the model in mixed mode loading conditions allow more realistic modelling of clay-infilled rock joints, which is more phenomenologically promising than the use of the current constitutive models in PFC2D such as the parallel bond model (PBM). The proposed model is implemented in DEM commercial codes (PFC2D) as a user-defined contact constitutive model. In parallel with this theoretical development, experimental works on shear behaviour of infilled materials and infilled rock joints under different normal loads are also carried out for the calibration of the cohesive model, and validation of the DEM based approach, respectively. Simulation results show excellent agreement with experimental counterparts demonstrating the effectiveness of the proposed cohesive model in reproducing the shear properties of clay-infilled rock joint. The proposed cohesive DEM framework, therefore, will facilitate better understanding of the shear mechanism of cohesive infilled rock joints.

1. Introduction

In highly fractured or randomly jointed rock mass or very soft rock, rock mass may be assumed isotropic and mechanical properties may be estimated using in-situ test methods or empirical approaches [1,2]. However, in many cases discontinuities mainly control failure mechanism and, therefore, it is crucial to estimate the shear behaviour of rock joints. The presence of infill material within a joint can significantly influence its shear strength. Infill thickness and asperity angle are the most important parameters controlling the shear behaviour of infilled rock joints [3–5]. The characterisation and prediction of the shear mechanism of infilled rock joints is a significant problem in rock engineering projects. For instance, Indraratna et al. [6] reported that using an oversimplified constitutive model in the design process, which neglected the role of infill material, could have contributed to the collapse of São Paulo metro station. Thus, improving the understanding of the shear behaviour of infilled rock joints for better prediction of failure is crucial to practical applications in mining and geotechnical engineering.

In recent decades, researchers and scholars have made great efforts, from the perspectives of laboratory tests [7–14] to study the shear behaviour of infilled rock joints. Although laboratory testing is the most common approach for investigating the shear mechanism and mechanical behaviour of infilled rock joints, experimental set up requires an enormous amount of resources. Generating a wide range of specimens with various asperity angles, having access to advanced laboratory apparatus, and time-consuming nature of the experimental procedure are the main issues making the laboratory investigation practically complicated and sometimes economically inefficient. Furthermore, observation of the failure mode throughout the testing procedure and afterwards is a difficult task, if not impossible. This may be occurred due to the disturbance of the infilled rock joint after sample removal from the shear box. To reduce the difficulties of laboratory investigations, some scholars developed empirical models [6,10]. However, empirical modelling is based on the data obtained from one case study which makes it difficult to generalise the formulation for further investigations. Furthermore, empirical formulas are based on a number of unknown fixed ratios and fitting parameters with no physical interpretation that increases the level of uncertainty of these approaches for real-world problems.

Alternatively, in the last several decades, computational methods have provided a versatile tool for simulating the failure behaviour of various geomaterials such as rock and soil. As the power of computers has been rising dramatically, computational methods as a

* Corresponding author.
E-mail address: mahdi.saadat@adelaide.edu.au (M. Saadat).

https://doi.org/10.1016/j.compgeo.2019.103109
Received 2 March 2019; Received in revised form 22 April 2019; Accepted 23 May 2019

complementary tool have become increasingly popular amongst scientists and engineers. As a promising alternative tool for scientific research, the numerical simulations could overcome the difficulties arising from laboratory testing [15]. Once being calibrated with the laboratory data, numerical modelling has the potential to solve complex scientific and engineering problems and obtain better insight in the relevant failure mechanisms of soil and rock through considerable variation in repeatability and robustness of the simulations [16].

The infill material within rock joint may be classified as being either cohesive (clay) or frictional (sand) [17]. In order to characterise the intrinsic failure mechanisms of the cohesive or frictional soil, these mechanisms should be phenomenologically incorporated in the constitutive relationship of the numerical models. The constitutive models are often incorporated in continuum- or discontinuum-based methods [18–22]. Characterising the morphological features of the infilled rock joint is a difficult and challenging task, particularly, reproducing the cohesive behaviour of the soil at micro/meso scale in which the softening response of the material and the gradual degradation of its cohesion needs to be explicitly simulated [20,21]. In that regard, continuum-based approach is considered to be too simple as they cannot adequately take into account the morphological characteristics of the infilled rock joint explicitly. As an alternative, discontinuum approaches have been considered as a promising numerical tool for characterising the softening response of different materials. Discontinuum approaches consider the material domain as an assembly of particles displacing independent of each other and interacting at pairwise contact [23–25]. Initially proposed by Cundall and Strack [26], Discrete Element Method (DEM) is an efficient simulation method providing insight into interparticle forces and microstructure evolution [27]. This method is capable of reproducing crack initiation and propagation processes with breaking the bond between particles. Despite being a promising numerical framework, DEM requires a suitable constitutive model describing the interaction between particles to characterise the mechanical behaviour of materials. A key benefit of DEM approach is that without prescribing the failure evolution laws, the macroscopic behaviour of the material can be reproduced as a result of a microscale damage [28–30].

Potyondy and Cundall [31] firstly developed bonded particle model (BPM) to reproduce the mechanical behaviour of materials by generating a collection of non-uniform-sized circular or rigid spherical particles that may or may not be bonded together. A new version of BPM known as a linear parallel bond model (PBM) is currently available via commercial DEM codes, particle flow code (PFC) [24]. This model assumes interparticle behaviour is perfectly brittle and has been successfully employed by many scholars to simulate rock material (e.g. Bahaaddini et al. [32], Bewick et al. [33], Cheng et al. [34], Cho et al. [35], Cho et al. [36], Cui [37], Wang et al. [38], Zhang et al. [39], Al-Halbouni et al. [40]). For cohesive soils, the PBM may still be employed to simulate their failure behaviour if DEM particles are generated at the molecular scale, which inhibits the practical application of DEM due to immense computational demand [20]. For making the numerical process time efficient, DEM particles are required to be created at granular scales. Therefore, the damage mechanism (e.g. cohesive softening response) have to be embodied in the constitutive contact model.

The shear stress-deformation relationships of cohesive soils are characterised by a peak strength followed by a gradual reduction in strength to a residual strength [41]. At a molecular scale, the strength of cohesive soils is governed mainly by the forces between clay particles, which composed of cohesion and friction components [42]. The shear failure of cohesive soils is associated with the gradual weakening of the bonds between clay particles (i.e. softening response at particle level). After peak shear strength is reached, strain localisation will occur, resulting in the development of a shear band [43]. With the progressive shearing, microscopic frictional interaction between localised surfaces occurs, leading to a macroscopic residual response of the clay [44]. In this context, the gradual degradation of cohesion between soil particles can be described by damage mechanics, while plasticity theory can characterise the frictional interaction.

Utili and Nova [45] proposed a DEM-based contact bond model based on Mohr-Coulomb failure criteria to simulate the mechanical behaviour of frictional cohesionless and cohesive soil. Obermayr et al. [46] modelled the cohesive behaviour of soil by adding an attractive normal force between DEM particles. Karakus et al. [47] employed Flat-Joint model [48] to characterize the mechanical behaviour of infilled rock joints. However, the investigations mentioned above lacked a general expression for gradual softening of the contacts, which precludes capturing the associative shear mechanism of cohesive soils. Despite a number of investigations on the mechanical behaviour of rock joints and soil-structure interface using DEM approach [32,49–52], very few researchers have focused on the explicit simulation of infilled rock joints, specifically, clay-infilled rock joints. For instance, Duriez et al. [53] used a non-cohesive DEM framework to simulate infilled rock joints. Their numerical sample consisted of a parallelepiped box filled with DEM particles representing the infill material. Although the type of infill material (cohesive or non-cohesive) was not declared, it can be deduced from their DEM framework that the focus of their study was on non-cohesive infilled rock joints. The rock joint configuration (i.e. asperities), which contributes to peak shear strength, was also neglected in the generation of DEM specimens.

In the present study, a series of experimental direct shear tests were conducted to observe the influence of asperity angle (20° and 30°) and infill thickness (6 and 12 mm) on the peak shear and residual strength of clay-infilled rock joints. The macroscopic cohesion and friction angle of clay (i.e. kaolin) were obtained by conducting direct shear tests under constant normal load (CNL) condition with 100, 200, and 300 kPa of normal stress magnitude. The laboratory observations showed that by decreasing the ratio of infill thickness to the asperity height, the peak shear strength of the infilled rock joint decreased. In parallel, a DEM model was generated taking into account the rock joint geometries and infill thickness. A straightforward cohesive contact model developed by Saadat and Taheri [54] was employed to model the softening response of the cohesive infill material. The model constitutive relationships were augmented with mixed-mode behaviour and softening response of the bonded contacts, which allowed us to reproduce the progressive damage of rock joint. The model was implemented in PFC2D, and its micro mechanical parameters were first calibrated with experimental data under 100 kPa normal stress. The calibration procedure was successfully verified by repeating two more numerical tests with 200 and 300 kPa normal stresses and comparing the results with the experimental counterparts. To further assess the applicability of the proposed numerical framework to laboratory scale problems, the calibrated model was used to simulate the mechanical and damage behaviour of rock joints containing cohesive infill material. The comparison between experimental and numerical results shows that the proposed cohesive DEM framework can reasonably reproduce the failure behaviour of clay-infilled rock joints with different infill thickness to asperity height ratio. This DEM study will enable us to understand better the influence of infill thickness, asperity height, and magnitude of normal stress on the failure mechanism of infilled rock joints in detail, which in turn allow us to improve the quality of design in rock engineering projects while reducing cost and increasing safety.

2. Experimental programme

2.1. Direct shear test on a cohesive soil

Before using the DEM-based cohesive model, the micro-parameters of the model should be calibrated against the macroscopic response of a cohesive soil in the laboratory. We used kaolin clay as infill material, which was commercially purchased from SIBELCO [55]. The details of infill properties are given in Table 1. A series of direct shear test was performed on the soil samples under different constant normal stresses

Table 1
The basic properties of the infilled material.

Property	
Unified soil classification system	CH
Specific gravity	2.58
Liquid limit, LL	58
Plastic limit, PL	28
Plasticity index	30
Optimum moisture content (%)	27
Maximum dry density ($\mathbf{kg/m^3}$)	1418

(σ_n^0) of 100 kPa, 200 kPa, and 300 kPa. The soil was mixed with water and then cut into a specimen having a dimension of 60 × 60 × 20 and inserted into the shear box for conducting the direct shear test. Two steel plates with the height of 20 mm were placed on the bottom and top part of the soil. Thus the total height was 60 mm. In the next stage, a vertical load was applied on the upper shear box. Axial loading was continued till stabilising the system, and then remained constant throughout the test. At the final stage, a constant horizontal velocity of 0.2 mm/min was applied on the lower shear box until reaching 8 mm of shear displacement while recording the shear stress and displacement. Three direct shear test under 100 kPa, 200 kPa, and 300 kPa were conducted, and the corresponding maximum shear stresses for each test were measured to identify the cohesion and friction angle of the cohesive soil (i.e. 21.3 kPa and 15.3°, respectively). The results in terms of shear stress-shear displacement, normal-shear displacement, and peak shear stress – normal stress relations are presented in Fig. 1. These macroscopic parameters will be used later on to calibrate the micro-mechanical parameters of the DEM-based cohesive model. Different stress stages were identified from laboratory observations (Fig. 1a), namely: elastic (I), pre-peak (II), softening (III), and residual (IV) stages. Initially, the soil showed a linear elastic stage (stage I). In stage I, the soil exhibited compressive response (negative normal displacement). After some shear displacement, the bond between soil particles began to break leading to a non-linear shear behaviour before reaching the maximum strength. It can be seen that the shear displacement at which stage II started was increased by increasing the magnitude of confining pressure. At low confining pressure (100 kPa), the soil exhibited insignificant softening behaviour, while at high normal stress magnitudes (200 and 300 kPa) obvious softening response was observed (stage III, Fig. 1a). The rate of compressive displacement was significantly reduced during stage II, and III (stages II and III, Fig. 1a). During stage III, the specimen showed negligible change in the normal displacement (stage III, Fig. 1a). The softening response was more pronounced when confining pressure is high, which was attributed to successive bond break at molecular level during this stage. With the progressive shear displacement of the specimens, a residual response was achieved (stage

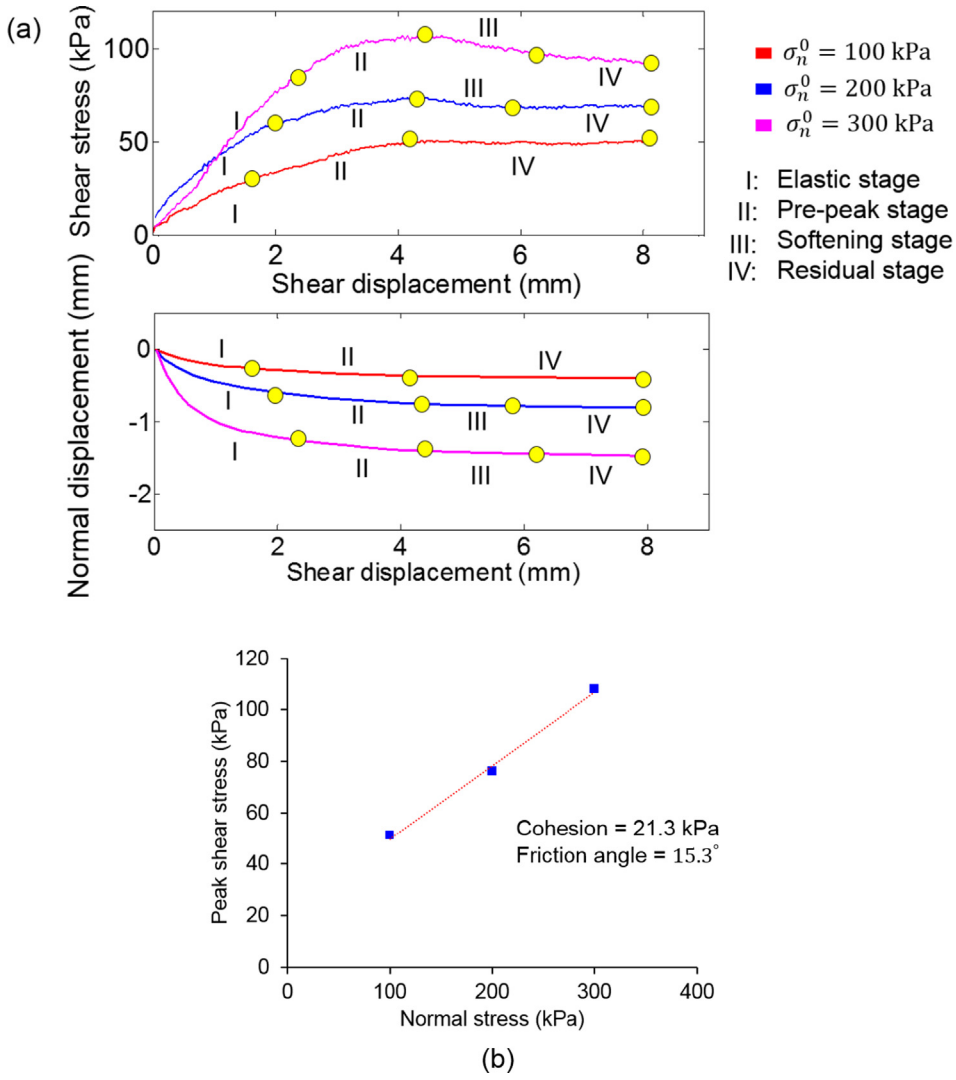

Fig. 1. Results of the direct shear test on the cohesive soil. (a) Shear stress-displacement curves under different normal stresses (σ_n^0). (b) Calculating cohesion and friction angle of the soil based on direct shear test results.

IV in Fig. 1a), which attributed to the frictional behaviour of the soil particles [44]. The normal displacement of the soil remained in constant value during stage IV. These observations were consistent with the previous studies conducted on cohesive soil (e.g. Lin [56]). The four different stages illustrated in Fig. 1a will be used later on as guidelines to calibrate the proposed DEM framework.

In the next step of the experimental program, a series of direct shear tests were carried out on infilled single asperity rock joints. Conducting direct shear test on natural rock joints was not considered due to a large number of potential parameters involved in the shearing process [29], therefore, making calibration and validation process complicated.

2.2. Direct shear test on infilled rock joints under CNL condition

Dental plaster was used for generating replica rock joints as to produce rock joint with single asperity with high strength. Once this material is mixed with water at a ratio of 3:1, it can be moulded in any shape to produce a high strength replica after curing. Artificial rock samples that had a triangular joint profile with base angles of 20° and 30° were generated and cured at a temperature of 80 °C for 14 days. The previous experimental investigations on infilled rock joint showed that the ratio of infill thickness (t) to asperity height (a) has a significant influence on the shear behaviour of infilled rock joints [4,13,12]. In non-planer rock joints, as t/a increases, the overall shear strength of the rock joint decreases [57]. Rock joints with idealized saw-tooth asperities are suitable for studying the shear behaviour of infilled rock joints [13,12,58], because they allow independent assessment of t/a. Thus, in the present study, we produced rock joints with different inclination angles to independently assess the shear behaviour of infilled rock joints. The geometrical configuration of rock joints is illustrated in Fig. 2. The height of the top and bottom of the rock-like specimen was considered to be 12 mm, which gives a total height of 24 mm. Thus, the laboratory specimens with infill thickness of 12 mm had a total height of 12 + 12 + 12 = 36 mm. We placed steel plates with a height of 12 mm on the top and bottom part of the experimental specimens. Dental plaster was used to attach the steel plates to the rock-like material to avoid losing the connection between rock and steel plates during shear. Similarly, for 6 mm infill thickness, we placed steel plates with a height of 15 mm on the top and bottom part of the rock to obtain a total height of 60 mm. The dimension of infill specimens are illustrated in Fig. 2b. As mentioned earlier, no asperity degradation was considered in the experimental program, and the test was conducted under 100 kPa and 300 kPa of constant normal stresses. The role of the replica was to provide a base restricted area for the infill material to shear after applying a normal stress and then a shear stress without occurring any asperity damage. The cohesive soil introduced in the previous section was used as the infill material.

The following procedure was followed for preparing the infilled rock joint specimens:

1- Plaster moulds were created to cast the synthetic rock samples. 3D printing technique was utilised to prepare the artificial joint surfaces with asperity angles of 20° and 30°. Both halves of the replica were created at the same session as two different negative moulds were in access for top and bottom half specimens.
2- The dental plaster was mixed with water at a ratio of 3:1 by mass to reach a low viscosity material that filled well into the moulds ensuring the escape of air bubbles. The casting procedure was completed in less than 10 min due to the fast curing rate of the dental plaster. The moulds then rested on a vibrating table for 10 min to eliminate any remaining air bubble as illustrated in Fig. 3a.
3- The samples were de-moulded after one hour (Fig. 3b). The rapid curing rate of the mixture accelerated this process. After that, the samples were left in the oven and cured for the next 14 days at 80 °C.
4- The cohesive clay was prepared as per the procedure introduced in Section 4.1. For creating the desired infill thickness (6 mm or 12 mm), different moulds were generated. The soil was conformed well to the moulds using a spatula. After that, a de-moulder was used to extrude the infill layer (Fig. 3c).
5- The final stage included placing the infill layer on the rock joints surface. The infill layer was placed on the bottom block and trimmed to reach the same dimension of the replica (Fig. 2d). After placing the top block on the infill layer, the whole sample was placed into the direct shear test machine to conduct experiment (Fig. 3e–f).

The direct shear tests were conducted using a GDS shear base system which is an electro-mechanical shear testing device. The shear box of this apparatus is made up of the top and bottom parts. A constant normal stress was applied on the upper shear box through a loading frame. The upper box was remained stationary during the shearing procedure. A horizontal velocity with a rate of 0.2 mm/min was applied to the bottom part to achieve the shearing of the infilled rock joint. Both normal and shear forces were applied using GDS electro-mechanical force actuators. The data acquisition system was connected to a PC running GDSLAB data acquisition software for monitoring the shear stress and displacement throughout the shearing procedure. Six different direct shear tests were carried out on infilled rock joints. For rock joint with asperity inclination of 30°, an infill layer with 6 mm and 12 mm thickness was considered and for those with 20° asperity angle, an infill layer of 12 mm was prepared. Notice that no asperity damage was occured during our laboratory testing, which was necessary to understand the infill thickness and asperity characteristics on the shear mechanism of infilled rock joints [13].

The results of direct shear test on infilled rock joints is illustrated in Fig. 4. Fig. 4a shows the shear stress-displacement, and normal-shear displacement curves. It can be seen that similar to cohesive soil shear behaviour (Fig. 1a), the clay-infilled rock joints also exhibited four different stages which were previously introduced in Section 2.1. However, higher peak and residual shear strengths were observed except for $t = 12$ mm and $\alpha = 20°$, which attributed to the presence of asperities. The normal-shear displacement curves of infilled rock joints were also different from the soil. It can be seen that increasing the magnitude of the normal stress significantly enhanced the peak and residual strength of the infilled rock joints. In each graph, the ratio of infill thickness (t) to asperity height (a), t/a, is given. The stress stages, and normal displacement response obtained for infilled rock joints are demonstrated at shear-stress displacement graph obtained for the specimen with $t = 12$ mm and $\alpha = 20°$, and the underlying shear mechanism is described as follows. At the initial stage of shearing (I), the shear stress is rapidly increased, which is referred to here as the elastic stage. The initial compression was observed for all specimens in this stage. During this phase, the shear stiffness of the infilled rock joint was controlled by the applied normal stress. At stage II, nonlinear hardening was observed in the shear stress-displacement graph. There were two main reasons contributing to the nonlinear pre-peak behaviour of the infilled rock joint. Firstly, the progressive shear displacement weakened the bond between soil particles, causing a reduction in the shear stiffness and thus, a nonlinear response was observed during stage II, which was similar to the mechanism observed in Fig. 1a. Secondly, due to infill squeezing between advancing asperities [6], the asperity interfaces approached each other causing an enhancement of asperity interference that was represented by pre-hardening behaviour at shear stress-displacement graph. This hardening behaviour, which was not the case in the specimens without rock joint (Fig. 1a), significantly increased the peak shear strength of infilled rock joints. For the smaller t/a ratio of 1.3 and 2.7, the initial compression of infilled rock joints was followed by dilation. The dilative response for t/a ratio of 1.3 was more pronounced under both 100 and 300 kPa of normal stress, which was attributed to asperity interference when the infill thickness was relatively small. For t/a ratio of 4.25, however, the compression was continued, and the infilled rock joint only exhibited a similar behaviour

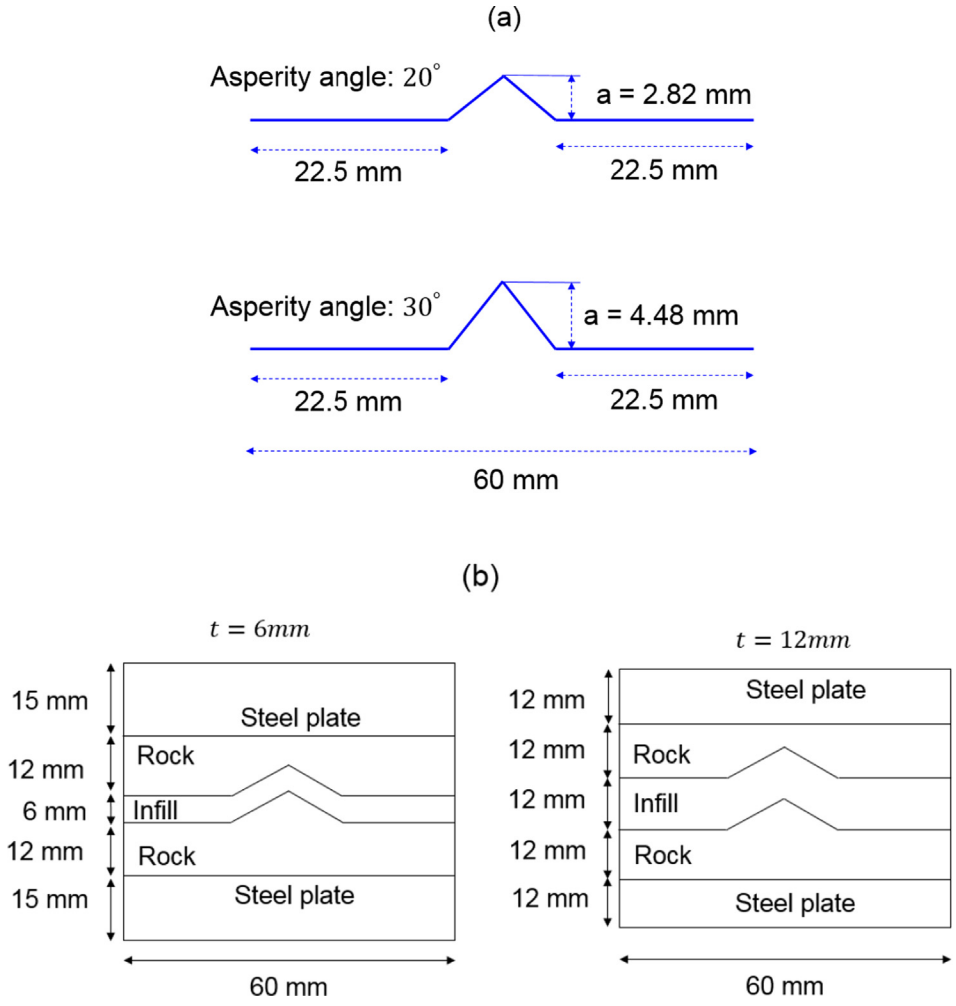

Fig. 2. (a) The geometrical configuration of infilled rock joints. (b) The dimension of infill specimens.

of soil compression. After peak shear strength was reached, due to progressive degradation of cohesion, the infilled rock joints demonstrated a post-peak softening response (stage III). Unlike soil behaviour, at low confining stress (100 kPa), a slight softening response was observable in infilled rock joints. This was due to an increase in the stress level, which caused more bond break in the infill material during the post-peak response. The laboratory results showed that, in all infilled rock joints, the softening intensity increased significantly with increasing the confining pressure. For the smaller t/a ratio of 1.3 and 2.7, the rate of dilation was reduced during stage III, whereas for /a ratio of

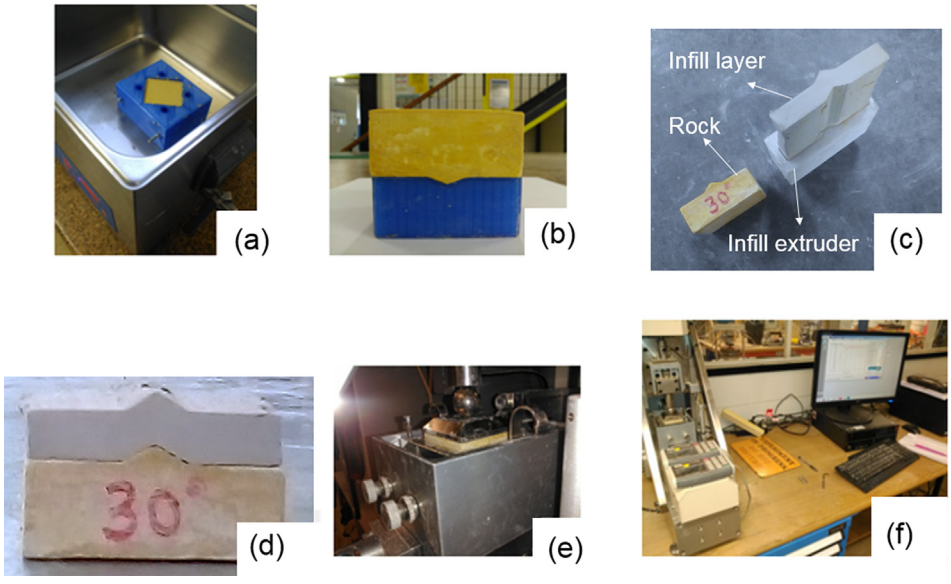

Fig. 3. Different steps of direct shear test on infilled single asperity rock joints. (a) Pouring the dental paste into the mould and vibrating the sample for 20 min. (b) Removing the sample from the mould. (c) Creating the desired infill thickness. (d) Placing the infill layer on rock joint surface. (e) Moving the specimen to the shear box. (f) Conducting the direct shear test and recording the data.

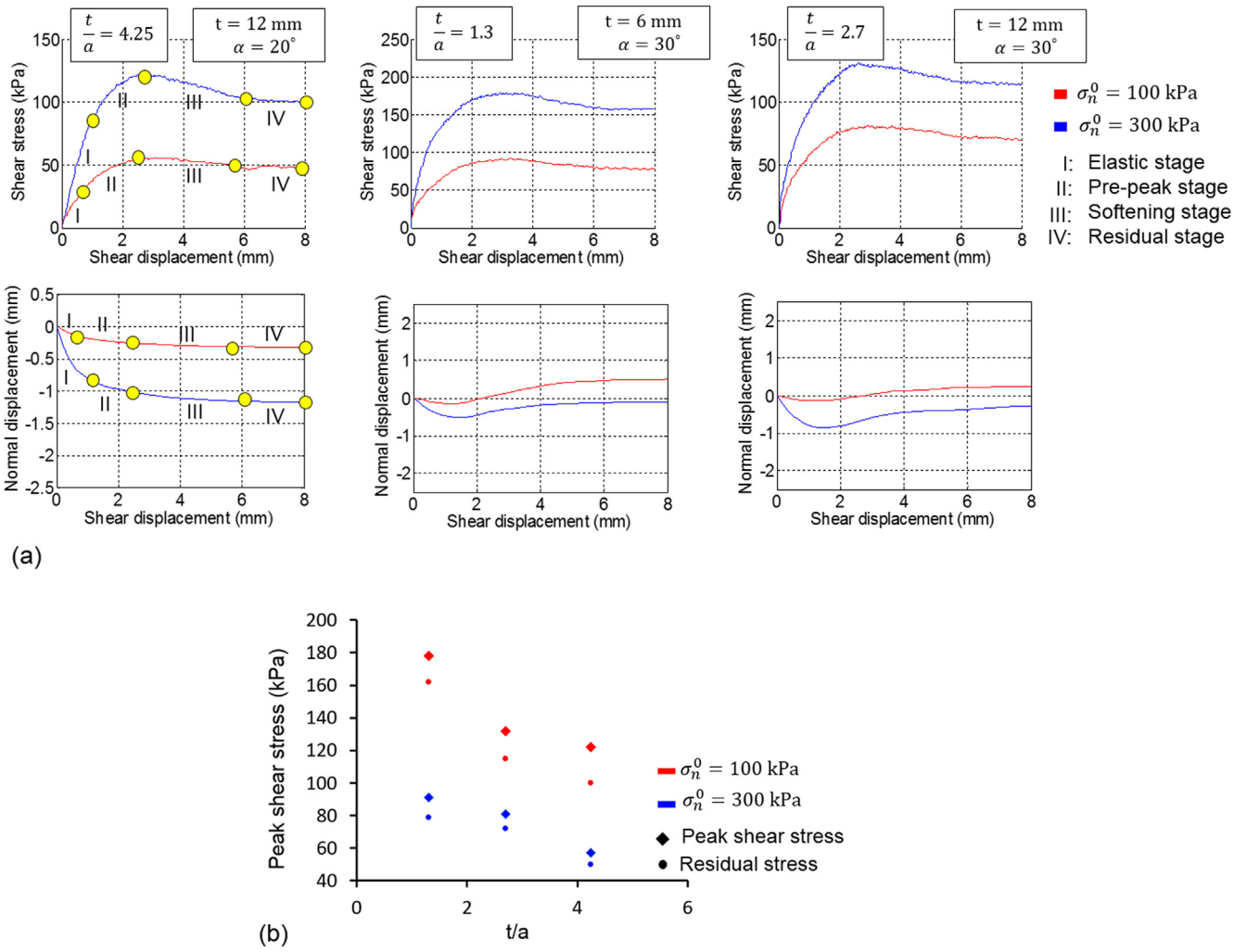

Fig. 4. The results of the direct shear test on infilled rock joints with different asperity angles and infill thicknesses. (a) Shear stress-displacement and normal-shear displacement curves. (b) Variation of peak and residual shear strengths with the t/a ratio.

4.25 the compression continued with a lower rate. During stage IV, the infilled rock joint exhibited a residual behaviour, which was attributed to the frictional response between soil particles. Notice that, the shear stress characteristics of other specimens (with different asperity angle and infill thickness) can be similarly interpreted. Our experimental observations was consistent with the previous laboratory investigations [6,59,60].

The laboratory results also showed that the geometrical configuration of rock joints influenced the peak and residual shear strengths. In order to better interpret the results based on rock joint geometrical properties, the peak and residual shear strengths of infilled rock joints were plotted against the t/a ratio, and the results are illustrated in Fig. 4b. The experimental study of Ladanyi and Archambault [8] demonstrated that higher shear strength will be achieved for infilled rock joints with steeper asperities, and the influence of infill thickness on peak shear strength is more pronounced for asperities with higher inclination angles. In the present study, we observed that by increasing the t/a ratio, the peak and residual shear strengths of the infilled rock joints exhibited a significant reduction (Fig. 4b). For t/a of 1.3, the peak and residual strengths at both 100 and 300 kPa of normal stress showed the highest values, while for t/a of 4.25 the shear behaviour of rock joint was governed by infill material, and as expected, the value of peak and residual strengths of the rock joint approached to those of cohesive soil. The experimental results will be used to validate the proposed calibrated DEM framework.

3. DEM background for modelling cohesive materials

The DEM was firstly proposed by Cundall and Strack [26] to study the mechanical behaviour of granular materials. The cohesive materials can be simulated as an assembly of rigid balls moving and interacting with each other at their contacts. A brief DEM background is presented in this section to show how a cohesive contact model can be incorporated in DEM to simulate the mechanical behaviour of the cohesive materials. The following Sections 2.1 and 2.2 can also be found in Potyondy and Cundall [31], Nguyen et al. [20], and Nguyen et al. [21] and more comprehensively in Itasca [24].

3.1. Law of motion

In DEM simulations, the governing equations are based on Newton's second law of motion. The resultant forces and moments acting upon a rigid particle can be described by two distinct components, the translational and rotational acceleration:

$$\vec{F_i} = m_i(\vec{u_i} - \vec{g}) \tag{1}$$

$$\vec{M_i} = \vec{\omega_i} I_i \tag{2}$$

where i denotes the order of particles in a particle assembly; $\ddot{x}_i$ is particle acceleration, ω_i is the rotational velocity of particle; I_i is the inertia tensor; g is the body force acceleration vector (e.g., gravitational

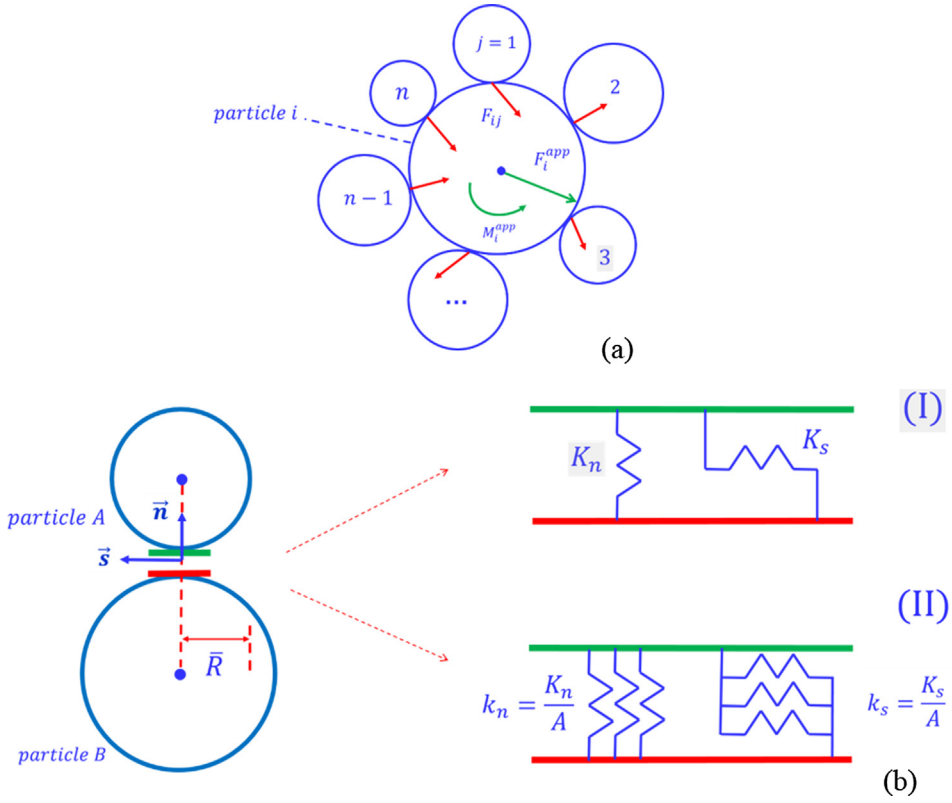

Fig. 5. Graphical illustration of DEM. (a) Force and moments acting upon a DEM particle (Modified from Nguyen et al. [20]). (b) Interaction between bonded contact: (I) force-displacement form, and (II) stress-displacement form.

loading); and F_i and M_i are the resultant force and moment respectively. The vectorial summation of all forces and moments acting upon a particle can be determined to calculate the resultant forces and moments as:

$$\vec{F_i} = \sum_j \vec{F_{ij}} + \vec{F_i}^{app} = \sum_j (\vec{F_{ij}}^n + \vec{F_{ij}}^s) + \vec{F_i}^{app} \tag{3}$$

$$\vec{M_i} = \sum_k \vec{F_{ij}}^s r_{ij} + \vec{M_i}^{app} \tag{4}$$

where r_{ij} is the distance from the centre of particle *i-th* and the contacting point of particle *i-th*. F_{ij}^n and F_{ij}^s are the normal and shear forces in the local coordinate system of the contact between particle i and j, respectively. $\vec{F_i}^{app}$ and $\vec{M_i}^{app}$ are the forces and moments applied on the particle i-th. The resultant forces and moments are illustrated in Fig. 5a. Fig. 5b illustrates the interactions between DEM particles in both force-displacement and stress-displacement forms.

The equations of motions in DEM are dynamic-based accumulating a kinetic energy in the system during numerical simulation. In the DEM codes used in the present study (PFC2D) mechanical damping and local damping are considered to dissipate the dynamic energy. The same approach suggested by Potyondy and Cundall [31] was adopted in this research to dissipate the kinetic energy and damp out the resulting acceleration of particles. The damping force and moment applied to each particle are proportional to the total forces and moments and can be added to the equation of motions such that the damped equations can be calculated as:

$$\vec{F_i}^{damp} = -\alpha(\vec{F_i} + m_i\vec{g})sign(\vec{u_i}) \tag{5}$$

$$\vec{M_i}^{damp} = -\alpha\vec{M_i}sign(\vec{\omega_i}) \tag{6}$$

where α is a nondimensional parameter known as global damping coefficient. A global damping of 0.7 is suggested to be sufficient in DEM [31] for dissipating the kinetic energy and remaining under quasi-static equilibrium condition during numerical simulation.

3.2. Contact constitutive law

Contacts play an essential role in DEM simulation as the interaction forces at contact micro scale characterise the collective macroscopic behaviour of the DEM particle assembly in the macroscopic scale. Once the motion of the particle is updated, a constitutive law can be applied to the contacts to compute the forces at the interfaces of two contacts. Such constitutive law defines the relationship between contact forces and particle displacements. The bonding contacts between two particles in DEM represent the binder portion among particles, and unlike cohesionless contacts, they are able to resist both tensile and compressive stresses [20]. The total force of each contact includes normal and shear components linked with the displacement of the particle with contact normal and shear stiffnesses. In that sense, the constitutive law of bonded contacts can be described incrementally as:

$$\Delta\vec{F} = \Delta F_n\vec{\boldsymbol{n}} + \Delta F_s\vec{\boldsymbol{s}} \tag{7}$$

$$\Delta F_n = K_n\Delta u_n^e \tag{8}$$

$$\Delta F_s = K_s\Delta u_s^e \tag{9}$$

where ΔF_n and ΔF_s are the incremental normal and shear components in normal ($\vec{\boldsymbol{n}}$) and shear ($\vec{\boldsymbol{s}}$) directions; K_n and K_s are contact normal and shear stiffness; Δu_n^e and Δu_s^e are incremental elastic displacements in normal and shear directions, respectively. The bonded contacts can be considered as a system of springs (Fig. 5b) with stiffnesses $k_n = K_n/A$ and $k_s = K_s/A$ where A is the bond cross section area. In 2D, $A = 2\bar{R}t$ where $\bar{R}$ is the radii of the smaller particle (Fig. 4,b). Thus, the force-displacement relationship defined in Eqs. (8) and (9) can be rewritten in stress-displacement form as:

$$\Delta\sigma_n = k_n\Delta u_n^e \tag{10}$$

$$\Delta\sigma_s = k_s \Delta u_s^e \tag{11}$$

where $\Delta\sigma_n$ and $\Delta\sigma_s$ are contact incremental normal and shear stresses. Any constitutive model characterising the bonded contact behaviour in DEM can be developed either in force-displacement or stress-displacement form. The same contact modelling concept was applied in the current research for proposing a new cohesive contact model by adopting the fundamentals of plasticity theory.

4. The proposed cohesive DEM framework

The proposed DEM approach simulates the mechanical interaction between soil grains bonded together with cohesive contacts. The cohesive behaviour of the soil at grain level was analogously modelled with shear failure characteristics at macroscopic scale. The elastic, yield and softening behaviour of the cohesive bonds were incorporated in the model using the framework of plasticity theory. This section briefly describes the constitutive relationships of the cohesive model.

4.1. The constitutive relationships of the cohesive contacts

In the present study, a new cohesive, contact model developed by Saadat and Taheri [54] was employed for simulating the shear behaviour of cohesive soil in DEM codes. There are various DEM-based cohesive models available in the literature (i.e. Nguyen et al. [20], Nguyen et al. [21], Le et al. [61]; and Le et al. [62]) that can be used for simulating cohesive contact behaviour. However, in the new cohesive DEM framework, the number of microproperties were reduced because it allows us to make the calibration procedure more straightforward. In addition, a simple cohesive contact model reduces the computational demand required for simulating large displacement of infilled rock joints.

In the proposed constitutive model [54], the relative displacement $\boldsymbol{u}(u_n, u_s)$ of the DEM contacts was decomposed into an elastic and plastic components to account for reversible and irreversible displacements:

$$\boldsymbol{u} = \boldsymbol{u}^e + \boldsymbol{u}^p \tag{12}$$

The contact normal and shear stresses are linked to their corresponding relative displacements and can be calculated by:

$$\sigma_n = k_n^0 (u_n - u_n^p) \tag{13}$$

$$\sigma_s = k_s^0 (u_s - u_s^p) \tag{14}$$

where σ_n and σ_s are normal and shear stresses in the bonding contacts; u_n and u_n^p are the total and plastic normal displacements; u_s and u_s^p are the total and plastic shear displacements; and k_n^0 and k_s^0 are the normal and shear stiffnesses, respectively.

The following yield function that accounts for the mixed-mode failure of DEM contacts was considered to determine the failure state at which softening of cohesive bonds starts to occur:

$$F(\sigma_n, \sigma_s, C) = \sigma_s + \mu\sigma_n - C = 0 \tag{15}$$

where μ is the friction coefficient of the contact and C is defined as:

$$C = C^0 e^{-\kappa u^p} \tag{16}$$

In Eq. (16), C^0 is the initial bond cohesion, κ is the softening parameter, and u^p is the contact's accumulated plastic displacement, which can be calculated from its increments, defined as:

$$du^p = \sqrt{(du_n^p)^2 + (du_s^p)^2} \tag{17}$$

A damage parameter ($0 \le D \le 1$) can be defined to measure the degradation of cohesive bonds during progressive shear displacement of the soil:

$$D = \frac{C^0 - C}{C^0} = 1 - e^{-\kappa u^p} \tag{18}$$

The value of the damage parameter introduced in Eq. (18) was determined for each contact at each numerical iteration and plotted graphically to enhance the interpretation of model performance. The cohesive contacts without bond-failure have $D = 1.0$, while the completely degraded contacts exhibit a damage value of $D = 0.0$. During the progressive softening stage, the cohesive contacts return: $0 < D < 1$.

Simulating dilation effect at microscopic level in DEM modelling requires incorporating the microstructural characteristics of the physical material in the model, which is difficult to achieve [20]. Alternatively, a dilatancy parameter that accounts for the dilation response of the cohesive contacts was considered using the following non-associative flow rule:

$$G(\sigma_n, \sigma_s) = \sigma_s + \beta\sigma_n \tag{19}$$

where β is the dilation coefficient. Consequently, the flow rule of incremental displacement can be expressed as:

$$du_n^p = d\lambda \frac{\partial G}{\partial \sigma_n} \tag{20}$$

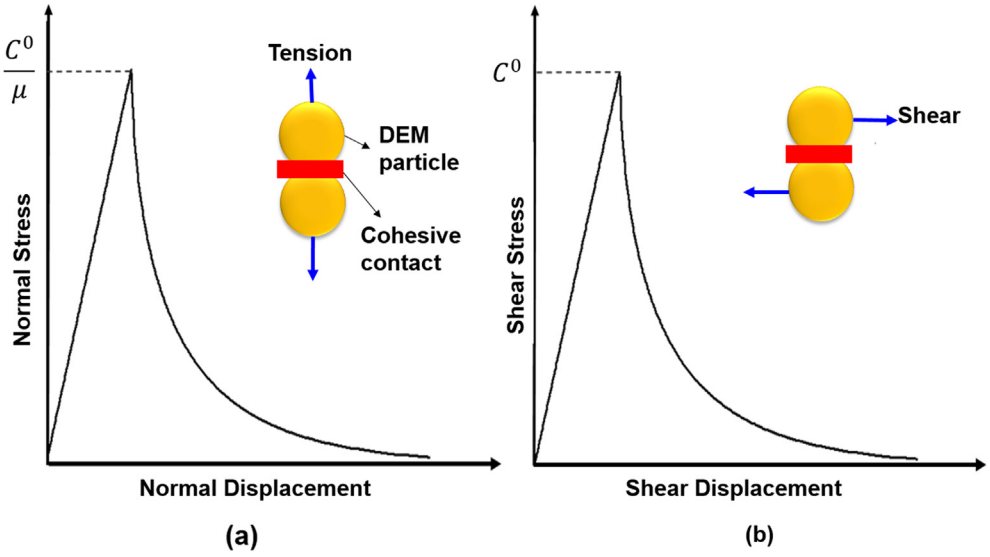

Fig. 6. Stress-displacement behaviour of the proposed cohesive contact model in (a) Mode I, and (b) Mode II [54].

$$du_s^p = d\lambda \frac{\partial G}{\partial \sigma_s} \tag{21}$$

where $d\lambda \geq 0$ is the plastic multiplier. Fig. 6 illustrates the behaviour of DEM contact in mode I and II. The linear elastic portion of stress-displacement curves defines the contact behaviour before failure ($D = 0.0$), followed by a non-linear stage that represents contact softening due to the progressive degradation of cohesion ($0 < D < 1$).

5. Establishment of the cohesive DEM

The proposed cohesive model represent the properties of cohesive contacts at the granular scale so that it requires highly sophisticated experiments to achieve the micromechanical parameters of the cohesive soil. In general, the mechanical parameters obtained from the standard laboratory testing cannot be imported directly into the DEM model as the macro-mechanical behaviour is synthesised at mesoscale. The remedy, however, is to calibrate the micro parameters by matching the results of DEM simulation with experimental data. This procedure has been used in DEM studies for obtaining the micromechanical properties of constitutive models [20,31,63]. Here the results of direct shear tests on cohesive soil was used for calibrating the micro parameters. Firstly, a metrical vessel containing a dense pack of interlocked particles was generated. After that, the procedure was continued by calibration of normal and shear stiffness of contacts (k_n and k_s) through matching the DEM results in the elastic stage. Then the peak shear stress was approximated by altering cohesion (C^0). The next step was to calibrate the softening parameter (κ) based on the post-peak response of the cohesive soil. Finally, friction and dilation coefficients (μ and β) were calibrated by fitting DEM response with the experimental observations. After the calibration procedure, the micro parameters were adopted to validate the proposed cohesive model through simulating the shear behaviour of infilled rock joints.

5.1. Generation of DEM specimen

A two-dimensional model was created in PFC 2D for simulating the same laboratory direct shear tests introduced in Section 4.1 and the micro-mechanical parameters of the cohesive constitutive model were calibrated by comparing the numerical simulation results with the physical response of the cohesive soil in direct shear testing. The height of laboratory specimen for the soil test was 60 mm out of which 20 mm was the height of soil sample, and 40 mm was the total height of steel plates placed on the top and bottom part of the soil (the height of each steel plate was 20 mm). A material vessel with a dimension of 60 mm × 50 mm was created and a particle assembly including nearly 11,000 balls was generated in PFC 2D. The height of the soil specimen was 20 mm, which was equal to the laboratory counterpart. The height of steel plates in the numerical specimen was reduced by 5 mm to make the numerical simulations time efficient. Since no damage was expected in steel plates, reducing the size had no influence on the numerical results. The particle size was controlled by the uniform distribution with minimum and maximum diameters of $D_{min} = 0.48$ mm and $D_{max} = 0.64$ mm respectively. Using uniform grain size distribution is common practice in DEM simulations as simulating real grain size distribution is nearly impossible [20,21,32,61,64]. The reason is that creating a particle assembly with the exact porosity of physical material requires a huge number of particles leading to inefficient computation [20]. A comprehensive instructions for generating material-genesis in PFC has been described by Potyondy and Cundall [31]. According to their study, an overall porosity of 16% can ensure the generation of a dense particle assembly in DEM. The same approach was adopted in this study to generate samples. After producing the numerical samples, the particles were divided into two groups namely, soil and plate particles (Fig. 7a). The steel plates used in the present study were assumed non-breakable and non-deformable as the strength and modulus of the steel plates were much larger in comparison with that of cohesive soil used. In the numerical setup, the height of the upper and lower steel plates was assumed to be 15 mm to reduce the number of particles representing the steel plates. This minimised the simulation time and made the numerical approach computationally efficient. This assumption was acceptable as there was no damage in the steel plates. Furthermore, there was no gravity acting on the model so that the mass of particles had no influence on the mechanical response of the system. The PBM was applied on the contacts between steel plate particles (Fig. 7b), and its microproperties were selected according to the literature [65], which include Young's modulus (200 GPa), shear to stiffness ratio (1.5), cohesion (800 MPa), and tensile strength (400 MPa).

The proposed cohesive model was installed on soil-soil contacts and soil-steel contacts (Fig. 7b). Fig. 7c shows the boundary condition applied to the system. The calibration procedure involved matching the numerical results of direct shear test of the cohesive soil under 100 kPa of constant normal stress with experimental counterparts. Then micromechanical parameters related to the cohesive soil are obtained, and finally the same micro parameters on the model are adopted for reproducing the shear behaviour of the cohesive soil under 200 kPa and 300 kPa of constant normal stresses. In the numerical models, the walls created during particle assembly generation were removed and 8 new walls were created for applying the boundary condition and performing the direct shear test (Fig. 7c). The upper block was kept stationary during the shearing procedure, and a constant horizontal velocity of 0.03 m/s was applied on wall 5. This velocity was chosen because it was observed through a series of numerical experiments that any value lower than this did not influence the overall stress-displacement curve and damage response of the models. The selected horizontal velocity allowed us to maintain the model in a quasi-static equilibrium condition while reducing the computational costs. The CNL condition was achieved by adopting a servo-controlled mechanism [24] and applying a desired constant normal stress on the wall 1. The reaction force in wall 5 was monitored and divided by the length of the specimen (60 mm) to calculate the shear stress, the horizontal displacement of wall 5 was measured during the shearing procedure to represent the shear displacement.

5.2. Microproperties calibration and model validation

The micro parameters needed to be calibrated were k_s^0, k_n^0, C^0, μ, β, and κ. The PFC software also allows altering the value of k_n^0 and k_s^0 after sample generation procedure enabling the user to generate a single specimen and repeat the tests for any desirable number of simulations. k_s^0 was calibrated through matching the simulation results with linear elastic part of the shear stress-displacement curve obtained from experiment. The k_n^0/k_s^0 ratio was assumed to be 1.8, and this assumption was further verified by obtaining the best fit from numerical simulations under various normal stress magnitudes. The desired peak shear stress was achieved by altering the cohesion of contacts (C^0). The friction coefficient (μ) was calibrated together with C^0 in such a way to return the best match in terms of peak shear strength. The reliability of this microproperty was further verified by comparing the macroscopic numerical friction angle with the experimental counterpart. After achieving satisfactory macroscopic elastic response and peak shear strength, by varying the value of softening parameter (κ), the damage response of the cohesive soil throughout the post-peak stage was approximated. It should be noted that the softening parameter has a simultaneous influence on the pre-peak, the peak, and the post-peak responses. So that this parameter was calibrated in such a way to reproduce the best overall response in terms of pre-peak hardening, peak, and softening stages. The dilation ratio (β) is the local property of the cohesive soil, which can only be identified with more sophisticated laboratory techniques. However, as mentioned by Nguyen et al. [20], this parameter can be calibrated by fitting with the experimental

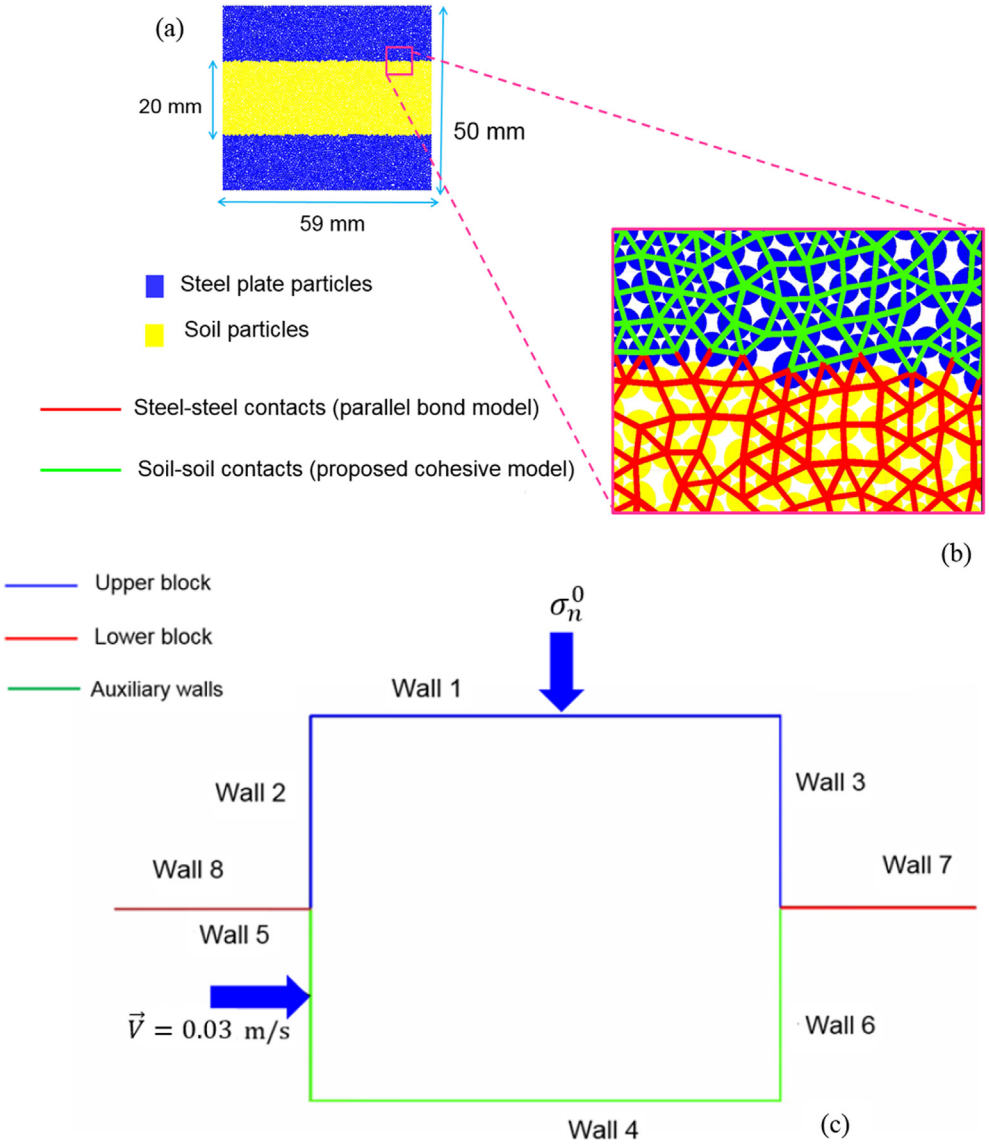

Fig. 7. Numerical specimen for conducting a direct shear test on cohesive soil. (a) Material vessel dimension and particle assembly including soil and steel particles. (b) The constitutive contact models installed for each contact group. (c) The boundary condition applied on the material vessel for conducting the direct shear test.

Table 2
The microproperties of the calibrated soil.

k_s^0 (GPa/m)	k_n^0/k_s^0	C^0 (kPa)	$\varkappa$ (1/m)	μ	β
0.7	1.8	23.5	18.0×10^3	0.32	0.2

observation. A parametric study of direct shear test was conducted in which β was varied in a range from 0.15 to 0.45. The numerical simulations exhibited that macroscopic response of the cohesive soil was virtually unaltered when varying the dilation coefficient in this range. The final set of microproperties obtained from calibration procedure are given in Table 2. The results of shear stress-displacement under 100 kPa of normal stress magnitude (σ_n^0) is given in Fig. 8a. As it can be observed, the macroscopic response of DEM simulation shows a very close agreement with the physical response of the experimental data.

For validating the proposed cohesive contact model, the same micro mechanical parameters obtained through calibration procedure under σ_n^0= 100 kPa were adopted to reproduce the macroscopic response of the cohesive soil under 200 kPa and 300 kPa. The results of the validation process are given in Fig. 8. Fig. 8a indicates that the proposed model can approximate the macroscopic behaviour of the cohesive soil with an excellent agreement. As Fig. 8a illustrates, an increase in the magnitude of normal stress showed higher shear stiffness and peak shear resistance.

In order to get a better insight regarding these observations, the damage evolution of cohesive soil was monitored during the shearing process, and the results are given in Fig. 8b. Based on Eq. (18), the amount of damage was calculated for each cohesive contact during the shearing procedure and shown graphically to derive a better interpretation of shear zone evolution in the soil contacts. Completely damaged contacts are shown in red (D = 1.0) and bonded contacts are shown in blue (D = 0.0). It can be observed from Fig. 8b that the number of bonded contacts (or contacts experienced linear elastic stage) was higher for a numerical specimen with σ_n^0=100 kPa compared to higher normal stress magnitudes. In fact, as the magnitude of normal stress increased, the reaction force required for shearing the specimen was raised leading to a significant increase in the shear stiffness. Consequently, more contacts experienced their yielding limits.

Fig. 1a illustrates that in the physical specimens the shear stiffness increases by an increase in the normal stress, while the same material was used in all the tests. Similarly, the increase in the shear stiffness of

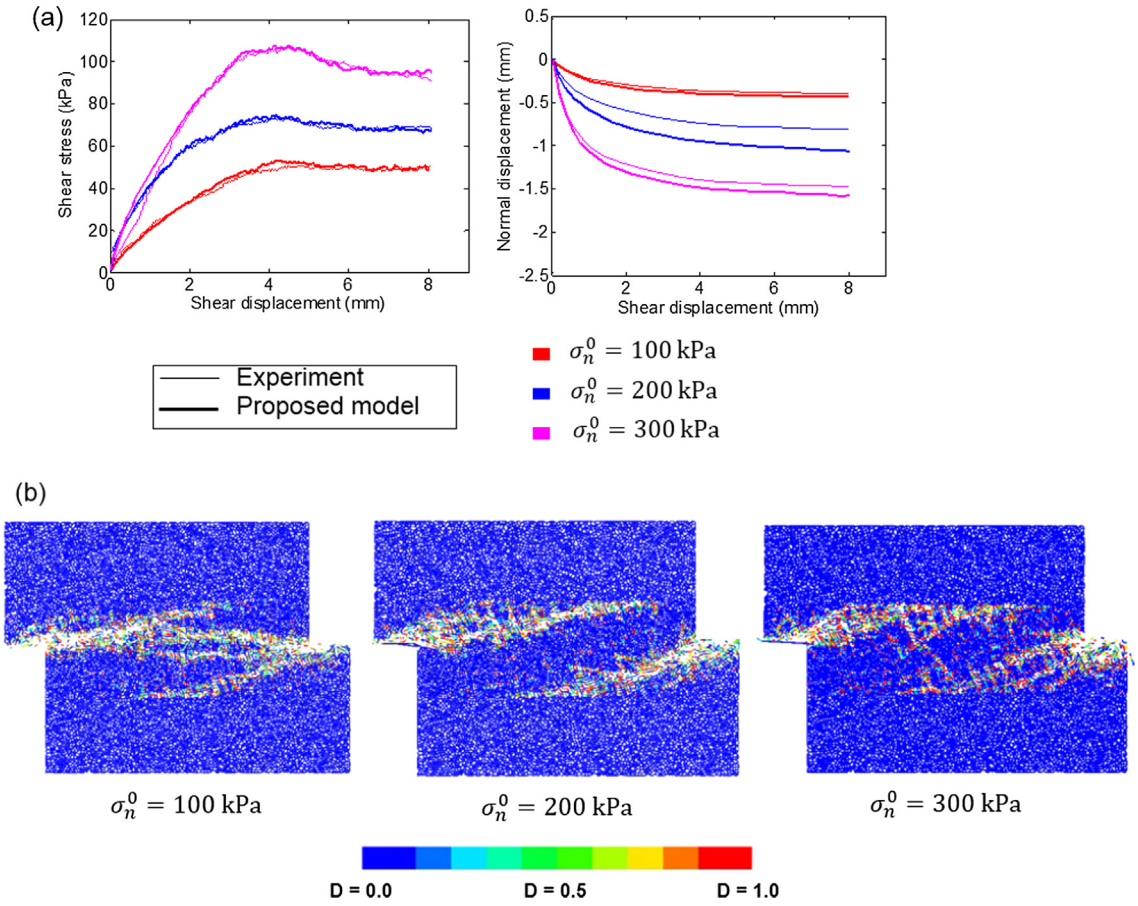

Fig. 8. The results of experimental and numerical direct shear test on cohesive soil under various constant normal stresses. (a) The shear stress-displacement and normal-shear displacement results of calibration of micro-mechanical parameters. (b) Damage evolution pattern in numerical samples.

the numerical specimen was due to an increase in the magnitude of normal stress (Fig. 8a). In fact, the same material, which was represented by one set of microproperties, was used in all simulations to ensure that the calibrated model was able to mimic the macroscopic response of the cohesive soil under different normal stresses. Others also confirmed this approach in the previous DEM studies [32,49,66,67].

To better interpret the damage evolution procedure in the material and to carefully observe the performance of the proposed cohesive model in reproducing the softening response at mesoscale, the value of damage in each contact was monitored at different stress stages introduced in Section 2.1, and the results are illustrated in Fig. 9. The points at which the damage evolution was monitored are marked with yellow circles on the graphs (Fig. 9a). Similar to the laboratory observations (Fig. 1a), the DEM shear mechanism of cohesive soil can be divided into four separate stages namely elastic, pre-peak, peak, and residual stages (Fig. 9a). The shear mechanism observed during numerical modelling is described in the following paragraphs.

During elastic phase (stage I in Fig. 9a), the cohesive contacts returned their elastic response so that the reaction force measured from the wall 5 (Fig. 7) only showed an overall elastic behaviour of the cohesive contacts. With the progressive increase in shear displacement, the shear force needed to move the specimen horizontally was significantly increased, resulting in the yielding of the cohesive contacts. The normal-shear displacement curve (Fig. 9a) showed initial compressive behaviour for all specimen, with the cohesive soil under 300 kPa exhibited the highest initial compression. From point "a" to point "b" of the shear stress-displacement graph (Fig. 9a), the pre-peak stage (stage II) was observed for both 100 and 300 kPa of normal stress. At point "a" (Fig. 9b, column a), the softening of cohesive contacts started, which mainly occurred at the upper left and lower right of the specimens. As expected, the number of yielding (softened) contacts ($0.0 < D < 1.0$) was higher at 300 kPa. Since in the yielding contacts $D < 1.0$, these contact therefore were still being able to carry stresses. On the other hand, a number of contacts at the central areas of the specimens were under elastic behaviour ($D = 0.0$), and could produce more stresses at grain level. Thus, the overall response of these softened and non-yielding bonds resulted in the pre-peak behaviour of the soil at the macroscopic scale. At the end of this stage (Fig. 9b, column b), the localised shear zones were largely extended, and the maximum shear strength of the soil was achieved. The numerical results showed that the damage response of the contacts was affected by the magnitude of applied normal stress. The numerical sample with $\sigma_n^0 = 300$ kPa produced more damaged contacts, while at σ_n^0=100 kPa they were less pronounced. It can also be observed from Fig. 9a that the shear stiffness of the specimens exhibited a gradual reduction (stage II), which attributed to the progressive contact softening and hence the growth of localised shear zones. The pre-peak phase (stage II), which regarded as a nonlinear elastic behaviour at macroscopic scale, was the natural consequence of the collective mechanical response of the DEM contacts, even though the nonlinear characteristics were not incorporated in the constitutive relationships of the proposed model. Notice that, phenomenologically, both yielding and non-yielding contacts are needed to capture the pre-peak nonlinear behaviour in the cohesive soil, which confirms the effectiveness and necessity of incorporating an exponential softening decay in the proposed DEM framework. During stage II, the rate of compression in the DEM particles reduced under both 100 and 300 kPa normal stress magnitude (stage II, Fig. 9a), which could be attributed to the growth of localised damage zone in the specimens (column b, Fig. 8b).

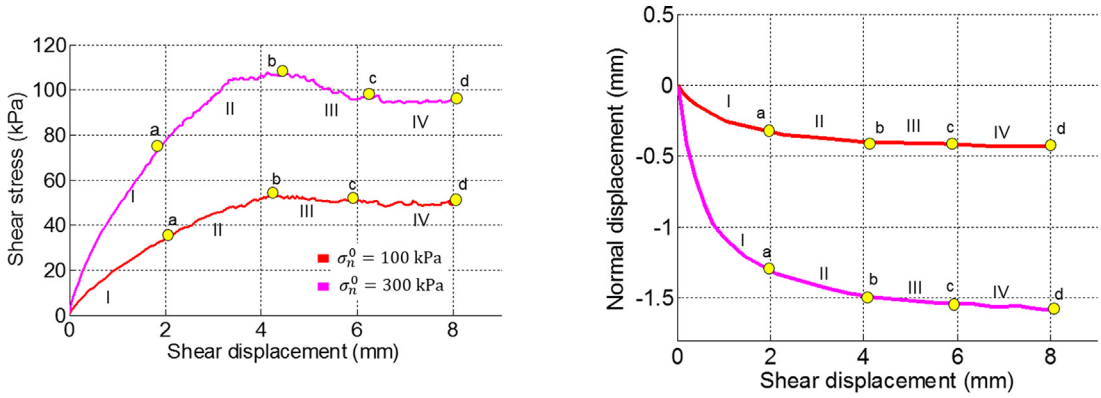

(a)

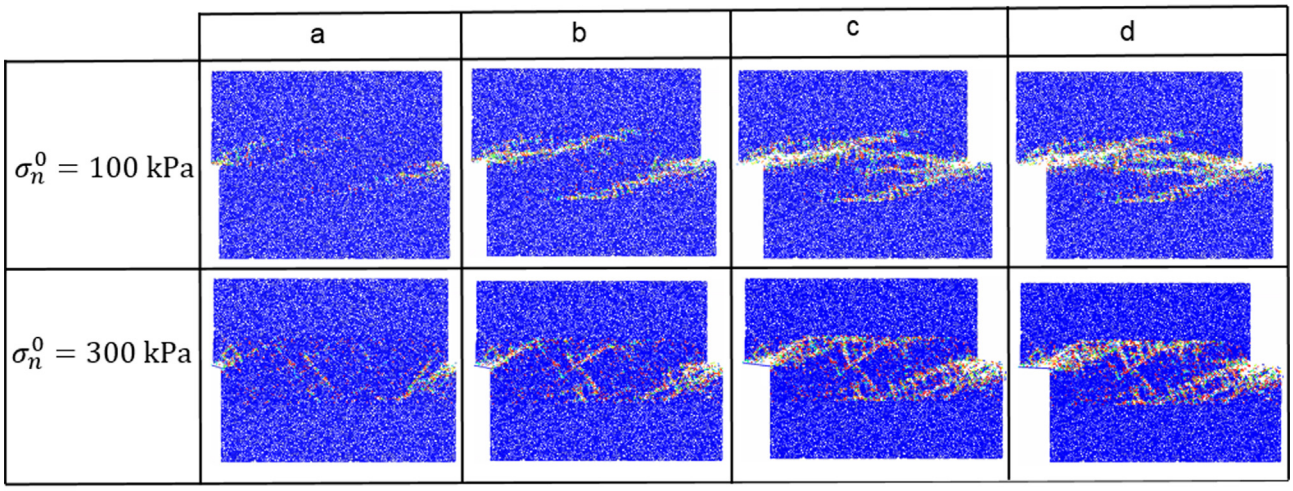

(b)

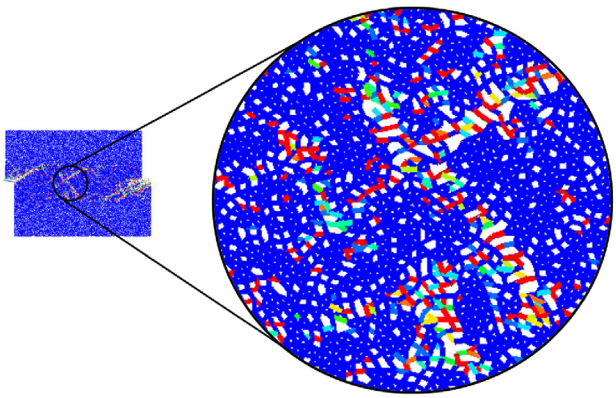

(c)

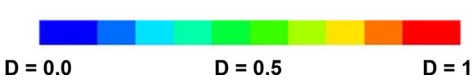

Fig. 9. Results of a direct shear test on a numerical sample. (a) The shear stress-displacement graph. (b) The evolution of damage in the cohesive contacts at different stress level. (c) A close-up view of damage evolution under 300 kPa of normal stress at point "b".

At peak shear strength (Fig. 9a, point "b"), the numerical specimen with σ_n^0= 300 kPa showed a higher number of damaged contacts (D = 1.0) at the centre than σ_n^0= 100 kPa (Fig. 9b, column b). This was due to the high magnitude of confining pressure, which caused the cohesive contacts in the middle of the specimen to come into their yielding limit, and display progressive damage behaviour. Fig. 9c illustrates a close up view of the contacts in the central part of the specimen with 300 kPa. It can be seen that in this particular region, the contacts exhibited both softening ($0 < D < 1$) and damaged (D = 1.0) responses, which was hardly detected at low confining stress. After reaching the peak shear strength, the specimens entered to stage III at

which the level of shear stress gradually declined. This macroscopic softening behaviour was mostly depended on the magnitude of applied normal stress which influenced the degree of contact resistance. Thus, it was observed that at the end of the softening stage (Fig. 9b, $\sigma_n^0 = 300$ kPa, column c), substantial damage was incurred to the contacts, which in turn intensified the macroscopic softening response in the numerical specimen with $\sigma_n^0 = 300$ kPa (Fig. 9a, stage III). In contrast, the mild softening stage under low confining pressure (Fig. 9a, $\sigma_n^0 = 100$ kPa, stage III) was attributed to the behaviour of the contacts, which remained mainly at their softening phase ($0.0 < D < 1.0$) (Fig. 9b, $\sigma_n^0 = 100$ kPa, column c). These numerical shear behaviour were reasonably consistent with the laboratory observations (Fig. 1a). During stage III, an insignificant change in the compressive behaviour of the DEM model was observed, which was due to the extension of localised damage (stage III, Fig. 9a). Finally, after nearly 6 mm of shear displacement, the residual shear strength was mobilized (Fig. 9a stage IV). During this stage, the shearing process progressed along the localised shear zones (i.e. damaged contacts in Fig. 9b, column c). It can be seen from Fig. 9a that during stage IV the shear strength of the models remained unchanged, which was associated with the growth of insignificant number of softened or damaged contacts in the localised shear zones (Fig. 9b, columns c and d). Similarly, the normal displacement of the models demonstrated a constant value (Fig. 9a).

The above mentioned DEM results demonstrated the capability of the proposed cohesive DEM framework in capturing the mechanical and failure behaviour of cohesive soil tested under CNL direct shear tests.

Fig. 10a and b illustrate the force-displacement law of PBM under tension and shear loading [24]. It can be seen that when a DEM contact reaches its yielding limit (either tensile or shear strength), the contact forces abruptly reduce to zero [24]. In fact, the PBM features no gradual degradation of contact strength after yield point. The force-displacement law depicted in Fig. 8a and b, clearly illustrates that the PBM produce no gradual strength degradation. If the PBM is augmented with a cohesive post-peak behaviour, e.g. an exponential decay function, it will be able to reproduce a gradual softening response after yield point.

Another numerical direct shear test was carried out using the same DEM setup (Fig. 7) and contact attribute. The only difference was that the cohesive model was replaced with the PBM. The PBM has four microproperties including normal and shear stiffness, tensile strength, and cohesion. The tensile strength and cohesion control the bond strength. The stiffness parameters of the PBM was kept the same as those of the cohesive model, and the cohesion of contacts was assigned as the same C^0 obtained in the calibration procedure. There was no direct way to measure the tensile strength of the soil at microscopic level, therefore this parameter was assumed as equal to the contact cohesion. The macroscopic shear stress-displacement obtained from PBM is illustrated in Fig. 10c. The PBM reproduced the same macroscopic elastic response as the proposed model. However, the peak and residual stresses could not be achieved by the PBM. The reason is that in the PBM when the contacts reached their yield limit (i.e. cohesive strength), the forces reduced abruptly to zero (Fig. 10a and b). Hence, the PBM contacts could not resist against shearing. Thus, at macroscopic scale, the overall response was a peak shear strength followed by a residual behaviour. In the cohesive model, however, some of the cohesive contacts returned their softening response ($0.0 < D < 1.0$) after yield limit, and some other were still in the linear elastic stage ($D = 0.0$). As a result, the overall macroscopic response of the model was a pre-peak stage before the peak shear strength. Notice that, one can alter the microproperties of the PBM to obtain a good match with the experimental data (e.g. Tamás et al. [68], Tamás et al. [69], and Tamás [70]). However, we believe that incorporating a softening response in the force-displacement law of the contacts allows us to achieve a more realistic phenomenological constitutive model for simulating the shear behaviour of clay-infilled rock joints.

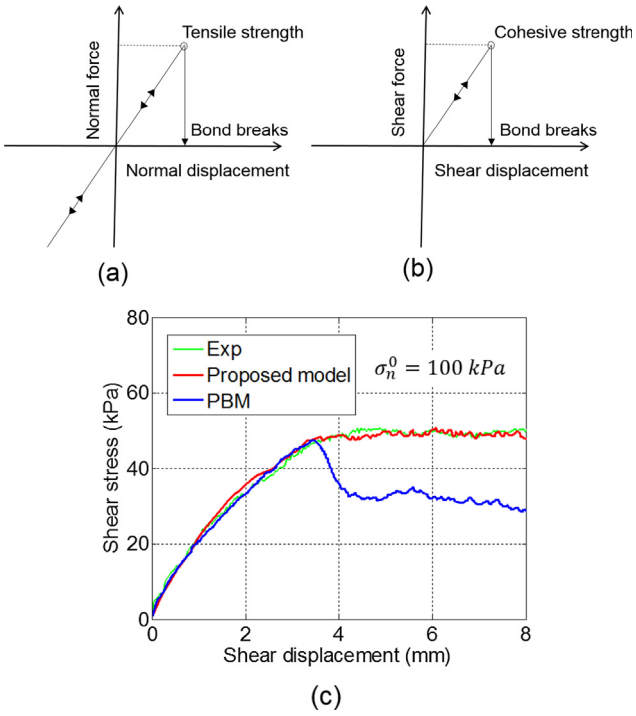

Fig. 10. The simulation results using PBM. Force-displacement law of the PBM in (a) tension, and (b) shear. (c) The shear-stress displacement curves obtained from the direct shear test.

5.3. Effect of shear rate on macroscopic response

In DEM modelling of the direct shear test, loading rate plays a significant role in macroscopic shear behaviour. A sufficiently small loading rate and a relatively high damping magnitude are required to ensure that the numerical specimen remains in quasi-static equilibrium, and there is no abrupt stress increase or unexpected macroscopic response within the DEM model [18]. A damping coefficient of 0.7 suggested by Potyondy and Cundall [31] was employed to approximate the quasi-static condition. The details of damping of particle motions can be found in [31]. Notice that using the same experimental loading rate of 0.2 mm/min in numerical modelling is computationally inefficient. Alternatively, a sufficiently small shear loading rate can be selected to maintain the model in quasi-static equilibrium [18]. In the present study, the direct shear test was repeated under different loading rates ranging from 0.01 to 0.2 m/s to identify the optimum shear loading rate. Fig. 11 illustrates the influence of shear rate on the macroscopic behaviour of the numerical specimen. The numerical results showed that the shear loading rate less than 0.03 m/s had negligible influence

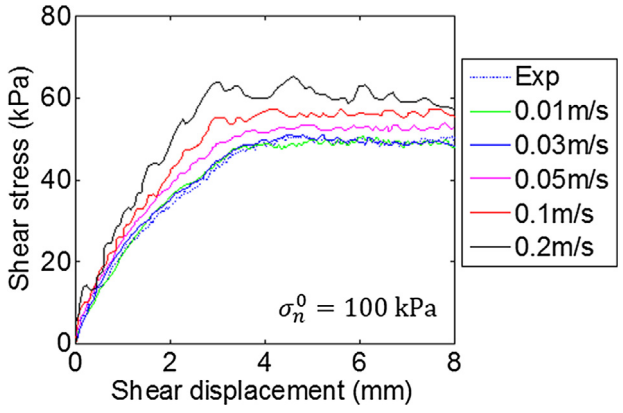

Fig. 11. The shear stress-displacement curves using various shear rate.

on the macroscopic response of the specimen. Thus this shear rate was deemed to be sufficient to achieve quasi-static equilibrium and used in the numerical model. This shear loading rate generated a mechanical timestep of roughly 1.2×10^{-7} s, which was automatically calculated by PFC software. Thus, the shear rate of 0.03 m/s can be interpreted to 36×10^{-7} mm/step. This means that 1 mm of shear displacement requires 360,000,000 computational steps. Others successfully followed this approach in previous DEM research [18,32].

5.4. Particle size optimisation

The size of DEM particles highly influences the macroscopic response of DEM simulation. Potyondy and Cundall [31] demonstrated that the size of DEM particles is an intrinsic parameter affecting the characterisation of the material. Thus it cannot be treated as a parameter that only controls the resolution of DEM simulation. They concluded that the particle size is the accurate representation of the effect of both packing and strength heterogeneity in DEM specimen. In fact, the number of DEM particles must be large enough to mimic the macroscopic physical response obtained from laboratory observation. Although increasing the number of particles is computationally inefficient, but an optimum particle size can be achieved by conducting a parametric study to ensure the convergence of the macroscopic results to the lowest possible size. Accordingly, four additional particle assemblies were generated and tested using the same micro parameters. Different models with various particle size were generated, and the ratio between the thickness of the soil (20 mm) and the average particle size was calculated (R_d). The results in Fig. 12, which demonstrates shear stress-shear displacement relations, show that a convergence can be achieved by decreasing the particle size confirming that the numerical specimen with $R_d = 13.15$ was appropriate for calibration purposes as it generated a material vessel with the lowest possible number of balls leading to an efficient computational time. However, the same particle size was used to generate the infill material with 6 mm of thickness (the details are given in Section 5.2) to examine the sensitivity of the macroscopic response to the particle size. The ratio between infill thickness and the average particle size was also calculated. According to these results, the DEM specimens with R_d of 0.047 and 0.038 failed to reproduce an appropriate macroscopic response, in terms of peak and residual behaviour. Models with R_d of 0.02 and 0.012 produced macroscopic results which were very close to the calibrated size (R_d= 0.028). Therefore, the model with minimum particle diameter (D_{min}) of 0.48 was chosen for the modelling purposes. Notice that the ratio between the maximum and minimum diameter (D_{min}/D_{max}) was considered to be 1.33 for all models.

5.5. Generation of infilled rock joints in DEM

To further illustrate the performance of the proposed cohesive DEM framework, simulations of direct shear test on infilled rock joints were conducted using the calibrated microproprties. Notice that the maximum height of the laboratory specimens, including infill material

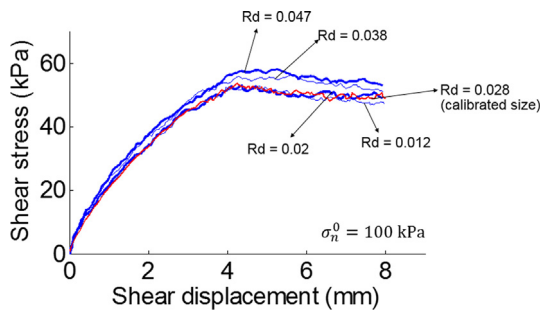

Fig. 12. Shear behaviour of DEM specimen with various particle sizes.

(t = 12 mm) and rock-like material, was 36 mm. In numerical models, the height was reduced to 30 mm to reduce the computational time. The dimension of numerical specimens are illustrated in Fig. 13a. This assumption was numerically reasonable because no damage was considered to occur in the rock sample [65]. Therefore, material vessels with the dimension of 60 × 30 (mm) were generated and filled with the particles having a size of D_{min} = 0.48 mm and D_{max} = 0.64 mm. The steps required for the generation of DEM specimen of infilled rock joint is demonstrated in the specimen of infilled rock joint is demonstrated in Fig. 13b. Firstly, a material vessel with a dimension of 60 × 30 was generated. In the next step, the mode was solved to reach equilibrium.

The particle assembly was then divided into two separate groups, namely infill particle and rock particle groups. The geometry of rock joints asperity angles of $20^{Å^\circ}$ and $30^{Å^\circ}$ was imported into PFC 2D for producing a single asperity rock joint. Then, based on the infill thickness the required particles for generating the infill layer were selected, and the desired infill thickness was achieved. As demonstrated in Fig. 14a, there were three different contact groups constructed in the system: rock-rock contacts, infill-infill contacts, and infill-rock contacts. The proposed cohesive model was installed on the infill-infill and infill-rock contact groups, and the PBM was installed on rock-rock contacts. The calibrated micro-mechanical parameters obtained in Section 5.2 was employed to simulate the failure behaviour of infill-infill contacts. The microproperties of rock-rock contacts were selected according to the literature [49], which include Young's modulus (9.0 GPa), shear to normal stiffness ratio (1.85), cohesion (22.0 MPa), and tensile strength (25.0 MPa). These contact properties allowed us to ensure the rock-rock contacts remained intact during simulations, without any asperity damage.

5.6. DEM simulation of the direct shear test of infilled joints

After sample generation, particle configuration, and contact model installation (Fig. 13), all the walls in the sample were removed, and new walls were generated to apply the new boundary condition and performing the direct shear test (Fig. 14b). Using the servo-controlled mechanism, the constant normal stress was applied to the top wall of the upper block (wall 1). The shearing procedure was achieved by applying a horizontal velocity of 0.03 m/s to the lower block (i.e. walls 4, 5, and 6). The horizontal reaction force of wall 4 was monitored and divided by the joint length (60 mm) to calculate the shear stress during the test. The horizontal displacement of the wall 4 was used to calculate shear displacement during shearing. The synthetic numerical specimens were sheared at two normal stresses of 100 kPa and 300 kPa. The shear behaviour of infilled rock joints simulated in DEM was compared with the experimental counterparts in Fig. 15a, and excellent agreement was observed. As can be seen in Fig. 15a, in all the numerical samples, the shear stress increased linearly from the beginning of the test, showed a pre-peak response before reaching the peak. Then the behaviour becomes strain softening with a gentle post-peak slope until the end of the shearing. Finally, the shear strength of the infilled rock joints remained at a constant residual level. Notice that the four stages observed in the laboratory specimens (Section 2.2) were accurately identified by the proposed DEM framework, which will be described later in this section.

The numerical specimens with t/a ratio of 1.3 and 4.25 returned the highest and the lowest peak shear strength respectively (Fig. 15a). For the specimen with 6 mm of infill thickness, the influence of asperity angle was more significant as it showed a higher peak shear stress. The macroscopic response in the laboratory investigation for 6 mm infill thickness was a combined asperity sliding and material softening. In the case of numerical samples with 12 mm of infill thickness, the greater number of cohesive contacts allowed them to have more control over the macroscopic shearing behaviour as the restriction provided by the asperity angle was reduced significantly. In fact, the wider space between joint surfaces enabled infilled particles to dominate the shear performance of the joint. This resulted in a dominating influence of

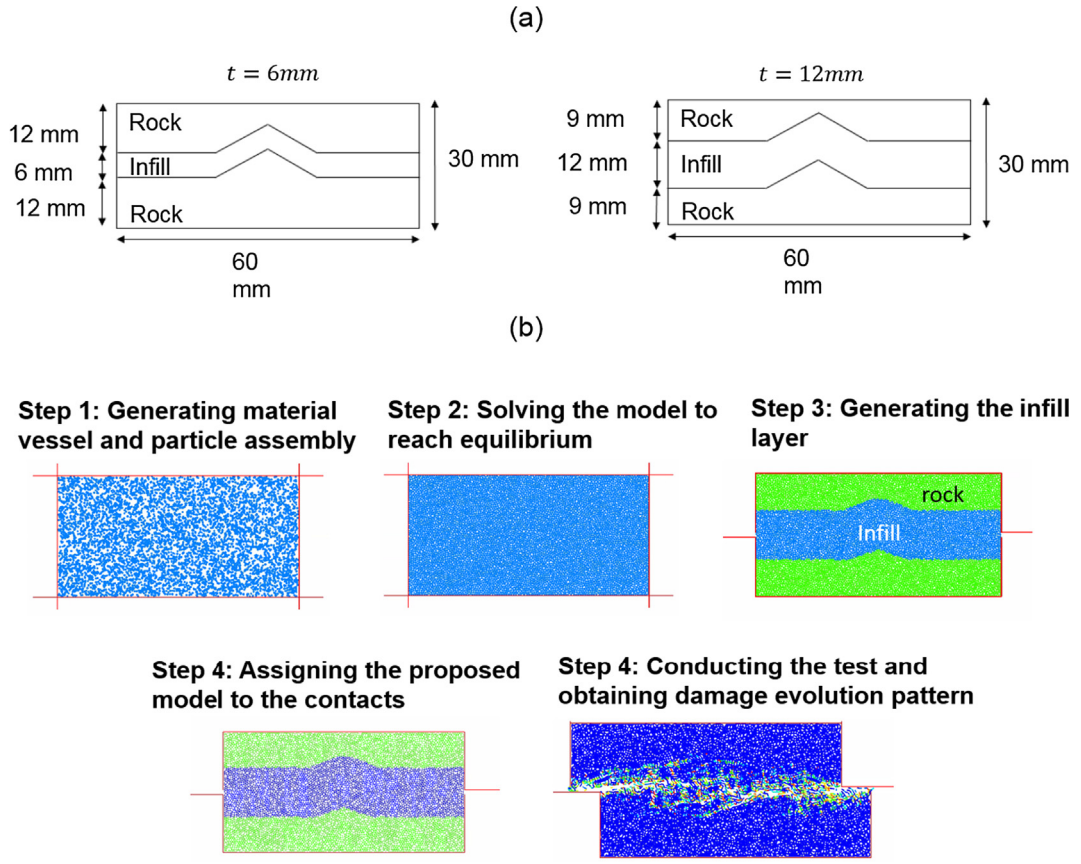

Fig. 13. (a) The dimension of numerical specimens. (b) Different steps for generation of particle assembly for conducting a numerical direct shear test on infilled rock joints.

infill contacts over asperity inclination, reducing the pre-peak hardening, and consequently a significant reduction in the peak shear stress. A detailed description of the shear mechanism of the infilled rock joint will be provided in the future in this section.

The normal-shear displacement curves (Fig. 15a) show that the numerical specimen were subjected to an initial compression during the elastic stage. This initial compression was followed by a dilative response for t/a ratio of 1.3 and 2.7. However, the numerical results showed that the dilatational behaviour of infilled rock joint reduced when the t/a ratio was 4.25. This was an indication that the asperity inclination angle no longer had great effect on the overall dilation behaviour of the DEM specimen. For the smaller t/a ratio of 1.3 and 2.7, the initial compression was more significant under 300 kPa, which was attributed to the higher compressive response of DEM particles due to greater normal stress magnitude.

The damage evolution of cohesive infill was monitored during the shearing process and the final results are given in Fig. 15b. Completely damaged contacts are shown in red ($D = 1.0$), bonded contacts are in blue ($D = 0.0$). It can be observed from Fig. 15b that the number of softened contacts ($0.0 < D < 1.0$) was higher for numerical specimens with a normal stress of 100 kPa. In contrast, at 300 kPa confining pressure, the number of damaged contacts ($D = 1.0$) was significantly higher, indicating the greater resistance of the infill layer against shearing.

The peak and residual strengths obtained from DEM simulation are plotted against t/a, and the results are illustrated in Fig. 16. The laboratory results are also included in Fig. 16 to make a better comparison. It can be seen from Fig. 16 that the peak and the residual strength of the infilled rock joints were very well captured by the proposed DEM framework. The numerical results showed that asperity interference highly influenced both the peak and residual strengths when $t/a < 2.67$, while at $t/a = 4.25$ the shear behaviour of the infilled rock joint was approximately governed by the infill material.

The value of damage in each infill contact was monitored at different shearing stages introduced in Section 2.1, and the results are illustrated in Fig. 17. For demonstration purposes, only the results of the numerical specimen with $t = 6$ mm and $\alpha = 30^{\circ}$ are analysed. The points at which the damage evolution was monitored are marked with yellow circles on the graphs (Fig. 17a), and their corresponding damage responses are illustrated in Fig. 17b. Fig. 17a illustrated the shear stress-displacement and normal-shear displacement curves of the DEM specimen. In the following paragraphs, the shear mechanism observed during numerical modelling of infilled rock joints is described.

The elastic phase (Fig. 17a, stage I) in the numerical models with infilled rock joint was similar to that of achieved for DEM soil specimens. However, the infilled specimens presented a higher value of shear stiffness, which was attributed to the higher resistance of the infill layer against shear displacement due to the presence of idealised asperities. During the elastic stage, the shear strength of the specimens was rapidly increased. Similar to the laboratory counterpart, the numerical specimen with 300 kPa confining pressure showed a higher value of shear stiffness. The normal-shear displacement curve (Fig. 17a) shows that the DEM specimens exhibited initial compression during stage I, which was due to the compressive response of DEM particles. This initial compression was higher under 300 kPa of normal stress magnitude. The corresponding damage evolution response of the numerical specimens at the end of the elastic stage (Fig. 17a, point "a") was monitored and depicted in Fig. 17b. It can be seen that under both 100 and 300 kPa of normal stress, some of the contacts at the upper left and lower right of the infill layer entered to their yielding limit ($0.0 < D < 1.0$) (Fig. 17a, point "a"). As expected the numerical specimen with $\sigma_n^0 = 300$ kPa exhibited more softened contacts at this point.

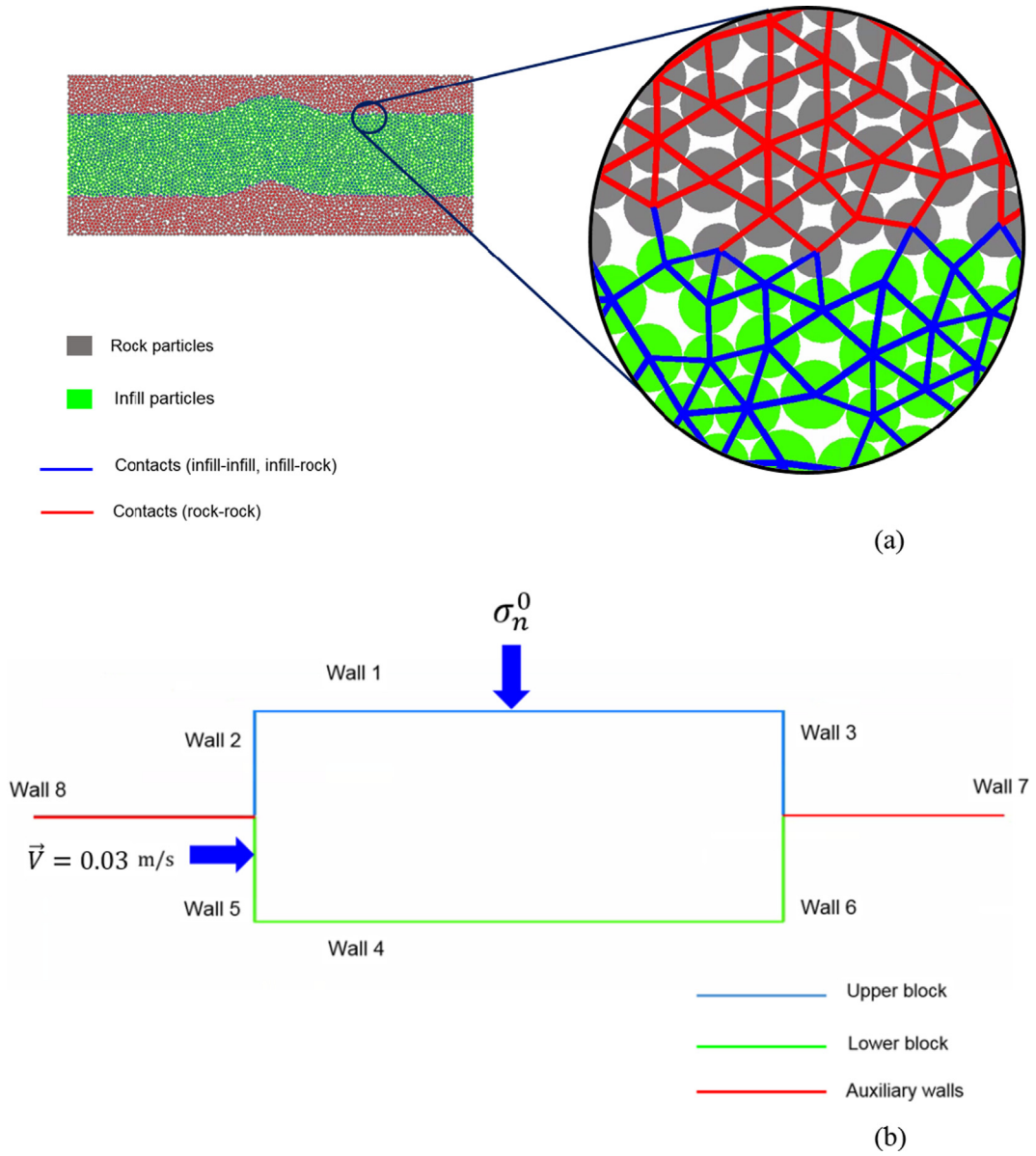

Fig. 14. The numerical sample including an infill layer after contact installation; the proposed cohesive model was installed on infill-infill, and infill-rock contacts and PBM was used to characterise rock-rock contacts. (a) Particle assembly and assignment of constitutive models. (b) The boundary condition required for conducting the direct shear test on infilled rock joints.

The accumulation of these softened contacts formed macroscopic localised shear zones. The numerical models displayed an overall nonlinear hardening response during stage II (Fig. 17a), which akin to the experimental samples, had two leading factors. Firstly, the nonlinearity of the shear stress-displacement curve was associated with the reduction in the shear stiffness, which was the results of the rapid growth in the number of yielding contacts ($0.0 < D < 1.0$). Secondly, the continuous shear displacement of the rock joint intensified the degree of asperity interference, which improved the resistance of DEM contacts against shearing. This produced a pre-hardening behaviour at macroscopic scale leading to a higher peak shear strength in infilled rock joints than that of soil itself (Fig. 17a, point "b"). It can be observed that in the numerical specimens with higher confining pressure, higher peak shear strength resulted at the end of stage II (Fig. 17a, point "b"). The normal-shear displacement curve (Fig. 17a, stage II) demonstrates that at point a, the dilative response of the infilled rock joints started, which was attributed to asperity interference as a result of progressive shear displacement of the rock joint. This occurred when the thickness of the infill layer was relatively thin.

During post peak stage (Fig. 17a, stage III), the number of yielding contacts started to increase within the infill layer, which is evident by the softening response of the shear stress-displacement curves. In particular, the intensity of softening was less pronounced at lower confining pressure (Fig. 17a, stage III, $\sigma_n^0 = 100$ kPa). This can be confirmed by the damage response of the contacts within the numerical specimens (Fig. 17b, point "c"), where very few completely failed contacts ($D = 1.0$) were observed for $\sigma_n^0 = 100$ kPa, whereas specimen with $\sigma_n^0 = 300$ kPa exhibited a considerable number of damaged contacts. The growth in the localised shear zone evolution was accelerated from this stage because more cohesive contacts started to soften. Physically, the softening process is associated with the gradual degradation of the inter-particle bonding followed by frictional interaction of soil particles in the localised shear zones. In this context, the micro-mechanical mechanism incorporated in the proposed DEM framework was able to very well capture the phenomenological aspects of cohesive soil failure at the macroscopic scale. The rate of dilation response of infilled rock

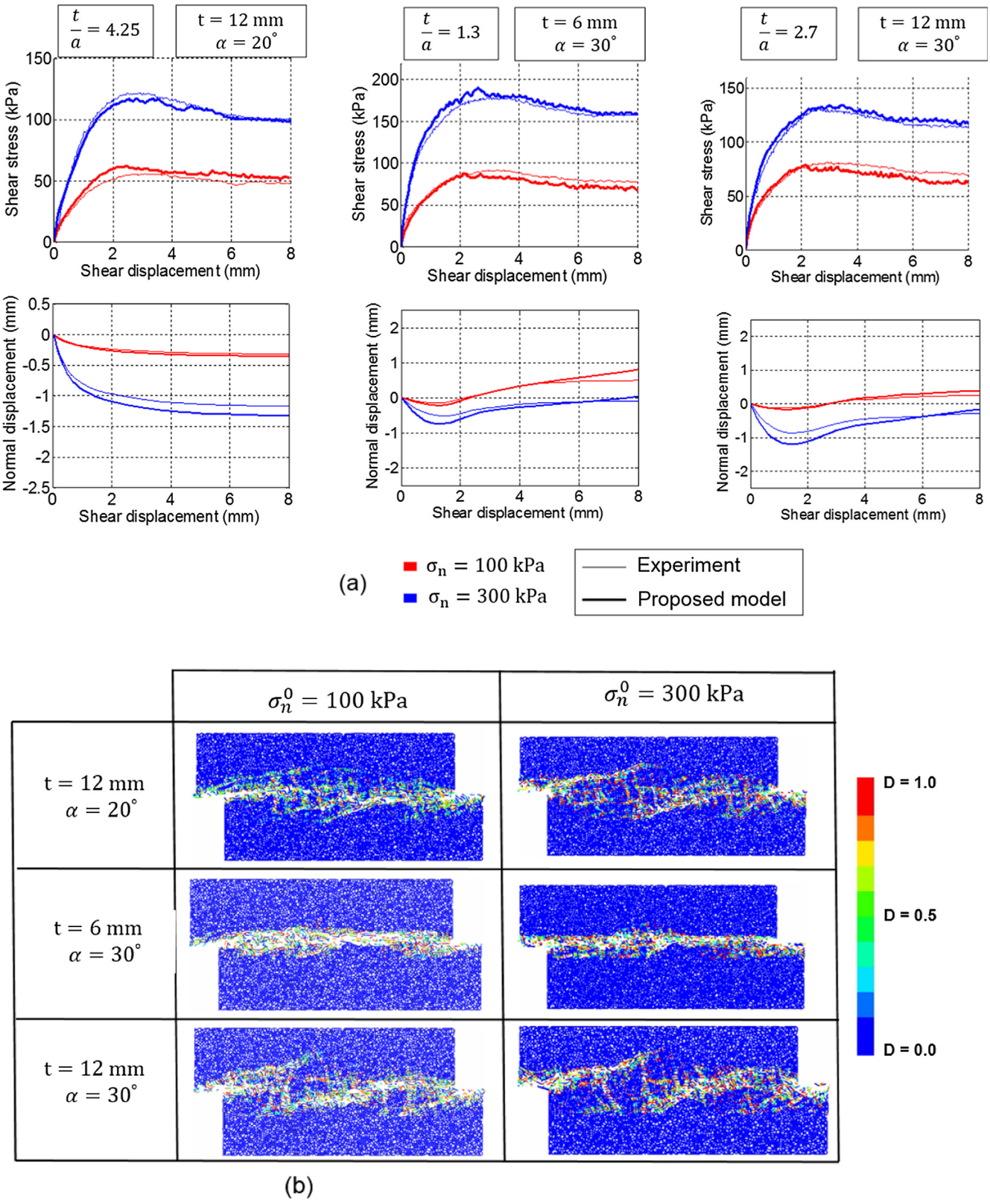

Fig. 15. Comparison of direct shear test results from the laboratory experiment and DEM simulations using the proposed cohesive model. (a) Comparison of the shear stress-displacement and normal-shear displacement curves from laboratory tests and DEM simulations for infilled rock joints with asperity angle of 20° and 30° and infill thickness of 6 and 12 mm. (b) Damage evolution in the numerical specimens.

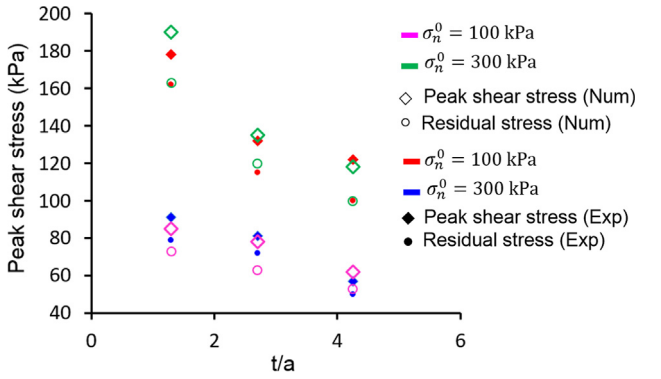

Fig. 16. The comparison between numerical and experimental peak and residual strength of the infilled rock joints.

joints reduced in stage III (Fig. 17a, stage III), which could be attributed to growth in the number of softening contacts, and the extension of the localised shear zone. During stage IV, the frictional behaviour of DEM particles at grain scale produced a macroscopic residual response in the shear stress-displacement curves (Fig. 17a, stage IV). The progressive shear displacement of the specimens during stage IV resulted in the extension of the localised shear zones, and accordingly the growth in the number of yielding contacts (Fig. 17b, point "d").

The procedure described above was observed for all of the numerical models. As demonstrated in Fig. 15a and b, the micro-mechanical behaviour of the cohesive contacts were affected by the magnitude of the normal stress thus the macroscopic response of the numerical samples in terms of both damage evolution and the peak and the residual shear stresses were changed. In the present research, we assumed no asperity damage. It can be observed from Fig. 17c that the damage only occurred in the infill layer. The DEM particles of the infill layer are not given in this plot to better demonstrate the cohesive contacts.

6. Conclusion

This paper presents a combined experimental-numerical investigation for the characterisation of the shear behaviour of clay-infilled rock joints. A series of laboratory direct shear tests were carried out on infilled rock joints filled with a cohesive soil. Idealised single asperity rock joints with a base angle of 20° and 30° were created and tested under CNL condition with 100 and 300 kPa of normal stress magnitude. The macroscopic properties of cohesive soil were also obtained from direct shear test results carried out on the soil. The experimental approach provided the macroscopic response of various infilled rock joints, while a proposed DEM framework supplied further insights into the failure mechanism and microscopic damage response of the cohesive soil. The microproperties of the proposed DEM framework were calibrated against the outcome of laboratory direct shear tests of cohesive soil. In particular, the cohesion and friction angle of the physical soil were numerically obtained similar to the experimental results. The calibrated DEM framework was then employed to reproduce the mechanical and failure behaviour of the infilled rock joints. The DEM results demonstrated a good agreement with the experimental counterparts. Based on the laboratory and DEM results, the following conclusions can be drawn:

1- The shear stress-displacement curves of the clay-infilled rock joints exhibited four different stages in both experimental and numerical observations. During stage I, the shear stress of the infilled rock joints was rapidly increased. A nonlinear hardening response was observed during stage II, which was associated with the progressive bond-break in the infill layer, and enhancement of asperity interference. Then the peak shear strength of the rock joint was achieved, following with a gradual softening response (stage III). Finally, due to frictional behaviour between infill particles, a macroscopic residual response was achieved.

2- The normal-shear displacement curves showed that the infilled rock joint exhibited an initial compression. A dilative behaviour for t/a ratio of 1.3 and 2.7 followed this initial compression. For the highest t/a ratio, however, the normal displacement of infilled rock joint approached to that of the soil itself.

3- The observations showed that the intensity of the softening response increased significantly with increasing the magnitude of normal stress. The numerical damage response showed that under high

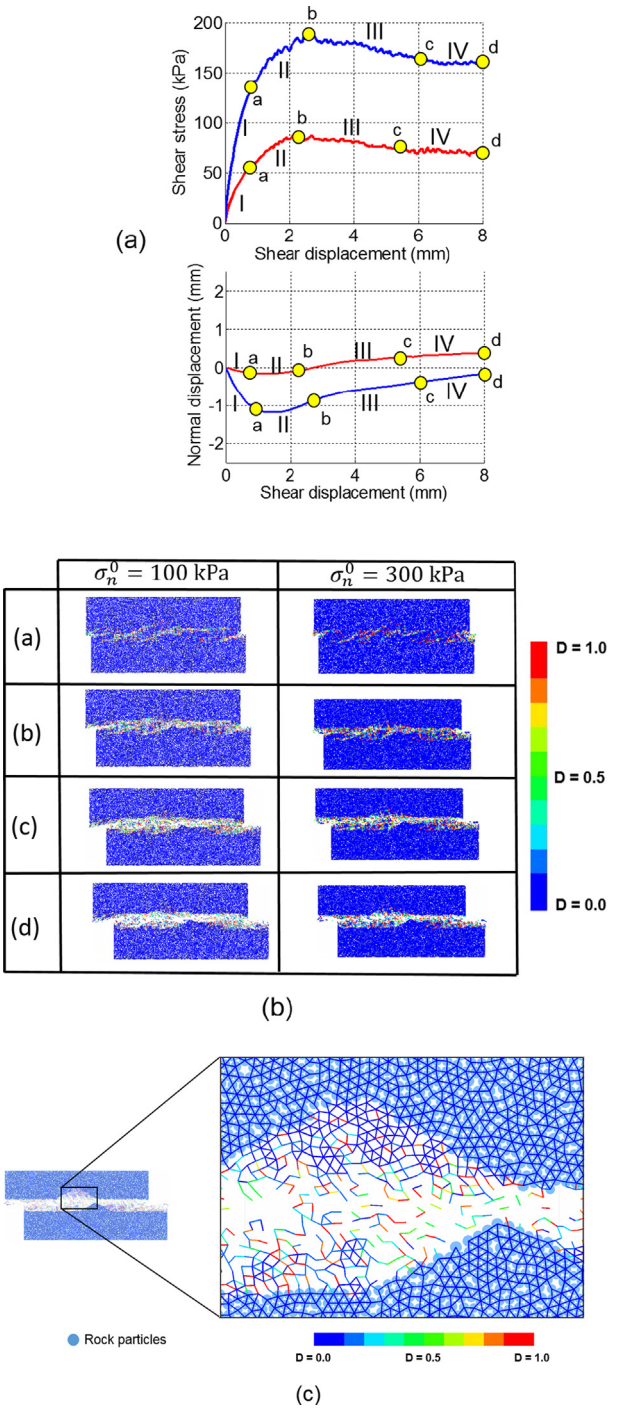

Fig. 17. Damage evolution in the infill layer ($\alpha = 30^{\circ}$ and $t = 6$ mm). (a) Shear stress-displacement curve for infilled rock joint. (b) Damage evolution pattern after different shear displacement. (c) Enlarged view of the damaged contacts in the infill layer (σ_n^0= 100 kPa).

confining pressure the number of completely failed contacts ($D = 1.0$) was proportionally higher than that of low confining stress.

4- The DEM results showed that localised shear zones at the point in which a transition from elastic behaviour to nonlinear elastic behaviour occurred. These localised shear zones largely extended during the shearing procedure, with a progressive increase in the number of yielding contacts ($0.0 < D < 1.0$). It was observed that, the DEM specimen with high confining pressure reproduced more completely damaged contacts compared to specimens with low normal stress magnitude.

5- The macroscopic behaviour of the numerical and experimental specimens in terms of peak and residual shear strengths were also interpreted based on t/a. Both numerical and laboratory results showed that the asperity interference was the major contributing factor for specimens with $t/a < 2.67$. However, when $t/a = 4.25$, the mechanical behaviour of the infilled rock joint was approximately governed by the infill layer.

Acknowledgment

The cohesive model used in this study was formulated based on a generic framework by Giang D. Nguyen (University of Adelaide) & Ha H. Bui (Monash University), with Giang D. Nguyen's help in the development and revision of the model. Critical comments by Giang D. Nguyen to improve the manuscript are acknowledged. The first author thanks Mr Sacha Emam from Itasca Consulting group for his invaluable help and comments during implementation and verification of the model in PFC software. The assistance of laboratory staff Mr Adam Ryntjes, Mr Gary Bowman, and Mr Simon Golding during experiments at the University of Adelaide is gratefully acknowledged. The first author acknowledges the helpful discussion with Mr Amin Soltani (University of Adelaide) about experimental setup. Professional editor, Leticia Mooney, provided copyediting and proofreading services, according to the guidelines laid out in the university-endorsed national 'Guidelines for editing research theses'.

Appendix A. Model implementation algorithm in PFC2D

The common approach for implementing the user-defined contact models in PFC is to write the stress-return algorithm in C++, and compile the code as Dynamic Link Library (DLL) files [24]. The DLL files can be executed whenever needed during numerical computations. The normal and shear stress of the cohesive contacts are updated based on their corresponding incremental relative displacement. The inelastic response of the contacts is determined by considering trial stress state [54]:

$$\sigma_n^{trial} = \sigma_n + k_n^0 du_n \tag{22}$$

$$\sigma_s^{trial} = \sigma_s + k_s^0 du_s \tag{23}$$

The value of yield function is then updated according to the Eq. (15). The cohesive contact enters to its softening stage if $F > 0$, and the normal and shear plastic displacements will be updated based on the flow rule with $d\lambda$ calculated from Taylor's expansion of the yield function as follows:

$$d\lambda = \frac{F^{trial}}{\frac{\partial F}{\partial \sigma_n} k_n^0 \frac{\partial G}{\partial \sigma_n} + \frac{\partial F}{\partial \sigma_s} k_s^0 \frac{\partial G}{\partial \sigma_s} + \frac{\partial F}{\partial C} \kappa C \sqrt{\left(\frac{\partial G}{\partial \sigma_n}\right)^2 + \left(\frac{\partial G}{\partial \sigma_s}\right)^2}} \tag{24}$$

Finally, the normal and shear stresses are corrected as follows:

$$d\sigma_n = d\sigma_n^{trial} + d\lambda(-k_n^0)\frac{\partial G}{\partial \sigma_n} \tag{25}$$

$$d\sigma_s = d\sigma_s^{trial} + d\lambda(-k_s^0)\frac{\partial G}{\partial \sigma_n} \tag{26}$$

The stress-return algorithm is operated on all yielding bonds with $F^{trial} > 0$ until 99.99% of the contact cohesion is damaged. At this point, the bond between two DEM particles is broken ($D = 1.0$). In the stress-return algorithm developed in C++, the corresponding DEM stresses, which are needed to compute F^{trial}, are obtained according to bond cross-sectional properties. This implementation approach was successfully followed by other researchers (e.g. Nguyen et al. [20,21]). The cross-sectional area ($\bar{A}$) of DEM contact in two dimensional space is defined as [24]:

$$\bar{A} = 2\bar{R} \tag{27}$$

where $\bar{R}$ is defined as:

$$\bar{R} = \begin{cases} \min(R^1, R^2), & ball - ball \\ R^1, & ball - facet \end{cases} \tag{28}$$

R^1 and R^2 are the radius of two adjoining DEM particles that bonded together. Potyondy and Cundall [31] proposed a deformability method, in which the normal stiffness of the contacts ($\bar{k}^n$) can be related to the elastic modulus of the contact ($\bar{E}_c$) as follows [24]:

$$\bar{k}^n = \frac{\bar{E}_c}{L} \tag{29}$$

where L can be determined as follows:

$$L = \begin{cases} R^1 + R^2, & ball - ball \\ R^1, & ball - facet \end{cases} \tag{30}$$

During calibration procedure normal to shear stiffness ratio $\bar{k}^n/\bar{k}^s$ was initiated to determine the shear stiffness of the contacts ($\bar{k}^s$) [67,71]. For calibration purposes in PFC2D, the user is allowed to alter the contact stiffnesses after assigning $\bar{E}_c$ [24], which is the approach followed in the present research.

References

[1] Taheri A, Tani K. Use of down-hole triaxial testing apparatus to estimate the mechanical properties of heterogeneous mudstone. Int J Rock Mech Min Sci. 2008;45:1390–402.
[2] Taheri A, Tani K. Developing of an apparatus for down-hole triaxial tests in a rock mass. Int J Rock Mech Min Sci. 2008;45:800–6.
[3] Indraranta B, Haque A, Aziz N. Shear behaviour of idealized infilled joints under constant normal stiffness. Geotechnique 1999;49:331–55.
[4] Oliveira DAF, Indraratna B, Nemcik J. Critical review on shear strength models for soil-infilled joints. Geomech Geoeng 2009;4:237–44.
[5] Mylvaganam J. Shear behaviour of normally consolidated and overconsolidated infilled rock joints under undrained triaxial conditions. Australia: University of Wollongong; 2007.
[6] Indraratna B, Oliveira D, Brown E, Assis A. Effect of soil-infilled joints on the stability of rock wedges formed in a tunnel roof. Int J Rock Mech Min Sci 2010;47:739–51.
[7] Barton N. A review of the shear strength of filled discontinuities in rock. Norwegian Geotechnical Institute Publication; 1974.
[8] Ladanyi B, Archambault G. Shear strength and deformability of filled indented joints. In: Proceedings of the 1st international symposium on the geotechnics of structurally complex formations, Capri, Italy, September 1977; 1977. p. 317–26.
[9] Lama R. Influence of clay infillings on shear behaviour of joints. In: 3rd congress of int assoc eng geol. Madrid; 1978.
[10] Papaliangas T, Lumsden A, Hencher S, Manolopoulou S. Shear strength of modelled filled rock joints. In: Proceedings of the international symposium on rock joints, Loen, Norway, June 1990; 1990. p. 275–82.
[11] Indraranta B, Welideniya H, Brown E. A shear strength model for idealised infilled joints under constant normal stiffness. Géotechnique. 2005;55:215–26.
[12] Shrivastava A, Rao K. Physical modeling of shear behavior of infilled rock joints under CNL and CNS boundary conditions. Rock Mech Rock Eng. 2018;51:101–18.
[13] Jahanian H, Sadaghiani MH. Experimental study on the shear strength of sandy clay infilled regular rough rock joints. Rock Mech Rock Eng 2015;48:907–22.
[14] Ma H, Liu Q. Prediction of the peak shear strength of sandstone and mudstone joints infilled with high water-cement ratio grouts. Rock Mech Rock Eng 2017;50:2021–37.
[15] Feng K, Montoya BM, Evans TM. Discrete element method simulations of bio-cemented sands. Comput Geotech 2017;85:139–50.
[16] Garcia FE, Bray JD. Modeling the shear response of granular materials with discrete element assemblages of sphere-clusters. Comput Geotech 2019;106:99–107.
[17] Indraratna B, Jayanathan M, Brown ET. Shear strength model for overconsolidated clay-infilled idealised rock joints. Géotechnique. 2008;58:55–65.
[18] Kazerani T, Zhao J. Micromechanical parameters in bonded particle method for modelling of brittle material failure. Int J Numer Anal Meth Geomech 2010;34:1877–95.
[19] Nguyen T, Bui H, Ngo T, Nguyen G. Experimental and numerical investigation of influence of air-voids on the compressive behaviour of foamed concrete. Mater Des 2017;130:103–19.
[20] Nguyen NHT, Bui HH, Nguyen GD, Kodikara J. A cohesive damage-plasticity model for DEM and its application for numerical investigation of soft rock fracture properties. Int J Plast 2017;98:175–96.
[21] Nguyen NHT, Bui HH, Nguyen GD, Kodikara J, Arooran S, Jitsangiam P. A thermodynamics-based cohesive model for discrete element modelling of fracture in cemented materials. Int J Solids Struct 2017;117:159–76.
[22] Mahabadi OK, Lisjak A, Munjiza A, Grasselli G. Y-Geo: New combined finite-discrete element numerical code for geomechanical applications. Int J Geomech 2012;12:676–88.
[23] Wang Y, Tonon F. Discrete element modeling of rock fragmentation upon impact in rock fall analysis. Rock Mech Rock Eng. 2011;44:23–35.
[24] Itasca. PFC (Particle Flow Code) Version 5.0. Minneapolis, USA: Itasca Consulting Group; 2016.
[25] Zhao Z. Gouge particle evolution in a rock fracture undergoing shear: a microscopic DEM study. Rock Mech Rock Eng 2013;46:1461–79.
[26] Cundall P, Strack O. A discrete numerical model for granular assemblies. Geotechnique 1979;29:47–65.
[27] Kia F, Montoya BM, Evans TM. Discrete element method simulations of bio-cemented sands. Comput Geotech 2017;85:139–50.
[28] Kazerani T, Yang Z, Zhao J. A discrete element model for predicting shear strength and degradation of rock joint by using compressive and tensile test data. Rock Mech Rock Eng 2012;45:695–709.
[29] Tatone B. Investigating the evolution of rock discontinuity asperity degradation and void space morphology under direct shear test. Toronto, Canada: University of Toronto; 2014.
[30] Wu K, Remond S, Abriak N, Pizette P, Becquart F, Liu S. Study of the shear behavior of binary granular materials by DEM simulations and experimental triaxial tests. Adv Powder Technol 2017;28:2198–210.
[31] Potyondy D, Cundall P. A bonded-particle model for rock. Int J Rock Mech Min Sci 2004;41:1329–64.
[32] Bahaaddini M, Sharrock G, Hebblewhite B. Numerical direct shear tests to model the shear behaviour of rock joints. Comput Geotech 2013;51:101–15.
[33] Bewick RP, Kaiser PK, DEM Bawden WF. Simulation of direct shear: 2. Grain boundary and mineral grain strength component influence on shear rupture. Rock Mech Rock Eng 2014;47:1673–92.
[34] Cheng K, Wang Y, Yang Q, Mo Y, Guo Y. Determination of microscopic parameters of quartz sand through tri-axial test using the discrete element method. Comput Geotech 2017;92:22–40.
[35] Cho N, Martin CD, Sego DC. Development of a shear zone in brittle rock subjected to direct shear. Int J Rock Mech Min Sci 2008;45:1335–46.
[36] Cho N, Martin CD, Sego DC, Jeon J. Dilation and spalling in axially compressed beams subjected to bending. Rock Mech Rock Eng 2010;43:123–33.
[37] Cui Y. Effect of joint type on the shear behavior of synthetic rock. Bull Eng Geol Environ 2018. https://doi.org/10.1007/s10064-018-1325-3.
[38] Wang P, Cai M, Ren F, Li C, Yang T. A digital image-based discrete fracture network model and its numerical investigation of direct shear tests. Rock Mech Rock Eng 2017;50:1801–16.
[39] Zhang Z, Cui Y, Chan DH, Taslagyan KA. DEM simulation of shear vibrational fluidization of granular material. Granular Matter 2018;20:71.
[40] Al-Halbouni D, Holohan EP, Taheri A, Schöpfer MPJ, Emam S, Dahm T. Geomechanical modelling of sinkhole development using distinct elements: Model verification for a single void space and application to the Dead Sea area. Solid Earth 2018;9:1341–73.
[41] Kalteziotis N. Progressive instability in strain-softening soil with particular reference to undrained bearing capacity. United Kingdom: University of Surrey; 1981.
[42] Wagner JF. Chapter 9 - mechanical properties of clays and clay minerals. In: Bergaya F, Lagaly G, editors. Developments in clay science. Elsevier; 2013. p. 347–81.
[43] D'Ignazio M, Länsivaara T. Shear bands in soft clays: Strain-softening behavior in finite element method. Rakenteiden mekaniikka. 2015;48:83–98.
[44] Tembe S, Lockner DA, Wong T-F. Effect of clay content and mineralogy on frictional sliding behavior of simulated gouges: Binary and ternary mixtures of quartz, illite, and montmorillonite. J Geophys Res: Solid Earth 2010;115.
[45] Utili S, Nova R. DEM analysis of bonded granular geomaterials. Int J Numer Anal Meth Geomech 2008;32:1997–2031.
[46] Obermayr M, Vrettos C, Eberhard P, Däuwel T. A discrete element model and its experimental validation for the prediction of draft forces in cohesive soil. J Terramech 2014;53:93–104.
[47] Karakus M, Liu Y, Zhang G, Tang H. A new shear strength model incorporating influence of infill materials for rock joints. Geomech Geophys Geo-Energy Geo-Resour 2016;2:183–93.
[48] Potyondy D. FC2D flat-joint contact model. Minneapolis: Itasca Consulting Group Inc; 2012.
[49] Oh J, Li Y, Mitra R, Canbulat I. A numerical study on dilation of a saw-toothed rock joint under direct shear. Rock Mech Rock Eng 2017;50:913–25.
[50] Cheng C, Chen X, Zhang S. Multi-peak deformation behavior of jointed rock mass under uniaxial compression: Insight from particle flow modeling. Eng Geol 2016;213:25–45.
[51] Jiang M, Jiang T, Crosta G, Shi Z, Chen H, Zhang N. Modeling failure of jointed rock slope with two main joint sets using a novel DEM bond contact model. Eng Geol 2015;193:79–96.
[52] Huang M, Chen Y, Gu X. Discrete element modeling of soil-structure interface behavior under cyclic loading. Comput Geotech 2019;107:14–24.
[53] Duriez J, Darve F, Donzé F. A discrete modeling-based constitutive relation for infilled rock joints. Int J Rock Mech Min Sci 2011;48:458–68.
[54] Saadat M, Taheri A. A numerical approach to investigate the effects of rock texture on the damage and crack propagation of a pre-cracked granite. Comput Geotech 2019;111:89–111.
[55] SIBELCO. Clay&Kaolin, https://www.sibelco.com/materials/clay-kaolin/; 2019 [accessed 11 April 2019].
[56] Lin C. Investigation of shear stress behaviour of compacted Kaolin clay mixed with salt solution. Australia: The University of Queensland; 2017.
[57] Indraratna B, Oliveira DAF, Brown ET, de Assis AP. Effect of soil–infilled joints on the stability of rock wedges formed in a tunnel roof. Int J Rock Mech Min Sci 2010;47:739–51.
[58] Lu Y, Wang L, Li Z, Sun H. Experimental study on the shear behavior of regular sandstone joints filled with cement grout. Rock Mech Rock Eng 2017;50:1321–36.
[59] Indraratna B, Premadasa W, Brown ET, Gens A, Heitor A. Shear strength of rock joints influenced by compacted infill. Int J Rock Mech Min Sci 2014;70:296–307.
[60] Indraratna B, Premadasa W, Brown ET. Shear behaviour of rock joints with unsaturated infill. Géotechnique 2013;63:1356–60.
[61] Le LA, Nguyen GD, Bui HH, Sheikh AH, Kotousov A, Khanna A. Modelling jointed rock mass as a continuum with an embedded cohesive-frictional model. Eng Geol 2017;228:107–20.
[62] Le LA, Nguyen GD, Bui HH, Sheikh AH, Kotousov A. Localised failure mechanism as the basis for constitutive modelling of geomaterials. Int J Eng Sci 2018;133:284–310.
[63] Shen Z, Jiang M, Thornton C. DEM simulation of bonded granular material. Part I: Contact model and application to cemented sand. Comput Geotech 2016;75:192–209.
[64] Feng S, Liu X, Chen H, Zhao T. Micro-mechanical analysis of geomembrane-sand interactions using DEM. Comput Geotech 2018;94:58–71.
[65] Shang J, Yokota Y, Zhao Z, Dang W. DEM simulation of mortar-bolt interface behaviour subjected to shearing. Constr Build Mater 2018;185:120–37.
[66] Bewick RP, Kaiser PK, Bawden WF, DEM Bahrani N. Simulation of direct shear: 1. Rupture under constant normal stress boundary conditions. Rock Mech Rock Eng 2014;47:1647–71.
[67] Hofmann H, Babadagli T, Yoon JS, Zang A, Zimmermann G. A grain based modeling study of mineralogical factors affecting strength, elastic behavior and micro fracture development during compression tests in granites. Eng Fract Mech 2015;147:261–75.
[68] Tamás K, Jóri IJ, Mouazen AM. Modelling soil–sweep interaction with discrete element method. Soil Tillage Res 2013;134:223–31.
[69] Tamás K, Kovács Á, Jóri IJ. The evaluation of the parallel Bond's properties in DEM modeling of soils. Periodica Polytechnica Mech Eng 2016;60:21–31.
[70] Tamás K. The role of bond and damping in the discrete element model of soil-sweep interaction. Biosyst Eng 2018;169:57–70.
[71] Liu G, Cai M, Huang M. Mechanical properties of brittle rock governed by micro-geometric heterogeneity. Comput Geotech 2018.

Appendix C (Paper 3)

Modelling Micro-cracking Behaviour of Pre-cracked Granite Using Grain-Based Element Model

Saadat M, Taheri A. (2019) Modelling Micro-cracking Behaviour of Pre-cracked Granite Using Grain-Based Distinct Element Model. *Rock Mechanics and Rock Engineering*. doi: 10.1007/s00603-019-01862-0

Statement of Authorship

Title of Paper	Modelling Micro-cracking Behaviour of Pre-cracked Granite Using Grain-Based Distinct Element Model
Publication Status	✓ Published ☐ Accepted for Publication ☐ Submitted for Publication ☐ Unpublished and Unsubmitted work written in manuscript style
Publication Details	Saadat M, Taheri A. (2019) Modelling Micro-cracking Behaviour of Pre-cracked Granite Using Grain-Based Distinct Element Model. Rock Mechanics and Rock Engineering. doi: 10.1007/s00603-019-01862-0

Principal Author

Name of Principal Author (Candidate)	Mahdi Saadat
Contribution to the Paper	Developed and wrote the formulation of the cohesive model Conducted the numerical modelling of pre-cracked Barre granite Analysed the numerical results Wrote the entire manuscript
Overall percentage (%)	80%
Certification:	This paper reports on original research I conducted during the period of my Higher Degree by Research candidature and is not subject to any obligations or contractual agreements with a third party that would constrain its inclusion in this thesis. I am the primary author of this paper.
Signature	Date: 07 August 2019

Co-Author Contributions

By signing the Statement of Authorship, each author certifies that:

i. the candidate's stated contribution to the publication is accurate (as detailed above);
ii. permission is granted for the candidate in include the publication in the thesis; and
iii. the sum of all co-author contributions is equal to 100% less the candidate's stated contribution.

Name of Co-Author	Dr Abbas Taheri		
Contribution to the Paper	Supervision of the technical work, revision of the manuscript		
Signature		Date	07 August 2019

End of the document

Rock Mechanics and Rock Engineering
https://doi.org/10.1007/s00603-019-01862-0

ORIGINAL PAPER

Modelling Micro-cracking Behaviour of Pre-cracked Granite Using Grain-Based Distinct Element Model

Mahdi Saadat[1] · **Abbas Taheri**[1]

Received: 7 November 2018 / Accepted: 20 May 2019

Abstract
In this paper, the micro-cracking behaviour of pre-cracked Barre granite is investigated using a grain-based distinct element model (GBM). We investigated and demonstrated a cohesive model in a distinct element code, PFC2D, to mimic the elastic and softening response of the intra-grain contacts in the GBM. The study employed the smooth-joint model to simulate the micro-cracking behaviour of grain interfaces. The grain size distribution, as well as the mineral constituent of Barre granite, was incorporated in the numerical model. The model was calibrated against uniaxial compressive strength and Brazilian split-tensile-strength tests. We found that the GBM framework successfully reproduced the macroscopic physical properties obtained from the laboratory tests. When calibration was complete, the geometries of pre-existing cracks, which were considered in the experimental testing, were imported into the numerical model and used to generate synthetic, pre-cracked Barre granite. The macroscopic cracking process in the generated numerical models was observed by monitoring the evolution of intra- and inter-granular micro-cracks. The cracking and coalescence behaviour of numerical pre-cracked granite revealed that the proposed GBM approach can replicate the macroscopic fracturing pattern of pre-cracked Barre granite with close agreement to the experimental observations. The crack initiation, coalescence, and peak axial stresses were also recorded during numerical testings, and a good agreement was also achieved between these simulated results and the laboratory data. The proposed GBM framework is promising for research into micro-cracking behaviour of pre-cracked crystalline rocks under compressive loading.

Keywords Discrete element modelling (DEM) · Grain-based model (GBM) · Pre-cracked crystalline rock · Cohesive contact model · Micro-cracking response

1 Introduction

The determination of rock mass strength and damage mechanism of granitic rocks is critical at the design and construction stages of civil and mining projects. Mining excavations at great depths generate challenges in the development of mining structures such as pillars and tunnels (Bahrani et al. 2011). Figure 1a illustrates an underground structure excavated in a massive to moderately jointed rock mass. As planes of weaknesses, discontinuities (e.g. joints) can affect the strength, deformation, and failure behaviour of rock masses (Brady and Brown 2004). Since discontinuities often have various characteristics, the scale at which they are studied is crucially important. Conducting large-scale in situ tests to determine the mechanical properties of rock mass are usually costly and challenging, especially around the excavation damaged zones (Hoek and Diederichs 2006). Alternatively, Farahmand et al. (2018) used a numerical approach to characterise the scale dependency of modulus and strength of a rock mass. They concluded that, for the numerical rock blocks with a height of less than 7 m, the rock mass properties remained relatively unchanged (Fig. 1b). They also observed that in the numerical specimens with 7 m height, the macroscopic cracks mostly formed around the pre-existing cracks, which is in agreement with the experimental observations of Moradian et al. (2016) obtained from small-scale Barre granite specimen (i.e. 152 mm × 76 mm) (Fig. 1c). Conducting laboratory tests on pre-cracked specimens (i.e. Fig. 1c) enhances our understating about the cracking processes and damage behaviour of rocks. The results of such experimental testing can serve as a basis for the

✉ Mahdi Saadat
mahdi.saadat@adelaide.edu.au

[1] School of Civil, Environmental and Mining Engineering, The University of Adelaide, Adelaide, Australia

Published online: 28 May 2019

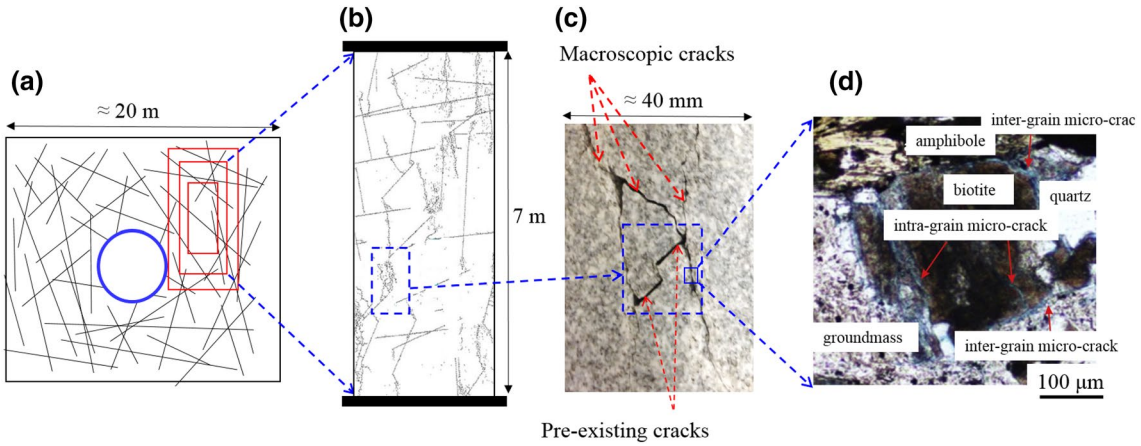

Fig. 1 **a** An underground structure (tunnel) excavated in a massive to moderately jointed rock mass. **b** Damage evolution in a large-scale numerical specimen containing randomly distributed fractures under compressive loading after Farahmand et al. (2018). **c** Damage evolution in laboratory-scale Barre granite due to coalescence of pre-existing cracks under compressive loading after Moradian et al. (2016). **d** Distribution of intragranular and intergranular micro-cracks under compressive loading (after Ündül et al. 2015)

development of constitutive models (i.e. in continuum methods) that can be used for the simulation of field-scale problems (Bobet and Einstein 1998). The macroscopic cracking response, however, is influenced by the microstructure of the rock at the grain scale (Wu et al. 2000). In this respect, studying the underlying mechanism of the initiation of inter- and intra-grain micro-cracks is crucial (Fig. 1d).

The development of macroscopic fractures due to the initiation and coalescence of inter- and intra-grain micro-cracks is the dominant damage mechanism influencing the mechanical behaviour and integrity of brittle rocks (Moradian et al. 2016; Morgan et al. 2013). Different parameters, such as grain shape and size, the type of minerals, and the presence of pre-existing cracks, affect the mechanical and failure responses of rock as a heterogeneous material. The mechanical behaviour of the rock mass is controlled by intact rock blocks and defects (i.e. joints, fractures, and cracks) (Taheri and Tani 2010). One of the main reasons for rock mass failure is the coalescence of pre-existing flaws (Yin et al. 2014; Zhou et al. 2018).

Many scientists have concluded that the mechanical and failure behaviours of crystalline rocks are highly influenced by inter- and intra-grain crack initiation and crack propagation at the mineral scale (Diaz et al. 2016; Rodríguez et al. 2016; Tavallali and Vervoort 2010; Tuğrul and Zarif 1999) (Fig. 1d). Therefore, studying the macroscopic failure and mechanical behaviour of pre-crack rock specimens is highly relevant during the process of rock mass characterisation, especially for the evaluation of rock mass strength (Bahrani and Kaiser 2016; Cao et al. 2016; Liu et al. 2018; Mayer and Stead 2017; Morgan et al. 2013).

The early laboratory investigation of the macroscopic cracking behaviours of rock was conducted by Brace and Bombolakis (1963). Later, others experimentally studied the mechanical behaviour of rock specimens that included pre-existing cracks (Bobet and Einstein 1998; Horii and Nemat-Nasser 1985; Li et al. 2005; Shen et al. 1995; Wong and Chau 1998). Rock-like materials were used in some of these studies to better illustrate the fracturing mechanism under uniaxial compressive loading (Bobet and Einstein 1998; Zhao et al. 2018). Various types of macroscopic cracks were identified by Zhou et al. (2014), including wing cracks, quasi-coplanar secondary cracks, oblique secondary cracks, out-of-plane tensile cracks and out-of-plane shear cracks. A high-speed video system was used by Miller and Einstein (2008) and Morgan et al. (2013) to observe crack initiation, propagation, and coalescence in Barre granite tested under uniaxial compressive loading. Moradian et al. (2016) used the acoustic emission (AE) technique. They identified various cracking levels of pre-cracked Barre granite during failure.

Although laboratory testing is the most common approach for studying the cracking behaviour of brittle crystalline rocks, conducting laboratory test on pre-existing specimens (especially natural crystalline specimens) is expensive, and highly time-consuming. In addition, investigating the influence of various parameters such as grain size distribution, mineral content, etc., on the mechanical and fracturing behaviour of the pre-cracked specimens is highly restricted in the laboratory environment.

Recent advancements in computational techniques have made numerical methods a promising alternative tool with which to study rock mass behaviour at a variety of scales. Using a stochastic distribution of grain properties (e.g. Weibull distribution), the influence of heterogeneity on the mechanical responses of a rock mass can be numerically

investigated (Gao et al. 2016). Advanced numerical methods have been used by many scientists to characterise the rock structure at the grain level (Bahrani and Kaiser 2016; Gao et al. 2016; Liu et al. 2018; Nicksiar and Martin 2014). The finite element method (FEM), distinct element methods (DEM), and the hybrid finite–discrete element methods (FDEM) are generally used for simulating the failure and deformation of rock. Of these numerical methods, DEM has been found to be a more promising tool for characterising the mechanical and failure behaviour of rocks. According to a review study conducted by Zhang and Wong (2018), both FEM and FDEM suffer from some issues such as difficulties in understanding the behaviour of individual cracks, and a dependency of micro-cracking responses on the fracturing mechanisms.

Two grain-based model (GBM) techniques—particle flow code (PFC) (Itasca 2016), and triangular and polygonal grains in UDEC (Gao et al. 2016; Kazerani and Zhao 2010) employ DEM principles during simulation. Both models characterise the heterogeneity and failure behaviour of crystalline rocks. These numerical methods have attractive advantages such as producing numerical crystalline specimens with similar geometrical characteristics to the physical specimen (Zhang and Wong 2018). Potyondy (2010a) developed the PFC-GBM model to represent the minerals of crystalline rock by a polygonal grain structure. According to Potyondy (2010a), an ideal polygonal structure generation procedure should reproduce a grain microstructure with similar topological and statistical properties of the physical specimen. The grain structure in PFC2D is generated based on the mineral content and size of each mineral. By using a random generation scheme, numerous GBM specimens with the same statistical volumetric percentages and size distributions but various distributions of minerals can be generated (Hofmann et al. 2015a). The axial splitting failure mode has frequently been observed in crystalline rocks (Bewick et al. 2014a, b; Potyondy 2010a; Zhang and Wong 2018), as a result of propagation and coalescence of micro-cracks along grain boundaries (Liu et al. 2018). An assembly of DEM particles represents the polygonal grain in PFC-GBM, and the contacts between these particles can be broken to mimic the development of intra-grain micro-cracks. The interfaces between the polygonal structures represent the grain boundaries. The DEM particles in PFC-GBM are laid along the interface and bonded together using an interface–contact constitutive model known as the smooth-joint model (SJM). The behaviour of inter-grain micro-cracks can be reproduced by breaking the bonds in boundary contacts. This approach has been widely used in the literature to simulate the micro-cracking behaviour of crystalline rocks (Bahrani et al. 2014; Hofmann et al. 2015a; Liu et al. 2018).

Although DEM has become a promising numerical technique to simulate the fracturing behaviour of crystalline rocks, the number of research studies on constitutive contact models is still limited. The parallel-bond model (PBM) proposed by Potyondy and Cundall (2004) is one of the earliest DEM-based contact models that characterises the mechanical behaviour of brittle rocks. The PBM, which is available in PFC-GBM framework, has been widely used in the literature as an intra-grain contact model that mimics the cracking behaviour of minerals (Hofmann et al. 2015a, b; Li et al. 2018; Liu et al. 2018). The contact forces in PBM are related to maximum normal, and shear stresses acting within the bonded contact (Itasca 2016). According to Potyondy and Cundall (2004), the bond strength in PBM is characterised by cohesion and tensile strength of the contact, and once either of the maximum stresses exceeds the bond strength, bond breakage occurs, and the contact is removed from the model. The bond break in PBM results in an abrupt reduction of contact forces to zero (Itasca 2016; Nguyen et al. 2017a, b), which releases an enormous amount of energy (Khazaei et al. 2015). However, in physical material the bond breakage occurs due to the weakening of the cohesional component of the rock in a gradual process (Hajiabdolmajid et al. 2002; Khazaei et al. 2015). According to Nguyen et al. (2017b), a huge number (e.g. millions) of DEM particles is required at microscale to simulate the microscale softening behaviour, which is hard to achieve, if not impossible (Nguyen et al. 2017b). As an alternative approach, many scholars suggest that by incorporating a softening response in the force–displacement law of PBM, the failure behaviour can be simulated more realistically at the particle level (Khazaei et al. 2015; Ma and Huang 2018a, 2018b; Nguyen et al. 2017a, b). A combination of damage mechanics and plasticity theory, which describe fracture as a gradual process of strength degradation and energy dissipation, has been considered to be an appropriate alternative to characterise the failure mechanism at the particle level (Nguyen et al. 2017a, b).

Another challenge involved in simulating the crystalline rocks using the PFC-GBM approach is the high number of micro-mechanical parameters incorporated in the constitutive models of inter- and intra-grain contacts. In this paper, a cohesive bond model proposed by Saadat and Taheri (2019) is employed that uses a single initial cohesion to define the contact strength, and the model produces a softening response in mode I (tensile), mode II (shear), and in mixed-mode cracking. There are different cohesive models available in the literature (Kazerani et al. 2012; Nguyen et al. 2017a, b; Pouya and Yazdi 2015). However, in the proposed cohesive model, the complexity of the previous models is reduced, and only one micro-parameter (cohesion) is considered to represent the contact strength to facilitate the calibration procedure (Saadat and Taheri 2019). For simulating the fracturing behaviour of grain boundaries, the smooth-joint model (Itasca 2016) is assigned to inter-grain contacts.

The focus of this research is to propose a grain-based model (GBM) framework augmented with a softening model that can mimic the mechanical and failure behaviour of pre-cracked crystalline rocks. This is because, despite the number of numerical studies using PFC-GBM for simulating the failure response of crystalline rocks, no comprehensive study in the literature investigates this approach's capability in reproducing the micro-cracking response of pre-cracked specimens using a cohesive contact model. The proposed GBM framework was calibrated against the experimental uniaxial compressive strength and Brazilian split-tensile-strength testing results using Barre granite. The calibrated model was then used for simulating the macroscopic mechanical and fracturing behaviour of physical pre-cracked Barre granite, and a good agreement was obtained. We found that using the proposed GBM framework, both inter- and intra-grain micro-cracking behaviour can be simulated. These capabilities provided a better insight into the influence of the microstructural features of the pre-cracked granite's failure mechanisms.

2 Grain-Based Modelling in PFC2D

In previous numerical simulations of hard rocks using PFC2D, the ratio between the tensile strength and uniaxial compressive strength was found to be overestimated when compared to experimental observations (Yoon et al. 2012). An efficient DEM approach should be able to characterise the fracturing mechanism of rocks with a close agreement to the experimental observations. A prerequisite in DEM-based studies is to calibrate the micro-mechanical properties of the contact model. In general, the Brazilian tensile strength (BTS) of the crystalline rocks is much lower than their UCS (Ma and Huang 2018a). In PBM, a high value of the micro-tensile strength and cohesion are needed to achieve a reasonable UCS that matches the experimental data. The set of micro-mechanical parameters achieved during UCS test cannot approximate the BTS, which is due to the high value of micro-tensile strength. If one reduces the micro-tensile strength to match the BTS with the experiment, the PBM contacts fail earlier in the UCS test, resulting in a lower axial strength compared to the laboratory counterpart (Potyondy 2012). The reason is that when a PBM contact fails either in tension or shear, the contact force reduces abruptly to zero, which inhibits matching the UCS (Potyondy 2012). Therefore, PBM cannot mimic the tension failure of rocks with an acceptable level of accuracy (Hofmann et al. 2015a).

The failure behaviour of pre-cracked Barre granite was extensively studied by Morgan et al. (2013) and Miller (2008). According to their experimental observations, at crack initiation stress, the initial macroscopic fractures in the pre-cracked granite are tensile cracks. Indeed, since PBM overestimates the BTS/UCS, the macroscopic tensile cracks and their corresponding crack initiation stress cannot be well captured by this model.

To overcome this issue, the clumped particle model was developed. In the clumped particle model, several DEM particles are clumped together to generate arbitrary shapes. It is used by many researchers to model crystalline rocks (Cho et al. 2007; Yoon et al. 2012). The main problem with clumped particles is that they are considered to be rigid bodies that cannot fail (Hofmann et al. 2015a). The clumped particle method cannot reproduce the intra-grain micro-cracking behaviour that has been extensively observed in the laboratory e.g. Moore and Lockner (1995). Hence, the grain-based modelling (GBM) approach was developed by Potyondy (2010a), to simulate the micro-cracking behaviour of grains and mineral interfaces. The two-dimensional PFC-GBM has been used extensively to simulate the mechanical behaviour of rocks (Bahrani and Kaiser 2016; Bahrani et al. 2014; Hofmann et al. 2015a; Liu et al. 2018). The PFC-GBM approach mimics the microstructural behaviour of crystalline rocks, and achieves a highly accurate ratio between tensile strength and uniaxial compressive strength.

The procedure to generate a grain-based model in PFC2D (Potyondy 2010a) is described as follows. Firstly, a particle assembly is generated with a desired mineralogical composition and grain size distribution (Fig. 2a). The DEM particles at this stage must have at least two contacts. Figure 2a illustrates a PFC2D model where the centre points of neighbouring DEM particles are connected. Secondly, a void must be defined as a closed chain of DEM particles and contacts (Fig. 2b). Thirdly, a network of polygons is created by joining the internal-void centroids (Fig. 2c). Before generating the mineral, DEM particles with fewer than three contacts are removed. Finally, a polygonal grain structure that mimics the mineral distribution of crystalline rock is formed (Fig. 2d). This polygonal grain structure then is employed to generate the GBM by being laid over a grain structure containing smaller DEM particles on a new particle assembly.

Figure 3 shows an example of a grain-based structure constructed in PFC2D. Figure 3a illustrates a particle assembly overlaid on a polygonal structure. In PFC-GBM, two sets of contacts are required: one set of contacts forming the grain boundaries (inter-grain contacts), and the other connecting the DEM particles inside the grains (intra-grain contacts) (Fig. 3b). In the present research, two different contact constitutive models are employed to simulate inter- and intra-grain micro-cracking behaviour.

3 DEM Contact Constitutive Models

The PFC-GBM approach generates a synthetic material that models a crystalline rock with a breakable polygonal grain structure (Bahrani et al. 2014). In the present study,

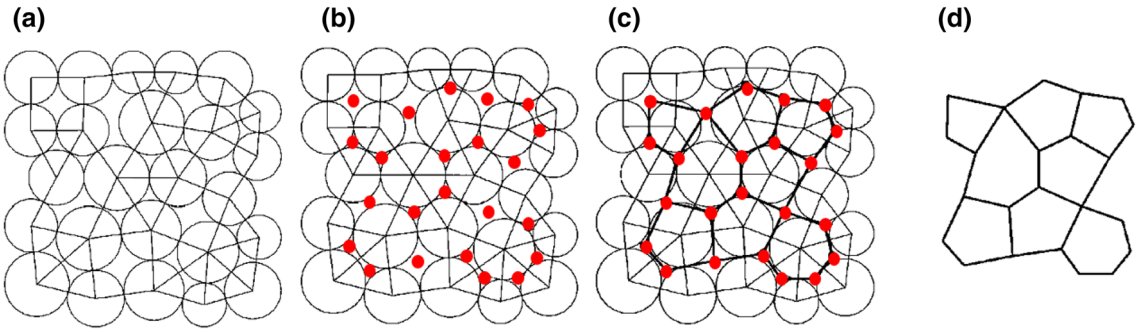

Fig. 2 The procedure of mineral structure generation: **a** creation of initial particle assembly, **b** detection of internal-void centroids, **c** generation of target polygonal structure, **d** construction of final grain structure and removing the initial particle assembly after (Potyondy 2010a)

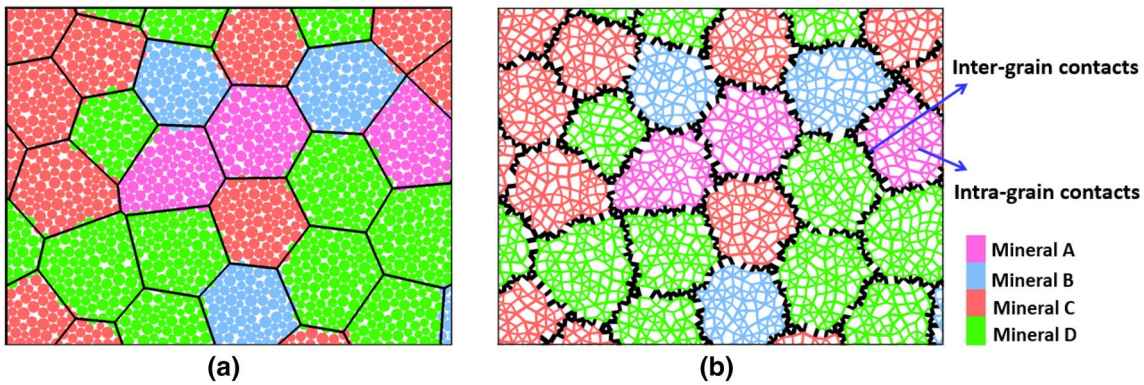

Fig. 3 An example of a grain-based model in PFC2D: **a** grain structures filled with DEM particles, coloured disks represent DEM particles, and black polygons depict grain interfaces; **b** inter- and intra-grain contacts in GBM

a cohesive model was installed on the intra-grain contacts. The smooth-joint model, which is an interface contact constitutive model, was assigned to the grain boundary contacts. Note that the smooth-joint model was employed as a non-cohesive interface model in the current study. This approach has been followed by many researchers in previous studies (Bahrani and Kaiser 2016; Bahrani et al. 2014; Bewick et al. 2014b; Liu et al. 2018). In future investigations, the cohesive constitutive model can be incorporated into the interface model to observe possible mechanical differences and, probably, new macroscopic fracturing patterns. This section describes the constitutive relationships of the cohesive model. More details regarding model validation can also be found in Saadat and Taheri (2019).

3.1 The Proposed Cohesive Model

This study used a new cohesive, constitutive model proposed by Saadat and Taheri (2019) for simulating the failure behaviour of intra-grain contacts in DEM codes. There are some cohesive models available in the literature (e.g. Le et al. (2017, 2018); Nguyen et al. (2017a, b) that can be used as contact models in DEM. However, in the new cohesive model, the number of microproperties was reduced because it allows the users to alleviate the complexity of the calibration scheme. Additionally, increasing the simplicity of the numerical algorithm makes the computations more time efficient.

In the proposed model (Saadat and Taheri 2019), the relative displacement $\boldsymbol{u}\left(\boldsymbol{u}_{\mathrm{n}}, \boldsymbol{u}_{\mathrm{s}}\right)$ of the contacts was decomposed into an elastic and plastic components to account for reversible and irreversible displacements in the contacts:

$$\boldsymbol{u} = \boldsymbol{u}^{\mathrm{e}} + \boldsymbol{u}^{\mathrm{p}}. \tag{1}$$

The normal and shear stresses are linked to the relative displacement of the contact between two particles, and can be calculated by:

$$\sigma_{\mathrm{n}} = k_{\mathrm{n}}^{0}\left(u_{\mathrm{n}} - u_{\mathrm{n}}^{\mathrm{p}}\right), \tag{2}$$

$$\sigma_{\mathrm{s}} = k_{\mathrm{s}}^{0}\left(u_{\mathrm{s}} - u_{\mathrm{s}}^{\mathrm{p}}\right), \tag{3}$$

where σ_{n} and σ_{s} are normal and shear stresses in the bonding contacts; u_{n} and $u_{\mathrm{n}}^{\mathrm{p}}$ are the total and plastic normal displacements; u_{s} and $u_{\mathrm{s}}^{\mathrm{p}}$ are the total and plastic shear displacements; and k_{n}^{0} and k_{s}^{0} are the normal and shear stiffnesses,

respectively. The contact deformability method should be used to achieve contact stiffnesses in DEM codes (Potyondy and Cundall 2004). This method will be discussed in Sect. 3.2.

3.1.1 Yield Criterion and Flow Rule

A yield function determines the failure state under which a bond-break between two DEM particles occurs. A simple yield function was used that accounts for the mixed-mode failure of the contacts, which allows the independent selection of the friction and strength components for the contacts:

$$F\left(\sigma_{\mathrm{n}}, \sigma_{\mathrm{s}}, C\right) = \sigma_{\mathrm{s}} + \mu\sigma_{\mathrm{n}} - C = 0, \tag{4}$$

where μ is the friction coefficient of the contact and C is defined as:

$$C = C^0 \mathrm{e}^{-\kappa u^{\mathrm{p}}}. \tag{5}$$

In Eq. 5, C^0 is the initial cohesion of the contacts, κ is the softening parameters, and u^{p} is the contact's accumulated plastic displacement, which can be calculated from its increments, defined as:

$$\mathrm{d}u^{\mathrm{p}} = \sqrt{(\mathrm{d}u_{\mathrm{n}}^{\mathrm{p}})^2 + \left(\mathrm{d}u_{\mathrm{s}}^{\mathrm{p}}\right)^2}. \tag{6}$$

In this study, a damage parameter ($0 \le D \le 1$) used to measure the level of the contact's deterioration, is defined as:

$$D = \frac{C^0 - C}{C^0} = 1 - \mathrm{e}^{-\kappa u^{\mathrm{p}}}. \tag{7}$$

The damage parameter introduced in Eq. 7 can be used to monitor the softening stage of the contacts. Fully bonded contacts have $D = 0$, and completely damaged contacts have $D = 1$.

At microscopic level, a dilatancy parameter is necessary to account for the dilation response of the contacts. A non-associative flow rule was considered to satisfy this requirement:

$$G\left(\sigma_{\mathrm{n}}, \sigma_{\mathrm{s}}\right) = \sigma_{\mathrm{s}} + \beta\sigma_{\mathrm{n}}, \tag{8}$$

where β is the dilation coefficient. Consequently, the flow rule of incremental displacement can be expressed as:

$$\mathrm{d}u_{\mathrm{n}}^{\mathrm{p}} = \mathrm{d}\lambda\frac{\partial G}{\partial \sigma_{\mathrm{n}}}, \tag{9}$$

$$\mathrm{d}u_{\mathrm{s}}^{\mathrm{p}} = \mathrm{d}\lambda\frac{\partial G}{\partial \sigma_{\mathrm{s}}}, \tag{10}$$

where $\mathrm{d}\lambda \ge 0$ is the plastic multiplier.

The inelastic behaviour of the contacts was updated via a semi-implicit algorithm, which calculated a trial stress as follows:

$$\sigma_{\mathrm{n}}^{\mathrm{trial}} = \sigma_{\mathrm{n}} + \mathrm{d}\sigma_{\mathrm{n}}^{\mathrm{trial}}, \tag{11}$$

$$\sigma_{\mathrm{s}}^{\mathrm{trial}} = \sigma_{\mathrm{s}} + \mathrm{d}\sigma_{\mathrm{s}}^{\mathrm{trial}}, \tag{12}$$

in which the trial stress increments were calculated as:

$$\mathrm{d}\sigma_{\mathrm{n}}^{\mathrm{trial}} = k_{\mathrm{n}}^0 \mathrm{d}u_{\mathrm{n}}, \tag{13}$$

$$\mathrm{d}\sigma_{\mathrm{s}}^{\mathrm{trial}} = k_{\mathrm{s}}^0 du_{\mathrm{s}}. \tag{14}$$

A Taylor expansion in the trial stress state gives:

$$F^{\mathrm{new}} = F^{\mathrm{trial}} + \frac{\partial F}{\partial \sigma_{\mathrm{n}}}\mathrm{d}\sigma_{\mathrm{n}}^{\mathrm{c}} + \frac{\partial F}{\partial \sigma_{\mathrm{s}}} d\sigma_{\mathrm{n}}^{\mathrm{c}} + \frac{\partial F}{\partial C}\frac{\partial C}{\partial u^{\mathrm{p}}}\mathrm{d}u^{\mathrm{p}}. \tag{15}$$

From Eqs. 5, 9, and 10, we will have:

$$\frac{\partial C}{\partial u^{\mathrm{p}}}\mathrm{d}u^{\mathrm{p}} = \mathrm{d}\lambda(-\kappa C\sqrt{\left(\frac{\partial G}{\partial \sigma_{\mathrm{n}}}\right)^2 + \left(\frac{\partial G}{\partial \sigma_{\mathrm{s}}}\right)^2}. \tag{16}$$

Substituting (12) and $\mathrm{d}\sigma_{\mathrm{i}}^{\mathrm{c}} = -k_{\mathrm{i}}^0 \mathrm{d}u_{\mathrm{i}}^{\mathrm{p}}$ (with "i" standing for "n", or "s") in (11), we obtain:

$$\begin{aligned} F^{\mathrm{new}} = F^{\mathrm{trial}} &- \mathrm{d}\lambda\frac{\partial F}{\partial \sigma_{\mathrm{n}}}k_{\mathrm{n}}^0\frac{\partial G}{\partial \sigma_{\mathrm{n}}} - \mathrm{d}\lambda\frac{\partial F}{\partial \sigma_{\mathrm{s}}}k_{\mathrm{s}}^0\frac{\partial G}{\partial \sigma_{\mathrm{s}}} \\ &- \mathrm{d}\lambda\frac{\partial F}{\partial C}\frac{\partial C}{\partial u^{\mathrm{p}}}\kappa C\sqrt{\left(\frac{\partial G}{\partial \sigma_{\mathrm{n}}}\right)^2 + \left(\frac{\partial G}{\partial \sigma_{\mathrm{s}}}\right)^2}. \end{aligned} \tag{17}$$

The plastic multiplier $\mathrm{d}\lambda$ can then be obtained as the solution of the equation $F^{\mathrm{new}} = 0$:

$$\mathrm{d}\lambda = \frac{F^{\mathrm{trial}}}{\frac{\partial F}{\partial \sigma_{\mathrm{n}}}k_{\mathrm{n}}^0\frac{\partial G}{\partial \sigma_{\mathrm{n}}} + \frac{\partial F}{\partial \sigma_{\mathrm{s}}}k_{\mathrm{s}}^0\frac{\partial G}{\partial \sigma_{\mathrm{s}}} + \frac{\partial F}{\partial C}\frac{\partial C}{\partial u^{\mathrm{p}}}\kappa C\sqrt{\left(\frac{\partial G}{\partial \sigma_{\mathrm{n}}}\right)^2 + \left(\frac{\partial G}{\partial \sigma_{\mathrm{s}}}\right)^2}}. \tag{18}$$

Therefore, the corrective stresses are determined as:

$$\mathrm{d}\sigma_{\mathrm{n}}^{\mathrm{c}} = \mathrm{d}\lambda\left(-k_{\mathrm{n}}^0\right)\frac{\partial G}{\partial \sigma_{\mathrm{n}}}, \tag{19}$$

$$\mathrm{d}\sigma_{\mathrm{s}}^{\mathrm{c}} = \mathrm{d}\lambda\left(-k_{\mathrm{s}}^0\right)\frac{\partial G}{\partial \sigma_{\mathrm{n}}}, \tag{20}$$

where $\mathrm{d}\sigma_{\mathrm{n}}^{\mathrm{c}}$ and $\mathrm{d}\sigma_{\mathrm{s}}^{\mathrm{c}}$ are corrective normal and shear stress, respectively. The total incremental stresses are finally obtained from:

$$\mathrm{d}\sigma_{\mathrm{n}} = \mathrm{d}\sigma_{\mathrm{n}}^{\mathrm{trial}} + \mathrm{d}\sigma_{\mathrm{n}}^{\mathrm{c}}, \tag{21}$$

$$\mathrm{d}\sigma_{\mathrm{s}} = \mathrm{d}\sigma_{\mathrm{s}}^{\mathrm{trial}} + \mathrm{d}\sigma_{\mathrm{s}}^{\mathrm{c}}. \tag{22}$$

The model behaviour in mode I and II is illustrated in Fig. 4. The linear elastic portion of stress–displacement curves defines the contact behaviour before failure, followed by a non-linear stage that represents contact softening due to the progressive degradation of cohesion.

3.2 Model Implementation in DEM Codes

The common approach for implementing the user-defined constitutive models in PFC is to write the stress-return algorithm in C++, and compile the code as Dynamic Link Library (DLL) files (Itasca 2016). The DLL files can be executed whenever needed in PFC. As is mentioned in Sect. 3.1, the model considers the stiffness of contact to update the normal and shear stresses. Thus, it was required in C++ to convert stresses to forces to develop the force–displacement law. This was achieved by considering bond cross-sectional properties of the contacts. This approach is successfully adopted by Nguyen et al. (2017a, b). In two-dimensional space, the cross-sectional contact area for two adjoining DEM balls is defined as (Itasca 2016):

$$\bar{A} = 2\bar{R},$$

where $\bar{R}$ can be measured as:

$$\bar{R} = \begin{cases} \min\left(R^1, R^2\right), \text{ball} - \text{ball} \\ R^1, \text{ball} - \text{facet} \end{cases}.$$

In the present study, in order to relate the normal stiffness of the contacts ($\bar{k}^{\mathrm{n}}$) to their elastic modulus ($\bar{E}_{\mathrm{c}}$), the deformability method proposed by Potyondy and Cundall (2004) was adopted. According to this method $\bar{k}^{\mathrm{n}}$ can be calculated as (Itasca 2016):

$$\bar{k}^{\mathrm{n}} = \frac{\bar{E}_{\mathrm{c}}}{L},$$

where L can be determined as follows:

$$L = \begin{cases} R^1 + R^2, \text{ball} - \text{ball} \\ R^1, \text{ball} - \text{facet} \end{cases}.$$

The normal to shear stiffness ratio $\bar{k}^{\mathrm{n}}/\bar{k}^{\mathrm{s}}$ can be initialised during the calibration procedure to calculate shear stiffness of the contacts ($\bar{k}^{\mathrm{s}}$). The normal ($\bar{k}^{\mathrm{n}}$) and shear ($\bar{k}^{\mathrm{s}}$) stiffness of the contact are regarded as micro-mechanical parameters of the proposed GBM framework. Since $\bar{k}^{\mathrm{n}}$ and $\bar{k}^{\mathrm{s}}$ represent the stiffness of the cement bridges at grain scale, it may require a highly sophisticated experimental approach to determine these local properties. Alternatively, they can be calibrated against the standard laboratory tests (i.e. uniaxial compression test) (Hofmann et al. 2015a; Liu et al. 2018).

4 Modelling Pre-cracked Granite

In general, the different minerals, pores, and defects in intact rocks control a rocks' mechanical and deformation behaviours (Liu et al. 2018). Better insight into the damage process and failure behaviour of brittle materials can be obtained by studying the processes of the propagation and coalescence of macroscopic cracks that initiate from pre-existing flaws. In the GBM approach, micro-cracks initiate and propagate in the numerical specimen due to bond failures in the inter- and intra-grain contacts. In the presence of pre-existing cracks, the macroscopic failure pattern, and the material strength are influenced by the initiation and propagation of micro-cracks that form around the inner- and outer-flaw-tip regions of the pre-existing flaws. Prior experimental observations have revealed that the flaw inclination angle has an effect on granite's fracturing processes (Miller and Einstein 2008; Morgan et al. 2013). In the following subsections, the calibration procedure of the GBM approach against laboratory data of Barre granite is described first. Then, the micro-parameters obtained during the calibration process are used to simulate the mechanical and cracking behaviours of Barre granite under uniaxial compression.

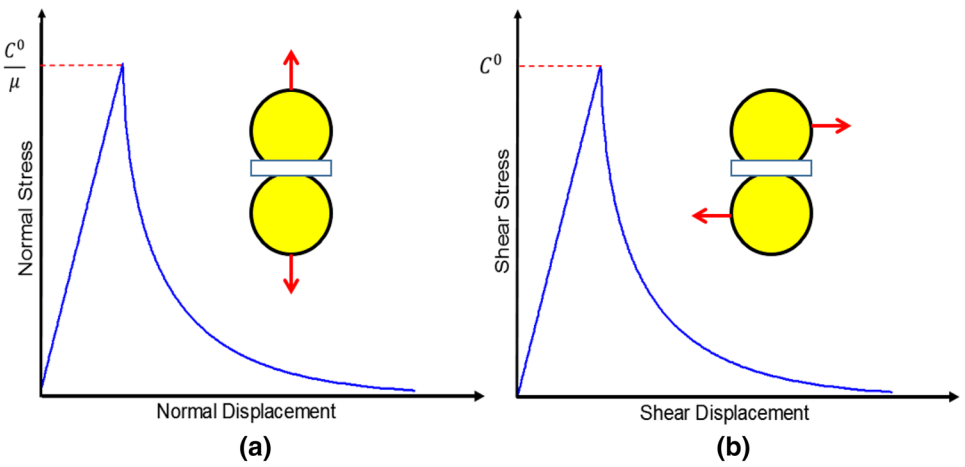

Fig. 4 Stress–displacement behaviour of the proposed cohesive contact model in **a** Mode I, and **b** Mode II

4.1 Calibration Procedure

The micro-mechanical parameters incorporated in the constitutive relationships of the cohesive and smooth-joint models are different from the macroscopic parameters measured in the laboratory. Therefore, the micro-mechanical parameters must be obtained in a calibration procedure (Bahrani et al. 2014; Farahmand et al. 2018; Liu et al. 2018). In the present study, the mechanical properties of Barre granite given by Miller (2008) and Morgan et al. (2013) were used to calibrate the proposed GBM framework. The calibration procedure involved altering the microproperties of the model until reaching a reasonable match between simulated macroscopic parameters and the laboratory test results. We used the results of the uniaxial compressive and Brazilian tensile tests of Barre granite to calibrate the GBM. The macroscopic parameters used in the calibration procedure included Young's modulus, the uniaxial compressive strength (UCS), Poisson's ratio, the Brazilian tensile strength (BTS), and the ratio of UCS/BTS.

4.1.1 Model Setup and Calibration

Barre granite approximately comprised 36% plagioclase, 32% quartz, 18% K-feldspar, 8% biotite, 3% muscovite, and 3% granophyre minerals (Morgan et al. 2013). The average grain size of Barre granite reported in the literature is 1.7 mm, with a minimum and maximum grain size of 0.87 mm and of 2.54 mm, respectively (Morgan et al. 2013). These data were used for generating the synthetic specimens illustrated in Fig. 5. Due to the small percentage of muscovite and granophyre minerals, each was categorised as "other minerals", together with biotite, during the specimen generation procedure. A unique set of micro-mechanical parameters were assigned to the DEM contacts that formed the "other minerals" group. In this research, the average grain size was slightly increased to 1.9 mm, which is still in the range of 0.87-2.54 mm, to make the numerical simulations computationally efficient. Increasing the average grain size to reduce computation time has also been adopted in previous GBM studies (Bewick et al. 2014b; Liu et al. 2018). These assumptions were required to reduce the complexity of numerical simulations and were verified by comparing them with the laboratory results.

We generated a rectangular specimen with a height of 152 mm and a width of 76 mm to simulate the uniaxial compression test (Fig. 6a). To produce reliable UCS results, particle sizes should be relatively small compared to the dimensions of the specimen (Munoz et al. 2016; Potyondy and Cundall 2004). Bahrani et al. (2014) and Hofmann et al. (2015a) suggested that at least five minerals are needed along the shorter dimension of the model to simulate a uniaxial test in PFC-GBM. In this research, a minimum particle radius of 0.2 mm was used, to ensure that each mineral was made of at least ten DEM particles. This increase in the number of DEM particles inside the grain allows for more realistic micro-cracking behaviour of the GBM. The numerical UCS specimen contains approximately 47,000 DEM particles.

ISRM (Ulusay 2015) suggested that the specimen diameter in the Brazilian tensile test ought to be at least ten times the average grain size. Accordingly, for simulating the Brazilian tensile test, a circular specimen with a diameter of 75 mm, containing approximately 18,000 DEM particles, was generated in PFC2D (Fig. 5b). A close-up view of the polygonal grain structure generated by GBM approach is illustrated in Fig. 5c.

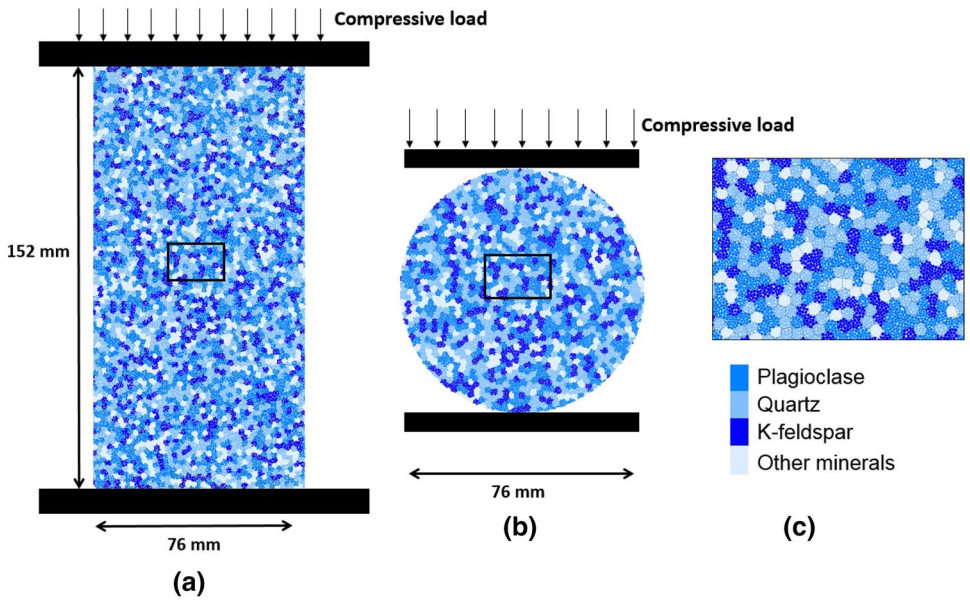

Fig. 5 Schematic of numerical test setups: **a** uniaxial compression test, **b** Brazilian tensile test, and **c** a close-up view of grain structure in synthetic Barre granite

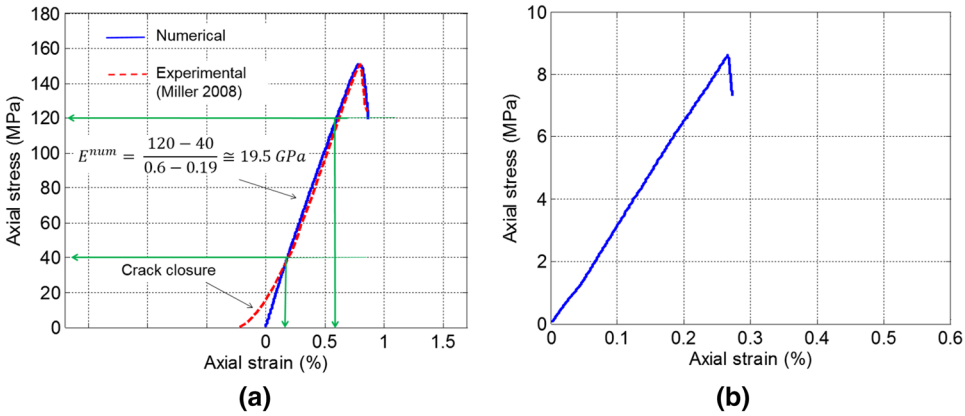

Fig. 6 Stress–strain curves obtained from numerical simulations: **a** uniaxial compression tests, and **b** Brazilian tensile test

The calibration procedure is performed by considering a set of micro-mechanical parameters and conducting uniaxial compression and Brazilian tensile tests until the macroscopic properties captured by the proposed GBM framework match the corresponding properties gained from the experimental tests. A summary of the GBM calibration can be found in Bahrani et al. (2014), in which the process was explained by reproducing the mechanical and fracturing behaviour of experimental intact and granulated Wombeyan marble. This process was also confirmed by Hofmann et al. (2015a) and Liu et al. (2018).

The following steps were carried out to calibrate the proposed GBM framework:

1. The first parameter calibrated was the rock's Young's modulus. A very high strength was assigned to the inter- and intra-grain contacts. Using a trial-and-error procedure, the linear portion of the UCS test curve was fitted to its experimental counterpart by altering the Young's modulus of the intra-grain contacts (E_c) and the shear and normal stiffness values of the smooth-joint model.
2. The Poisson's ratio of the model was calibrated by altering the shear-to-normal stiffness ratio of the cohesive contacts, and the shear and normal stiffnesses of the smooth-joint contacts. This step was carried out in an iterative process with step 1.
3. The Brazilian tensile test was conducted after calibrating the rock's Young's modulus. This was used to obtain the macroscopic tensile strength of the rock by varying the tensile strength of the inter-grain contacts in the smooth-joint model. The tensile strength of the smooth-joint model was reduced at this step to achieve the closest possible macroscopic tensile strength compared to the same value obtained from laboratory tests. The friction angle and friction coefficient of the smooth-joint model was also calibrated at this stage. A low value tensile strength needed to be assigned to the inter-grain contact at this stage, in order to obtain the macroscopic tensile strength of the Barre granite (Hofmann et al. 2015a; Liu et al. 2018).
4. Finally, the maximum axial strength (UCS) of the Barre granite was calibrated by altering the micro-properties of the cohesive model: Cohesion (C^0), the softening parameter (κ), and the friction and dilation coefficients (μ, β).

The stress–strain curves of the uniaxial compressive test and the Brazilian tensile test are depicted in Fig. 6. The micro-mechanical parameters obtained from the calibration procedure are listed in Table 1, and the macroscopic results of both the experimental and numerical tests are given in Table 2. Note that there is a discrepancy between the stress–strain results (Fig. 6a) from the beginning of loading until axial stress equal to 40 MPa, even the overall stiffnesses of the stress–strain results obtained from the numerical modelling and the experimental study are similar. The discrepancy is mainly due to a bedding error measurement (Munoz et al. 2016; Taheri and Tani 2008), and to the closure of existing micro-cracks in the experimental measurement at the beginning of loading, during the crack-closure stage (Taheri et al. 2016; Zeng et al. 2018). These two phenomena create a curvature at the beginning of loading in the experimental measurement, which cannot be captured by the numerical model. Since a constant value for the stiffness of inter- and intra-grain contacts needed in the GBM approach, a linear elastic response was reproduced by the model, even at the beginning of the numerical test. Therefore, no curvature of numerical stress–strain curve (i.e. crack closure) was observed. The linear portion of the stress–strain graph (Fig. 6a) was used to calibrate the Young's modulus of the rock (Potyondy 2010a). The reliability of the numerical models can be validated by comparing the numerical results with the Young's modulus, UCS, tensile strength, and Poisson's ratio of the rock (Farahmand et al. 2018; Li et al. 2018; Potyondy 2010a; Potyondy and Cundall 2004). In the present study, the mechanical parameters of Barre granite were captured by the proposed GBM framework. Therefore,

Table 1 Calibrated micro-mechanical parameters for simulating the macroscopic behaviour of Barre granite

Micro-mechanical parameters of the grains (the cohesive contacts)					
Element	Parameter	Grain 1 plagioclase	Grain 2 quartz	Grain 3 K-feldspar	Grain 4 other
Particles forming grains	Minimum particle radius forming grain, R_{min} (mm)	0.2	0.2	0.2	0.2
	Maximum to minimum radius ratio, R_{max}/R_{min}	1.66	1.66	1.66	1.66
Cohesive model	Young's modulus, $\bar{E}_c$ (GPa)	12.5	14.0	10.5	5.8
	Normal to shear stiffness ratio, $(\bar{k}^n/\bar{k}^s)$	2.0	1.0	2.0	1.5
	Cohesion, (C^0) (MPa)	125	165	125	90
	Friction ratio, (μ)	0.55	0.55	0.55	0.55
	Dilation ratio, (β)	0.22	0.22	0.22	0.22
	Softening parameter κ (1/m)	12×10^6	15×10^6	12×10^6	10×10^6
Micro-mechanical parameters of the grain boundaries (the smooth-joint contacts)					
Smooth-joint model	Normal stiffness, $(\bar{k}_n)$ (GPa)	87,000			
	Shear stiffness, $(\bar{k}_s)$ (GPa)	47,000			
	Tensile strength, (σ_c) (MPa)	9.0			
	Cohesion, (C^{sj}) (MPa)	150			
	Friction angle, (φ) (°)	82			
	Friction coefficient, (μ^{sj})	0.92			

Table 2 Laboratory test results compared to the numerically observed results for calibrated Barre granite

Property	(Experimental[a])	Numerical
Uniaxial compressive strength (MPa)	151	150
Young's modulus (GPa)	19.2	19.9
Poisson's ratio	0.16	0.19
Brazilian tensile strength (MPa)	5.08–10.65	8.4

[a]Experimental data from Miller (2008) and Morgan et al. (2013)

the underestimation of the initial crack closure had negligible implications on the outcome of the present study. This assumption was verified in the early attempts of PFC-GBM approach (Potyondy 2010a, b), which is widely adopted in the current GBM investigations (Farahmand et al. 2018; Li et al. 2018; Liu et al. 2018; Peng et al. 2017). In Sect. 5, the selected microproperties will be further validated by simulating the pre-cracked Barre granite specimens.

Figure 6b depicts the stress–strain curve of the Brazilian tensile test. It shows a linear elastic phase, a peak tensile strength, and an abrupt reduction of axial loading. Note that the stress–strain curve related to the Brazilian tensile test is not provided by Miller (2008). Therefore, only the peak tensile strength obtained from the numerical simulation was compared with experimental observations. This calibration approach was also followed in a number of previous numerical studies (Bahrani et al. 2014; Bewick et al. 2014b; Hofmann et al. 2015a; Liu et al. 2018).

The final macroscopic fracturing responses observed in the uniaxial compressive and Brazilian tensile tests are illustrated in Figs. 7, 8, respectively. The macroscopic fracturing response of the specimen under uniaxial compression is illustrated in Fig. 7a. For more clarity, the micro-cracking pattern of uniaxial test is shown separately.

It can be seen from Fig. 7b that the grain boundary micro-cracks dominated the specimen. This observation is in agreement with Mosher et al. (1975) who experimentally studied the fracturing characteristics of granite and found that the macroscopic tensile cracks that formed subparallel to the direction of compressive loading dominate the failure of brittle rocks. At pre-peak, the intra-grain contacts entered to their yielding limit (softening behaviour). After cohesion degradation ($D = 1.0$), bond-break occurred and intra-grain micro-cracks initiated. At some locations in the specimen (Fig. 7b), the interaction between inter- and intra-grain micro-cracks formed the macroscopic shear cracks, which was consistent with the macroscopic shear failure observed in brittle crystalline rocks (Hofmann et al. 2015a; Li et al. 2018). The majority of micro-cracks propagated and developed along the axial direction. Macroscopic fractures generated in brittle crystalline rocks under uniaxial compression are often dominated by cracks at the micro-level, in a direction approximately perpendicular to the loading plates. The failure mode observed in the present study's numerical simulation is called "axial splitting", which is in agreement with previous observations (Potyondy 2010a). Figure 8 shows that no intra-grain micro-cracks were observed during

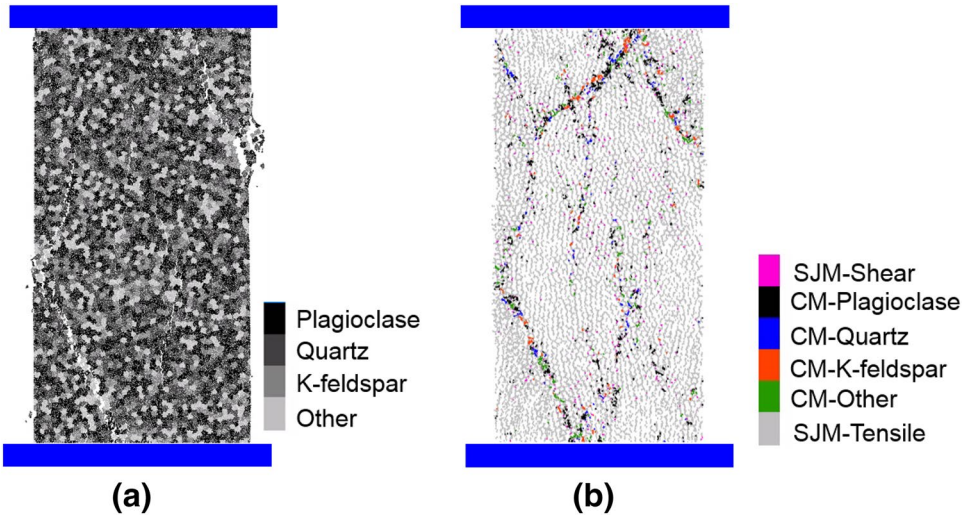

Fig. 7 The final numerical results obtained from uniaxial compression test: **a** macroscopic fractures developed during axial loading and **b** propagation of inter- and intra-grain micro-cracks in the specimen (*SJM* smooth-joint model, and *CM* cohesive model)

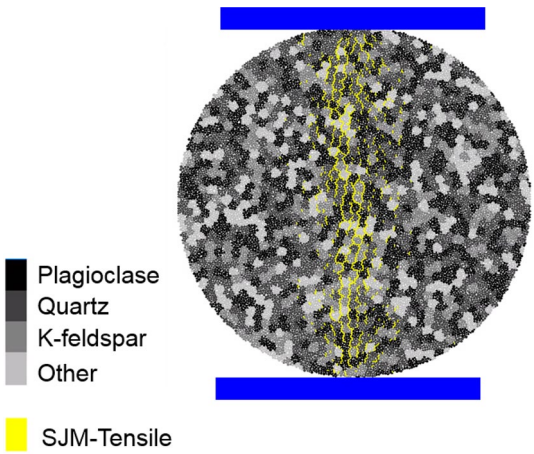

Fig. 8 Evolution of macroscopic tensile cracks in Brazilian specimen after failure

the Brazilian tensile test and only inter-grain micro-cracks presented during simulation. This was attributed to the low tensile strength assigned on the grain interface contacts, which resulted in the early initiation of inter-grain micro-cracks and the failure of the GBM specimen (Hofmann et al. 2015a, b; Liu et al. 2018; Saadat and Taheri 2019). The progressive coalescence of these tensile micro-cracks formed macroscopic tensile fractures, which extended towards the loading plates.

4.1.2 Random Distribution of Mineral Grains

Ideally, the topological and statistical properties of the GBM specimens should be similar to those of the physical rock (Potyondy 2010a). Voronoi tessellation is widely used, but the topological and statistical properties of the crystalline rock cannot be realistically generated by this method (Potyondy 2010a). The PFC's two-dimensional disk-packing scheme has been used by many scholars to generate polycrystalline microstructure (Bahrani et al. 2014; Hofmann et al. 2015a; Potyondy 2010a), which gives an appropriate match between synthetic and real grain microstructure (Potyondy 2010a). However, the sensitivity of the calibrated model to the random distribution of the grains should be examined by considering several distributions for the minerals. To do so, five seed numbers were considered to generate various GBM specimens with a different random distribution of the minerals. The results showed that the Young's modulus varied only between 19.5 and 20.5 GPa, and the Poisson's ratio varied between 0.17 and 0.19. The UCS varied between 148 and 153 MPa, and the Brazilian tensile strength varied between 8.2 and 8.8 MPa. The GBM investigation of Saadat and Taheri (2019) also revealed that the mechanical parameters of Aue granite showed insignificant variation with random distribution of minerals. However, we will demonstrate in Sect. 5.3.2 that the crack distribution pattern can be influenced by the random distribution of grains. Hofmann et al. (2015a) also emphasised that the change in the distribution of grain had significant influence on the fracture pattern as a result of inhomogeneities. The variation in the numerical results is well within the variation of the mechanical parameters of the physical Barre granite. Therefore, it was meaningful to employ the calibrated parameters for conducting uniaxial compression test on pre-cracked specimens.

4.2 Numerical Model Setup for Pre-cracked Specimens

The GBM approach was used to carry out a numerical simulation of pre-cracked granite, to validate the proposed GBM framework and evaluate its potential in reproducing the macroscopic fracturing behaviour and strength responses of physical specimens. We adopted the micro-mechanical

parameters obtained during the calibration procedure, and the macroscopic responses of the pre-cracked granite were simulated. The specimen dimension for the experimental UCS test was 152 mm (height) × 76 mm (width), and the same specimen size was used for conducting compression tests on pre-cracked specimens Miller (2008). The same specimen size was used for generating the GBM specimens in PFC2D. The geometries of pre-existing flaws were generated in PFC2D as per the information provided in the experimental study conducted by Miller (2008) (illustrated in Fig. 9). The pre-existing flaws were created in the physical Barre granite using an OMAX waterjet, which produced a crack with a thickness of 1.5 mm (Miller 2008; Morgan et al. 2013). The same thickness size was imported into PFC2D for generating the pre-cracked GBM specimens. After importing the geometries into the software, the pre-existing cracks were developed by removing the DEM particles.

In the specimens tested in the current study, the ligament length (L) and bridging angle (α) were considered to be constant, but the inclination angle (θ) was varied. The flaw length ($2a$) was equal to 13 mm and, the ligament length was equal to a for all specimens. The bridging angle was equal to 60°, and the flaw inclination angles of 0°, 30°, 30°, and 75° were simulated. The crack initiation, coalescence, and peak axial stresses were monitored during testing, and the crack propagation pattern and failure modes of the numerical specimens were compared with the experimental data. The values of crack initiation, coalescence, and peak axial stresses were obtained during numerical testing, using the definitions given by Miller and Einstein (2008), and Morgan et al. (2013). The crack initiation stress refers to the stress at which the first macroscopic crack initiates from the tips or the surface of the pre-existing flaw. The coalescence stress refers to the stress magnitude at which the pre-existing flaws link together and coalesce due to the expansion of macroscopic fractures in the bridging area. The peak axial stress is the stress at which the maximum axial strength of the specimens is achieved.

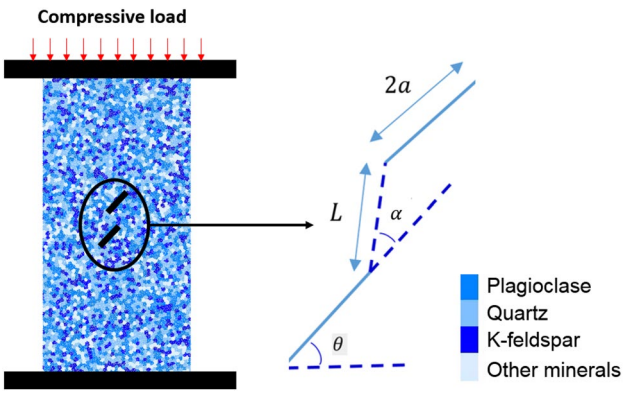

Fig. 9 Grain-based pre-cracked Barre granite in PFC2D and geometrical configuration of pre-existing cracks

5 Fracture Behaviour of Pre-cracked Granite

The microproperties of calibrated Barre granite were used to simulate the cracking behaviour of pre-cracked specimens. The following subsections discuss the micro-cracking and stress behaviours of the numerical specimens. In Sect. 5.1, a comparison to the experimental data is presented for $\theta = 30^{\circ}$ followed by a comprehensive discussion on the underlying failure mechanism. Both micro- and macroscopic characteristics (i.e. grain crushing) uniquely observed in the GBM specimens are also discussed. In Sect. 5.2, the fracture behaviour of pre-cracked specimens with various flaw configurations is presented. Finally, in Sect. 5.3 the influence of grain microstructure (i.e. random distribution of the minerals) on the mechanical and fracture behaviour of the pre-cracked specimens is discussed.

5.1 Numerical Simulation of Pre-cracked Barre Granite with $\theta = 30^{\circ}$

The results of the uniaxial compression loading tests for the numerical and experimental specimens are illustrated in Fig. 10. The complete stress–strain curves of the numerical specimens, with a flaw inclination angle of 30°, and three different experimental counterparts, are illustrated in Fig. 10a. The numerical results were compared with the average values obtained from the experimental results. The micro-cracking behaviour, and the development of macroscopic cracks in the flaw zone at different stages of loading are illustrated in Fig. 11b, c, and d. In Miller's (2008) study, for each experimental test, a simplified sketch of the final fracture pattern was provided including macroscopic cracks, white patching, and crushing zone (see laboratory fracturing patterns in Fig. 10b, c, and d). It can be seen from Fig. 10 that there was a discrepancy between the experimental results in terms of stress–strain curve and fracturing pattern, which may be attributed to the meandering path defined by the mineral boundaries (Morgan et al. 2013). Since the microstructure and the meandering paths in each specimen were different, the macroscopic fracturing responses and hence the stress–strain curves in the physical specimens (Fig. 10a) showed some variations.

According to Morgan et al. (2013), in Barre granite, visible regions of mineral lightning occurred on the surface of the specimen before fracturing, which was called "white patching". Two types of white patching were observed in Barre granite: linear and diffusive white patching (Miller 2008) as illustrated in Fig. 11. Linear white patching can travel along the grain boundary to form grain boundary

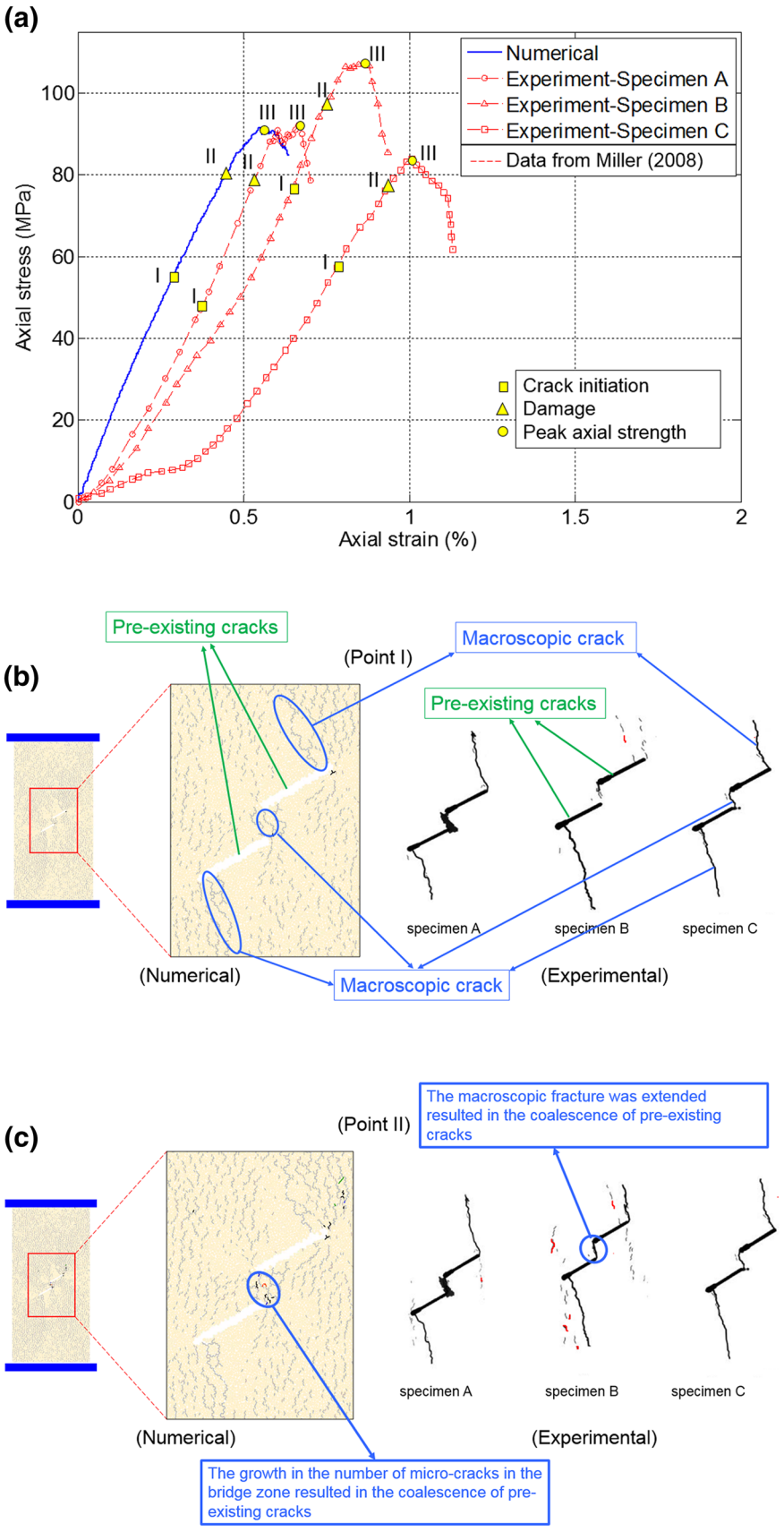

Fig. 10 Numerical and experimental results for a specimen with $\theta = 30^{\circ}$: **a** numerical and experimental stress–strain curves, the crack initiation, crack damage, and peak axial stresses are marked at each graph; **b** crack initiation stress (point I); **c** crack damage stress (point II); **d** peak stress (point III) Experimental results were modified from Miller (2008)

Fig. 10 (continued)

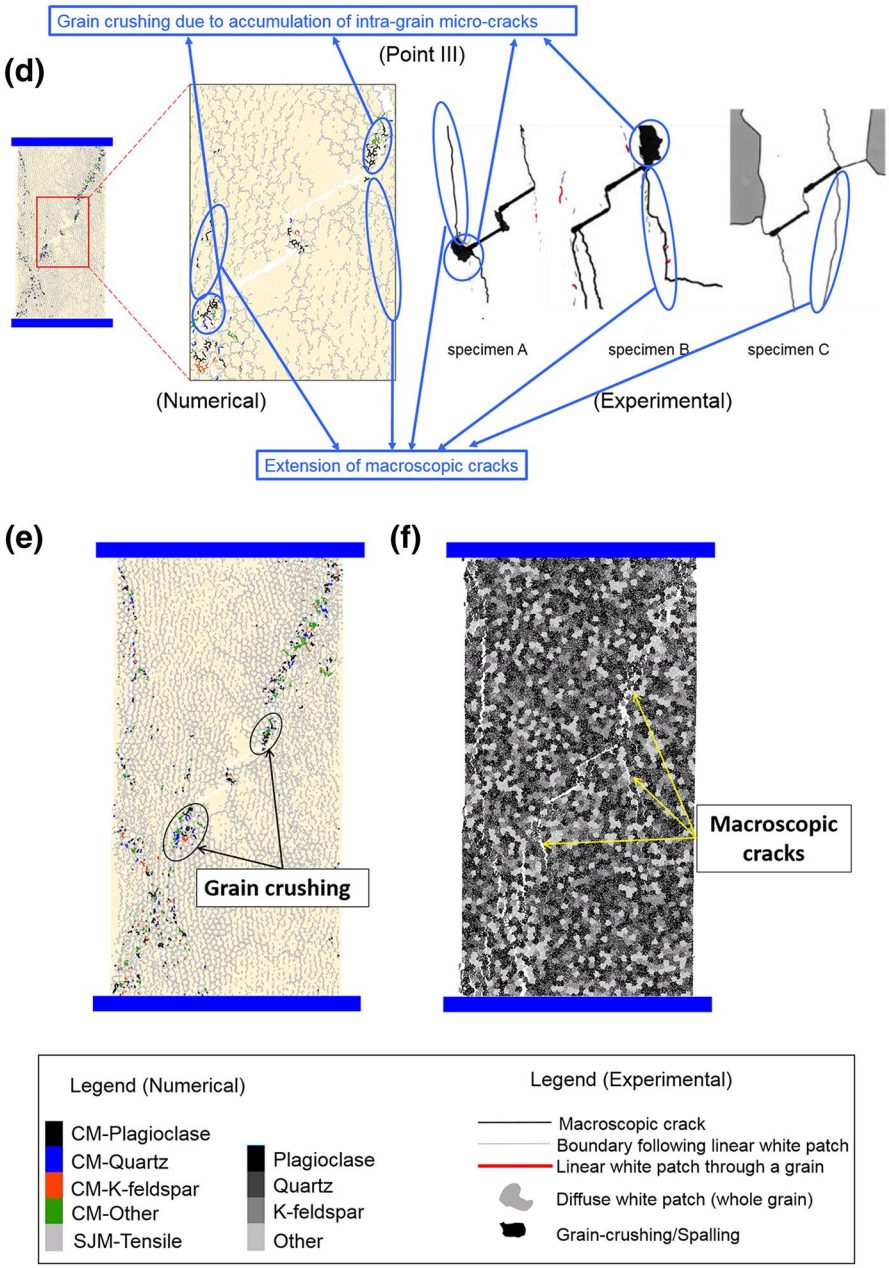

Fig. 11 Different types of white patching observed in Barre granite. **a** Linear white patching (grain boundary and intragranular). **b** Diffusive white patching modified from Morgan et al. (2013)

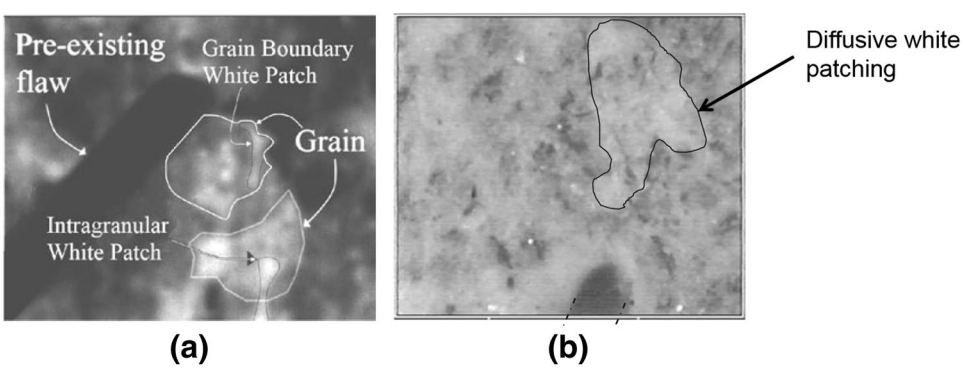

white patching, or travel through a mineral to create intragranular white patching (Fig. 11a). Grain boundary white patches appear in the specimen before crack initiation along the grain boundaries. In diffusive white patching, multiple minerals lightened entirely with no preferential direction (Fig. 11b). Diffusive white patching is mostly associated with shear cracking, but in some specimens, it can appear before both tensile and shear cracking (Morgan et al. 2013). In the GBM specimens, the inter- and intra-grain micro-cracks were monitored to compare the numerical cracking behaviour with the experimental counterparts.

The remainder of this subsection discusses the micro- and macroscopic failure mechanisms of pre-cracked granite, which were observed during the numerical simulations. It provides relevant comparisons with the experimental results.

The numerical results exhibited a linear-elastic behaviour from the beginning of the test until the simulation reached crack initiation stress (point I in Fig. 10a). Unlike the pre-cracked numerical specimen, the laboratory specimens showed an initial non-linear behaviour similar to intact rock. The reason is similar to that explained in Sect. 4.1.1. That is, that at the crack initiation stress magnitude (Fig. 10b), initial macroscopic cracks appeared in the flaw areas due to bond breakage in the inter-grain contacts. As a result of the low tensile strength of the inter-grain micro-cracks, the contact boundaries initially failed in the linear elastic stage. The progressive coalescence of the inter-grain micro-cracks formed large, sub-vertical cracks, and when the density of the inter-grain micro-cracks was sufficiently high, macroscopic fractures developed that were nearly parallel to the direction of the axial loading (Fig. 10b).

The experimental observations of Morgan et al. (2013) on pre-cracked Barre granite revealed that macroscopic tensile cracks typically follow the grain boundaries and are "jagged" in shape. Figure 12 illustrates a schematic representation of the grain boundary tensile crack observed in Barre granite by Morgan et al. (2013) and Moradian et al. (2016). In our numerical simulations, we observed the same failure pattern during the propagation of macroscopic tensile cracks.

In GBM, due to the random, polygonal shape of Voronoi elements that were generated to mimic the minerals, the grain boundaries were jagged in shape. Thus, the inter-grain micro-cracks were propagated in a meandering, jagged path that was dictated by the grain interfaces (Fig. 10b). The simulations revealed that the tensile wing cracks initiated near flaw tips, and they propagated vertically towards the loading walls (Fig. 10b). This was similar to the pattern observed in the experiments. Figure 10b shows that, at the crack initiation stress, some inter-grain micro-cracks appeared in the bridging area. However, according to the laboratory observations, the coalescence of the pre-existing crack did not occur at crack initiation stress magnitude, because further loading was needed in order to widen the tensile cracks in the bridging zone and fully link the flaws (Miller 2008). At crack initiation stress either grain breakage (specimen A), or tensile cracks (specimen B and C) presented in the bridging area (Fig. 10b). However, it was not until reaching the crack coalescence stress magnitude that the macroscopic fractures fully developed and the coalescence of the pre-existing cracks occurred. Similarly, in the numerical specimens, after macroscopic crack initiation further loading was needed to cause the coalescence of the pre-existing cracks (Fig. 10c).

The stress magnitude at which the coalescence of pre-existing cracks occurred was defined as the coalescence stress by Miller (2008). In the current study, this stress magnitude is called damage stress. At the crack damage stress magnitude (Fig. 10c), a sufficiently high number of inter- and intra-grain micro-cracks initiated from the inner- and outer-tip regions. The macroscopic tensile cracks formed at point I expanded, and larger macroscopic cracks around the flaw tips were formed. In the GBM simulation, the extension of the macroscopic crack inside the bridging area resulted in crack coalescence.

From point II until the peak axial stress (point III), a non-linear behaviour was observed in the numerical stress–strain

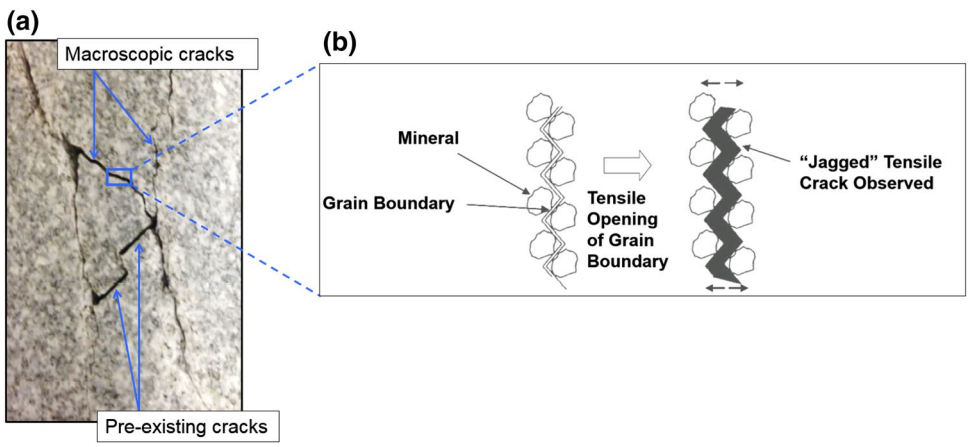

Fig. 12 **a** Macroscopic cracks in pre-cracked Barre granite modified from Moradian et al. (2016). **b** Jagged shape tensile cracks developed along the meandering path defined by the mineral boundaries (modified from Morgan et al. 2013)

curve (Fig. 10a), which was the result of a progressive macroscopic crack extension around the flaw tips and other areas of the specimen. Finally, at a stress magnitude of 92.8 MPa (point III in Fig. 10a), the maximum numerical axial strength was achieved, the specimen completely failed, and the axial stress dropped accordingly. It can be seen that, at point III (Fig. 10d), the simulated macroscopic fractures expanded and developed in a direction parallel to the compressive loading. A localised, macroscopic fracture path was exhibited near the flaw tips, which was the consequence of inter- and intra-grain micro-crack coalescence. In the laboratory specimens (A and B), this behaviour was identified as grain crushing. Our numerical observations presented in Fig. 10, confirm that the proposed GBM framework has the capability to reproduce the macroscopic stress–strain response and fracturing behaviour of pre-cracked Barre granite.

One of the factors that effectively controls the degree of grain crushing in the physical Barre granite is the mineral strength. Increasing the mineral strength reduces the grain breakage, therefore less intra-grain micro-cracks appear during the failure of Barre granite. The experimental observations showed that the Barre granite has strong minerals (e.g. quartz) which inhibit the severe breakage of the minerals under uniaxial compressive loading (Morgan et al. 2013). However, in the experimental pre-cracked specimens, some localised grain crushing was evident around the tips of the pre-existing flaws, which in turn was associated with the large sliding displacement along the surface of macroscopic fractures (Morgan et al. 2013). Similarly, in the GBM specimen, we found that the bond breakage occurred in the minerals in the vicinity of macroscopic fracture interfaces (Fig. 10e and f). Numerical simulations show that the large sliding displacement of the minerals along the surfaces of macroscopic fractures caused failure of intra-grain contacts, which resulted in the localised grain crushing.

In the numerical specimens, a relatively high number of unconnected grain boundary micro-cracks appeared away from the major macroscopic fractures (i.e. point III in Fig. 10d). This was due to the low value of the microscopic tensile strength assigned to the grain boundary contacts. In the experimental specimens, however, the unconnected micro-cracks may not be visible, but this does not mean that they are not present in the specimen (Hofmann et al. 2015a).

5.2 The Effect of Flaw Inclination Angle

In order to further validate the sensitivity of the proposed GBM framework to the orientation of pre-existing cracks, different numerical specimens with various flaw inclination angles were generated in PFC2D, and the results were compared with the laboratory data (Miller 2008).

Figure 13 illustrates the results of comparing the fracture pattern obtained from the GBM simulations at peak axial stress. The results revealed that the GBM model can successfully reproduce the experimental, macroscopic fracturing response. Note that the fracturing behaviour for $\theta = 30^{\circ}$ was discussed in Sect. 5.1. The numerical results showed that the macroscopic fractures initiated from the tips and surfaces of pre-existing flaws, and developed in an upward direction. The orientation of macroscopic cracks that are parallel to the applied stress also support the notion that tensile cracking is the dominant failure mode in GBM specimens. Both the inter- and intra-grain micro-cracks contributed to the process of fracture development in the numerical specimens. However, the majority of micro-cracks initiated due to the failure of boundary contacts.

It can be seen in Fig. 13 that the coalescence pattern observed in the GBM simulations was slightly different from those gained from the experimental observations. This is mainly due to the fact that, during specimen generation in PFC2D, the minerals were randomly produced. This meant that the paths generated by the grain boundaries were slightly different from those of laboratory specimens, and resulted in a modest variation in the coalescence pattern. However, the fracturing responses obtained from modelling were in agreement with those observed in the laboratory specimens. It will be shown in Sect. 5.3.2 that in the GBM specimens the coalescence pattern can be affected by the randomness of the distribution of the minerals.

5.3 The Influence of Grain Microstructure

The calibrated model was run three more times with different random seed numbers, which allowed us to investigate the influence of the grain microstructure on the mechanical and fracture behaviour of the GBM specimens. In the following subsections, the stress analysis of the models, and the variation in the macroscopic fracture pattern are presented.

5.3.1 Stress Analysis

Figure 14 depicts the average crack initiation, coalescence, and peak axial stresses for both numerical and experimental specimens. It can be seen from Fig. 14 that different random distribution of minerals leads to a slight variation in the stress results. However, the numerical results are in agreement with the experimental data. In intact rock specimens (e.g. specimens without pre-existing cracks), the crack initiation stress can be defined as a point where the Poisson's ratio starts to increase (Zhang and Wong 2013). The crack initiation stress of intact specimen is generally about 0.3–0.5 times of the peak strength (Brace et al. 1966; Martin 1993; Zhang and Wong 2012). However, in the physical pre-cracked Barre granite specimens, the crack initiation stress was defined as the stress magnitude corresponding to the appearance of the initial macroscopic cracks around the

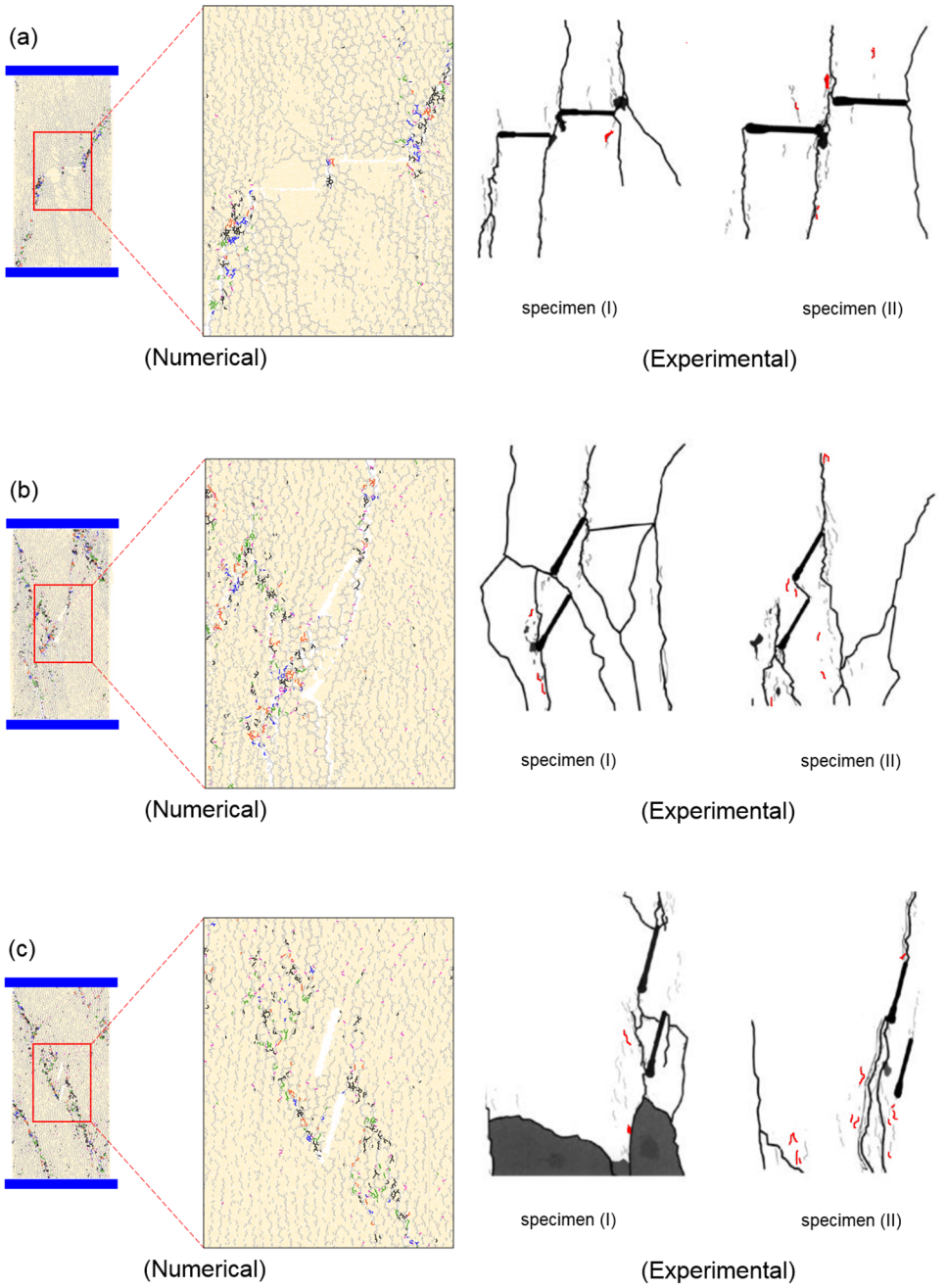

Fig. 13 Fracture pattern obtained from proposed GBM approach at peak axial strength versus experimental observations after Miller (2008): **a** $\theta = 0^{\circ}$, **b** $\theta = 60^{\circ}$, **c** $\theta = 75^{\circ}$

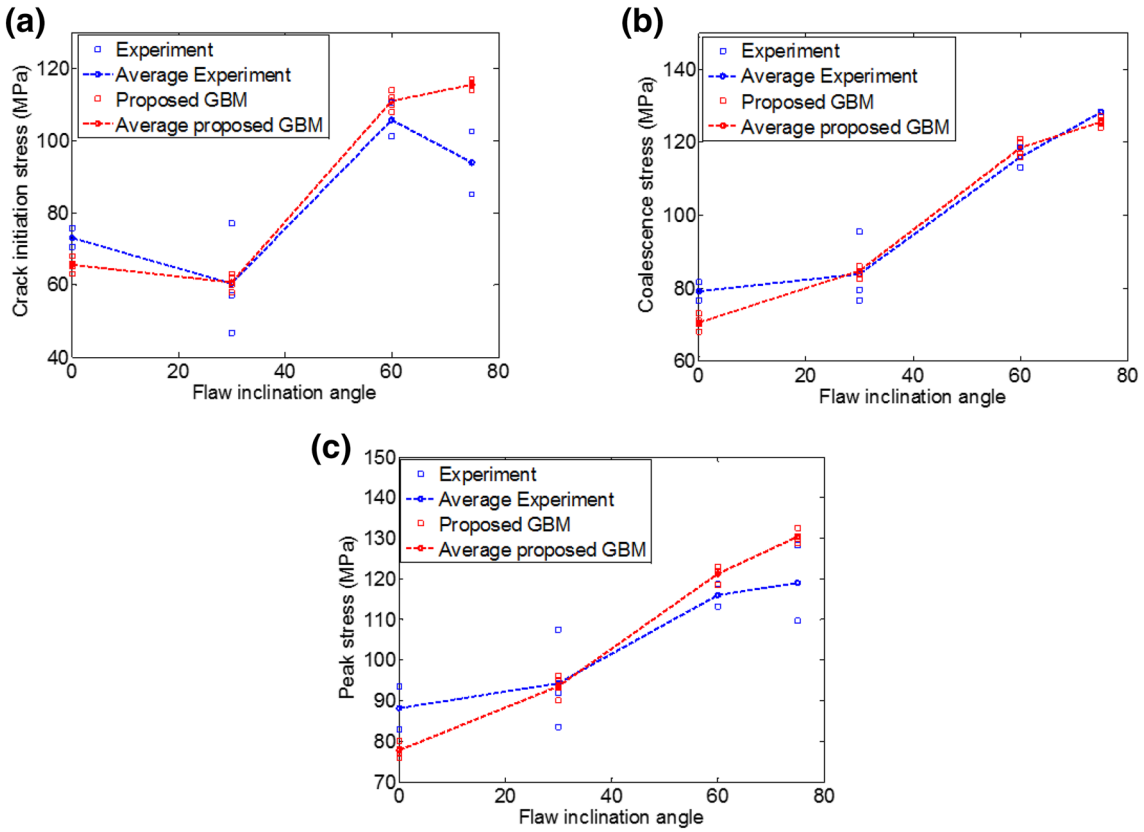

Fig. 14 The influence of flaw inclination angle on the mechanical response of pre-cracked Barre granite (numerical results versus experimental observations): **a** crack initiation stress, **b** coalescence stress, **c** peak stress

tips or on the surface of the pre-existing flaw (Miller 2008; Morgan et al. 2013). Wong and Einstein (2009) measured the stress corresponding to the initial observable macroscopic crack in the flaw region as the crack initiation stress of pre-cracked gypsum and Carrara marble. Zhang and Wong (2012) also adopted the same approach in their numerical study to obtain crack initiation stress of single-flawed rock-like specimens. Similarly, we monitored the crack initiation stress corresponding to the appearance of the first macroscopic cracks around the tips or on the surface of the pre-existing flaws. This enabled us to make a better comparison with the same values obtained from laboratory counterparts (Miller 2008). Hence, the crack initiation stresses obtained from this approach are much higher than those of intact specimens, especially for flaw inclination angles of 60° and 75° (Miller 2008; Morgan et al. 2013; Zhang and Wong 2012).

From Fig. 14a, the numerical crack initiation stress decreased with a low slope when the flaw inclination angle increased from 0° to 30°. In comparison, when the flaw inclination angle increased from 30° to 75° the crack initiation stress increased with a high slope. We believe that the stress concentration and random distribution of minerals are the possible reasons for the variation of the crack initiation stress in the GBM specimens. At $\theta = 0^{\circ}$, since the loading direction was perpendicular to the flaw surface, the stress concentration in the flaw region was significantly high, which caused the failure of the inter-grain contacts at a stress magnitude of approximately 70% of the peak axial strength. The slight decrease in the crack initiation stress at $\theta = 30^{\circ}$ could be attributed to the randomness of the distribution of the grains. As it mentioned by Morgan et al. (2013), the macroscopic tensile cracks in Barre granite followed a meandering path created by the grain boundaries. In the GBM specimens, the meandering paths are defined by the random generation of polygons representing the grains. For the GBM specimen with $\theta = 30^{\circ}$ the bond breakage of the inter-grain contacts initiated at a slightly lower stress magnitude, which caused a rapid growth of the macroscopic tensile crack along the meandering paths. It can be seen from Fig. 13a that the macroscopic tensile cracks were initially perpendicular to the surface of the pre-existing crack, which was attributed to the creation of the weakest possible meandering paths along this direction. Due to progressive compression, the macroscopic tensile cracks extended rapidly and aligned parallel with the loading direction (Fig. 13a). For $\theta > 30°$, the

influence of the pre-existing crack was gradually reduced, therefore, the bond-break in the inter-grain contacts occurred at higher crack initiation stresses. In fact, they required more loading to initiate the primary macroscopic tensile cracks.

By increasing the flaw inclination angle, the value of the numerical peak axial strength was increased with the highest magnitude achieved at an inclination angle of 75° (Fig. 14c). The same trend was observed during experimental tests. At 75° in one of the laboratory specimens, the coalescence between pre-existing flaws did not occur (Miller 2008). As a result, only one value of crack damage stress is presented in Fig. 14b for this test. Ideally, if the exact topological and statistical properties of the physical specimen were incorporated in the numerical modelling, the simulation response would be more similar. However, the aim of numerical simulations is not to incorporate the exact statistical and topological properties in the model, but rather to provide a match to real specimens (Saadat and Taheri 2019). According to Potyondy (2010a), using disk-packing scheme for specimen generation, which was also used in the present research, can provide a good match with the physical microstructure. Nonetheless, it can be seen in Fig. 13 that the coalescence pattern observed in the GBM simulations was slightly different from those gained from the experimental observations. This is mainly because, during specimen generation in PFC2D, the minerals were randomly produced. This means that the paths generated by the grain boundaries are slightly different from those of laboratory specimens, and resulted in a modest variation in the coalescence pattern. This difference between crack distribution of GBM and laboratory results was also highlighted by the previous researchers such as Hofmann et al. (2015a) and Bahrani et al. (2014). However, they concluded that these differences were inevitable, and thus they considered the outcome of their GBM simulations successful. Similarly, the fracturing responses obtained from modelling are regarded to be in agreement with those observed in the laboratory specimens. It will be shown in Sect. 5.3.2 that in the GBM specimens the coalescence pattern can be affected by the randomness of the distribution of the minerals.

5.3.2 Fracture Pattern Analysis

Figure 15 shows the distribution of inter- and intra-grain micro-cracks (I), and the development of macroscopic fractures (II) in the GBM specimens with different seed number. As expected, change in the randomness of the distribution of grains resulted in the inhomogeneous spatial distribution of the micro-cracks. It was observed that, for the flaw inclination angles investigated, the change in the distribution pattern of intra-grain micro-cracks was more pronounced than inter-grain micro-cracks, which was attributed to the inhomogeneity in the mineral grains (Hofmann et al. 2015a). For instance, in Seed 2 (Fig. 15b-I) the accumulation of intra-grain micro-cracks (grain crushing) at the outer tips of the pre-existing cracks was more conspicuous than Seed 1 and 3. The random distribution of minerals also impacted the development of macroscopic fractures. It can be seen from Fig. 15b-II that for Seed 1, an anti-wing crack developed above the left tip of the lower flaw, which was not the case in Seed 2 and 3 (the anti-wing crack is circled for emphasis). The same behaviour was also observed for $\theta = 60^{\circ}$, where anti-wing cracks formed in Seed 1 and 2, but Seed 3 only exhibited wing crack growth. Macroscopic cracks often originate at the tips of flaws, but in Seed 1 ($\theta = 0^{\circ}$), one macroscopic fracture initiated from the flaw surface and extended vertically towards the loading plate (Fig. 14a-II, Seed 1). The results also showed that the coalescence pattern of the pre-existing cracks was influenced by the grain microstructure. For example, for $\theta = 75^{\circ}$ (Fig. 15d-II), different coalescence patterns were observed. In Seed 1 and 2, the outer flaw tips were connected with macroscopic fractures, whereas in Seed 3 the right tips of two flaws coalesced. Miller (2008) also observed that the coalescence pattern in the pre-cracked Barre granite was highly influenced by the grain microstructure. Although the fracture pattern was influenced by the inhomogeneity of minerals, in the GBM specimens simulated, the fractures were formed subparallel to the loading direction, which is the common failure mode in the brittle rocks (Liu et al. 2018; Potyondy 2010a; Tang et al. 2000).

The growth of macroscopic fractures in pre-cracked Barre granite is the direct consequence of the failure of grain boundaries and the grain breakage. The laboratory observations of Morgan et al. (2013) and Miller (2008) showed that the distribution of macroscopic fractures in the pre-cracked Barre granite was influenced by the topological and statistical properties of the minerals.

6 Conclusion

Discontinuities and pre-existing cracks influence the failure mechanisms of rock in engineering projects such as tunnelling and underground mining. In this research, a PFC-GBM approach was used to investigate the influence of pre-existing flaws on the mechanical and failure behaviours of Barre granite under uniaxial compressive loading.

A DEM-based cohesive model was employed to simulate the failure behaviour of intra-grain micro-cracks. An initial cohesion defined the strength of intra-grain contacts as a micro-mechanical parameter. A softening parameter was incorporated into the cohesive, constitutive relationships, to simulate the damage behaviour of the intra-grain contacts during the post-peak stage. When the contact cohesion was completely damaged, a micro-crack appeared perpendicular

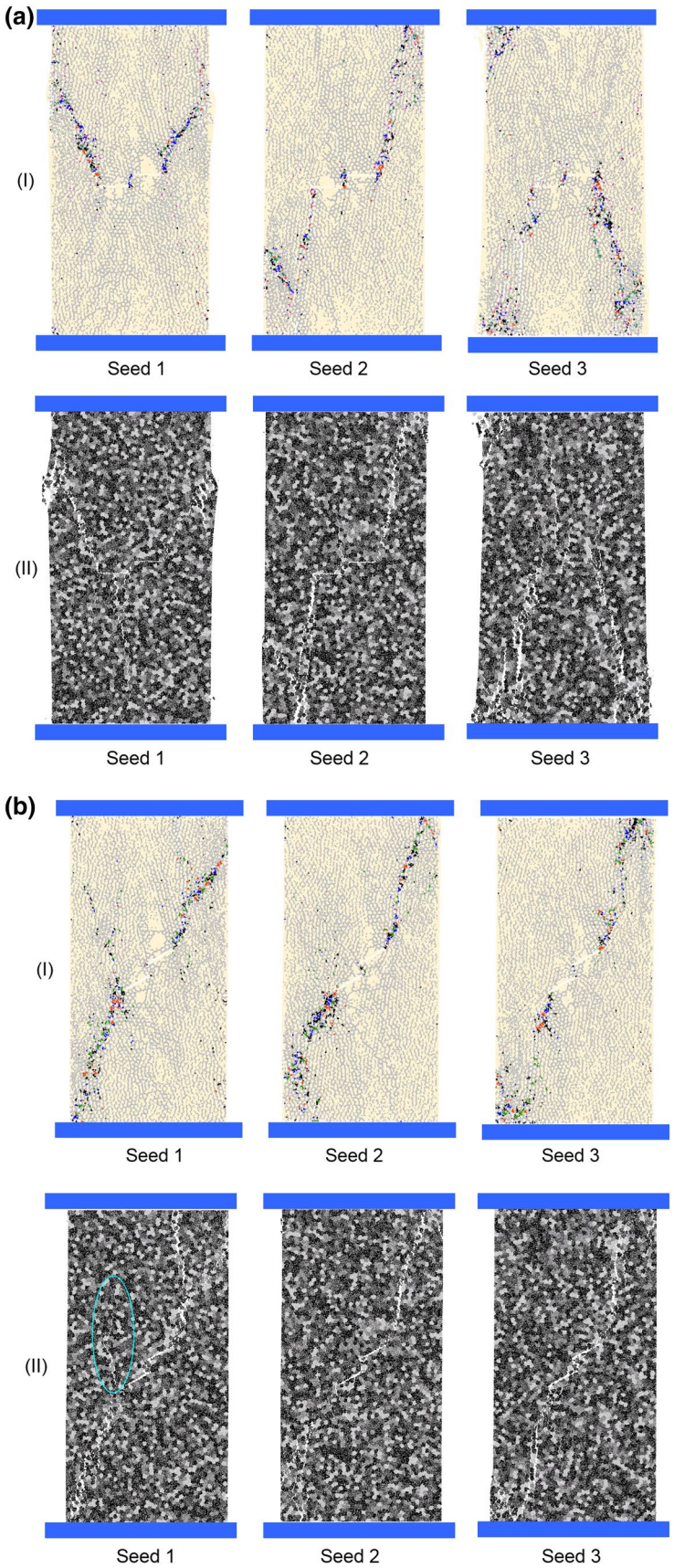

Fig. 15 Distribution of micro-cracks (I) and macroscopic fractures (II) in the pre-cracked GBM specimens. **a** $\theta = 0^{\circ}$, **b** $\theta = 30^{\circ}$, **c** $\theta = 60^{\circ}$, **d** $\theta = 75^{\circ}$

Fig. 15 (continued)

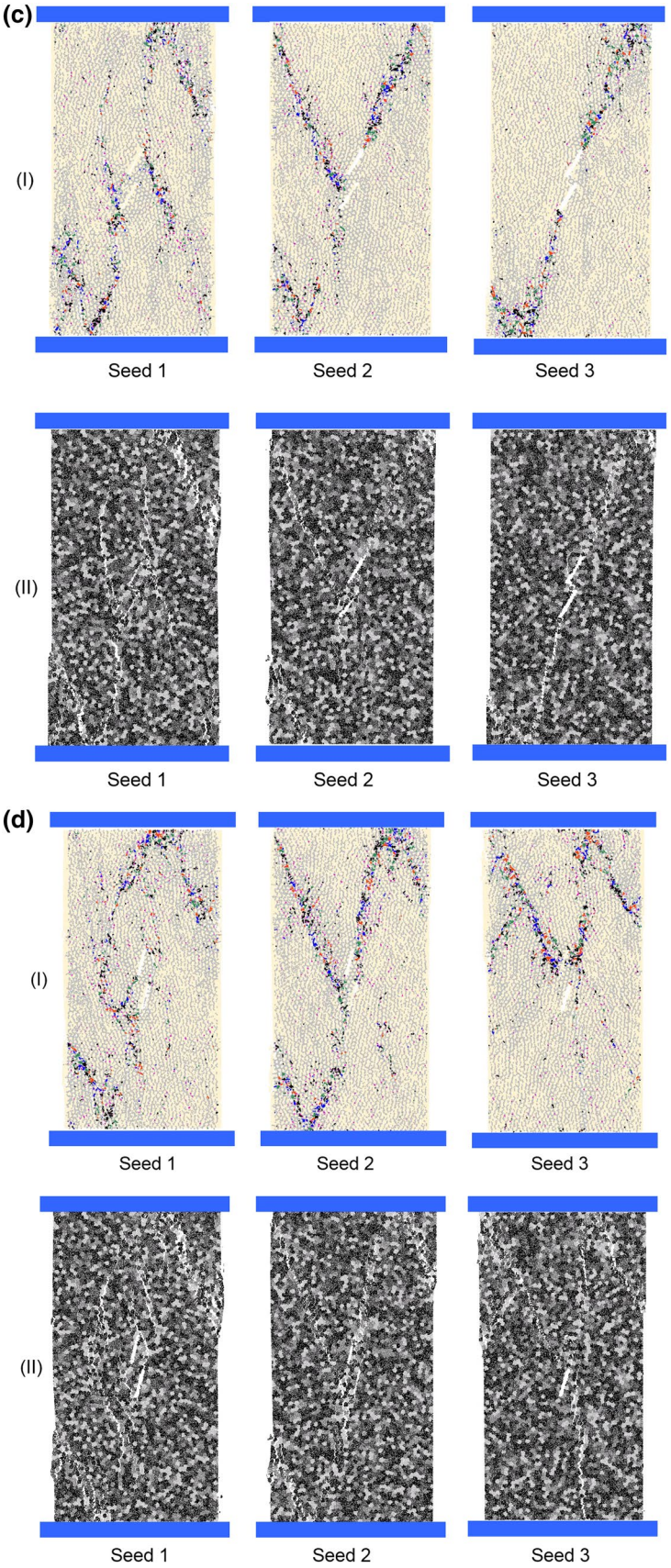

to the contact that mimics the intra-granular cracking response. The smooth-joint model was assigned to the inter-grain contacts to simulate the micro-cracking behaviour of the grain boundaries. The proposed GBM framework was successfully calibrated against the uniaxial compressive and Brazilian tensile experimental results. Pre-cracked granite specimens were generated in PFC2D to demonstrate the capability of the model in reproducing the macroscopic behaviour of physical specimens. Moreover, the influence of the flaw inclination angle on the overall cracking response of pre-cracked numerical specimens was studied.

From the analysis of the stress–strain curves obtained from numerical simulations, we observed that the macroscopic crack pattern at the crack initiation, damage, and peak axial stresses of double-flawed Barre granite can be reproduced by the proposed GBM framework. The numerical simulations showed that, by increasing the flaw inclination angle, the peak axial stress increases. Increasing the inclination angle of pre-existing cracks also showed the same incremental effect on crack initiation and the crack's damage stresses. The macroscopic fracturing patterns achieved in the numerical simulations also suggest that the modes of macroscopic crack initiation and propagation observed in the laboratory specimens, at least phenomenologically, can be identified by the proposed GBM framework. The numerical modelling revealed that the first macroscopic tensile cracks initiated from the tips and surfaces of the pre-existing cracks, and that they propagated upward towards the loading plates. It was also found that the formation of macroscopic fractures in the flaw region can be attributed to the initiation and coalescence of the inter-grain micro-cracks that formed due to the failure of the smooth-joint model contacts. The GBM simulations showed that the intra-grain micro-cracks begin to initiate and develop in the model before reaching the crack damage stress. The coalescence of pre-existing flaws occurred due to the combined interactions of the inter- and intra-grain micro-cracks.

This numerical modelling approach can be used for further investigations, such as studying the effects of grain size, mineralogy, and contact strength on the failure mechanism of crystalline rocks. The micro-cracking features, based on the current GBM approach, such as the extension and development of macroscopic cracks due to the progressive coalescence of inter- and intra-grain micro-cracks, which eventually led to the formation of macroscopic fracturing zones around the flaw tips and the coalescence of pre-existing cracks, will serve as guidelines for future experimental tests. The proposed GBM framework provided a cost-effective approach that helps in the determination of crack initiation, damage, and peak axial stresses of crystalline rocks, which are essential in the development of constitutive models (i.e. continuum models) that can be used for large-scale simulation of mining structures.

Acknowledgements The cohesive model used in this study was formulated based on a generic framework by Giang D. Nguyen (University of Adelaide) and Ha H. Bui (Monash University), with Giang D. Nguyen's help in the development and revision of the model. The first author is grateful to Mr Sacha Emam from Itasca Consulting group who provided consultation during implementation and verification of the model in PFC2D software. Professional editor, Leticia Mooney, provided copyediting and proofreading services, according to the guidelines laid out in the university-endorsed national 'Guidelines for editing research theses'.

Compliance with ethical standards

Conflict of interest The first author declares that he has no conflict of interest. The second author declares that he has no conflict of interest.

References

Bahrani N, Kaiser PK (2016) Numerical investigation of the influence of specimen size on the unconfined strength of defected rocks. Comput Geotech 77:56–67. https://doi.org/10.1016/j.compgeo.2016.04.004

Bahrani N, Valley B, Kaiser PK, Pierce M (2011) Evaluation of PFC2D grain-based model for simulation of confinement-dependent rock strength degradation and failure processes. Paper presented at the 45th US Rock Mechanics/Geomechanics Symposium, San Francisco, California

Bahrani N, Kaiser PK, Valley B (2014) Distinct element method simulation of an analogue for a highly interlocked, non-persistently jointed rockmass. Int J Rock Mech Min Sci 71:117–130. https://doi.org/10.1016/j.ijrmms.2014.07.005

Bewick RP, Kaiser PK, Bawden WF (2014a) DEM Simulation of Direct Shear: 2. Grain Boundary and Mineral Grain Strength Component Influence on Shear Rupture. Rock Mech Rock Eng 47:1673–1692. https://doi.org/10.1007/s00603-013-0494-4

Bewick RP, Kaiser PK, Bawden WF, Bahrani N (2014b) DEM Simulation of Direct Shear: 1. Rupture Under Constant Normal Stress Boundary Conditions. Rock Mech Rock Eng 47:1647–1671. https://doi.org/10.1007/s00603-013-0490-8

Bobet A, Einstein HH (1998) Fracture coalescence in rock-type materials under uniaxial and biaxial compression. Int J Rock Mech Min Sci 35:863–888. https://doi.org/10.1016/S0148-9062(98)00005-9

Brace WF, Bombolakis EG (1963) A note on brittle crack growth in compression. J Geophys Res 68:3709–3713. https://doi.org/10.1029/jz068i012p03709

Brace WF, Paulding BW, Scholz C (1966) Dilatancy in the fracture of crystalline rocks. J Geophys Res 71:3939–3953. https://doi.org/10.1029/jz071i016p03939

Brady BHG, Brown ET (2004) Rock Mechanics for Underground Mining, 3rd edn. Kluwer Academic Publishers, Netherlands

Cho N, Martin CD, Sego DC (2007) A clumped particle model for rock. Int J Rock Mech Min Sci 44:997–1010. https://doi.org/10.1016/j.ijrmms.2007.02.002

Diaz MB, Jung SG, Zhuang L, Kim KY, Yeom S, Shin HS (2016) Effect of cleavage anisotropy on hydraulic fracturing behavior of pocheon granite. Paper presented at the 50th US. Rock Mechanics/Geomechanics Symposium, Houston, Texas

Farahmand K, Vazaios I, Diederichs MS, Vlachopoulos N (2018) Investigating the scale-dependency of the geometrical and mechanical properties of a moderately jointed rock using a synthetic rock mass (SRM) approach. Comput Geotech 95:162–179. https://doi.org/10.1016/j.compgeo.2017.10.002

Gao F, Stead D, Elmo D (2016) Numerical simulation of microstructure of brittle rock using a grain-breakable distinct element grain-based model. Comput Geotech 78:203–217. https://doi.org/10.1016/j.compgeo.2016.05.019

Hajiabdolmajid V, Kaiser PK, Martin CD (2002) Modelling brittle failure of rock. Int J Rock Mech Min Sci 39:731–741. https://doi.org/10.1016/S1365-1609(02)00051-5

Hoek E, Diederichs MS (2006) Empirical estimation of rock mass modulus. Int J Rock Mech Min Sci 43:203–215. https://doi.org/10.1016/j.ijrmms.2005.06.005

Hofmann H, Babadagli T, Yoon JS, Zang A, Zimmermann G (2015a) A grain based modeling study of mineralogical factors affecting strength, elastic behavior and micro fracture development during compression tests in granites. Eng Fract Mech 147:261–275. https://doi.org/10.1016/j.engfracmech.2015.09.008

Hofmann H, Babadagli T, Zimmermann G (2015b) A grain based modeling study of fracture branching during compression tests in granites. Int J Rock Mech Min Sci 77:152–162. https://doi.org/10.1016/j.ijrmms.2015.04.008

Horii H, Nemat-Nasser S (1985) Compression-induced microcrack growth in brittle solids: axial splitting and shear failure. J Geophys Res Solid Earth 90:3105–3125. https://doi.org/10.1029/jb090ib04p03105

Itasca Consulting Group Inc (2016) PFC manual, version 5.0, Minneapolis

Kazerani T, Zhao J (2010) Micromechanical parameters in bonded particle method for modelling of brittle material failure. Int J Numer Anal Method Geomech 34:1877–1895. https://doi.org/10.1002/nag.884

Kazerani T, Yang ZY, Zhao J (2012) A discrete element model for predicting shear strength and degradation of rock joint by using compressive and tensile test data. Rock Mech Rock Eng 45:695–709. https://doi.org/10.1007/s00603-011-0153-6

Khazaei C, Hazzard J, Chalaturnyk R (2015) Damage quantification of intact rocks using acoustic emission energies recorded during uniaxial compression test and discrete element modeling. Comput Geotech 67:94–102. https://doi.org/10.1016/j.compgeo.2015.02.012

Le LA, Nguyen GD, Bui HH, Sheikh AH, Kotousov A, Khanna A (2017) Modelling jointed rock mass as a continuum with an embedded cohesive-frictional model. Eng Geol 228:107–120. https://doi.org/10.1016/j.enggeo.2017.07.011

Le LA, Nguyen GD, Bui HH, Sheikh AH, Kotousov A, Khanna A (2018) Localised failure mechanism as the basis for constitutive modelling of geomaterials. Int J Eng Sci 133:284–310

Li Y-P, Chen L-Z, Wang Y-H (2005) Experimental research on pre-cracked marble under compression. Int J Solids Struct 42:2505–2516. https://doi.org/10.1016/j.ijsolstr.2004.09.033

Li XF, Zhang QB, Li HB, Zhao J (2018) Grain-based discrete element method (gb-dem) modelling of multi-scale fracturing in rocks under dynamic loading. Rock Mech Rock Eng 51:3785–3817. https://doi.org/10.1007/s00603-018-1566-2

Liu G, Cai M, Huang M (2018) Mechanical properties of brittle rock governed by micro-geometric heterogeneity. Comput Geotech. https://doi.org/10.1016/j.compgeo.2017.11.013

Ma Y, Huang H (2018a) DEM analysis of failure mechanisms in the intact Brazilian test. Int J Rock Mech Min Sci 102:109–119. https://doi.org/10.1016/j.ijrmms.2017.11.010

Ma Y, Huang H (2018b) A displacement-softening contact model for discrete element modeling of quasi-brittle materials. Int J Rock Mech Min Sci 104:9–19. https://doi.org/10.1016/j.ijrmms.2018.02.007

Martin CD (1993) The strength of massive Lac du Bonnet granite around underground openings. University of Manitoba, Winnipeg

Mayer JM, Stead D (2017) Exploration into the causes of uncertainty in UDEC grain boundary models. Comput Geotech 82:110–123. https://doi.org/10.1016/j.compgeo.2016.10.003

Miller JT (2008) crack coalescence in granite. MSc Thesis, Massachusetts Institute of Technology

Miller JT, Einstein HH (2008) Crack Coalescence tests on granite. Paper presented at the 42nd US Rock Mechanics Symposium (USRMS), San Francisco, California

Moore DE, Lockner DA (1995) The role of microcracking in shear-fracture propagation in granite. J Struct Geol 17:95–114. https://doi.org/10.1016/0191-8141(94)E0018-T

Moradian Z, Einstein HH, Ballivy G (2016) Detection of cracking levels in brittle rocks by parametric analysis of the acoustic emission signals. Rock Mech Rock Eng 49:785–800. https://doi.org/10.1007/s00603-015-0775-1

Morgan SP, Johnson CA, Einstein HH (2013) Cracking processes in Barre granite: fracture process zones and crack coalescence. Int J Fract 180:177–204. https://doi.org/10.1007/s10704-013-9810-y

Mosher S, Berger RL, Anderson DE (1975) Fracturing characteristics of two granites. Rock Mech 7:167–176. https://doi.org/10.1007/bf01246723

Munoz H, Taheri A, Chanda EK (2016) Pre-peak and post-peak rock strain characteristics during uniaxial compression by 3D digital image correlation. Rock Mech Rock Eng 49:2541–2554. https://doi.org/10.1007/s00603-016-0935-y

Nguyen NHT, Bui HH, Nguyen GD, Kodikara J (2017a) A cohesive damage-plasticity model for DEM and its application for numerical investigation of soft rock fracture properties. Int J Plast 98:175–196. https://doi.org/10.1016/j.ijplas.2017.07.008

Nguyen NHT, Bui HH, Nguyen GD, Kodikara J, Arooran S, Jitsangiam P (2017b) A thermodynamics-based cohesive model for discrete element modelling of fracture in cemented materials. Int J Solids Struct 117:159–176. https://doi.org/10.1016/j.ijsolstr.2017.03.027

Nicksiar M, Martin CD (2014) Factors affecting crack initiation in low porosity crystalline rocks. Rock Mech Rock Eng 47:1165–1181. https://doi.org/10.1007/s00603-013-0451-2

Peng J, Wong LNY, Teh CI (2017) Effects of grain size-to-particle size ratio on micro-cracking behavior using a bonded-particle grain-based model. Int J Rock Mech Min Sci 100:207–217. https://doi.org/10.1016/j.ijrmms.2017.10.004

Potyondy D (2010a) A grain-based model for rock: approaching the true microstructure. In: Proceedings Rock Mechanics in the Nordic Countries,2010

Potyondy D (2010b) PFC2D Grain-Structure Generator. PFC2D Example on Itasca website. Itasca Consulting Group, Inc, Minneapolis

Potyondy D (2012) A flat-jointed bonded-particle material for hard rock. Paper presented at the 46th U.S. Rock Mechanics/Geomechanics Symposium, Chicago, Illinois

Potyondy D, Cundall P (2004) A bonded-particle model for rock. Int J Rock Mech Min Sci 41:1329–1364

Pouya A, Yazdi P (2015) A damage-plasticity model for cohesive fractures. Int J Rock Mech Min Sci 73:194–202

Cao R-H, Cao P, Lin H, Pu C-z OuK (2016) Mechanical behavior of brittle rock-like specimens with pre-existing fissures under uniaxial loading: experimental studies and particle mechanics approach. Rock Mech Rock Eng 49:763–783. https://doi.org/10.1007/s00603-015-0779-x

Rodríguez P, Arab PB, Celestino TB (2016) Characterization of rock cracking patterns in diametral compression tests by acoustic emission and petrographic analysis. Int J Rock Mech Min Sci 83:73–85. https://doi.org/10.1016/j.ijrmms.2015.12.017

Saadat M, Taheri A (2019) A numerical approach to investigate the effects of rock texture on the damage and crack propagation of a pre-cracked granite. Comput Geotech 111:89–111. https://doi.org/10.1016/j.compgeo.2019.03.009

Shen B, Stephansson O, Einstein Herbert H, Ghahreman B (1995) Coalescence of fractures under shear stresses in experiments. J Geophys Res Solid Earth 100:5975–5990. https://doi.org/10.1029/95jb00040

Taheri A, Tani K (2008) Developing of an apparatus for down-hole triaxial tests in a rock mass. Int J Rock Mech Min Sci 45:800–806

Taheri A, Tani K (2010) Assessment of the stability of rock slopes by the slope stability rating classification system. Rock Mech Rock Eng 43:321–333. https://doi.org/10.1007/s00603-009-0050-4

Taheri A, Yfantidis N, Olivares C, Connelly B, Bastian T (2016) Experimental study on degradation of mechanical properties of sandstone under different cyclic loadings. Geotech Test J 39:673–687. https://doi.org/10.1520/gtj20150231

Tang CA, Liu H, Lee PKK, Tsui Y, Tham LG (2000) Numerical studies of the influence of microstructure on rock failure in uniaxial compression—Part I: effect of heterogeneity. Int J Rock Mech Min Sci 37:555–569. https://doi.org/10.1016/S1365-1609(99)00121-5

Tavallali A, Vervoort A (2010) Failure of layered sandstone under Brazilian test conditions: effect of micro-scale parameters on macro-scale behaviour. Rock Mech Rock Eng 43:641–653. https://doi.org/10.1007/s00603-010-0084-7

Tuğrul A, Zarif IH (1999) Correlation of mineralogical and textural characteristics with engineering properties of selected granitic rocks from Turkey. Eng Geol 51:303–317. https://doi.org/10.1016/S0013-7952(98)00071-4

Ulusay R (2015) The ISRM suggested methods for rock characterization, testing and monitoring: 2007–2014. Springer, Berlin, pp 47–48

Wong RHC, Chau KT (1998) Crack coalescence in a rock-like material containing two cracks. Int J Rock Mech Min Sci 35:147–164. https://doi.org/10.1016/S0148-9062(97)00303-3

Wong LNY, Einstein HH (2009) Crack coalescence in molded gypsum and Carrara marble: part 1 macroscopic observations and interpretation. Rock Mech Rock Eng 42:475–511. https://doi.org/10.1007/s00603-008-0002-4

Wu XY, Baud P, T-f Wong (2000) Micromechanics of compressive failure and spatial evolution of anisotropic damage in Darley Dale sandstone. Int J Rock Mech Min Sci 37:143–160. https://doi.org/10.1016/S1365-1609(99)00093-3

Yin P, Wong RHC, Chau KT (2014) Coalescence of two parallel pre-existing surface cracks in granite. Int J Rock Mech Min Sci 68:66–84. https://doi.org/10.1016/j.ijrmms.2014.02.011

Yoon JS, Zang A, Stephansson O (2012) Simulating fracture and friction of Aue granite under confined asymmetric compressive test using clumped particle model. Int J Rock Mech Min Sci 49:68–83. https://doi.org/10.1016/j.ijrmms.2011.11.004

Zeng W, Yang S-Q, Tian W-L (2018) Experimental and numerical investigation of brittle sandstone specimens containing different shapes of holes under uniaxial compression. Eng Fract Mech 200:430–450. https://doi.org/10.1016/j.engfracmech.2018.08.016

Zhang X-P, Wong LNY (2012) Cracking processes in rock-like material containing a single flaw under uniaxial compression: a numerical study based on parallel bonded-particle model approach. Rock Mech Rock Eng 45:711–737. https://doi.org/10.1007/s00603-011-0176-z

Zhang X-P, Wong LNY (2013) Crack initiation, propagation and coalescence in rock-like material containing two flaws: a numerical study based on bonded-particle model approach. Rock Mech Rock Eng 46:1001–1021. https://doi.org/10.1007/s00603-012-0323-1

Zhang Y, Wong LNY (2018) A review of numerical techniques approaching microstructures of crystalline rocks. Comput Geosci 115:167–187. https://doi.org/10.1016/j.cageo.2018.03.012

Zhao C, Ym Zhou, Cf Zhao, Bao C (2018) Cracking processes and coalescence modes in rock-like specimens with two parallel pre-existing cracks. Rock Mech Rock Eng. https://doi.org/10.1007/s00603-018-1525-y

Zhou XP, Cheng H, Feng YF (2014) An experimental study of crack coalescence behaviour in rock-like materials containing multiple flaws under uniaxial compression. Rock Mech Rock Eng 47:1961–1986. https://doi.org/10.1007/s00603-013-0511-7

Zhou X-P, Zhang J-Z, Wong LNY (2018) Experimental study on the growth, coalescence and wrapping behaviors of 3D cross-embedded flaws under uniaxial compression. Rock Mech Rock Eng 51:1379–1400. https://doi.org/10.1007/s00603-018-1406-4

Appendix D (Paper 4)

A numerical approach to investigate the effects of rock texture on the damage and crack propagation of a pre-cracked granite

Saadat M, Taheri A. (2019) A numerical approach to investigate the effects of rock texture on the damage and crack propagation of a pre-cracked granite. *Computers and Geotechnics 111*: 89-111. doi: https://doi.org/10.1016/j.compgeo.2019.03.009

Statement of Authorship

Title of Paper	A numerical approach to investigate the effects of rock texture on the damage and crack propagation of a pre-cracked granite
Publication Status	✓ Published ☐ Accepted for Publication ☐ Submitted for Publication ☐ Unpublished and Unsubmitted work written in manuscript style
Publication Details	Saadat M, Taheri A. (2019) A numerical approach to investigate the effects of rock texture on the damage and crack propagation of a pre-cracked granite. Computers and Geotechnics 111: 89-111. doi: https://doi.org/10.1016/j.compgeo.2019.03.009

Principal Author

Name of Principal Author (Candidate)	Mahdi Saadat		
Contribution to the Paper	Developed and wrote the formulation of the cohesive model Conducted the numerical modelling of Aue granite with different grain size Analysed the numerical results Wrote the entire manuscript		
Overall percentage (%)	80%		
Certification:	This paper reports on original research I conducted during the period of my Higher Degree by Research candidature and is not subject to any obligations or contractual agreements with a third party that would constrain its inclusion in this thesis. I am the primary author of this paper.		
Signature		Date	07 August 2019

Co-Author Contributions

By signing the Statement of Authorship, each author certifies that:

i. the candidate's stated contribution to the publication is accurate (as detailed above);
ii. permission is granted for the candidate in include the publication in the thesis; and

iii. the sum of all co-author contributions is equal to 100% less the candidate's stated contribution.

Name of Co-Author	Dr Abbas Taheri		
Contribution to the Paper	Supervision of the technical work, revision of the manuscript		
Signature		Date	07 August 2019

End of the document

Computers and Geotechnics 111 (2019) 89–111

Contents lists available at ScienceDirect

Computers and Geotechnics

journal homepage: www.elsevier.com/locate/compgeo

Research Paper

A numerical approach to investigate the effects of rock texture on the damage and crack propagation of a pre-cracked granite

Mahdi Saadat*, Abbas Taheri

School of Civil, Environmental and Mining Engineering, The University of Adelaide, Australia

ARTICLE INFO

Keywords:
Discrete element modelling (DEM)
Grain based modelling (GBM)
Cohesive constitutive model
Pre-cracked granite
Micro-cracks

ABSTRACT

A grain-based distinct element model (GBM) is used to investigate the influence of grain size on the fracturing response of pre-cracked granite. A cohesive model is developed and implemented in distinct element codes to mimic the elastic and softening response of the intra-grain contacts in GBM. The model was calibrated to uniaxial compression and Brazilian tensile tests performed on Aue granite. The results show that pre-cracked specimens with larger grain size produce more softening contacts leading to a higher axial strength. A lower peak axial strength is observed for numerical specimens with single pre-existing crack.

1. Introduction

The focus of this study is on the failure and mechanical behaviour of single- and double-flawed rock specimens under uniaxial compression. The mechanical and failure behaviour of rock as a heterogeneous material is controlled by various parameters, such as grain shape and size, the type of minerals, and the existence of pre-existing flaws.

Rock masses contain discontinuities (ie. joints, fractures, and cracks), and their various geometrical patterns determine the strength of the material [1]. The coalescence of two pre-existing cracks is the primary cause of rock mass failure [2].

In underground and surface mining structures, rock mass stability is profoundly affected by the propagation and coalescence of macroscopic cracks initiating from the pre-existing flaws, on various rock mass scales. The macroscopic cracking process is the dominant damage mechanism controlling the mechanical behaviour and the integrity of brittle rocks [3].

Fig. 1 illustrates various scales of rock mass failure that must be addressed during the design procedure of underground openings. In Fig. 1(a, b), the large-scale characterisation of discontinuities is depicted. The macroscopic coalescence of defects and their mechanical behaviour was numerically studied by Farahmand et al. [4] (Fig. 1b), who addressed the scale-dependency of jointed rock masses. In a small-scale investigation, a Barre granite specimen containing two artificially generated pre-existing cracks was tested by Morgan et al. [3] (Fig. 1c). Fig. 1d illustrates the propagation of inter-and intra-grain micro-cracks at the microscopic scale.

The dominant damage mechanism controlling the mechanical behaviour and integrity of brittle rock, on various scales, can be understood by comprehensively investigating the propagation and coalescence of cracks that initiate from pre-existing flaws (Morgan et al. [3]). Therefore, studying the macroscopic failure responses and mechanical behaviours of rock masses, including pre-existing flaws, is critical during the process of rock mass characterisation, especially for the evaluation of rock mass strength [5,6].

Brace and Bombolakis [8] conducted one of the early laboratory investigations into the process of macroscopic cracking under compression. The coalescence process of pre-existing cracks has been experimentally studied by many researchers [3,9–14]. In some of these studies, rock-like materials were created to better illustrate the fundamental, macroscopic cracking process involved (e.g. [11]). Other scientists (e.g. [3,14]) generated pre-existing cracks in natural rocks to observe macroscopic cracks emanating from the flaws.

In research conducted by Miller and Einstein [14] and Morgan et al. [3], a high-speed video system was used to observe crack initiation, propagation, and coalescence in Barre granite. The studies described the progression and patterns of white patching, followed by the macroscopic cracking procedure of that material. In 2014, Zhou et al. [15] studied the crack coalescence behaviour of rock-like materials containing multiple flaws, and concluded that specimens containing multiple flaws may produce five types of cracks at or near the tips of pre-existing cracks. Those types included wing cracks, quasi-coplanar secondary cracks, oblique secondary cracks, out-of-plane tensile cracks and out-of-plane shear cracks.

Nevertheless, there are very few experimental studies available that focus on the influence of grain size distribution and rocks' mineral

* Corresponding author.
E-mail address: mahdi.saadat@adelaide.edu.au (M. Saadat).

https://doi.org/10.1016/j.compgeo.2019.03.009
Received 17 October 2018; Received in revised form 2 February 2019; Accepted 12 March 2019
Available online 15 March 2019

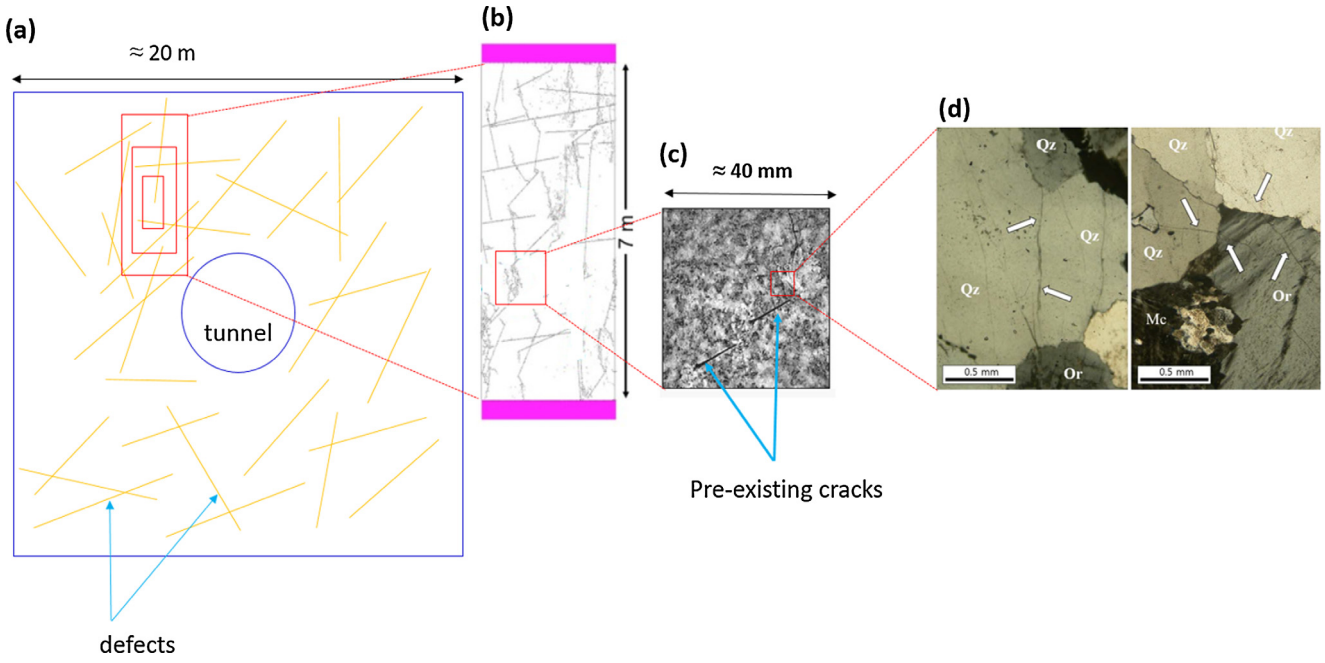

Fig. 1. (a) An underground structure (tunnel) excavated in highly jointed rock mass, (b) damage evolution in a large-scale numerical specimen containing randomly generated discrete fracture networks (DFNs) under compressive loading (after [4]), (c) small-scale damage evolution in Barre granite due to coalescence of pre-existing cracks under compressive loading (after [3]), (d) propagation of intragranular (left) and intergranular (right) micro-cracks after compressive testing (Qz:Quartz, Or: Orthoclase, Mc: microcline) (after [7]).

constituents on their mechanical behaviour, the cracking process, or coalescence responses (e.g. [3,16]). To the best of our knowledge, the study conducted by Morgan et al. [3] is the only experimental research that highlighted the importance of grain size on crack initiation, propagation and coalescence in specimens containing pre-existing flaws. The main reason is the difficulty and complexity of these experimental investigations. Preparing specimens with flaws, and then carefully monitoring their behaviour under pre-defined loading, is very difficult and extremely time-consuming.

This is why advanced computational methods have been adopted as an alternative tool in rock mechanics research. Of the various numerical methods, the discrete element method (DEM) [17] has proved to be a useful tool, one used by many scientists to overcome the financial risks and operating limitations of the experimental approach in geotechnical engineering [16,18–20]. Particle flow codes (PFC) is a promising numerical code based on DEM. It was developed by Cundall [21] and has been used by many scientists to solve rock engineering problems [22–25]. Some scientists use the DEM approach to investigate the influence of pre-existing cracks on the damage mechanisms of rock and rock-like materials. For instance, Zhang and Wong [16] used PFC2D to simulate the cracking process of a rock-like material containing a single flaw, under uniaxial compression. They concluded that the DEM approach could capture both primary and secondary macroscopic cracks that develop at the tip or surface of the flaw. Later, Zhang and Wong [26] used PFC2D to mimic the coalescence behaviour of rock-like materials including two pre-existing flaws. Their numerical approach revealed some insight regarding the initiation of cracks at a distance far from the flaw tip. It also demonstrated the coalescence of pre-existing cracks due to the propagation of steeply inclined-to-vertical macroscopic, tensile cracks.

In the above-mentioned works and other similar studies (e.g. [20,27,28]), the influence of tensile cracking in grain boundaries, and grain breakage around the tip and surface of the pre-existing crack, was neglected. In fact, the previously mentioned DEM-PFC simulations cannot capture the inter- and intra-grain micro-cracking process and reproduce a realistic damage response at both micro- and macroscopic scales. Rock heterogeneity is the direct consequence of a diversified rock microstructure that controls the mechanical and failure behaviour of brittle rocks. According to the research conducted by Diederichs [29], the material's heterogeneity can generate tensile stress inside the rock sample when it is subjected to compressive loading. Therefore, it is essential to incorporate the influence of material heterogeneity in any model of the mechanical and damage behaviour of rocks.

The grain-based model (GBM) developed by Potyondy [30] constructs a deformable, polygonal, mineral-like model that mimics the microstructural properties of rock. Many researchers have used GBM to investigate the mechanical behaviour of various rock types. Bahrani et al. [31] used GBM to numerically simulate the fracturing behaviour of both intact and granulated Wambyen marble. Later, Bahrani and Kaiser [5] adopted GBM to investigate the influence of specimen size on the strength of intact and defected rocks. They generated a Discrete Fracture Network (DFN) to reproduce defects in the synthetic, DEM specimens. They concluded that depending on the angle between the loading direction and the orientation of the defects, the strength of the specimens may increase, decrease, or fluctuate according to the size of the specimen. Bewick et al. [32] used GBM to mimic the fracturing processes, and the mechanism resulted in the shear rupture of intact (non-jointed) brittle rock. After calibrating the GBM, they conducted a parametric study to investigate the influence of the aspect ratio of the specimens on the shear strength and shear rupture process of the synthetic DEM samples. Peng et al. [33] used the GBM approach to investigate the influence of grain size-to-particle ratios on the micro-cracking process. Their numerical approach revealed that the uniaxial compressive strength (UCS) and Young's modulus decrease as particle size increases.

Nevertheless, there is no comprehensive study available that investigates the effect of the inter- and intra-gran micro-cracking process, the strength of the various mineral, and the mineral constituent on both the failure pattern and mechanical response of the specimens containing pre-existing cracks. Little is known about the cracking behaviours and mechanical responses of rock specimens containing pre-existing, microscopic cracks. Furthermore, there is no comprehensive study available that examines the capabilities of the GBM approach in reproducing the micro- and macro-cracking behaviour of specimens

including pre-existing cracks. We also have minimal knowledge of the influence of grain size distribution on the macroscopic cracking response of pre-existing flaws, or of its influences on the overall mechanical performance of brittle rocks. We believe that the micro-cracking response of grain boundaries, and the breakage process of grains, leading to the coalescence of pre-existing cracks in brittle rocks, require further investigation.

In this study, the PFC-GBM approach is used to generate numerical specimens based on the microstructure of Aue granite, and to assign its mineral constituent to numerical grains produced in PFC. In order to mimic the cracking behaviour of intra-grain contacts forming a mineral, a new cohesive model (CM) was developed and implemented in PFC2D. The smooth-joint model (SJM), which is a built-in constitutive model in PFC [34], was assigned to the inter-grain contacts. We calibrated the micro-mechanical parameters of the CM, as well as SJM, against experimental data.

We then investigate the effect of the grain size distribution on micro- and macro-cracking behaviour, and the damage mechanism of single- and double-flawed numerical specimens. To do so, we generated models with three different size distribution scenarios, and conducted uniaxial compression tests. Lastly, the damage response and micro-crack propagation in intra-grain contacts are discussed ahead of the conclusions.

2. Constitutive relationships

A GBM framework is developed in the present study to simulate the microstructure of pre-cracked Aue granite. The GBM model is capable of handling any number of mineral types with different range of grain size. The mineral constituent and grain size can be linked in a logical fashion using Voronoi tessellation structure that allow us to mimic the microstructure of crystalline rock [35]. In the proposed GBM framework, the DEM particles inside a grain are bonded using a cohesive contact model which produces deformable and breakable minerals. The fracturing behaviour of grain interfaces is simulated by the smooth-joint model that controls the behaviour of the contacts regardless of their orientation along the interfaces [31]. The cohesive model and the smooth-joint model are separately solved in the simulations. In DEM modelling, the calculations alternate between the application of Newton's second law to the DEM balls and a force-displacement constitutive model at contact level. The motion of DEM particles is determined by Newton's second law, while the constitutive model is used to update the contact forces arising from the relative motion of the contacts [34]. In the proposed GBM framework, the forces arising from the relative motion of inter-grain contacts are updated via the smooth-joint model, while the forces arising from the relative motion of intra-grain contacts are updated via the cohesive model. The constitutive relationships of the cohesive model is described in Section 2.1. The kinematic variables and the force-displacement law of the smooth-joint model is given in Section 2.2.

2.1. The proposed cohesive contact model

We developed a new cohesive constitutive model for this study, for simulating the failure behaviour of intra-grain contacts in DEM codes. There are a number of cohesive models available in the literature [36–39] that can be used as contact models in DEM. However, this study makes an effort to reduce the number of micro-mechanical parameters that need to be incorporated into the cohesive model. This allows its users to alleviate the complexity of calibration, because fewer micro-mechanical parameters need to be calibrated. Additionally, by reducing the number of micro-mechanical parameters, and by increasing the simplicity of the computational algorithm, we made the numerical simulations more time-efficient.

The relative displacement $\boldsymbol{u}(u_n, u_s)$ of the contacts is decomposed into elastic and plastic components, to account for reversible and irreversible displacements in the contacts:

$$\boldsymbol{u} = \boldsymbol{u}^e + \boldsymbol{u}^p \tag{1}$$

The normal and shear stresses are linked to the relative displacements of the contacts between two particles, and can be calculated as follows:

$$\sigma_n = k_n^0(u_n - u_n^p) \tag{2}$$

$$\sigma_s = k_s^0(u_s - u_s^p) \tag{3}$$

where σ_n and σ_s are normal and shear stresses in the bonding contacts; u_n and u_n^p are the total and plastic normal displacements; u_s and u_s^p are the total and plastic shear displacements; k_n^0 and k_s^0 are the normal and shear stiffnesses, respectively.

2.1.1. Yield criterion and flow rule

In the cohesive mode, a yield criterion is necessary to determine the stress states under which the contact failures occur, and plastic displacement starts to accumulate. In order to model the contact failure under mixed-mode conditions, a simple yield function that allows the strength and friction of the contacts to be chosen independently is considered. To satisfy this requirement, and keep the model as simple as possible, the following yield function is proposed:

$$F(\sigma_n, \sigma_s, C) = \sigma_s + \mu\sigma_n - C = 0 \tag{4}$$

where μ is the friction coefficient of the contact, and C is defined as follows:

$$C = C^0 e^{-\kappa u^p} \tag{5}$$

In Eq. (5), C^0 is the initial cohesion of the contacts, κ is the softening parameter, and u^p is the accumulated plastic displacement of the contact that can be calculated from its increments:

$$du^p = \sqrt{(du_n^p)^2 + (du_s^p)^2} \tag{6}$$

In this study, a damage parameter ($0 \le D \le 1$), used to measure the level of the contact's deterioration, is defined as:

$$D = \frac{C^0 - C}{C^0} = 1 - e^{-\kappa u^p} \tag{7}$$

Note that the softening parameter may not imply a physical meaning. The parameter must be incorporated in the relationships to simplify the model [37,38]. Later, in DEM simulations, the damage parameter (D) can be monitored for each contact. It can be illustrated graphically to evaluate the state of damage in the numerical system. $D = 0$ shows that the contact is fully bonded, and $D = 1$ shows that the contact has completely failed. The model's behaviour in modes I and II is illustrated in Fig. 2. The linear, elastic portion of the stress-displacement curves defines the contact behaviour before failure, followed by a non-linear stage that represents contact softening that occurs due to the progressive degradation of cohesion.

During DEM simulations based on particle sliding, the dilation effect can be achieved. However, the circular shape and microstructural features of the particles are not analogous to physical materials, so that obtaining the same physical dilative response at the contact level is an arduous task. Therefore, for DEM modelling, a dilatancy parameter is necessary to account for the dilation effect of the material at the mesoscale. Considering a flow rule including a dilatancy parameter enables us to follow the rigorous procedure of developing the model using the framework of plasticity theory. In this regard, a non-associative flow rule was defined as follows:

$$G(\sigma_n, \sigma_s) = \sigma_s + \beta\sigma_n \tag{8}$$

where β is the dilation coefficient. Consequently, the flow rule of incremental displacement can be expressed as:

$$du_n^p = d\lambda \frac{\partial G}{\partial \sigma_n} \tag{9}$$

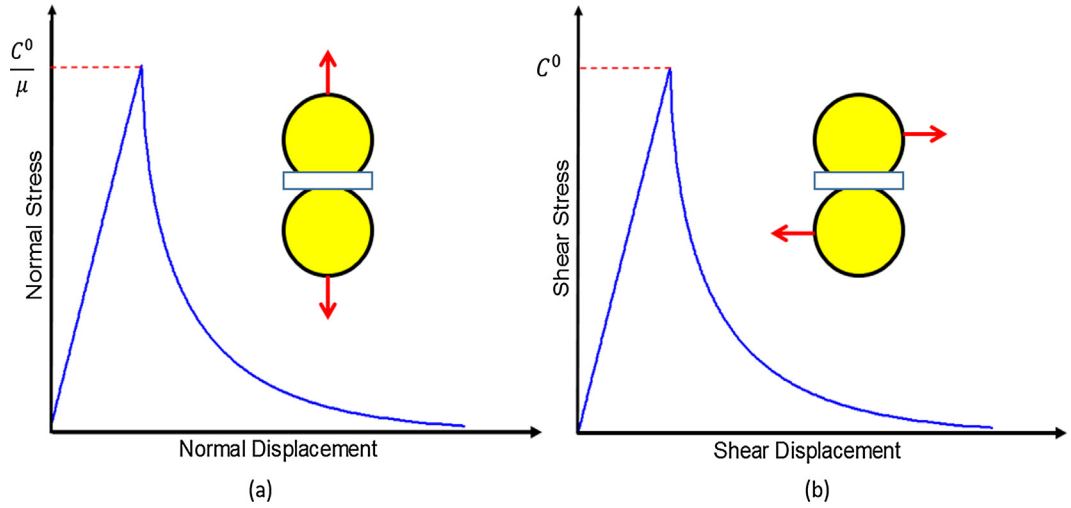

Fig. 2. Stress-displacement behaviour of the proposed cohesive contact model in (a) Mode I, and (b) Mode II.

$$du_s^p = d\lambda \frac{\partial G}{\partial \sigma_s} \tag{10}$$

where $d\lambda \geq 0$ is the plastic multiplier.

A semi-implicit algorithm is used to update the stress in the case of the contact's inelastic behaviour. Following this algorithm, a trial stress state is used to check if inelastic behaviour takes place, indicated by $F^{trial} = F(\sigma_n^{trial}, \sigma_s^{trial}, C) > 0$, where the trial stresses are:

$$\sigma_n^{trial} = \sigma_n + d\sigma_n^{trial} \tag{11}$$

$$\sigma_s^{trial} = \sigma_s + d\sigma_s^{trial} \tag{12}$$

In which the trial stress increments are calculated as:

$$d\sigma_n^{trial} = k_n^0 du_n \tag{13}$$

$$d\sigma_s^{trial} = k_s^0 du_s \tag{14}$$

A Taylor expansion at the trial stress state gives:

$$F^{new} = F^{trial} + \frac{\partial F}{\partial \sigma_n} d\sigma_n^c + \frac{\partial F}{\partial \sigma_s} d\sigma_n^c + \frac{\partial F}{\partial C}\frac{\partial C}{\partial u^p} du^p \tag{15}$$

From Eqs. (5), (9), and (10), we will have:

$$\frac{\partial C}{\partial u^p} du^p = d\lambda \left(-\kappa C \sqrt{\left(\frac{\partial G}{\partial \sigma_n}\right)^2 + \left(\frac{\partial G}{\partial \sigma_s}\right)^2}\right) \tag{16}$$

Substituting (12) and $d\sigma_i^c = -k_i^0 du_i^p$ (with "i" standing for "n", or "s") in (11), we get:

$$F^{new} = F^{trial} - d\lambda \frac{\partial F}{\partial \sigma_n} k_n^0 \frac{\partial G}{\partial \sigma_n} - d\lambda \frac{\partial F}{\partial \sigma_s} k_s^0 \frac{\partial G}{\partial \sigma_s} - d\lambda \frac{\partial F}{\partial C} \kappa C \sqrt{\left(\frac{\partial G}{\partial \sigma_n}\right)^2 + \left(\frac{\partial G}{\partial \sigma_s}\right)^2} \tag{17}$$

the plastic multiplier $d\lambda$ can then be obtained as solution of the equation $F^{new} = 0$:

$$d\lambda = \frac{F^{trial}}{\frac{\partial F}{\partial \sigma_n} k_n^0 \frac{\partial G}{\partial \sigma_n} + \frac{\partial F}{\partial \sigma_s} k_s^0 \frac{\partial G}{\partial \sigma_s} + \frac{\partial F}{\partial C} \kappa C \sqrt{\left(\frac{\partial G}{\partial \sigma_n}\right)^2 + \left(\frac{\partial G}{\partial \sigma_s}\right)^2}} \tag{18}$$

The corrective stresses is determined as:

$$d\sigma_n^c = d\lambda (-k_n^0) \frac{\partial G}{\partial \sigma_n} \tag{19}$$

$$d\sigma_s^c = d\lambda (-k_s^0) \frac{\partial G}{\partial \sigma_n} \tag{20}$$

where $d\sigma_n^c$ and $d\sigma_s^c$ are corrective normal and shear stresses, respectively.

The total incremental stresses are finally obtained from:

$$d\sigma_n = d\sigma_n^{trial} + d\sigma_n^c \tag{21}$$

$$d\sigma_s = d\sigma_s^{trial} + d\sigma_s^c \tag{22}$$

The cohesive model in the present study was developed based on a generic plasticity framework. The constitutive relationships was developed based on stress and displacement of DEM contacts. The proposed cohesive model was implemented in C++ and compiled as dynamic link library (DLL) files that could be loaded in PFC2D whenever needed. In the implementation algorithm developed in C++, the DEM forces were converted to stresses according to bond cross-sectional properties. This was necessary to measure the F^{trial} in every time-step. This implementation approach was successfully followed by other researchers (e.g. [37,38]).

The bond cross-sectional area ($\bar{A}$) in two dimensional space is defined as [34]:

$$\bar{A} = 2\bar{R} \tag{23}$$

where $\bar{R}$ is defined as:

$$\bar{R} = \begin{cases} \min(R^1, R^2), & ball - ball \\ R^1, & ball - facet \end{cases} \tag{24}$$

R^1 and R^2 are the radius of two adjoining particles that come into contact. Potyondy and Cundall [40] proposed a deformability method, in which the normal stiffness of the contacts ($\bar{k}^n$) can be related to the elastic modulus of the contact ($\bar{E}_c$) as follows [34]:

$$\bar{k}^n = \frac{\bar{E}_c}{L} \tag{25}$$

where L can be determined as follows:

$$L = \begin{cases} R^1 + R^2, & ball - ball \\ R^1, & ball - facet \end{cases} \tag{26}$$

During calibration procedure normal to shear stiffness ratio $\bar{k}^n/\bar{k}^s$ was initiated to determine the shear stiffness of the contacts ($\bar{k}^s$) [41,42]. In C++ algorithm the contact deformability method was adopted to obtain shear and normal stiffness of the contacts which were necessary to calculate σ_n and σ_s from Eqs. (2) and (3), respectively.

2.2. The smooth-joint model

The smooth-joint model simulates the micro-cracking behaviour of

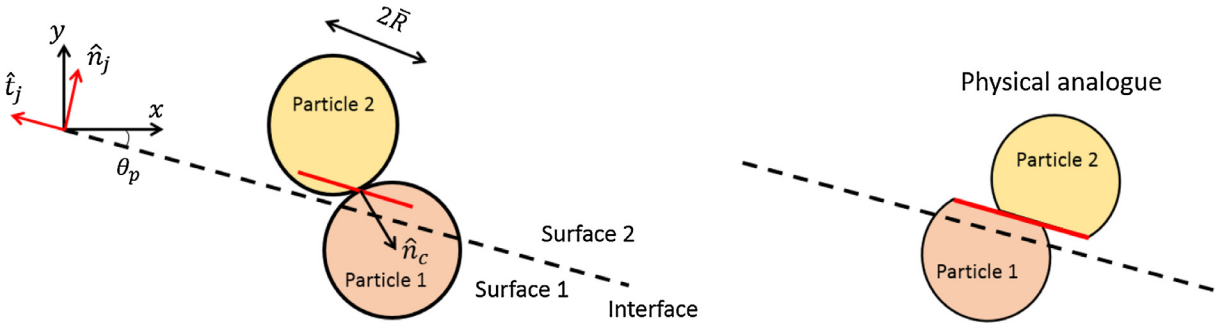

Fig. 3. The smooth-joint model application in PFC2D (modified from [34]).

an interface in PFC software (Itasca [34]). The smooth-joint constitutive model is assigned to the DEM particles lying on the opposite side of the interface. The DEM particles intersected by this model are allowed to overlap and pass through one another. Fig. 3 illustrates the performance DEM particles intersected by the smooth-joint model. The orientation of interface (Fig. 3) in 2D is defined as the unit normal vector acting on the interface [34]:

$$\hat{\boldsymbol{n}}_{\boldsymbol{j}} = (\mathbf{sin}\theta_{\boldsymbol{p}}, \mathbf{cos}\theta_{\boldsymbol{p}}) \tag{27}$$

where θ_p is the dip angle of the interface. $\hat{\boldsymbol{n}}_{\boldsymbol{c}}$ in Fig. 3 is defined as the unit normal vector of the contact between two adjacent DEM particles. The smooth-joint interface consists of two coincident surfaces (shown as surface 1 and 2 in Fig. 3). If and only if $\hat{\boldsymbol{n}}_{\boldsymbol{j}}.\ \hat{\boldsymbol{n}}_{\boldsymbol{c}} \geq 0$, then particle 2 lies in surface 2. The strength of smooth-joint contact mode is defined by the tensile strength, cohesion, and friction angle. When a smooth-joint contact fails (either in tension or shear), the contact maintain a residual strength defined by the smooth-joint friction coefficient. The details about updating the smooth-joint model force-displacement law for a bonded joint can be found in the manual of PFC2D [34]. By employing the smooth-joint model, the existing bond between two DEM particles are removed and a set of elastic springs are assigned over a rectangular-shaped cross section. The cross sectional area of the smooth-joint model can be calculated as [34]:

$$\boldsymbol{A} = 2\bar{\boldsymbol{R}}\boldsymbol{t} \tag{28}$$

where t and $\bar{R}$ are the thickness ($t = 1.0$) and radius of smooth-joint model crass-section, respectively. Note that $\bar{R} = \lambda min(R^1, R^2)$, where R^1 and R^2 are particles radii, and λ is radius multiplier which is usually taken as 1.0.

The constitutive relationships of the smooth-joint model was comprehensively described by Itasca [34]. A summary of the model behaviour can also be found in [23]. The smooth-joint force is resolved into normal and shear forces as follows:

$$\mathbf{F} = -\boldsymbol{F}_{\boldsymbol{n}}\hat{\boldsymbol{n}}_{\boldsymbol{j}} + \mathbf{F}_{\mathbf{s}} \tag{29}$$

The normal force is updated as follows:

$$\boldsymbol{F}_{\boldsymbol{n}} = (\boldsymbol{F}_{\boldsymbol{n}})_0 + \bar{\boldsymbol{k}}_{\boldsymbol{n}}\boldsymbol{A}\Delta\boldsymbol{\delta}_{\boldsymbol{n}}^{\boldsymbol{e}} \tag{30}$$

$(F_n)_0$ is the smooth-joint normal force at the beginning of the timestep, $\bar{k}_n$is the normal stiffness, A is the bond cross-sectional area, and $\Delta\delta_n^e$ is the normal displacement increment. The trial shear force can be calculated as:

$$\mathbf{F}_{\boldsymbol{s}}^{*} = (\mathbf{F}_{\mathbf{s}})_0 - \bar{\boldsymbol{k}}_{\boldsymbol{s}}\boldsymbol{A}\Delta\boldsymbol{\delta}_{\boldsymbol{s}}^{\boldsymbol{e}} \tag{31}$$

where $(\mathbf{F}_s)_0$ is the shear force at the beginning of the timestep, $\bar{k}_s$ is the shear stiffness, and $\Delta\delta_s^e$ is the shear displacement increment. The shear strength of the contact can be considered as $F_s^{\mu} = -\mu^{sj}F_n$, where μ^{sj} is the friction coefficient of the contact. The micro-mechanical parameters that control the bond strength are tensile strength (σ_c) and cohesion (c). The shear strength of the contact is calculated from simple Mohr-Coulomb ($\tau_c = \sigma_c\tan(\varphi) + c$). The force–displacement law for a bonded contact is illustrated in Fig. 4. When the bond is not in tension, the shear force is limited by:

$$\mathbf{F}_{\mathbf{s}} = \begin{cases} \mathbf{F}_{\boldsymbol{s}}^{*}, ||\mathbf{F}_{\boldsymbol{s}}^{*}|| < \boldsymbol{F}_{\boldsymbol{s}}^{\boldsymbol{\mu}} \\ \boldsymbol{F}_{\boldsymbol{s}}^{\boldsymbol{\mu}}\,(\mathbf{F}_{\boldsymbol{s}}^{*}/||\mathbf{F}_{\boldsymbol{s}}^{*}||),\ otherwise \end{cases} \tag{32}$$

If $F_n \geq \sigma_c A$, then the contact fail in tension mode (Fig. 4a) and $F_n = |\mathbf{F}_s| = 0.0$; otherwise if $|\mathbf{F}_s^*| \geq \tau_c A$ the contact is broken in shear mode, and the shear force of the contact is updated by Eq. (32) (Fig. 4b).

3. Modelling procedure

Since the micro-mechanical parameters incorporated in the proposed cohesive model represent the cement bridges of minerals at grain level, it may require advanced laboratory techniques to identify the local parameters of the material. Alternatively, the model parameters can be calibrated against the results of standard experimental tests such as unconfined compression and Brazilian tensile tests. This calibration approach has been extensively used in current DEM investigations due to lack of laboratory techniques to measure the properties of crystalline rocks at mineralogical scale [5,31,32,35,42–44]. Thus, the same approach was adopted in the present study. The procedure for calibrating the micro-mechanical parameters of GBM against laboratory results of Aue granite is described in the Section 3.1. After calibration of micro-mechanical parameters, three different scenarios were generated to numerically investigate the influence of rock texture on the behaviour of pre-cracked Aue granite. A description on rock texture, the process of generating different grain size scenarios, and model set up is provided in Section 3.2.

3.1. Model set up and calibration

To set up and calibrate the proposed cohesive model by adopting the GBM approach in PFC2D, we used experimental results from unconfined compressive tests, and a Brazilian tensile test. The micro-mechanical properties of the cohesive GBM approach were achieved, such that the macroscopic behaviour of the numerical simulation matches the observed, experimental macroscopic properties (ie. uniaxial compressive strength, tensile strength, Young's modulus) of Aue granite. The cohesive and smooth-joint models were assigned as intra- and inter-grain constitutive models, respectively. The cohesive and smooth-joint models are solved separately in the simulations. The yield limit of each model functions separately, which means if the yield limit is reached in one model, it will not affect the other model simulation.

The following assumptions were made in the calibration process:

1) The smooth-joint model was assigned to the grain boundary contacts with the same micro-parameters such that the behaviour of inter-grain contacts at a microscopic level was defined by tensile strength, cohesion, and friction angle before bond-break and friction coefficient after contact failure.
2) Cohesion (C^0), friction coefficient (μ), dilation coefficient (β), and

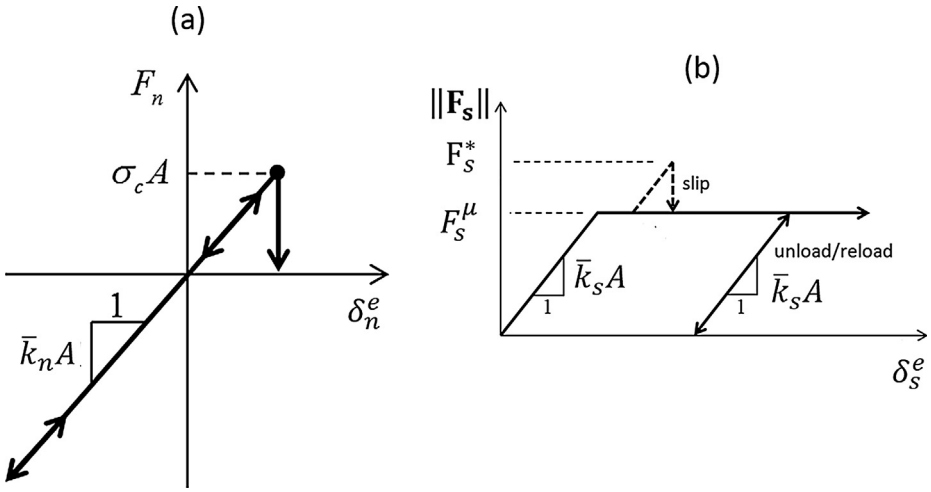

Fig. 4. Force-displacement law in the smooth-joint model. (a) Normal force versus normal displacement, (b) shear force versus shear displacement (modified from [34]).

softening parameter (κ) define the peak strength envelope of the cohesive contacts. Different micro-mechanical properties were assigned to the four different minerals, including quartz, plagioclase, orthoclase, and mica.

3) The contact deformability method [40] was adopted so that the normal and shear stiffness values for each contact were calculated according to the contact Young's modulus (E_c) and the size of two particles bonded with that contact.

The mineral sizes and mineral content of Aue granite were taken from [41]. The data related to average grain size and mineral content is given in Table 1. According to Hofmann et al. [41] the mineral size of Aue granite varies from 0.9 to 1.8 mm; hence, the standard deviation of grain size for each mineral was considered within this range to build the necessary polygons in GBM. In GBM approach, the distribution of minerals is generated randomly. The algorithm proposed by Potyondy [45] was used in the current research for random generation of minerals. This approach for generating random distribution of minerals was technically approved and followed in many PFC-GBM studies [5,31,32,41,42,46]. A comprehensive description of PFC-GBM algorithm can be found in [30,45]. Note that there are infinite number of seeds that can be generated by the algorithm available in PFC-GBM. However, it has been a common approach in PFC-GBM investigations to generate one seed for each mineral size (i.e. each scenario) and investigate the influence of grain size on the behaviour of crystalline rocks [33,35,41,42]. This parametric study approach is significant, because by altering only one parameter and fixing the others, the influence of a particular parameters can be revealed (i.e. grain size).

A Brazilian tensile test and a uniaxial compression test were simulated and calibrated against experimental data (ie., tensile strength, uniaxial compressive strength, Poisson's ratio, and Young's modulus).

The following steps were carried out to calibrate the model:

1) The grain size distribution of the numerical specimens was assigned according to Table 1.
2) In the next step, the Young's modulus of the rock was calibrated which is controlled by the Young's modulus of intra-grain contacts ($\bar{E}_c$) and the shear and normal stiffnesses of inter-grain contacts. At this step only the linear elastic response of the GBM specimen needed to be monitored so that the micro-mechanical parameters that controlled the peak axial strength of the specimen (i.e. C^0) were assigned to be relatively high. Note that after successfully calibrating the elastic properties of rock, the micro-mechanical parameters that influences the strength of the GBM specimen were calibrated in steps 4 and 5.
3) The Poisson's ratio of the model was calibrated by altering the shear-to-normal stiffness ratio of the cohesive contacts, and the shear and normal stiffness values of smooth-joint contacts. This step was carried out in an iterative process with step 2.
4) The Brazilian tensile test was conducted to obtain the macroscopic tensile strength of the rock by varying the tensile strength of the inter-grain contacts in the smooth-joint model. The tensile strength of the smooth-joint model was reduced at this step in order to achieve the closest possible macroscopic tensile strength when compared to the same value obtained from the laboratory testing. The friction angle, friction coefficient, and the cohesion of the smooth-joint model was also altered to achieve a good agreement between numerical results and experimental observations. Note that a proportionately high value of cohesion was assigned on inter-grain contacts (150 MPa) to avoid any shear failure during the Brazilian test [41,42]. This allowed us to control the tensile failure of the numerical Brazilian splite tensile test, and successfully calibrate the tensile strength of the smooth-joint model contacts.
5) The UCS was calibrated by altering the micro-properties of the cohesive model: cohesion (C^0), softening parameter (κ), friction and dilation coefficients (μ, β). As micro-mechanical parameters affect various rock mechanical parameters, several iterations were undertaken between step 1 and 5 to achieve satisfying micro-mechanical properties for the GBM framework. This calibration approach have been used by other scholars (e.g. Hofmann et al. [41] and Farahmand et al. [4]).

Table 1
Mineral content and size for Aue granite [47–49].

	Quartz	Plagioclase	Orthoclase	Mica
Mineral content (%)	30	40	20	10
Avg. mineral diameter (mm)	1.45 ± 0.35	1.35 ± 0.45	1.35 ± 0.45	1.2 ± 0.3

The dimensions of the experimental samples for the UCS test were 100 mm (height) × 50 mm (diameter), and the Brazilian test's physical disk had a diameter of 50 mm. To make the numerical approach computationally efficient, we generated a numerical specimen of 50 mm (height) × 25 mm (diameter). Fig. 5 shows the synthetic rock samples generated for the Brazilian tensile and uniaxial compressive tests. The black mesh lines in Fig. 5 show the mineral structure. We reduced the sample size to obtain time-efficient simulations as has also been done by other researchers in GBM studies (e.g. [31,41]). The effect of scale is

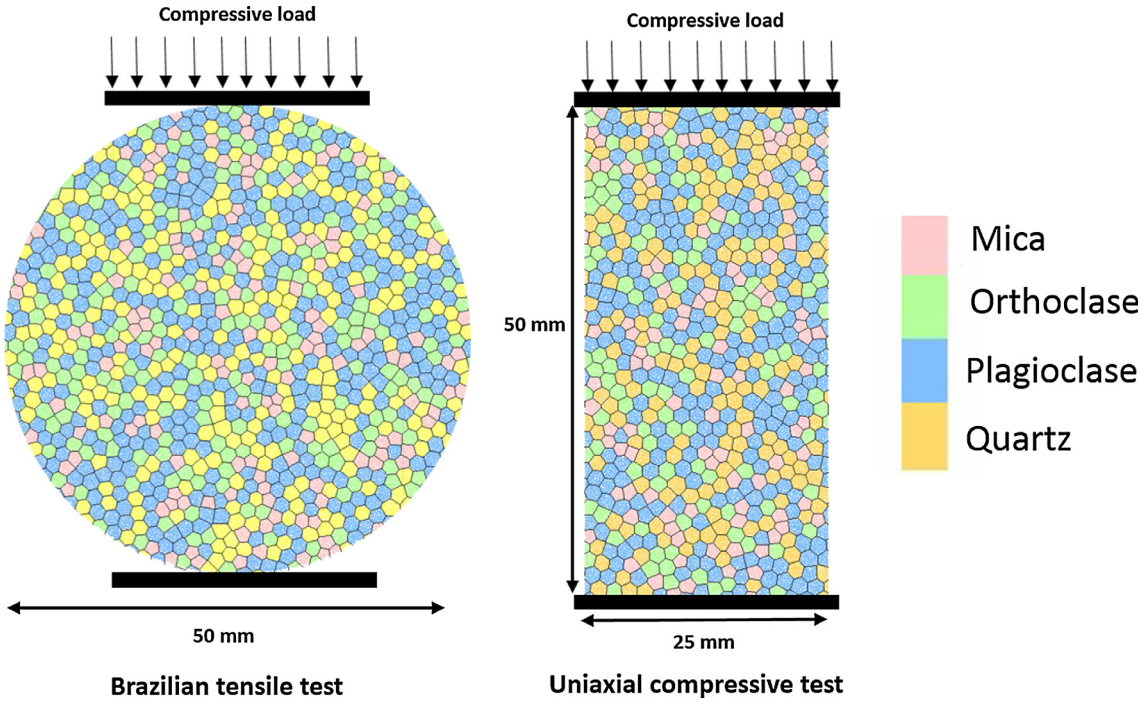

Fig. 5. Schematic of numerical test setups. The black lines indicate the grain boundary.

not significant, according to Potyondy and Cundall [40] and Hofmann et al. [41], provided the particle sizes are relatively small compared to the dimensions of the specimen. The uniaxial compression test was conducted by applying a vertical load on the upper wall. In order to avoid any ball-facet overlap, a relatively high normal stiffness (10% higher than the ball-ball average stiffness) was assigned to the walls [23]. The same set up was considered for the Brazilian tensile test. Note that the uniaxial compression and the Brazilian tensile tests were setup in a way to have frictionless ball-wall contacts. With this arrangement, an ideal rock-platen condition can be achieved which prevents the loading plates from inhibiting the rock bulging [34].

The micro-parameters for Aue granite are listed in Table 2, and the macroscopic properties of Aue granite from the laboratory testing and numerical simulations are compared in Table 3.

Table 3 shows that the strength properties of intact rock determined by the numerical model, such as tensile strength, and uniaxial compressive strength, are in good agreement with the experimental results. The inter-grain micro-cracks developed during uniaxial testing were parallel to the direction of axial loading. The failed specimen in Fig. 6a

Table 3
Macroscopic properties of Aue granite (Yoon et al. [47]) and GBM approach.

Property	Aue granite (Experimental)	Aue granite (Numerical)
Uniaxial compressive strength (MPa)	134 ± 7	135
Young's modulus (GPa)	48 ± 8	49
Poisson's ratio	0.19	0.2
Brazilian tensile strength (MPa)	8 ± 1	7.54

Table 2
Micro-mechanical parameters obtained from calibration procedure of Aue granite.

Element	Parameter	Grain 1 Quartz	Grain 2 Plagioclase	Grain 3 Orthoclase	Grain 4 Mica
Particles forming grains	Minimum particle radius forming grain, Rmin (mm)	0.1	0.1	0.1	0.1
	Maximum to minimum radius ratio, R_{max}/R_{min}	1.66	1.66	1.66	1.66
Cohesive model	Young's Modulus, $\bar{E}_c$ (GPa)	62	52	42	32
	Normal to shear stiffness ratio, $(\bar{k}^n/\bar{k}^s)$	1.0	2.0	2.0	1.5
	Cohesion, (C^0) (MPa)	118	95	95	60
	Friction ratio, (μ)	0.58	0.6	0.6	0.55
	Dilation ratio, (β)	0.22	0.25	0.25	0.2
	Average normal stiffness, $(\bar{k}^n_{avg})$ (GPa)	245,000	210,000	185,000	163,000
	Average shear stiffness, $(\bar{k}^s_{avg})$ (GPa)	245,000	119,000	121,000	136,000
	Softening parameter, κ (1/m)	25,000,000	18,000,000	18,000,000	15,000,000
Micro-mechanical parameters of the grain boundaries (the smooth joint contacts)					
Smooth-joint model	Normal stiffness, $(\bar{k}_n)$ (GPa/m)	106,000			
	Shear stiffness, $(\bar{k}_s)$ (GPa/m)	28,500			
	Tensile strength, (σ_c) (MPa)	8			
	Cohesion, (C^{sj}) (MPa)	150			
	Friction angle, (φ) (°)	80			
	Friction coefficient, (μ^{sj})	0.95			

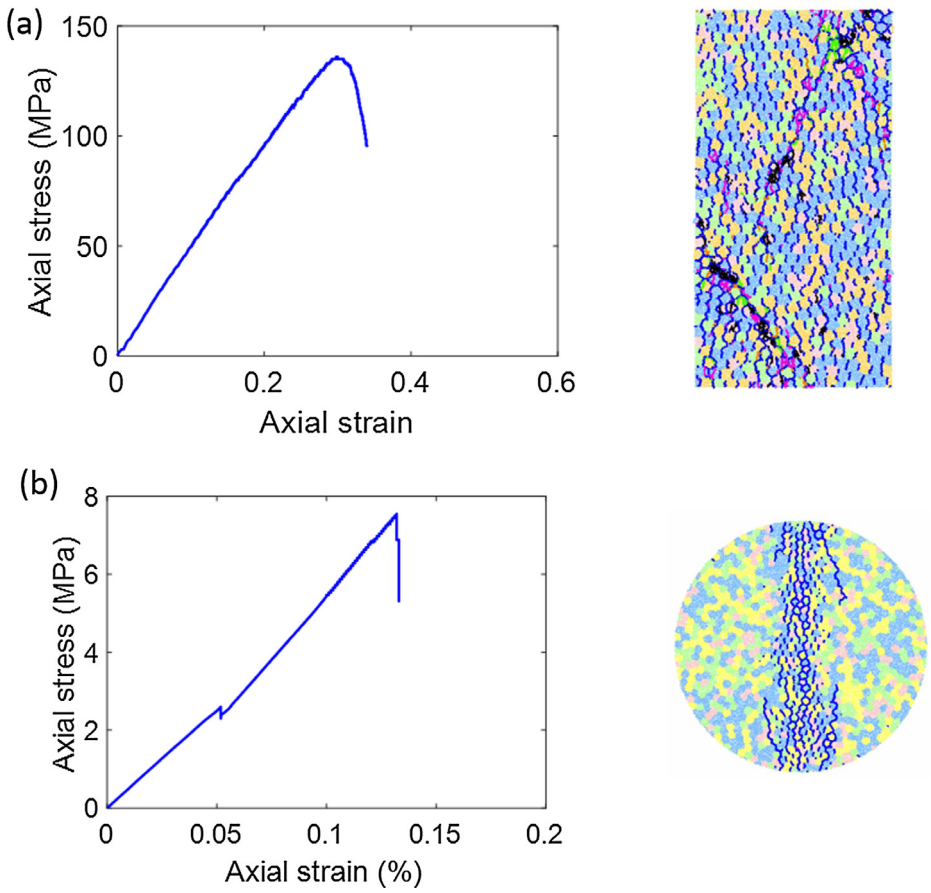

Fig. 6. The numerical response of the intact granite under (a) uniaxial compression, and (b) Brazilian tensile test.

shows that macroscopic fractures were formed in the specimen due to the interaction of the inter- and intra-grain micro-cracks. In the case of the Brazilian test however (Fig. 6b), the failure of the specimen was due to development of macroscopic tensile fractures formed as a result of bond-break in the inter-grain contacts (SJ model).

As shown in Table 3, the cohesive GBM approach successfully captures the macroscopic properties, especially the tensile strength derived from the Brazilian test. The ratio of the uniaxial compressive strength to the tensile strength derived from the Brazilian test is 17.9, which is within the range of the experimental counterpart (15.6–18.1). This reveals that the cohesive GBM approach developed in this study is capable of simulating the macroscopic mechanical properties of rock by replicating the microstructure of rock at a granular level. As the macro-mechanical properties obtained from the numerical simulations (Table 3) match the experimental counterpart, the micro-mechanical properties given in Table 2 can be used to model the mechanical behaviour of Aue granite.

The random distribution of the grains and DEM particles are important in GBM study, and the sensitivity of the calibrated model to these factors should be evaluated before using the calibrated GBM for performing parametric study [41]. To investigate the effect of the randomness of the distribution of the grains having the same grain size and mineral content, the calibrated model was run seven more times with a variety of seed numbers for the grain distribution and the DEM particle distribution. The results showed that the Young's modulus varied only between 48 and 50 GPa, and the Poisson's ratio varied between 0.19 0.21. The UCS and Brazilian tensile strength varied between 133.4 and 136.8 MPa, and 7.2 to 8.5 MPa, respectively. Similarly, with the various seed number for the distribution of DEM particles in the model, the Young's modulus varied between 47 and 49, and the Poison's ratio varied between 0.18 and 0.22. The results also showed that the UCS and Brazilian tensile strength varied between 132.8 and 135.2 MPa, and 7.1 to 8.2 MPa, respectively. The variation in the numerical results is very well within the variation of the mechanical parameters of the physical Aue granite. Therefore, it was meaningful to employ the calibrated parameters for conducting more investigations.

3.2. Generating pre-cracked granite with different grain sizes

In mineralogy, grain size is a parameter that can be used for classifying crystalline rocks. A widely used method for measuring the grain size in a physical rock is to analyse a thin section of the specimen using a polarized microscope. Generally, the shape of minerals is not spherical and a particular grain approaches the shape of a polygon. In nature, we may find a specific rock with various grain sizes. For instance, Fig. 7 illustrates three thin sections of an Australian sandstone with various grain sizes (i.e. fine, medium, and coarse grained sandstone).

We considered three different grain size scenarios to investigate the influence of grain size on the strength, cracking, and damage responses of single- and double-flawed specimens. The average grain diameter considered in each scenario is given in Table 4. The grain size for scenario 1 is equal to the grain size of the experimental Aue granite (calibrated model). The size of quartz for scenario 1 was also different from the other minerals (1.45 ± 0.35 mm). For scenario 2 and 3, the average size of quartz was considered to be 3.2 mm and 4.3 mm, respectively. The average size for other minerals (plagioclase, orthoclase, and mica) was assumed to be 1.6 mm and 3.0 mm for scenario 2 and 3, respectively. For scenario 2 and 3, the average grain size of quartz was considered to be different from other minerals to achieve a heterogeneous mineral size distribution. Hence, the average grain size increased with scenario number which allowed us to have different grain

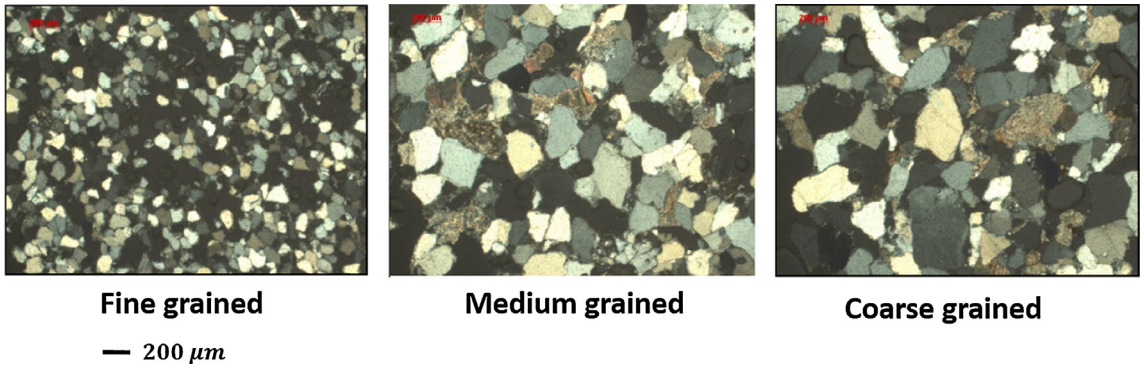

Fig. 7. Various grain sizes observed in three types of Australian sandstones [50].

Table 4
Overview of various scenarios with different mineral size distribution considered to investigate the influence of grain size heterogeneity on the simulation results of single- and double-flawed specimens.

	Avg. mineral diameter (mm)			
	Quartz	Plagioclase	Orthoclase	Mica
Scenario 1	1.45 ± 0.35	1.35 ± 0.45	1.35 ± 0.45	1.2 ± 0.3
Scenario 2	3.2	1.60	1.6	1.6
Scenario 3	4.3	3.0	3.0	3.0

size categories for comparison purposes. Note that the grain sizes presented in Table 4 indicate the average size of each mineral. The grain-based single- and double-flawed synthetic specimens, as well as the geometry of the double-flawed samples, are illustrated in Fig. 8a, b and Fig. 8c, respectively. The ligament length in double-flawed specimens was always equal to the length of the flaw. The flaw length was considered to be 4 mm, and the inclination angle was varied ($\theta = 0^{\circ}$, 15°, 30°, 45°, 60°, 75°). The pre-existing cracks in the double-flawed specimens were generated to be left-stepping flaws, with bridging angles of 60°. The specimen dimensions were equal to the models generated during the calibration process (50 mm high and 25 mm wide).

The scenarios considered in the present study had a grain size almost equivalent to that of the physical specimen. An ideal grain-generation algorithm should be able to produce a mineral microstructure which is similar to the statistical and topological properties of the physical specimen. However, the aim of numerical simulations is not to incorporate the exact grain microstructure in the model, but rather to provide the best possible match with the real specimens. In the present study, a grain-based disk-packing scheme proposed by Potyondy [30] was employed to generate the polycrystalline structure of Aue granite. It has been observed in the previous investigations that disk-packing scheme, which is available in PFC2D [34], gives a perfect match with the physical specimens in terms of microstructural properties [30,41,42,45,51], compared to other grain-generation algorithms available in UDEC and 3DEC software packages [30].

In previous GBM research conducted by Hofmann et al. [41] on the same granite, the average grain size adopted in the parametric study ranged from 0.5 to 5 mm. According to Hofmann et al. [41], if there are less than five minerals along the shorter dimension of the model, you need to increase the size of the specimens. In our study, however, the average mineral size was slightly reduced in the large-grain-size specimens (scenario 3) to 4.3 mm for quartz, and 3 mm for the rest of minerals. This resulted in approximately 5–7 minerals along the shorter dimension of the specimen, which maintained the same dimensions and

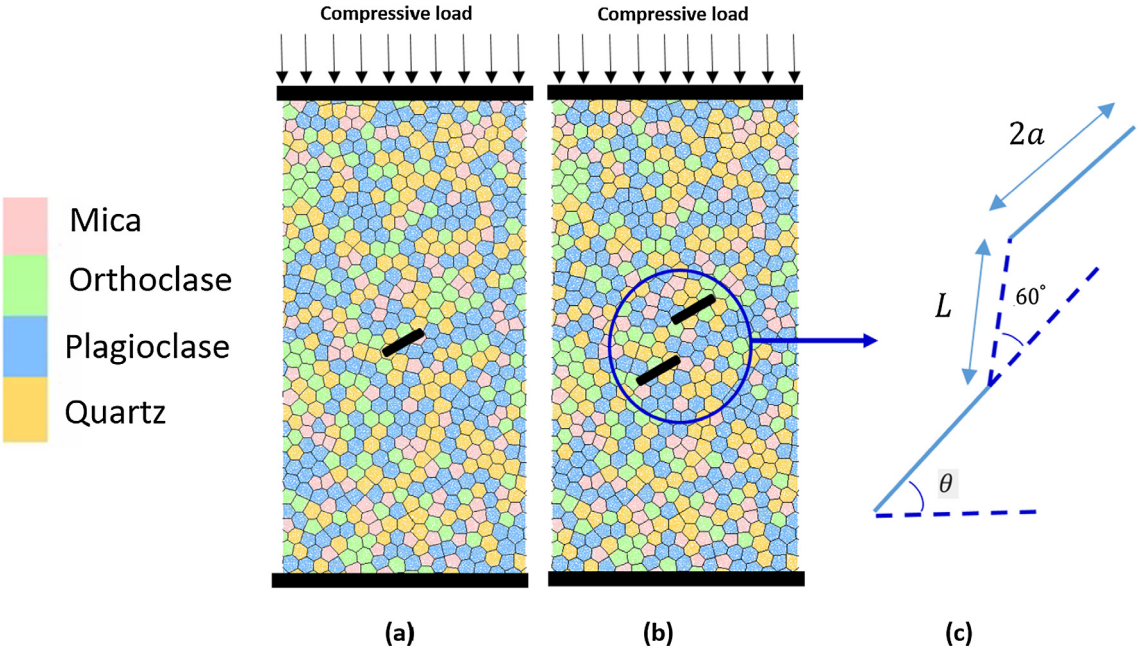

Fig. 8. The grain-based numerical model of (a) single-flawed and (b) double-flawed specimens. The black lines indicate the grain boundary. (c) The geometry of pre-existing cracks in double-flawed specimen defined by flaw inclination angle (θ), bridge angle (60°), bridge length (L), and flaw length (2a).

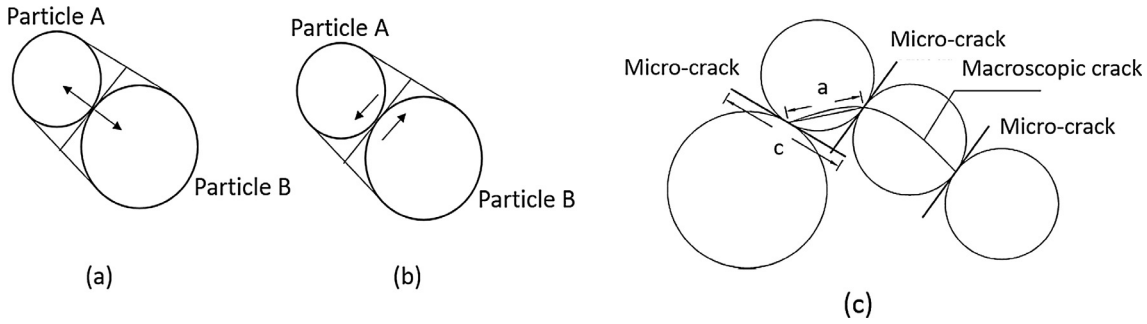

Fig. 9. Definition of micro-cracks and macroscopic crack in PFC software: (a) tensile crack; (b) shear crack (adopted from Diederichs [53]); (c) construction of macroscopic cracks (adopted from Zhang and Wong [16]).

made the simulations more time-efficient.

It should be mentioned that all the numerical models for the pre-cracked granite were constructed with the same distribution of minerals (i.e. the same seed number was used to generate the randomness of the distribution of the minerals). In order to generate the GBM specimens for performing parametric study on mineral size, the algorithm proposed by Potyondy [45] was used which is capable of generating a specimen with the desired polygon size. This approach for generating a random distribution of minerals has been practised in many PFC-GBM studies [5,31,32,41,42,46]. It has been a common approach in PFC-GBM to generate one seed for each mineral size (i.e. each scenario) and investigate the influence of grain size on the behavior of crystalline rocks [33,35,41,42].

The micro-mechanical properties of the calibrated Aue granite model were employed to investigate the influence of mineral size (see Table. 4) on the mechanical and fracturing behavior of pre-cracked GBM specimens. Notice that, since the micro-mechanical parameters in the present study (i.e. C^0) were calibrated against a physical Aue granite specimen, it was meaningful to employ the same set of calibrated parameters for conducting parametric study on grain size. By considering the micro-mechanical parameters (i.e. C^0) to be constant, and varying the grain size, we would be able to recognize the influence of mineral size on the mechanical and fracturing behavior of pre-cracked specimens. The benefit of this approach is that once the micro-mechanical parameters representing a physical granite sample with known grain size are gained, they can be employed for conducting a further parametric study on various influential parameters such as grain size, mineral content, etc. It should be mentioned that this methodology has been used by other researchers and demonstrated promising ability to shed more light on the mechanical behavior of crystalline rocks [33,35,41–44,52]. Accordingly, in the present study, the same approach was adopted for investigating the influence of rock texture on the macroscopic behavior of pre-cracked Aue granite.

In Section 4, we will assign the calibrated micro-mechanical parameters in each scenario to investigate the micro- and macro-cracking responses of the single- and double-flawed models under uniaxial compressive loading.

4. The results of numerical simulations

In this section, we investigate the influence of the grain size distribution on crack initiation and propagation, and the failure mechanism of single- and double-flawed specimens. We obtain the micro-cracking pattern from the failure of inter- and intra-grain contacts, and monitor the damage evolution patterns in the mineral contacts by tracking the damage parameter (D) defined in the cohesive constitutive model (Eq. (7)).

The micro-cracking process in brittle rocks is closely related to mineral grains, pores, and pre-existing flaws. By characterising the micro-cracking process concerning the mineral size distribution, we can enhance our understanding of the macroscopic damage behaviour of brittle rocks. As mentioned in Section 3, the mineral composition and the distribution of the grain size of various minerals can be simulated using the PFC-GBM approach. One of the merits of this numerical tool is that the influence of the grain size distribution on the mechanical behaviour and cracking responses of the minerals can be captured.

We generated different numerical specimens with a small grain size (Scenario 1), medium grain size (Scenario 2), and large grain size (Scenario 3) to assess the fracturing and failure behaviour of single flaw specimens under uniaxial compression. The mineral content assigned for these numerical specimens was similar to the calibrated specimen. We observed that the grain size profoundly affected the number of both inter- and intra-grain micro-cracks, and the mechanical responses of the numerical specimens.

4.1. Monitoring micro-cracks in GBM

In DEM modelling, the breakage of inter- and intra-grain contacts can simulate the nucleation of a micro-crack. In the current numerical study, an inter-grain micro-crack formed when the smooth joint contact between adjacent boundary particles was broken. Each micro-crack was represented as a single straight line, with a length equal to the average diameter of its particles. The accumulation of certain number of micro-cracks forms a macroscopic crack. Fig. 9 illustrates a schematic view of micro-crack initiation in DEM. According to Diederichs [53], the centroid of the micro-crack lies along the line connecting the centres of adjacent particles (Fig. 9a,b). Zhang and Wong [16] defined the centroid of two adjacent micro-cracks as a, and the length of the longest micro-crack as c (Fig. 9c). When $a/c \leq 1$, the two micro-cracks were treated as single micro-crack [16]. A macroscopic crack was formed in the model when three or more micro-cracks initiated. Fig. 10 illustrates the initiation of micro-cracks in a pre-cracked specimen ($\theta = 0^{\circ}$). It can be seen that the breakage of inter-grain contacts resulted in the formation of macroscopic cracks on the surface of pre-existing flaw (Fig. 10a). A close-up view of the flaw region is presented in Fig. 10b, which shows how the accumulation of a number of inter-grain micro-cracks could form a macroscopic crack. In the current study, the inter- and intra-grain micro-cracks were graphically monitored; different colours were assigned to different types of micro-cracks. The approach suggested by Zhang and Wong [16] to measure the crack initiation stress was adopted in this research, which is the stress at which the first macroscopic tensile cracks form in the flaw regions (either at the tips or on the surface). The same method was used to monitor the macroscopic cracks that formed due to the coalescence of inter- and intra-grain micro-cracks. To trace the macroscopic tensile cracks (ie. at the level of crack initiation stress), we graphically plotted the micro-cracks that formed along the grain boundaries.

4.2. PFC-GBM modelling of brittle rocks including a single flaw

Three different numerical specimens with various grain size distribution were generated. The specimens had the same mineral type

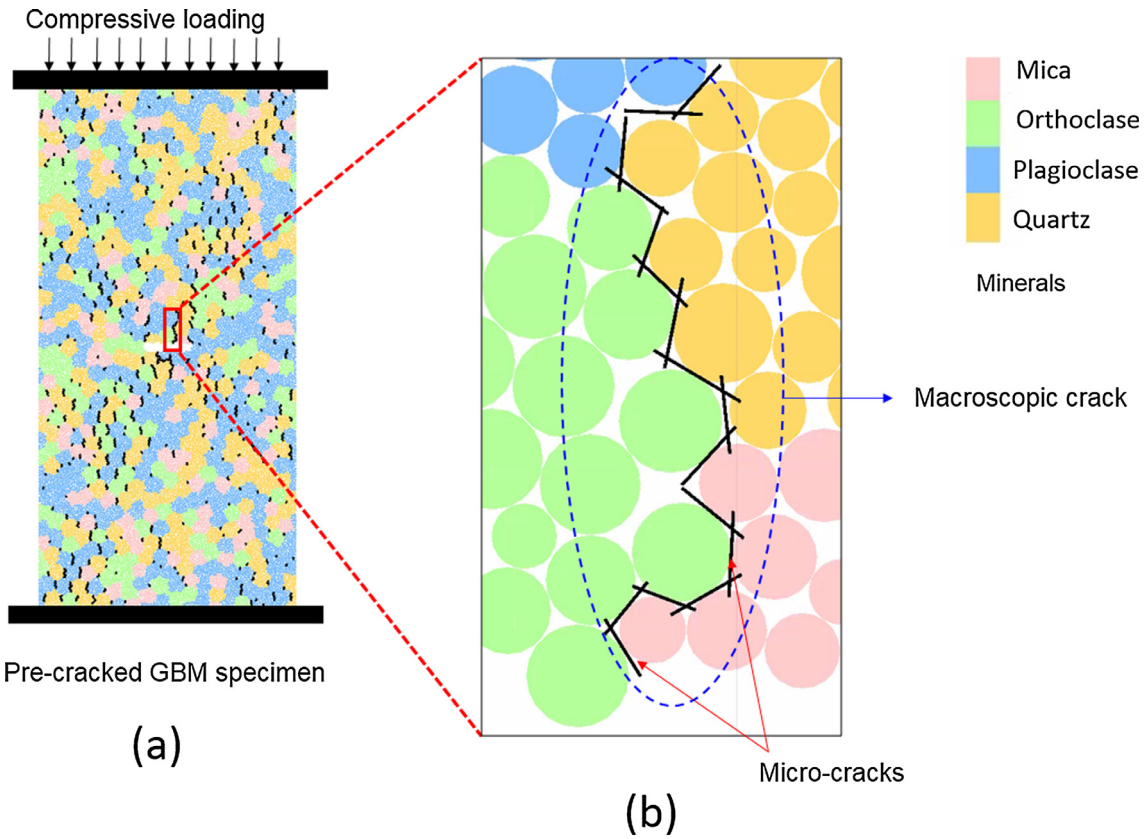

Fig. 10. Nucleation of micro-cracks in GBM, and development of macroscopic cracks. (a) Development of macroscopic cracks in a pre-cracked numerical specimen ($\theta = 0^{\circ}$), the black lines indicate macroscopic cracks. (b) A close-up view of the formation of a macroscopic crack on the surface of pre-existing flaw. The black lines represent micro-cracks.

(quartz, plagioclase, orthoclase, and mica). Numerical specimens with single and double pre-existing cracks were generated by removing the DEM particles according to the aperture, length, and inclination angle of the flaws. It has frequently been observed in the experimental studies that tensile wing cracks are the most common form of cracks that initiate in single and double flawed specimens [16,54,55]. The experimental observations of Wong and Einstein [54], for instance, showed that the tensile wing cracks were always the first cracks initiated during uniaxial compression testing.

In order to provide a comprehensive analysis of PFC-GBM modelling of the macroscopic and microscopic fracturing behaviour of brittle rocks including pre-existing cracks, we monitored the initiation, development, and coalescence of inter- and intra-grain micro-cracks and linked them with the axial stress-strain curves. To make this paper more concise, only the macroscopic axial stress-strain curves of specimens with $\theta = 30^{\circ}$ and their corresponding micro-cracking behaviour at different loading points are presented as a typical example showing the failure mechanism.

One of the important factors affecting the potential of spalling around underground mining excavations is the crack initiation stress [16,44,56]. The initiation of cracks from pre-existing flaws controls the dominant failure mechanisms and mechanical behaviour of brittle rocks on a variety of scales [3]. Therefore, in the following sub-sections, the crack initiation stress and its corresponding micro-cracking responses are presented. Additionally, the final failure mode of the models is provided, and we discuss the influence of grain size and flaw inclination angles on the distribution of inter-and intra-grain micro-cracks.

4.2.1. The failure mechanism of single-flawed specimens (example from $\theta = 30^{\circ}$)

The axial stress-strain curves and the micro-cracking behaviour of the specimens that included a single, pre-existing crack with an inclination angle of 30° is illustrated in Fig. 11. Different stress levels were considered in this graph as points I, II, and III. The point I showed the stress level at which the initiation of macroscopic cracks on the surface or at the tips of the pre-existing cracks was observed. The stress level at which the coalescence between inter- and intra-grain micro-cracks was occurred is marked as point II. The point III corresponds to the peak axial strength of the GBM specimens. It can be seen that the grain size profoundly influenced the micro-cracking and macroscopic behaviour of the numerical specimens with a single flaw. For single-flawed specimens, the numerical behaviour was monitored in three distinct points: Initiation of primary cracks (I), extension of macroscopic cracks (II), failure of the model and peak axial strength (III). The crack initiation stress (I) increased from 39.6 MPa for scenario 1, to 49.6 MPa for scenario 2, but reduced to 36.9 for scenario 3. The initiation of tensile cracks at point I in all of the specimens was found to be due to the failure of the inter-grain contacts (SJ model). It is clear in Fig. 11 that the grain boundaries control the crack initiation pattern (I in Fig. 11b, c, and d), and that the mineral size can highly influence the pattern of tensile crack initiation as inter-grain micro-cracks grow. We also found that, apart from the tip area, other inter-grain micro-cracks are formed in the different parts of the specimens (I). However, the length of the macroscopic tensile cracks was longer around the flaw tips compared to other regions, especially for scenario 1 and 2 (I in Fig. 11b and c). During compressive loading of the specimens, intra-grain contacts started to enter to their yielding limit. At this point, the stress-displacement of intra-grain contacts appeared as a softening response. After complete degradation of cohesion (C^0) and reaching the final stage of softening behaviour ($D = 1.0$), the intra-grain micro-cracks were initiated. These intra-grain micro-cracks mostly tended to initiate from macroscopic tensile fractures that were previously formed from

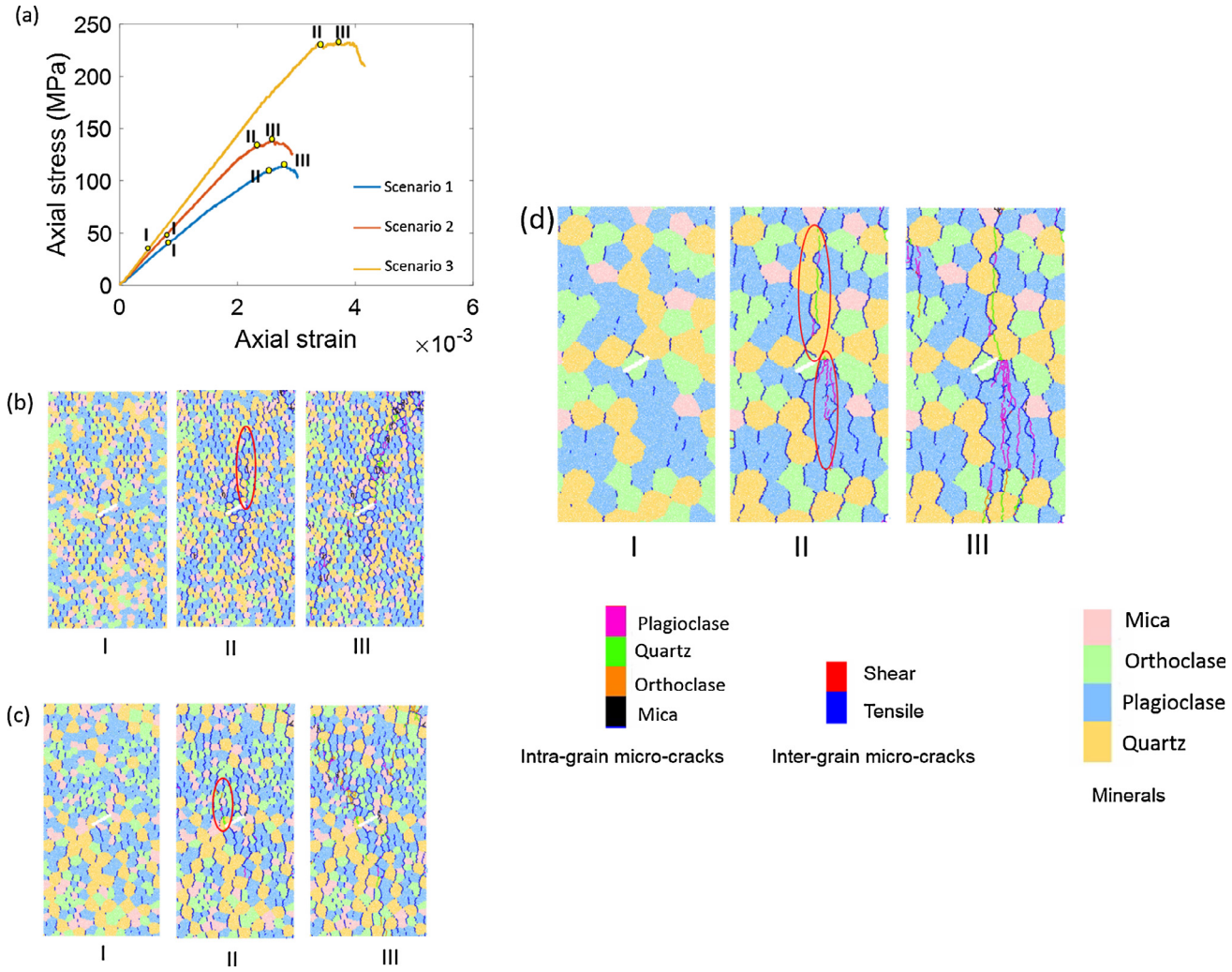

Fig. 11. The macroscopic failure behaviour of numerical specimens with $\theta = 30^{\circ}$ (a) the complete axial stress-strain curves, (b) scenario 1, (c) scenario 2, (d) scenario 3.

the flaw tips due to bond-breakage in inter-grain contacts. Accordingly, a progressive coalescence between inter- and intra-grain micro-cracks occurred, which resulted in the formation of a much larger macroscopic fractures. The corresponding point where the interaction between inter- and intra-grain micro-cracks was observed, is marked as point II in stress-strain graphs (II in Fig. 11b, c, and d). It can also be observed that from point I to point II, all numerical specimens experienced a significant growth in inter-grain micro-cracks in the direction parallel to the applied compressive loading, leading to the extension of macroscopic tensile cracks.

The progressive failure of intra-grain contact leads to peak axial strength (III). The corresponding peak axial stresses for scenarios 1, 2, and 3 are 103, 132, and 231 MPa, respectively; they show a significant increase in the intra-grain micro-crack initiation stress with increasing the grain size (Fig. 11a)., which is consistent with the observations of Hofmann et al. [41], Gui et al. [57], and Peng et al. [33]. According to Hofmann et al. [41], bond-breaks occur faster in the parallel bond model, since the stress on the bond is higher in smaller grains, and they result in a significant reduction in the axial strength. Similarly, since the cohesion (C^0) for all three scenarios in the current cohesive model are equal, the intra-grain contacts in the minerals with higher stress concentrations reach their complete damage state ($D = 1.0$) much earlier, leading to a significant reduction in the strength of the material. In scenario 3, only one grain boundary was formed around the pre-existing crack, which was connected to the flaw tips. Consequently, this weak inter-grain interface could easily fail at a lower axial stress to form a primary, macroscopic tensile crack. However, in scenario 3, despite it having the lowest crack initiation stress, the grains showed a higher resistance against compressive loading. This is because the stress concentration in the minerals was lower, leading to a much higher peak axial strength. The possible reason for having the lowest crack initiation stress in scenario 3 might be attributed to the dimension of the grains surrounded the pre-existing crack. Due to the large dimension of the grains in scenario 3, the macroscopic crack could initiate along one interface (which was straight), while in scenario 1 and 2, due to smaller grain sizes, the same sized macroscopic crack had to be initiated along multiple grain boundaries (i.e. jagged shape interface). It was believed that the jagged interfaces in scenario 1 and 2 acted as rough interfaces (i.e. interfaces with irregular asperities), but in the contrary, the straight interfaces in scenario 3 acted as planar interfaces (i.e. smooth interfaces). Accordingly, in scenario 3 when $\theta \leq 30^{\circ}$, the inter-grain micro-crack could rapidly grow along the straight grain interfaces to form macroscopic cracks at the early stages of compressive loading. In scenario 1 and 2, however, more time stepping was required to initiate the micro-cracks along the jagged shaped grain interfaces and develop a macroscopic crack. However, in scenario 3 when $\theta > 30^{\circ}$, as the angle between the loading direction and the pre-existing crack was reduced, the contribution of low stress concentration in the flaw zone was more pronounced leading to relatively higher crack initiation stresses.

The graphical representation of intra-grain micro-cracks in Fig. 11b,

c, and d revealed that the propagation of intra-grain micro-cracks at peak (III) was more pronounced for scenario 3 compared to other grain sizes, which was due to a larger number of DEM particles inside the minerals. It can be seen that at the onset of failure (III), the density of both inter- and intra-grain micro-cracks increased, and smaller grain size in specimens showed a higher number of micro-cracks. The macroscopic cracks formed in all scenarios as a direct consequence of progressive coalescence between inter- and intra-grain micro-cracks that initiated from the pre-existing flaws at the centre of the specimen. The formation of these macro-cracks is the major reason for the failure of the rock mass at field scale (Fig. 1a).

The localized macroscopic shear fractures also formed in the specimens (Fig. 11b, c, and d; III), which were the result of interaction between inter- and intra-grain micro-cracks. Notice that the macroscopic shear fractures began to generate when the intra-grain micro-cracks appeared in the specimens, which initiated due to grain sliding. This fracture mechanism was previously observed by Morgan et al. [7]. According to their experimental research, in crystalline rocks such as granite, the localized shear cracking is associated with the relative sliding along the fracture interfaces that are already developed in the specimen [7]. This numerical simulations were also consistent with the macroscopic shear fractures observed in the GBM study of brittle rocks [4,5].

4.2.2. Initial cracks in the single-flaw specimens

The initial macroscopic cracks that developed around the flaw tip are illustrated in Fig. 12. The blue lines depicted in the figures are tensile inter-grain micro-cracks formed as a result of bond-break in SJ contacts, in tensile mode. The laboratory observations of Morgan et al. [3] showed that tensile cracks typically propagated along a meandering path created by the grain boundaries. Therefore, the shape of tensile cracks around pre-existing cracks is always “jagged” rather than smooth. The numerical observations in the current study also showed the same jagged pattern in the development of propagated macroscopic cracks. The jagged pattern in the development of macroscopic tensile cracks in the numerical simulations is associated with the shape of the Voronoi tessellations that were created during the sample generation procedure.

The crack initiation stress is given under each specimen (Fig. 12). We can see that, for all grain sizes, the crack initiation increased with an increasing flaw inclination angle. For scenario 2, when $\theta > 0^{\circ}$ the crack initiation stress was approximately 10 MPa higher than scenario 1. Monitoring inter-grain micro-cracks for scenarios 1 and 2 (Fig. 12a-c and Fig. 12a′-c′) revealed that for θ equal to 0°, 15°, and 30°, the first tensile cracks were relatively close to the middle surface of the flaw. In comparison, when θ was equal to 45°, 60°, and 75°, the first crack growth occurred in the inter-granular boundaries, away from the centre and close to the flaw tip (Fig. 12d–f and Fig. d′–f′). In scenario 3, for $\theta \leq 30^{\circ}$,the crack initiation stress was lower than for scenarios 1 and 2, but it raised significantly to a peak axial strength for 60° and 75°,leading to the presence of a few intra-grain micro-cracks (Fig. 12e″-f″). As mentioned in Section 4.2.1, in scenario 3, specimens with high flaw inclination angles (i.e. $\theta > 30^{\circ}$) were significantly influenced by the low stress concentration, which resulted in a higher crack initiation stresses. At 60° and 75°, the low stress concentration was more effective resulting in a higher axial stress to fully grow the macroscopic cracks around the flaw.

4.2.3. Failure behaviour of single-flaw specimens

A progressive increase in uniaxial compressive loading leads to the development of secondary macroscopic cracks and failure of the specimens at peak stress. The complete stress-strain curves for all numerical samples are illustrated in Fig. 13, and the fracture patterns at peak axial strength are shown in Fig. 14. It is clear from Fig. 13 that the maximum axial stress for scenario 1 was the lowest when the inclination angle was equal to 15°. For $\theta > 15^{\circ}$, there was an increase in the maximum axial strength of the material. For scenario 3 (the largest grain size), the lowest possible maximum axial strength occurred at $\theta = 30^{\circ}$, and for $\theta > 30^{\circ}$ there was an increase in the strength of the specimens. The results for scenario 2 (medium grain size), however, were significantly different. At $\theta = 30^{\circ}$ and $\theta = 60^{\circ}$, the lowest axial strengths were reached. We believe this is due to different mineral distributions around the flaw region when the inclination angle changes. For this scenario, the weakest mineral (mica) was present around the right side of the flaw’s tip. Since the cohesion of mica was the lowest value (ie. 60 MPa) compared to other minerals, it predominantly influenced the evolution of intra-grain micro-cracks around the tip region. Fig. 13 also shows that all specimens in each scenario underwent the same elastic behaviour before macroscopic cracks propagated.

Fig. 14 shows that an increase in compressive loading resulted in a dramatic rise in the number of both inter- and intra-grain micro-cracks. The secondary macroscopic cracks around the flaw’s tip propagated due to the bond-break in the intra-grain contacts, and the progressive coalescence between the inter- and intra-grain micro-cracks. The laboratory observations of Morgan et al. [3] showed that the secondary macroscopic cracks had a powdery residue, indicating grain breakage. According to Morgan et al. [3], mineral breakage was associated with a sizeable sliding displacement along the surface of the crack. Other laboratory investigations (e.g. [58–60]) also found that micro-cracks generally initiate from the grain interfaces, and that the intra-grain micro-cracks will be formed at high applied stress. In the present study’s GBM numerical simulations, the initiation of micro-cracks was mostly caused by stress concentration at the inter-grain contacts (grain boundaries), and the intra-grain micro-cracks initiated when the applied stress was high. The majority of micro-cracks in the numerical specimens propagated and extended in a direction parallel to the maximum axial stress. This failure mechanism at the microscopic level is known as axial splitting [30,61], and it was observed in all numerical specimens regardless of their grain size. We can see in Fig. 14e-f, Fig. 14e′-f′, and Fig. 14e″-f″ that numerical specimens with $\theta \geq 60^{\circ}$ produced fewer intra-grain micro-cracks, and the failure of these specimens occurred due to the progressive coalescence between the inter-grain micro-cracks. This can be attributed to the fact that, as the flaw inclination angle increased, the behaviour of the numerical specimens came closer to intact rock, which lead to a reduction in the number of intra-grain micro-cracks [42]. It was observed that for $\theta < 45^{\circ}$, the number of intra-grain micro-cracks around the tip region was increased by increasing the grain size (Fig. 14a–c, a′–c′, and a″–c″). One possible reason is that an increase in the grain size leads to an overall increase in the strength of the specimens, so that more damaged contacts (intra-grain micro-cracks) are produced to reach the failure state.

4.3. PFC-GBM modelling of brittle rocks including a double flaw

The linkage of pre-existing flaws (crack coalescence) is an important phenomenon in nature [14], as it controls the failure mechanism of materials [3]. In this regard, numerical specimens containing double flaws were generated and tested under uniaxial compressive loading. The results are summarised in three different subsections. An example of a failure mechanism for $\theta = 30^{\circ}$ is given in Section 4.3.1. The results of initial crack development and failure mode in the specimens are given in Sections 4.3.2 and 4.3.3, respectively. Finally, the damage responses of specimens at the microscopic level is analysed in Section 5.

4.3.1. The failure mechanism of double-flaw specimens (example from $\theta = 30^{\circ}$)

Fig. 15 illustrates the stress-strain curves for numerical specimens with $\theta = 30^{\circ}$, and their corresponding micro-cracking behaviour. Different stress levels were considered in this graph as points I, II, III, and IV. The point I showed the stress level at which the initiation of macroscopic cracks on the surface or at the tips of the pre-existing flaws was

Fig. 12. Initiation of primary macroscopic cracks for the specimens with different inclination angles and grain sizes. The crack initiation stress and the peak stress (in parentheses) are given below each numerical specimen. The blue lines indicate the inter-grain micro-cracks. The first row (a–f) shows scenario 1, the second row (a′–f′) shows scenario 2, and the third raw (a″–f″) shows scenario 3. (For interpretation of the references to colour in this figure legend, the reader is referred to the web version of this article.)

observed. The stress level at which the development of macroscopic tensile cracks inside the bridging area occurred was presented by point II. For double-flaw specimens, a coalescence stress (point III) was considered in the stress-strain curves to monitor the onset of flaw coalescence. The peak axial strength of the GBM specimens was indicated by point IV. The micro-cracks developed at various points of loading are also monitored during the simulations, and are shown in Fig. 15b–d. According to Fig. 15, the increase in the grain size resulted in an increase in the peak axial strength. At point I, for all numerical specimens, the inter-grain micro-cracks were initiated in the bridging area of the flaw system. It can be seen in Fig. 15b–d that the inter-grain micro-cracks were only initiated in this particular area because the

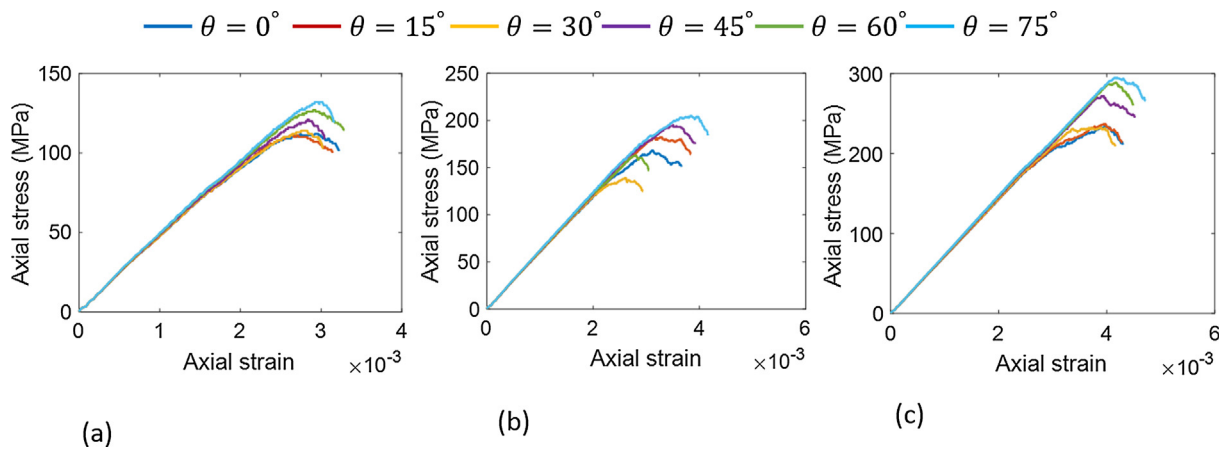

Fig. 13. Complete axial stress-strain curves for single-flawed specimens: (a) scenario 1, (b) scenario 2, (c) scenario 3.

stress concentration was relatively high. The crack initiation stress was slightly raised by increasing the grain size (the results are quantitatively compared in Section 4.3.2).

The macroscopic tensile cracks propagated in the bridging zone at point II. At point III, the coalescence of pre-existing cracks was observed in all scenarios; it occurred due to the rapid extension and development of macroscopic cracks in the bridging area. In all numerical specimens, the macroscopic tensile cracks that were the result of progressive linkage of inter-grain micro-cracks, were formed from the flaw tips. The micro-cracks developed until point II are grain boundary tensile cracks, which initiated as a result of bond-break in the SJ model. A small tensile strength needed to be assigned to the inter-grain contacts during the calibration procedure in order to match the Brazillian tensile test results. This early coalescence of pre-existing cracks due to the initiation of inter-grain micro-cracks may not be observable during experimental testing. However, it does not mean that they are not present in the physical specimens [41]. In the numerical simulations, the macroscopic cracks fully developed in the bridging zone due to progressive compressive loading, leading to flaw coalescence at point III. The axial stress-strain curve in Fig. 15a shows that the large grain size specimens required a higher axial stress to reach point II. This may contribute to the longer length of the grain boundaries in this specimen, as the inter-grain contacts required more time-stepping and, consequently, more axial stress to fully develop and form the macroscopic tensile crack.

At point III, intra-grain micro-cracks started to initiate. In all three scenarios, more inter-grain micro-cracks initiated and formed macroscopic tensile cracks, which propagated in the loading direction. The progressive coalescence between the inter- and intra-grain micro-cracks caused non-linear behaviour in the axial stress-strain curves before reaching the peak axial strength. The intra-grain micro-cracks tended to initiate from the flaw tips in scenarios 1 and 2. However, in scenario 3 the intra-grain micro-cracks appeared in the bridging area and at the flaw tips. This was mainly because of the presence of larger minerals in the bridging area. In fact, only one mineral was generated in the bridging area in scenario 3, and due to a higher number of DEM particles, it tended to produce more intra-grain micro-cracks. By the continuous loading of the numerical specimens, more intra-grain contacts (with the cohesive model) reached their yielding limit, generating intra-grain micro-cracks. The interaction between inter- and intra-grain micro-cracks formed macroscopic fractures in a direction parallel to the maximum axial stress. This leads to the failure of the specimens at point IV, where the peak axial strength was achieved. As shown in Fig. 15b-d, the number of intra-grain micro-cracks increased significantly at peak axial strength, and the macroscopic cracks were fully propagated, extending parallel to the direction of axial loading.

4.3.2. Initial cracks in the double-flaw specimens

To gain a better insight into the crack initiation pattern and coalescence of primary macroscopic cracks, we monitored the state of the numerical specimens at the time the primary macroscopic cracks initiated. The results are illustrated in Fig. 16. This figure shows that the macroscopic cracks in all numerical specimens initiated from the surface of pre-existing flaws and propagated vertically towards the loading DEM walls. Similar to single-flawed specimens, the inter-grain micro-cracks were initiated due to the bond-failure in SJ contacts. Fig. 16 shows that the macroscopic cracks initiated from the middle portion of the flaws, and that they shifted towards the tips with an increase in the inclination angle. In scenario 3, the macroscopic cracks only followed the grain boundary provided by orthoclase in the inner tip area due to the large diameter of the grains. In fact, for this specimen, the bridging zone was dominated by this mineral, a meandering path defined the propagation of the inter-grain micro-cracks as a result. Note that the calibrated contact strength (C^0) for orthoclase and plagioclase are equal, while the same value is different for quartz and mica. This difference between the mineral strength may change the cracking response in the bridging zone. For instance, the weakest mineral (mica) has the potential to develop more micro-cracks leading to grain crushing in the inner tip area. However, in such circumstance, many other factors (i.e. stress concentration, flaw inclination angle, and etc.) may influence the results. Scenario 3 showed that, for $\theta \geq 60^{\hat{A}\circ}$ (Fig. 16e″–f″), since the angle between pre-existing crack and loading direction was relatively small compared to other specimens, the influence of pre-existing flaw was less pronounced leading to a relatively higher crack initiation stress. In fact, for $\theta \geq 60^{\hat{A}\circ}$ more time stepping was needed for the initiation of the micro-cracks and the formation of macroscopic crack. This resulted in the initiation of fewer micro-cracks in the bridging area compared to other specimens.. This shows that both inclination angle and grain size can influence the initiation of primary tensile cracks. The stress at which the initial tensile cracks formed in the flaw system was monitored, and is given below each specimen in Fig. 16. The results revealed that crack initiation stress was increased when the inclination angle of the flaw was increased, and when the rate of increase was higher for scenario 3. These numerical findings were consistent with the laboratory observations of Barre granite [14] containing left-stepping pre-existing cracks.

4.3.3. Failure behaviour of double-flaw specimens

A progressive increase in uniaxial compressive loading leads to the development of secondary macroscopic cracks and the failure of the specimens at peak stress. The complete stress-strain curves for all numerical samples are illustrated in Fig. 17, and the fracture patterns at peak levels are shown in Fig. 18.

The axial stress-strain curves in Fig. 17 show that almost all

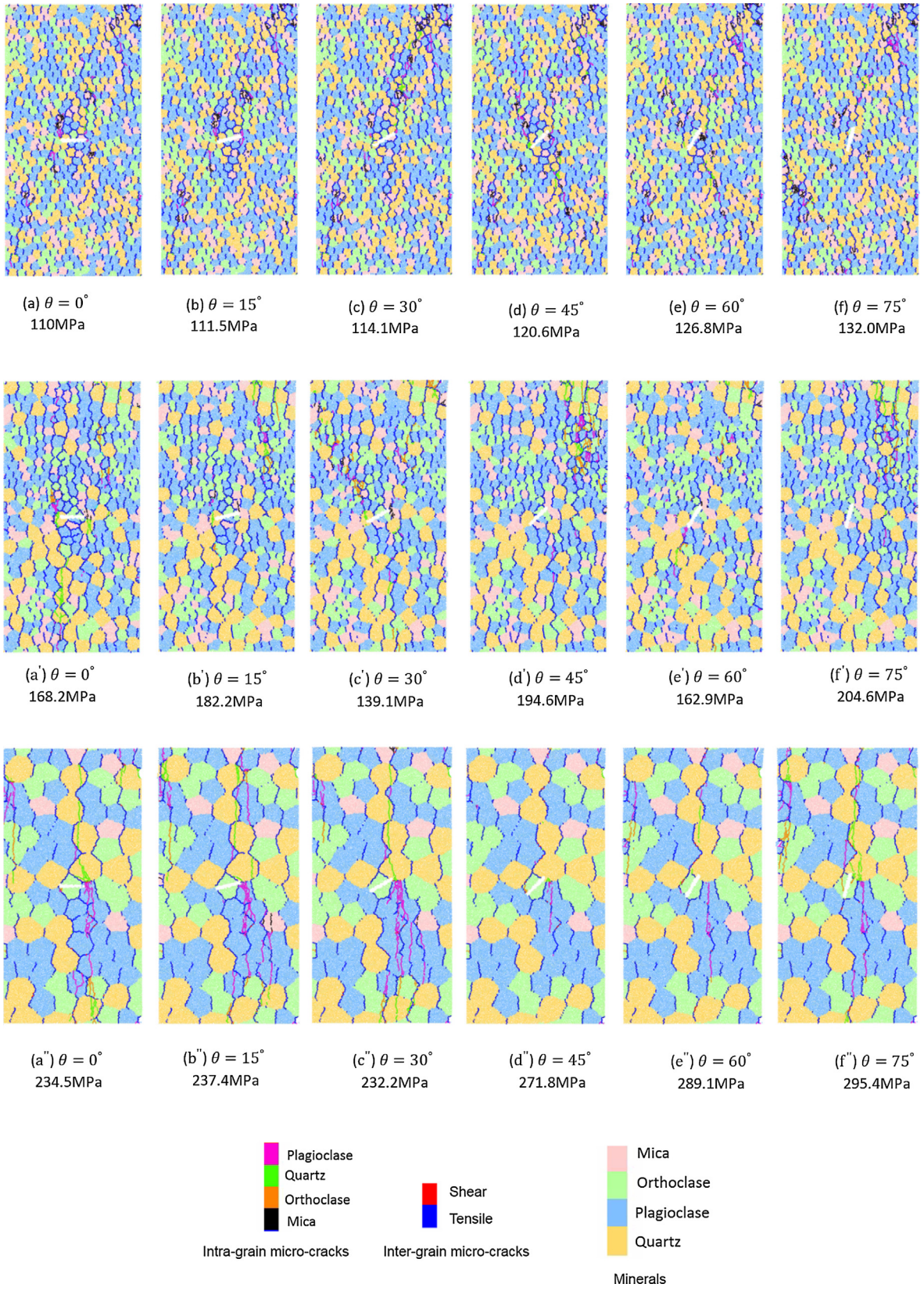

Fig. 14. Final fracture pattern including inter- and intra-grain micro-cracks. The first row (a–f) shows scenario 1, the second row (a′–f′) shows scenario 2, and the third raw (a″–f″) shows scenario 3.

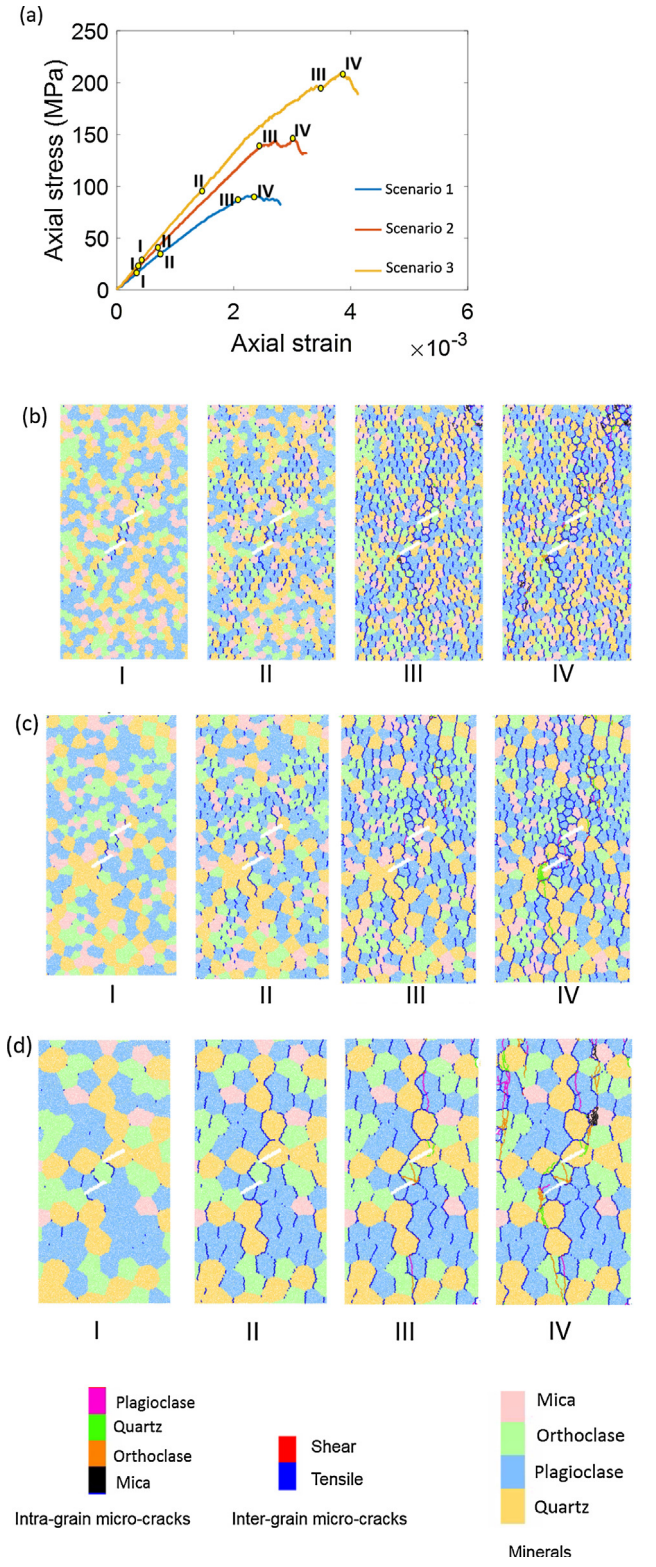

Fig. 15. The macroscopic failure behaviour of double-flawed specimens with $\theta = 30^{Å^\circ}$, (a) complete axial stress-strain curves, (b) scenario 1, (c) scenario 2, (d) scenario 3.

specimens in the same scenario underwent the same elastic behaviour before macroscopic cracks propagated. The results revealed that the specimens exhibited a more brittle failure response with an increase in the flaw inclination angle. As indicated in Fig. 17, the peak strength gradually increased following an increase in the grain size. The flaw inclination angle was also found to influence the peak strength in each scenario. For relatively low inclination angles ($\theta \leq 30^{Å^\circ}$), the peak strength decreased, but increased when θ increased from $45^{Å^\circ}$ to $75^{Å^\circ}$. At $\theta \leq 30^{Å^\circ}$ pre-hardening and post-peak softening behaviours were observed that showed the influence of the flaw inclination angle on the overall macroscopic response of the specimens.

During the design procedure of underground structures, pre-hardening and post-peak softening is of great importance because such behaviour can control the stability or instability of the rock blocks surrounding the tunnel. A more comprehensive understanding of the mechanical and failure behaviours of rock can help designers to better predict the residual behaviour of failed rock blocks. In underground mining for instance, the residual and deformation characteristics of rock are more important than its peak axial strength, because it is crucial in achieving both the stability and optimal support of the tunnel [62].

The results presented in Fig. 18 indicate the coalescence behaviour observed in double-flaw specimens. Both inter- and intra-grain micro-cracks evolved at the onset of failure. As mentioned in Section 3, the inter-grain micro-cracks propagate due to a low tensile strength assigned to the SJ contacts. The linkage of these inter-grain micro-cracks generates macroscopic tensile cracks that exist in both the inner and outer flaw regions. According to Morgan et al. [3], the main reason for shear cracking is the size and shear strength of the grains. Increasing the shear strength of the minerals reduces the number of shear cracks. The strength of the minerals (intra-grain contacts) in the current study's GBM simulations were controlled by the cohesion (C^0) obtained during the calibration procedure. The growth of intra-grain micro-cracks was the result of the gradual degradation of bond cohesion, and finally of the bond-break in the contacts inside the minerals.

At failure point, macroscopic cracks extended from the outer flaws' tips as a result of the combined inter- and intra-grain micro-crack growth. However, different coalescence patterns of pre-existing cracks were obtained when the grain size changed. Fig. 18 shows that scenarios 1 and 2 produced almost identical coalescence patterns. For scenarios 1 and 2, the inter-grain micro-cracks in the bridging zone formed macroscopic cracks leading to the coalescence of pre-existing cracks. The primary macroscopic cracks were fully grown from the tips and surface of the flaws, towards the direction parallel to the maximum axial stress. In scenario 3, at $\theta \leq 30^{Å^\circ}$ the inter-grain micro-cracks developed in orthoclase caused the coalescence of pre-existing cracks. In contrast, at $45^{Å^\circ}$ and $60^{Å^\circ}$relatively few intra-grain micro-cracks were developed in the orthoclase, but the number of micro-cracks increased significantly in the plagioclase and quartz. For specimens with an inclination angel of $75^{Å^\circ}$, however, a combination of plagioclase and orthoclase micro-cracks resulted in the coalescence of pre-existing cracks. Overall, it was observed that compared to scenarios 1 and 2, the large grain size specimens (scenario 3) produced a higher number of intra-grain micro-cracks in the bridging area.

5. Axial strength and damage evolution

In general, intact rock contains various mineral grains that produce different micro-cracking responses when the sample is loaded. The pre-existing flaws and pores may also alter the failure behaviour as well as the axial strength and mechanical properties of intact rocks. In dense, brittle rocks, the boundaries between the minerals' grains are the weakest elements and can be regarded as the major source of micro-crack initiation and propagation. In the GBM approach, these inter-grain contacts are well simulated using the smooth-joint model. However, the micro-cracking response inside the mineral grains is also of great importance as the coalescence and interaction between the inter- and intra-grain contacts control the overall mechanical behaviours of rock. This part analyses the maximum axial strength of the numerical specimens, and their damage evolution responses after complete failure.

Fig. 16. Initiation of primary macroscopic cracks for the specimens with different inclination angles and grain sizes. The crack initiation stress and the peak stress (in parentheses) are given below each numerical specimen. The blue lines indicate the inter-grain micro-cracks. The first row (a–f) shows scenario 1, the second row (a′–f′) shows scenario 2, and the third raw (a″–f″) shows scenario 3. (For interpretation of the references to colour in this figure legend, the reader is referred to the web version of this article.)

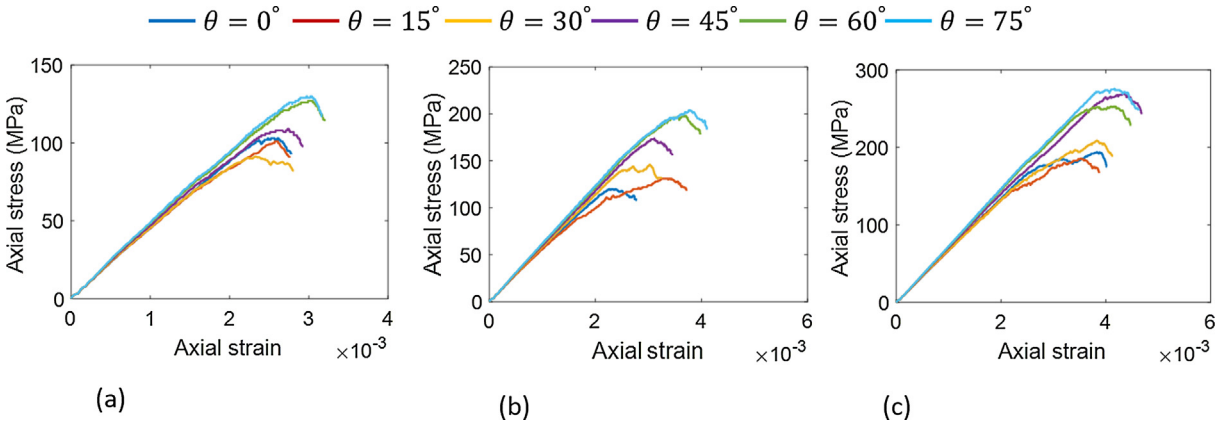

Fig. 17. Complete axial stress-strain curves for double-flawed specimens: (a) scenario 1, (b) scenario 2, (c) scenario 3.

5.1. Maximum axial strength of the specimens

The peak axial stresses obtained from uniaxial compressive tests are depicted in Fig. 19. The peak axial strength in scenario 3 (Fig. 19c) is the highest compared to the other scenarios. The results show that the single-flaw specimens returned a significantly higher peak axial strength compared to the double-flaw specimens, in all scenarios. However, as the flaw inclination angle (θ) increased, the peak axial strength of the double-flaw samples gradually approached that of the single-flaw specimens. For single-flaw specimens, in scenario 1 and 3 the peak axial strength experienced a gradual increase by an increase in θ. In scenario 2, however, we observed a fluctuation in the value of maximum strength, which was attributed to the grain size and the distribution of minerals around the pre-existing crack. The results also revealed that the mineral size changed the inclination angle at which the lowest possible axial strength occurred. For instance, in scenario 1, the lowest axial strength was achieved at $\theta = 30^{Å^\circ}$; in scenarios 2 and 3 the same value was obtained at $\theta = 0^{Å^\circ}$ and $\theta = 15^{Å^\circ}$, respectively.

5.2. Damage evolution inside the minerals

In this study, a proposed cohesive model was assigned to the intra-grain contacts to study the micro-cracking response and the microscopic and macroscopic damage evolution mechanisms in the minerals. When the intra-grain contact reached their yielding regions, they exhibited softening behaviours before being completely broken. By monitoring the damage parameter (D) defined in the cohesive model (Eq. (7)), the damage state of the intra-grain contacts could be numerically evaluated. This lets us investigate the influence of the grain size on the microscopic softening responses of the intra-grain contacts in their post-peak regions, for both single- and double-flaw specimens. The evolution of damage in single- and double-flaw specimens at failure point, with various grain sizes, is illustrated in Figs. 20 and 21, respectively.

The results showed that the grain size had a significant influence on the damage mechanisms and softening responses of the intra-grain contacts. For the both single- and double-flaw specimens, the numerical models with calibrated grain sizes showed almost no softening intra-grain contacts (Figs. 20a and 21a). In fact, the contacts, coming to their failure point, reproduced their softening behaviour very quickly, and broke more quickly. In comparison, the numerical specimens with medium and large grain sizes showed more softening contacts (Figs. 20b, c and 21b, c). Moreover, we observed that, for all grain sizes, the macroscopic cracks passed through a mineral and initiated the intra-grain micro-cracks in the stress concentration zone. For scenarios 2 and 3, the number of particles—and consequently the number of contacts forming a mineral is higher than the number of particles and contacts in scenario 1. A higher number of particles in the grains increased the possibility that the intra-grain contacts would display their softening responses ($0 < D < 1.0$) without being completely damaged. In the softening contacts, the stress was gradually reduced, allowing the contacts to show more resistance against failure. By increasing the number of softening contacts within the grains (or increasing the grain size), the maximum strength of the numerical specimen was significantly increased. As mentioned in Section 4, the specimens tend to produce intact (or flaw-less) rock behaviour at high inclination angles. Consequently, the failure behaviour of the specimens is dominated by the bond-break in the inter-grain contacts. The same behaviour was also observed for scenario 1 and scenario 2 at $\theta \geq 60^{Å^\circ}$ where the number of either damaged or softening contacts experienced a significant reduction. In double-flaw specimens, both softening ($0.0 < D < 1.0$) and failed contacts ($D = 1.0$) contribute to the coalescence of pre-existing cracks.

6. Conclusions

Discontinuities and pre-existing defects profoundly influence the failure behaviour of rock in engineering projects such as tunnelling and underground mining. In this research, the PFC-GBM was used to investigate the influence of grain size distribution on the mechanical and cracking responses of Aue granite rock specimens containing a single and double flaw under uniaxial compression. A cohesive model was developed and implemented in discrete element codes (PFC2D) to simulate the failure behaviour of intra-grain micro-cracks. The smooth-joint model was adopted to mimic the failure responses of grain boundaries. The proposed GBM framework was successfully calibrated against the uniaxial compression and Brazilian testing. Three different scenarios were examined, to investigate the influence of grain size on cracking, strength, and damage behaviour of the numerical specimens.

For both single-and double-flaw specimens, the strength of the material increased significantly with an increase in mineral size. The numerical simulation showed that the primary macroscopic cracks initiated from the surface or tip of a flaw, as a direct consequence of bond-break in the inter-grain contacts. These macroscopic cracks developed along a meandering path created by the boundaries between the grains, leading to a jagged-shaped macroscopic crack around the pre-existing cracks. For low-flaw inclination angles, the inter-grain micro-cracks initiated from the middle portion of the flaw. In the samples with high inclination angles, the inter-grain micro-cracks shifted towards the tips of the flaws. This was not the case for the samples with large grain sizes, as the location of flaw tips was highly controlled by the size of minerals. This lead to the initiation of inter-grain micro-cracks around the tip area for all inclination angles. For double-flaw specimens with large grain size distributions (scenario 3), the bridging zone was generated inside orthoclase. This mineral had a dominant influence on the micro-cracking and coalescence responses in the inner tip region.

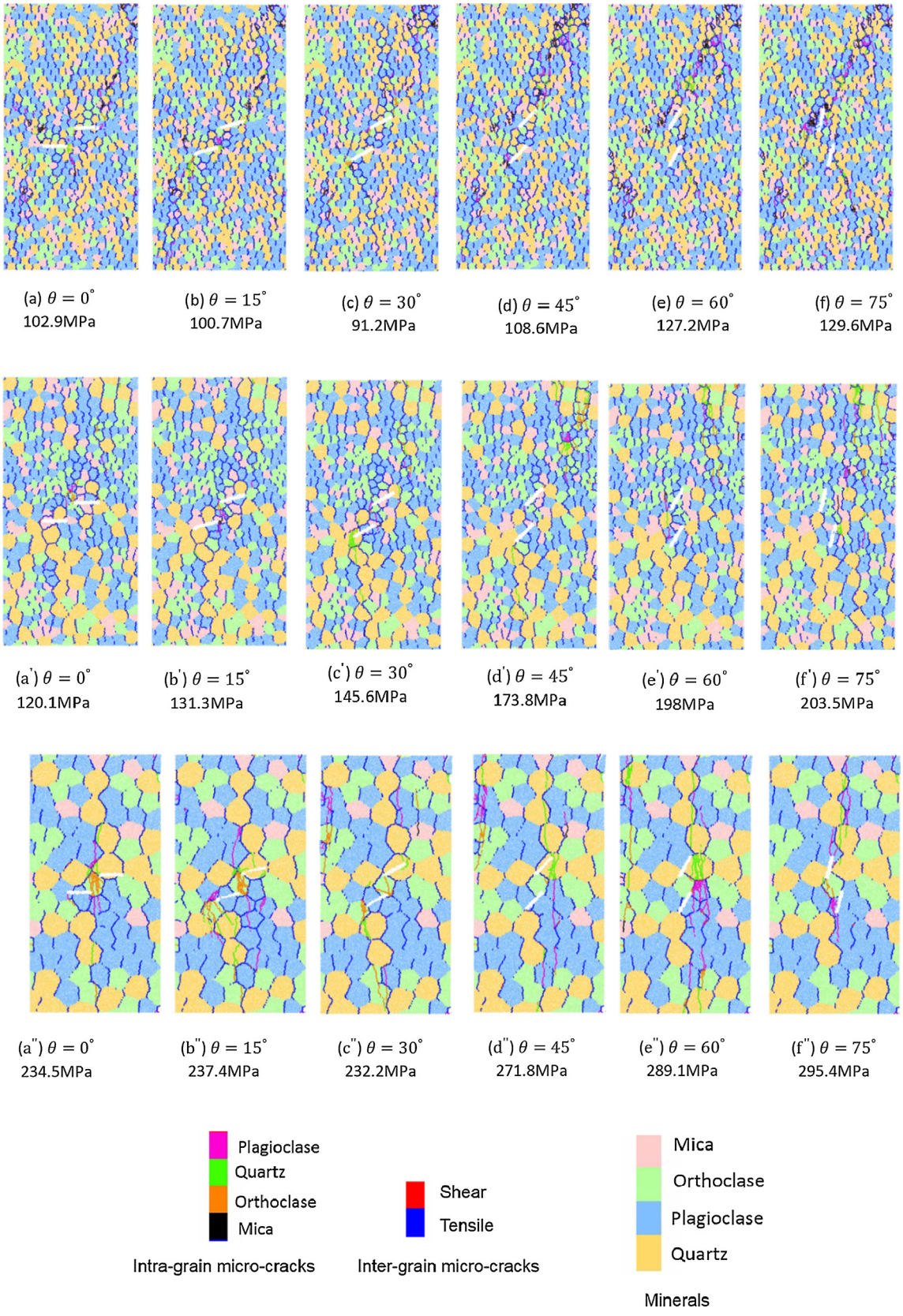

Fig. 18. Final fracture pattern including inter- and intra-grain micro-cracks. The first row (a–f) shows scenario 1, the second row (a′–f′) shows scenario 2, and the third raw (a″–f″) shows scenario 3.

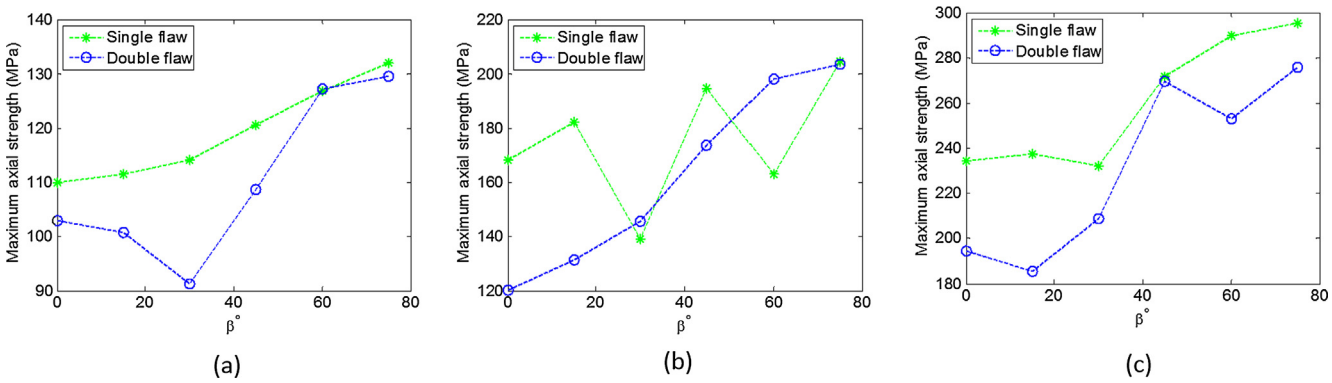

Fig. 19. Maximum axial strength of the single- and double-flawed specimens with different mineral size (a) scenario 1, (b) scenario 2, (c) scenario 3.

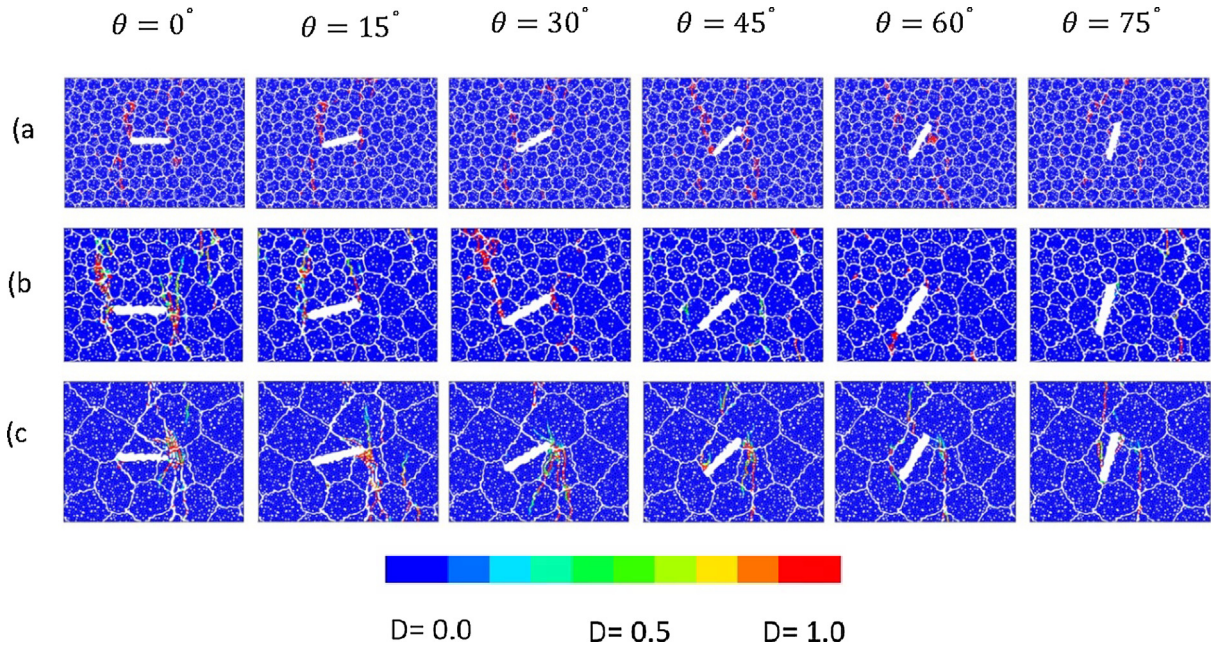

Fig. 20. Damage evolution of intra-grain contacts at peak stress for single-flawed specimens (a) scenario 1, (b) scenario 2, (c) scenario 3.

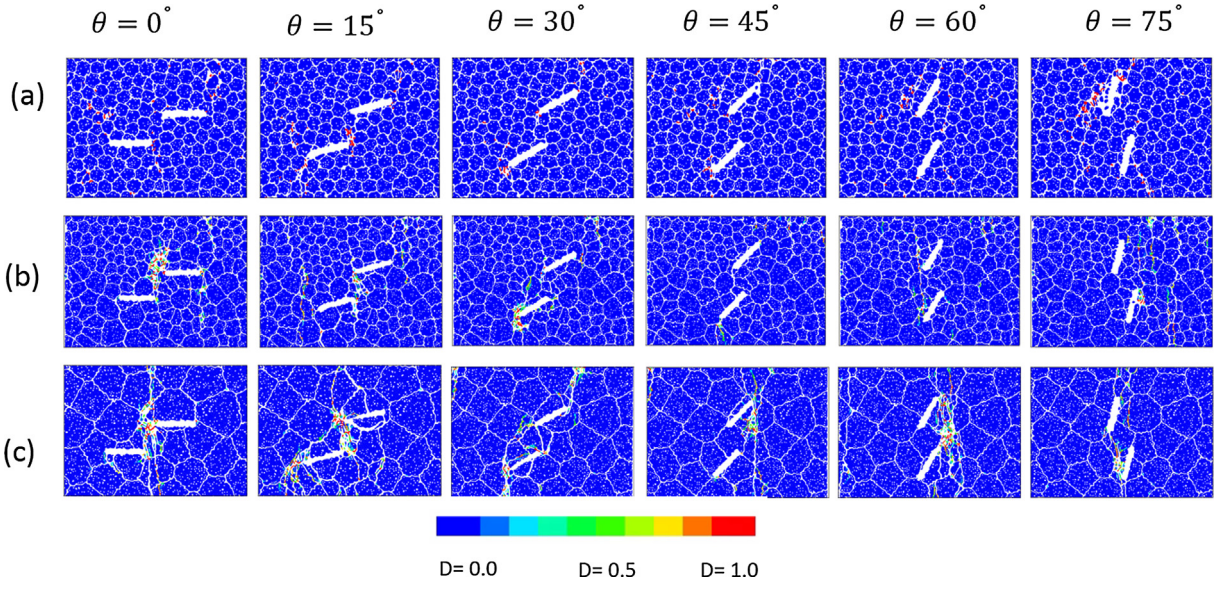

Fig. 21. Damage evolution of intra-grain contacts at peak stress for double-flawed specimens (a) scenario 1, (b) scenario 2, (c) scenario 3.

This study showed that two major factors are important in the macroscopic responses of the material: The grain size and the inclination angle of pre-existing cracks. In double-flaw specimens, the coalescence of pre-existing cracks occurred due to the linkage of inter- and intra-grain micro-cracks and production of softening contacts when the flaws have low inclination angles. By increasing the inclination angle, the number of intra-grain micro-cracks and softening contacts in the bridging area reduced significantly, and the coalescence occurred as a result of inter-grain micro-crack propagation.

Acknowledgment

The cohesive model used in this study was formulated based on a generic framework by Giang D. Nguyen (University of Adelaide) & Ha H. Bui (Monash University), with Giang D. Nguyen's help in the development and revision of the model. Critical comments by Giang D. Nguyen to improve the manuscript are acknowledged. The first author thanks Mr Sacha Emam from Itasca Consulting group for his invaluable help and comments during implementation and verification of the model in PFC software. Professional editor, Leticia Mooney, provided copyediting and proofreading services, according to the guidelines laid out in the university-endorsed national 'Guidelines for editing research theses'.

References

[1] Taheri A, Tani K. Assessment of the stability of rock slopes by the slope stability rating classification system. Rock Mech Rock Eng 2010;43:321–33.
[2] Yin P, Wong RHC, Chau KT. Coalescence of two parallel pre-existing surface cracks in granite. Int J Rock Mech Min Sci 2014;68:66–84.
[3] Morgan SP, Johnson CA, Einstein HH. Cracking processes in Barre granite: fracture process zones and crack coalescence. Int J Fract 2013;180:177–204.
[4] Farahmand K, Vazaios I, Diederichs MS, Vlachopoulos N. Investigating the scale-dependency of the geometrical and mechanical properties of a moderately jointed rock using a synthetic rock mass (SRM) approach. Comput Geotech 2018;95:162–79.
[5] Bahrani N, Kaiser PK. Numerical investigation of the influence of specimen size on the unconfined strength of defected rocks. Comput Geotech 2016;77:56–67.
[6] Mayer JM, Stead D. Exploration into the causes of uncertainty in UDEC Grain Boundary Models. Comput Geotech 2017;82:110–23.
[7] Diaz MB, Jung SG, Zhuang L, Kim KY, Yeom S, Shin HS. Effect of Cleavage Anisotropy on Hydraulic Fracturing Behavior of Pocheon granite. In: 50th US Rock Mechanics/Geomechanics Symposium. American Rock Mechanics Association. Houston, Texas; 2016.
[8] Brace WF, Bombolakis EG. A note on brittle crack growth in compression. J Geophys Res 1963;68:3709–13.
[9] Horii H, Nemat-Nasser S. Compression-induced microcrack growth in brittle solids: axial splitting and shear failure. J Geophys Res Solid Earth 1985;90:3105–25.
[10] Shen B, Stephansson O, Einstein Herbert H, Ghahreman B. Coalescence of fractures under shear stresses in experiments. J Geophys Res Solid Earth 1995;100:5975–90.
[11] Bobet A, Einstein HH. Fracture coalescence in rock-type materials under uniaxial and biaxial compression. Int J Rock Mech Min Sci 1998;35:863–88.
[12] Wong RHC, Chau KT. Crack coalescence in a rock-like material containing two cracks. Int J Rock Mech Min Sci 1998;35:147–64.
[13] Li Y-P, Chen L-Z, Wang Y-H. Experimental research on pre-cracked marble under compression. Int J Solids Struct 2005;42:2505–16.
[14] Miller JT, Einstein HH. Crack Coalescence Tests on Granite. In: The 42nd US Rock Mechanics Symposium (USRMS). American Rock Mechanics Association, San Francisco, California; 2008.
[15] Zhou XP, Cheng H, Feng YF. An experimental study of crack coalescence behaviour in rock-like materials containing multiple flaws under uniaxial compression. Rock Mech Rock Eng 2014;47:1961–86.
[16] Zhang X-P, Wong LNY. Cracking processes in rock-like material containing a single flaw under uniaxial compression: a numerical study based on parallel bonded-particle model approach. Rock Mech Rock Eng 2012;45:711–37.
[17] Cundall PA, Strack ODL. A discrete numerical model for granular assemblies. Géotechnique 1979;29:47–65.
[18] Karatela E, Taheri A. Three-dimensional hydro-mechanical model of borehole in fractured rock mass using discrete element method. J Nat Gas Sci Eng 2018;53:263–75.
[19] Karatela E, Taheri A, Xu C, Stevenson G. Study on effect of in-situ stress ratio and discontinuities orientation on borehole stability in heavily fractured rocks using discrete element method. J Petrol Sci Eng 2016;139:94–103.
[20] Zhang X-p, Zhang Q, Wu S. Acoustic emission characteristics of the rock-like material containing a single flaw under different compressive loading rates. Comput Geotech 2017;83:83–97.
[21] Cundall P. A computer model for simulating progressive, large scale movements in blocky rock systems. In: International symposium on rock fracture. Nancy, France; 1971.
[22] Kazerani T, Zhao J. Micromechanical parameters in bonded particle method for modelling of brittle material failure. Int J Numer Anal Meth Geomech 2010;34:1877–95.
[23] Bahaaddini M, Sharrock G, Hebblewhite B. Numerical direct shear tests to model the shear behaviour of rock joints. Comput Geotech 2013;51:101–15.
[24] Mehranpour MH, Kulatilake PHSW, Xingen M, He M. Development of new three-dimensional rock mass strength criteria. Rock Mech Rock Eng 2018.
[25] Liu J, Wang J, Wan W. Numerical study of crack propagation in an indented rock specimen. Comput Geotech 2018;96:1–11.
[26] Zhang X-P, Wong LNY. Crack initiation, propagation and coalescence in rock-like material containing two flaws: a numerical study based on bonded-particle model approach. Rock Mech Rock Eng 2013;46:1001–21.
[27] Lee H, Jeon S. An experimental and numerical study of fracture coalescence in pre-cracked specimens under uniaxial compression. Int J Solids Struct 2011;48:979–99.
[28] Huang Y-H, Yang S-Q, Ranjith PG, Zhao J. Strength failure behavior and crack evolution mechanism of granite containing pre-existing non-coplanar holes: experimental study and particle flow modeling. Comput Geotech 2017;88:182–98.
[29] Diederichs MS. Manuel Rocha medal recipient rock fracture and collapse under low confinement conditions. Rock Mech Rock Eng 2003;36:339–81.
[30] Potyondy D. A grain-based model for rock: approaching the true microstructure. In: Proc rock mech in the Nordic countries; 2010. 10p.
[31] Bahrani N, Kaiser PK, Valley B. Distinct element method simulation of an analogue for a highly interlocked, non-persistently jointed rockmass. Int J Rock Mech Min Sci 2014;71:117–30.
[32] Bewick RP, Kaiser PK, Bawden WF, Bahrani N. DEM simulation of direct shear: 1. Rupture under constant normal stress boundary conditions. Rock Mech Rock Eng 2014;47:1647–71.
[33] Peng J, Wong LNY, Teh CI. Effects of grain size-to-particle size ratio on micro-cracking behavior using a bonded-particle grain-based model. Int J Rock Mech Min Sci 2017;100:207–17.
[34] Itasca. PFC (Particle Flow Code) Version 5.0. Itasca Consulting Group, Minneapolis, USA; 2016.
[35] Lan H, Martin CD, Hu B. Effect of heterogeneity of brittle rock on micromechanical extensile behavior during compression loading. J Geophys Res: Solid Earth 2010;115.
[36] Le LA, Nguyen GD, Bui HH, Sheikh AH, Kotousov A, Khanna A. Modelling jointed rock mass as a continuum with an embedded cohesive-frictional model. Eng Geol 2017;228:107–20.
[37] Nguyen NHT, Bui HH, Nguyen GD, Kodikara J. A cohesive damage-plasticity model for DEM and its application for numerical investigation of soft rock fracture properties. Int J Plast 2017;98:175–96.
[38] Nguyen NHT, Bui HH, Nguyen GD, Kodikara J, Arooran S, Jitsangiam P. A thermodynamics-based cohesive model for discrete element modelling of fracture in cemented materials. Int J Solids Struct 2017;117:159–76.
[39] Le LA, Nguyen GD, Bui HH, Sheikh AH, Kotousov A, Khanna A. Localised failure mechanism as the basis for constitutive modelling of geomaterials. Int J Eng Sci; 2018 (in press).
[40] Potyondy D, Cundall P. A bonded-particle model for rock. Int J Rock Mech Min Sci 2004;41:1329–64.
[41] Hofmann H, Babadagli T, Yoon JS, Zang A, Zimmermann G. A grain based modeling study of mineralogical factors affecting strength, elastic behavior and micro fracture development during compression tests in granites. Eng Fract Mech 2015;147:261–75.
[42] Liu G, Cai M, Huang M. Mechanical properties of brittle rock governed by micro-geometric heterogeneity. Comput Geotech 2018.
[43] Hofmann H, Babadagli T, Zimmermann G. A grain based modeling study of fracture branching during compression tests in granites. Int J Rock Mech Min Sci 2015;77:152–62.
[44] Nicksiar M, Martin CD. Factors affecting crack initiation in low porosity crystalline rocks. Rock Mech Rock Eng 2014;47:1165–81.
[45] Potyondy D. PFC2D Grain-Structure Generator. PFC2D Example on Itasca website, Itasca Consulting Group, Inc, Minneapolis, MN, May 28. 2010.
[46] Bewick RP, Kaiser PK, Bawden WF. Shear rupture under constant normal stiffness boundary conditions. Tectonophysics 2014;634:76–90.
[47] Yoon JS, Zang A, Stephansson O. Simulating fracture and friction of Aue granite under confined asymmetric compressive test using clumped particle model. Int J Rock Mech Min Sci 2012;49:68–83.
[48] Zang A. Akustische Emissionen beim Sprödbruch von Gestein. Habilitationsschrift, Scientific Technical Report STR97/19. Univ Potsdam, Germany; 1997.
[49] Zang A, Wagner FC, Stanchits S, Janssen C, Dresen G. Fracture process zone in granite. J Geophys Res Solid Earth 2000;105:23651–61.
[50] Wasantha PLP, Ranjith PG, Zhao J, Shao SS, Permata G. Strain rate effect on the mechanical behaviour of sandstones with different grain sizes. Rock Mech Rock Eng 2015;48:1883–95.
[51] Li XF, Zhang QB, Li HB, Zhao J. Grain-Based Discrete Element Method (GB-DEM) modelling of multi-scale fracturing in rocks under dynamic loading. Rock Mech Rock Eng 2018;51:3785–817.
[52] Wong LNY, Peng J, Teh CI. Numerical investigation of mineralogical composition effect on strength and micro-cracking behavior of crystalline rocks. J Nat Gas Sci Eng 2018;53:191–203.
[53] Diederichs MS. Instability of hard rockmasses, the role of tensile damage and relaxation. UWSpace; 2000.
[54] Wong LNY, Einstein HH. Systematic evaluation of cracking behavior in specimens containing single flaws under uniaxial compression. Int J Rock Mech Min Sci 2009;46:239–49.

[55] Jin J, Cao P, Chen Y, Pu C, Mao D, Fan X. Influence of single flaw on the failure process and energy mechanics of rock-like material. Comput Geotech 2017;86:150–62.
[56] Diederichs MS. The 2003 Canadian Geotechnical Colloquium: Mechanistic interpretation and practical application of damage and spalling prediction criteria for deep tunnelling. Can Geotech J 2007;44:1082–116.
[57] Gui YL, Zhao ZY, Ji J, Wang XM, Zhou KP, Ma SQ. The grain effect of intact rock modelling using discrete element method with Voronoi grains. Géotechnique Lett 2016;6:136–43.
[58] Kranz RL. Microcracks in rocks: a review. Tectonophysics 1983;100:449–80.
[59] Tapponnier P, Brace WF. Development of stress-induced microcracks in Westerly Granite. Int J Rock Mech Min Sci Geomech Abstracts 1976;13:103–12.
[60] Akesson U, Hansson J, Stigh J. Characterisation of microcracks in the Bohus granite, western Sweden, caused by uniaxial cyclic loading. Eng Geol 2004;72:131–42.
[61] Tang CA, Liu H, Lee PKK, Tsui Y, Tham LG. Numerical studies of the influence of microstructure on rock failure in uniaxial compression — Part I: effect of heterogeneity. Int J Rock Mech Min Sci 2000;37:555–69.
[62] Gao F, Kang H. Experimental study on the residual strength of coal under low confinement. Rock Mech Rock Eng 2017;50:285–96.

Appendix E (Paper 5)

A cohesive grain based model to simulate shear behaviour of rock joints with asperity damage in polycrystalline rock

Saadat M, Taheri A. (2019) A cohesive grain based model to simulate shear behaviour of rock joints with asperity damage in polycrystalline rock. *Computers and Geotechnics (UNDER REVIEW)*

Statement of Authorship

Title of Paper	A cohesive grain based mode to simulate shear behaviour of rock joints with asperity damage in polycrystalline rock
Publication Status	☐ Published ☐ Accepted for Publication ✓ Submitted for Publication ☐ Unpublished and Unsubmitted work written in manuscript style
Publication Details	Saadat M, Taheri A. (2019) A cohesive grain based mode to simulate shear behaviour of rock joints with asperity damage in polycrystalline rock. Computers and Geotechnics (Under Review)

Principal Author

Name of Principal Author (Candidate)	Mahdi Saadat		
Contribution to the Paper	Developed and wrote the formulation of the cohesive model Conducted the numerical modelling on different granitic rocks Analysed the numerical results Wrote the entire manuscript		
Overall percentage (%)	80%		
Certification:	This paper reports on original research I conducted during the period of my Higher Degree by Research candidature and is not subject to any obligations or contractual agreements with a third party that would constrain its inclusion in this thesis. I am the primary author of this paper.		
Signature		Date	07 August 2019

Co-Author Contributions

By signing the Statement of Authorship, each author certifies that:

i. the candidate's stated contribution to the publication is accurate (as detailed above);
ii. permission is granted for the candidate in include the publication in the thesis; and

iii. the sum of all co-author contributions is equal to 100% less the candidate's stated contribution.

Name of Co-Author	Dr Abbas Taheri		
Contribution to the Paper	Supervision of the technical work, revision of the manuscript		
Signature		Date	07 August 2019

End of the document

A cohesive grain based model to simulate shear behaviour of rock joints with asperity damage in polycrystalline rock

Mahdi Saadat*, Abbas Taheri

School of Civil, Environmental and Mining Engineering, The University of Adelaide, Australia

Corresponding author:

Mahdi Saadat*

Mailing address: School of Civil, Environmental and Mining Engineering, The University of Adelaide, Australia

Email: mahdi.saadat@adelaide.edu.au

Tel: +61 831 31673

Mobile phone: +61498812260

Abstract

A cohesive grain based model is proposed to simulate the fracture behaviour of polycrystalline rocks. The model was employed to characterize the cracking response of both inter- and intra-grain contacts in the grain based model (GBM). The model was implemented in distinct element codes and its ability to mimic the mechanical and failure behaviour of polycrystalline rocks was demonstrated through calibration of several granitic rocks including Adelaide black granite, Eibenstock II granite, and Aue granite. The calibrated model of Aue granite was used to assess the effect of joint roughness coefficient (JRC) on asperity damage and shear mechanism of rock joints (i.e. grain crushing) under constant normal load (CNL) and constant normal stiffness (CNS) conditions. The bond-break in intra-grain contacts contributed to asperity damage in form of grain crushing. The numerical observations showed that under CNS condition asperity damage increased with increasing initial normal stress and JRC, and rough rock joints exhibited more dilative response.

Keywords: Cohesive grain based model; Polycrystalline rocks; Rock joint; CNS condition

1- Introduction

The focus of this study is on the brittle failure of polycrystalline rocks (i.e. granite) using cohesive based distinct element method (DEM). Various parameters control the mechanical and damage response of crystalline rocks, such as microstructural properties of grains (i.e. shape and size), mineral constituents, pre-existing defects, cavities, etc [1-4].

The macroscopic fracture process is the dominant damage mechanism controlling the mechanical response and the integrity of crystalline rocks [5]. It has been repeatedly observed in the experimental and numerical studies that the microstructural characteristics of crystalline rocks control the micro-cracking process of the mineral itself, and hence the overall macroscopic response of rock including strength, deformability, and fracture pattern [1, 3, 6-10]. At microscopic scale, the failure process of brittle rocks involves initiation, extension, and acumulation of inter- and intra-grain micro-cracks [2, 10]. Therefore, an appropriate description of microstructural properties and the interaction between polycrystalline minerals is essential for understanding the macroscopic mechanical behaviour of brittle rocks [11].

The presence of natural discontinuities around orebodies can have a profound influence on the stability and safety of mining structures [12]. Therefore, an appropriate assessment of rock joint shear behaviour is necessary for the design and construction procedure of mining

excavations. The experimental observations revealed that, in polycrystalline rocks, the macroscopic shear behaviour of rock joint highly depends on the micro-texture of rock specimen [13]. Thus, not only the surface roughness characteristics [14-16], but also the microstructural properties of the host rock should be taken into account for evaluating the rock fall hazards caused by the shear failure of rock joints [13, 17, 18]. In conventional rock joint studies, constant normal load (CNL) boundary condition was used to investigate the shear mechanism where the normal stress remains constant during the direct shear test, and rock joint surface dilates freely during shearing [19]. However, in underground mining, the normal stress may vary due to restriction provided by neighbouring rock blocks, which represent a constant normal stiffness (CNS) condition [19-23]. The importance of CNS condition in field situation has been emphasised by several research scholars (e.g. Indraratna et al. [19], Park et al. [20], Shrivastava and Rao [24]). Therefore, apart from microstructural properties of crystalline rock, the influence of CNS condition is essential in the study of rock joint shear behaviour.

As an alternative to experimental tests, the grain based model (GBM) employs DEM principles to produce numerical crystalline specimens with similar microstructural properties to the physical specimen, which can mimic the cracking behaviour of inter- and intra-grain contacts [25, 26]. Many research scholars employed advanced numerical techniques to characterise the microstructural behaviour of crystalline rocks (e.g. Bahrani and Kaiser [8], Bewick et al. [27], Li et al. [1], Liu et al. [2]). The experimental observations revealed that in physical crystalline specimen the bond breakage occurs due to the weakening of the cohesional component of the minerals and grain interfaces in a gradual process [10, 28]. The parallel-bond model (PBM) [29], and the smooth joint model (SJM) [30] are the most common contact models used in PFC-GBM research [7, 25, 31] to simulate the fracture behaviour of crystalline rocks. PBM and SJM, however, are incapable of reproducing the gradual softening response at the contact level. In fact, in PBM, when the contact forces exceed the bond strength, bond-break occurs, which results in an abrupt reduction of contact forces to zero [29]. Similarly in SJM, while the contact is broken in tension, both normal and shear forces reduce abruptly to zero [30]. If SJM contact is in the shear state, a frictional force-displacement response with zero dilation is resulted [30]. Therefore, neither PBM nor SJM can exhibit a cohesive softening response after the yield limit. Notice that using PBM and SJM as GBM contact models may demonstrate satisfactory match with the physical specimen (e.g. Hofmann et al. [7], Bahrani et al. [31], and Liu et al. [2]), and can still be employed in GBM studies. However, augmenting the force-displacement laws of the PBM and SJM with a gradual softening response, which observed in the experimental tests

[5, 10], allows us to achieve a more realistic phenomenological constitutive model for simulating the cracking response of crystalline rocks.

In our previous numerical research, we developed a DEM based cohesive contact model to study the influence of rock texture on the macroscopic damage and mechanical response of granitic rock using PFC-GBM approach [32]. The cohesive contact model (CCM) was implemented in PFC2D, and assigned to the intra-grain contacts. We used the SJM as inter-grain contact model in our previous research [32]. In the present study, we implemented the DEM based cohesive model in the force-displacement law of the SJM to achieve a cohesive interface model, which we denote as cohesive SJM (CSJM). We applied CCM and CSJM on the intra- and inter-grain contacts, respectively. The new PFC-GBM framework was calibrated against the uniaxial compressive and Brazilian tensile tests performed on Aue granite. The micro-cracking behaviour of the model was analysed according to the damage response of the inter- and intra-grain contact. The numerical models demonstrated a good match with the experimental counterparts. To further validate the model, the macroscopic cracking response of asymmetric uniaxial test conducted on Aue granite was performed, and the results were compared with the laboratory observations.

To the best of author's knowledge, there is no numerical study to examine the potential of PFC-GBM approach in the assessment of rock joint shear behaviour. In the present study, we employed the proposed cohesive GBM to numerically investigate the shear behaviour of rock joints with a focus on the micro-texture of asperities. To do so, we imported the geometrical characteristics of three different rock joints with different joint roughness coefficients (JRC) into the numerical models. After that, numerical direct shear tests under constant normal load (CNL), and constant normal stiffness (CNS) were conducted.

2- Constitutive relationships of the contacts

In the present study, a cohesive, contact model (CCM) developed by Saadat and Taheri [32] was employed for simulating the fracture behaviour polycrystalline rock. There are various DEM-based cohesive models available in the literature (e.g. Le et al. [33], Nguyen et al. [34], Nguyen et al. [35]; and Le et al. [36]). However, we simplified the relationships to reduce the calibration procedure of GBM approach. In addition, a simple cohesive contact model reduces the computational demand. The formulations of the model can be found in detail in our previous

research [32]. In this section, the microproperties of the model and force-displacement law are briefly described.

The relative displacement $\boldsymbol{u}(u_n, u_s)$ of the DEM contacts was decomposed into an elastic and plastic components to account for reversible and irreversible displacements:

$$\boldsymbol{u} = \boldsymbol{u}^e + \boldsymbol{u}^p \tag{1}$$

The contact normal and shear stresses are linked to their corresponding relative displacements and can be calculated by:

$$\sigma_n = k_n^0(u_n - u_n^p) \tag{2}$$

$$\sigma_s = k_s^0(u_s - u_s^p) \tag{3}$$

where σ_n and σ_s are normal and shear stresses in the bonding contacts; u_n and u_n^p are the total and plastic normal displacements; u_s and u_s^p are the total and plastic shear displacements; and k_n^0 and k_s^0 are the normal and shear stiffnesses, respectively.

The model features a yield function to account for mixed-mode failure:

$$F(\sigma_n, \sigma_s, C) = \sigma_s + \mu\sigma_n - C = 0 \tag{4}$$

where μ is the friction coefficient of the contact and C is defined as:

$$C = C^0 e^{-\kappa u^p} \tag{5}$$

In Eq. 5, C^0 is the initial bond cohesion, κ is the softening parameter, and u^p is the contact's accumulated plastic displacement, which can be calculated from its increments, defined as:

$$du^p = \sqrt{(du_n^p)^2 + (du_s^p)^2} \tag{6}$$

A damage parameter ($0 \leq D \leq 1$) can be defined to measure the degree of damage in the cohesive contacts:

$$D = \frac{C^0 - C}{C^0} = 1 - e^{-\kappa u^p} \tag{7}$$

The damage parameter introduced in Eq. 7 was included in the implementation algorithm which enabled PFC2D to graphically present the damage response in DEM contacts. When the contact is fully bonded the damage parameter takes a value of $D = 0.0$, whereas a completely

damaged contact returns $D = 1.0$. During the contact softening, the associative damage will be $0 < D < 1$.

In DEM, simulating microscopic dilation response requires incorporating the microstructural characteristics of the material in the model, which is a difficult task to achieve [34]. Alternatively, the dilative response of cohesive contacts was taken into account using the following non-associative flow rule:

$$G(\sigma_n, \sigma_s) = \sigma_s + \beta\sigma_n \tag{8}$$

Fig 1 illustrates the behaviour of DEM contact in mode I (tension) and II (shear). The cohesive model can be either employed as inter-grain or intra-grain contact model. The intra-grain contact model was called CCM, and the microproperties of the model contained a subscript of CCM (e.g. C^0_{CCM}). The inter-grain contact model was called cohesive, smooth joint model (CSJM), and the microproperties of the model contained a subscript of CSJM (e.g. C^0_{CSJM}). The CSJM is a modified version of the smooth joint model (SJM). The details of the SJM can be found in [30] and [37]. The microproperties of the model include C^0, μ, κ, β, k_n^0, and k_s^0. Notice that for intra-grain contacts, we employed contact deformability method [29], which links the contact stiffnesses to its Young's modulus ($\bar{E}$). The details of identifying $\bar{E}$ and contact stiffnesses can be found in our previous study [32].

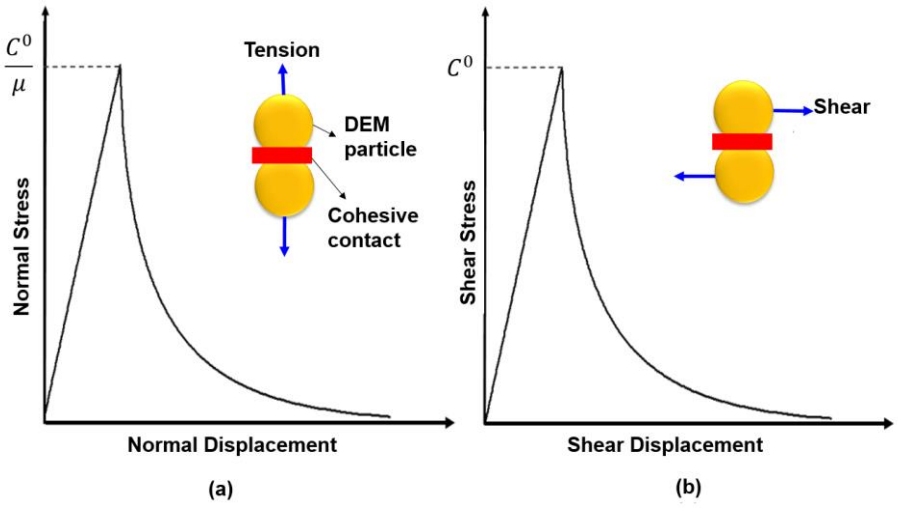

Fig 1 The behaviour of DEM contacts in (a) tension, and (b) shear.

The CCM and CSJM are separately solved in the simulations. In DEM modelling, the calculations alternate between the application of Newton's second law to the DEM balls and a force-displacement constitutive model at the contacts. The motion of DEM particles is

determined by Newton's second law, while the constitutive model is used to update the contact forces arising from the relative motion of the balls at the contact locations [30]. When updating the ball kinematics or when solving the constitutive laws at the contacts at a given time, each ball or each contact is processed independently, therefore any modification in the contact force, for instance, is not propagated instantaneously and does not affect neighbouring contacts within the same iteration. Instead, any change in the system will potentially alter the model state for the next iteration. In the GBM framework, the forces arising from the relative motion of inter-grain contacts are updated via the CSJM, while the forces arising from the relative motion of intra-grain contacts are updated via the CCM.

3- Validation of cohesive GBM

In GBM approach, a random generation algorithm is required to construct the polygonal microstructure of the model. In this section, the microstructural properties of three different granitic rocks were incorporated into the GBM to generate different numerical specimens. We used an algorithm proposed by Potyondy [25] for random generation of polycrystalline microstructures, which has been extensively used in the previous GBM studies (e.g. Saadat and Taheri [32], Hofmann et al. [7]). The complete details of this algorithm can be found in [25]. In section 3-1, we will introduce a comprehensive calibration procedure to analyse the significance of cohesive modelling. We will also demonstrate in section 3-1 that non-cohesive GBM (e.g. PBM-SJM) is unable to reproduce the macroscopic behaviour (i.e. load-displacement curve) of brittle rock (e.g. granite). In section 3-2, the ability of the model in reproducing the macroscopic behaviour of Eibenstock II granite in UCS, Brazilian, and triaxial tests with different confining pressures (σ_3) will be investigated. In section 3-3, we will compare the numerical fracture pattern of Aue granite under asymmetric uniaxial and confining tests with their experimental counterparts.

3-1 Calibration of Adelaide black granite

According to the previous experimental and numerical investigations the polycrystalline rocks exhibit a gradual cohesive-frictional damage response during failure [10, 28]. This gradual damage development in polycrystalline rock is more pronounced under three-point bending tests on single-edge-notched beam in which the global load-displacement curve exhibits obvious softening response [38]. There are experimental evidences from three-point bending (TPB) tests on the single-edge-notched beam that the development of fracture process zone (FPZ) in polycrystalline rock (e.g. granite) is attributed to propagation of macroscopic tensile

cracks, which in turn is the result of the progressive coalescence of micro-cracks along cleavage planes in minerals [38]. Therefore, it is needed to incorporate a softening response in the constitutive relationships of DEM contacts to achieve a more realistic numerical outcome. Notice that non-cohesive contact models (e.g. PBM) are incapable of reproducing the gradual softening behaviour of soft rock in three-point bending test of rock [34]. In this section, we demonstrate a process for calibration of Adelaide black granite using three experimental tests: uniaxial compression test, Brazilian tensile strength test, and three-point bending tets.

The thin section analysis of experimental specimen showed that Adelaide black granite consists of 45-50% plagioclase, 20-25% pyroxene, 10% biotite, 5% amphibole, 5% magnetite, and 1-2% quartz [38]. The average grain size of Adelaide black granite reported in the literature is 2.5 mm, with a minimum and maximum grain size of 0.02 mm and 6.5 mm, respectively [38]. Due to the small percentage of amphibole, magnetite, and quartz, each was categorised as "other minerals" during specimen generation procedure, and a unique set of micro-properties (CCM) were assigned on its DEM contacts. These simplifications were needed to reduce the complexity of numerical simulation process and was also adopted in our previous GBM research [39]. These data were used to build the GBM models and calibrate the model's micro-properties. A systematic calibration procedure, as outlined in the flowchart presented in Fig 2, was followed in order to determine a set of appropriate micro-properties that was able to reproduce the macroscopic mechanical behaviour (e.g. UCS) and the global load-displacement of three-point bending test of a physical specimen. The calibration aimed to achieve a set of microproperties which could reproduce the similar macroscopic behaviour of the experimental specimens (e.g. Young's modulus, Poisson's ratio, etc.). The CCM and CSJM were assigned as intra- and inter-grain contact models, respectively. The following points were considered during the calibration process:

1- The CSJM was assigned to the contacts representing mineral interfaces such that the mechanical behaviour of grain boundary at the contact level is defined by contact strength (i.e. C^0_{CSJM}). When the contact reaches its yield limit, the mechanical behaviour of the contact is controlled by the softening parameter (κ_{CSJM}) until bond-break occurs. After bond-break, the contact behaviour is controlled by the friction coefficient (μ_{CSJM}).
2- The peak strength envelop of the intra-grain contact (i.e. the contact inside a mineral) are defined by C^0_{CCM} , μ_{CCM}, β_{CCM}, and κ_{CCM}. Different microproperties (e.g. C^0_{CCM}) were assigned to the four minerals, including quartz, plagioclase, orthoclase, and mica.

3- We employed the contact deformability method [29] to calibrate the Young's modulus of intra-grain contacts ($\bar{E}_{CCM}$). The normal and shear stiffness of CSJM ($k^0_{n,CSJM}$, $k^0_{s,CSJM}$) were assigned explicitly.

The details of the calibration procedure can be found in our previous GBM study [32]. Here, we briefly described the calibration steps:

1- The macroscopic Young's modulus of the specimen was mainly controlled by $\bar{E}_{CCM}$, and $k^0_{n,CSJM}$, $k^0_{s,CSJM}$. We only needed to obtain the linear elastic response of the specimen (i.e. macroscopic Young's modulus), therefore we assigned a high value for the strength microproperties (e.g. C^0_{CCM}). The unconfined compressive test was carried out in this step (Fig 2a).
2- The Poisson's ratio of the model was calibrated by altering $k^0_{n,CSJM}/k^0_{s,CSJM}$ and $k^0_{n,CCM}/k^0_{s,CCM}$ ratios. It was necessary to repeat this step in an iterative process with step 1.
3- The macroscopic Brazilian tensile strength (BTS) of the model was calibrated by carrying out the Brazilian tensile test (Fig 2b). In this step, an appropriate value for the inter-grain cohesion (C^0_{CSJM}) was identified. Notice that in the GBM approach the macroscopic tensile strength is characterised by the strength of inter-grain contacts [7, 32]. The relative inter-grain microproperties that control the macroscopic tensile behaviour of Brazilian disk was also calibrated at this stage (i.e. μ_{CSJM}, and β_{CSJM}). We altered these micro-mechanical properties until achieving a good agreement between the numerical results and experimental counterparts.
4- The uniaxial compressive strength (UCS) was calibrated by choosing appropriate intra-grain properties (i.e. C^0_{CCM}, μ_{CCM}, and β_{CCM}). The inter-grain microproperties obtained from step 3 were assigned to the inter-grain contact in this step. As microproperties influence different macroscopic properties, several iterations were undertaken between step 1 and 4 to identify a satisfying set of microproperties.

Notice that the above mentioned steps were used to calibrate the deformability parameters of the model (e.g. Young's modulus, UCS), but κ_{CCM} and κ_{CSJM} were selected by fitting the post-peak response of numerical TPB test with its laboratory counterpart. The results of TPB test on notched sample of Adelaide black granite carried out by Parisio et al. [38] were chose for this purpose. The laboratory setup and loading condition are illustrated in Fig 3. The rock beam was supported by two roller at the bottom, and the specimen was loaded by a roller located at

the mid-span of the rock beam at the top [38]. The same test setup was used in PFC2D to support and load the beam. The uniaxial compression test was carried out by applying a vertical load on the upper wall. In order to prevent ball-facet overlap, a relatively high stiffness was assigned to the walls (10 % higher than the average ball-ball stiffness). The ball-wall contacts were considered to be frictionless, which prevents the loading plates from inhibiting the rock bulging [32].

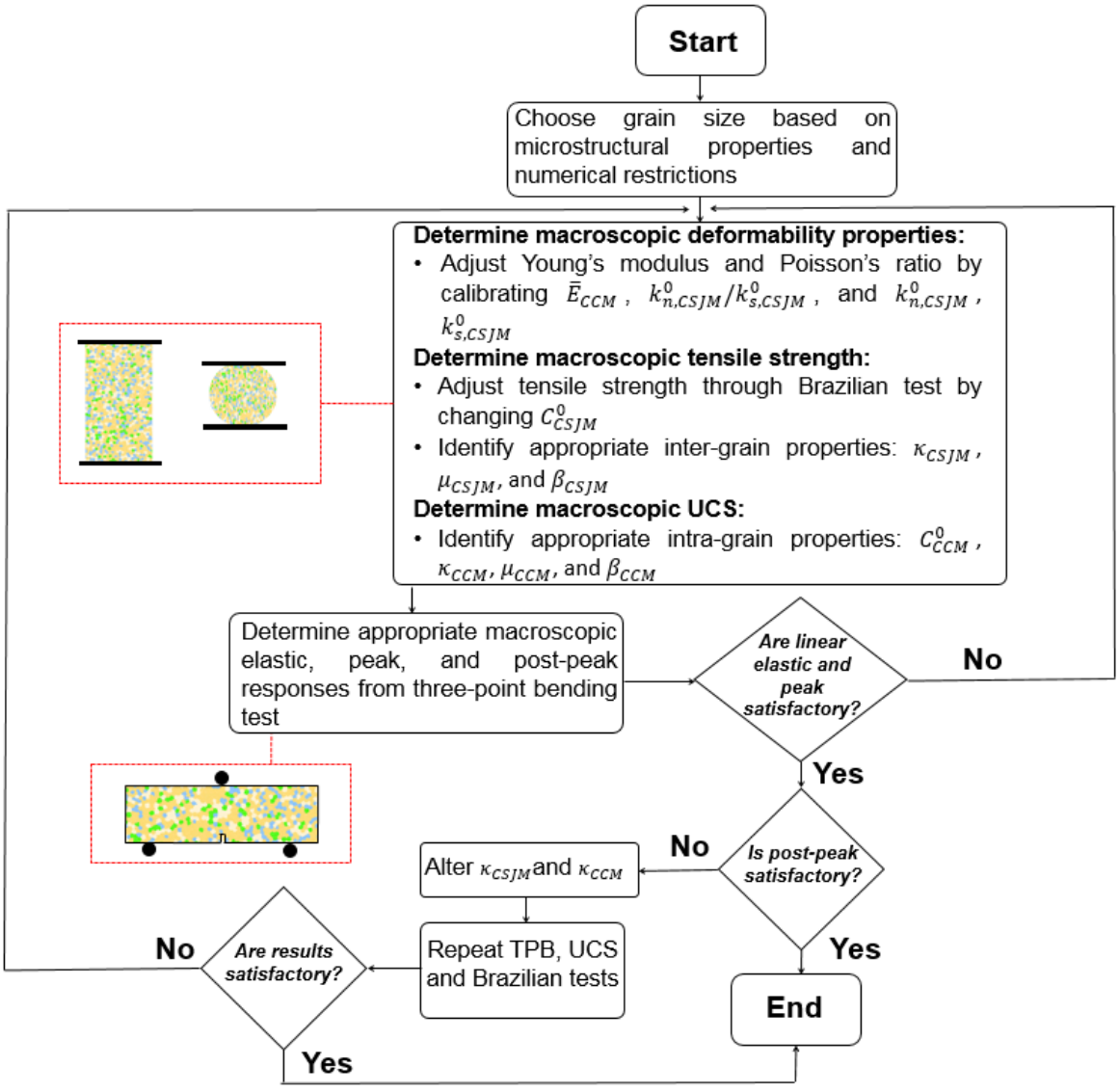

Fig 2 Flowchart illustrating the calibration procedure of the proposed cohesive GBM

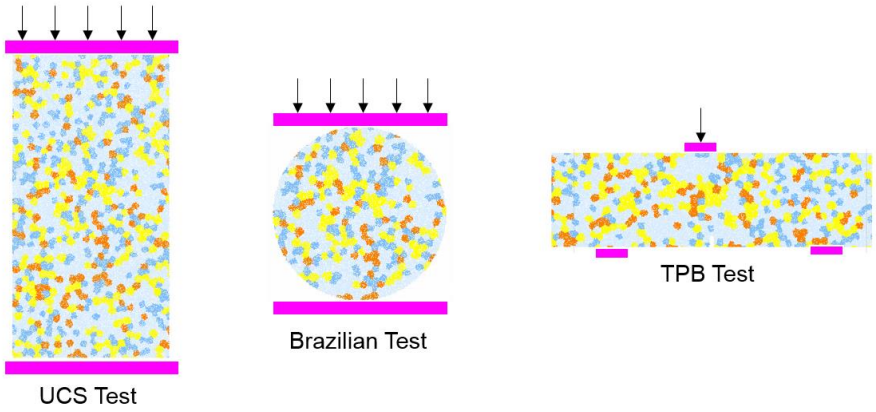

Fig 3 Numerical setups of different calibration tests

The calibrated micro-properties and a comparison between numerical and experimental macroscopic data are given in Table 1 and Table 2, respectively. You can see that the calibrated GBM model was able to reproduce the laboratory data with a good match. Another GBM simulation of TPB test was performed using the same numerical setup, boundary condition, and microstructural characteristic. The only difference was that the cohesive contact constitutive models were replaced by PBM (intra-grain contacts) and SJM (inter-grain contacts). The elastic properties and deformation characteristics of PBM and SJM contacts were kept the same as those of the CCM and CSJM, while the tensile strength and cohesive micro-parameters were calibrated to produce the best fit with the peak load of the laboratory specimen.

Table 1 Micro-mechanical parameters obtained from the calibration procedure of Adelaide black granite

Element	Parameter	Grain 1 Pyroxene	Grain 2 Plagioclase	Grain 3 Biotite	Grain 4 Others
Particles forming grains	Minimum particle radius forming grain, R_{min} (mm)	0.15	0.15	0.15	0.15
	Maximum to minimum radius ratio, R_{max}/R_{min}	1.66	1.66	1.66	1.66
Cohesive model	Young's Modulus, $\bar{E}_{CCM}$ (GPa)	120	105	105	85
	Normal to shear stiffness ratio, $(k^0_{n,CCM}/k^0_{s,CCM})$	1.0	2.0	2.0	1.5

	Cohesion, (C^0_{CCM}) (MPa)	160	145	110	145
	Friction ratio, (μ_{CCM})	0.50	0.55	0.50	0.55
	Dilation ratio, (β_{CCM})	0.25	0.25	0.20	0.25
	Softening parameter, κ_{CCM} (1/m)	15,000,000	8,000,000	5,000,000	8,000,000

Micro-mechanical parameters of the grain boundaries (the smooth joint contacts)

Smooth-joint model	Normal stiffness, ($k^0_{n,CSJM}$) (GPa/m)	250,000
	Shear stiffness, ($k^0_{n,CSJM}$) (GPa/m)	130,000
	Cohesion, (C^0_{CSJM}) (MPa)	8.7
	Friction ratio, (μ_{CSJM})	0.45
	Dilation ratio, (β_{CSJM})	0.25
	Softening parameter, κ_{CSJM} (1/m)	1,000,000

Table 2 Macroscopic properties of Adelaide black granite [38] and GBM approach

Property	Adelaide black granite granite (Experimental)	Adelaide black granite (Numerical)
Uniaxial compressive strength (MPa)	180	185
Young's modulus (GPa)	102	105
Poisson's ratio	0.24	0.28
Brazilian tensile strength (MPa)	10.9	11.5

The comparison between experiment and GBM simulation for the applied load magnitude against the crack mouth opening displacement (CMOD) curves is illustrated in Fig 4. Fig 4a

illustrates the global load-displacement curves and Fig 4b shows the macroscopic fracture patterns. The load-CMOD curve in the numerical simulation using the proposed cohesive GBM framework satisfactorily matches with the experimental counterpart (Fig 4a). During the loading procedure, the GBM specimen was exhibited to undergo three distinct stages including initial linear elastic, hardening before reaching the peak, and finally gradual softening until the specimen was completely failed. The macroscopic hardening behaviour of the load-CMOD curve was the direct consequence of the collective response of cohesive inter- and intra-grain contacts, even though the proposed cohesive contact model featured no hardening characteristics at the contact level. During the softening stage, the inter-grain contacts the surrounding the crack tip area gradually softened, resulting in a softening response in the macroscopic load-CMOD curve, which exhibited a good match with the experimental counterpart. Nevertheless, the GBM with PBM and SJM contact models could not capture a promising hardening response as the tensile strength of inter-grain contacts were totally damaged at the moment the bond strength was reached. Therefore, the specimen reached its peak load and entered to softening stage. As it can be seen, the softening response of the GBM with PBM and SJM was not perfectly matched with the experimental results, which was due to lack of microscopic strain-softening behaviour. Notice that one can alter the micro-properties of PBM and SJM to achieve a satisfactory peak load, but it is obvious that macroscopic softening behaviour will not be captured as PBM and SJM has no micro-parameter that controls the contact's post-peak behaviour. The inability of PBM in reproducing the post-peak softening behaviour in TPB test was also investigated by Nguyen et al. [34] and Nguyen et al. [35]. In Fig 4b a comparison between the fracture distribution in the numerical specimen and the distribution of acoustic emission (AE) events from the laboratory analysis is depicted. Notice that the damage contour plots of the numerical analysis of Parisio et al. [38] are also shown in Fig 4b. The proposed cohesive GBM is able to capture the FPZ very well.

We simulated two more TPB test with different softening parameter (κ_{CSJM}) to demonstrate how this micro-property influences the overall post-peak response of the specimen (Fig 4c). You can see from Fig 4c that the specimen with higher κ_{CSJM} (i.e. lower softening behaviour at contact level) exhibited less macroscopic softening during post-peak, while the specimen with lower κ_{CSJM} (i.e. higher softening behaviour at contact level) could reproduce a relatively higher peak load and hence a more pronounce macroscopic softening behaviour.

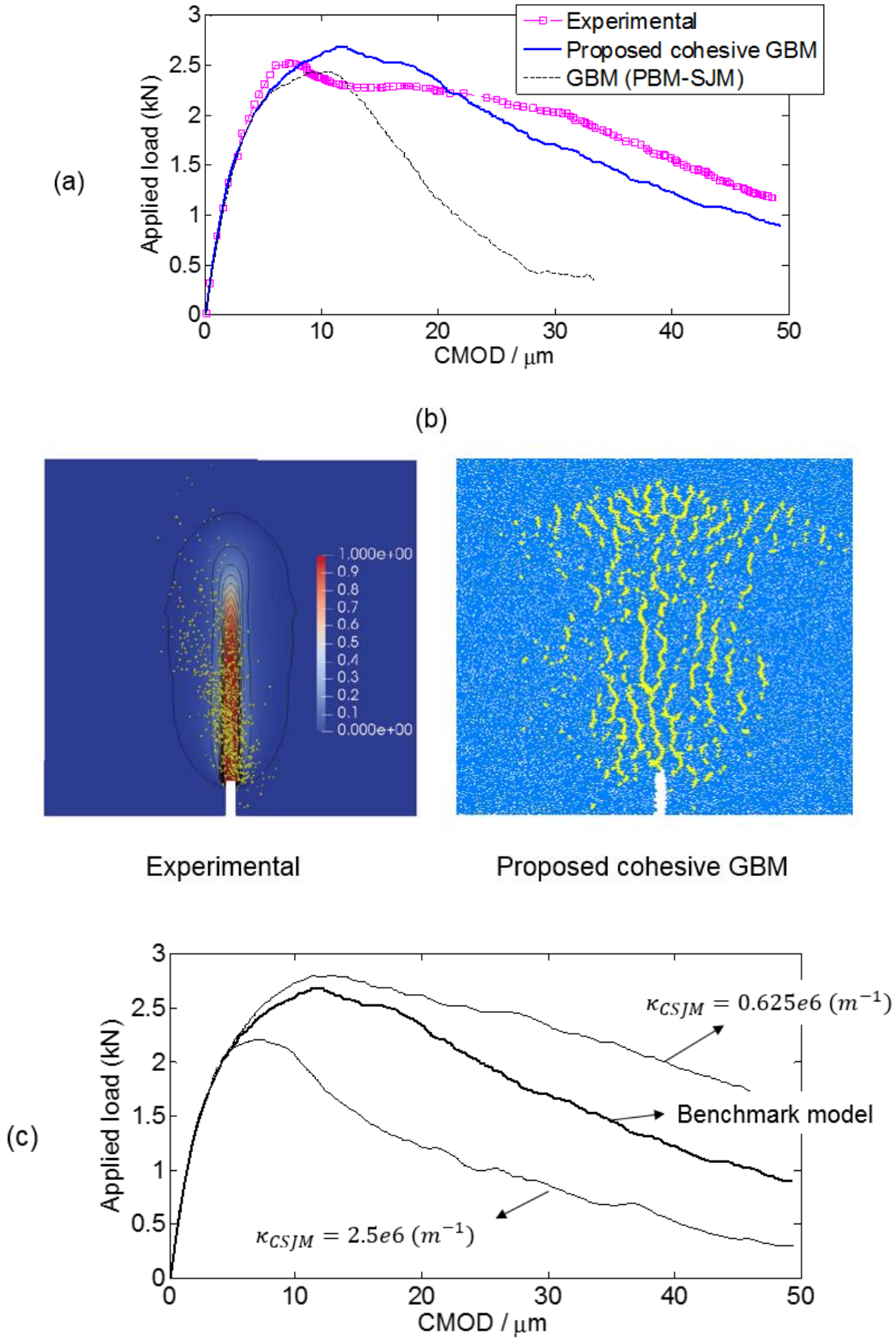

Fig 4 The results of TPB tests. (a) and (b) Comparison of experimental [38] and numerical results; the yellow lines in (b) show the distribution of micro-cracks in the GBM specimen. (c) The results of the parametric study on the softening parameter of CSJM.

3-2 Simulation of Eibenstock II granite

Eibenstock II granite consists of 44% quartz, 24% plagioclase, 21% orthoclase, and 11% mica [7]. The minimum and maximum grain size of this granite are 0.49 mm and 1.79 mm, respectively, with an average grain size of 1.14 mm [7]. The same procedure (steps 1-4) introduced in section 3-1 was used to calibrate the model. The microproperteis of Eibenstock II granite is given in Table 3. The simulation and experimental results are illustrated in Fig 5. You can see from stress-strain curves in Fig. 5a that the simulation results agree with the experimental counterparts. Fig 5b shows the distribution of macroscopic cracks in GBM specimens including inter- and intra-grain micro-cracks. The numerical results revealed that even under uniaxial loading condition, obvious grain crushing occurred, which is consistent with the laboratory observations. Figure 5b shows that with increasing confining pressure (σ_3), the induced inter- and intra-grain micro-cracks formed macroscopic fracture zones, which are similar to those of experimental specimens. Fig 5c shows a relation between indirect tensile strength versus strain of the Brazilian test. The average tensile strength of Eibenstock II granite was 7.0 MPa [40], which was very well reproduced by the proposed cohesive GBM (Fig 5c). You can also see that the macroscopic fracture response of the numerical specimen agrees with the laboratory observation (Fig 5d). Notice that in Brazilian tensile strength test, only inter-grain micro-cracks (small black lines in Fig 5d) appeared in the GBM specimen, which was due to the small microscopic tensile strength of inter-grain contacts (C^0_{CSJM}) required to match the numerical results with experimental observations. These results were consistent with the previous GBM investigations (e.g. [2, 7, 32, 39, 41]).

Table 3 Micro-mechanical parameters obtained from the calibration procedure of Eibenstock II granite

Element	Parameter	Grain 1 Quartz	Grain 2 Plagioclase	Grain 3 Orthoclase	Grain 4 Mica
Particles forming grains	Minimum particle radius forming grain, R_{min} (mm)	0.15	0.15	0.15	0.15
	Maximum to minimum radius ratio, R_{max}/R_{min}	1.66	1.66	1.66	1.66
Cohesive model	Young's Modulus, $\bar{E}_{CCM}$ (GPa)	45	35	30	25

	Normal to shear stiffness ratio, ($k^0_{n,CCM}/k^0_{s,CCM}$)	1.0	2.0	2.0	1.5
	Cohesion, (C^0_{CCM}) (MPa)	105	82	82	45
	Friction ratio, (μ_{CCM})	0.50	0.55	0.55	0.50
	Dilation ratio, (β_{CCM})	0.22	0.25	0.25	0.2
	Softening parameter, κ_{CCM} (1/m)	15,000,000	8,000,000	8,000,000	5,000,000

Micro-mechanical parameters of the grain boundaries (the smooth joint contacts)

Smooth-joint model	Normal stiffness, ($k^0_{n,CSJM}$) (GPa/m)	85,000
	Shear stiffness, ($k^0_{n,CSJM}$) (GPa/m)	12,500
	Cohesion, (C^0_{CSJM}) (MPa)	5.7
	Friction ratio, (μ_{CSJM})	0.40
	Dilation ratio, (β_{CSJM})	0.25
	Softening parameter, κ_{CSJM} (1/m)	1,200,000

(a)

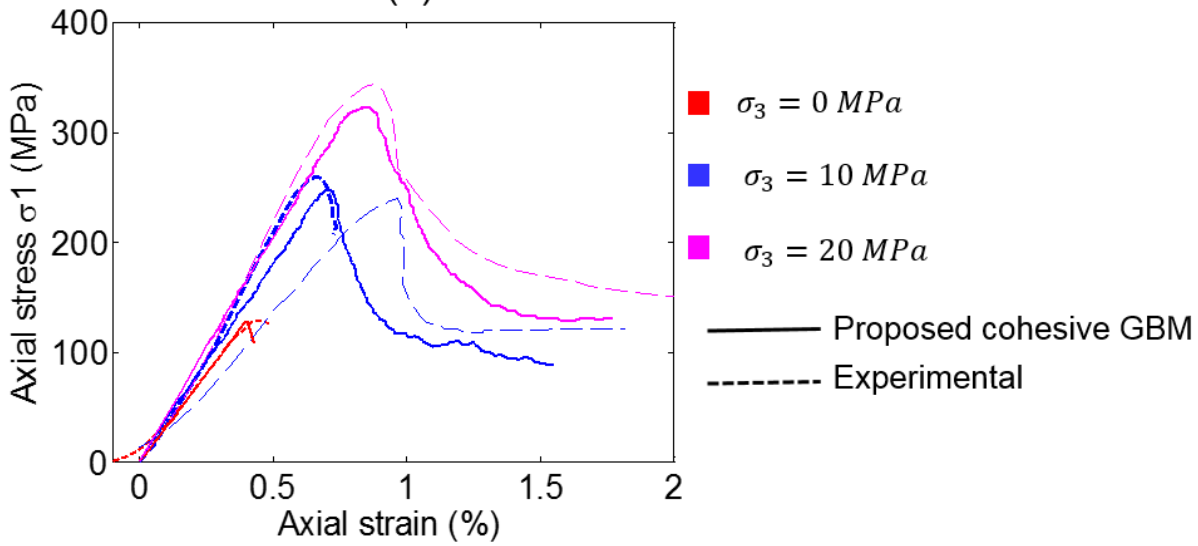
Axial stress σ1 (MPa)
400
300
200
100
0
0
0.5
1
1.5
2
Axial strain (%)
$\sigma_3 = 0\ MPa$
$\sigma_3 = 10\ MPa$
$\sigma_3 = 20\ MPa$
Proposed cohesive GBM
Experimental

(b)

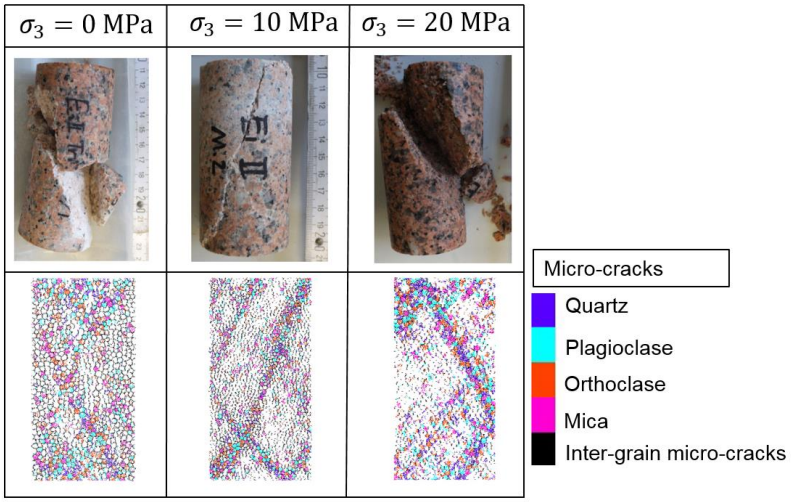
$\sigma_3 = 0$ MPa
$\sigma_3 = 10$ MPa
$\sigma_3 = 20$ MPa
Micro-cracks
Quartz
Plagioclase
Orthoclase
Mica
Inter-grain micro-cracks

(c)

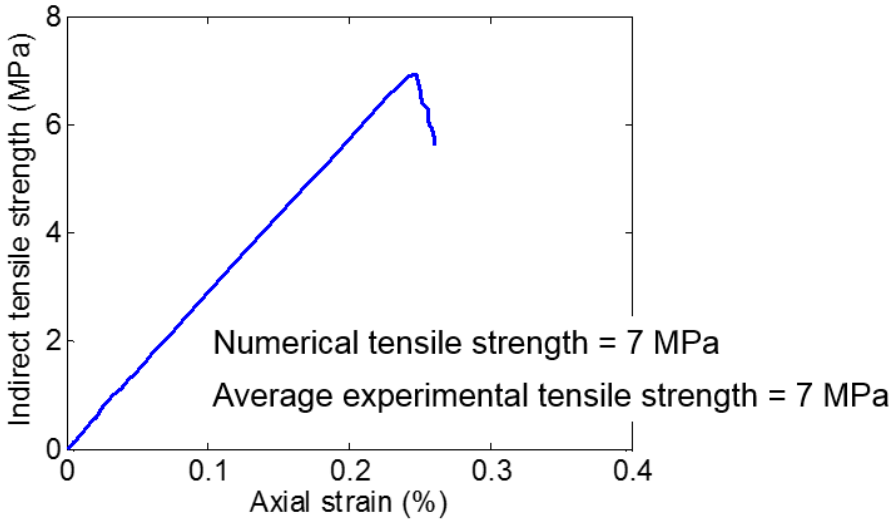
Indirect tensile strength (MPa)
8
6
4
2
0
0
0.1
0.2
0.3
0.4
Axial strain (%)
Numerical tensile strength = 7 MPa
Average experimental tensile strength = 7 MPa

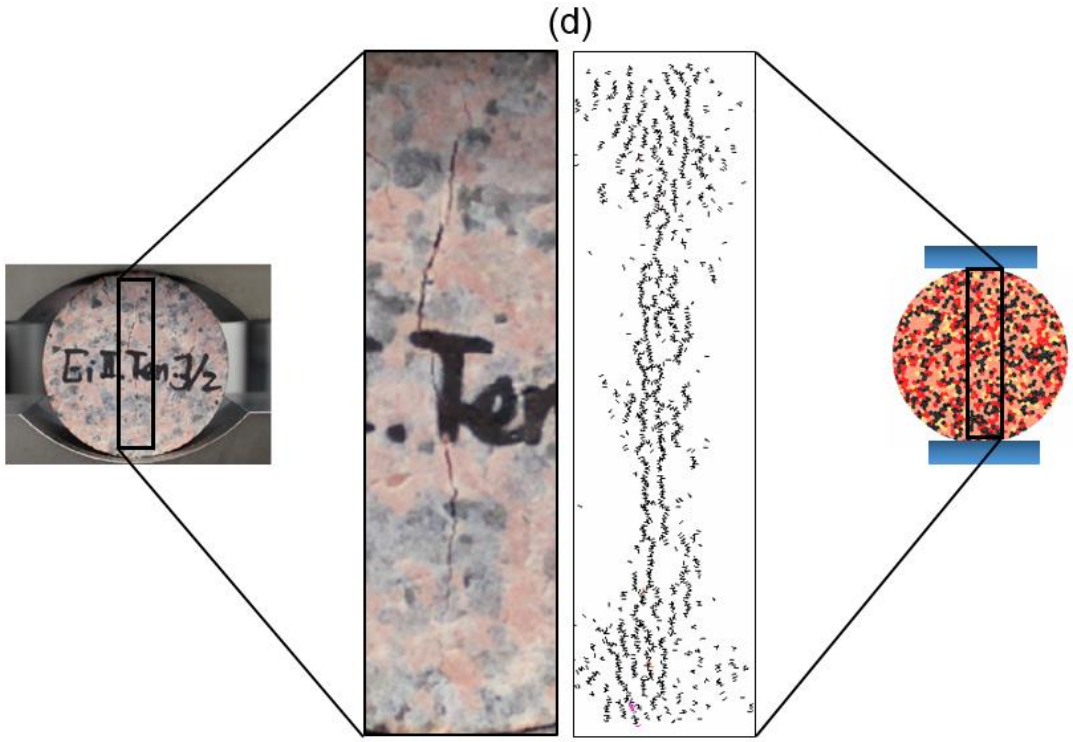

Fig 5 Simulation of Eibenstock II granite using the proposed cohesive GBM. (Experimental results from Tan [40]) (a) Stress-strain curves after compressive tests under various confining pressures (Notice that there are two experimental tests with $\sigma_3 = 10\ MPa$ and one of them is depicted by dashed thick blue lines and the other by dashed think blue line). (b) Macroscopic crack distribution in GBMs and their experimental counterparts. (c) The results of numerical Brazilian test. (d) Macroscopic tensile crack distribution in the GBM specimen and its experimental counterpart.

3-3 Simulation of Aue granite

The red Aue granite from Blauenthal/Germany (syeno–monzo-granite) [7] was simulated in this section. The mineral size and content are given in Table 1. According to Hofmann et al. [7] the grain size varies from 0.9 to 1.8 mm; hence, the grain size standard deviation within this given range was used to generate GBM specimens. The dimension of the laboratory specimen for the unconfined compressive test was 100 mm (height) × 50 mm (diameter), and the diameter of the Brazilian disk was 50 mm. The GBM specimens with the same dimensions were generated in the present research.

Table 4 Mineral content and size for Aue granite [42-44]

	Quartz	Plagioclase	Orthoclase	Mica
Mineral content (%)	30	40	20	10
Avg. mineral diameter (mm)	1.45±0.35	1.35±0.45	1.35±0.45	1.2±0.3

The experimental results from unconfined and confined compressive and Brazilian tensile tests of Aue granite were used for calibration purposes.

The microproperties of calibrated Aue granite is listed in Table 2, and the macroscopic parameters of both numerical and experimental observations are given in Table 3. Fig 6 illustrates the numerical stress-strain graph and corresponding failure state of the specimen at peak. The numerical results show that the macroscopic cracks were formed in the specimen as a result of interaction between inter- and intra-grain micro-cracks.

Table 5 Micro-mechanical parameters obtained from the calibration procedure of Aue granite

Element	Parameter	Grain 1 Quartz	Grain 2 Plagioclase	Grain 3 Orthoclase	Grain 4 Mica
Particles forming grains	Minimum particle radius forming grain, R_{min} (mm)	0.15	0.15	0.15	0.15
	Maximum to minimum radius ratio, R_{max}/R_{min}	1.66	1.66	1.66	1.66
Cohesive model	Young's Modulus, $\bar{E}_{CCM}$ (GPa)	62	52	42	32
	Normal to shear stiffness ratio, $(k^0_{n,CCM}/k^0_{s,CCM})$	1.0	2.0	2.0	1.5
	Cohesion, (C^0_{CCM}) (MPa)	118	95	95	60
	Friction ratio, (μ_{CCM})	0.58	0.6	0.6	0.55
	Dilation ratio, (β_{CCM})	0.22	0.25	0.25	0.2

	Average normal stiffness (GPa)	245,000	210,000	185,000	163,000
	Average shear stiffness, (GPa)	245,000	119,000	121,000	136,000
	Softening parameter, κ_{CCM} (1/m)	25,000,000	18,000,000	18,000,000	15,000,000

Micro-mechanical parameters of the grain boundaries (the smooth joint contacts)

Smooth-joint model	Normal stiffness, ($k^0_{n,CSJM}$) (GPa/m)	106,000
	Shear stiffness, ($k^0_{n,CSJM}$) (GPa/m)	28,500
	Cohesion, (C^0_{CSJM}) (MPa)	7.0
	Friction ratio, (μ_{CSJM})	0.45
	Dilation ratio, (β_{CSJM})	0.25
	Softening parameter, κ_{CSJM} (1/m)	1,500,000

Table 6 Macroscopic properties of Aue granite [42] and GBM approach

Property	Aue granite (Experimental)	Aue granite (Numerical)
Uniaxial compressive strength (MPa)	134±7	138
$\boldsymbol{\sigma_{1@10MPa}}$	256	248
$\boldsymbol{\sigma_{1@40MPa}}$	456	436
Young's modulus (GPa)	48±8	50
Poisson's ratio	0.19	0.22

Brazilian tensile strength (MPa)	8±1	8.3

Fig 7 illustrates the results of the Brazilian tensile test and the corresponding damage response of inter-grain contacts at different tensile stress magnitudes. In GBM approach, the macroscopic tensile strength of the model is controlled by the microscopic tensile strength of the inter-grain contacts [25]. In the previous PFC-GBM studies, SJM has been extensively employed to simulate the micro-cracking behaviour of inter-grain contacts. In the present study, CSJM was proposed and assigned to inter-grain contact, which modelled the gradual softening of grain boundaries. In CSJM, when the contact reaches its yield limit, the softening response of the contact begins. D_{CSJM} demonstrates the degree of damage in the inter-grain contacts, and can be plotted graphically to depict the localized damage response of inter-grain contacts. We monitored the damage state of grain boundaries at different stress magnitudes to observe the effectiveness of CSJM in reproducing the mechanical behaviour of Aue granite. In Fig 7b, an enlarged view of the inter-grain contacts is illustrated below each specimen to better exhibit the softening response of grain-boundary contacts. It can be seen that from point "a" to point "c" the number of soften contacts ($0.0 < D_{CSJM} < 1.0$) significantly increased, with the majority of the damage occurred in the middle portion of the Brazilian disk, point "b", and extended towards the loading plates, point "c" (Fig 7b).

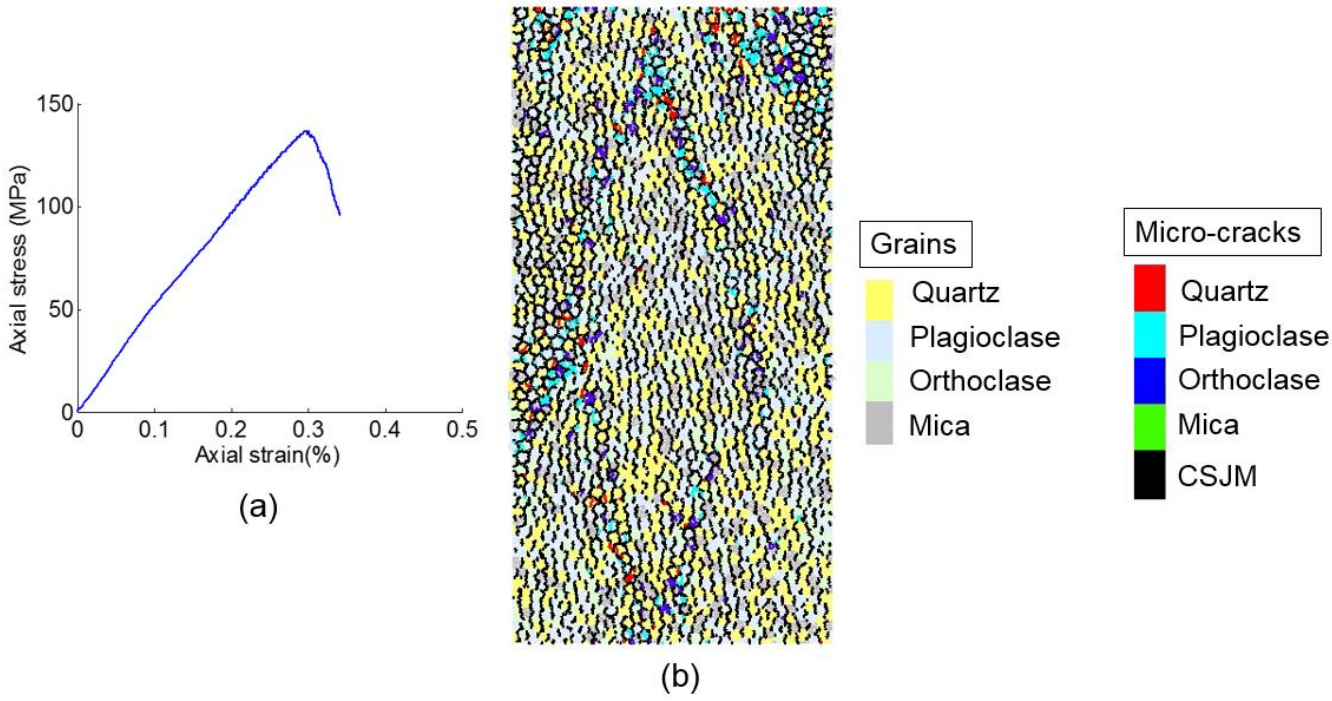

Fig 6 The numerical behaviour of Aue granite under uniaxial compression loading. (a) Axial stress-strain curve. (b) Fracture distribution at peak axial stress.

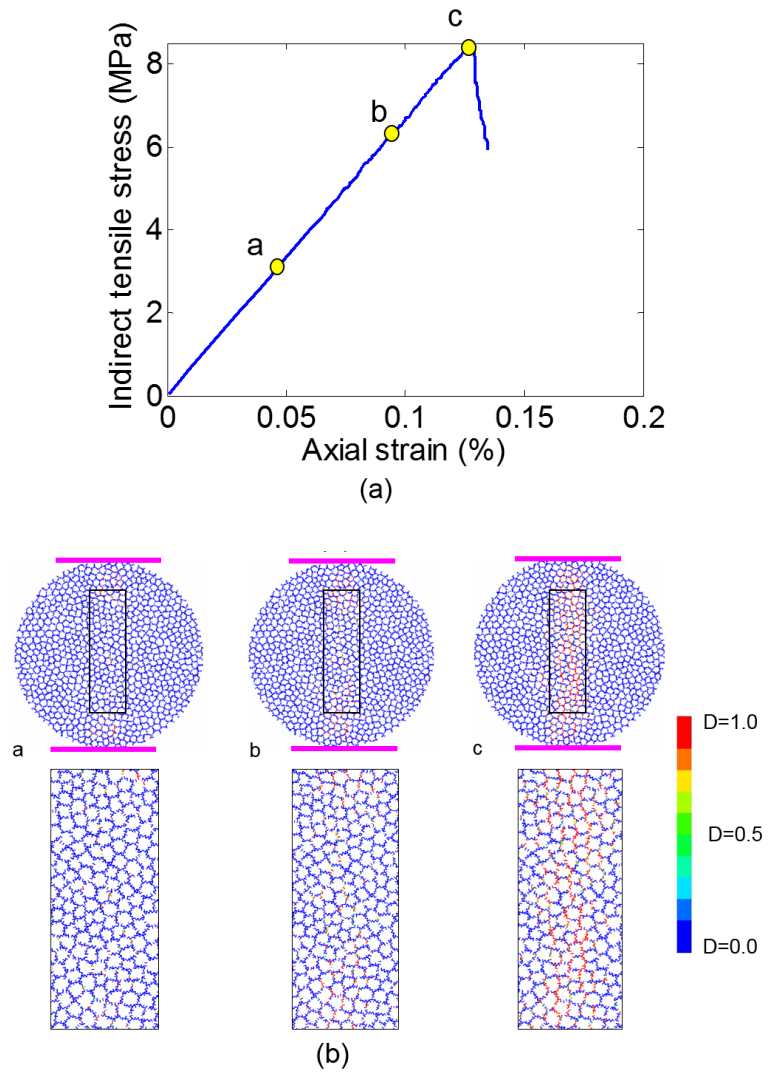

Fig 7 The Brazilian tensile test. (a) Axial stress-strain curve. (b) Microscopic damage response in the cohesive inter-grain contacts.

To further validate the abilities of the proposed cohesive model, a series of uniaxial and triaxial asymmetric tests were simulated using the cohesive GBM framework. Fig 8 illustrates the experimental (Fig 8a) and numerical (Fig 8a) setup of the asymmetric test. The length of top loading wall was shortened to 30 mm (specimen diameter was 50 mm), leaving the upper left portion of the specimen (20 mm) free of compressive loading [42]. As stated by Yoon et al. [42], I asymmetric testing aims to observe the development of shear rupture zone in the specimens, which is an important failure mechanism in deep mining structures [45]. Fig 9 illustrates a comparison between fracture behaviour of laboratory uniaxial and triaxial asymmetric tests and the micro-cracking response of the proposed cohesive GBM. The laboratory observations showed that at atmospheric pressure, the cracks initiated at the edge (3D) or point (2D) of the asymmetric steel loading platen, and developed sub-vertically towards the stationary steel platen (Fig 9 a and b, $\sigma_3 = 0\ MPa$) [42, 46]. You can see that in the

proposed GBM framework very well captured this failure pattern, with the sub-vertical macroscopic cracks were formed due to the progressive coalescence of inter- and intra-grain micro-cracks. At 10 and 40 MPa confining pressure, cracks were initiated at the edge of loading platen and propagated towards the loaded portion of the specimens (Fig 9 a and b, $\sigma_3 = 10$ and $40\ MPa$) [42, 46]. You can see from Fig 9c ($\sigma_3 = 10$ and $40\ MPa$) that the GBM specimen exhibited a close failure pattern to its laboratory counterparts. Notice that in the numerical specimen more unconnected inter-grain micro-cracks developed away from the major fracture. This is because a very small tensile strength is required to match the Brazilian tensile strength results [7, 32, 39]. The micro-cracks that may have developed away from the major fracture could not be observed in the physical specimens. However this does not mean that these micro-cracks do not exist [7]. Therefore, the GBM results seem to fit the laboratory observations reasonably well, and the macroscopic behaviour can be reproduced.

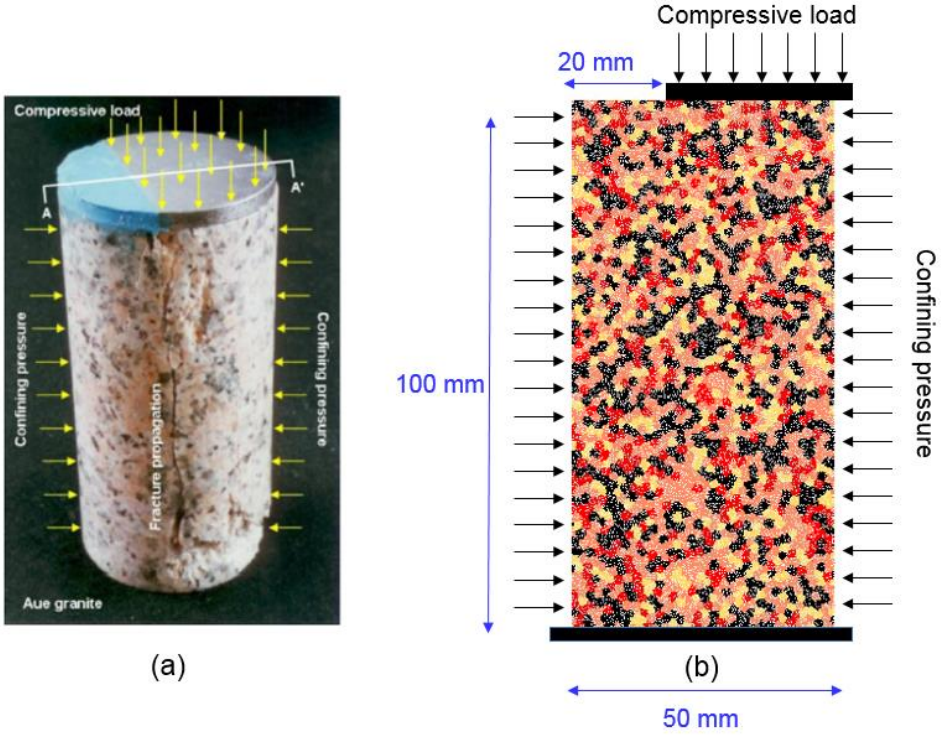

Fig 8 The specimen setup for the asymmetric test. (a) Laboratory setup [42]. (b) Numerical setup.

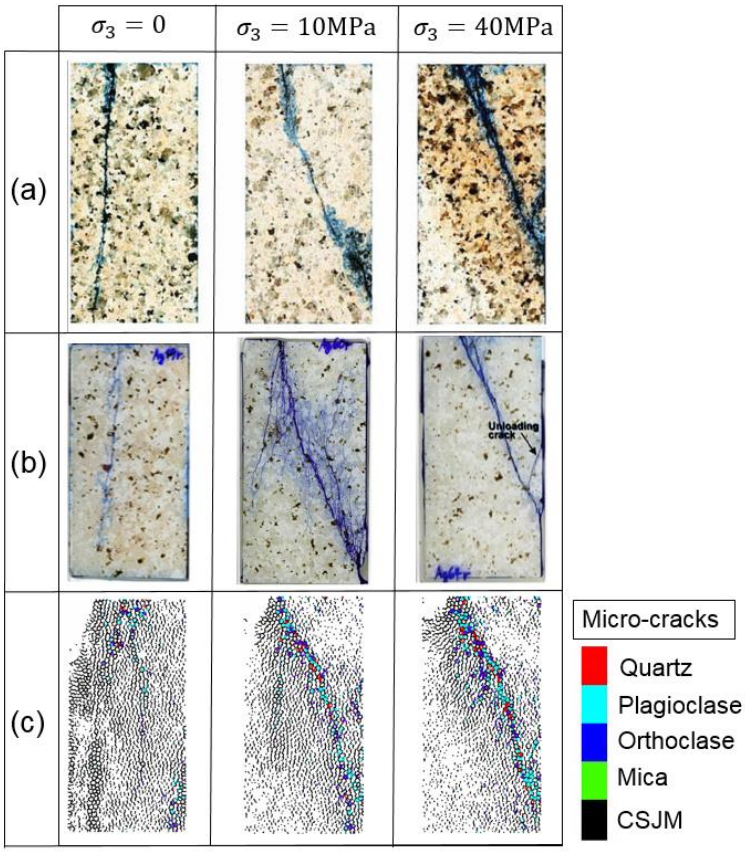

Fig 9 Comparison of the crack distribution of asymmetric uniaxial and triaxial tests at 10 and 40 MPa confining pressure with the micro-cracking response of the GBM specimens. (a) Experimental results from Stanchits and Dresen [46]. (b) Experimental results from Yoon et al. [42]. (c) The macroscopic fracture behaviour and micro-crack distribution in GBM specimens.

In Fig 10 the numerical observations of Hofmann et al. [7] and Yoon et al. [42] are illustrated. Hofmann et al. [7] used GBM modelling with PBM-SJM constitutive models and Yoon et al. [42] employed clumped particle model to simulate Aue granite. You can see from Fig 9 that, unlike GBM simulation of Hofmann et al. [7] (Fig 10a) and Yoon et al. [42] (Fig 10b), in the present GBM specimen obvious grain crushing was observed with an intense concentration along the major fracture, which was closer to the physical behaviour.

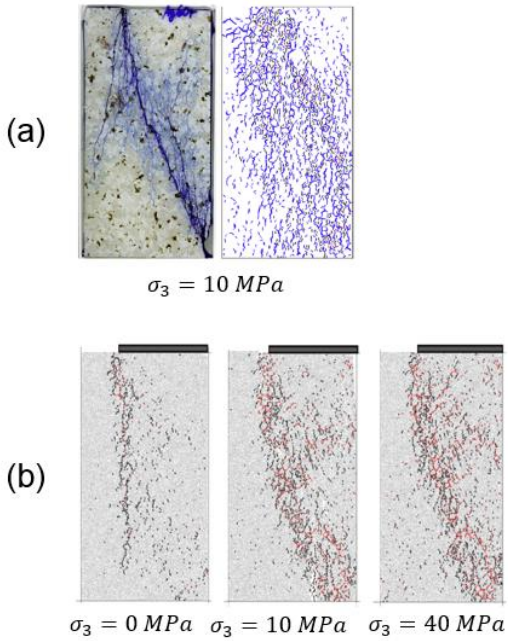

Fig 10 Numerical crack pattern observed in asymmetric tests of Aue granite by (a) Hofmann et al. [7] and (b) Yoon et al. [42].

5- Rock joint shear behaviour using cohesive GBM

5-1 Influence of JRC and CNS condition on rock joint behaviour

In order to study the impact of surface roughness of rock joints and microstructural characteristic of polycrystalline rock on the overall shear behaviour GBM specimens, we selected three different natural rock joint profiles with known JRC values of 4.6 (smooth), 10.2 (rough), and 17.5 (very rough), which were measured by Bahaaddini [47]. The surface configuration of rock joint profiles is depicted in Fig 11. Hereafter, the GBM specimens with JRC values of 4.6, 10.2, and 17.5 are called JP1, JP2, and JP3, respectively. The direct shear tests performed under both CNL and CNS conditions. The numerical setup under CNL and CNS conditions are illustrated in Fig 12. The increment of initial normal stress magnitudes (σ_n^0) under CNS condition is expressed as [19]:

$$d\sigma_n^0 = k^{cns} \times d\delta_n \tag{9}$$

where k^{cns} is constant normal stiffness at an external boundary, and $d\delta_n$ is the increment of normal displacement. The applied normal stress on rock joint surface can be determined as:

$$\sigma_n^{cns} = \sigma_n^0 + d\sigma_n^0 \tag{10}$$

k^{cns} is the major parameter that controls the shear mechanism under the CNS condition. Different researchers used various CNS stiffness values in DEM studies. For instance, Bewick et al. [48] suggested CNS stiffnesses of 10, 30, and 100 GPa/m for GBM simulations of intact

sandstone with average UCS and Young's modulus of 140 MPa, and 44 GPa, respectively. Shang et al. [22] assumed CNS stiffness values of 1, 10, and 30 GPa/m to numerically study the shear behaviour of incipient rock joints of Horton Formation Siltstone under CNS condition. The average UCS and Young's modulus of their specimen, respectively, were approximately 140 MPa, and 35 GPa. In the present study, a k^{cns} of 15GPa/m was considered for Aue granite to carry out CNS direct shear tests.

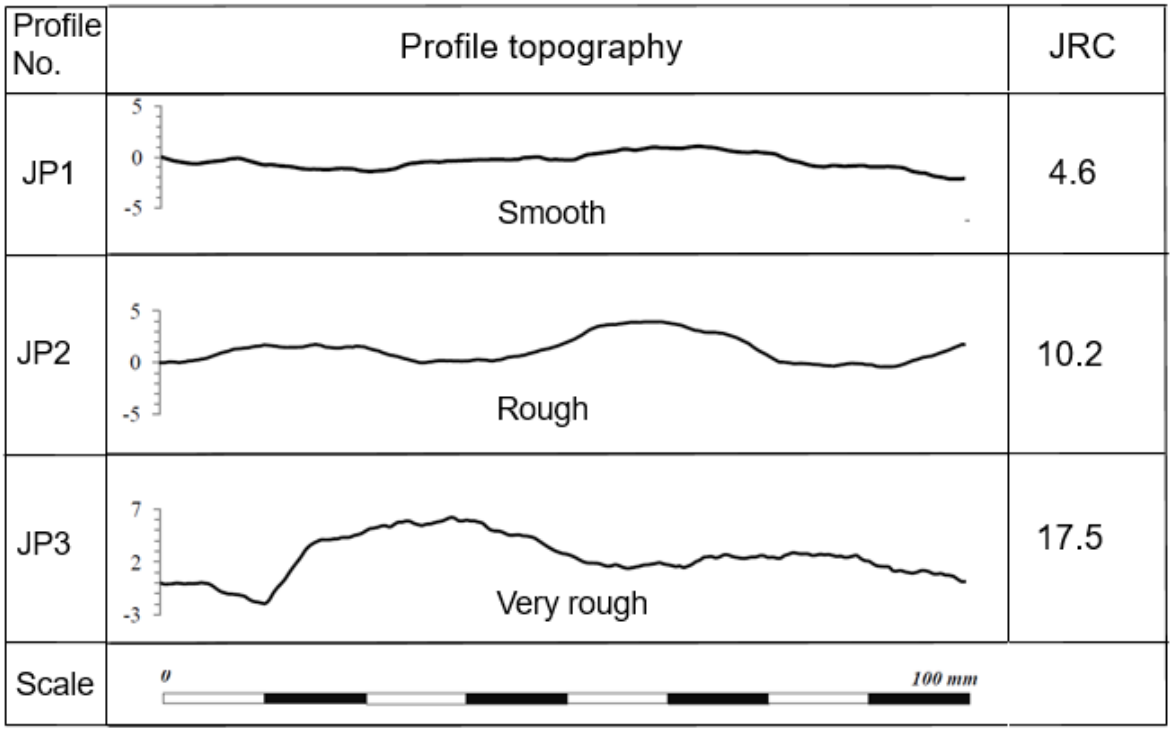

Fig 11 Natural rock joint profiles used in the GBM approach (modified from [47])

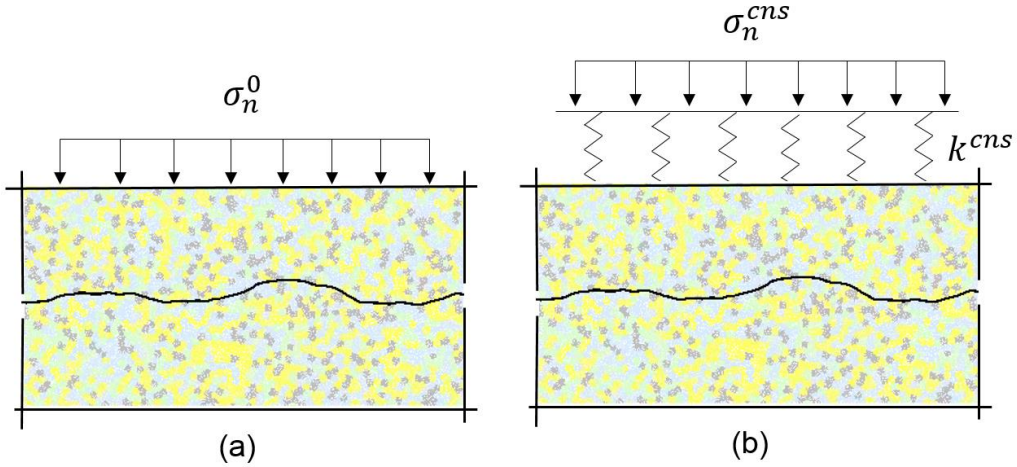

Fig 12 Direct shear test setup of GBM specimen under (a) CNL, and (b) CNS conditions.

The SJM was applied to the DEM particles forming the rock joint interface. The macroscopic data for calibrating SJM microproperties were not available. However, it often the case in numerical investigations that one set of microproperties can be assumed to represent the mechanical behaviour of rock joint [8, 49]. Gutiérrez-Ch et al. [23] suggested a value between 1 and 10 for k_n^{SJM}/k_s^{SJM} to simulate direct shear tests using SJM. The microproperties of SJM include normal stiffness (k_n^{SJM}), shear stiffness (k_s^{SJM}), and friction ratio (μ^{SJM}). In the present study, a set of microproperties representing the mechanical behaviour of rock joint was assumed for investigating the influence of surface roughness and CNS condition on rock joint shear behaviour. The value of k_n^{SJM} and k_s^{SJM} were considered to be 10,000 and 2,500 GPa/m, respectively. The friction ratio (μ^{SJM}) was assumed to be 0.75.

The results of the numerical direct shear test for JP2 under different initial normal stress magnitudes (σ_n^0) are presented in Fig 13. We have used three different terms suggested by Bahaaddini et al. [37] for describing the shear mechanism of rock joints: 'asperity sliding', 'asperity wear', and 'asperity shear-off'. 'Asperity damage' is a term used by the authors by which the degradation of asperities was described. When the degradation of asperities was high, we used descriptive terms such as 'sever asperity damage' and 'pronounced asperity damage'. We also used the term 'minor asperity damage' to describe low-intensity asperity degradation, and 'grain crushing' to refer to the development of intra-grain micro-cracks [5, 39]. Asperity sliding occurs under low normal stress where the walls of rock joint slide freely over each other [37]. This may be followed by minor asperity damage which is evident by very few intra-grain contacts and slight concentration of inter-grain contacts around the critical asperity areas (see CNL specimen with $\sigma_n^0 = 2\ MPa$, Fig 13b). Asperity wear takes place under medium normal stress magnitude [37], and causes higher asperity damage in the forms of grain crushing. This shear mechanism exhibits a higher concentration of inter-grain micro-cracks, which cancan be seen in CNL specimen with $\sigma_n^0 = 7\ MPa$, Fig 13b. Finally, when the applied normal stress magnitude is high, the rock joint tends to demonstrate the asperity shear-off mechanism [37]. This shear behaviour is usually followed by pronounced asperity damage which is the direct consequence of severe grain crushing and high concentration of inter-grain micro-cracks around the critical asperity areas. Figure 13b shows an instance of asperity shear-off in CNL specimen with $\sigma_n^0 = 7\ MPa$.

The shear stress-displacement graphs (Fig 13a) showed that the slope of the linear elastic stage of the GBMs increased with increasing σ_n^0. The results demonstrated that all GBMs, under CNS condition, exhibited a higher peak shear strength. For $\sigma_n^0 = 2\ MPa$ a distinct peak shear strength could not be recognized, which was due to a progressive increase of applied normal stress. For medium and high σ_n^0 (i.e. 7 and 14 MPa), a distinct peak shear strength could be observed under CNS, but there was still a slight increase in the shear strength during post peak.

The CNL models exhibited a higher dilative response compared to CNS models (Fig 13a). The fracture response of GBMs showed that the asperity degradation in CNS models was more pronounced than those undertaken under CNL condition (Fig 13b). These behaviours were attributed to an increase in the magnitude of normal stress in the CNS condition. The CNL models showed a transition from asperity sliding mode ($\sigma_n^0 = 2\ MPa$) to asperity wear ($\sigma_n^0 = 7\ MPa$) and asperity shear off ($\sigma_n^0 = 14\ MPa$) modes by increasing σ_n^0 (Fig 13a and b).

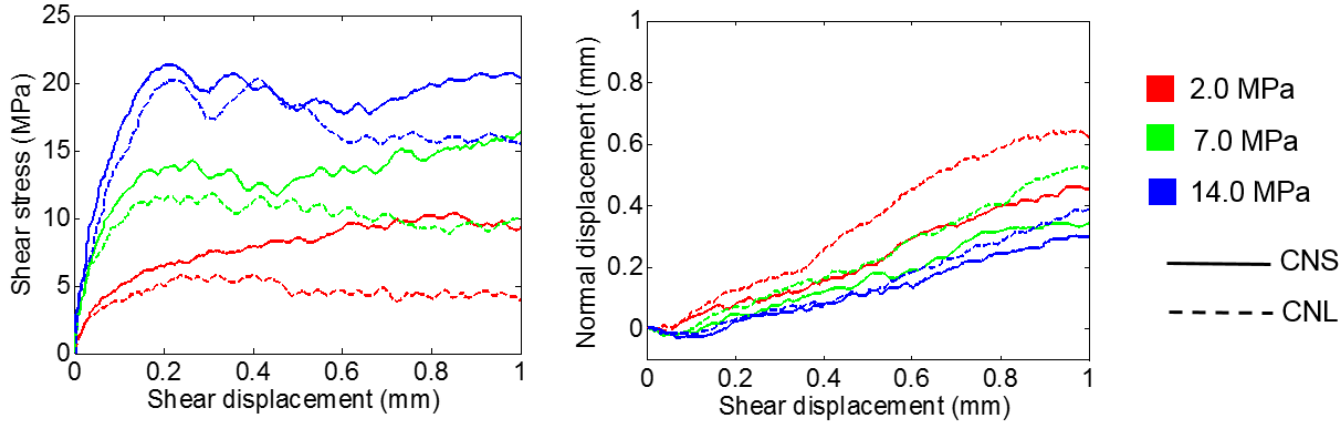

(a)

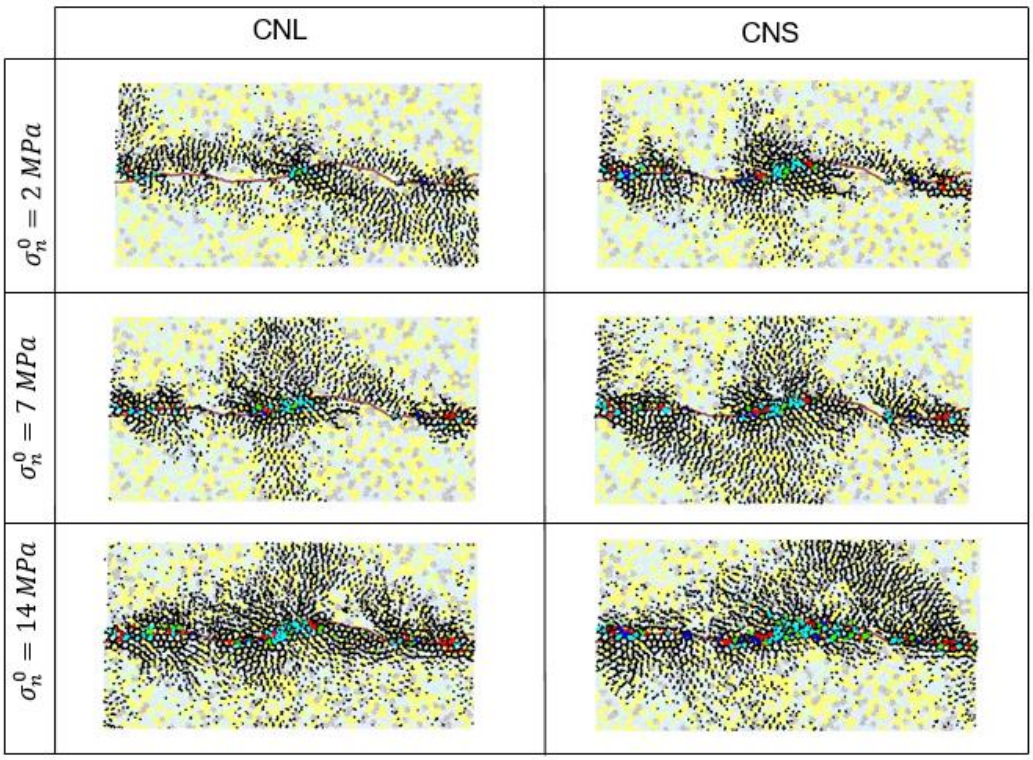

(b)

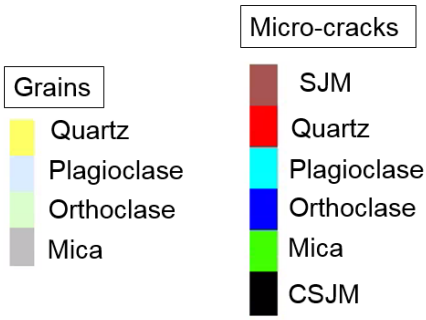

Fig 13 The result of the direct shear test on GBM specimen under CNL and CNS conditions: (a) shear stress-displacement and normal-shear displacement graphs; (b) distribution of inter- and intra-grain micro-cracks.

The macroscopic fracture behaviour of GBMs in Fig 13b shows that in all GBMs, asperity damage occurred due to bond-break in the intra-grain contact, which resulted in grain crushing in critical asperities. The experimental investigations of Morgan et al. [5] showed that mineral strength highly controls the degree of grain crushing in polycrystalline rocks. The GBM results (Fig 13b) revealed that when the shear mechanism was asperity sliding (i.e. $\sigma_n^0 = 2\ MPa$), the grain crushing was not significant. In contrast, in GBMs with higher σ_n^0 more intra-grain cracks were promoted resulting in a more pronounced localized asperity degradation. The distribution pattern of inter-grain micro-cracks (black lines in Fig 13b) showed that by increasing σ_n^0, the inter-grain micro-cracks tended to develop vertically towards the top loading wall. The numerical simulations revealed that grain crushing (i.e. localized asperity damage) was more pronounced under CNS condition. This may be attributed to asperity interlocking as a result of an increase in the applied normal stress under CNS condition, which prevented the rock joint surface from slipping along the irregularities. As a results, the critical asperities exhibited more resistance against shearing leading to more grain crushing.

In order to better analyse the asperity degradation of rock joints under CNS condition during the shear procedure, the fracture distribution pattern of GBM (JP2) with 2.0 and 14.0 MPa of σ_n^0 was monitored at four different shear stress magnitudes, and the results are illustrated in Fig 14. In the pre-peak stage (point "a", Fig 14), both GBMs demonstrated the formation of inter-grain micro-crack around the critical asperity areas. When $\sigma_n^0 = 14.0\ MPa$ a slight grain crushing is observed. With further shear displacement, the number of inter- and intra-grain micro-cracks enhanced in the GBMs (point "b", Fig 14). The peak shear strength occurred in GBM with $\sigma_n^0 = 14.0\ MPa$ at point "b", while no recognizable peak was observed for the test at $\sigma_n^0 = 2.0\ MPa$. Then, the GBM with $\sigma_n^0 = 14.0\ MPa$ experienced a softening stage during

which a high degree of bond-break occurred in inter-grain contacts (point "c", Fig 14). A pronounced localized asperity damage (i.e. grain crushing) was also observed at this point. In comparison, the GBM with $\sigma_n^0 = 2.0\ MPa$ showed minor asperity damage, and the inter-grain micro-cracks developed around the rock joint surface (point "c", Fig 14). At the end of the shearing stage (point d), severe asperity damage occurred in the GBM with $\sigma_n^0 = 14.0\ MPa$, and inter-grain micro-cracks coalesced to form larger grain boundary fractures apart from the rock joint interface. In contract at point "d", the GBM with $\sigma_n^0 = 2.0\ MPa$ exhibited a low intensity of asperity damage, and the formation of tensile fractures was less severe. Notice that the extension of tensile fractures was the result of progressive coalescence of inter-grain micro-cracks, which are demonstrated by accumulation of fractures in grain bountries (i.e. black lines) demonstrated in Fig 14. The extension of tensile fractures along grain boundaries was the results of assigning small contact strength (C_{CSJM}^0) to the inter-grain contacts in order to match the experimental Brazilian tensile strength. This is the pivotal aspect of GBM simulation [7, 32]. These numerical observations are consistent with the fracture behaviour of physical specimens. For instance, the experimental results of Meng et al. [13] on granite with irregular rock joints showed that apart from asperity damage, several tensile fractures were initiated and distributed into the rock specimen away from rock joint profile.

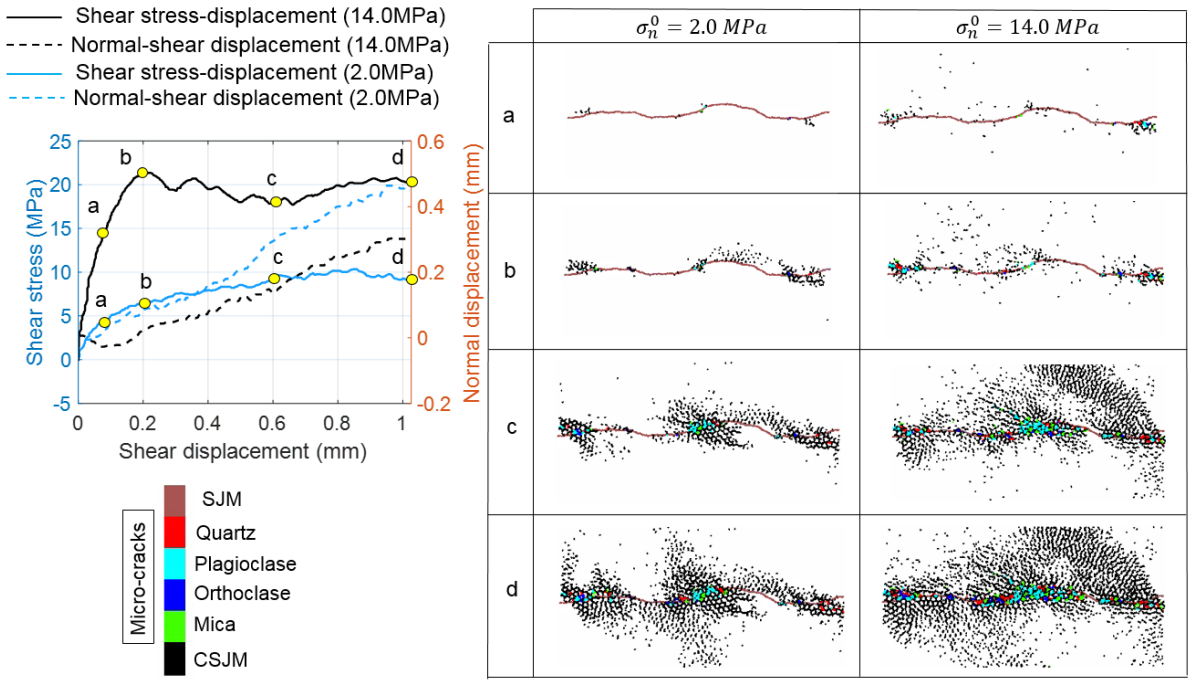

Fig 14 Asperity degradation of GBMs with different σ_n^0 under CNS condition (JP2)

In order to assess the influence of JRC on the shear mechanism and fracture behaviour of GBM specimen under CNS condition, the numerical direct shear tests were carried out using JP1, JP2, and JP3 (Fig. 4) with $\sigma_n^0 = 2.0\ MPa$. Fig 15 illustrates the shear stress-displacement and normal-shear displacement relations, and the fracture distribution in GBMs. As expected, by increasing the value of JRC, the peak shear strength and normal displacement seincrease (Fig 15a). The GBM with JP2 and JP3 showed severe asperity damage, whereas JP1 exhibited dominant asperity sliding (Fig 15a) with slight asperity damage (Fig 15b). The results showed that the shear stress in JP2 gradually increased after 0.2 mm of shear displacement, which was due to the effect of CNS condition. This behaviour was not observed in JP1 and JP3. These numerical results were consistent with the experimental observations of Indraratna et al. [19].

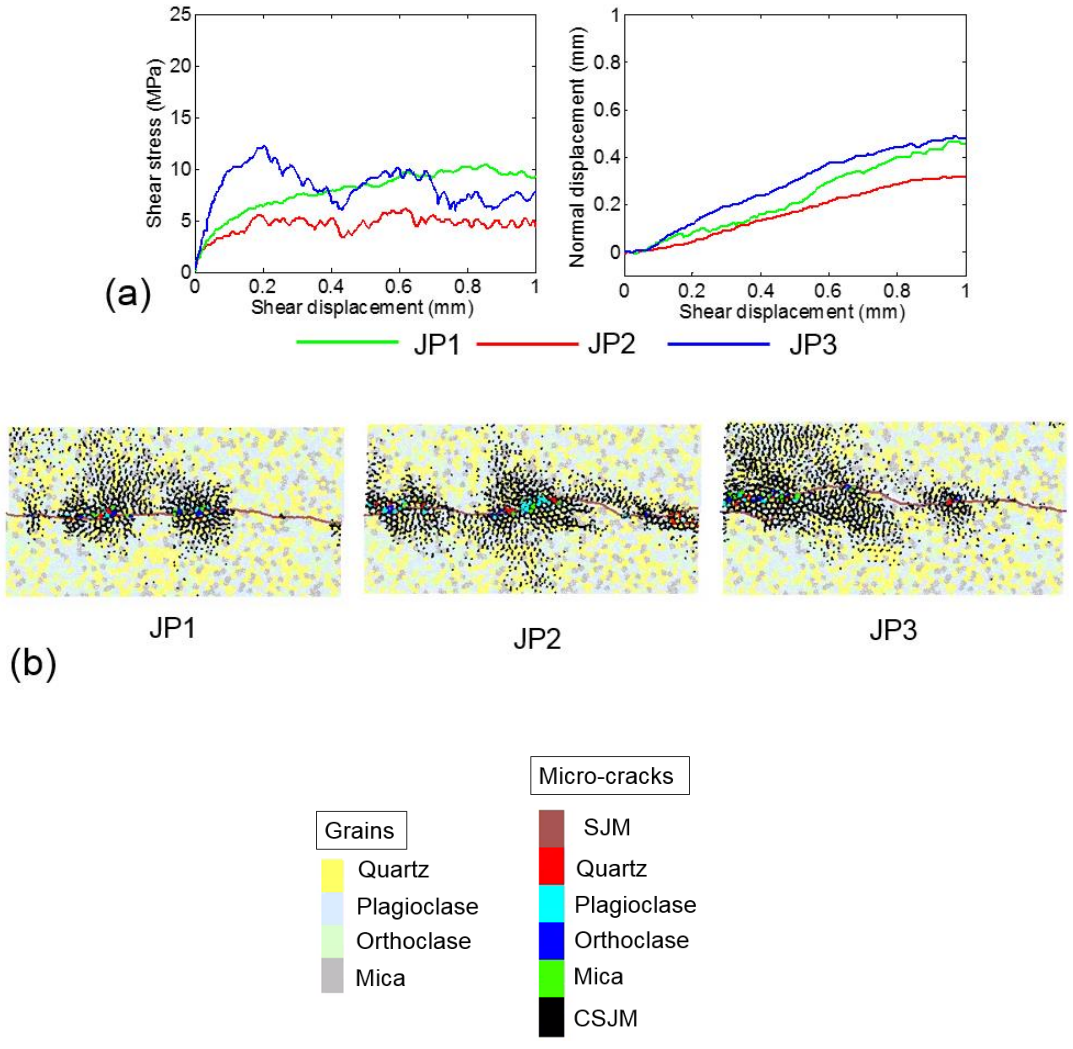

Fig 15 The numerical direct shear test results on rock joints with different surface roughness under CNS condition. (a) The shear stress-displacement and normal-shear displacement curves (b) The fracture distribution and asperity damage in GBM specimens.

5-2 Influence of grain size on the shear behaviour of rock joint

We generated three distinct grain size scenarios given in Table 7, which are similar to our previous research studying the effect of rock texture on macroscopic behaviour of pre-cracked polycrystalline rocks [32]. This enables us to investigate the influence of grain size on macroscopic behaviour of rock joint (JP2). To do so, we have conducted 18 numerical direct shear tests in PFC2D to examine the effect of rock texture on macroscopic shear behaviour of rock joints under both CNL and CNS conditions. The peak shear stress and peak dilation angle of the numerical specimens were measured, and the results of this parametric study are illustrated in Fig 16.

Table 7 Overview of various grain size scenarios for investigating the influence of grain size heterogeneity on the shear mechanism of rock joint

	Average mineral diameter (mm)			
	Quartz	Plagioclase	Orthoclase	Mica
Fine grain	1.45±0.35	1.35±0.45	1.35±0.45	1.2±0.3
Medium grain	3.2	1.6	1.6	1.6
Coarse grain	4.3	3.0	3.0	3.0

You may see that at $\sigma_n^0 = 2\ MPa$ the grain size has a negligible influence on the peak shear stress and peak dilation angle of rock joint under both CNL and CNS conditions. At σ_n^0 of 7 and 14 MPa, the effect of grain size was more pronounced .The highest peak shear stresses and the lowest peak dilation angles are observed at σ_n^0 = 14 MPa , respectively (Fig 16) . The increase in the shear stress of rock joints was attributed to the higher asperity strength because an increase in the grain size relatively rises the UCS of GBMs [7, 32, 50]. The reduction in peak dilation angle might be due to severe asperity damage. As it can be seen in Fig. 16a, the influence of CNS condition on peak shear strength was more pronounced under $\sigma_n^0 = 2\ MPa$, which was due to the predominant asperity sliding mechanism resulting from low confining stress [19]. Nonetheless, the peak dilation angle of CNS specimens showed lower values compared to their CNL counterparts regardless of σ_n^0 magnitude, which was attributed to a

progressive increase of applied normal stress under CNS condition.

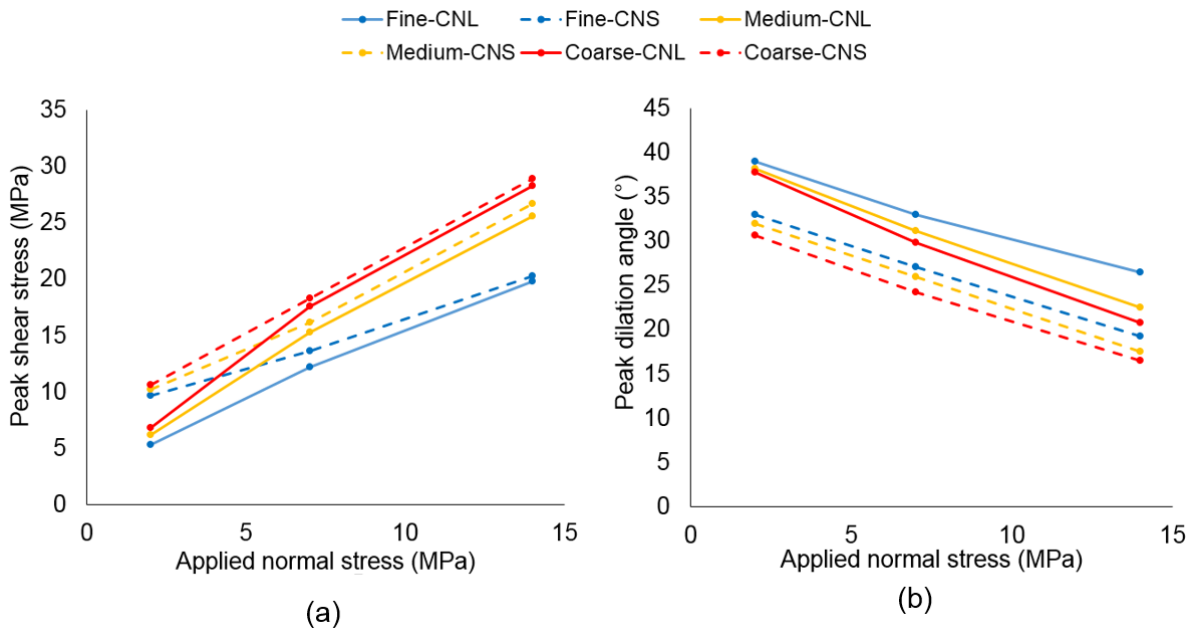

Fig 16 The effect of grain size on the (a) peak shear stress, and (b) peak dilation angle of rock joint (JP2)

6- Conclusion

A cohesive GBM framework was proposed and implemented in PFC2D to simulate the fracture behaviour of polycrystalline rocks. The gradual softening response of inter- and intra-grain contacts was simulated by incorporating an exponential damage evolution function to the force-displacement laws. The damage response of the contacts could be controlled by a softening parameter, which defined as a microproperty in the constitutive relationships. The model was calibrated with the experimental results of uniaxial compression, and Brazilian tensile tests carried out on Aue granite. The model exhibited good capability in reproducing the macroscopic behaviour of granitic specimen. Thus, the proposed GBM framework can be used as an alternative tool to an experimental approach to obtain new insight regarding the fracture behaviour of polycrystalline rocks.

The calibrated model was employed for investigating the asperity damage mechanism of rock joints with various surface roughness under both CNL and CNS conditions. Three rock joint profiles were digitized and imported into PFC2D to produce jointed polycrystalline specimens. The numerical results indicated that the response of rock joints under CNS was greatly controlled by asperity damage (i.e. grain crushing), the extent of which increased with increasing σ_n^0 and surface roughness. The normal displacement of rock joints increased with increasing JRC, and reduced with increasing σ_n^0. The asperity damage was occurred in GBMs

as a result of grain crushing which was due to bond-break in the intra-grain contacts, an effect that was more severe in rough rock joints.

Acknowledgment

The cohesive model used in this study was formulated based on a generic framework by Giang D. Nguyen (University of Adelaide) & Ha H. Bui (Monash University), with Giang D. Nguyen's help in the development and revision of the model. Critical comments by Giang D. Nguyen to improve the manuscript are acknowledged. The first author thanks Mr Sacha Emam from Itasca Consulting group for his invaluable help and comments during implementation and verification of the model in PFC software. The comments from Dr. David O. Potyondy from Itasca Consulting group regarding rock joint simulation in PFC2D are highly appreciated.

References

[1] Li XF, Li HB, Zhao J. The role of transgranular capability in grain-based modelling of crystalline rocks. Computers and Geotechnics. 2019;110:161-83.
[2] Liu G, Cai M, Huang M. Mechanical properties of brittle rock governed by micro-geometric heterogeneity. Computers and Geotechnics. 2018.
[3] Wang X, Cai M. Modeling of brittle rock failure considering inter- and intra-grain contact failures. Computers and Geotechnics. 2018;101:224-44.
[4] Gao F, Stead D, Elmo D. Numerical simulation of microstructure of brittle rock using a grain-breakable distinct element grain-based model. Computers and Geotechnics. 2016;78:203-17.
[5] Morgan SP, Johnson CA, Einstein HH. Cracking processes in Barre granite: fracture process zones and crack coalescence. International Journal of Fracture. 2013;180:177-204.
[6] Nicksiar M, Martin CD. Factors Affecting Crack Initiation in Low Porosity Crystalline Rocks. Rock Mechanics and Rock Engineering. 2014;47:1165-81.
[7] Hofmann H, Babadagli T, Yoon JS, Zang A, Zimmermann G. A grain based modeling study of mineralogical factors affecting strength, elastic behavior and micro fracture development during compression tests in granites. Engineering Fracture Mechanics. 2015;147:261-75.
[8] Bahrani N, Kaiser PK. Numerical investigation of the influence of specimen size on the unconfined strength of defected rocks. Computers and Geotechnics. 2016;77:56-67.
[9] Tuğrul A, Zarif IH. Correlation of mineralogical and textural characteristics with engineering properties of selected granitic rocks from Turkey. Engineering Geology. 1999;51:303-17.
[10] Hajiabdolmajid V, Kaiser PK, Martin CD. Modelling brittle failure of rock. International Journal of Rock Mechanics and Mining Sciences. 2002;39:731-41.
[11] Park J-W, Park C, Song J-W, Park E-S, Song J-J. Polygonal grain-based distinct element modeling for mechanical behavior of brittle rock. International Journal for Numerical and Analytical Methods in Geomechanics. 2017;41:880-98.
[12] Taheri A, Tani K. Assessment of the Stability of Rock Slopes by the Slope Stability Rating Classification System. Rock Mechanics and Rock Engineering. 2010;43:321-33.
[13] Meng F, Wong LNY, Zhou H, Wang Z. Comparative study on dynamic shear behavior and failure mechanism of two types of granite joint. Engineering Geology. 2018;245:356-69.
[14] Barton N, Choubey V. The shear strength of rock joints in theory and practice. Rock mechanics. 1977;10:1-54.

[15] Grasselli G, Egger P. Constitutive law for the shear strength of rock joints based on three-dimensional surface parameters. International Journal of Rock Mechanics and Mining Sciences. 2003;40:25-40.
[16] Kazerani T, Yang ZY, Zhao J. A Discrete Element Model for Predicting Shear Strength and Degradation of Rock Joint by Using Compressive and Tensile Test Data. Rock Mechanics and Rock Engineering. 2012;45:695-709.
[17] Wang X, Kang H, Gao F. Numerical investigation on the shear behavior of jointed coal mass. Computers and Geotechnics. 2019;106:274-85.
[18] Yang X-X, Qiao W-G. Numerical investigation of the shear behavior of granite materials containing discontinuous joints by utilizing the flat-joint model. Computers and Geotechnics. 2018;104:69-80.
[19] Indraratna B, Thirukumaran S, Brown ET, Zhu S-P. Modelling the Shear Behaviour of Rock Joints with Asperity Damage Under Constant Normal Stiffness. Rock Mechanics and Rock Engineering. 2015;48:179-95.
[20] Park J-W, Lee Y-K, Song J-J, Choi B-H. A Constitutive Model for Shear Behavior of Rock Joints Based on Three-Dimensional Quantification of Joint Roughness. Rock Mechanics and Rock Engineering. 2013;46:1513-37.
[21] Thirukumaran S, Indraratna B. A review of shear strength models for rock joints subjected to constant normal stiffness. Journal of Rock Mechanics and Geotechnical Engineering. 2016;8:405-14.
[22] Shang J, Zhao Z, Ma S. On the shear failure of incipient rock discontinuities under CNL and CNS boundary conditions: Insights from DEM modelling. Engineering Geology. 2018;234:153-66.
[23] Gutiérrez-Ch JG, Senent S, Melentijevic S, Jimenez R. Distinct element method simulations of rock-concrete interfaces under different boundary conditions. Engineering Geology. 2018;240:123-39.
[24] Shrivastava AK, Rao KS. Physical Modeling of Shear Behavior of Infilled Rock Joints Under CNL and CNS Boundary Conditions. Rock Mechanics and Rock Engineering. 2018;51:101-18.
[25] Potyondy D. A grain-based model for rock: Approaching the true microstructure. In: Proc Rock Mech in the Nordic Countries, 10p. 2010.
[26] Zhang Y, Wong LNY. A review of numerical techniques approaching microstructures of crystalline rocks. Computers & Geosciences. 2018;115:167-87.
[27] Bewick RP, Kaiser PK, Bawden WF, Bahrani N. DEM Simulation of Direct Shear: 1. Rupture Under Constant Normal Stress Boundary Conditions. Rock Mechanics and Rock Engineering. 2014;47:1647-71.
[28] Khazaei C, Hazzard J, Chalaturnyk R. Damage quantification of intact rocks using acoustic emission energies recorded during uniaxial compression test and discrete element modeling. Computers and Geotechnics. 2015;67:94-102.
[29] Potyondy D, Cundall P. A bonded-particle model for rock. Int J Rock Mech Min Sci. 2004;41:1329-64.
[30] Itasca. PFC manual, version 5.0, Minneapolis. 2016.
[31] Bahrani N, Kaiser PK, Valley B. Distinct element method simulation of an analogue for a highly interlocked, non-persistently jointed rockmass. International Journal of Rock Mechanics and Mining Sciences. 2014;71:117-30.
[32] Saadat M, Taheri A. A numerical approach to investigate the effects of rock texture on the damage and crack propagation of a pre-cracked granite. Computers and Geotechnics. 2019;111:89-111.
[33] Le LA, Nguyen GD, Bui HH, Sheikh AH, Kotousov A, Khanna A. Modelling jointed rock mass as a continuum with an embedded cohesive-frictional model. Engineering Geology. 2017;228:107-20.
[34] Nguyen NHT, Bui HH, Nguyen GD, Kodikara J. A cohesive damage-plasticity model for DEM and its application for numerical investigation of soft rock fracture properties. International Journal of Plasticity. 2017;98:175-96.

[35] Nguyen NHT, Bui HH, Nguyen GD, Kodikara J, Arooran S, Jitsangiam P. A thermodynamics-based cohesive model for discrete element modelling of fracture in cemented materials. International Journal of Solids and Structures. 2017;117:159-76.
[36] Le LA, Nguyen GD, Bui HH, Sheikh AH, Kotousov A, Khanna A. Localised failure mechanism as the basis for constitutive modelling of geomaterials. International Journal of Engineering Science. 2018;accepted & in press.
[37] Bahaaddini M, Sharrock G, Hebblewhite B. Numerical direct shear tests to model the shear behaviour of rock joints. Computers and Geotechnics. 2013;51:101-15.
[38] Parisio F, Tarokh A, Makhnenko R, Naumov D, Miao X-Y, Kolditz O, et al. Experimental characterization and numerical modelling of fracture processes in granite. International Journal of Solids and Structures. 2019;163:102-16.
[39] Saadat M, Taheri A. Modelling Micro-cracking Behaviour of Pre-cracked Granite Using Grain-Based Distinct Element Model. Rock Mechanics and Rock Engineering. 2019.
[40] Tan X. Hydro-Mechanical Coupled Behavior of Brittle Rocks - Laboratory Experiments and Numerical Simulations. Freiberg, Germany: Universität Bergakademie 2013.
[41] Hofmann H, Babadagli T, Zimmermann G. A grain based modeling study of fracture branching during compression tests in granites. International Journal of Rock Mechanics and Mining Sciences. 2015;77:152-62.
[42] Yoon JS, Zang A, Stephansson O. Simulating fracture and friction of Aue granite under confined asymmetric compressive test using clumped particle model. International Journal of Rock Mechanics and Mining Sciences. 2012;49:68-83.
[43] Zang A. Akustische Emissionen beim Sprödbruch von Gestein. Habilitationsschrift, Scientific Technical Report STR97/19. Germany: Univ Potsdam; 1997.
[44] Zang A, Wagner FC, Stanchits S, Janssen C, Dresen G. Fracture process zone in granite. Journal of Geophysical Research: Solid Earth. 2000;105:23651-61.
[45] Bewick RP, Kaiser PK, Bawden WF. Shear rupture – two case studies from a deep mine. In: Hudyma M, Potvin Y, editors. Seventh International Conference on Deep and High Stress Mining. Perth: Australian Centre for Geomechanics; 2014. p. 641-58.
[46] Stanchits S, Dresen G. Separation of Tensile and Shear Cracks Based on Acoustic Emission Analysis of Rock Fracture. In: Non-Destructive Testing in Civil Engineering (NDT-CE), International Symposium. Berlin; 2003.
[47] Bahaaddini M. Numerical study of the mechanical behaviour of rock joints and non-persistent jointed rock masses. Sydney, Australia: The University of New South Wales; 2014.
[48] Bewick RP, Kaiser PK, Bawden WF. Shear rupture under constant normal stiffness boundary conditions. Tectonophysics. 2014;634:76-90.
[49] Zhou J, Zhang L, Pan Z, Han Z. Numerical studies of interactions between hydraulic and natural fractures by Smooth Joint Model. Journal of Natural Gas Science and Engineering. 2017;46:592-602.
[50] Peng J, Wong LNY, Teh CI. Effects of grain size-to-particle size ratio on micro-cracking behavior using a bonded-particle grain-based model. International Journal of Rock Mechanics and Mining Sciences. 2017;100:207-17.